Hydrodynamique des systèmes minéralisés péri-granitiques : étude du gisement à W-Sn-(Cu) de Panasqueira (Portugal)

Gaëtan Launay

UNIVERSITÉ D'ORLÉANS

ÉCOLE DOCTORALE ENERGIE, MATERIAUX, SCIENCES DE LA TERRE ET DE L'UNIVERS

Institut des Sciences de la Terre d'Orléans

THÈSE présentée par :

Gaëtan LAUNAY

soutenue le : **19 Décembre 2018**

pour obtenir le grade de : **Docteur de l'université d'Orléans**

Discipline/ Spécialité : Sciences de le Terre/Métallogénie

Hydrodynamique des systèmes minéralisés péri-granitiques : étude du gisement à W-Sn-(Cu) de Panasqueira (Portugal)

THÈSE dirigée par :

Stanislas SIZARET	Professeur, université d'Orléans
Laurent GUILLOU-FROTTIER	Ingénieur-Chercheur, BRGM

RAPPORTEURS :

David DOLEJS	Professeur, Université de Freiburg
Christoph HEINRICH	Professeur, ETH Zürich

JURY :

Michel PICHAVANT (Président)	Directeur de Recherches, ISTO
David DOLEJS	Professeur, Université de Freiburg
Christoph HEINRICH	Professeur, ETH Zürich
Daniel KONTAK	Professeur, Université Laurentienne Sudbury
Philip WEIS	Docteur, GFZ Postdam
Stanislas SIZARET	Professeur, université d'Orléans
Laurent GUILLOU-FROTTIER	Ingénieur-Chercheur, BRGM

« Deux petites souris tombent dans un sceau plein de crème. La première souris abandonne très vite la lutte et se noie. La deuxième souris ne renonce pas, elle se débat tant et tant qu'elle finit par transformer la crème en beurre et sort du sceau. A partir de cet instant je suis la deuxième souris »

Steven Spielberg, Arrête-moi si tu peux

Remerciements

Arrivé au terme de ces trois années palpitantes et très enrichissantes tant sur le plan scientifique qu'humain, il est temps pour moi de remercier les nombreuses personnes qui ont contribués de près ou de loin au bon déroulement de cette expérience unique. Je tiens en premier lieu à remercier mes directeurs de thèse Stanislas Sizaret et Laurent Guillou-Frottier pour la confiance qu'ils m'ont accordé et pour la liberté de recherche dont j'ai pu profiter tout au long de ces trois années de doctorat. Je vous remercie de m'avoir encouragé et guidé mais aussi pour la pédagogie et la patience dont vous avez fait preuve et pour le soutien que vous m'avez apporté notamment lors de mes nombreuses périodes de doute. Je vous remercie également de m'avoir formé à l'art de la rédaction scientifique en m'apportant vos nombreux conseils lors la rédaction de mes premiers articles.

Je remercie également tous les membres du jury David Dolejs, Christoph Heinrich, Phillip Weis, Daniel Kontak et Michel Pichavant qui ont accepté d'évaluer avec un regard critique et objectif le travail présenté au sein de ce manuscrit.

Je tiens également à remercier tout particulièrement Eric Gloaguen pour, sa passion, son enthousiasme, son accompagnement sur le terrain et pour avoir partagé avec moi ses connaissances encyclopédiques des systèmes minéralisés. Les nombreuses discussions et échanges que nous avons eus tout au long de ces trois dernières années ont permis d'améliorer grandement le travail présenté dans ce manuscrit. Je souhaite également remercier Jérémie Melleton et Phillipe Lach pour leurs contributions scientifiques et leur aide lors de la caractérisation géochimique des quartz.

Je remercie chaleureusement Yannick Branquet pour ses conseils, son aide précieuse lors de la réalisation des modèles numériques et ses judicieuses remarques et corrections. Je suis très heureux que cette collaboration ait conduit à la soumission d'une publication. Par la même occasion j'en profite pour remercier toute l'équipe de métallogénie de l'université de Rennes 1 (Phillipe Boulvais et Marc Poujol) pour leur accueil très chaleureux lors de mes venues à Rennes ainsi que pour les moments de convivialité que nous avons partagé.

Je tiens également à remercier Rémi Champallier et Colin Fauguerolles avec qui j'ai eu plaisir de travailler lors de la réalisation des différentes expériences présentées dans cette étude. Sans vous la réalisation de ces expériences aurait été impossible et une partie importante de ce travail n'aurait jamais vu le jour.

Je souhaite également remercier Charles Gumiaux pour son aide sur le terrain, et pour l'organisation de la campagne de gravimétrie réalisée en partenariat avec les collègues de l'université de Porto (Ricardo Ribeiro, Alexandre Lima, Fernando Noronha).

Je remercie chaleureusement les géologues et le personnel de la mine de Panasqueira (Filipe Pinto et Paulo Ferraz) pour leur aide et pour l'accès à la mine et aux forages dont j'ai pu bénéficier au cours de ces trois années. Je souhaite également remercier les collègues Portugais de l'université de Porto pour leur accueil chaleureux et les échanges que nous avons pu avoir.

Merci à Laurent Bailly pour son aide en pétrographie et au mini MEB ainsi que pour les nombreuses discussions fructueuses que nous avons pu avoir lors des réunions d'avancement.

Merci à Sylvain Janiec et Gabriel Badin pour les nombreuses lames minces qu'ils ont produite dans le cadre de ce travail. Je souhaite également remercier Ida di Carlo, Patricia Benoist et Sylvain Janiec pour leur aide précieuse lors des nombreuses séances MEB et microsondes dont j'ai pu bénéficier. Je souhaite également remercier tous les collaborateurs académiques pour leur aide et leur conseil lors de l'acquisition des données présentées de cette étude : Marc Poujol pour les datations U-Pb sur apatite, Bleuenn Guéguen pour l'analyse des éléments en trace dans les micas, Ida Di Carlo pour les nombreuses séances MEB et microsonde, Hubert Haas pour les mesure de porosité et de densité et Phillipe Penhoud pour les analyses DRX.

Je souhaite également remercier toute l'équipe de DGR-MIN, Isabelle Duhamel-Achin, Laurent Guillou-Frottier, Eric Gloaguen, Jérémie Melleton, Laurent Bailly, Nicolas Charles, Sébastien Colin, Guillaume Vic, Matthieu Chevillard, Lucile Esnee et Antony Pochon, pour leur accueil chaleureux et pour les moments d'échange que nous avons partagé lors des pauses cafés.

Sur le plan personnel je souhaite remercier toute ma famille et plus particulièrement mes parents qui m'ont soutenu tout au long du cursus universitaire qui m'a conduit jusqu'ici. Je suis conscient de la chance que j'ai et je vous serais éternellement reconnaissant. Je souhaite également remercier mon ordinateur pour avoir tenu le coup jusqu'au bout même si Dieu sait que cela s'est parfois montré très difficile…

Enfin je souhaite remercier Marie à qui je dédie ce manuscrit pour son soutien sans faille et sans lequel je n'aurais jamais tenu le coup au cours de ces trois dernières années.

Tables des matières

Chapitre I : Introduction générale et problématique

Mise en contexte :

Ce travail de thèse s'inscrit dans le cadre du projet de recherche « New Ores » (instrument de financement européen « Eramin ») réalisé en partenariat entre l'Université de Lorraine, l'Institut des Sciences de la Terre d'Orléans (ISTO), le Bureau de Recherches Géologiques et Minières (BRGM), l'Université de Porto, l'Université de Lisbonne, le Laboratoire National de l'Energie et de la Géologie (LNEG, Portugal) et la société Beralt Tin & Wolfram (exploitant de la mine de Panasqueira, Portugal). Ce projet a pour principal objectif de développer de nouveaux modèles métallogéniques de genèse des gisements péri-granitiques à W-Sn-(Nb-Ta-Li), afin d'en améliorer les guides de prospection. Cet intérêt croissant porté aux gisements à W-Sn découle notamment de l'augmentation de la consommation mondiale en tungstène et en métaux rares au cours des 2 dernières décennies liée à l'essor de nouvelles technologies. Les gisements à W-Sn de type veines et greisen représentent une part importante des réserves mondiales en W et constituent l'objet central de ce travail de thèse. Afin d'appréhender les différents enjeux scientifiques, économiques et sociétaux liés à l'étude de ce type de gisement, ce premier chapitre propose un état des connaissances subdivisé en 3 parties.

La première partie (I) est dédiée aux propriétés et aux différents usages du tungstène dans le domaine industriel afin d'appréhender les intérêts économiques de ce métal. Un bref aperçu de la répartition des réserves mondiales est également présentés afin d'identifier les zones favorables et les cibles prioritaires d'un point de vue géologique.

La seconde partie (II) constitue une revue métallogénique des gisements à W-Sn de type veine et greisen. Les notions abordées portent principalement sur (i) le comportement géochimique du tungstène, (ii) les relations spatiales et génétiques entre minéralisations à W-Sn et intrusions granitiques, (iii) les caractéristiques du magmatisme associés aux gisements à W-Sn, (iv) la typologie et le modèle génétique de formation des gisements de type veines et greisen, et (v) l'importance de la transition magmatique-hydrothermale lors de la formation de ce type de gisement. Cette revue métallogénique est organisée en suivant l'ordre chronologique des différents processus magmatiques et hydrothermaux impliqués au cours de la formation des gisements à W-Sn. Cette partie a pour principal objectif de mettre en évidence l'importance des processus hydrothermaux (circulation de fluides) lors de la formation des gisements de type veines et greisen.

La troisième partie (III) est focalisée sur les processus de circulation hydrothermale impliqués lors de la mise en place des minéralisations péri-granitiques. La circulation de fluides hydrothermaux étant indispensable au transport, à la concentration et au piégeage des métaux, cette troisième partie a pour but (i) de présenter les principaux paramètres hydrodynamiques contrôlant la circulation hydrothermale en environnement péri-granitique (ii) d'introduire les différents rétrocontrôles existant entre la circulation de fluide, la déformation et les altérations hydrothermales, rétrocontrôles qui seront par la suite au cœur de ce travail de thèse et (iii) d'identifier les mécanismes potentiels pouvant contrôler et/ou améliorer la circulation hydrothermale en environnement péri-granitique.

Cet état des connaissances a pour objectifs d'identifier les principales lacunes scientifiques justifiant ce travail de thèse et de définir les principaux questionnements de cette étude.

I- Enjeux économiques et sociétaux

1. Propriétés et usages du tungstène

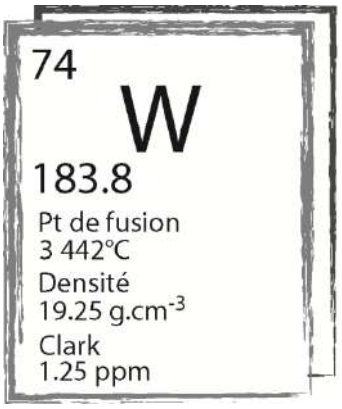

Le tungstène (W) fut découvert en 1783 par deux frères espagnols José and Fausto de Elhuyar qui isolèrent ce métal à partir de la wolframite. Ces découvreurs le nommèrent wolfram, mais le nom de tungstène fut finalement adopté par l'IUPAC en 2005. Néanmoins, le symbole W fut conservé pour rappeler l'histoire de la découverte de cet élément. Son nom officiel provient du suédois *tung* « lourd » et *sten* « pierre » signifiant littéralement pierre lourde due à la densité très élevée de ce métal. Cet élément de tous les extrêmes présente le point de fusion le plus élevé de tous les éléments chimiques et se caractérise par une grande résistance à la corrosion chimique (attaque acide et oxydation) et mécanique en raison de sa dureté élevée (7.5 sur l'échelle de Mohs). Dans la nature, le tungstène est peu abondant (1.25 ppm dans la croute terrestre) et se présente principalement sous la forme de wolframite, un tungstate mixte de fer et de manganèse ($FeMnWO_4$) ou bien sous la forme de scheelite ($CaWO_4$).

En raison de ses propriétés uniques, le tungstène est utilisé sous de nombreuses formes (Fig. 1a) et trouve de nombreuses applications industrielles notamment dans le développement de nouvelles technologies. Sous sa forme métal (17% du W produit), le tungstène entre notamment dans la fabrication des filaments pour ampoules à incandescence, des contacteurs électroniques mais aussi dans la fabrication des résistances chauffantes des fours industriels. En raison de son caractère hautement réfractaire, le tungstène métal est également un des principaux constituants employés dans l'élaboration du revêtement de la chambre à plasma du réacteur à fusion nucléaire du projet ITER (Fig. 1b). Les alliages et les superalliages de tungstène (21%) sont utilisés pour confectionner des pièces nécessitant une haute résistance à la température telles que les réacteurs d'avion. Sous forme de carbures (55%), le tungstène est utilisé pour produire différents outils devant résister à l'usure et à la corrosion tel que les outils de coupe, les forets, les trépans de forage mais encore les billes de stylos. Enfin, sous forme d'oxyde, le tungstène est un des rares composés électrochromes (changement de couleurs réversible en présence d'un champ électrique) entrant dans la fabrication de « verres intelligents »

(Fig. 1c). Ces verres présentent un très grand potentiel technologique notamment dans la construction de bâtiments éco-énergétiques en réduisant considérablement la quantité d'énergie consommée par la climatisation, l'éclairage ou le chauffage.

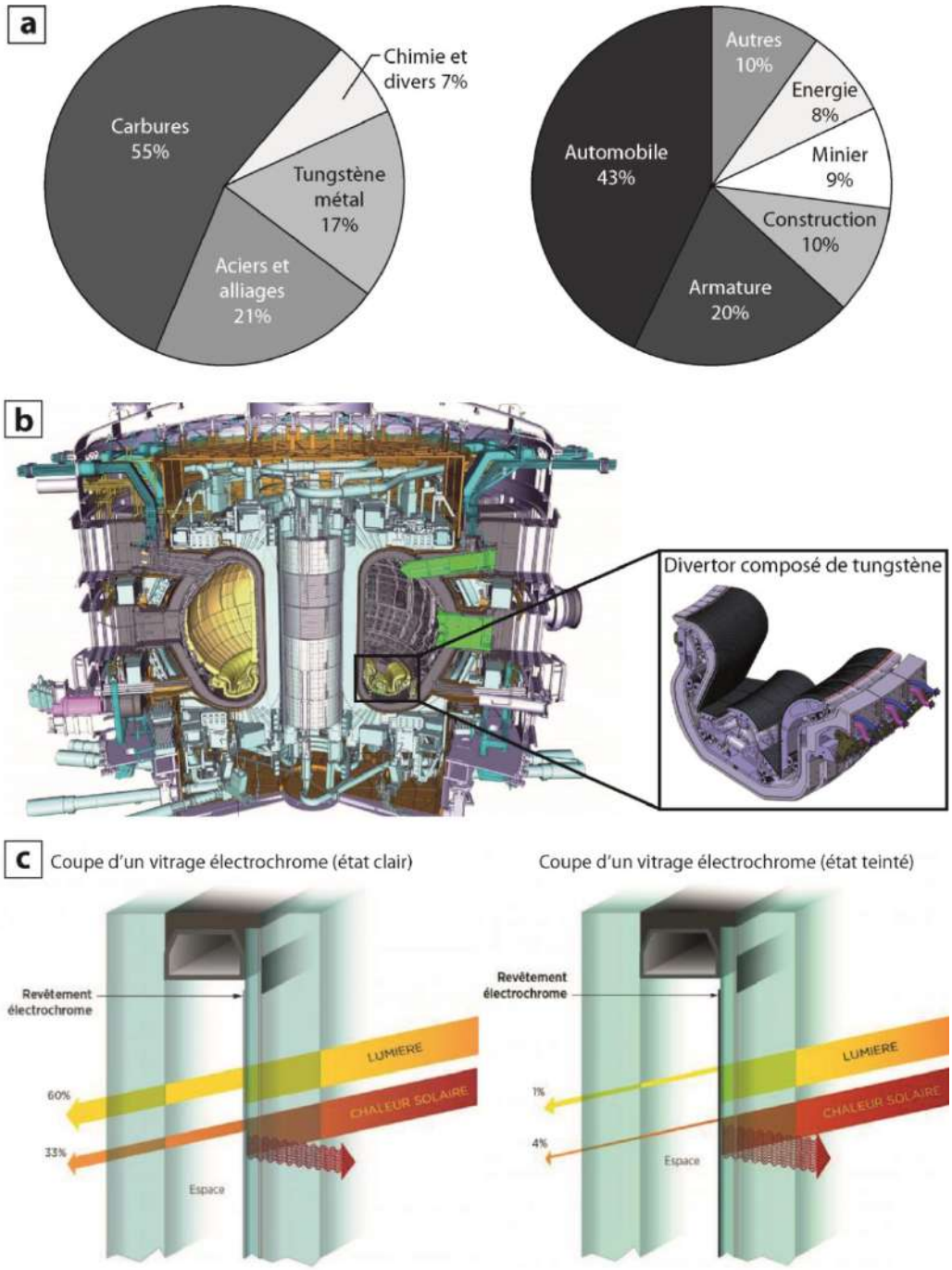

Figure 1 (a) Répartition des différentes filières industrielles utilisant le tungstène (ITIA 2015) (b) Représentation schématique du réacteur à fusion nucléaire (Tokamak) du projet ITER. Le tungstène entre dans la composition des divertors présents à la base du réacteur (www.iter.org). (c) Schéma présentant le principe de fonctionnement des vitrages intelligents électrochromes composés d'oxyde de tungstène (www.sageglass.com).

2. Répartition mondiale des réserves, de la production et de la consommation en tungstène

En raison de ses caractéristiques uniques et de ses nombreuses applications dans la recherche et le développement de nouvelles technologies, la demande mondiale en W a pratiquement doublé entre 1989 et 2016 passant de 50 kt à plus de 90 kt par an (Fig. 2). Cette augmentation de la demande et de la consommation est largement imputable au développement industriel de la Chine qui représente à elle seule 64% de la consommation mondiale. Les réserves connues en tungstène sont évaluées à 3.5 Mt (USGS report 2017-2018). Environ 52% de ces réserves sont localisées en Chine (Fig. 3a), qui assure à elle seule près de 83% de la production mondiale de tungstène (Fig. 3b). Même si la Chine consomme plus de la moitié du tungstène qu'elle produit (≈ 67%), sa forte production lui permet de dominer très largement le marché mondial du tungstène. A l'inverse la production annuelle Européenne (≈ 3.3 kt) ne permet pas de subvenir à ses propres besoins industriels (≈ 11.6 kt) (Fig. 3b). Or, la recherche et le développement (R&D) autour du tungstène constitue une activité très importante en France (verres électrochromes, airbus, projet ITER…) et plus largement en Europe. De ce fait, son approvisionnement peut être considéré comme sensible en raison de la forte domination chinoise sur le marché mondial du tungstène. En raison de cette forte dépendance, le tungstène a été reconnu comme « métal critique » par la commission Européenne (Fig. 3c) encourageant de ce fait le financement de nombreux projets de recherche visant à réévaluer le potentiel minier en Europe. Au regard de la répartition géographique des provinces métallogéniques à tungstène, il s'avère que les principaux gisements exploités aujourd'hui dans le monde correspondent à des régions actuellement ou anciennement actives d'un point de vue magmatique.

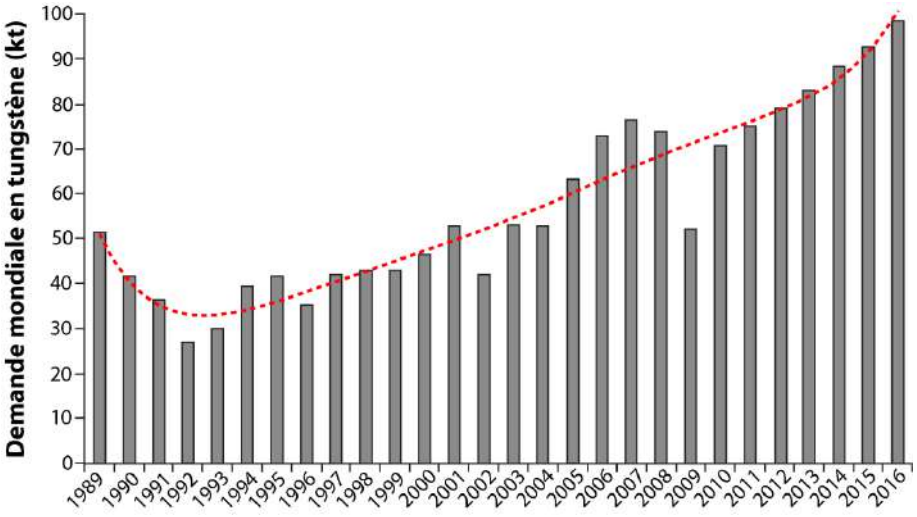

Figure 2 Evolution de la consommation mondiale de W entre 1989 et 2016 (source ITIA Roskill).

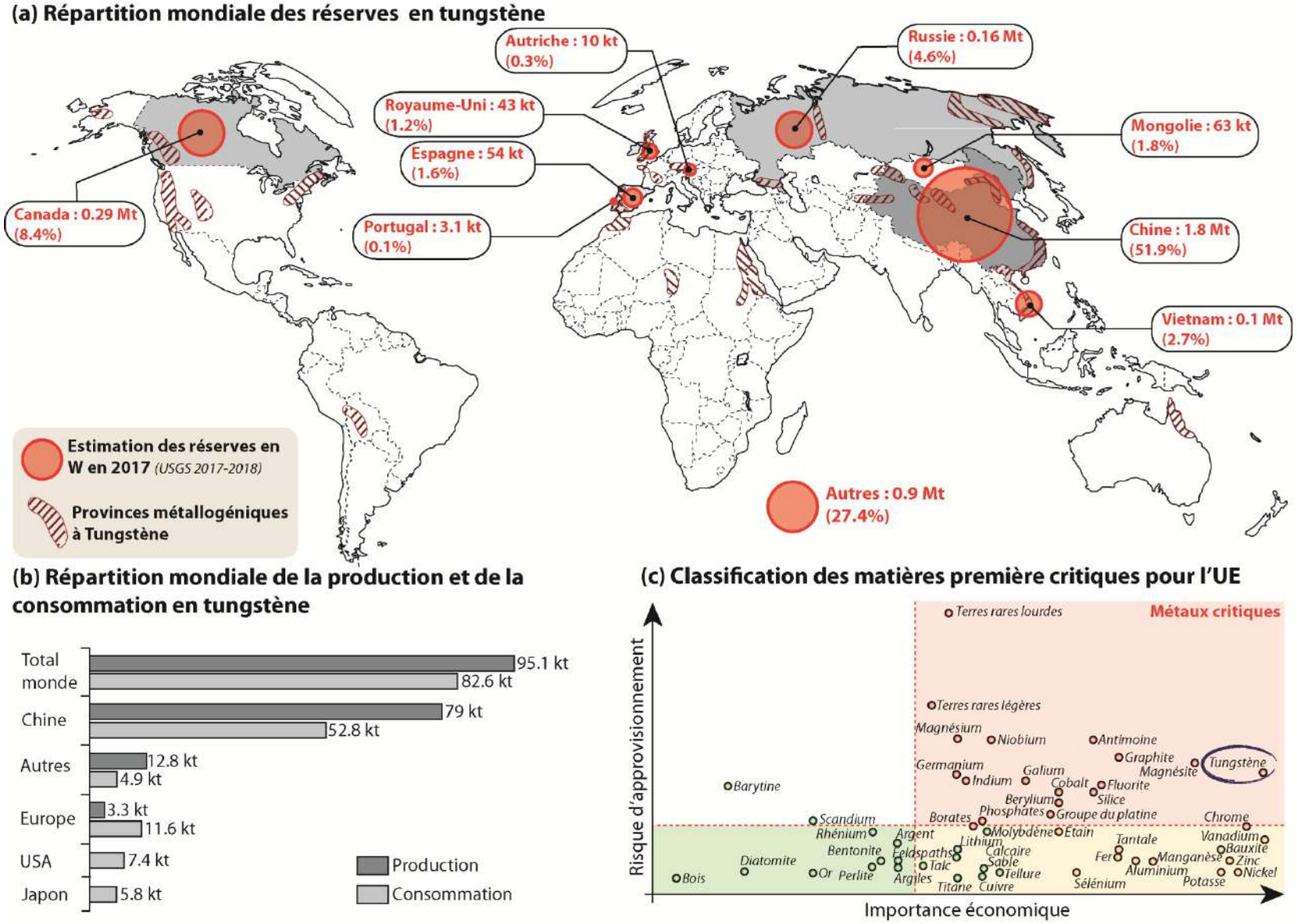

Figure 3 Répartition mondiale (a) des réserves (USGS 2017-2018) (b) de la production (USGS 2018) et de la consommation (ITIA 2015) de tungstène (c) Diagramme présentant la criticité des principales matières premières en fonction de leur importance économique et de leur risque d'approvisionnement (modifié d'après le rapport de la commission Européenne 2014). Le tungstène entre dans la catégorie des métaux dits critiques.

II- Caractéristiques métallogéniques des gisements péri-granitiques à W-Sn

1. Comportement géochimique du tungstène

Lors de la formation de la Terre par accrétion de météorites et de planétésimaux (Fig. 4a), les nombreux impacts ont entrainé un échauffement important de la planète déclenchant la différenciation terrestre. Lors de la première étape de différenciation (60 Ma après l'accrétion terrestre), les éléments sidérophiles tels que le tungstène ont préférentiellement migré vers le centre de la Terre pour former le noyau (Fig. 4b) appauvrissant considérablement le manteau en tungstène (Lee et Halliday, 1995; Newsom et *al*., 1996). A l'inverse, les éléments lithophiles ayant une forte affinité avec les phases silicatés tel que le hafnium (Hf) se sont concentrés dans le manteau primitif. La désintégration du hafnium 182 étant incomplète lors de la formation du noyau, la désintégration du stock restant de ^{182}Hf en ^{182}W causa le renouvellement du stock de tungstène dans le manteau (Fig. 4b).

Lors de la formation de la croûte continentale par fusion partielle du manteau, les éléments incompatibles (D < 1) présentant une forte affinité pour les liquides silicatés tels que le tungstène ont été extrait du manteau et ont préférentiellement migré avec les magmas jusqu'à la surface pour former la croûte continentale juvénile (Fig. 4c). L'extraction de la majeure partie du tungstène présent dans le manteau primitif explique les concentrations relativement importantes dans la croûte continentale (1100 ppb) par rapport aux autres réservoirs terrestres (Newsom, 1990; O'Neill, 1991 ; Newsom et *al*., 1996).

A travers cet exemple de processus, il apparait que le magmatisme constitue un mécanisme privilégié pour mobiliser et concentrer le tungstène et donc générer des gisements économiquement intéressant. Le caractère incompatible du tungstène rend ce métal particulièrement mobile lors des processus de fusion de partielle (mantellique ou crustale), mais également lors de la cristallisation fractionnée qui a probablement pour effet de concentrer le tungstène dans les derniers liquides issus du refroidissement de chambres magmatiques. Les régions marquées par le processus de recyclage crustal impliqué lors des différentes orogénèses représentent donc certainement des zones favorables à la formation de gisements de tungstène (Romer et Kroner, 2016). Dans la suite de ce manuscrit le mot tungstène sera remplacé par son symbole chimique W

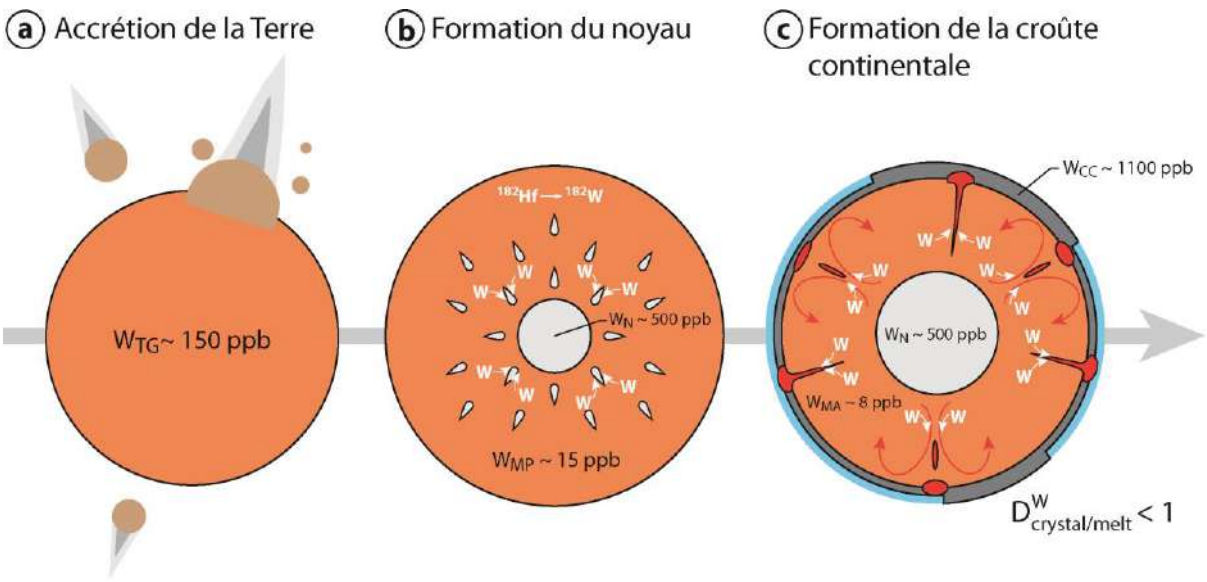

Figure 4 Comportement géochimique du tungstène lors des différentes étapes de différenciation terrestre. L'évolution de la concentration en tungstène dans les différents réservoirs est indiquée à chaque étape de différenciation (modifiée d'après www.mantleplumes.org). W_{TG} : concentration en W dans la Terre globale (valeur chondritique), W_N : concentration en tungstène dans le noyau, W_{MP} : concentration en tungstène dans le manteau primitif, W_{MA} : concentration en tungstène dans le manteau appauvrit, W_{CC} : concentration en tungstène dans la croûte continentale.

2. Relations spatiales et génétiques entre intrusions granitiques et minéralisations à W-Sn

2.1 Contexte géodynamique et géologique de formation des gisements à W-Sn

La répartition spatiale des minéralisations à W-Sn à travers le monde montre que celles-ci apparaissent principalement en contexte d'hypercollision continentale associées à des intrusions granitiques tardi-orogéniques (Fig. 5a) (Jébrak et Marcoux, 2008). Les différents massifs granitiques formés lors de l'orogénèse Hercynienne constituent de parfaits exemples illustrant le fort lien spatial existant entre intrusions granitiques et minéralisations à W-Sn (Fig. 5b). La distribution temporelle de l'abondance des différents types de gisements à W-Sn montre que la majeure partie des systèmes exploités aujourd'hui dans le monde se sont formés au cours de l'orogénèse Hercynienne et de l'orogénèse Cimmérienne (Fig. 5c) (Denisenko et Rundquist, 1986). Ces relations spatio-temporelles entre minéralisations à W-Sn et contexte orogénique mettent en évidence le rôle prépondérant du magmatisme continental post-orogénique dans la formation des gisements à W. L'intense activité magmatique liée aux phases tardi-orogéniques de l'orogénèse Hercynienne a conduit à la formation des nombreuses provinces métallogéniques à W observées en Europe telles que la province Ibérique, les Cornouailles

Anglaises, le massif Armoricain, le massif Central et le massif de Bohème (Stemprok, 1981; Derré, 1982; Romer et Kroner, 2016).

En fonction du type d'encaissant, de la profondeur de mise en place, du contexte géologique et structural local et des différents processus magmatiques et hydrothermaux impliqués au cours de leur formation, une grande variété de gisements à W-Sn ont été décrit au sein de ces provinces métallogéniques (Černý et *al*., 2005; Romer et Kroner, 2016) :

- Les skarn se développent principalement le long des contacts entre intrusifs et encaissants carbonatés. La minéralisation est concentrée au sein d'auréoles réactionnelles résultant de l'interaction entre l'intrusion granitique et les roches carbonatées (Salau, France; Los Santos, Espagne).
- Les « breccia pipe » résultant de la formation de brèches hydrauliques explosives minéralisées (Borralha, Portugal; Puy-les-Vignes, France).
- Les granites à métaux rares se caractérisent par des compositions très évoluées (fortement enrichies en Sn, W, Nb, Ta, Li) et présentent une minéralisation disséminée dans l'ensemble de la masse granitique (Beauvoir, France; Argemela, Portugal).
- Les gisements disséminés de type greisen (Cinovec-Zinwald, République Tchèque; Panasqueira, Portugal).
- Les gisements de type veines (Panasqueira, Portugal; Montbelleux, France; Hemerdon, Angleterre).

Chacun de ces corps minéralisés montrent des relations spatiales très fortes avec des intrusions granitiques généralement interprétées comme étant la principale source de tungstène (Černý et *al*., 2005; Romer et Kroner, 2016). Les greisen et les minéralisations de type veine sont couramment associés au sein d'un même système et représentent près de la moitié des réserves mondiales de W.

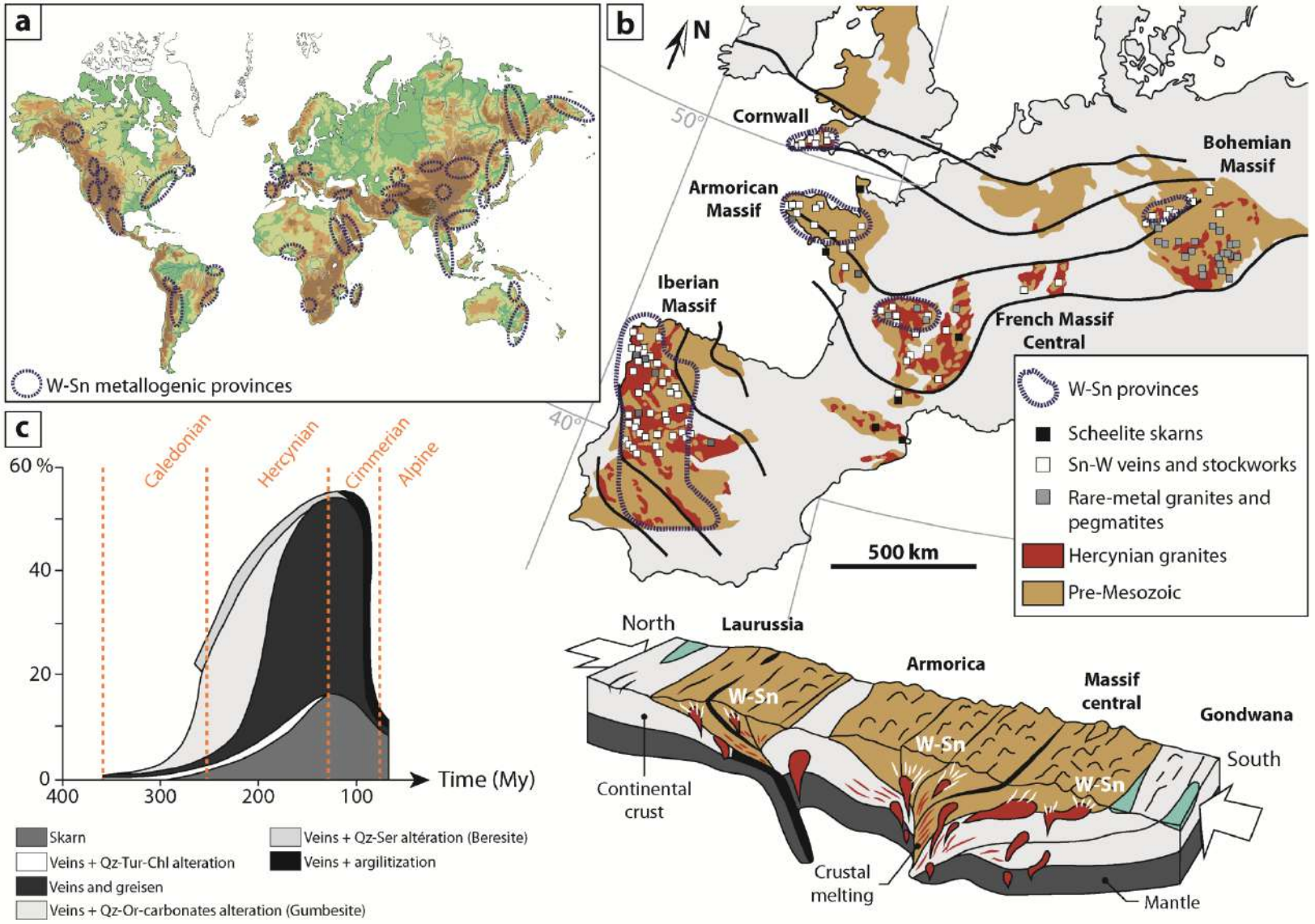

Figure 5 (a) Répartition mondiale des provinces métallogéniques à W-Sn, montrant les relations spatiales entre massifs granitiques formés en contexte de collision continentale et minéralisations à W-Sn (d'après Romer et Kroner, 2016). (b) Localisation des principales provinces métallogéniques à W-Sn au sein de la chaine Hercynienne Européenne montrant de fortes relations spatiales entre les granites Hercyniens et les différents types de gisement à W-Sn (d'après Stemprok, 1981). La coupe géologique montre le contexte géodynamique de formation des granites associés aux minéralisations à W-Sn. (c) Répartition temporelle des différents types de gisements à W-Sn au cours des temps géologiques et des différentes orogénèses (d'après Zaraisky et *al.*, 1995).

2.2 Caractéristiques du magmatisme associé aux minéralisations à W-Sn

Les minéralisations à W-Sn sont généralement associées à des granites évolués de type-S riches en minéraux hydroxylés (muscovite) (Fig. 6a). Ces granites majoritairement péralumineux sont souvent marqués par un enrichissement important en éléments lithophiles (Nb, Ta, Li, F, Rb, Cs) et par de faibles teneurs en Ti, Mg, Ca, Sr, Ba et Zr (Lehmann, 1990; Förster et *al*., 1999; Breiter et *al*., 2005). Ces granites peuvent aussi bien cristalliser en conditions réduites (ilménite series) qu'en conditions oxydantes (magnétites series), suggérant des états redox (fO_2) variables d'un gisement à l'autre (Fig. 6b) (Pollard, oral communication). Cette variabilité de la fO_2 peut être imputée à la nature de l'encaissant (carbonates, métasédiments riches en matière organique, gneiss…) avec lequel le granite s'équilibre lors de sa mise en place, ou bien au type(s) de roche(s) ayant fondu pour donner naissance aux magmas granitiques (Robb, 2005). Les magmas parents de ces granites se mettent généralement en place à faible profondeur (2 à 5 km de profondeur) et sont issus de la fusion partielle de roches alumineuses d'origine crustale (métapelites) en réponse à l'épaississement de la croûte continentale lors des orogènes (Clark et *al*., 2011; Romer et Kroner, 2016). Une cristallisation fractionnée poussée de ces magmas granitiques peut conduire à un enrichissement extrême des derniers liquides silicatés en éléments incompatibles et solubles tels que W, Sn, Nb, Ta, Li aboutissant à la formation de gisements péri-granitiques (Linnen et *al*., 1995 et 1996; Linnen et Keppler, 1997; Linnen, 1998b ; Robb, 2005). Le recyclage de roches d'origine crustale enrichies en éléments lithophiles (Ta, Li, B, Be, In, Ge and Ga) et en W-Sn telles que les métapélites et les gneiss peut être un processus majeurs de pré-concentration des métaux au sein des magmas granitiques (Romer et Kroner, 2016). Cependant, ce transfert en W, Sn et métaux rares depuis les protolithes vers les magmas granitiques dépend fortement de la composition minéralogique des roches sources. En effet, la présence de minéraux incorporant l'étain et le tungstène tels que la biotite, la magnétite ou le rutile et restant généralement au sein des restites (résidu de fusion) et peuvent être la cause de magmas granitiques pauvres en métaux (Lehmann, 1990; Müller and Halls, 2005). A l'inverse, d'importantes altérations supergènes (weathering) des roches sources sédimentaires peuvent conduire à un enrichissement important des protolithes en W, Sn et métaux rares et donc être à l'origine de magmas granitiques très enrichies en métaux (Romer et Kroner, 2016). Ces différents mécanismes de pré-concentrations des métaux au sein des roches

sources sédimentaires, ont conduit Romer et Kroner (2016) a proposé le modèle conceptuel présenté en Figure 6c.

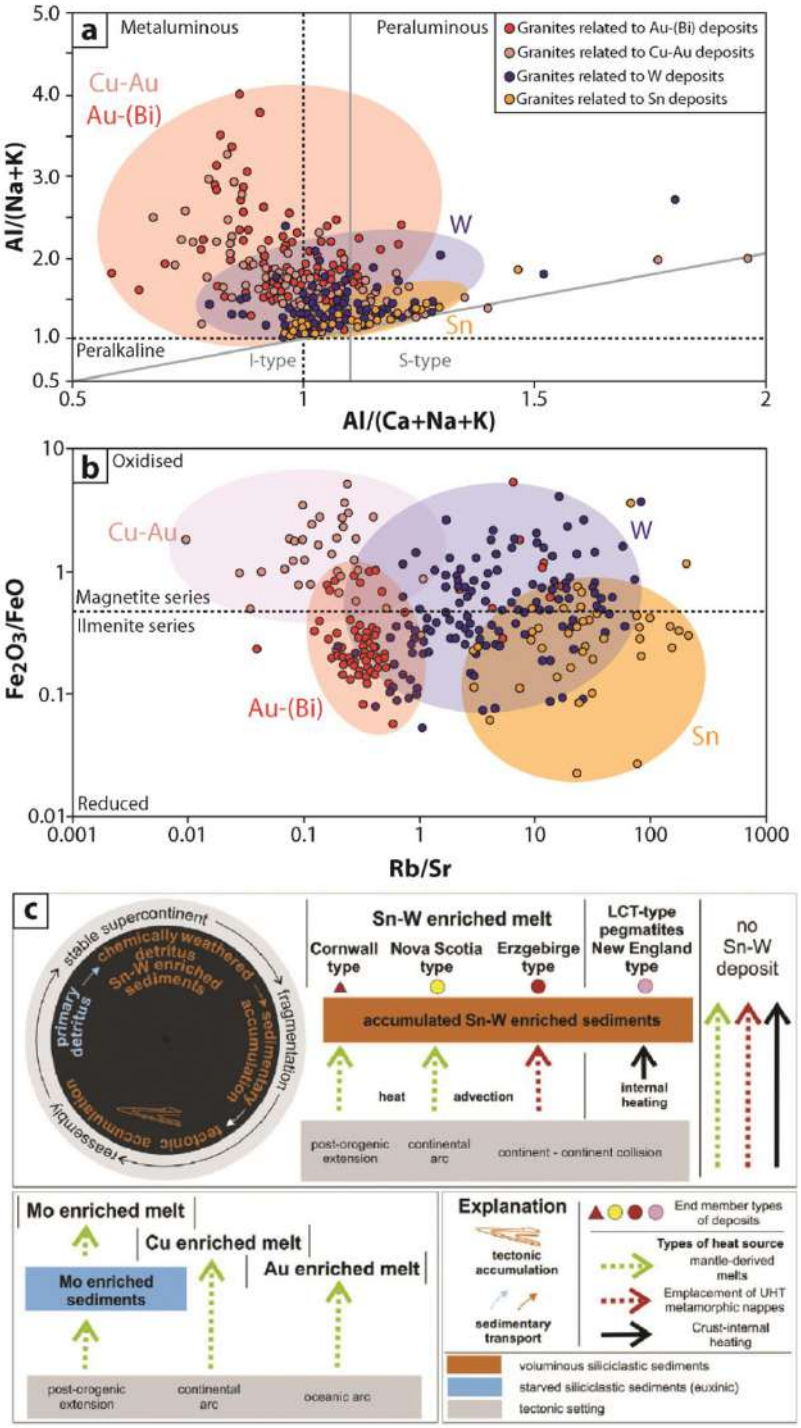

Figure 6 Caractéristiques géochimiques de granites associés à des minéralisations à tungstène. A titre de comparaison, la composition de granitoïdes associés à des gisements de Cu-Au (porphyres cuprifères), Au-(Bi) et Sn (porphyres à étain) sont également représentés (a) Classification de Chappell &White (1992) (b) Classification d'Ishihara (1977) (modifiée d'après Pollard). (c) Modèle conceptuel présentant les différents paramètres contrôlant la genèse des magmas granitiques associés aux gisements à W-Sn, Cu et Mo. Ce modèle met notamment l'accent sur le rôle du recyclage des roches sources sédimentaires enrichies en métaux (Romer et Kroner, 2016).

3. Les gisements de type veines et greisen : typologie et modèle génétique de formation

3.1 Caractéristiques morphologiques des gisements de type veines et greisen

L'exploitation des gisements de type veine et greisen représente près de 50 % de la production mondiale en W. Les gisements de type veines et greisen se développent généralement au toit et en bordure de coupoles constituant les apex (parties apicales) d'intrusions granitiques majoritairement polyphasées et plus vastes en profondeur (Fig. 7a). Ces intrusions montrent souvent un enrichissement en éléments incompatibles vers les faciès les plus différenciés et les plus récents (Jébrak et Marcoux, 2008). Des zonalités minéralogiques et chimiques marquées sont souvent observées à l'échelle de la coupole. Les zones les plus proches des coupoles sont souvent plus riches en W et Sn, tandis que les zones plus distales sont généralement plus riches en en Cu, Pb et Zn et plus pauvres en W et Sn. Dans ce type de gisements (i) l'étain et le tungstène sont rarement en quantités économiques équivalentes (W > Sn ou Sn > W) (Jébrak et Marcoux, 2008) et (ii) la minéralisation est présente sous deux formes : disséminée au sein du greisen ou sous formes de veines de quartz minéralisées (Fig. 7a).

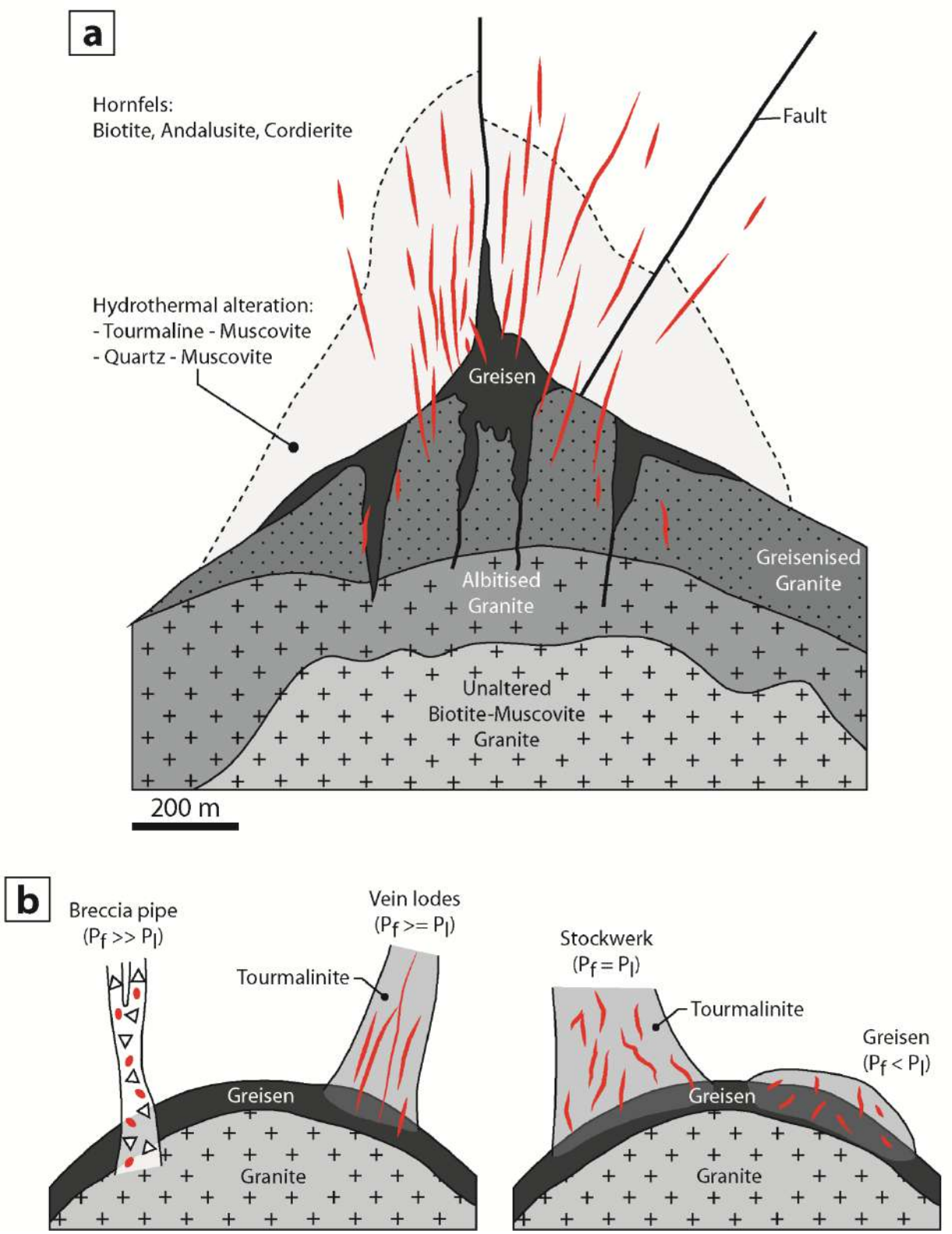

Figure 7 (a) Représentation schématique des gisements de type « veines et greisen » présentant les relations génétiques et spatiales entre l'intrusion granitique et le système filonien portant la minéralisation à W-Sn. Les différents types d'altération communément observés dans ce type de gisements (greisenisation et tourmalinisation) sont également représentés (modifiée d'après Shcherba, 1970). (b) Morphologies des minéralisations à W-Sn de type de veines et greisen en fonction du rapport entre pression fluide (P_f) et pression lithostatique (P_l) (modifiée d'après Jébrak et Marcoux, 2008).

3.1.1 Les minéralisations de type greisens

Les greisens sont des roches métasomatiques formées par l'altération hydrothermale de granites au cours d'intenses interactions fluides-roches conduisant à la transformation complète des minéraux magmatiques primaires (feldspath et biotite) du granite en un assemblage à quartz-muscovite, quartz-muscovite-topaze ou à quartz-topaze dans certains cas (Stemprok, 1987; Pollard et *al*., 1988; Pirajno, 1992; Černý et *al*., 2005). Les greisens peuvent également contenir des quantités variables de zinnwaldite, lépidolite et micas lithinifères marquant une forte occurrence de lithium au sein des fluides responsables de la greisenisation. Cette altération intervient généralement en fin de cristallisation dans les parties apicales de granites évolués (coupoles) à des conditions de pression de l'ordre de 1- 2 kbar et à des températures variant entre 400 à 450°C (Fig. 8) (Stmeprok, 1987; Zaraisky et *al*., 1995). Les greisens sont très souvent associés aux minéralisations à W-Sn de type veines mais peuvent également être présents dans certains gisements de type breccia pipe (Puy les Vignes, Harlaux, 2016). Dans le cas d'encaissants gneissiques ou granitiques, les greisens peuvent à la fois se développer dans le granite intrusif et dans l'encaissant (Echassières-Montebras). En fonction de la localisation et de l'étendu de la zone altérée, les greisens peuvent être classés en deux catégories :

- Les greisens fissuraux présents aux épontes de veines et/ou de fractures recoupant les intrusions granitiques (Cligga Head, Angleterre). Leur extension est généralement faible (jusqu'à 10 cm) et restreinte aux épontes de veines (Hall, 1971).
- Les greisens massifs se développent principalement dans les parties apicales des intrusions granitiques (coupoles) et le long des contacts entre intrusifs et encaissant. Les greisens massifs constituent des gisements à fort tonnage et faible teneur dont la puissance peut atteindre plusieurs centaines de mètres (200-300 m) (Cinovec, East Kemptville) (Halter, 1998; Zaraisky et *al*., 1995). Ceux-ci présentent des minéralisations disséminées à wolframite, cassiterite et sulfures (molybdénite, chalcopyrite, sphalérite…) (Taylor, 1979; Ŝtemprok, 1987; Pollard et *al*., 1988). Les greisens massifs sont fréquemment soulignés par des zones d'altération feldspathique de type albitisation et/ou microclinisation (Fig. 7a et 8) (Shcherba 1970, Pirajno, 1992).

Les nombreuses études réalisées sur les greisens suggèrent que la greisenisation résulte du passage de fluides acides (Fig. 8) aux salinités modérée (3 à 10 wt%), et riches

en Na, K et en éléments incompatibles (B, F, Li, Sn, W). Ces fluides sont souvent interprétés comme étant d'origine magmatique et la greisenisation comme étant un processus d'auto-métasomatose intervenant lors de la transition magmatique-hydrothermale (Stemprok, 1987; Pollard et *al*., 1988; Pirajno, 1992; Zaraisky et *al*., 1995; Halter et al., 1998 ; Černý et *al*., 2005). De ce fait les altérations hydrothermales de type greisen constituent d'excellent traceurs de la transition magmatique –hydrothermale.

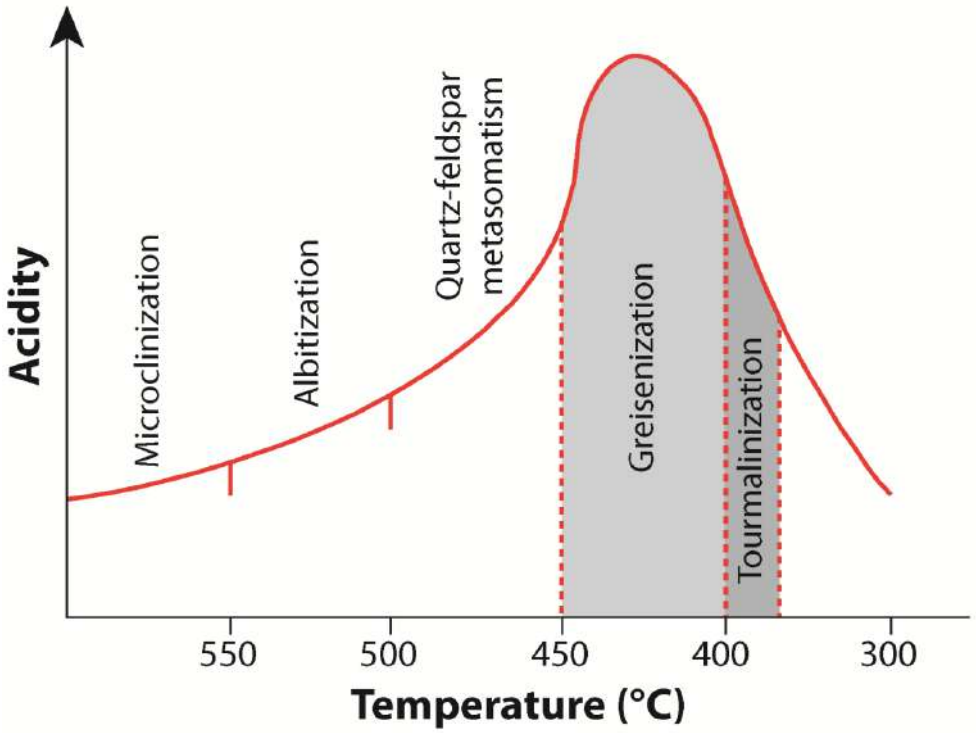

Figure 8 Evolution de la température et de l'acidité des fluides associées aux principales phases d'altération hydrothermale observées au sein des gisements à W-Sn de type veines et greisen (modifiée d'après Zaraisky et *al*., 1995).

3.1.2 Les minéralisations de type veines

Ces minéralisations se présentent sous la forme de veines de quartz de géométrie et de puissance variable (stockwerk, filons, veines simples et étroits, essaims de veines parallèles ou brèches). Les veines se forment principalement dans l'encaissant mais peuvent également se développer dans les parties apicales des intrusions granitiques (Fig. 7a). Des textures de type crack-and-seal, syntaxial ou composé sont couramment observées au sein de ces veines témoignant d'une histoire hydrothermale polyphasée et pulsatile, au cours de laquelle les veines enregistrent plusieurs phases d'ouverture et de remplissage. L'ouverture de ces veines est largement contrôlée par le contexte structural local et régional, régissant la pression lithostatique (P_l). Les phases d'ouverture peuvent

également être influencées par les instabilités mécaniques induites par la cristallisation et le refroidissement du granite sous-jacent. La morphologie des veines est également fortement contrôlée par les conditions locales de perméabilité et de pression fluides générées par le magma et son cortège de fluides (Fig. 7b) (Jébrak et Marcoux, 2008) :

- Des pressions fluides faibles ($P_f < P_l$) et un environnement peu perméable aboutissent au piégeage des fluides dans l'espace intergranulaire du granite conduisant à la formation d'un greisen massif à minéralisation disséminée au sommet des coupoles granitiques.
- Des conditions de pression fluide équilibrées avec la contrainte lithostatique ($P_f = P_l$) conduisent à une fracturation étendue et à la formation d'un stockwerk.
- Des conditions de pressions fluides lithostatiques ($P_f > = P_l$) peuvent entrainer la formation de puissants filons parallèles partant des coupoles granitiques. En fonction du contexte structural local, ces filons peuvent présentés des orientations variables (subhorizontaux, subverticaux, divergents, parallèles).
- Des conditions de pressions fluides supralithostatiques ($P_f >> P_l$) en environnement peu perméable peuvent provoquer une rupture explosive entrainant la formation de brèche hydraulique composant les breccia pipe partant des coupoles granitiques.

Dans ces veines de quartz, la minéralisation contient en proportions variables la suite métallique W, Sn, Mo, Bi sous forme de wolframite, cassiterite, molybdénite. La phase à W-Sn est souvent suivie et recoupée par une phase tardive à sulfures massifs (chalcopyrite, sphalerite, pyrite, arsénopyrite, stannite, galène) apportant un cortège important de métaux valorisants (Cu, Pb, Zn et Ag) (Cornouailles Anglaises, Panasqueira…). Ces différentes phases de minéralisation sont généralement également présentes au sein des greisens massifs associées aux veines, suggérant donc que la formation des greisens et des veines résultent de la circulation des mêmes fluides (Korges et *al*., 2017).

La formation des veines s'accompagne également d'altérations hydrothermales précoces borées aboutissant à la formation de tourmalinite (contenu en tourmaline >15 %) le long des épontes des veines (Pirajno, 2009) (Fig. 7a et 7b). Ces tourmalinites se développent généralement à partir des épontes et peuvent se propager sur des distances très importantes. D'un point de vue chronologique et thermique, la tourmalinisation intervient de manière plus ou moins concomitante à la greisenisation (Fig. 8) et peut être suivie par une phase d'altération à muscovite-quartz.

3.2 La transition magmatique-hydrothermale : un processus clé dans la formation des gisements de type veines et greisen

La transition magmatique hydrothermale constitue un évènement majeur marqué par la cristallisation complète des intrusions granitiques et au cours duquel un système magmatique-hydrothermal évolue d'un stade dominé par des processus magmatiques (cristallisation fractionnée et concentration des éléments incompatibles) vers un stade dominé par la circulation de fluides hydrothermaux (Fig.9) (Burnham et Ohmoto, 1980; Halter et Webster, 2004). Cette transition est une étape décisive marquée par la convergence de différents paramètres physico-chimiques et de mécanismes favorables à la concentration des métaux et à la formation de gisements. C'est notamment au cours de la transition magmatique-hydrothermale qu'interviennent (i) la concentration des éléments incompatibles et des métaux (W, Sn) dans les liquides magmatiques résiduelles (ii) l'expulsion potentielle de fluides magmatiques-hydrothermaux enrichis en éléments incompatibles et en métaux (W, Sn, Li…), (iii) le transport du W par les fluides hydrothermaux jusqu'au système filonien, et (iv) de forts contrastes thermomécaniques induisant des instabilités mécaniques causant l'ouverture des structures drainantes qui vont ensuite piéger les fluides portant les minéralisations à W-Sn.

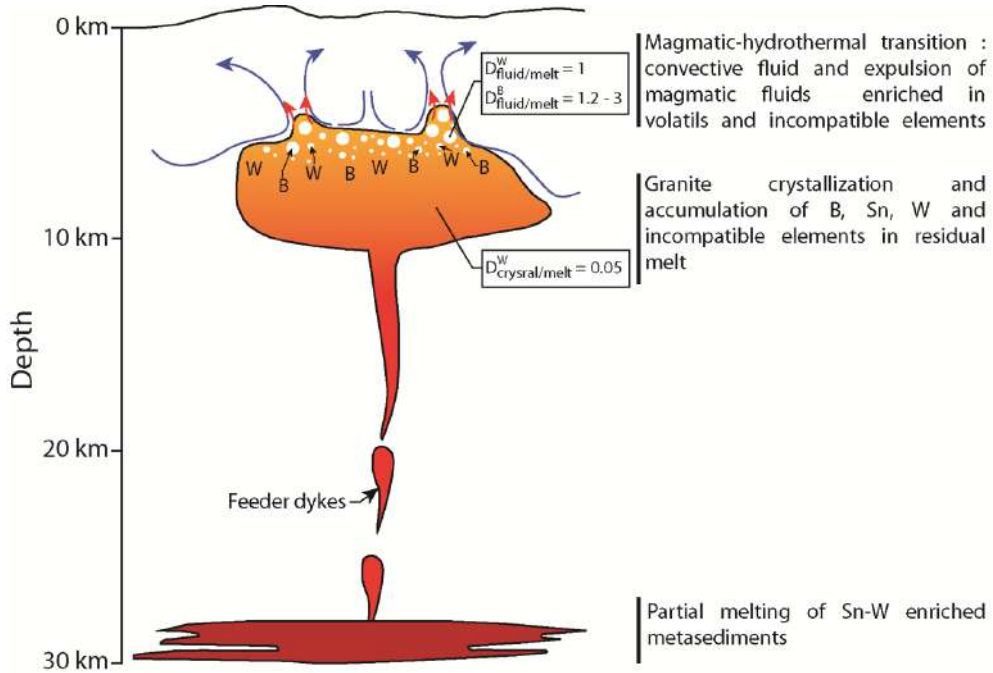

Figure 9 Représentation schématique des processus magmatiques et hydrothermaux conduisant à la formation des gisements péri-granitiques à W-Sn. Cette figure met l'accent sur l'importance de la transition magmatique-hydrothermale (d'après Robb, 2005 et Chelle-Michou, 2017). Les coefficients de partage (D) du W et du B entre phase fluide et magma silicaté et sont également indiqués.

3.2.1 Concentration et expulsion du W et des éléments incompatibles lors de la transition magmatique-hydrothermale

La cristallisation fractionnée des granites de type-S constitue un mécanisme efficace pour concentrer certains éléments. En effet, des éléments tels que le W, Sn Li et B présentent un comportement incompatible marqué causant leur accumulation dans les liquides silicatés résiduels (Fig. 9). Lorsque ces liquides évolués atteignent la saturation en H_2O, la phase fluide exsolvée du magma interagit avec les liquides enrichis en éléments incompatibles et en métaux entrainant la mobilisation et le transport de ces derniers jusqu'au système filonien lors des phases hydrothermales. Dans le cas du tungstène, le coefficient de partage fluide/magma granitique relativement faible ($D^{W}_{fluide/magma} \approx 1$) suggère que le W sera efficacement concentré dans les magmas granitiques avant que ces derniers atteignent la saturation en eau (Robb, 2005). L'analyse des inclusions fluides réalisée dans le cas du gisement à W-Sn de Panasqueira (Lecumberri-Sanchez et *al*., 2017) et du porphyre à Cu-Mo de Butte (Rusk et *al*., 2004) montre que les fluides minéralisateurs associés à ce type de système peuvent présenter des teneurs relativement importantes en Na et K et en éléments incompatibles lithophiles notamment en Li et B et en métaux (Cu, Zn et Pb) (Fig. 10a). Le W quant à lui présente des concentrations non négligeables (10-100 ppm) suggérant que le transport chimique de ce dernier par les fluides hydrothermaux est suffisamment efficace lors de la transition magmatique-hydrothermale pour potentiellement former les minéralisations à W observées au sein des veines.

Les coefficients de partage du bore entre phase fluide et magma silicaté ($D^{B}_{magma/fluide}$) déterminés expérimentalement par Pichavant (1981) London (1988) et Schatz et *al*., (2004) ont montré que le B est préférentiellement mobilisé par la phase fluide s'ex-solvant lors de la transition magmatique-hydrothermale ($D^{B}_{magma/fluide} < 1$) (Fig. 10b). L'expulsion de fluides riches en B est donc vraisemblablement responsable des altérations de type tourmalinisation communément observés au sein des gisements à W-Sn de type veine et greisen. Ces altérations constituent de ce fait d'excellents marqueurs de la transition magmatiques-hydrothermale pouvant être utilisé afin de tracer les processus physico-chimiques intervenant lors de cet évènement clé.

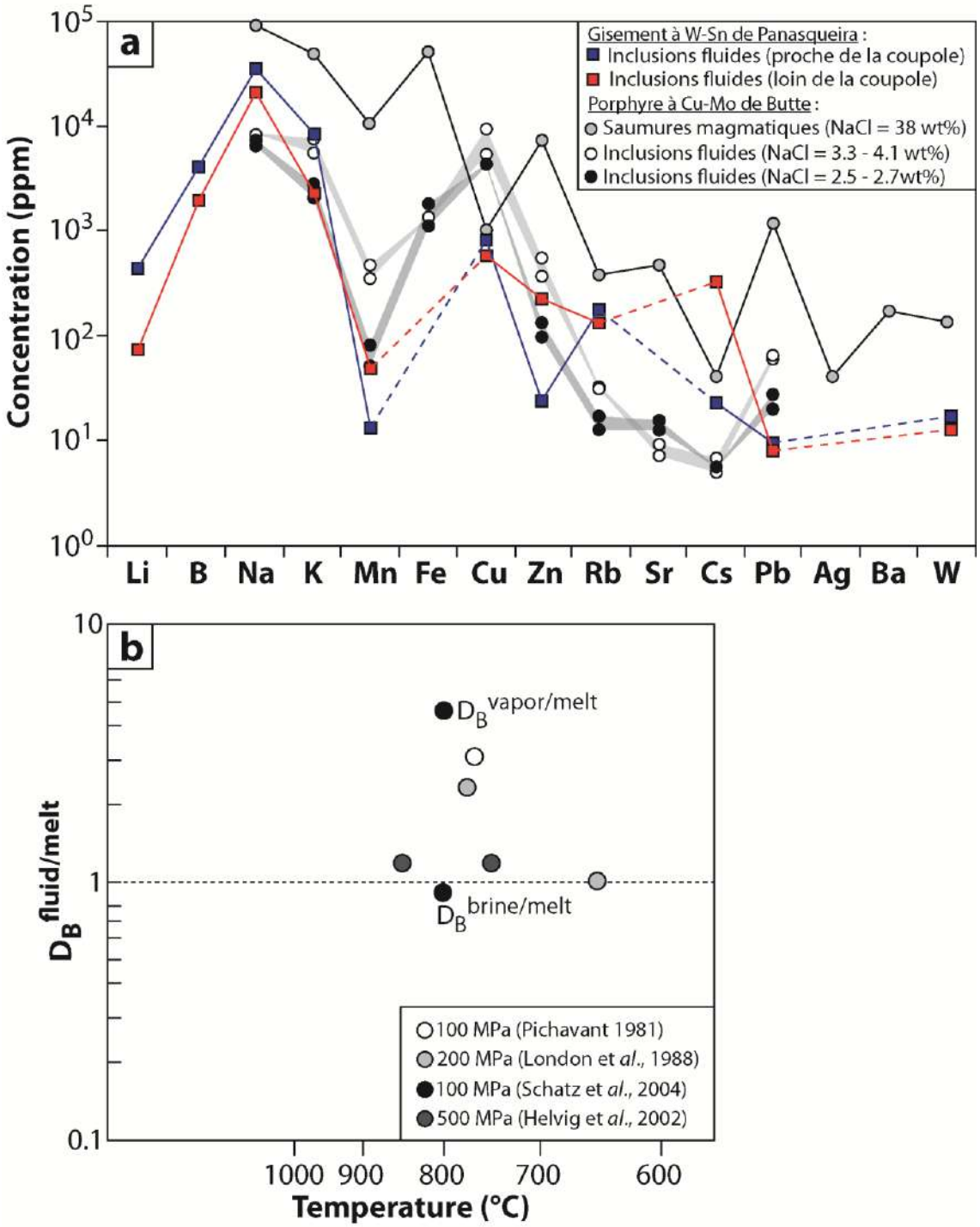

Figure 10 (a) Caractéristiques géochimiques des saumures hydrothermales et des inclusions fluides associées aux minéralisations à Cu-Mo de Butte (Rusk et *al.*, 2004) et aux minéralisations à W-Sn de Panasqueira (Lecumberri-Sanchez et *al.*, 2017). (b) Coefficients de partage du bore entre liquide silicaté et fluide hydrothermal déterminés pour différentes conditions de pression et de température (modifiées d'après Schatz et *al.*, 2004).

3.2.2 Caractéristiques physico-chimiques et isotopiques des fluides minéralisateurs

Afin de contraindre les caractéristiques physico-chimiques et la (ou les) source(s) des fluides porteurs des minéralisations à W-Sn, de très nombreuses études portant sur l'analyse des inclusions fluides et la détermination des signatures en isotopes stables des fluides ont été menés dans de nombreux cas de gisements à W-Sn. La compilation des données d'inclusions fluides réalisées par Naumov (2011) montre que le dépôt de la wolframite intervient à des conditions de température généralement comprises entre 200 et 400°C et de pression principalement comprises 50 et 250 MPa mais pouvant atteindre dans certains cas des valeurs très élevées imputables à des états de suppressions fluides induites par l'expulsion de fluides magmatiques (Fig. 11a) (Naumov, 2011). Les fluides minéralisateurs présentent une large gamme de salinité (équivalent NaCl) comprise entre 0.1 et 80 wt% avec des valeurs moyennes généralement comprises entre 1 et 10 wt% (Fig. 11b). Il s'agit généralement de fluides aquo-carboniques biphasés avec un contenu en gaz extrêmement variable d'un gisement à l'autre voir absent dans certains cas (Fig. 11c) (Naumov, 2011). Cette phase gazeuse généralement dominée par le CO_2 (56.1 mol%) peut également contenir en proportion moins importantes du CH_4 (30.7 mol%), N_2 (13.2 mo%) ainsi que du H_2S en très faible quantité (0.01 mol%) (Fig. 11c) (Naumov, 2011). La présence de ces volatils (CO_2-CH_4-N_2) est compatible avec des fluides d'origine métamorphiques (métasédimentaires). Néanmoins, la présence de cubes de sel dans certains cas témoigne de la présence de saumures hypersalées d'origine magmatique dans les systèmes hydrothermaux à W-Sn (Audétat *et al.,* 2000). Il en ressort donc que la formation des gisements magmatique-hydrothermaux à W-Sn résultent de l'interaction de plusieurs sources de fluides.

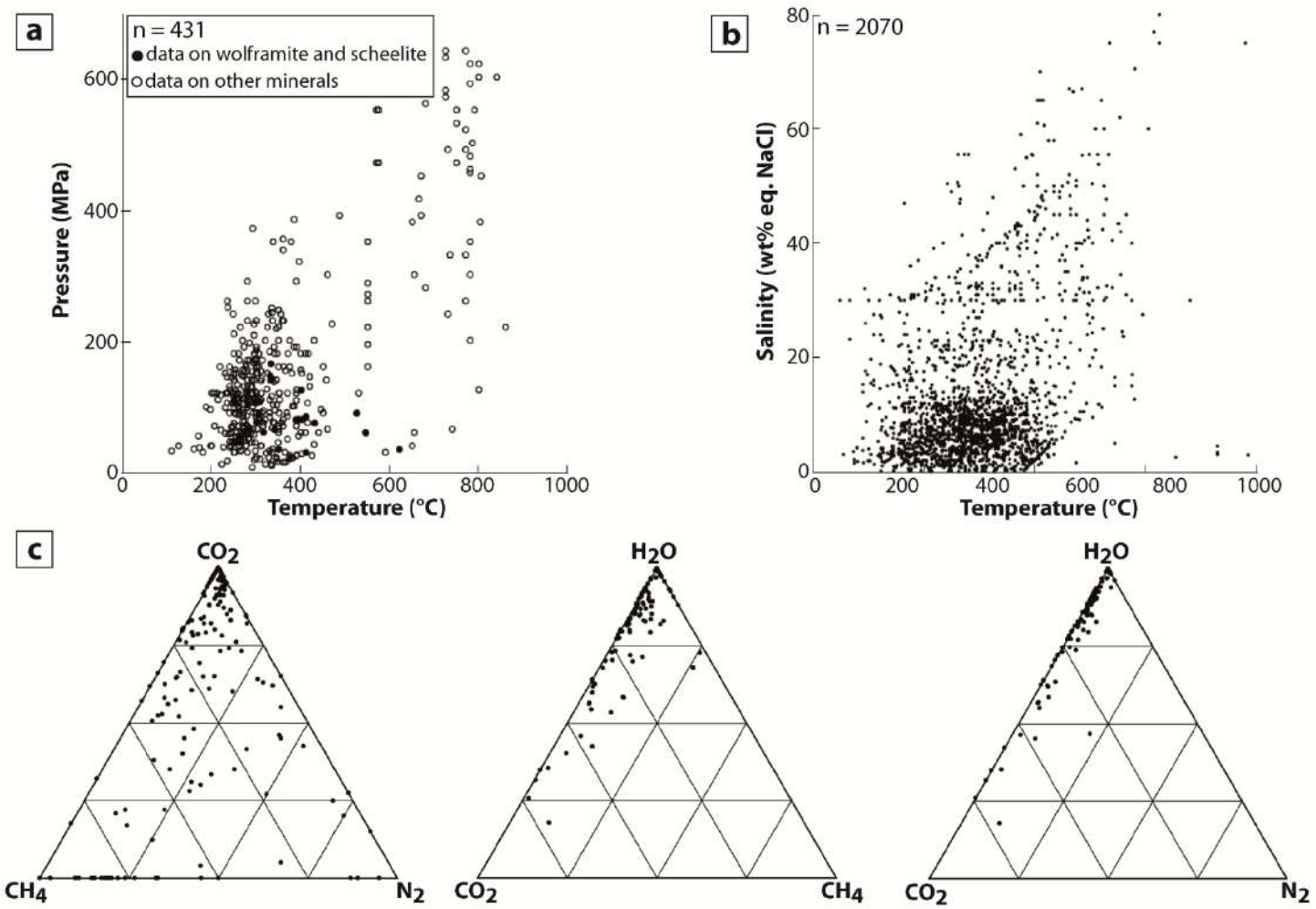

Figure 11 Compilation des données microthermométriques (températures et pression) (a), des valeurs de salinité (b) et des données compositionnelles des inclusions fluides (c) analysées au sein des différents types de gisements à W-Sn présent à travers le monde (modifié d'après Naumov, 2011).

Les compositions isotopiques en $\delta^{18}O$ et δD des fluides associées aux minéralisations à W-Sn présentent des signatures très variables d'un gisement à l'autre mais également au sein d'un même gisement (Fig. 12). Ces signatures peuvent aussi bien refléter (i) des interactions fluides/roches hétérogènes conduisant à l'équilibration des fluides minéralisateurs avec les différentes roches en présence (métamorphiques), ou bien (ii) l'implication de fluides magmatiques, météoriques et métamorphiques en proportions plus ou moins importantes en fonction du gisement considéré. Ces différentes sources de fluide peuvent intervenir au cours de différentes phases de minéralisation, ou bien au cours d'une même phase suggérant des processus de mélanges entre des fluides salés, chauds et riches en métaux (W, Sn, Li, B…) d'origine magmatique et des fluides externes peu salés, froids et riches en CO_2-CH_4-N_2 d'origine météorique et/ou métamorphique. En fonction des proportions de ces différentes sources de fluide dans les systèmes magmatique-hydrothermaux, ces phénomènes de mélange peuvent provoquer la dilution des fluides magmatiques salés expliquant d'une part, la forte dispersion de salinité (différent degré de dilution), et d'autre part la grande variabilité du contenu en gaz (CO2-CH4-H2) observées au sein des inclusions fluides.

La présence de ces différentes sources de fluides va être fonction de nombreux paramètres tels que la profondeur de mise en place, le type d'encaissant et de sa capacité à tamponner la composition chimique des fluides et implique des processus de circulation très différents faisant intervenir des mécanismes et des forces motrices variées qui seront abordées dans la partie suivante (III).

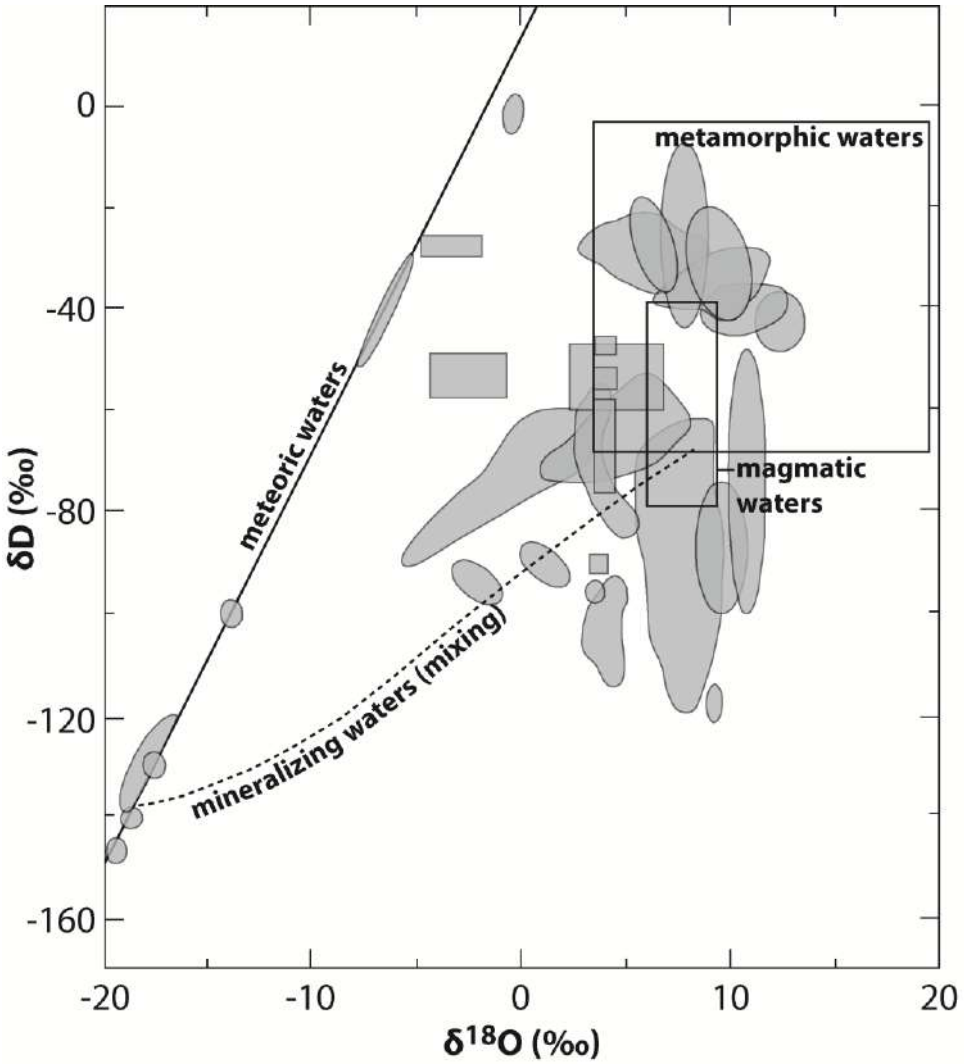

Figure 12 Compilation des compositions isotopiques en $\delta^{18}O$ et δD (en ‰) des fluides minéralisateurs responsables de la formation de différents gisements à W-Sn présent dans le monde (modifié d'après Legros, 2017).

3.2.3 Mobilité du tungstène dans les solutions hydrothermales

La formation des gisements de type veine et greisen résulte du transport chimique efficace du tungstène et de son accumulation au cours des différents processus magmatiques-hydrothermaux. La mobilité du W dans les solutions hydrothermales a fait l'objet de nombreuses études thermodynamiques (Inova et Khodakowsky, 1968; Inova, 1966; Wood et Samson, 2000) et expérimentales (Bryzgalin, 1976; Bryzgalin et *al*., 1971; Foster, 1977; Wesolowski, 1984; Wood, 1992). Ces études ont montré que la solubilité du W dans les fluides hydrothermaux dépend des conditions de pression et de température (Fig. 13), mais également des caractéristiques physicochimiques des fluides minéralisateurs (pH, fO_2, composition…). Si la valence du tungstène peut varier de (2+) à (6+), celui-ci est généralement transporté sous son état d'oxydation (6+) dans les fluides

hydrothermaux (Wood et Vlassopoulose, 1989). Le pH de la solution via la concentration en HCl dans le fluide ne semble pas avoir d'effet sur la quantité totale de W pouvant être transportée par le fluide (Fig. 13a) (Wood, 1992). A l'inverse la concentration en NaCl et KCl semble affecter significativement la solubilité du W (Fig. 13b). En effet, les données expérimentales obtenues par Bryzgalin (1976), Foster (1977) et Wesolowski (1984) démontrent que la solubilité en W mesurée augmente systématiquement lorsque la concentration en NaCl et KCl dans la solution augmente. Ces résultats expérimentaux suggèrent clairement un transport plus efficace du W dans des solutions hypersalines comparables aux saumures hydrothermales potentiellement libérées en fin de cristallisation d'intrusions granitiques (Audétat *et al.*, 2000； Rusk et *al.*, 2004). De plus, l'étude des inclusions fluides réalisées dans de nombreux cas de gisements hydrothermaux à W a révélé que la formation de la wolframite/scheelite résulte de la circulation de fluides riches en Na-K-Ca-Cl avec des salinités variables comprises entre 1 et 80 wt% (Naumov, 2011). Si les différents résultats expérimentaux semblent être cohérents avec de nombreux cas naturels, le rôle exacte des chlorures (Cl) et des alcalins (Na et K) lors du transport du W reste encore aujourd'hui sujet à controverse. En effet, les complexes de tungstène chlorurés (WCl_6 ou $WOCl_4$) n'étant pas stables en conditions hydrothermales (Ivanova, 1966; Schröcke et *al.*, 1984), ces derniers ne contribuent donc pas au transport chimique du tungstène qui va être principalement présent dans les fluides sous la forme de tungstate : WO_4^0, $HW0_4^-$, $H_2WO_4^0$, $NaWO_4^-$ et $NaHWO_4^0$ (Wood, 1990; Wood, 1992; Wood et Samson, 2000). La salinité et l'activité en KCl et NaCl dans le fluide jouent donc probablement un rôle indirect soit en équilibrant les charges de la solution hydrothermale, soit en participant à la formation de certains complexes :

$$WO_{3(s)} + NaCl_{(aq)} + H_2O = HWO_{4\,(aq)}^- + Na_{(aq)}^+ + HCl_{(aq)}$$

$$WO_{3(s)} + NaCl_{(aq)} + H_2O = NaWO_{4\,(aq)}^- + H_{(aq)}^+ + HCl_{(aq)}$$

$$WO_{3(s)} + NaCl_{(aq)} + H_2O = HNaWO_{4(aq)} + HCl_{(aq)}$$

$$WO_{3(s)} + KCl_{(aq)} + H_2O = HWO_{4\,(aq)}^- + K_{(aq)}^+ + HCl_{(aq)}$$

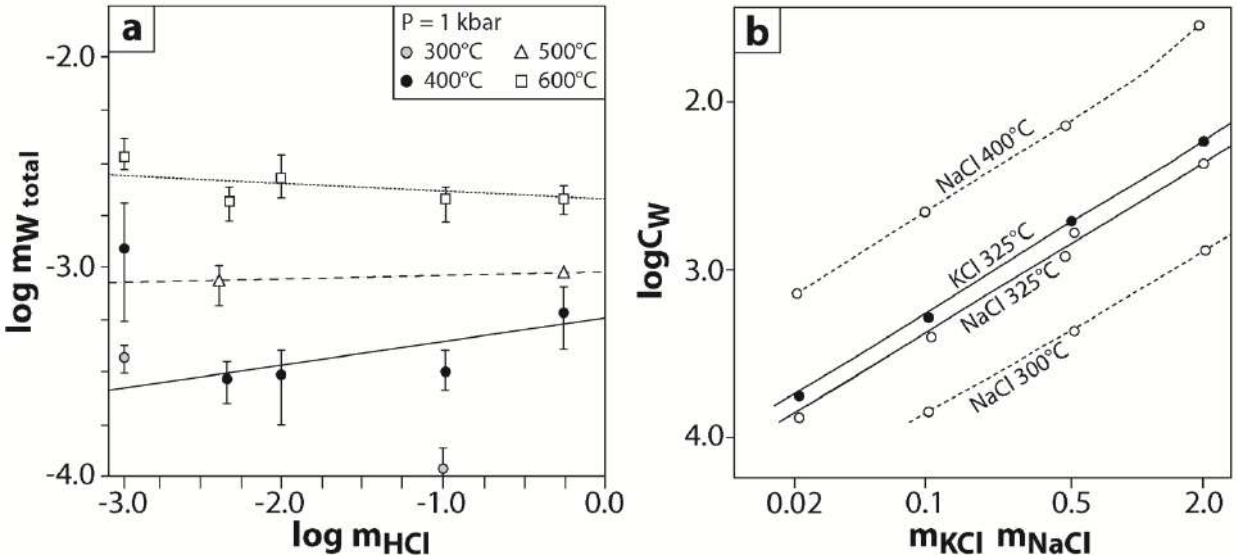

Figure 13 (a) Evolution de la solubilité du tungstate dans les fluides hydrothermaux en fonction de la concentration en HCl (Wood, 1992) et (b) de la concentration en NaCl, HCl pour différentes conditions de température (Bryzgalin, 1976)

3.2.4 Effets des instabilités mécaniques induites par la transition magmatique-hydrothermale

La mise en place et la cristallisation d'apex granitiques lors de la transition magmatique-hydrothermale peut affecter significativement l'état de contrainte locale au sein de l'encaissant par le développement et le maintien d'instabilités thermomécaniques (Guillou-Frottier et Burov, 2003 ; Gloaguen et *al*., 2014). En effet, les modèles numériques de Guillou-Frottier et Burov (2003) montrent que la mise en place d'apex granitiques peut s'accompagner d'une localisation des contraintes et donc de la déformation au niveau des apex (Fig. 14). Pour un contexte tectonique et structural donné, cette localisation de la déformation peut provoquer l'ouverture et le développement de fractures et de failles préférentiellement au niveau des apex granitiques (Guillou-Frottier et Burov, 2003). Ces structures vont ensuite drainer et piéger les fluides minéralisateurs au niveau des apex expliquant ainsi les relations spatiales systématiquement observées entre coupoles granitiques et minéralisation filoniennes.

Néanmoins ces modèles ne prennent pas en compte la circulation des fluides dont l'organisation est un paramètre critique dans la localisation des minéralisations. Par ailleurs, l'expulsion potentielle de fluides lors de la transition magmatique-hydrothermale peut constituer un mécanisme important lors de l'ouverture de ces drains. Comme mentionné précédemment, des pressions fluides élevées peuvent être à l'origine de l'ouverture des veines composant les gisements à W-Sn. La conjonction entre le

développement d'instabilités mécaniques et des pressions de fluides élevées préférentiellement situées au niveau des apex peuvent être à l'origine de la localisation des minéralisations au niveau des zones apicales des intrusions granitiques. Cependant le rôle des apex sur la focalisation et l'organisation des circulations de fluides reste peu contraint.

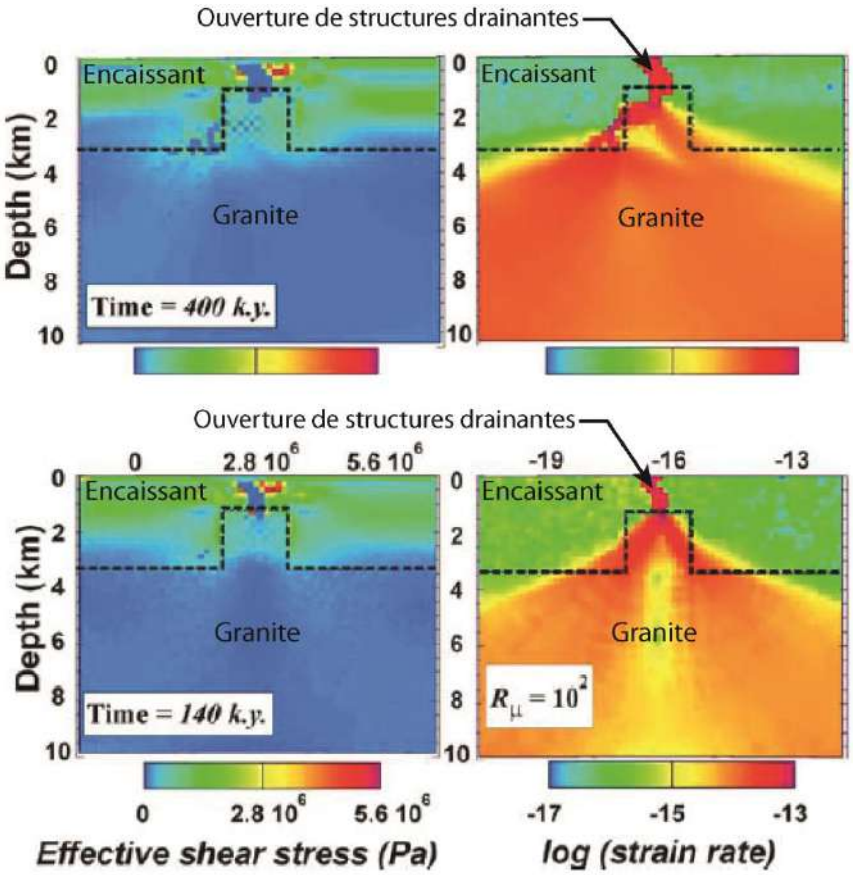

Figure 14 Effet de la mise en place d'un apex granitique sur la localisation de la déformation. La ligne en pointillés noir correspond au contact granite-encaissant (d'après Guillou-Frottier et Burov, 2003).

III- L'hydrothermalisme péri-granitique

1. Genèse des gisements hydrothermaux

Comme mentionné précédemment, l'hydrothermalisme péri-granitique constitue l'étape finale de formation des gisements à W-Sn. La formation de gîtes hydrothermaux peut être décrite par un modèle conceptuel divisé en 3 étapes principales (Fig. 15) :

- (i) Dans un premier temps, les métaux sont lessivés et mobilisés au sein d'un large volume de roche source par des fluides aqueux riches en ligands (Cl, F, OH, H_2S) qui constituent d'excellents agents de transport d'éléments dissouts tels que les métaux. Dans le cas des gisements péri-granitiques à W-Sn, l'origine des fluides est souvent multiple et généralement différente de celle des métaux qui peuvent à la fois provenir des liquides magmatiques résiduels enrichis en incompatibles (Li, B, W, Sn…) et des roches encaissantes (métasédiments).
- (ii) Les fluides hydrothermaux chargés en métaux sont ensuite collectés au sein de structures ou de facies lithologiques perméables permettant leur migration sur d'importantes distances. Lors de cette étape de transport, la focalisation d'un large volume de fluides minéralisateurs au sein de ces structures perméables cause une augmentation locale du flux métallique. La formation d'un gisement de grande taille repose sur l'efficacité de cette focalisation des flux sur le long terme. Celle-ci dépend elle-même de la disponibilité de structures drainantes tout au long de l'activité hydrothermale et implique donc des processus d'ouverture et de maintien des structures perméables efficaces et actifs tels que des conditions de pression fluide élevées et un contexte structural actif.
- (iii) D'importants changements des conditions physico-chimiques au sein de ces zones de focalisation des flux peuvent provoquer la déstabilisation des complexes métalliques au sein de la solution hydrothermale entrainant alors le dépôt des métaux sous la forme de concentration minérale. Cette étape de piégeage est généralement déclenchée par des changements de température, de pression, de pH (neutralisation) et de conditions redox (fO_2) ou à l'adjonction dans le fluide d'éléments provenant des roches encaissantes tels que le fer ou le calcium pouvant provoquer respectivement le dépôt de la wolframite et de la scheelite (Lecumberri-Sanchez et al., 2017). Ces changements sont généralement induits par des processus de mélanges entre les fluides chauds et minéralisés et des fluides

externes froids et non minéralisés, mais aussi par d'importantes interactions fluides-roches provoquant également les altérations hydrothermales observées au sein de ces gisements.

La concentration des métaux au sein d'un volume final restreint par rapport à la roche source de départ constitue le point déterminant de la formation d'un gisement hydrothermal. Au cours de ces différentes étapes peuvent intervenir des mécanismes d'enrichissement causés par l'extraction et le dépôt séquentiel de certains métaux. Par ailleurs, les gisements hydrothermaux sont souvent marqués par la juxtaposition de plusieurs cycles de mobilisation-transport-dépôt des métaux conduisant à la formation de systèmes minéralisés complexes, polyphasés et polymétalliques.

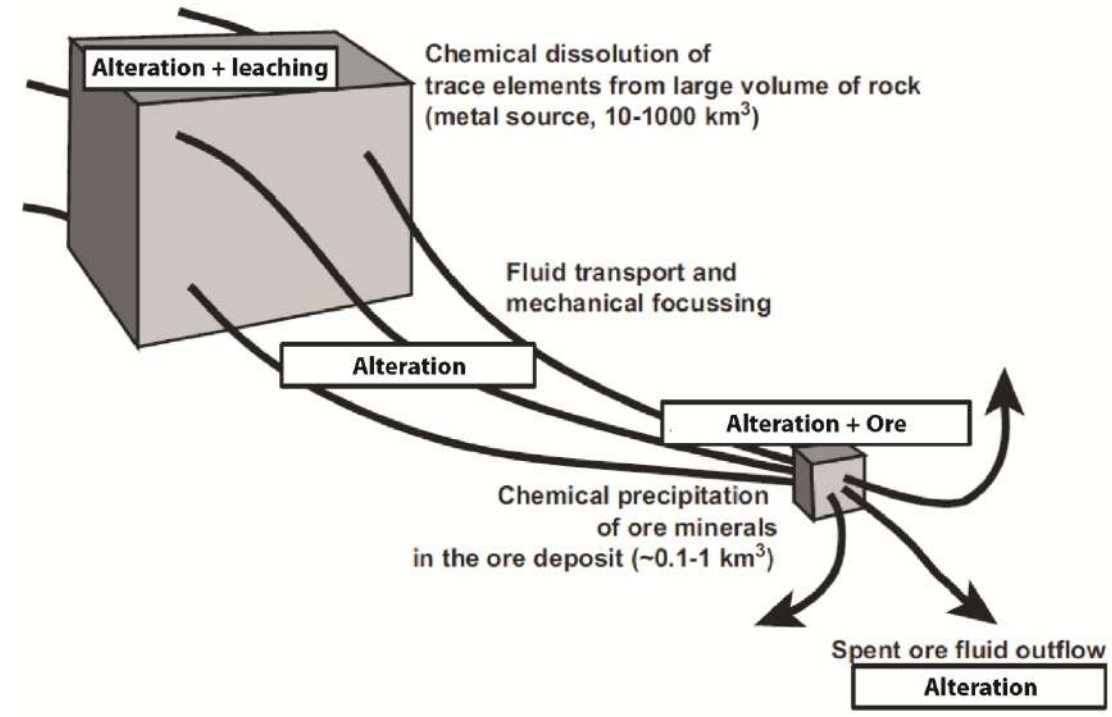

Figure 15 Modèle conceptuel présentant les trois étapes de formation d'un gisement hydrothermal (source-transport-dépôt) (d'après Heinrich, 1996 communication orale).

2. La circulation hydrothermale péri-granitique : équations physiques et forces motrices des écoulements

2.1 Loi physiques décrivant les écoulements de fluide et le transport des métaux en contexte hydrothermal

Comme mentionné précédemment, la formation d'un gisement hydrothermal d'intérêt économique dépend de la capacité du système à transporter et à focaliser efficacement les fluides porteurs de la minéralisation. Ce processus de transfert peut être décrit et modélisé en couplant les équations de transport de la chaleur et de soluté en milieu poreux et la loi de Darcy.

(i) L'équation de transport de la chaleur :

Cette équation décrit l'évolution de la température du fluide hydrothermal et de son milieu lors du transfert de chaleur par convection et conduction :

$$\rho_m Cp_m \frac{\delta T}{\delta t} = \lambda \Delta T - \rho_f Cp_f \boldsymbol{v_f}.\nabla T + Q$$

avec ρ_m et ρ_f (kg.m^{-3}) la masse volumique du milieu et du fluide, Cp_m et Cp_f (J.kg^{-1}.K^{-1}) les capacité thermiques du milieu et du fluide, λ (W.m^{-1}.K^{-1}) le coefficient de conductivité thermique, $\boldsymbol{v_f}$ (m.s^{-1}) la vitesse d'écoulement du fluide et Q (W.m^{-3}) la production de chaleur du milieu.

(ii) L'équation de transport de soluté en milieu saturé :

Cette équation décrit l'évolution de la concentration (C) en soluté au sein du fluide hydrothermal transitant à travers un milieu poreux :

$$\frac{\delta C}{\delta t} = -\varphi \boldsymbol{v_f} \nabla C + \varphi D.\nabla^2 C + \varphi Q$$

Avec t (s) le temps, φ la porosité du milieu, $\boldsymbol{v_f}$ (m.s^{-1}) la vitesse d'écoulement du fluide, D (m².s^{-1}) le coefficient de diffusion du soluté considéré et Q (kg.m^{-3}) un terme source pouvant être négatif en cas de précipitation ou positif en cas de dissolution.

Le transfert thermique et chimique décrit par ces deux équations se compose d'un terme diffusif et d'un terme advectif. Le transport diffusif des métaux dépend directement des gradients de concentration et du coefficient de diffusion de l'élément considéré. Les coefficients de diffusion sont principalement thermo-dépendants et généralement compris entre 10^{-9} et 10^{-8} m².s^{-1} en contexte hydrothermal. Ce mode de transport intervient donc

principalement à petite échelle lors de processus locaux d'interaction fluide-roche conduisant notamment à la formation des auréoles métasomatiques. La diffusion est donc généralement considérée comme négligeable dans le transport des métaux à plus grande échelle. L'advection correspond au transport d'une quantité additive (chaleur et élément chimique) par une phase fluide et dépend directement de la vitesse d'écoulement du fluide dans le système hydrothermal. Des vitesses d'écoulement élevées assurent un flux chimique important et permettent de transporter une grande quantité de métaux à grande échelle. L'advection constitue donc le mode de transfert préférentiel des métaux au sein des gisements hydrothermaux. Le nombre de Péclet (*Pe*) décrit le rapport entre l'advection et la diffusion et permet donc d'évaluer directement l'efficacité du transport chimique et thermique au sein d'un système hydrothermal :

$$Pe = \frac{v_f L}{D}$$

avec v_f (m.s^{-1}) la vitesse d'écoulement du fluide, L (m) la longueur carcatéristique du système et D (m².s^{-1}) le coefficient de diffusion. Pour des *Pe* faibles, la diffusion est le mode transfert dominant et le transport des métaux peut être considéré comme inefficace et négligeable. Inversement, des nombres de Péclet élevés correspondent à un mode de transfert dominé par l'advection et donc à un transport efficace des métaux. La formation d'un gisement de grande taille et économiquement intéressant implique donc des vitesses d'écoulement du fluide élevées. La vitesse d'écoulement constitue un paramètre hydrodynamique critique difficile à évaluer sur le terrain, néanmoins quelques rares estimations sont présentes dans la littérature (Thompson, 1977; Oelkers, 1997; Dolejs, 2015) (Fig. 16). Ces estimations montrent que la formation d'un gisement de type veine requiert des vitesses élevées comprises entre 10^{-7} et 10^{-5} m.s^{-1} et des nombres de Péclet supérieurs à 100 pour des coefficients de diffusion de 10^{-9} m².s^{-1} (Dolejs, 2015).

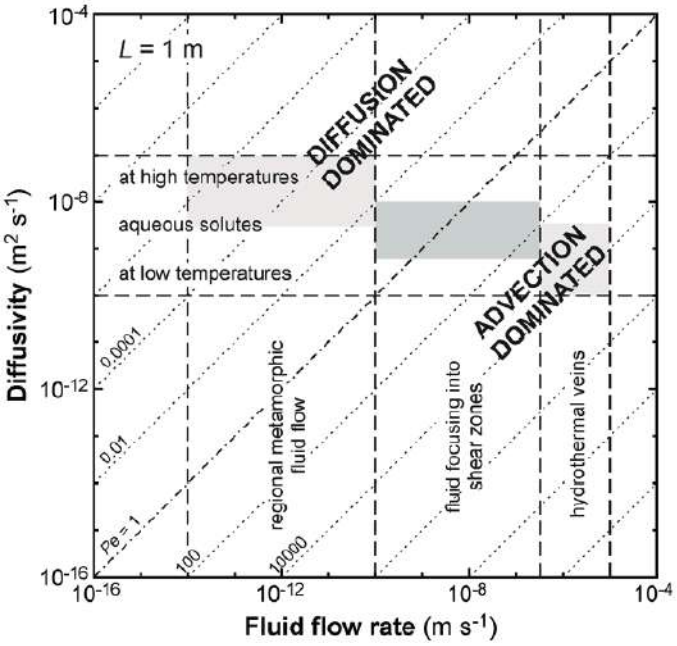

Figure 16 Répartition des modes de transport par advection et diffusion dans l'espace vitesse-diffusion. Les gammes de vitesses estimées pour les différents types d'environnement géologiques et hydrothermaux sont également représentées. Les lignes en pointillés serrés correspondent aux nombres de Péclet (*Pe*). Les domaines en gris correspondent aux gammes de vitesses-diffusion pour les veines hydrothermales, les shear zones et le métamorphisme régional (Dolejs, 2015).

(iii) La loi de Darcy :

La vitesse d'écoulement du fluide à moyenne et grande échelle peut être calculée et simulée à partir de la loi de Darcy qui décrit les écoulements de fluides en fonction du gradient de pression et de la perméabilité du milieu. :

$$\boldsymbol{q} = -\frac{\boldsymbol{k}}{\mu_f}(\nabla P - \rho_f g)$$

Avec $\boldsymbol{q}$ (m.s^{-1}) la vitesse de Darcy, $\boldsymbol{k}$ (m²) la perméabilité du milieu, μ_f (Pa.s) la viscosité dynamique du fluide, ρ_f (kg.m^{-3}) la masse volumique du fluide et g (9.81 m².s^{-1}) le coefficient d'accélération gravitationnelle. Les vitesses de Darcy peuvent être converties en vitesse d'écoulement du fluide dans le milieu poreux en prenant en compte la porosité :

$$\boldsymbol{v_f} = \frac{q}{\varphi}$$

Le couplage de la loi de Darcy avec les équations physiques précédemment décrites permet de simuler de façon fine le fonctionnement d'un système hydrothermal et le transport des métaux et de chaleur à travers la croûte. Dans ce couplage, la perméabilité constitue un paramètre critique ayant un impact majeur sur les écoulements de fluides minéralisateurs et donc sur l'efficacité du transport de métaux au sein d'un système hydrothermal. Les différents mécanismes pouvant affecter la perméabilité d'un système hydrothermal seront décrits dans la partie suivante.

2.2 Les principales forces motrices impliquées lors de l'hydrothermalisme péri-granitique

La mise en mouvement des fluides et la vitesse de circulation de ces derniers sont directement contrôlées par des gradients de pression et de température. Dans le cas des gisements péri-granitiques, les principales forces motrices impliquées lors de la circulation des fluides minéralisateurs sont la convection hydrothermale et des états de surpression fluide induite par l'expulsion de fluides magmatiques (Fig. 17) (Chi et Xue, 2011; Ingebritsen et Appold, 2012).

Les conditions de surpression fluide correspondent à un excès de pression fluide par rapport à la pression hydrostatique à une profondeur donnée. Cette surpression se traduit par de forts gradients de pression latéraux et verticaux conduisant à la mise en mouvement des fluides depuis les zones de hautes pressions vers les zones de plus basses pressions. Lorsque les conditions de pression fluides sont supralithostatique ($P_f > P_{litho}$) d'importants rétrocontrôles entre la perméabilité et la pression fluide peuvent intervenir et conduire à l'ouverture de structures perméables. L'expulsion de fluides magmatiques dans les parties apicales des intrusions granitiques (coupoles et apex) constitue la principale force motrice des écoulements de fluides lors de la transition magmatique-hydrothermale et peut expliquer l'ouverture de structures drainantes (veines, stockwerk…) au niveau de ces zones apicales (Fig. 17a).

La convection hydrothermale est induite par des changements de densité de la phase fluide qui affectent les forces de flottabilité entrainant le plongement des fluides froids plus denses et la remontée des fluides chauds moins denses. Ces changements de densité sont généralement induits par des variations importantes de température et/ou de salinité du fluide. Une augmentation importante de la température lors de la mise en place et lors du refroidissement d'une intrusion granitique peut conduire à la mise en place forcée de boucles convectives autour de l'intrusion dont la taille est fonction de l'étendu de l'intrusion (Fig. 17b) (Norton et Cathles, 1979; Cathles, 1977; Gerdes et *al*., 1998; Eldursi et *al*., 2009). Les fluides impliqués lors de cette convection sont généralement d'origine météorique et métamorphique. Leur mise en mouvement peut provoquer le lessivage et la mobilisation des métaux disséminés au sein des encaissants (Eldursi et *al*., 2009; Eldursi et *al*., 2018).

Si l'expulsion de fluides magmatiques correspond à un évènement ponctuel (« single pass ») intervenant théoriquement qu'une seule fois par intrusion granitique (plusieurs fois si intrusions polyphasées), les fluides mobilisés par la convection peuvent réaliser

plusieurs cycles de mobilisation-transport-dépôt (« multiple pass ») aboutissant à la formation de gisements généralement polyphasés. Le manque de contrainte ne permet pas de définir clairement le rôle exact de chacun de ces modes de circulation ni de déterminer au cours de quelles étape ceux-ci interviennent. Ces deux modes de circulation peuvent aussi bien intervenir de manière concomitante au cours d'un même stade minéralisateur, ou bien de façon polyphasé au cours d'un continuum débutant par des processus d'expulsion lors de la transition magmatique hydrothermal suivi par des circulations convectives lors du refroidissement des intrusions granitiques (Fig. 17).

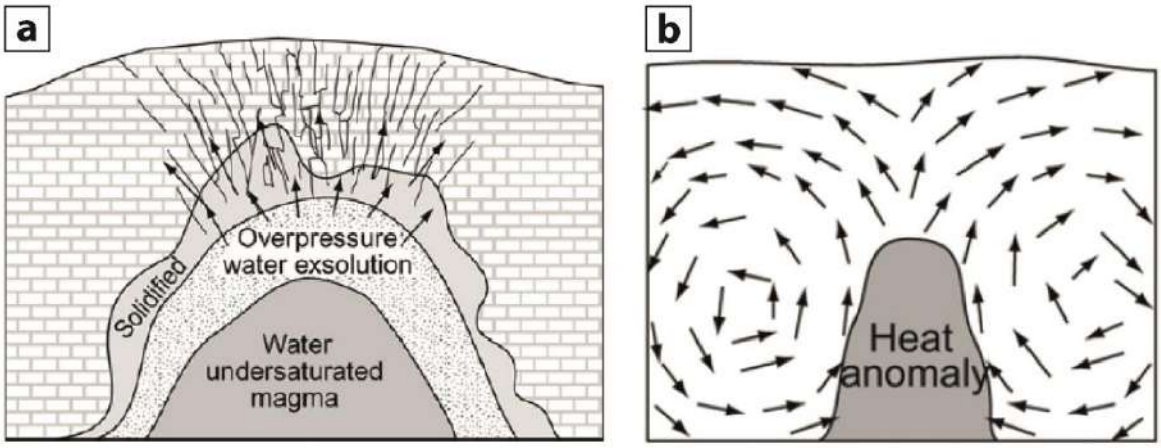

Figure 17 Modèles schématiques présentant les différents types de circulation hydrothermale ainsi que les forces motrices associées impliquées en environnement péri-granitique (d'après Chi et Xue, 2011). (a) Expulsion de fluides magmatiques en sommet de coupole granitique provoquant des conditions de surpression fluides. (b) Convection hydrothermale péri-granitique induite par l'anomalie thermique que constitue l'intrusion granitique.

3. La perméabilité : un paramètre critique lors de la circulation hydrothermale

Comme mentionné par Richards and Tosdal (2001) "*The mantra of hydrogeologists and … ore deposits geologists alike is 'permeability, permeability, permeability'…*" la perméabilité représente un paramètre critique dans le fonctionnement des systèmes hydrothermaux. En effet, les vitesses d'écoulement du fluide et donc l'efficacité du transport de chaleur et de métaux par advection à travers la croûte sont directement contrôlées par la perméabilité des roches rencontrées. La formation de gisements d'intérêt économique implique donc des perméabilités suffisamment élevées pour permettre le drainage et la focalisation d'un large volume de fluides minéralisateurs. La perméabilité présente une forte variabilité en fonction du type de roche en présence et constitue un paramètre dynamique pouvant évoluer significativement au cours des différents processus

géologiques impliqués dans les systèmes hydrothermaux (Ingebritsen et Appold, 2012; Ingebritsen and Gleeson, 2015).

3.1 Perméabilités des roches associées aux gisements à W-Sn de type veine et greisen

La perméabilité d'une roche correspond à sa capacité à laisser circuler un fluide. La perméabilité et la porosité sont généralement intrinsèquement liées (Fig. 18a) (Moeck, 2014 ; Luijendijk & Gleeson, 2015). Même si certains contre-exemples existent (argilites, ponces volcaniques), des porosités importantes sont généralement garantes de perméabilités matricielles élevées (basalte, grès, calcaires), alors que des roches peu poreuses sont généralement marquées par de faibles perméabilités (roches cristallines et métamorphiques) (Fig. 18b). Les gisements à W-Sn de type veines et greisen se mettent généralement en place au sein de socles composés de roches cristallines et métasédimentaires affectées par un métamorphisme plus ou moins important en fonction de la profondeur de mise en place du système magmatique-hydrothermal.

Ces roches présentent généralement de faibles porosités (0-15 %) et donc de faibles valeurs de perméabilité comprises entre 10^{-17} et 10^{-21} m² dans le cas de facies intacts et non altérés (Fig. 18a et 18b) (Brace, 1984; Evans et *al*., 1997; Sonney and Vuataz, 2009; Ingebritsen et Appold, 2012; Walter, 2016). Ces faibles valeurs de perméabilité dans les granites et les roches encaissantes semblent être d'une part peu favorable à l'extraction des fluides magmatiques, mais également peu favorable au développement d'un système hydrothermal péri-granitique. Néanmoins, la perméabilité de ces roches est susceptible d'être affectée de façon significative par des phénomènes de fracturation et d'altération hydrothermale que nous détaillerons dans la suite de cette partie.

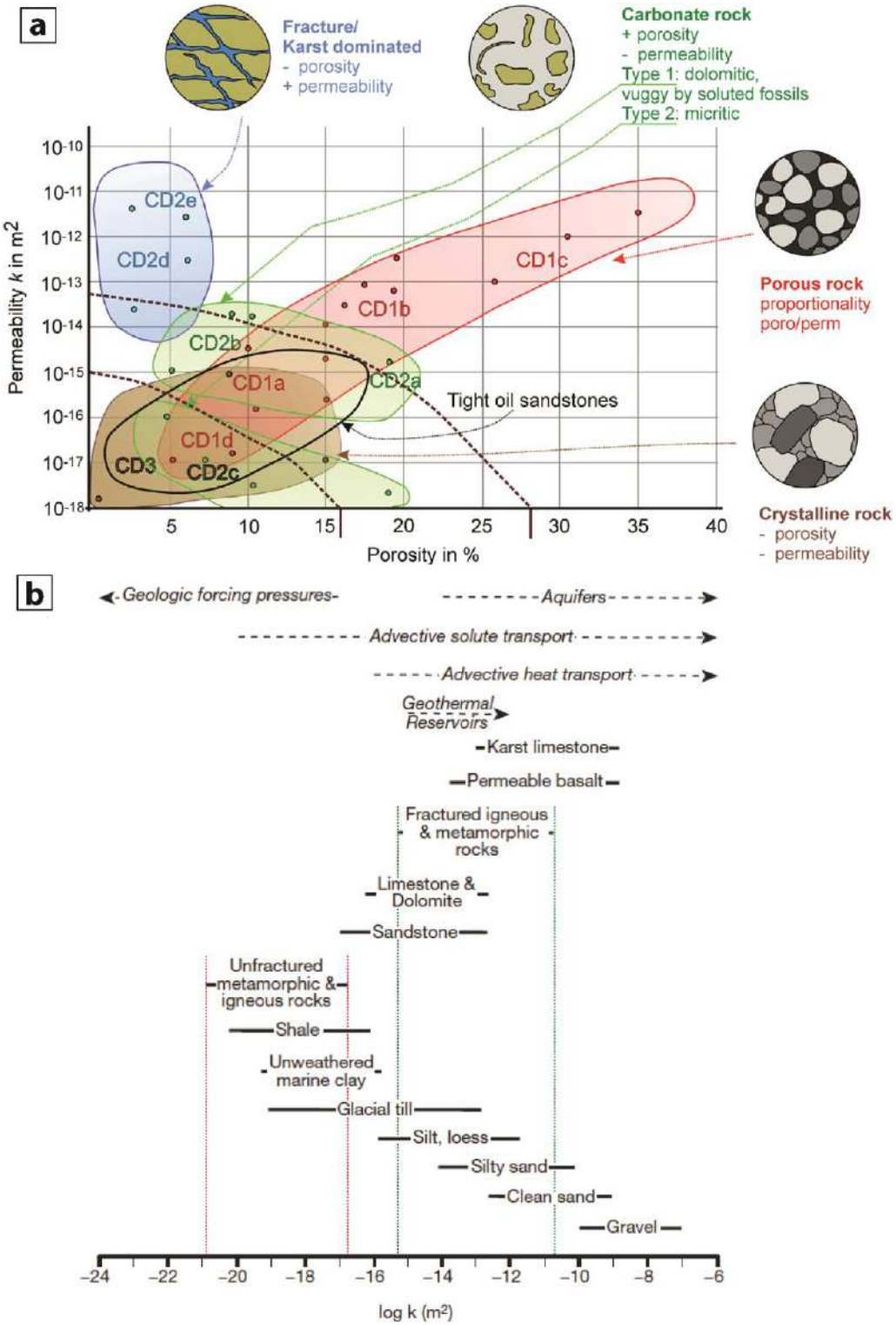

Figure 18 (a) Relation entre porosité et perméabilité au sein de différents réservoirs géothermiques et hydrothermaux (d'après Moeck, 2014). (b) Gammes de perméabilité observées au sein des principales roches composant la croûte terrestre. Les valeurs limites de perméabilités nécessaires au fonctionnement de certains processus de circulation sont également représentées (d'après Ingebritsen et Appold, 2012). Les gammes de perméabilité et de porosité matricielles au sein des roches cristallines et métamorphiques sont en apparences faibles (lignes en pointillés rouges) mais peuvent être améliorées par des processus de fracturation et d'altération hydrothermale (ligne en pointillés verts).

3.2 La perméabilité : un paramètre dynamique

La perméabilité a été reconnue comme étant un paramètre dynamique évoluant en temps et en espace au cours des différents processus géologiques impliqués lors du fonctionnement des systèmes hydrothermaux (Manning et Ingebritsen, 1999; Ingebritsen et Appold, 2012; Ingebritsen et Gleeson, 2015). La déformation, la fracturation, les conditions de surpression fluide, la dissolution/précipitation et les altérations hydrothermales sont autant de processus pouvant affecter significativement la perméabilité d'un système hydrothermal. Ces processus permettent notamment d'expliquer comment des systèmes initialement imperméables peuvent évoluer vers des systèmes perméables et favorables aux écoulements de fluides et donc au transport efficace de métaux.

3.2.1 Evolution de la perméabilité avec la profondeur

La profondeur de mise en place a un effet très important sur la perméabilité intrinsèque (Ingebritsen and Manning, 1999; Ingebritsen et Appold, 2012; Ingebritsen et Gleeson, 2015) (Fig. 19). En effet, l'augmentation de la contrainte lithostatique avec la profondeur cause la compaction et la fermeture des fractures présentes au sein des roches causant de ce fait une baisse de la porosité et de la perméabilité suivant des lois généralement exponentielles (Fig. 19a et 19b). En contions de sub-surface, les perméabilités sont généralement élevées et comprises entre 10^{-16} et 10^{-12} m² alors qu'elles sont comprises entre 10^{-20} et 10^{-18} m² dans la croûte inférieure (20-25 km). Le passage de la transition ductile-fragile constitue un autre mécanisme entrainant une baisse significative de la perméabilité expliquant les faibles valeurs observées au sein de la croûte inférieure. Par conséquent, un système hydrothermal se mettant en place à faible profondeur sera plus vigoureux et donc plus favorable à la formation d'un gisement de grande taille. Inversement, la circulation hydrothermal d'un système mis en place dans la croûte moyenne et profonde sera fortement inhibée en raison de la faible perméabilité des roches et sera donc peu favorable à la formation d'un gisement d'intérêt économique. Les gisements péri-granitiques à W-Sn se forment généralement à des profondeurs comprises en 2 et 5 km correspondant à des perméabilités relativement faibles (10^{-18} à 10^{-16} m²).

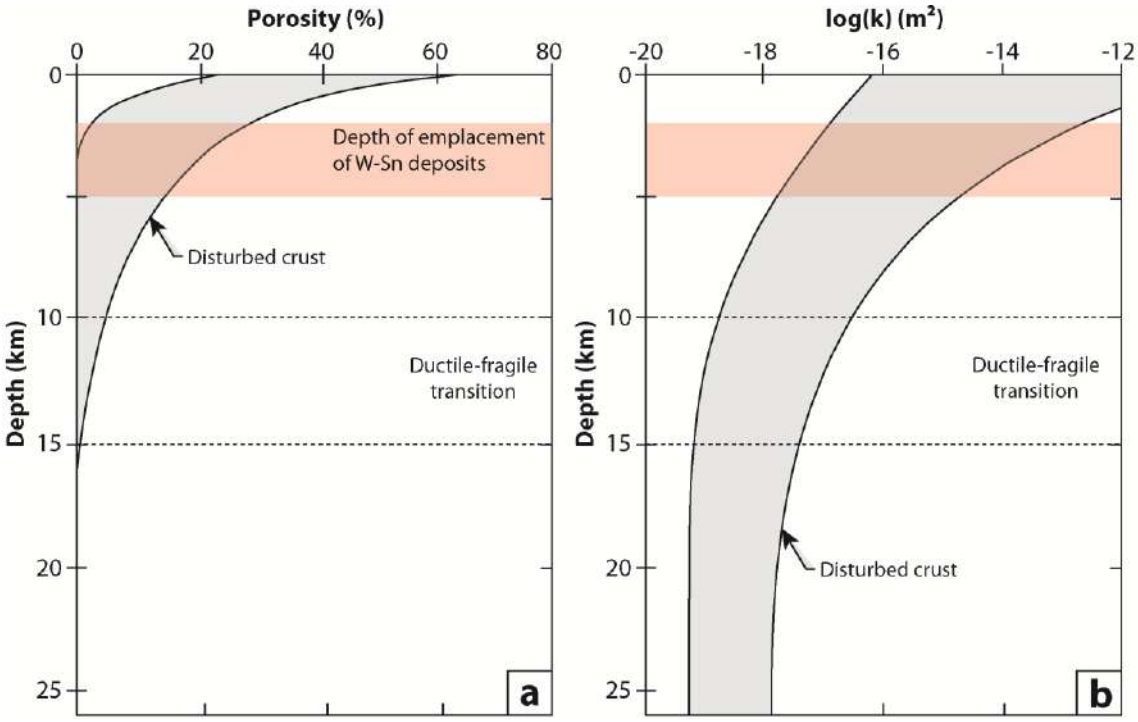

Figure 19 Evolution de la porosité (a) et de la perméabilité (b) en fonction de la profondeur (d'après Manning et Ingebritsen, 1999; Moore et Saffer, 2001).

3.2.2 Effets de la déformation/fracturation

La localisation préférentielle des minéralisations et des zones d'altération hydrothermale au sein de structures géologiques (failles, fractures, fentes de tension et shear zones) a rapidement conduit les géologues à considérer la déformation et la fracturation comme des mécanismes majeurs pour améliorer la perméabilité des systèmes hydrothermaux (Sibson, 1992, 1996 et 2001; Cox, 2002; Sibson and Rowland, 2003; Cox, 2010). Par la suite, les relations entre perméabilité et déformation/fracturation ont fait l'objet de nombreuses études expérimentales réalisées sur différents types de roches. Les expériences de fracturation réalisées par Tenthorey et Fitz Gerald (2006) sur granite ont démontré que la facturation pouvait augmenter la perméabilité de plusieurs ordres de grandeur et donc améliorer significativement la perméabilité d'une roche initialement imperméable (10^{-19} m²) (Fig. 20a). Le même type d'observation a été réalisé par Coelho et *al*., (2015) sur des roches caractéristiques de l'hydrothermalisme océanique (basalte, épidosite, métadiabase) (Fig. 20b). Cette étude a également démontré que les fractures et les réseaux de microcracks formés lors de la fracturation peuvent être rapidement scellés et cicatrisés conduisant à une baisse progressive de la perméabilité jusqu'à sa valeur initiale (Fig. 20b). Ces résultats expérimentaux suggèrent que la perméabilité générée par

fracturation est transitoire et effective sur un laps de temps court impliquant donc que le système de fractures soit régulièrement ré-ouvert (contexte structural actif) pour maintenir des valeurs de perméabilité élevées.

Les expériences réalisées par Zhang et *al*., (1994a) ont montrés que la déformation ductile correspondant par analogie au fonctionnement des shear zones peut également augmenter de manière significative la perméabilité par le développement de bandes de cisaillement perméables (Fig. 20c). Ce processus est d'autant plus efficace pour des pressions fluides élevées démontrant que des conditions de surpression fluides peuvent également être responsables de perméabilité élevée en favorisant l'ouverture de structures perméables (Fig. 20c).

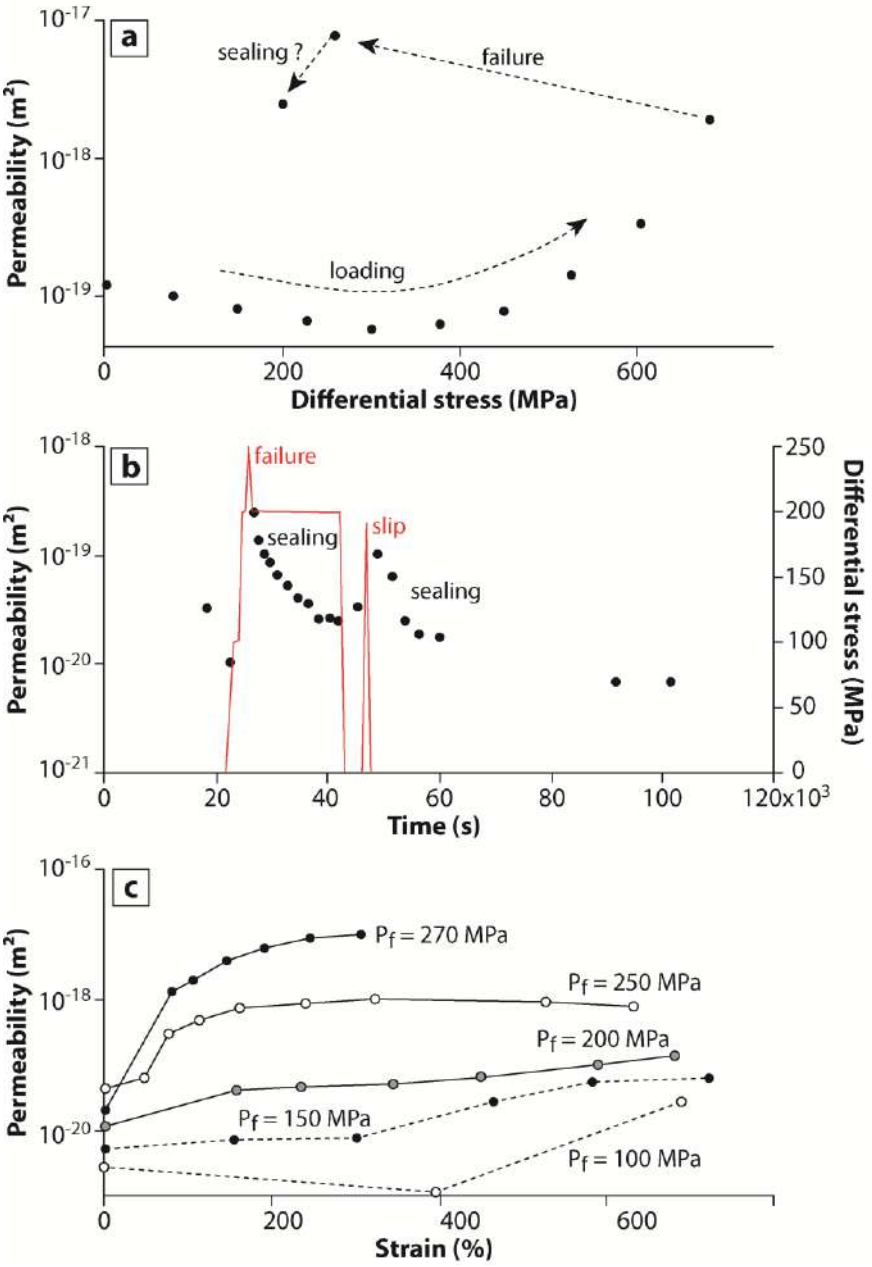

Figure 20 (a) Effet de la fracturation sur la perméabilité d'un échantillon de granite (d'après Tenthorey et Fitz Gerald, 2006). (b) Effet de la fracturation sur la perméabilité d'un échantillon de métadiabase (d'après Coelho et al., 2015). Après l'augmentation de perméabilité induite par la fracturation, la perméabilité diminue et retourne à sa valeur initiale en raison de la cicatrisation des microcracks. (c) Effet de la déformation ductile sur la perméabilité d'un échantillon de marbre. La pression fluide a également un effet majeur sur l'augmentation de perméabilité induite par la déformation (d'après Zhang et al., 1994a).

3.2.3 Effets des altérations hydrothermales

Les transformations minéralogiques induites par les réactions d'altération hydrothermale peuvent également constituer un mécanisme efficace pour améliorer ou réduire la perméabilité d'une roche (Putnis, 2002; Jamtveit et *al*., 2008; Putnis and Austrheim, 2010; Pollok et *al*., 2011; Booden and Simpson, 2011; Putnis and John, 2010; Jonas et *al*., 2014; Putnis, 2015). En fonction des variations de volume (ΔV) entre les minéraux produits et les minéraux altérés, de la porosité peut être produite ou bien scellée affectant de ce fait la perméabilité de la roche. La serpentinisation constitue l'exemple le plus représentatif de ce type de processus. En effet, la transformation des olivines et des

pyroxènes en serpentine lors de l'hydrothermalisme océanique s'accompagne d'une expansion très importante de la phase solide ($\Delta V \approx 30\text{-}55$ %) pouvant sceller les réseaux de pores et de microcracks présents dans la roche (Coleman, 1971; O'Hanley, 1992). Les expériences de serpentinisation réalisées par Farough et *al*., (2016) ont montré que la serpentinization d'une péridotite pré-fracturée s'accompagnait d'une baisse rapide et importante de la perméabilité (Fig. 21a) induite par le colmatage et le remplissage des joints de grains et des microcracks. Le phénomène inverse a également été étudié par Tenthorey et Cox (2003) (Fig. 21b). Ces auteurs ont démontré que la rétromorphose d'une serpentinite en péridotite s'accompagnait d'une augmentation importante de la perméabilité pouvant affecter significativement le transfert de fluide lors de la déshydratation des plaques plongeantes en zone de subduction.

Les rares études expérimentales (Moore et *al*., 1983; Tenthorey et Fitz Gerald, 2006) réalisées sur l'altération hydrothermale de roches granitiques ont été réalisés à partir d'un fluide simple composé d'eau déminéralisée et donc peu réactif. Ces études ont montré que les interactions entre ce fluide et les échantillons de granite pouvaient conduire à une baisse significative de la perméabilité induite par la précipitation d'argiles inhibant de ce fait la circulation de fluide à travers les roches granitiques (Fig. 21c). Cependant, les systèmes minéralisés péri-granitiques à W-Sn sont associés à des fluides plus complexes et plus acides dont les interactions avec les roches granitiques peuvent conduire à la formation d'une grande variété de roches métasomatiques telles que les greisens. Les transformations minéralogiques associés à ce type d'altération sont totalement différentes de celles obtenues lors des expériences réalisées par Moore et *al*., (1983) et par Tenthorey et Fitz Gerald (2006). Les résultats expérimentaux décrits précédemment ne s'appliquent donc pas au cas des greisens.

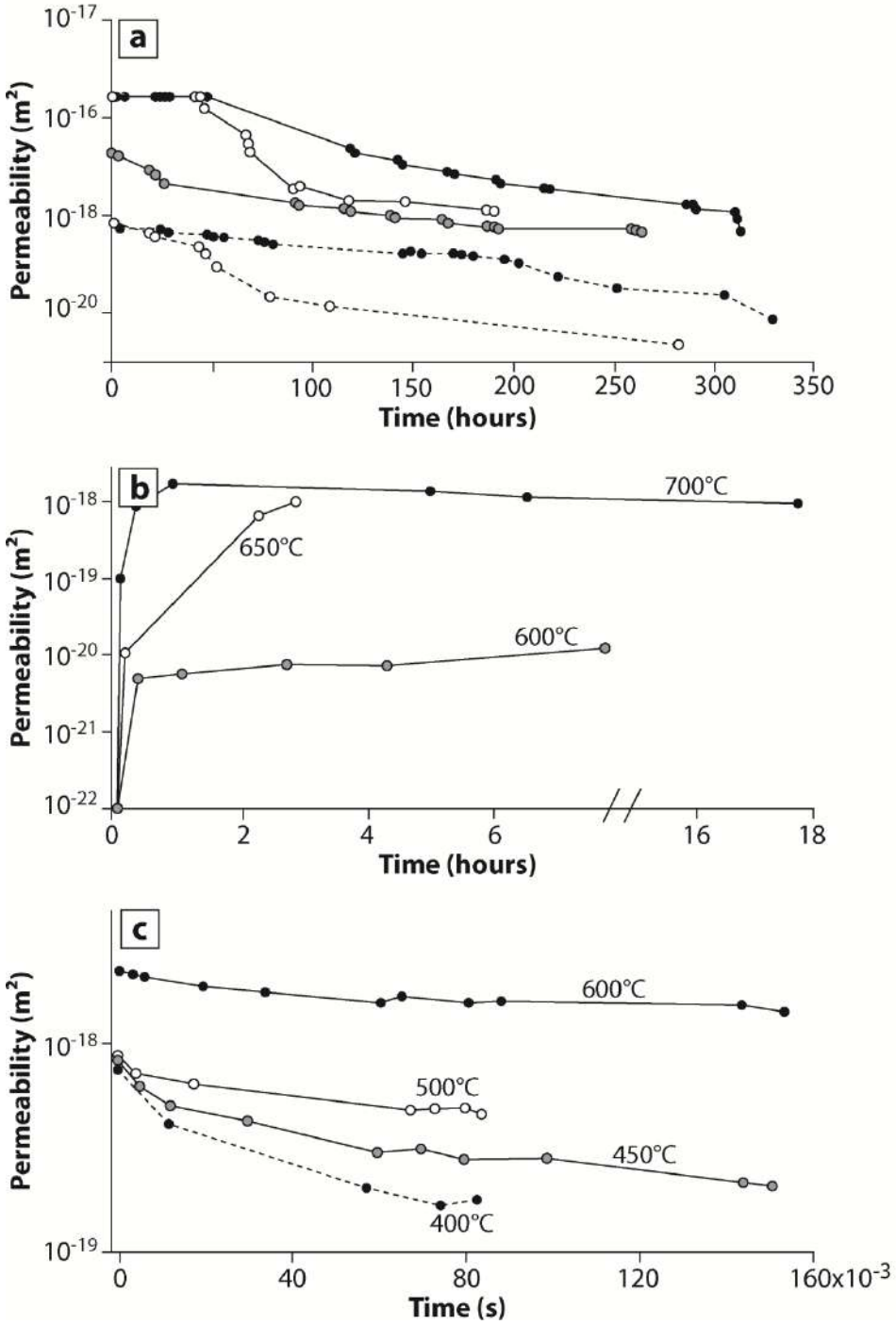

Figure 21 (a) Effet de la serpentinisation sur la perméabilité, ces expériences ont été réalisées à partir de différents échantillons de péridotite (d'après Farough et *al*., 2015). (b) Effet de la rétromorphose de la serpentine en olivine sur la perméabilité. Ces expériences ont été réalisées à différentes températures (d'après Tenthorey et Cox, 2003). (c) Effet de l'altération de type argile sur la perméabilité de roche granitique. Ces expériences ont été réalisées à différentes températures (d'après Tenthorey et Fitz Gerald, 2006).

3.2.4 Implications de la perméabilité dynamique lors de la circulation hydrothermale

Basée sur le couplage d'équations physiques et de paramètres physico-chimiques, la modélisation numérique représente un outil puissant pour étudier le processus de circulation hydrothermale autour et dans les intrusions granitiques, mais aussi pour prédire en temps et en espace les zones favorables à la minéralisation. Bien que la circulation hydrothermale péri-granitique ait fait l'objet de nombreux modèles numériques (Norton et Cathles, 1979; Cathles, 1977; Gerdes et *al*., 1998; Cui et al., 2001; Eldursi et *al*., 2009; Gruen et *al*., 2012 et 2014; Eldursi et *al*., 2018), le caractère dynamique de la perméabilité est rarement considéré dans ces études. Cependant, de récentes études (Weis et *al*., 2012 et 2015; Scott et Driesner, 2018) prenant en compte les couplages et les rétrocontrôles entre la déformation, les altérations hydrothermales et la perméabilité ont montré que le caractère dynamique de la perméabilité peut voir des effets majeurs sur l'organisation de la circulation hydrothermale, les flux et donc sur la localisation de la minéralisation.

Les modèles numériques réalisés par Weis et *al*., (2012) et (2015) sur les gisements de type porphyre ont montré que les conditions de surpression fluides induites par l'expulsion de fluides magmatiques sont indispensables à l'ouverture de structures perméables causant ensuite la focalisation et le piégeage des fluides minéralisateurs (Fig. 22a). Ces modèles démontrent également que la perméabilité dynamique est indispensable à la mise en place et à la stabilisation de fronts de précipitation des métaux dans les parties apicales des intrusions granitiques (Fig. 22a).

Les modèles réalisés récemment par Scott et Driesner (2018) ont démontré que la dissolution et la précipitation du quartz lors de la circulation hydrothermale péri-granitiques pouvaient affecter significativement la perméabilité de l'encaissant et donc les flux locaux en gérant de fortes hétérogénéités de perméabilité (Fig. 22b). En effet, les zones marquées par de fort taux de dissolution du quartz présentent des perméabilités élevées alors que les zones caractérisées par de fort taux de précipitation présentent de faibles perméabilités. Ces fortes hétérogénéités de perméabilité ont des effets majeurs sur les flux en entrainant la focalisation des décharges hydrothermales dans les zones plus perméables qui constituent de ce fait des zones favorables à la précipitation de métaux (Fig. 22b). Ces deux études démontrent qu'il est indispensable de considérer les différents couplages et rétrocontrôles entre perméabilité, déformation et altération hydrothermale

afin de développer des modèles numériques rendant compte de la complexité des systèmes hydrothermaux et suffisamment précis pour être utilisés comme outil prédictif.

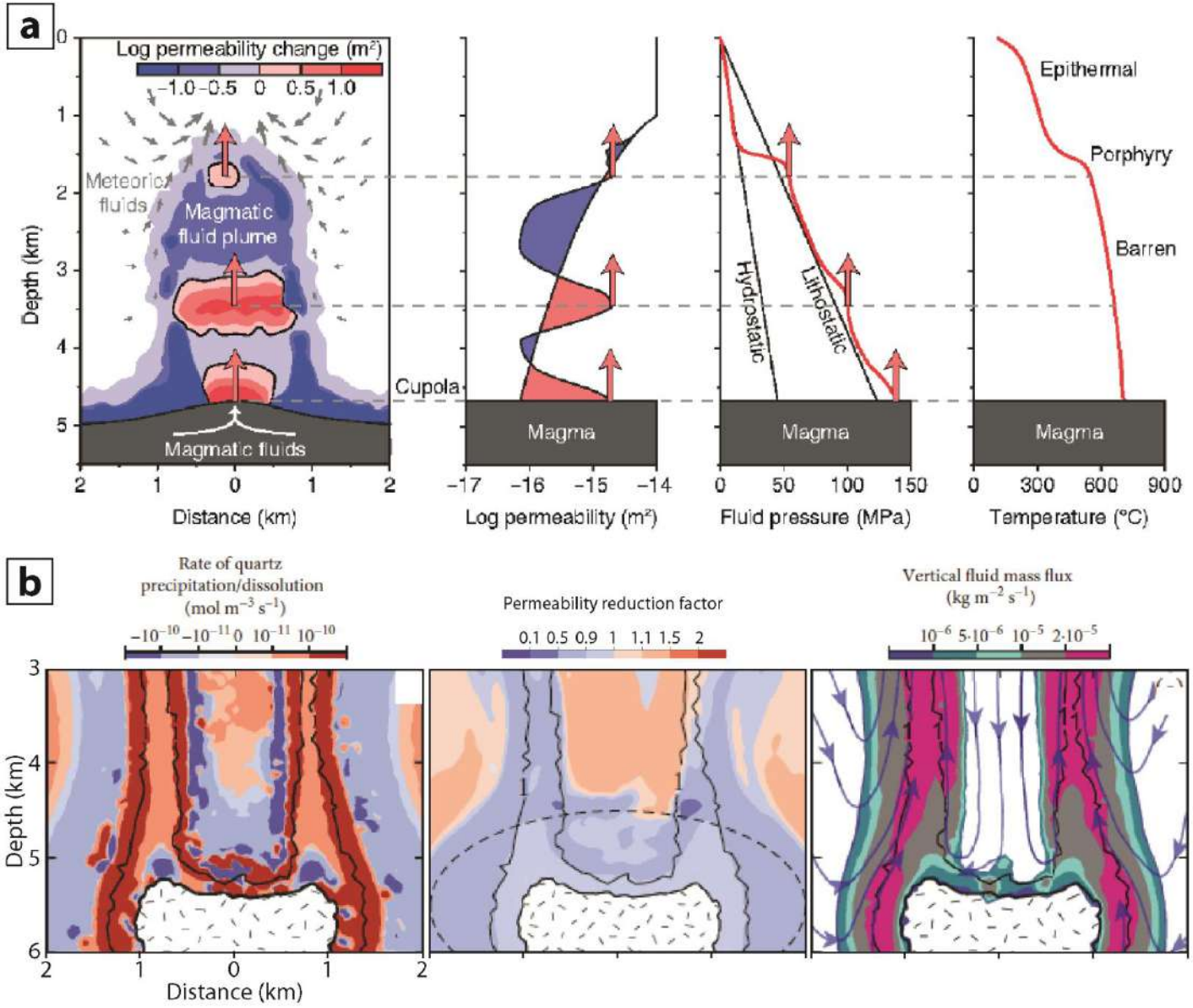

Figure 22 Exemples de modèles numériques prenant en compte certains processus mécaniques et chimiques ayant un effet significatif sur la perméabilité dynamique en environnement péri-granitique. (a) Effet de conditions de surpression fluide induite par l'expulsion de fluide magmatique sur la perméabilité de l'encaissant en contexte de porphyre cuprifère (d'après Weis et *al.*, 2012). (b) Effet de la précipitation et de la dissolution du quartz sur la perméabilité autour d'intrusions granitiques (d'après Scott et Driesner, 2018).

3.2.5 Processus pouvant affecter la perméabilité dans les gisements à W-Sn de type veine et greisen

Les nombreuses études minéralogiques et pétrologique réalisées sur les gisements de type veine et greisen ont montré que la greisenisation est souvent marquée par le développement de textures poreuses (Halter et *al*., 1996; Stemprok et *al*., 2014 ; Kontak et *al*., 2011). En effet, les rares mesures de porosité réalisées sur ce type de gisement montrent que la greisenisation s'accompagne d'une augmentation significative de la porosité totale et de la porosité connectée (Fig. 23) (Blecha et *al*., 2012; Machek et *al*., 2013; Müller-Huber et Börner, 2017). Cela suggère donc que les transformations minéralogiques impliquées lors de la greisenisation peuvent potentiellement affecter la perméabilité des intrusions granitiques via la génération de pores. Cette altération marquant la transition magmatique-hydrothermale peut donc constituer un processus majeur en améliorant la circulation des fluides et le transport des métaux dans un système initialement peu perméable.

A l'instar des systèmes de type porphyre, la formation des gisements de types veines et greisen est souvent associée à des conditions de surpression fluide lors de la transition magmatique-hydrothermal. De telles conditions peuvent être favorables à l'ouverture de structures perméables et donc à la formations des systèmes filoniens. Cependant, le rôle et l'existence de telles conditions de pression fluides restent à être démontré.

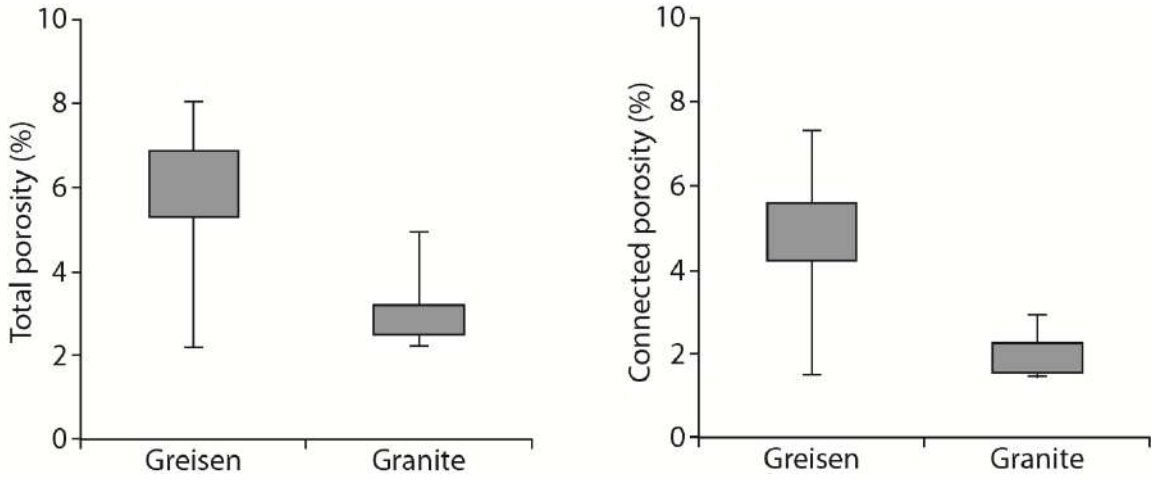

Figure 23 Gammes de porosité totale et de porosité connectée mesurées dans le greisen composant le complexe de Nebelstein (Autriche) (d'après Müller-Huber et Börner, 2017).

IV- Problématique et objectifs de cette étude

Comme mentionné précédemment dans l'état de l'art, la formation des gisements à W-Sn de type veine et greisen résulte de la succession de nombreux processus magmatiques et hydrothermaux dont la transition magmatique-hydrothermale représente un évènement charnière et décisif. Les caractéristiques pétrologiques et géochimiques des différents processus magmatiques ainsi que les sources et les caractéristiques physico-chimiques des fluides minéralisateurs ont fait l'objet de nombreuses études et sont donc relativement bien contraintes. En revanche, les aspects hydrodynamiques (vitesse et direction d'écoulement) ainsi que les aspects physiques de la circulation hydrothermale péri-granitique lors de la transition magmatique-hydrothermale demandent à être mieux contraint afin de proposer de nouveaux modèles métallogéniques prenant en compte la complexité de ces systèmes.

En effet, le transport des métaux lors de la circulation hydrothermale repose avant tout sur un processus physique qui est l'advection et dont l'efficacité dépend directement de la vitesse d'écoulement des fluides dans le système hydrothermal. Le manque de contrainte de terrain permet difficilement d'appréhender et d'évaluer en temps et espace les valeurs de vitesse d'écoulement des fluides impliqués dans le transport des métaux lors de la transition magmatique-hydrothermale. Celles-ci peuvent néanmoins être estimés grâce à une méthode réactualisée reposant sur l'étude des bandes de croissance minérale. En outre, cette méthode permet également de déterminer les paléo-directions d'écoulement qui constitue un autre paramètre majeur permettant, d'une part d'identifier les centres d'émanation des fluides minéralisateurs et de contraindre les gradients de pression qui représentent l'une des principales forces motrices impliquées lors de la circulation hydrothermale péri-granitique. De plus, le rôle exact des apex granitiques ainsi que les effets de la géométrie du toit des intrusions granitiques dans l'organisation des circulations hydrothermales et donc dans la localisation des minéralisations restent peu étudiés. Par ailleurs, la formation des gisements de type veine et greisen impliques des roches initialement peu perméables et donc peu favorable à l'extraction des fluides magmatiques, mais également peu favorable au développement d'un système hydrothermal péri-granitique permettant la formation de gisements économiques. Face à ce paradoxe, il apparait donc clairement que la perméabilité constitue un paramètre dynamique évoluant au gré de la déformation et des altérations hydrothermales. En effet,

des conditions de surpression fluides lors de l'ouverture des veines ainsi que la porosité générée lors de la greisenisation sont susceptibles d'améliorer significativement la perméabilité des roches lors de la formation des gisements de type veine et greisen. Cependant, les effets et les implications de ces différents rétrocontrôles demandent à être déterminés.

Se posent alors les questions suivantes :

- **Quels sont les contrôles structuraux de la minéralisation filonienne de Panasqueira ? Quel est leur lien avec le contexte structural et géologique régionale ?**
- **Comment s'organise la circulation hydrothermale péri-granitique lors de la transition magmatique-hydrothermale ? Quels sont les effets des apex granitiques dans la focalisation des décharges hydrothermales ?**
- **Quels sont les rétrocontrôles entre pression fluide et l'ouverture des veines lors de la transition magmatique-hydrothermale ?**
- **Quelles sont les relations génétiques entre les minéralisations filoniennes à W-Sn et les altérations de type greisen ?**
- **Quels sont les effets de la greisenisation sur la perméabilité et donc sur la circulation des fluides minéralisateurs au sein des intrusions granitiques ?**
- **Quels sont les implications d'un tel rétrocontrôle sur l'extraction des fluides magmatiques et la focalisation de décharges hydrothermales ?**
- **Comment et quand interviennent les différents modes (expulsion et convection) de circulation lors de l'hydrothermalisme péri-granitique ? Quelles sont les relations entre ces différents modes de circulation et les différentes phases minéralisatrices ?**

Cette étude a pour objectif d'apporter des éléments de réponse à ces différentes questions en employant une approche pluridisciplinaire couplant : (i) travail de terrain (étude structurale et étude pétrologique de la greisenisation) (**Chapitre II**) (ii) reconstruction des paléo-circulation hydrothermale lors de la transition magmatique-hydrothermale via l'analyse texturale des bandes de croissance minérale (**Chapitre III**), (iii) étude pétrologique et géochimique des relations génétiques entre greisenisation et minéralisations filonienne (**Chapitre IV**), (iv) détermination expérimentale des effets de

la greisenisation sur les caractéristiques pétrophysiques des roches (porosité densité et perméabilité) (**Chapitre V**) et (v) modélisation numérique de la circulation hydrothermale péri-granitique intégrant l'évolution de la perméabilité dynamique lors des interactions fluide-roche ainsi que la production de fluide magmatique lors de la transition magmatique-hydrothermale (**Chapitre VI**). Ce travail de recherche est centré sur le cas du gisement à W-Sn-(Cu) de Panasqueira. Ce gisement de classe mondiale encore exploité aujourd'hui constitue un exemple de référence pour étudier les processus magmatiques et hydrothermaux conduisant à la formation d'un gisement à W-Sn de grande taille. En effet, en raison des nombreux travaux miniers (galeries) et des nombreuses campagnes de forages le gisement de Panasqueira offre des conditions d'affleurement exceptionnelles facilitant l'observation des structures minéralisées, des faciès d'altérations, des relations génétiques entre intrusions granitiques et le réseau de veine. Ce gisement a donc fait l'objet de nombreuses études géochimiques, minéralogiques (Thadeu, 1951; Clark, 1964; Kelly and Rye, 1979; Bussink, 1984; Snee et al., 1988; Polya, 1988 et 1989; Polya et *al*., 2000; Noronha et *al*., 1992; Lüders, 1996; Lourenço, 2002) et structurales (Foxford et *al*., 1991 et 2000; Jacques et *al*., 2017) visant à contraindre les conditions de formation, les sources et les caractéristiques géochimiques des fluides associées à la minéralisation à W-Sn de Panasqueira. Fort de ces données et des contraintes hydrodynamiques et géologiques apportées par cette étude, un modèle métallogénique de formation du gisement de Panasqueira prenant à la fois en compte la physique des écoulements ainsi que les caractéristiques géochimiques des fluides sera proposé à la fin de cette étude (**Chapitre VI**). Les résultats obtenus au cours de cette étude sont présentés à travers 5 chapitres principalement rédigés sous la forme d'article scientifique.

References

A-B

Audétat, A., Günther, D. & Heinrich, C. A. 2000 - Magmatic-hydrothermal evolution in a fractionating granite: A microchemical study of the Sn-W-F-mineralized Mole Granite (Australia) - Geochimica et Cosmochimica Acta, 64, pp.3373-3393.

Blecha, V., Stemprok, M. 2012. Petrophysical and geochemical characteristics of late Variscan granites in the Karlovy Vary Massif (Czech Republic) – implications for gravity and magnetic interpretation at shallow depths. Journal of Geosciences. 65 - 85.

Booden, M.A., Mauk, J.L., Simpson, M.P. 2011. Quantifying Metasomatism in Epithermal Au-Ag Deposits: A Case Study from the Waitekauri Area, New Zealand. *Economic Geology* ; 106 (6): 999–1030.

Brace, W. (1984). Permeability of crystalline rocks : New in situ measurements. *Journal of Geophysical Research : Solid Earth*, 89(B6) :4327–4330.

Breiter, K., Müller, A., Leichmann, J., Gabašová, A., 2005. Textural and chemical evolution of a fractionated granitic system: the Podlesí stock, Czech Republic. Lithos 80, 323–345.

Bryzgalin, O.V., 1976, On the solubility of tungstic acid in aqueous salt solutions at high temperatures: Geochemistry International, v. 13, p. 155–159.

Bryzgalin, O.V., Ivanova, G.F., Studenikova, Z.V., Shcherbina, A.N. 1971. Tungsten and Molybdenum in Post-magmatic Processes. In: Geokhimja volframa i molibdena, pp 63-80. Moscow, Nauka.

Burnham, C.W., and Ohmoto, H., 1980, Late-stage processes of felsic magmatism. In: Ishihara, S., and Takenouchi, S. (Eds.), Granitic magmatism and related mineralization: Tokyo, Japan, Mining Geology Special Issue 8, pp. 1–11.

Bussink, R.W. 1984. Geochemistry of the Panasqueira Tungsten-Tin Deposit, Portugal. Geol. Ultraiectina.

C

Cathles L.M. 1977. An analysis of the cooling of intrusives by Ground-Water convection which including boiling. Econo. Geol. 77. 804-826.

Černý, P., Blevin, P.L., Cuney, M. and London, D. 2005. Granite-Related Ore Deposits. In: J.W. Hedenquist, J.F.H. Thompson, R.J. Goldfarb, and J.R. Richards (eds.). Economic Geology - One Hundredth Anniversary Volume, 337–370.

Chappell, B. W. & White, A. J. R. 1992 - I- and S-type granites in the Lachlan Fold Belt - Transactions of the Royal Society of Edinburgh, 83, pp.1-26

Chelle-Michou, C., Rottier, B., Caricchi, L. and Simpson, G. 2017. Tempo of magma degassing and the genesis of porphyry copper deposits. Nature Scientific Reports 7, Article number: 40566.

Chi, G. Xue, C. 2011. An overview of hydrodynamic studies of mineralization. GEOSCIENCE FRONTIERS 2(3) (2011) 423-438.

Clark, A. H. 1964. Preliminary study of the temperatures and confining pressures of granite emplacement and mineralization, Panasqueira, Portugal: Inst. Mining MetallurgyTrans., 73, 813-824.

Clark, C., Fitzsimmons, I.C.W., Healy, D., 2011. How does the continental crust get really hot? Elements 7, 235–240.

Coelho, G., Branquet, Y., Sizaret, S., Arbaret, L., Champallier, R., Rozenbaum, O. 2015. Permeability of sheeted dykes beneath oceanic ridges: Strain experiments coupled with 3D numerical modeling of the Troodos Ophiolite, Cyprus. Tectonophysics, Elsevier, 2015, 644-645, pp.138-150.

Coleman, R. G. 1971. Petrologic and geophysical nature of serpentinites, Geol. Soc. Am. Bull., 82(4), 897–918.

Commission européenne 2014. Mémo 14/377.

Cox, S.F., 2002, Fluid flow in mid- to deep crustal shear systems: Experimental constraints, observations on exhumed high fluid flux shear systems, and implications for seismogenic processes: Earth Planets Space, v. 4, p.1121−1125.

Cox, S.F., 2010. The application of failure mode diagrams for exploring the roles of fluid pressure and stress states in controlling styles of fracture-controlled permeability enhancement in faults and shear zones Geofluids 10, 217–233.

Cui, X., Nabelek, P.I., Liu, M. 2001. Heat and fluid flow in contact metamorphic aureoles with layered and transient permeability, with application to the Notch Peak aureole, Utah. JOURNAL OF GEOPHYSICAL RESEARCH, VOL. 106, NO. B4, PAGES 6477-6491.

D

Denisenko, V.K., Rundquist, D.V. 1986. Tungsten-bearing zones and provinces of the world. Geology of Tungsten, UNESCO publication chapter.

Derré, C. 1982. Caractéristiques de la distribution des gisements à étain-tungstène dans l'ouest de l'Europe. Mineral. Deposita 17:55-77.

Dolejs, D., 2015. Quantitative characterization of hydrothermal systems and reconstruction of fluid fluxes: the significance of advection, disequilibrium, and dispersion. SGA proceedings 13th SGA Biennial Meeting.

E

Eldursi, K., Branquet, Y., Guillou-Frottier, L., Marcoux, E. 2009. Numerical investigation of transient hydrothermal processes around intrusions: Heat-transfer and fluid-circulation controlled mineralization patterns. Earth and Planetary Science Letters 288, 70-83.

Eldursi, K., Branquet, Y., Guillou-Frottier, L., Martelet, G., Calcagno, P. 2018 Intrusion-Related Gold Deposits: new insights from gravity and hydrothermal integrated 3D modeling applied to the Tighza gold mineralization (Central Morocco) Journal of African Earth Sciences.

Evans, J. P., Forster, C. B., and Goddard, J. V. 1997. Permeability of fault-related rocks, and implications for hydraulic structure of fault zones. *Journal of structural Geology*, 19(11):1393–1404.

F

Farough, A. 2015. An experimental study on characterization of physical properties of ultramafic rocks and controls on evolution of fracture permeability during serpentinization at hydrothermal conditions, PhD dissertation, 95 pp., Va. Tech, Blacksburg.

Farough, A., D. E. Moore, D. A. Lockner, and R. P. Lowell 2016. Evolution of fracture permeability of ultramafic rocks undergoing serpentinization at hydrothermal conditions: An experimental study, Geochem. Geophys. Geosyst., 17, 44–55.

Foster R. P. 1977. Solubility of scheelite in hydrothermal chloride solutions. Chem. Geol. 20, 27-43.

Förster, H.-J., Tischendorf, G., Trumbull, R.B., Gottesmann, B., 1999. Late-collisional granites in the Variscan Erzgebirge, Germany. Journal of Petrology 40, 1613–1645.

Foxford, K.A., Nicholson, R., Polya, D.A., 1991a. Textural evolution of W-Cu-Sn bearing hydrothermal quartz veins at Minas da Panasqueira, Portugal. Mineralogical Magazine 55, 435-445.

Foxford, K.A., Nicholson, R., Polya, D.A., Hebblethwaite, R.P.B. 2000. Extensional failure and hydraulic valving at Minas da Panasqueira, Portugal: Evidence from vein spatial distributions, displacements and geometries. J. Struct. Geol. 22, 1065–1086.

G

Gerdes, M.L., Baumgartner, L.P., Person, M., 1998. Convective fluid flow through heterogeneous country rocks during contact metamorphism. J. Geophys. Res. 103, 23,983–24,003.

Gloaguen, E., Branquet, Y., Chauvet, A., Bouchot, V., Barbanson, L. and Vigneresse, J.L. 2014. Tracing the Magmatic/Hydrothermal Transition in Regional Low-Strain Zones: The Role of Magma Dynamics in Strain Localization at Pluton Roof, Implications for Intrusion-Related Gold Deposits. Journal of Structural Geology 58: 108–121.

Gruen, G., Weis, P., Driesner, T., deRonde, C.E.J., Heinrich, C.A., 2012. Fluid-flow patterns at Brothers volcano, southern Kermadec arc: insights from geologically constrained numerical simulations. Econ. Geol.107 (8), 1595–1611.

Gruen, G., Weis, P., Driesner, T., Heinrich, C.A., De Ronde, C.E.J. 2014.Hydrodynamic modeling of magmatic–hydrothermal activity at submarine arc volcanoes, with implications for ore formation. Earth and Planetary Science Letters 404 (2014) 307–318

Guillou-Frottier, L., Burov, E. 2003. The development and fracturing of plutonic apexes: implications for porphyry ore deposits. Earth & Planetary Science Letters, 214, 341-356.

H

Hall, A. 1971. Greisenisation in the granite of Cligga Head, Cornwall. Proceedings of the Geologists' Association 82(2).

Halter, W.E., Williams-Jones, A.E., Kontak, D.J. 1996. The role of greisenization in cassiterite precipitation at the East Kemptville tin deposit, Nova Scotia. *Economic Geology*, 91 (2): 368–385.

Halter, W.E., Williams-Jones, A.E., Kontak, D.J. 1998. Origin and evolution of the greisenizing fluid at the East Kemptville tin deposit, Nova Scotia, Canada. *Economic Geology*, 93 (7): 1026–1051

Halter, W.E., Webster, J.D. 2004. The magmatic to hydrothermal transition and its bearing on ore-forming systems-Preface. Chemical Geology, 210(1): 1-6.

Harlaux, M., 2016. Tungsten and rare-metal (Nb, Ta, Sn) hydrothermal metallogenic systems in the late-variscan orogenic context: example of the French Massif Central (Doctoral dissertation, Université de Lorraine).

Heinrich, C. 1996. Oral communication.

I

Ingebritsen, S.E., Appold, M.S. 2012. The physical hydrogeology for ore deposits. Econ Geol 107:559–584

Ingebritsen, S. E., Gleeson, T., 2015 Crustal permeability: Introduction to the special issue. Geofluids, Volume15, Issue1-2

Ingebritsen, S.E., Manning, C.E. 1999. Geologic implications of a permeability–depth curve for continental crust. Geology 27, 1107–1110.

Ivanova, G.F., 1966, Thermodynamic evaluation of the possibility of tungsten transport as halogen compounds: Geochemistry International, v. 2, p. 964–973.

Ivanova, G.F., and Khodakovsky, I.L., 1968, Transport of tungsten in hydrothermal solutions: Geochemistry, v. 5, p. 779–780.

Ishihara, S. 1977 - The magnetite-series and ilmenite-series granitic rocks - Mining Geology, 27, pp.293-305.

ITIA, 2015. Tungsten, Global Industry, Markets & Outlook.

J

Jébrak M., Marcoux E., 2008. Géologie des ressources minérales. Géologie Québec. 685p.

Jamtveit, B., Malthe-Sørenssen, A., Kostenko, O. 2008. Reaction enhanced permeability during retrogressive metamorphism. Earth and Planetary Science Letters. Volume 267, Issues 3–4, 620-627.

Jonas, L., John, T., King, H.E., Geisler, T., Putnis,A. 2014. The role of grain boundaries and transient porosity in rocks as fluid pathways for reaction front propagation. Earth and Planetary Science Letters, Volume 386, 64-74.

K

Kelly, W.C., Rye, R.O. 1979. Geologic, fluid inclusion and stable isotope studies of the tin-tungsten deposits of Panasqueira, Portugal. Econ Geol 74:1721–1822

Kontak, D.J. & Kyser, K. 2011. A fluid inclusion and isotopic study of an intrusion-related gold deposit (IRGD) setting in the 380 Ma South Mountain Batholith, Nova Scotia, Canada: evidence for multiple fluid reservoirs. Miner. Deposita, Volume 46, Issue 4, pp 337–363.

Korges, M., Weis, P., Lüders, V., Laurent, O. 2018. Depressurization and boiling of a single magmatic fluid as a mechanism for tin-tungsten deposit formation. Geology, January 2018; v. 46; no. 1; p. 75–78.

L

Lecumberri-Sanchez, P., Vieira, R., Heinrich, C.A., Pinto, F., Wälle, M. 2017. Fluid-rock interaction is decisive for the formation of tungsten deposits. Geology 45, 579–582.

Lee, D.C., Halliday, A.N. 1995. Hafnium-tungsten chronometry and the timing of terrestrial core formation. Nature, 378, 771-774.

Legros, H. 2017. Les systèmes métallogéniques hydrothermaux à tungstène et métaux rares (Nb-Ta-Li-Sn) de la période Jurassique-Crétacé au sud de la province de Jiangxi (Chine). Sciences de la Terre. Université de Lorraine. Français.

Lehmann, B., 1990. Metallogeny of Tin. Springer-Verlag, Berlin (211 pp.).

Linnen RL, Pichavant M, Holtz F, Burgess S (1995) The effect of fO2 on the solubility, diffusion, and speciation of tin in haplogranitic melt at 850 °C and 2 kbar. Geochim Cosmochim Acta 59: 1579-1588.

Linnen, R.L., Pichavant, M., Holtz, F., 1996. The combined effects of fO2 and melt composition on SnO2 solubility and tin diffusivity in haplogranitic melts. Geochimica et Cosmochimica Acta 60, 4965–4976.

Linnen, R. L. 1998 - Depth of emplacement, fluid provenance and metallogeny in granitic terranes: a comparison of western Thailand with other tin belts - Mineralium Deposita, 33, pp.461-476.

Linnen, R.L., Keppler, H., 1997. Columbite solubility in granitic melts: consequences for the enrichment and fractionation of Nb and Ta in the Earth's crust. Contributions to Mineralogy and Petrology 128, 213– 227. doi:10.1007/s004100050304.

London, D., Hervig, R.L., Morgan VI, G.B. 1988. Melt – vapor solubilities and elemental partitioning in peraluminous granite – pegmatite systems: experimental results with Macusani glass at 200 MPa. Contrib. Mineral. Petrol. 99, 360– 373.

Lourenço A.A.M.M.A. 2002. Paleoíluidos e mineralizações associadas às fases tardias da Orogenia Hercínica.Tese submetida à Faculdade de Ciências da Universidade do Porto para obtenção do grau de Doutor em Geologia.

Lüders, V., 1996. Contribution of infrared microscopy to fluid inclusion studies in some opaque minerals (Wolframite, Stibnite, Bournonite) : Metallogenic implications. Economic Geology, Vol. 91, 8, 1462-1468.

Luijendijk E, Gleeson T (2015) How well can we predict permeability in sedimentary basins? Deriving porositypermeability algorithms for non-cemented sand and clay mixtures. Geofluids, 15, B04203, 67–83.

M

Machek, M., Roxerová, Z., Janoušek, V., Staněk, M., Petrovský, E., René, M. 2013. Petrophysical and geochemical constraints on alteration processes in granites. Stud Geophys. Geod., Volume 57, Issue 4, pp 710–740.

Manning, C.E., Ingebritsen, S.E., 1999. Permeability of the continental crust: implications of geothermal data and metamorphic systems. Rev. Geophys. 37, 127–150.

Moeck, I. S. 2014. Catalog of geothermal play types based on geologic controls. *Renewable and Sustainable Energy Reviews*, 37 :867–882.

Moore, D., Morrow, C., Byerlee, J.D. 1983. Chemical reactions accompanying fluid flow through granite held in a temperature gradient. Geochimica et Cosmochimica Acta. 47. 445-453.

Moore, J.C., Saffer, D.M. 2001.Updip limit of the seismogenic zone beneath the accretionary prism of southwest Japan: an effect of diagenetic to low-grade metamorphic processes and increasing effective stress. Geology, 29: 183-186.

Müller, A., Halls, C., 2005. Rutile – the tin–tungsten host in the intrusive tourmaline breccia at Wheal Remfry, SW England. In: Mao, J., Bierle F.P. (Eds.), Mineral Deposit Research: Meeting the Global Challenge. Proceedings of the Eighth Biennial SGA Meeting. Springer Berlin Heidelberg, pp 441–444.

Müller-Hubner, E., Börner, F. 2017. Multi-parameter petrophysical charcaterization of Variscan greisen rocks from the Southern Bohemian Batholith (Austria) and the Eastern Erzgebirge Volcano-Plutonic Complex (Germany). Austrian Journal of Earth Sciences, Vol. 110/1, 78-100.

N

Naumov, V.B., Dorofeev, V.A., Mironova, O.F., 2011. Physicochemical parameters of the formation of hydrothermal deposits: a fluid inclusion study. I. Tin and tungsten deposits. Geochemistry International 49, 1002-1021.

Newsom, H. E. 1990. Accretion and core formation in the Earth: Evidence from siderophile elements. In Origin of the Earth (eds. H. E. Newsom and J. H. Jones) pp. 273–288, Oxford University Press, Oxford.

Newsom, H. E., Sims, K.W.W., Noll, Jr. P.D., Jaeger, W. L., Maehr, S. A., and Bessera, T.B. 1996. The depletion of W in the bulk silicate Earth. Geochm. Cosmochim. Acta 60, 1155–1169.

Noronha, F., Doria, A., Dubessy, J., Charoy, B., 1992. Characterization and timing of the different types of fluids present in the barren and ore-veins of the W-Sn deposit of Panasqueira, Central Portugal. Mineralium Deposita 27, 72-79. doi:10.1007/BF00196084

Norton, D., Cathles, L.M. 1979. Thermal aspects of ore deposition. In: Barnes, H.L. (Ed.), Geochemistry of Hydrothermal Ore Deposits, second ed. John Wiley and Sons, New York, pp. 611e631.

O

Oelkers EH (1997) Physical and chemical properties of rocks and fluids for chemical mass transport calculations. Rev Min 34:131-191.

O'Hanley, D. S. 1992, Solution to the volume problem in serpentinization, Geology, 20(8), 705–708.

O'Neill, H. St. C. 1991. The origin of the Moon and the early history of the Earth. A chemical model. Part 2: The Earth. Geochmi. Cosmochim. Acta 55, 1159-1172.

P

Pichavant, M., 1981. An experimental study of the effect of boron on a water-saturated haplogranite at 1 Kbar vapour pressure. Contributions to Mineralogy and Petrology 76, 430-439.

Pirajno, F. 1992. Greisen systems. In: Hydrothermal Mineral Deposits. Springer, Berlin, Heidelberg, 280-324.

Pirajno, F., 2009. Skarn systems. In Hydrothermal Processes and Mineral Systems (pp. 535580). Springer Netherlands.

Pollard, P.J. Granites and related tungsten deposits. Personal communication.

Pollard, P.J., Taylor, R.G., Cuff, C. 1988. Genetic Modelling of Greisen-Style Tin Systems. In: Hutchison C.S. (eds) Geology of Tin Deposits in Asia and the Pacific. Springer, Berlin, Heidelberg, pp 59-72.

Pollok, K., Putnis, C.V., Putnis, A. 2011. Mineral replacement reactions in solid solution-aqueous solution systems: Volume changes, reactions paths and end-points using the example of model salt systems. Am J Sci March 2011 311:211-236.

Polya, D.A. 1989. Chemistry of the main-stage ore-forming fluids of the Panasqueira WCu(Ag)-Sn deposit, Portugal: implications for models of ore genesis. Econ. Geol. 84, 1134–1152.

Polya, D.A. 1988a, Efficiency of hydrothermal ore formation and the Panasqueira W-Cu-(Ag)-Sn vein deposit: Nature, v. 333, p. 838-841.

Polya, D.A., Foxford, K.A., Stuart, F., Boyce, A., Fallick, A.E. 2000. Evolution and paragenetic context of low δD hydrothermal fluids from the Panasqueira W-Sn deposit, Portugal: New evidence from microthermometric, stable isotope, noble gas and halogen analyses of primary fluid inclusions. Geochim. Cosmochim. Acta 64, 3357–3371.

Putnis, A. 2002. Mineral replacement reactions: from macroscopic observations to microscopic mechanisms. *Mineralogical Magazine*, 66 (5): 689–708.

Putnis, A., Austrheim, H. 2010. Fluid-induced processes: metasomatism and metamorphism. Geofluids, 10: 254-269.

Putnis, A. and John, T. 2010. Replacement processes in the earth's crust. Elements: an international magazine of mineralogy, geochemistry, and petrology. 6 (3): pp. 159-164.

Putnis, A. 2015. Transient Porosity Resulting from Fluid–Mineral Interaction and its Consequences. *Reviews in Mineralogy and Geochemistry*, 80 (1): 1–23.

R

Richards, J.P., and Tosdal, R.M., 2001, Preface: Reviews in Economic Geology, v. 14, p. vi.

Robb, L. 2005. Introduction to Ore-forming Processes. Blackwell Publishing, Malden, MA, 373 p.

Rusk, B., Reed, M., Dilles, J.H., Klemm, L., and Heinrich, C.A., 2004, Compositions of magmatic hydrothermal fluids determined by LA-ICP-MS of fluid inclusions from the porphyry copper-molybdenum deposit at Butte, Montana: Chemical Geology, v. 210, p. 173–199.

S

Schatz, O.J., Dolejs, D., Stix, J., Williams-Jones, A.E., Layne, G.D. 2004. Partitioning of boron among melt, brine and vapor in the system haplogranite–H2O–NaCl at 800 °C and 100 MPa. Chemical Geology 210 (2004) 135– 147.

Schröcke, H., Trumm, A., and Hochleitner, R., 1984, Über den Transport von Wolfram und den Absatz von Wolfram-Doppel-Oxiden in fluiden wässrigren Lösungen: Geochimica et Cosmochimica Acta, v. 48, p. 1791–1805.

Scott, S.W. and Driesner, T. 2018. Permeability Changes Resulting from Quartz Precipitation and Dissolution around Upper Crustal Intrusions. Geofluids, Volume 2018, Article ID 6957306, 19 pages.

Shcherba, G. N. 1970. Greisens. Int Geol Rev 12: 114–255

Sibson, R.H. 1992. Implications of fault-valve behaviour for rupture nucleation and recurrence. Tectonophysics, 211, 283–93.

Sibson, R. H. 1996. Structural permeability of fluid-driven fault-fracture meshes. *Journal of Structural Geology*, 18(8):1031–1042.

Sibson, R. H. 2001, Seismogenic framework for hydrothermal transport and ore deposition: Reviews in Economic Geology, v. 14, p. 25−50.

Sibson, R.H., and Rowland, J.V., 2003, Stress, fluid pressure, and structural permeability in seismogenic crust, North Island, New Zealand: Geophysical Journal International, v. 154, p. 584−594.

Snee, L.W., Sutter, J.F., Kelly, W.C. 1988. Thermochronology of economic mineral deposits; dating the stages of mineralization at Panasqueira, Portugal, by high-precision 40Ar/39Ar age spectrum techniques on muscovite. Econ Geol 83:335–354

Sonney, R. and Vuataz, F.-D. 2009. Numerical modelling of alpine deep flow systems: a management and prediction tool for an exploited geothermal reservoir (lavey-les-bains, switzerland). *Hydrogeology Journal*, 17(3): 601–616.

Stemprok, M. 1981. Tin and tungsten deposits of the west-central European Variscides. Proceedings of the fifth quadrennieal IAGOD Symposium.

Stemprok, M. 1987. Greisenization (a review). Geol Rundsch , Springer-Verlag 76: 169.

Štemprok, M., Dolejš, D., Holub, F.V. 2014. Late Variscan calc-alkaline lamprophyres in the Krupka ore district, Eastern Krušné hory/Erzgebirge: their relationship to Sn-W mineralization. Journal of Geosciences, volume 59, issue 1, 41 – 68.

T

Taylor, R.G. 1979. Geology of tin deposits. Developments in economic geology, Volume 11, Elsevier, 543p.

Tenthorey, E., Cox, S. 2003. Reaction-enhanced permeability during serpentine dehydration. Geology. 31. 10.1130/G19724.1.

Tenthorey, E., Gerald, J.D., 2006. Feedbacks between deformation, hydrothermal reaction and permeability evolution in the crust: Experimental insights. Earth Planet. Sci. Lett. 247, 117-129.

Thadeu, D. 1951. Geologia do couto mineiro da Panasqueira. Comunic Serv Geol Port 32:5–64.

Thompson AB (1997) Flow and focusing of metamorphic fluids. In Jamtveit B, Yardley B (eds) Fluid flow and transport in rocks. Mechanisms and effects. Chapman & Hall, London, p 299-314.

U-W

USGS, 2018. Tungsten. Mineral Commodity Summaries. 178-179.

Walter, B. 2016. Réservoirs de socle en contexte extensif : genèse, géométries et circulations de fluides : exemples du rift intracontinental du lac Albert (Ouganda) et de la marge proximale d'Ifni (Maroc). PhD thesis, Université de Lorraine.

Weis P, Driesner T, Heinrich C.A., 2012. Porphyry-copper ore shells form at stable pressure-temperature fronts within dynamic fluid plumes. Science, 338, 1613–6.

Weis, P. 2015. The dynamic interplay between saline fluid flow and rock permeability in magmatic hydrothermal systems. Volume15, Issue1-2.

Wesolowski, D., Drummond, S.E., Mesmer, R.E., and Ohmoto, H., 1984, Hydrolysis equilibria of tungsten(VI) in aqueous sodium chloride solutions to 300°C: Inorganic Chemistry, v. 23, p. 1120–1132.

Wood, S.A., and Vlassopoulos, D., 1989, Experimental determination of the hydrothermal solubility and speciation of tungsten at 500°C and 1 kb: Geochimica et Cosmochimica Acta, v. 53, p. 303–312.

Wood, S.A., 1990a, Do tungsten chloride complexes contribute to the genesis of hydrothermal tungsten deposits? [abs.]: Goldschmidt Conference, 2nd, Baltimore, Maryland, May 2–4, 1990, Abstract Volume, p. 92.

Wood, S.A. 1992. Experimental determination of the solubility of WO3(s) and the thermodynamic properties of H2WO4(aq) in the range 300–600°C at 1 kbar: Calculation of scheelite solubility, Geochimica et Cosmochimica Acta, Volume 56, Issue 5, Pages 1827-1836.

Wood, S.A., Samson, I.M. 2000. The Hydrothermal Geochemistry of Tungsten in Granitoid Environments: I. Relative Solubilities of Ferberite and Scheelite as a Function of T, P, pH, and *m*NaCl. *Economic Geology* Vol. 95, 2000, pp. 143–182.

Z

Zaraisky, G.P., Stoyanovskaya, F.M. 1995. Experimental modeling of gain and loss of rare metals (W, Mo, Sn) during greisenization and alkalic metasomatism of leucocratic granite. Experiment in Geosciences, No. 4, pp 19-21.

Zhang, S., Cox, S.F., Paterson, M.S., 1994a. The influence of room temperature deformation on porosity and permeability in calcite aggregates. J. Geophys. Res. 99, 15761-15775.

Chapter II Geological and structural setting of the W-Sn-(Cu) Panasqueira ore deposit

I- Geology and metallogeny of the Iberian Massif

1. The European Variscan belt

The European Variscan belt corresponds to the eastern part of a large Paleozoic belt extending on both sides of the Atlantic Ocean. The Variscan belt formed during the late Paleozoic (late Devonian to Carboniferous, 370-290 Ma) and resulted from the convergence and the collision of two major paleocontinents, the Gondwana to the South and the Laurussia (Avalonia, Baltica and Siberia) to the North that caused ultimately the formation of the Pangea (Fig. 1) (Matte, 1986 et 2001; Kroner et Romer, 2013).

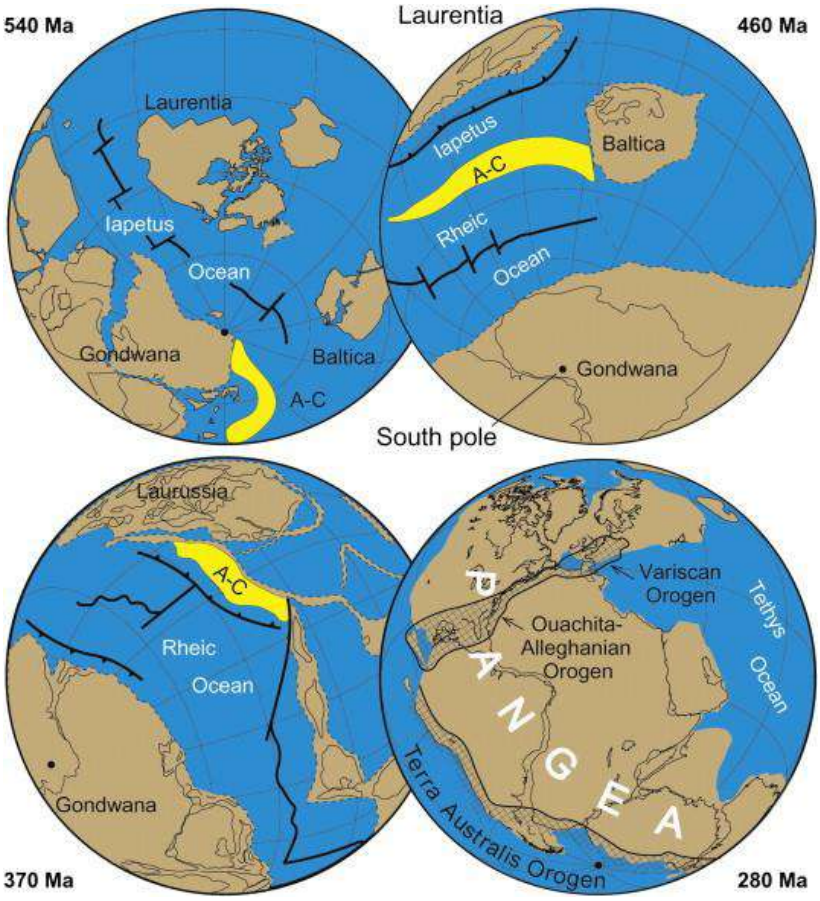

Figure 1 Paleogeographic reconstructions of the Variscan orogeny (adapted by Nance et *al.*, 2012 from Scotese, 1997; Cocks and Torsvik, 2002; Stampfli and Borel, 2002). A-C correspond to the Avalonia micro-continent.

The European Variscan Belt extends over 3000 km for 700-800 km of width and outcrops in several isolated massifs like the Iberian Massif, the Armorican Massif, the Cornwall, the French Massif Central, the Ardennes, the Bohemian Massif, the Alpine External Crystalline Massif, and the Corso-Sarde Massif (Fig. 2a) (Matte, 2001; Faure et *al.*, 2009; Martínez Catalán et *al.*, 2009; Kroner et Romer, 2013; Ballèvre et *al.*, 2014; Diez Fernández et *al.*, 2016). Petro-structural, geophysical and paleontological studies have highlighted the implication of several Gondwana-derived microcontinents like

Avalonia and Armorica during the Variscan orogeny (Cocks et Fortey 1982; Van der Voo 1983; Perroud 1985; Paris et Robardet 1990 et 1994). The occurrence of several oceanic sutures (Iapetus and Rheic Ocean) through the European Variscan Belt is consistent with the existence of these microcontinents and emphasizes that the Variscan belt encompasses a polyphased history that integrates several collision stages (Abalos et *al*., 2002; Martínez Catalán et *al*., 2009; Ballèvre et *al*., 2014; Díez Fernández et *al*., 2016). In simplified cross section, the Variscan belt is characterized by a general fan-like shape divided by sutures and thrusts marked by opposite sense of vergences that were probably inherited from the subduction of the different oceanic domains (Fig. 2b) (Matte, 1986). From structural, petrological and paleontological criteria the Variscan Belt can be subdivided in several tectono-metamorphic domains including (i) external zones constituted by Proterozoic basement surmounted by a Paleozoic sedimentary cover moderately deformed and weakly affected by metamorphism during the Variscan orogeny and (ii) internal zones including relics of oceanic sutures, which were affected by HP-LT and HT-LP metamorphism and strong deformation related to the burying and thrusting related to the emplacement of nappes. The boundaries between these domains correspond to major Variscan thrusts, shear zones and oceanic sutures that can be traced through the Variscan bet (Fig. 2a). Due to the complex history of the Variscan orogeny, the correlation between the different structural domains and the structuration of the European Variscan belt are still debated.

The exhumation of high pressure and high temperature rocks, the activity of crustal shear zones during the late stages of the Variscan orogeny caused the genesis and emplacement of a large amount of crustal derived granites that reflect the recycling of the thickened crust (Kroner and Romer, 2013). This extensive magmatic activity yielded to the formation of numerous occurrences of granitic intrusions notably observed in the Iberian, the Armorican and the Bohemian Massifs. The emplacement of these granites was accompanied by the formation of several W-Sn metallogenic provinces deposits through the Variscan Belt (Romer and Kroner, 2016) (see **Fig.5 in Chapter I**).

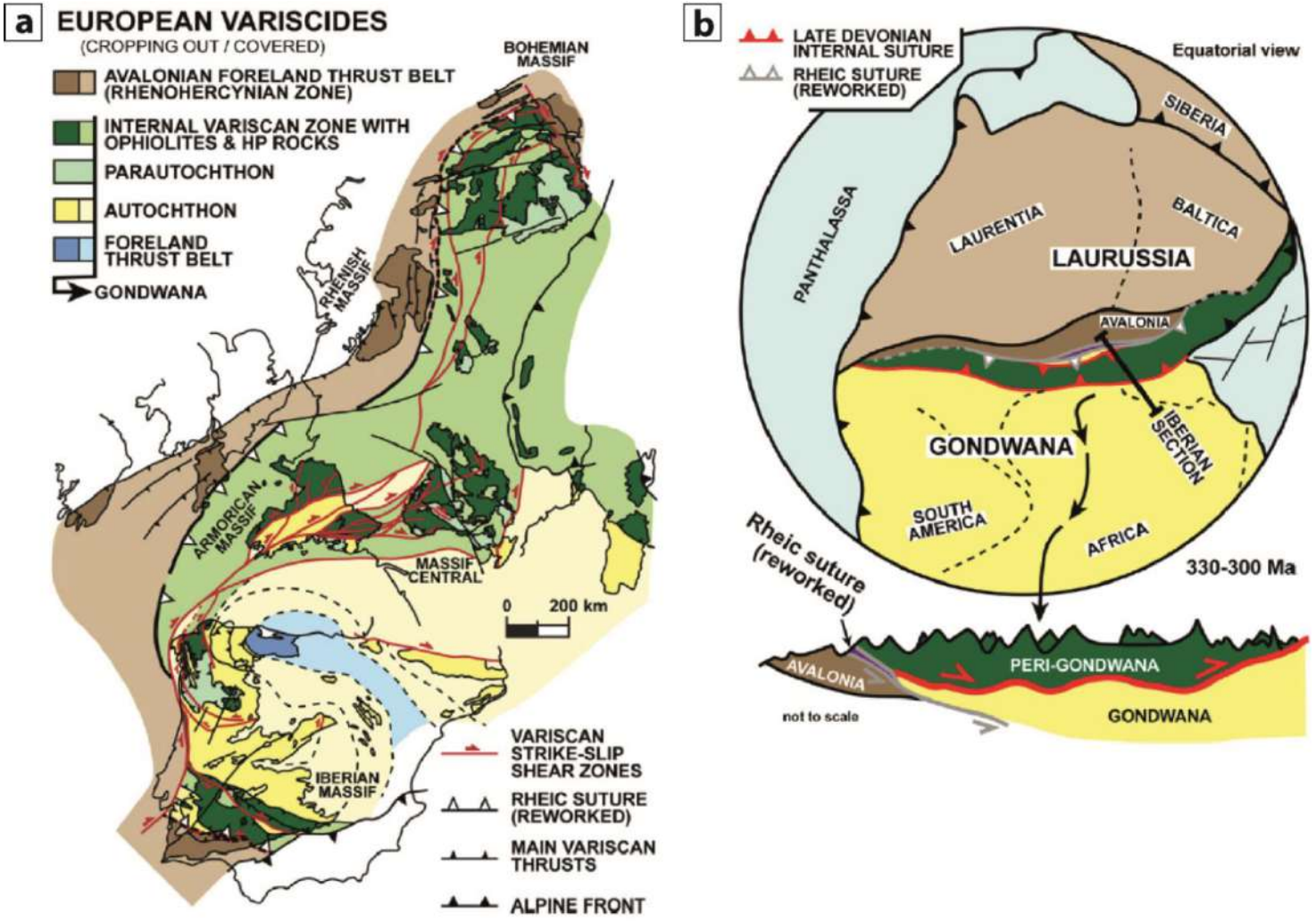

Figure 2 (a) Structural map of the European Variscan belt displaying the different tectonic domains and the main Variscan thrust and shear zones. (b) Reconstruction of the Variscan paleogeography during the Variscan orogeny (330-300 Ma), and simplified cross section showing the general fan-like shape of the Variscan belt (From Díez Fernández and Arenas, 2015).

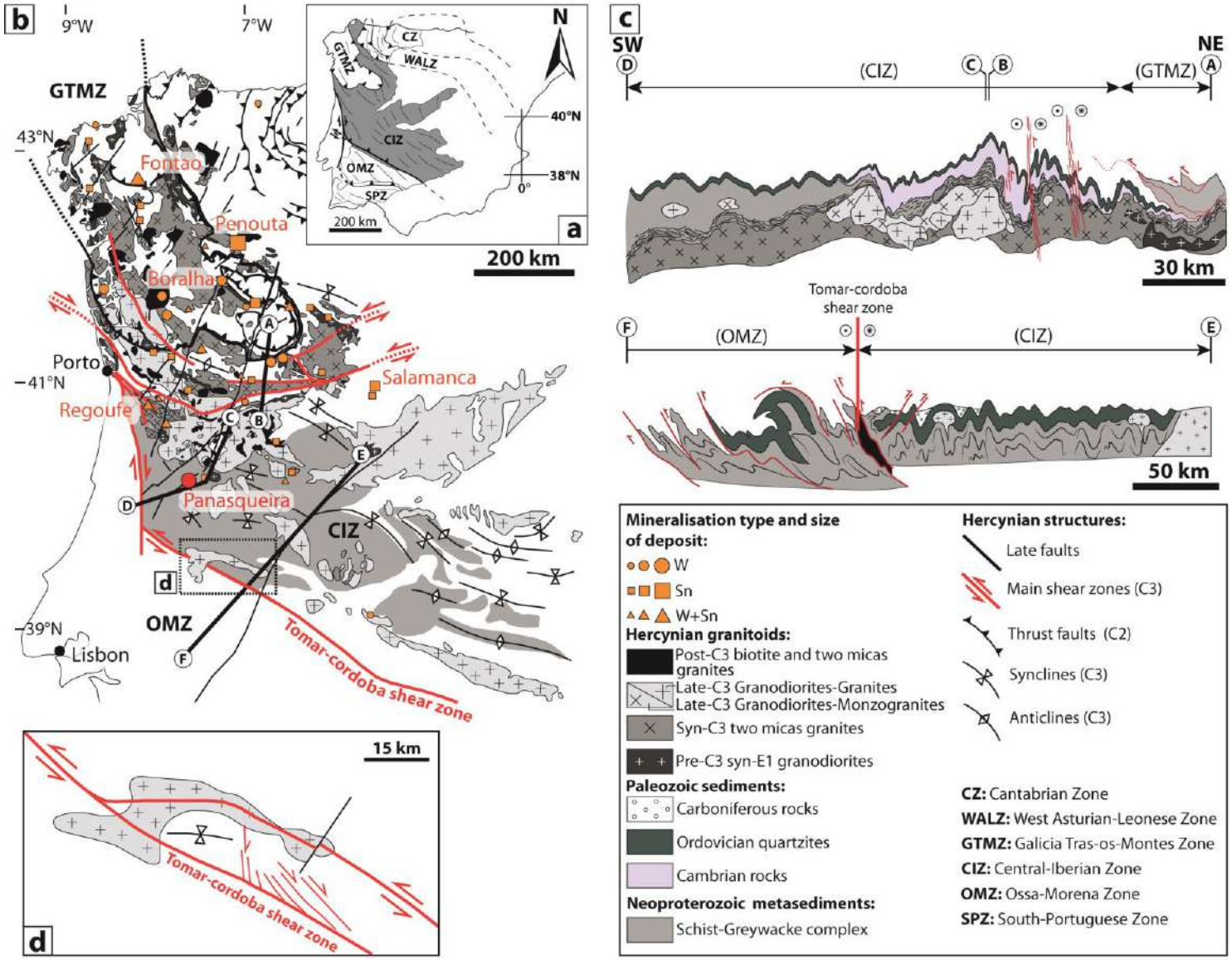

Figure 3 (a) Tectonic map of the Variscan Iberian massif showing the main tectonostratigraphic domains defined by Julivert et *al.*, (1972). CZ: Cantabrian Zone, WALZ: West Asturian-Leonese Zone, GTMZ: Galicia Tràs-os-Montes Zone, CIZ: Central Iberian Zone, OMZ: Ossa-Morena Zone and SPZ: South Portuguese Zone. (b) Synthetic map displaying the tectono-magmatic and the metallogenic setting of the CIZ. This map exhibits notably the spatial relationships between the main Variscan shear zones (C3) and the granitic intrusions as well as the spatial and the genetic link between the Variscan granites and the Sn-W ore deposits (realized from Pereira et *al.*, 1993; Dias et *al.*, 1998; Diez Fernandez and Pereira, 2016). (c) Synthetic geological cross sections across the southern part of the CIZ displaying the main Variscan structures and the relationships between these structure and the Variscan granitic intrusions (section (A-D) is modified from Diez Fernandez and Pereira, 2016 and the section (E-F) from Martínez Poyatos et *al.*, 2012). (d) Detailed map view of the Tomar-Cordoba shear zone displaying the relationship between the ductile shear zone and the domino faults system formed during the C3 deformation event (from Sanderson et *al.*, 1991).

2. The Central Iberian Zone (CIZ)

The Iberian massif represents the southwestern branch of the European Variscan Belt (Fig. 2a). According to the scheme proposed by Lötze (1945) and modified by Julivert et *al*. (1972) the Iberian Massif can be divided into six tectonic domains (from north to south): the Cantabrian Zone (CZ), the West Asturian-Leonese Zone (WALZ), the Galicia-Trás-os-Montes Zone (GTMZ), the Central Iberian Zone (CIZ), the Ossa-Morena Zone (OMZ), and the South Portuguese Zone (SPZ) (Fig. 3a). These zones are mainly composed of Paleozoic and Neoproterozoic metasedimentary sequences that cover the Cadomian basement of the Gondwana and that were intruded by a large volume of granitic intrusions during the late stages of the Variscan orogeny (Martínez Catalán et *al*., 2007). The boundaries between these zones correspond to major thrust and shear zones that can be followed through the Variscan Belt (Fig. 2a).

The Central Iberian Zone (CIZ) constitutes the axial zone of the Iberian Massif and corresponds to the margin of Gondwana, which was overlapped in the North by a set of far-travelled allochthonous units that compose the GTMZ (Fig. 3b and 3c) (Díez Fernández and Arenas, 2015). These thrust sheets correspond to slices of continental and oceanic crusts that were transported from the outboard to the inner part of the Gondwana's margin at the beginning of the continental collision (Arenas et *al*., 2016; Martínez Catalán et *al*., 2009; Díez Fernández et *al*., 2016). To the South, the CIZ is separated to the OMZ by the Tomar-Badajoz-Cordoba shear zone that is characterized by a left lateral transpressive flower structure with a strike-slip displacement from SE to NW (Fig. 3b and 3c) (Burg et *al*., 1981; Matte, 1986; Sanderson et *al*., 1991; Azor et *al*., 1994). This ductile shear zone is locally associated with a set of N-S to NW-SE trending faults that are antithetic to the main shear zone and form "domino" type geometry (Fig. 3d) (Sanderson et *al*., 1991).

The CIZ is mainly composed of the Schist-Greywacke-Complex (SGC) intruded by a large volume of granitoïd intrusions resulting from an extensive magmatism event during the latest stages of the orogeny (Dias et *al*., 1998) (Fig. 3b and 3c). The SGC consists of a thick (8-11 km) folded metasedimentary sequence composed of late Neoproterozoic schists and greywackes affected by a regional greenschist metamorphism during the Variscan orogeny (Schermerhorn, 1955; Ribeiro, 1990; Rodríguez Alonso et *al*., 2004; Martínez Catalán et *al*., 2007). These metasedimentary rocks consist mainly of a non-

fossiliferous terrigenous sequence of interlayered beds of green to dark-grey slates and siltites with discontinuous layers of greywackes, conglomerates and sandstones that can locally reach 1 km of thickness (Schermerhorn, 1955; Meireles et *al*., 2013). The SGC is uncomformably overlain by an incomplete Paleozoic sedimentary sequence mainly composed of Ordovician quartzite, which forms elongated NW-SE synclines and anticlines structures formed during the C3 deformation stage (Fig. 3b and 3c) (Martínez Poyatos et *al*., 2001; Díez Fernández and Pereira, 2016; Dias da Silva et *al*., 2017).

2.1 The main deformation stages observed in the CIZ

Three compressional (C1 to C3) and two extensional (E1 to E2) tectonic events have been distinguished in the CIZ (Fig. 4) (Dias da Silva et *al*., 2010; Martínez Catalán et *al*., 2014). C1 and C2 correspond to a continuous compressional event, which has occurred between 360 and 330 Ma mainly in the northern part of the CIZ in response to the continental collision between the Gondwana and the Laurussia (Dias et *al*., 1998; Simancas et *al*., 2003). The C1 stage (D1 in Dias et *al*., 2013; Dias and Ribeiro, 1995) is related to a NE-SW shortening and caused the moderate formation of tight to open folds with sub-horizontal axes and NW-SE subvertical axial planes associated with a penetrative axial planar cleavage (S1) (Fig. 4). This first deformation stage is accompanied by a low grade metamorphism belonging to the greenschist facies (chlorite or biotite zone). The C2 stage (D2 in Dias et *al*., 2013; Dias and Ribeiro, 1995) is related to the nappe emplacement, which led to the development of recumbent folds associated with sub-horizontal shear zones and sub-horizontal penetrative foliation (S2) (Fig. 4) (Diez Balda et *al*, 1995). The emplacement of these thrust sheets led to crustal thickening and was accompanied by a Barrovian metamorphism in the northern part of the CIZ (Escuder Viruete et *al*., 1994; Rubio Pascual et *al*., 2013).

The crustal thickening caused by the first compressional stages (C1+C2) triggered the gravitational collapse of the orogenic belt in the northwestern part of the CIZ. This collapse led to synorogenic extension (E1) in continuity with the C2 stage (Fig. 4). This extension induced the exhumation of several migmatite core complexes (Díez-Montes 2007; Villar Alonso 1992; Díez Fernández and Pereira 2016; Pereira et *al*. 2017), which were accompanied by the emplacement of syn-E1 granitoids presenting granodioritic compositions and ages ranging between 347 and 318 Ma (Fig. 3b and 4) (Dias et *al*., 1998; Gutiérrez-Alonso et *al*. 2018).

The last compressional stage C3 (D3 in Dias et *al*., 2013; Dias and Ribeiro, 1995) is characterized by a transpressional deformation, which led to the generation of tight and upright folds with NW-SE subvertical axial planes (S3), affecting notably the Ordovician quartzite that formed the elongated NW-SE synclines and anticlines cartographic fold pattern observed today (Fig. 3b and 3c). This folding is associated with the formation of subvertical strike-slip ductile shear zones, with ENE-WSW strike and sinistral shear sense and conjugated dextral NNW-SSE ductile shear zones (Fig. 3b, 3c and 4). These ductile shear zones were accompanied and controlled the emplacement of a large amount of crustal derived granites that result from the partial melting of the thickening continental crust. From the ages of the oldest granites affected by the C3 deformation stage (syn-C3), the age of this final compressional stage was estimated between 318 and 300 Ma (Fig. 4) (Díez Montes and Gallastegui 1992; Gutiérrez-Alonso et *al*., 2015). The C3 ductile deformation is followed by brittle deformation stage marked by the development of NE-SW, NNE-SSW and NW-SE sinistral brittle shear zones that controlled the emplacement of the post-kinematic (post-C3) granitoïds (295 to 285 Ma) (Fig. 4) (Pereira et *al*., 1993; Martínez Catalán et *al*., 2014). These brittle shear zones are also commonly associated with W-Sn mineralization related to granitic intrusions in the northern part of the Iberian Massif (Dias et *al*., 2003; Mateus et *al*., 2001; Mateus and Noronha, 2010).

At the end of the Variscan orogeny, the collapse of the orogenic belt is associated with a generalized post-orogenic extension (E2) induced by a pure shear with sub-vertical compression. Finally, the Iberian Massif was affected by an important uplift during the Alpine orogeny whose the vertical displacement can reach up to 1000 m (Fig. 5) (Ribeiro et *al*., 1990; Janssen et *al*., 1993; Zeck et *al*., 1992; Andeweg, 2002; Cloetingh et *al*., 2002). These vertical motions were controlled by a set of NE-SW reverse faults (like the Lousa-Seia and the Cebola faults) that delimit and separate rigid blocks.

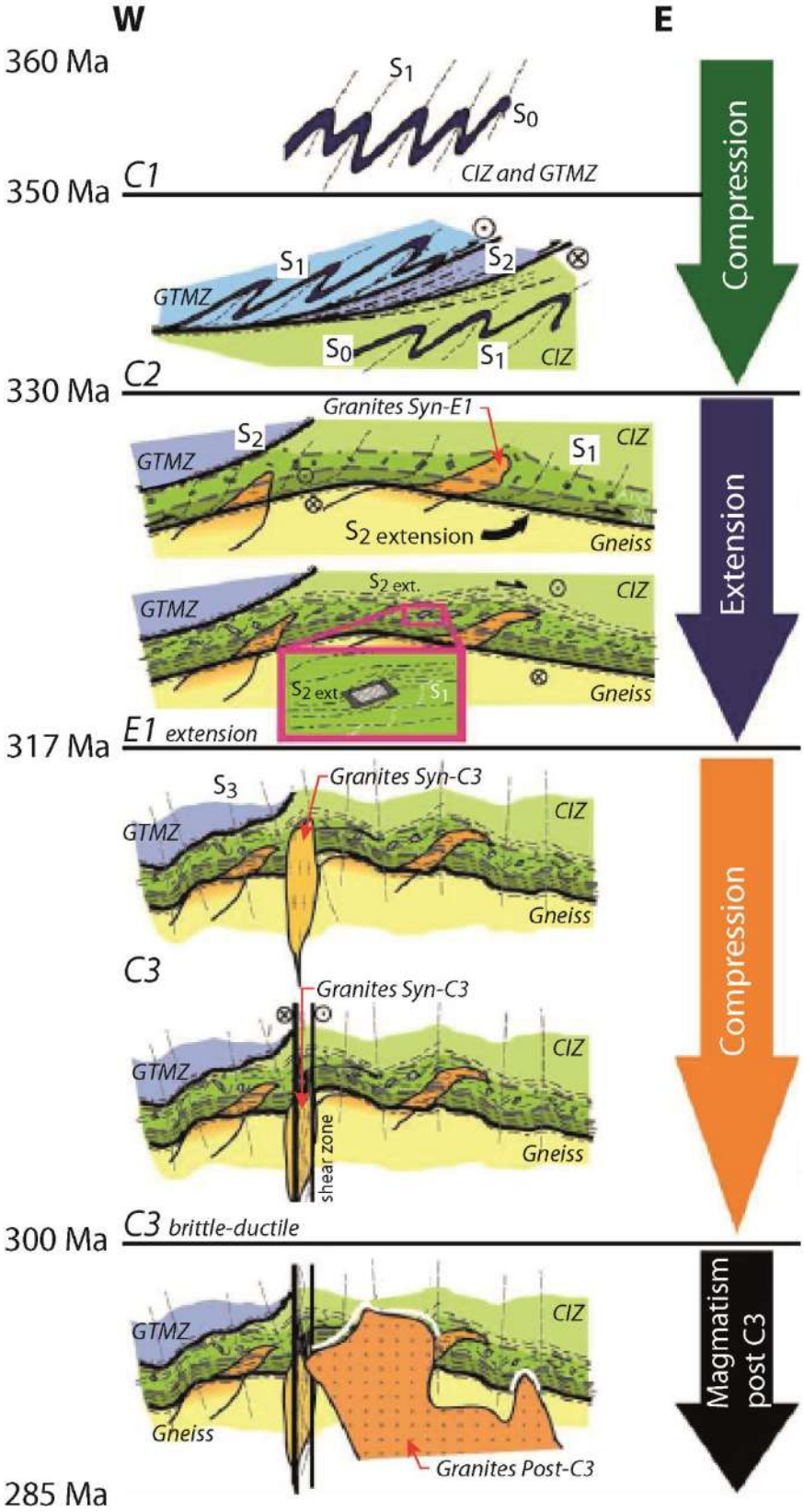

Figure 4 Tectono-magmatic evolution of the Central Iberian zone during the Variscan orogeny. This schematic representation displays the main compressional (C1, C2 and C3) and extensional (E1) stages, as well as the different generations of granitic intrusions. (From Dias da Silva et *al*., 2010).

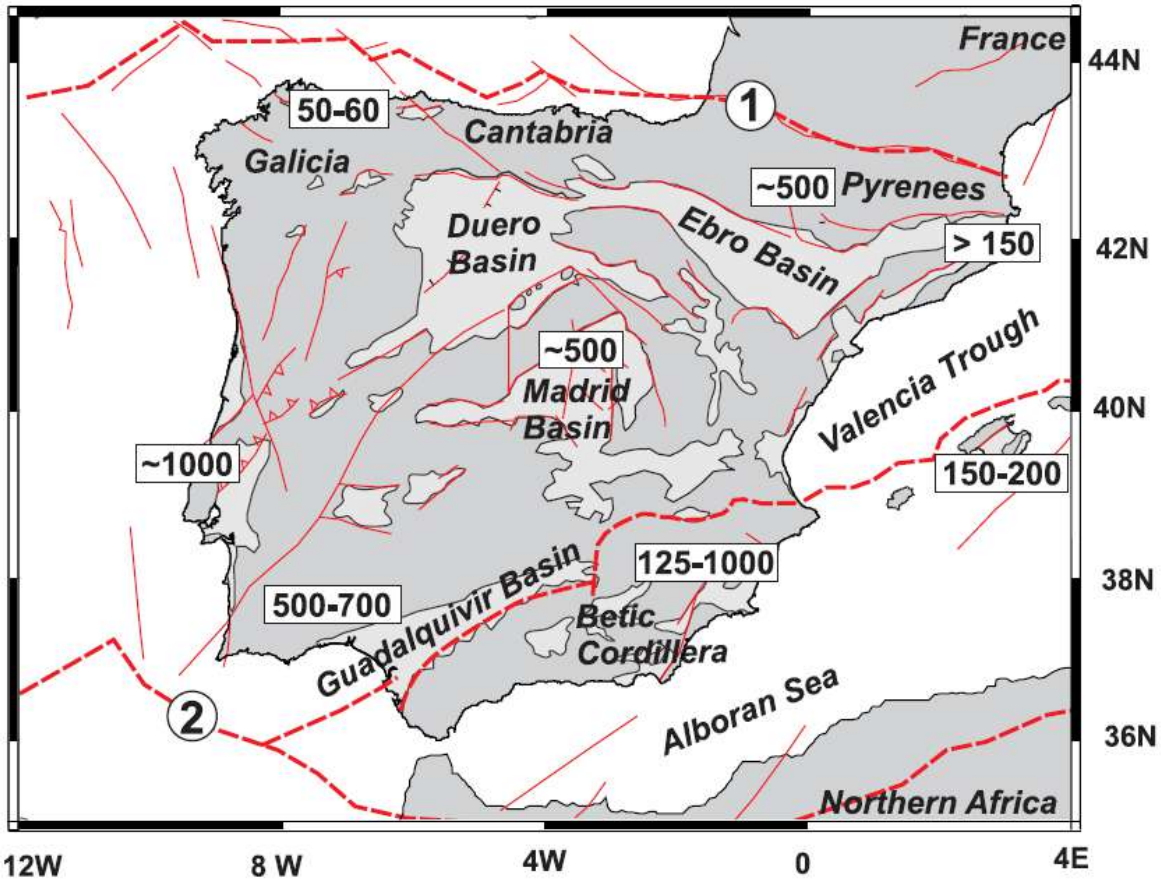

Figure 5 Structural map of the Iberian peninsula showing the main structures related to general uplift induced by the Alpine orogeny. Number in boxes corresponds to quantitative estimation of the vertical displacement (in meters) of the Pliocene-Quaternary uplift observed in Iberia (modified by Cloetingh et *al.*, 2002 from Janssen et *al.*, 1993; Zeck et *al.*, 1992; Andeweg, 2002).

2.2 The Variscan magmatism of the CIZ

A large volume of granitic intrusions were emplaced in the CIZ during the post-collisional stages of the Variscan orogeny (325 to 295 Ma) and formed a NW-SE 600 km-wide band (Ferreira et al., 1987; Dias et al., 1998). This extensive magmatic activity results from (i) the strong crustal thickening induced by the Variscan orogeny and (ii) a high heat production induced by the disintegration of radiogenic elements (U, Th, K) present in rocks composing the thickened continental crust (Villesca et *al.*, 1998, Bea et *al.*, 1999). Nevertheless, implications of basic mantle derived magmas have also been described in some part of the Iberian Massif (Dias et *al.*, 1998; Castro et *al.*, 1999).

Based on their petrological characteristics and emplacement ages relatively to the main Variscan event C3 (D3 in Dias et *al.*, 1998), granitic intrusions have been classified by Ferreira et *al.* (1987) and Dias et *al.* (1998) as: pre-C3 and syn-E1 granitoïds (319-313 Ma), syn-to late-C3 granitoïds (311-306 Ma), late to post-C3 granitoïds (300 Ma) and

post-C3 granitoïds (296-290 Ma). The most part of the CIZ granitoïds are syn-to-post tectonic and were emplaced defining alignments closely related to the C3 ductile and brittle shear zones (Fig. 4b and 6) (Iglesias and Ribeiro, 1981; Ferreira et *al*., 1987; Orejana et *al*., 2012).

The pre-C3 and syn-E1 granitoïds are granodiorites that form syn-tectonic massifs elongated parallel to crustal structures related to the C2 and E1 deformation stages. These granodiorites exhibit porphyritic textures and are often associated with mafic and ultramafic rocks like gabbro, dolerite and diorite.

The syn-C3 biotite granitoïds are characterized by calc-alkaline (leucomonzogranites) to aluminopotassic (two micas leucogranites) affinities and Sr-Nd signatures that emphasize hybridization and interactions between mantle and crustal derived magmas (Simoes et *al*., 1997; Dias et *al*., 1998). These granitoïds form extensive batholiths elongated parallel to the ductile shear zones formed during the C3 deformation event.

The late-C3 granitoïds include (i) biotite dominant monzogranite formed by anatectic processes and (ii) strongly peraluminous two-mica granites that clearly result from the melting of the metasedimentary rocks composing the continental crust (Dias et *al*., 1992). These two types of granitoïds are generally associated and form large zoned massifs with porphyritic monzogranites in the external part of the massifs and two micas peraluminous granites in the inner part.

The post-C3 granitoïds are late granodiorites characterized by subalkaline and ferro-potassic affinities and result of hybridization between alkaline and calc-alkaline magmas (Mendes et *al*., 1997). These latest intrusions form subcircular massifs that crosscut the structures developed during the C3 deformation event. These granodiorites are mainly located in the northern part of the CIZ and seem to be associated with the NNE-SSW brittle faults system.

The syn-C3 and the late-D3 granitic massifs represent volumetrically the most important part of the Variscan magmatism and are spatially and genetically associated with numerous Sn-W-Li-(Nb-Ta) ore deposits and indices (Fig. 3b).

2.3 Metallogenic setting of the CIZ

The Iberian massif represents a large part of the Sn-W metallogenic province of the European Variscan Belt (Romer and Kroner, 2016). The Sn-W hydrothermal deposits are mainly associated with deformation stages and magmatism related to the post-collisional events (Fig. 3b) (Schermerhorn, 1981; Derré, 1982; Mateus and Noronha, 2010). In the Iberian Peninsula, the deposits extend from Galicia in the North to the Southwestern part of Spain (Fig. 3b). The main Sn-W districts including the W-Sn-(Cu) Panasqueira ore deposit are hosted by the CIZ (Fig. 3b). These deposits are mainly related to syn- to late-C3 Variscan granites and are usually located in the apical portions of granitic cupolas that correspond to apophyses of a more extended granitic intrusion at depth. These granites are generally highly fractionated porphyritic two micas granites or leucogranites enriched in volatiles and incompatibles elements (Li, Rb, F, Nb, Ta, Sn, and W). The type of mineralization varies mainly from disseminated ores in massive greisen (Panasqueira, Regoufe) and highly evolved granites (Penouta, Argemela), to veins and stockworks developed within the granite and the host rocks (Panasqueira, Logrosán, Regoufe). Some occurrences of skarn (Los Santos) and breccia pipe (Borralha) can be also found in the CIZ.

The Sn-W deposits of the Iberian Massif are generally polyphased and can be summarized by a first high-temperature W-Sn oxides stage followed by a lower temperature sulfide stage (Noronha et *al*., 1992 and 1999). A regional spatial metal zoning equivalent to zonation described in equivalent Sn-W provinces like the Cornwall is inferred from the distribution pattern of W-Sn, Cu and Pb-Zn-Cu. Tourmalinization and greisenization are the main metasomatic alterations respectively observed in the metasedimentary host rocks and the upperpart of granite intrusion associated to W-Sn mineralization (Schermerhorn, 1956; Thadeu,1965b). The greisenization of the upper part of the granitic cupolas occurred generally simultaneously with the formation of the mineralized stockworks and quartz veins. The massive greisens formed during this metasomatic activity constitute low-grade high-tonnage Sn-W deposits that can be exploited in some cases. The mineralized quartz veins that host cassiterite and wolframite constitute the large part of W-Sn ore deposits exploited by most mines (Panasqueira, Borralha and Barruecopardo). These veins occur both inside the apical portions of granite intrusions and within the country rocks. The veins are strongly controlled by the late deformation stages and follow generally preexisting fractures planes, tension gashes and

schistosity planes that affect the country rocks (Ribeiro and Pereira, 1982). Elevated fluid pressure conditions related to the expulsion of late magmatic fluids can generally constitute another important mechanism during the vein opening. Some deposits like Panasqueira present the particularity of sub horizontal vein systems which the origin and the mechanism of formation are still debated.

II- Structural control of the W-Sn-(Cu) mineralization of Panasqueira

1. Regional geological and structural setting

1.1 The Beira Baixa province

The W-Sn-(Cu) Panasqueira ore deposit is located in the Beira Baixa province about 35 km west of the Fundão city (Fig. 6a). This region occupies the southern flank of the Serra da Estrela massif, which represents a large complex of granitic intrusions mainly emplaced during the late to post orogenic stages. To the south, the Beira Baixa region is limited by the Tomar-Badajoz-Cordoba shear zone, which separates the CIZ from the OMZ. Country rocks composing this region consist of two distinct metasedimentary series (Thadeu, 1951, 1979) (Fig. 6b):

- A thick (several thousand meters thick) metasedimentary cover composed of marine flyschoid series that correspond to the schist-greywacke complex (SGC), which is locally named "Beira schist". These metasedimentary rocks are probably Neoproterozoic and are mainly composed of chlorite, quartz, sericite and albite. Certain facies can exhibit layers rich in organic matter (about 0.17 % according to Bussink, 1984) and syngenetic sulfides (pyrite). This flyschoid series was affected by greenschist metamorphism and was strongly deformed and folded during the Variscan orogeny. During this regional metamorphism the clay sediments were transformed into sericite-chlorite slates. A network of lenticular milky barren quartz veins (locally called "Seixo Bravo") is present in the vertical foliation planes of the Beira schist. This Seixo Bravo corresponds to quartz exudation formed during the regional metamorphism.
- The Beira schist formation is uncomformably overlain by a thin sedimentary series mainly composed of quartzite and slate of Ordovician age. This formation is subdivided into 3 units: (i) a lower unit mainly composed of thick Armorican quartzite (metasandstone), in which fine layers of slates can be locally observed, (ii) a middle unit composed of sandstone interlayered with pelites, in which numerous quartzite beds can be observed and (iii) an upper unit mainly composed of siltstone and pelites with arkosic sandstone beds.

These metasedimentary rocks were intensely deformed and folded during the Variscan orogeny (Fig. 6a and 6c). The occurrences of kilometric cartographic folds with NW-SE axes and NW-SE striking thrust faults emphasize that the Beira Baixa province was affected by a regional NE-SW horizontal shortening (Fig. 6a and 6c). This region is particularly rich in Sn-W deposits and indices, such as Gois, Argemela, Fundão and Panasqueira that are spatially related to non-outcropping granite intrusions (Fig. 6). The presence of these intrusions at depth is evidenced by the occurrences of large spotted schist aureoles that formed during the thermal metamorphism induced by the emplacement of these granites (Fig. 6a and 6c). Beira Baixa province was affected by the Alpine uplift observed at the Iberian massif. The vertical displacement induced by this uplift is accommodated by regional NE-SW faults like the Lousà-Seia, the Cebola and the Sobreira Formosa faults (Thadeu, 1949; Cloetingh et *al*., 2002).

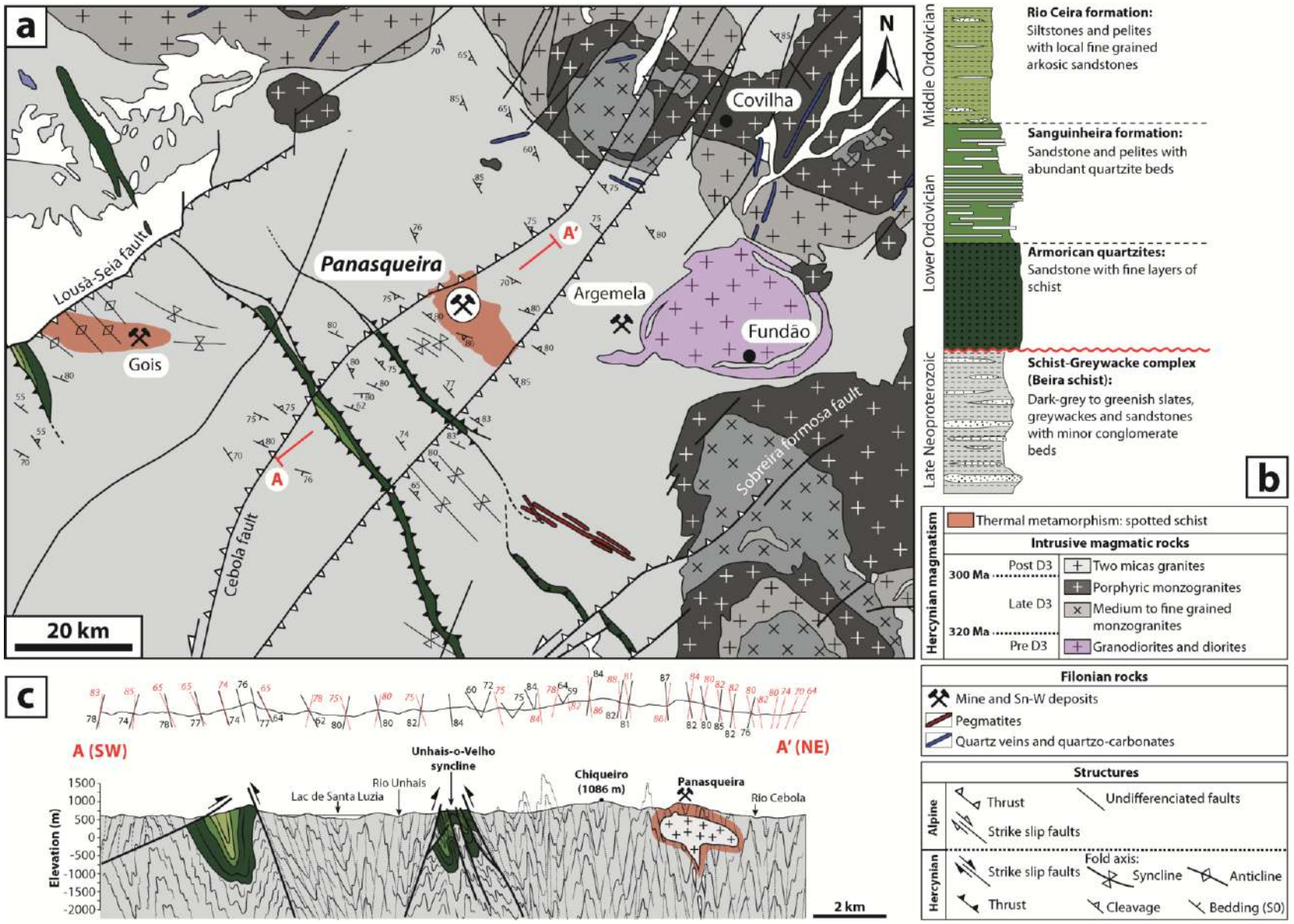

Figure 6 Geological and structural setting of the Beira Baixa province. (a) Geological map, (b) stratigraphy and (c) cross section of the Beira Baixa province. The cross section (A-A') was realized through the NW-SE cartographic folds (Ordovician quartzite) and the W-Sn-(Cu) Panasqueira ore deposit.

1.2 The Unhais-o-Velho syncline

As previously mentioned, the Ordovician sedimentary cover observed in the Beira Baixa province was intensively folded during the compressive deformation induced by the Variscan orogeny (Fig. 6c). The Rio Zêzere valley exposes a complete cross-section through the Unhais-o-Velho syncline that permits to observe the macroscopic structures formed during the regional NE-SW shortening (Fig. 7). This syncline is located at approximatively 10 km southwest of the Panasqueira mine (Fig. 6a).

The Armorican quartzite composing this syncline exhibits tight, upright and isoclinal folds (several tens of meters) characterized by isolated fold hinges, that are separated from each other by thrusts (Fig. 7a to 7c). These folds are characterized by sub-horizontal NW-SE axes (plunge between 4 and 17°) and bedding (S_0) dipping between 10 and 85° to the NE-SW (Fig. 7a to 7d). In more pelitic layers a discrete vertical axial plane cleavage can be locally observed in mesoscopic folds (Fig. 7d) and establishes link between the regional foliation and folds formed during the regional horizontal shortening. Thrusts are characterized by NW-SE strike and dip ranging from 25 to 85° to the NE-SW (Fig. 7a, 7e and 7f). These thrusts are usually preferentially located in the fold hinges (Fig. 6e).

These different structures emphasized that the region of Panasqueira was affected by an intense NE-SW compression, which led to strong horizontal shortening with vertical stretching.

Figure 7 Structural characteristics of the Ordovician quartzite syncline of Unhais-o-Velho. (a) Panoramic photograph of the folded Ordovician quartzite outcropping along the "Rio Zêzere" river. The lower-hemisphere equal-area stereoplots show the orientation of stratigraphy (S_0), fold axes and reverse faults observed in the Unhais-o-Velho syncline. (b), (c) and (d) mesoscale folds observed in the Armorican quartzite, and emphasizing a NE-SW shortening. Note the development of a discrete planar axial cleavage (S_1). (e) and (f) reverse faults and fault gouge emphasizing a NE-SW shortening.

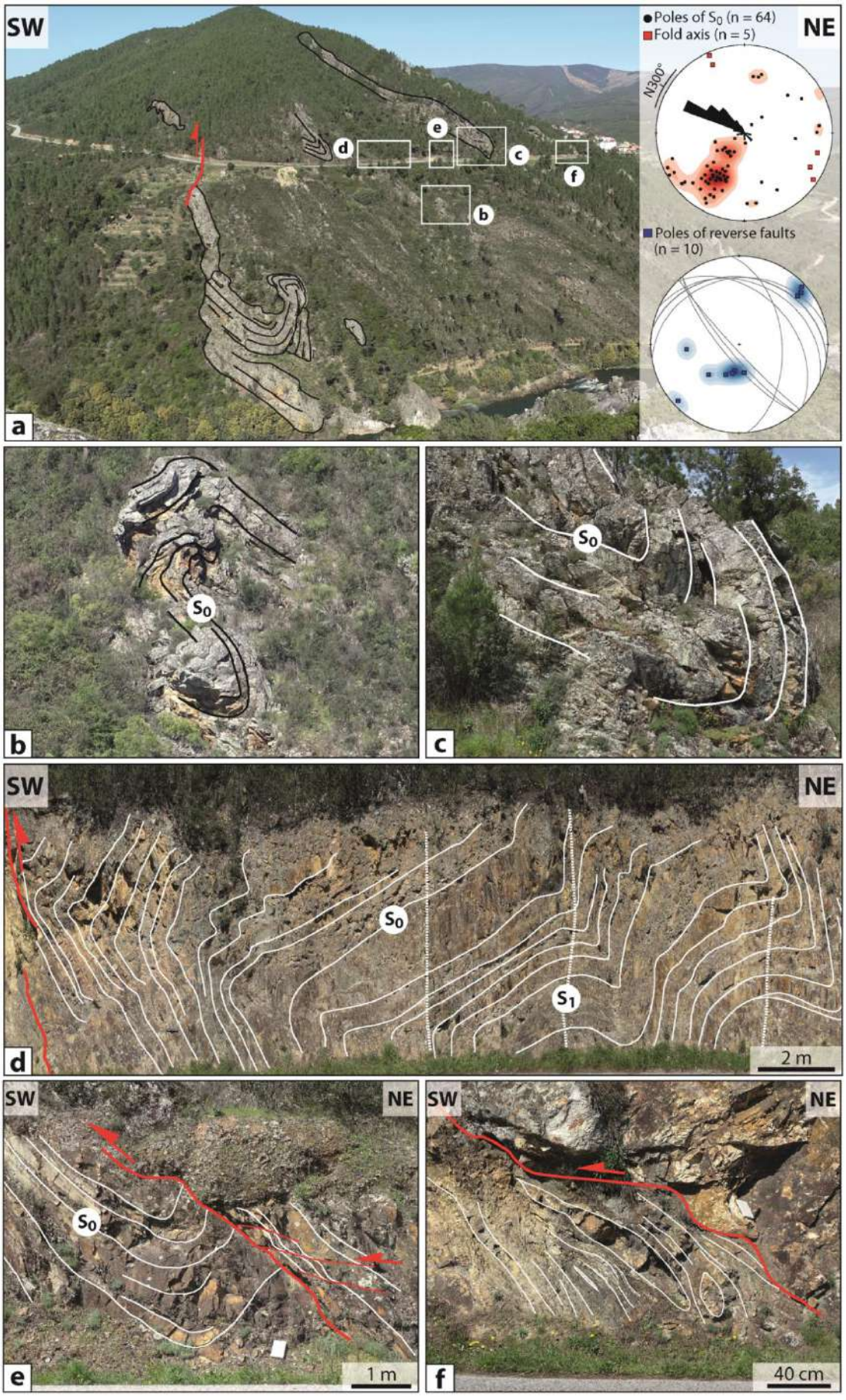
SW
NE
Poles of S_0 (n = 64)
Fold axis (n = 5)
N300°
Poles of reverse faults (n = 10)
a
b
c
d
e
f
S_0
S_1
2 m
1 m
40 cm

1.3 The Beira schist structures

1.3.1 The folds

Like Ordovician sedimentary cover, Beira schist were affected by intense folding leading to the formation of tight, upright and isoclinal folds (Fig. 6 and 8). The NE-SW horizontal shortening induced by the regional compression was so intense that folds were extremely elongated vertically and bedding (S_0) was transposed in parallel to the axial planar cleavage of the resulting isoclinal folds (foliation S_1) (see stereograms in Fig. 8). However, fold hinges have locally been preserved and the structural relationships between folding and the regional foliation (S_1) can be observed (Fig. 8).

As displayed in Figure 8a, mesoscale syncline and anticline locally observed in Beira schist (sector of Chiqueiro) are characterized by NW-SE sub-horizontal axes. This folding was accompanied by the development of a pervasive slaty vertical axial planar cleavage (Fig. 8b and 8c). This cleavage, which corresponds to the regional pervasive foliation, strikes NW-SE and dips sub-vertically to the NE or SW (Fig. 8b and 8c). Folds were crosscut by conjugate brittle strike-slip faults system composed of a series of N-S trending subvertical dextral faults and a series of E-W trending subvertical sinistral faults.

Vertical stretching lineation and boudinage of vertical quartz veins parallel to the foliation planes can be easily observed from thin sections (Fig. 9a and 9b). The occurrences of symmetric vertical pressure shadow (fig. 9c) suggest a pure shear with horizontal flattening and vertical stretching. These structures emphasize that the regional compression led to an intense NE-SW horizontal shortening and strong vertical stretching consistent with structures described in the Unhais-o-Velho syncline and with the folding of Beira schist formation.

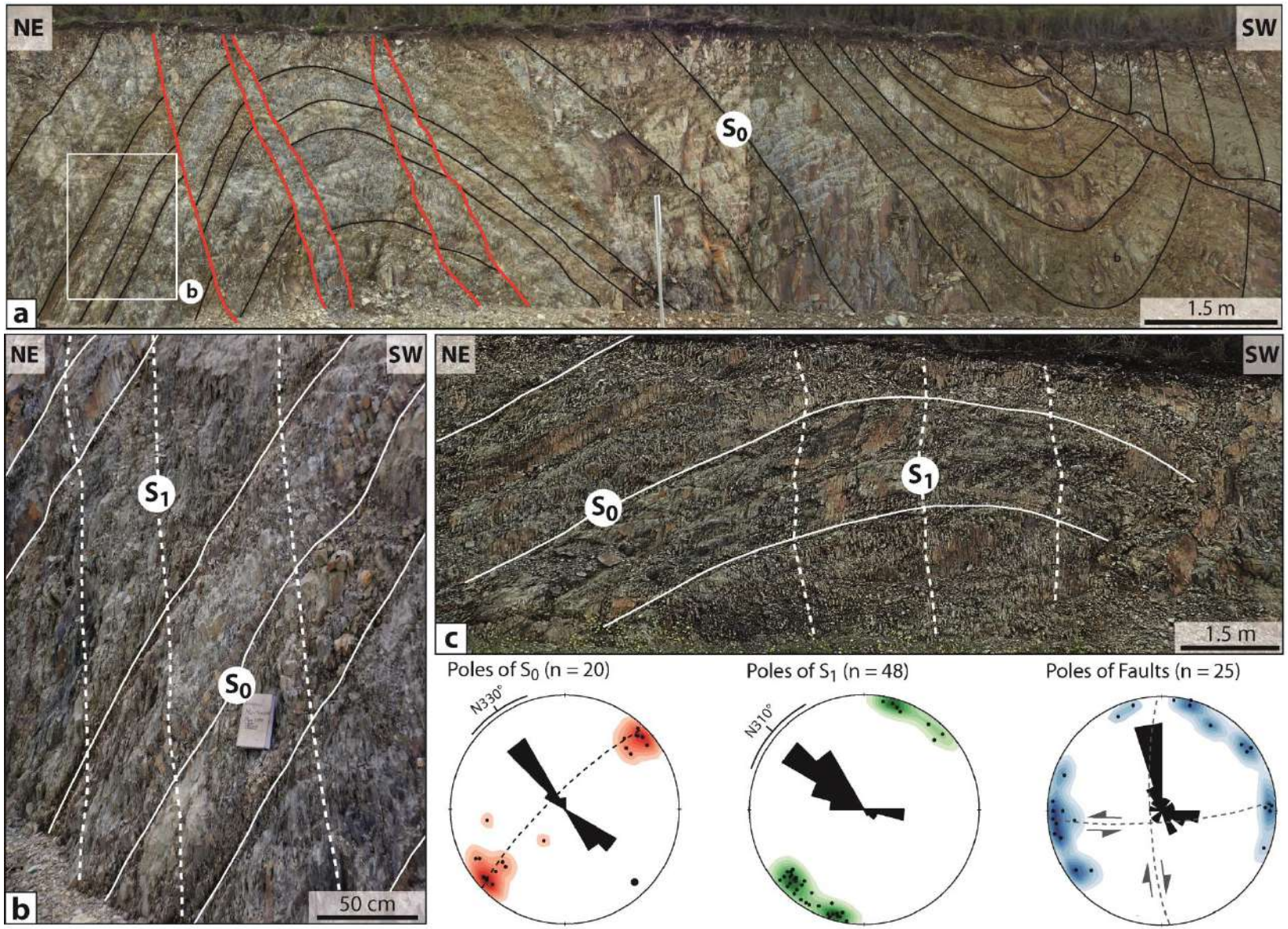

Figure 8 Photographs showing relationships between folding, the regional foliation (S_1) and faults affecting the Beira schist formation (outcrops in the sector of Chiqueiro). (a) Panoramic photography displaying mesoscale anticline and syncline. (b) and (c) Zooms on fold limb and fold hinge showing the bedding (S_0) and the axial planar cleavage corresponding to the regional foliation (S_1). The lower-hemisphere equal-area stereoplots show the orientation of stratigraphy (S_0), axial planar cleavage and faults observed in the sector of Chiqueiro.

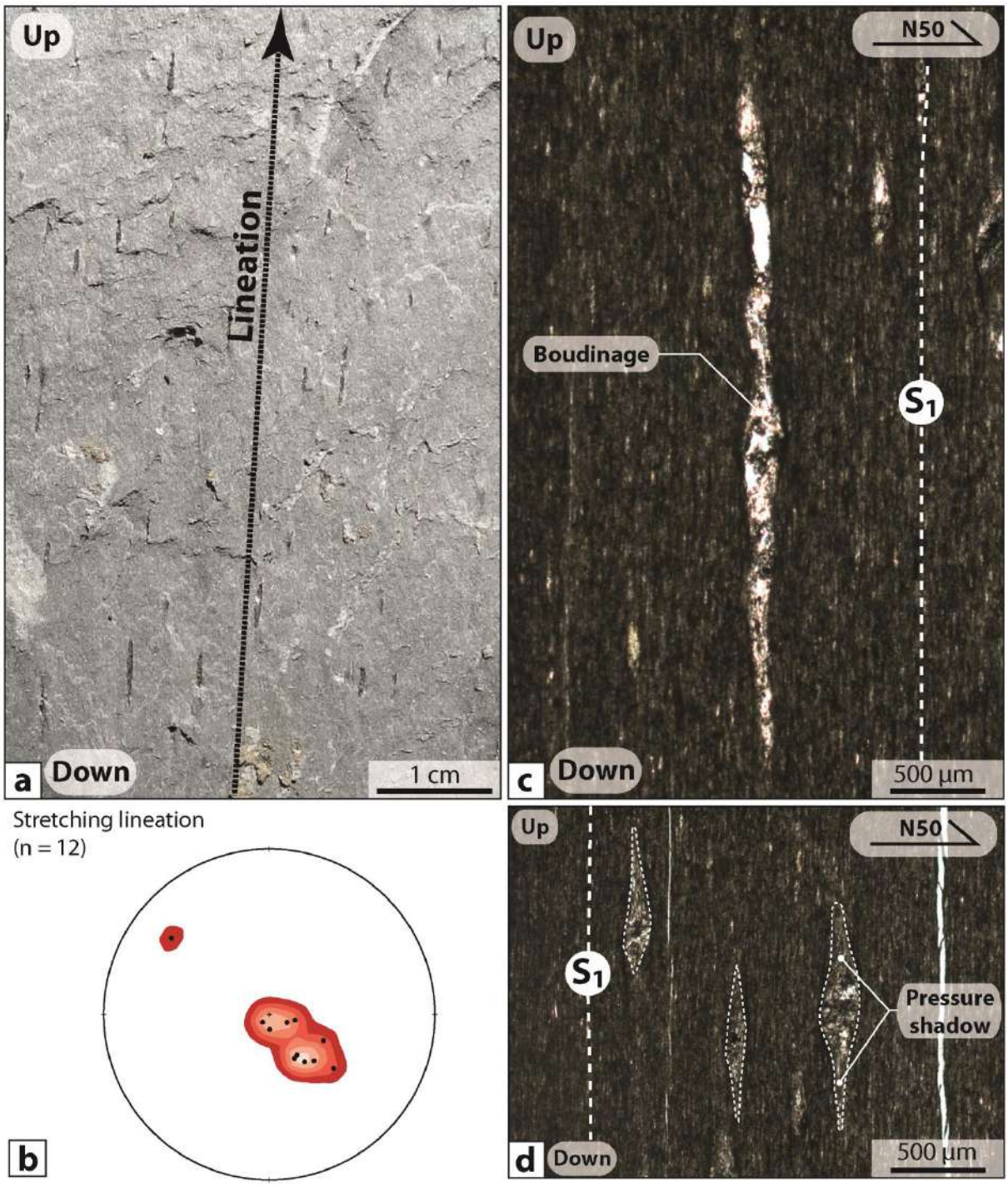

Figure 9 Vertical stretching lineation observed in the Beira schist formation close to the Panasqueira deposit (sector of Chiqueiro). (a) Photograph showing vertical stretching lineation recorded by chlorite (b) Lower-hemisphere equal-area stereoplot showing trend and plunge of the stretching lineation observed on the field. (c) and (d) Photomicrographs (transmitted light) showing boudinage and pressure shadow microstructures emphasizing a vertical stretching.

1.3.2 Horizontal barren quartz veins

Beira schist can locally host flat-lying to shallowly dipping barren quartz veins and veinlets (from 1 to 10 cm thick) (Fig. 10). These flat veins crosscut and postdate clearly the regional vertical foliation (Fig. 10a). They can locally form en echelon arrays and can be interpreted as horizontal tension gashes that could be opened in response to the regional NE-SW horizontal shortening. These veins were opened without significant shear displacements and their vertical dilation is clear and can be observed by the perfect matching offsets on opposite vein walls. In some cases, these veins were folded (with sub-horizontal fold axis) and affected by the vertical foliation, which was refracted in veins due to the more competent nature of quartz compared to the metasedimentary host rocks (Fig. 10 b to d). These veins were formed without any metasomatic alteration of the proximal host rock suggesting that they were probably related to metamorphic processes rather than to hydrothermal processes.

The opening of this barren quartz vein (Fig. 10e) is compatible with the regional NE-SW shortening and with the strong vertical stretching documented from folds, stretching lineation and from the vertical boudinage.

Figure 10 Structural characteristics of sub-horizontal barren quartz veins present in the Beira Baixa province close to the Panasqueira deposit (road between Paul and Barco). (a) Sub-horizontal barren quartz veins crosscutting the vertical foliation of Beira schist. (b) Horizontal quartz tension gashes folded during the regional NE-SW shortening. (c) and (d) Zooms on folded horizontal quartz tension gashes showing refraction of the vertical foliation due to the more competent nature of quartz veins. (e) Lower-hemisphere equal-area stereoplots showing the orientation of the regional foliation (S1) and poles of barren quartz veins.

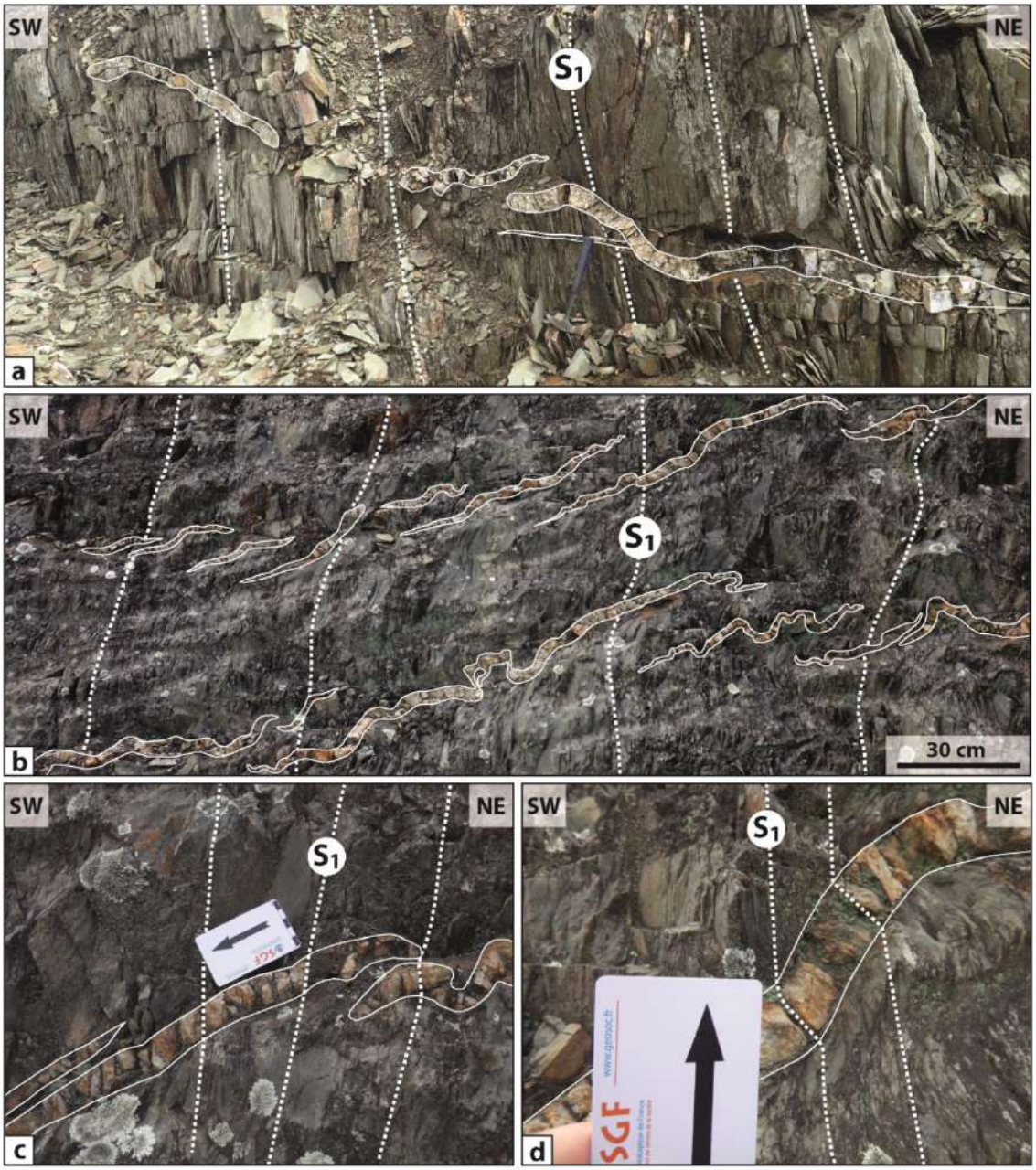

e Poles of S_1 (n = 14)

Poles of barren quartz veins (n = 18)

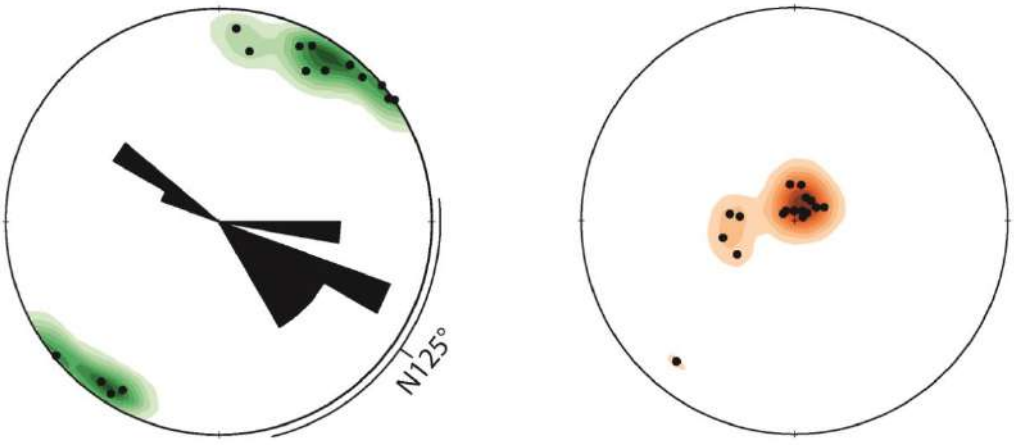

1.3.3 Brittle-ductile faults

As previously mentioned, the Variscan orogeny led to the formation of different brittle-ductile fault systems (Fig. 11 and 12). These structures include NW-SE-striking subvertical thrusts that occur as (i) en echelon arranged extensional veins defining vertical shear zones (Fig. 11a) and (ii) brittle-ductile vertical shear bands (Fig. 11b and c). These shear bands are generally sub-parallel to the regional foliation and exhibit clear vertical shearing (top to the SW or NE), which locally led to the transposition of the foliation (S_1) into the shear bands (Fig. 11c). The occurrences of isolated fold hinges and boudinaged quartz veins in some shear bands (Fig. 11b) indicate that vertical shearing and boudinage process (previously described) could occur during the same deformation event.

A second set of brittle-ductile faults comprising sub-vertical sinistral shear bands striking E-W (Fig. 12a to 12c) and conjugate dextral shear bands striking N-S (Fig. 12d) can be observed regionally. This lateral shearing led to the formation of (i) C-S structures marked by the transposition of the regional foliation (S_1) into the shear bands (C) (Fig. 12d) and (ii) en echelon-arranged tension gashes depicting shear zones on horizontal sections (Fig. 12c). The brittle equivalent of these shear zones is expressed as conjugate dextral N-S trending and sinistral E-W trending strike-slip faults (Fig. 12e). The sub-horizontal slickenside striation observed on these faults (Fig. 12 f and 12g) are consistent with the horizontal displacements observed in the ductile shear zones.

As previously mentioned, these ductile-brittle faults postdate the folding event. However, the stress field related to these faults is compatible with those related to the early folding event. Indeed, these brittle-ductile fault systems involve a NE-SW shortening related to a regional compression. Accordingly, the shearing deformation and the early folding stage could occur during a same continuum of deformation.

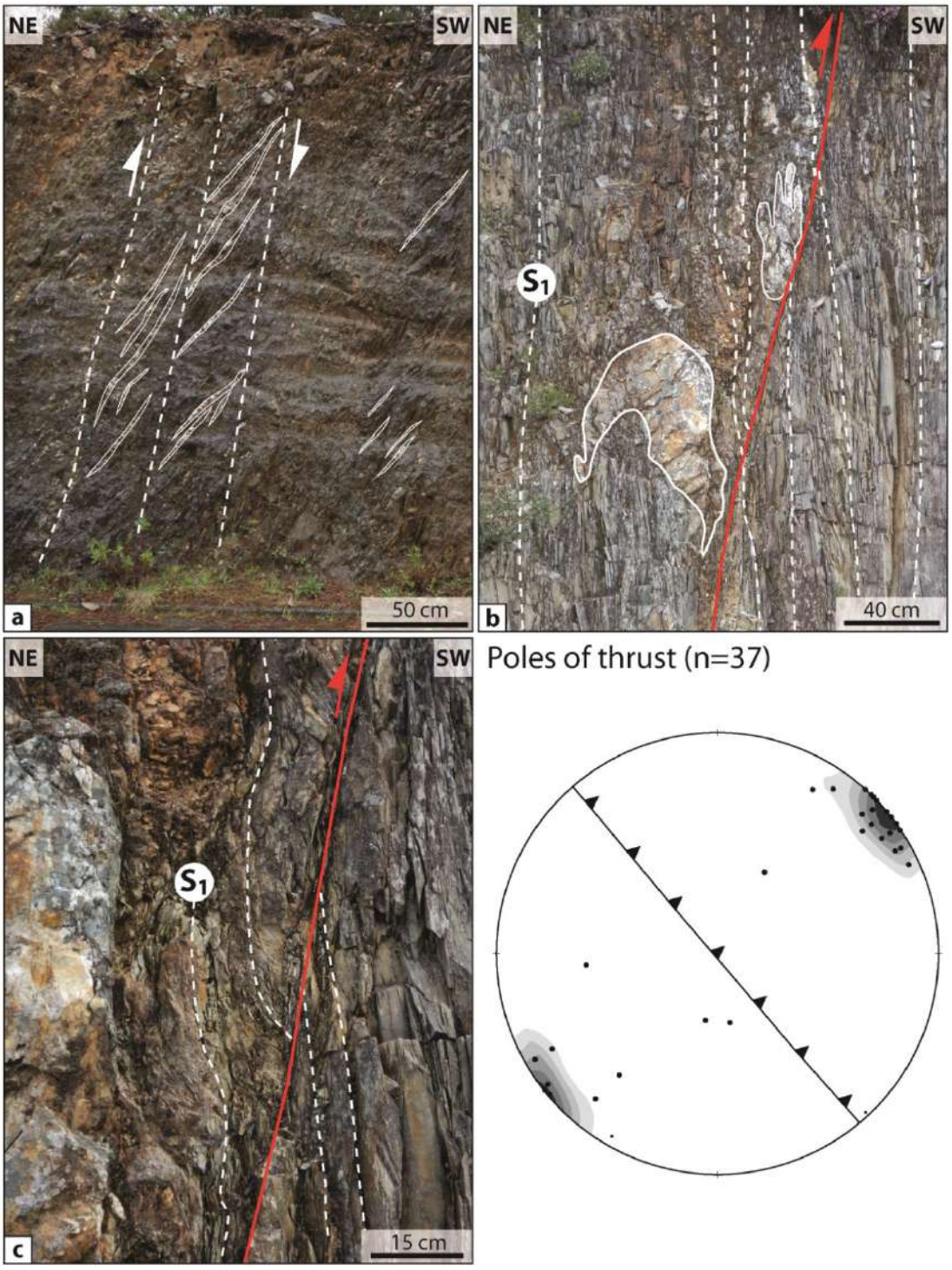

Figure 11 Vertical brittle-ductile thrust faults present in the Beira Baixa province close to the Panasqueira deposit (road between San Jorge de Beira and Barroca Grande). (a) En echelon-arranged extensional veins defining a sub-vertical shear band characterized by a reverse sense of shear (top to the SW). (b) Vertical shear band with reverse sense of shear. This shear band was accompanied by folding and boudinage of quartz exudation. (c) Zoom on the shear band displayed on (b). The lower-hemisphere equal-area stereoplot shows the orientation of poles of the brittle-ductile thrust faults.

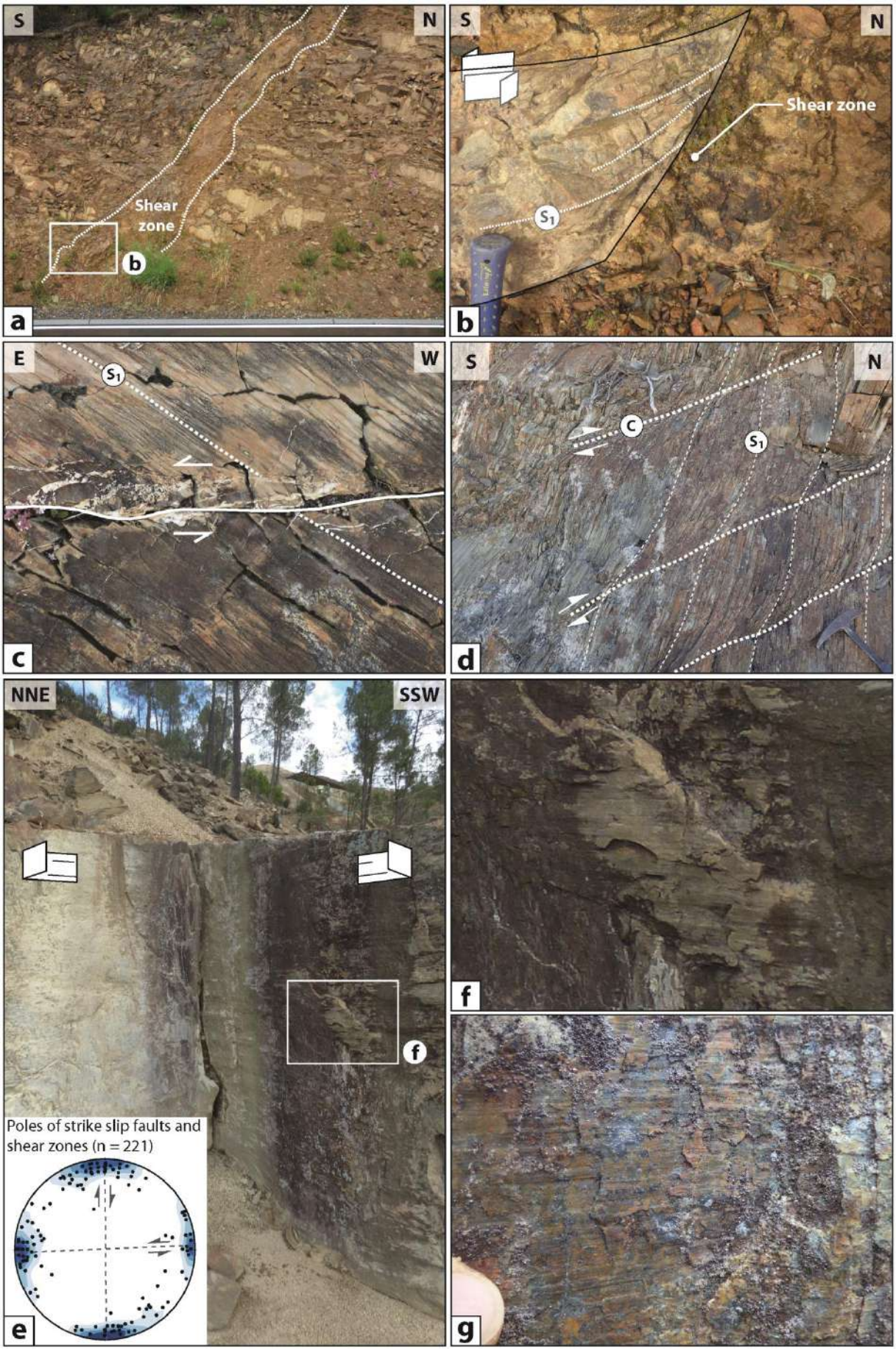
S
N
Shear zone
b
a
S
N
Shear zone
S1
b
E
W
S1
c
S
N
C
S1
d
NNE
SSW
f
Poles of strike slip faults and shear zones (n = 221)
e
f
g

Figure 12 Subvertical brittle-ductile strike-slip faults present in the Beira Baixa province close to the Panasqueira deposit. (a) E-W trending sinistral ductile shear band located in the sector of Cabeço do Pilão (Southeastern part of the Panasqueira district). (b) Zoom on the shear band displayed in (a) showing the transposition of the regional foliation (S_1) induced by the shearing. (c) En echelon-arranged extensional veins defining E-W trending sinistral shear band. (d) S-C structure defining N-S trending dextral shear zone. (e) Conjugate brittle strike-slip faults with N-S trending dextral fault and E-W trending sinistral fault. (f) and (g) zooms on fault planes showing orientations of lineation on slip surfaces, with (f) sinistral displacement and (g) dextral displacement

1.4 Structural analysis and regional stress field

Structures observed in the Beira Baixa region and structural data are summarized as stereograms in Figure 13. This structural synthesis permits to constrain the regional stress field, in which the hydrothermal system of Panasqueira was formed. According to this synthesis, all the structures observed in the Beria Baixa region were likely formed during a same compressive event involving a regional horizontal NE-SW shortening. This shortening (Z) has first induced an intensive horizontal flattening in the NE-SW directions accompanied by a strong vertical stretching (X) leading to the formation of tight and upright folds (with NW-SE axes) and vertical stretching lineation on foliation planes resulting from folding. This NE-SW horizontal shortening and this vertical stretching were so intense that (i) bedding was transposed in parallel to the regional foliation, (ii) fold hinges and quartz rich layers were vertically boudined and (iii) subvertical brittle-ductile thrust were developed to accommodate this intense deformation. The transposition of bedding parallel to the regional foliation explain the strong variable dips of S_0-S_1 intersection lineation that range between 5 and 80° and form a NW-SE trend consistent with the regional fold axes. This vertical stretching caused also the formation of sub-horizontal extensional barren quartz veins, which were subsequently folded (with sub-horizontal fold axes) in response to the NE-SW horizontal shortening.

This compressive stage was followed by a transpressional deformation event, during which vertical conjugate C-S shear bands and strike-slip faults were formed with N-S trending dextral shear system and E-W trending sinistral shear system. The formation of these structures is compatible with the regional NE-SW horizontal shortening responsible of the regional folding. Accordingly, this late transpressional deformation event and the early folding stage could occur during a same continuum of deformation involving a NE-SW maximum compression direction consistent with regional structural models proposed for the CIZ (Abalos et al., 2002; Martínez Catalán et *al*., 2014; Dias da Silva, 2014).

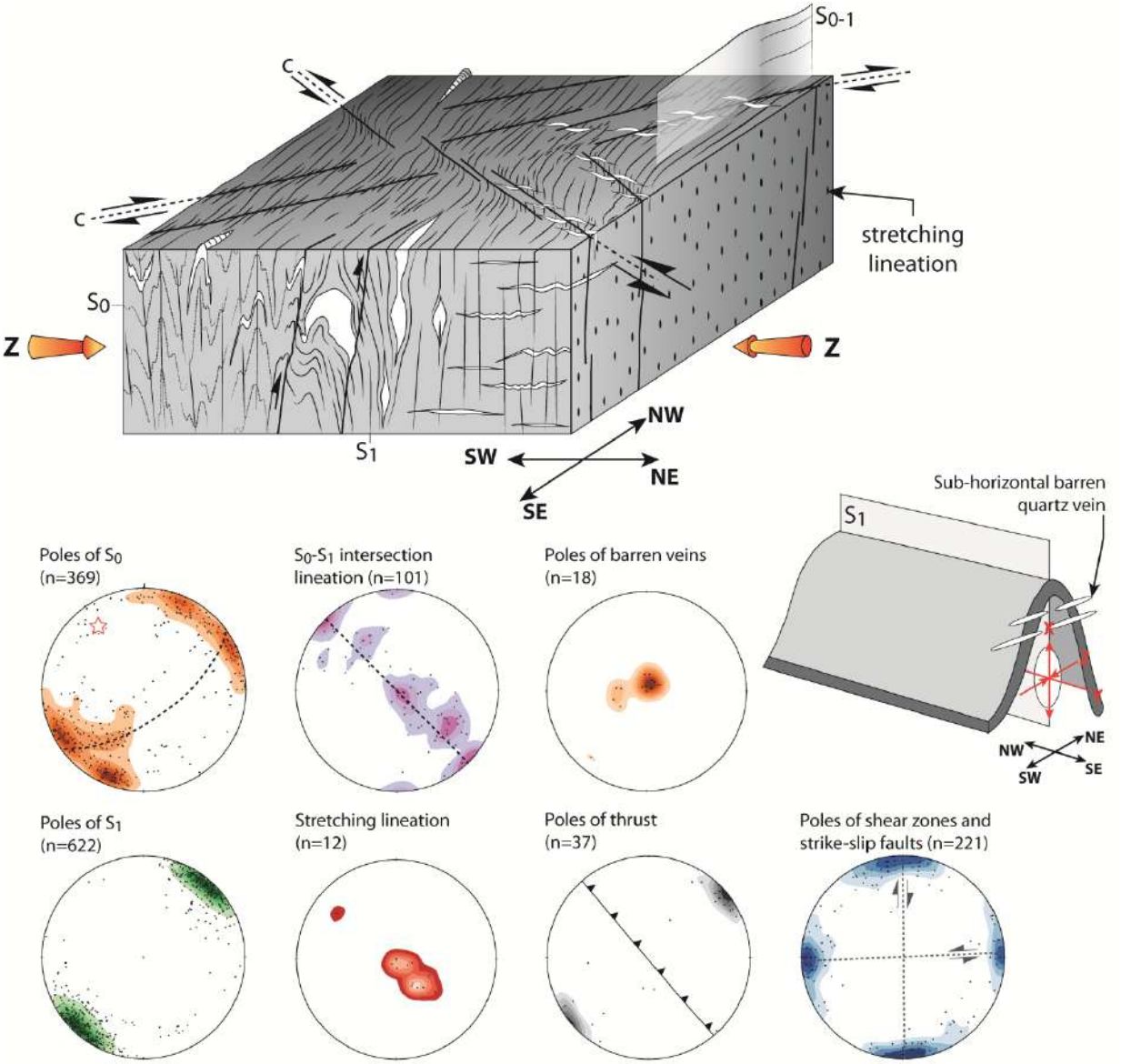

Figure 13 Synthesis of structural data and structures observed in the Beira Baixa province close to the Panasqueira deposit. All of these structures were formed during the same compressive event involving NE-SW shortening (Z).

2. Structural controls of the W-Sn-(Cu) mineralization of the Panasqueira district

2.1 Geological and structural setting of the W-Sn-(Cu) Panasqueira ore deposit

In the Panasqueira district, the Beira schist was affected by thermal metamorphism, during which metapelites were converted into spotted schist in response to the emplacement of an underlying S-type granite (Fig.14 Fig. 15a to15c) (Clark, 1964; Bussink 1984). This thermal metamorphism produced an extensive aureole of spotted schist best developed in the more argillaceous layers. These spots include mainly biotite and chiasolite and, to a lesser extent cordierite (Fig. 14) (Thadeu, 1951; Clark, 1969; Kelly and Rye, 1979). From this paragenesis and KFMASH petrogenetic grid we constrain a field of pressure and temperature conditions corresponding to the stability field of spotted schist paragenesis formed during the emplacement of the Panasqueira granite. Accordingly, the thermal metamorphism induced by the granite emplacement could occur at temperature ranging between 450 and 650°C for maximum pressure condition of 2.5 kbar (Fig. 14).

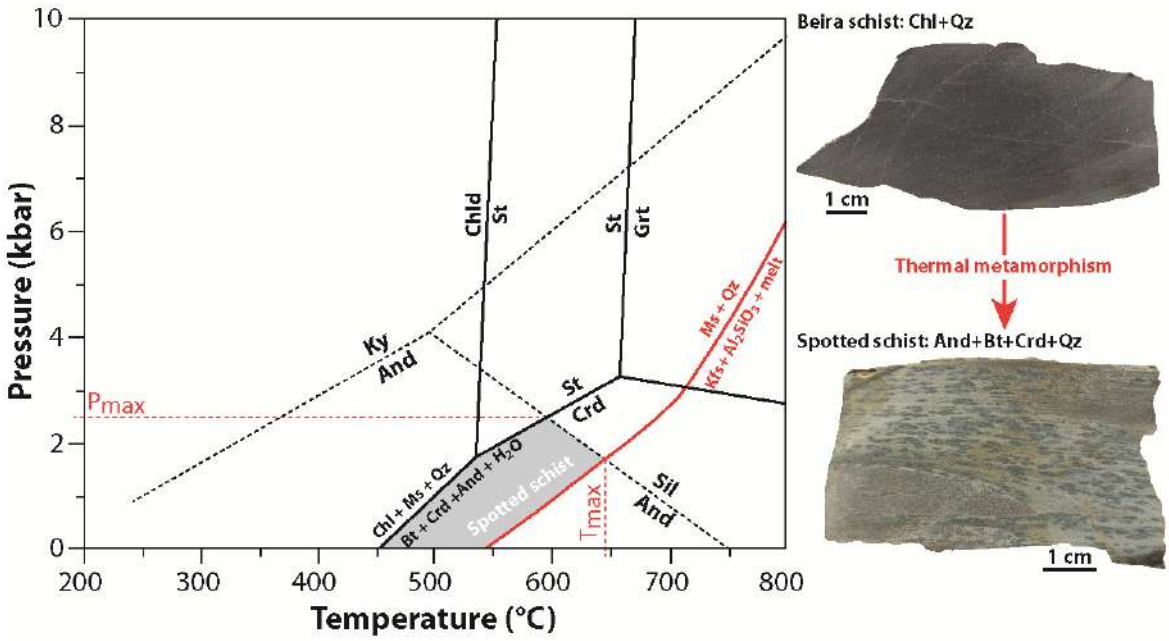

Figure 14 Samples of Beira schist and spotted schist from the Panasqueira deposit displaying effect of thermal metamorphism induced by the emplacement of the Panasqueira granite. KFMASH petrogenetic grid showing stability field (P and T conditions) of the paragenesis composing the spotted schist.

Although this granite is not outcropping, its lateral extent is inferred from the surface distribution of spotted schist and from drill holes distributed over the Panasqueira district (Fig.15a and 15b). This small intrusive body is characterized by an elliptical shape elongated in the NW-SE direction (7.5 x 4.5 km) with a thickness that can locally reach 2 km (Hebblethwaite and Antao, 1982; Thadeu, 1951; Kelly and Rye 1979; Clark, 1964; Ribeiro, 2018). This elongated shape can be related to the regional NE-SW horizontal shortening, which could occur during the granite emplacement. This granite is limited by the Alpine Cebola fault to the north-west and the Rio Zêzere fault to the south-east (Fig.15a and 15c). The important uplift induced by these large-scale Alpine structures led to important vertical displacements (up to 200-500 m) of the rigid blocks delimited by these faults. This uplift locally controlled by the Cebola and the Rio Zêzere faults could preserve the Panasqueira deposit from erosion.

As exposed by underground mining works and drill cores from the sector of Barroca Grande, the upper part of the granite intrusion is marked by the presence of a quartz-muscovite greisen cupola, around which the highest concentration of economic mineralized veins are concentrated (Fig. 15a and 15c). This greisen cupola is capped by approximatively 15 m of massive unmineralised quartz (silica cap) that could be emplaced in void space opened by the contraction of the intrusive body (Thadeu, 1951; Kelly and Rye, 1979). As evidenced from the interpolated trajectories of the penetrative vertical foliation (S_1), the foliation was locally affected by the presence of shear zones that caused the transposition of the regional NW-SE trending foliation into the NNW-SSE trending shear zones (Fig 15b). These inferred shear zones match with N-S trending faults exposed in the mine working and on the field (Fig. 15b). These faults, which belong to the brittle-ductile shear system induced by late transpressional deformation described previously, were initiated with strike-slip movements during the Variscan orogeny and were reactivated during the Alpine orogeny. The greisen cupola is aligned in the trend of these shear zones (Fig. 15b). Accordingly, these local shear zones could control and promote the emplacement of the cupola.

In the sector of Barroca Grande-Panasqueira, the W-(Sn)-Cu mineralization is hosted by a dense network of low dipping veins crosscutting the vertical foliation of the Beira schist and the greisen cupola (Fig.15c). This veins network is connected at depth with the greisen cupola and centered above it and extends over an area of 6 km² for a depth extension about 200-300 meters (Fig.14a and 14c) (Kelly and Rye 1979; Poyla et *al*.,

2000). The ore zone shows an asymmetric disposition with a maximum development in the southwestern part of the cupola. As suggested by Blattler (1985) this ore zone disposition could be related to the steeply southwest dipping of the granite roof underneath (Fig. 15a) that could control the preferential localization of structural weakness in the metasedimentary host rocks. Although the mineralized veins are essentially sub-horizontal, number of steeply dipping ore veins locally named "Galo veins" occurs in the vicinity of the cupola. A second mineralized zone present in the sector of Cabeço do Pião (southeastern part of the Panasqueira deposit) suggests the existence of another granite apophysis at depth. The occurrence of numerous veins and greisenized aplites in this sector supports this hypothesis.

In the following we describe the structural control of the mineralized veins system exposed in the sector of Barroca Grande and Cabeço do Pião and we compare these structures with the regional stress field previously constrained from the structural setting of the Beira Baixa province.

Figure 15 Geological and structural setting of the W-Sn-(Cu) Panasqueira ore deposit. (a) Geological map of the Panasqueira ore deposit showing the elevation (above the sea level) of the granite roof. (b) Interpolated foliation trajectories emphasizing occurrences of NNW-SSE trending dextral shear zone close the greisen cupola (data source Beralt Tin & Wolfram S.A.). (c) Geological cross sections (A-A') and (B-B') displaying the spatial relationship between mineralized veins and the underlying granite. The cross section (B-B') displays the vertical motion induced by the Alpine faults (Cebola fault, the Rio Zezêre and the 8E fault).

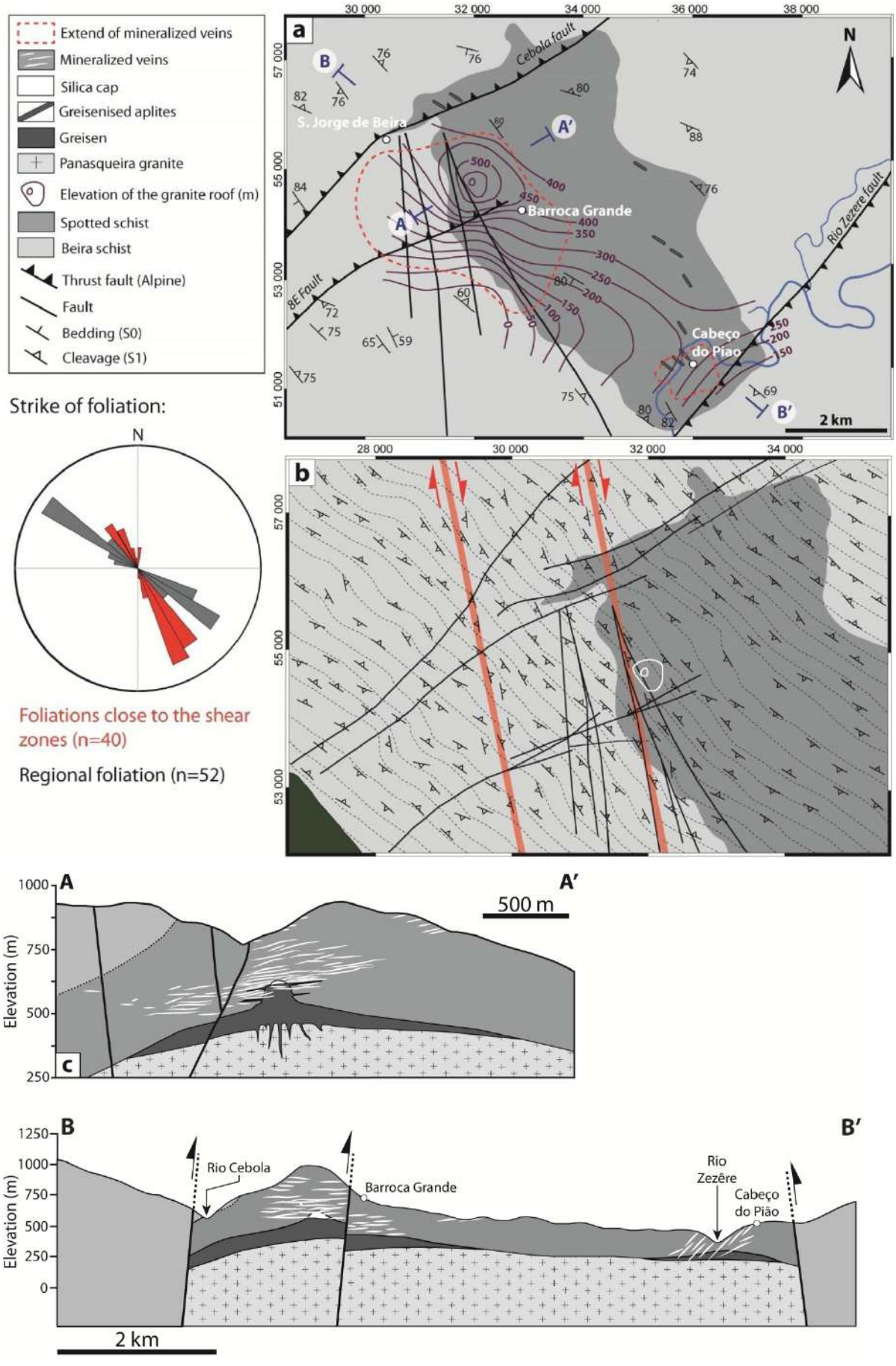
Extend of mineralized veins
Mineralized veins
Silica cap
Greisenised aplites
Greisen
Panasqueira granite
Elevation of the granite roof (m)
Spotted schist
Beira schist
Thrust fault (Alpine)
Fault
Bedding (S0)
Cleavage (S1)
Strike of foliation:
N
Foliations close to the shear zones (n=40)
Regional foliation (n=52)
a
b
c
Cebola fault
S. Jorge de Beira
Barroca Grande
Cabeço do Pião
Rio Zezere fault
BE Fault
2 km
500 m
Elevation (m)
Rio Cebola
Barroca Grande
Rio Zezêre
Cabeço do Pião

2.2 Sector of Barroca-Grande-Panasqueira

2.2.1 The folded barren quartz veins "Seixo Bravo"

As described previously the Beira Baixa region is characterized by the occurrence of barren horizontal extensional quartz veins, which were folded with varying degrees of intensity during the regional NE-SW horizontal shortening. These barren folded quartz veins are also present in the W-Sn-(Cu) Panasqueira deposit and are generally characterized by thickness ranging from 1 to 100 cm (Fig. 16). These veins locally names "Seixo Bravo" formed tight and upright folds with sub-horizontal NW-SE fold axes (Fig. 16a and 16b). In the most deformed cases, these veins were vertically boudined and fold hinges were isolated in response to the strong vertical stretching. This stretching can be also accommodated by the formation of sub-vertical thrusts that affect generally the fold hinges (fig. 16c). Although, these deformed quartz veins are generally barren, epigenetic sulfide (arsenopyrite and chalcopyrite) and tourmaline mineralizations can be observed in some cases (Fig. 16c) and are related to the mineralization stages that occurred in the flat mineralized vein swarm. These folded barren quartz veins are always crosscut by the ore-bearing flat veins (Fig. 16c and 16d) and hence predate clearly the hydrothermal mineralizing events of Panasqueira. Photomicrograph displayed in Figure 16e shows that folding of the metasedimentary cover can also be observed close to the mineralized veins despite the strong metasomatic alteration related to the hydrothermal activity of Panasqueira. Accordingly, the formation of mineralized veins of Panasqueira occurred after the folding of the Beira schist formation.

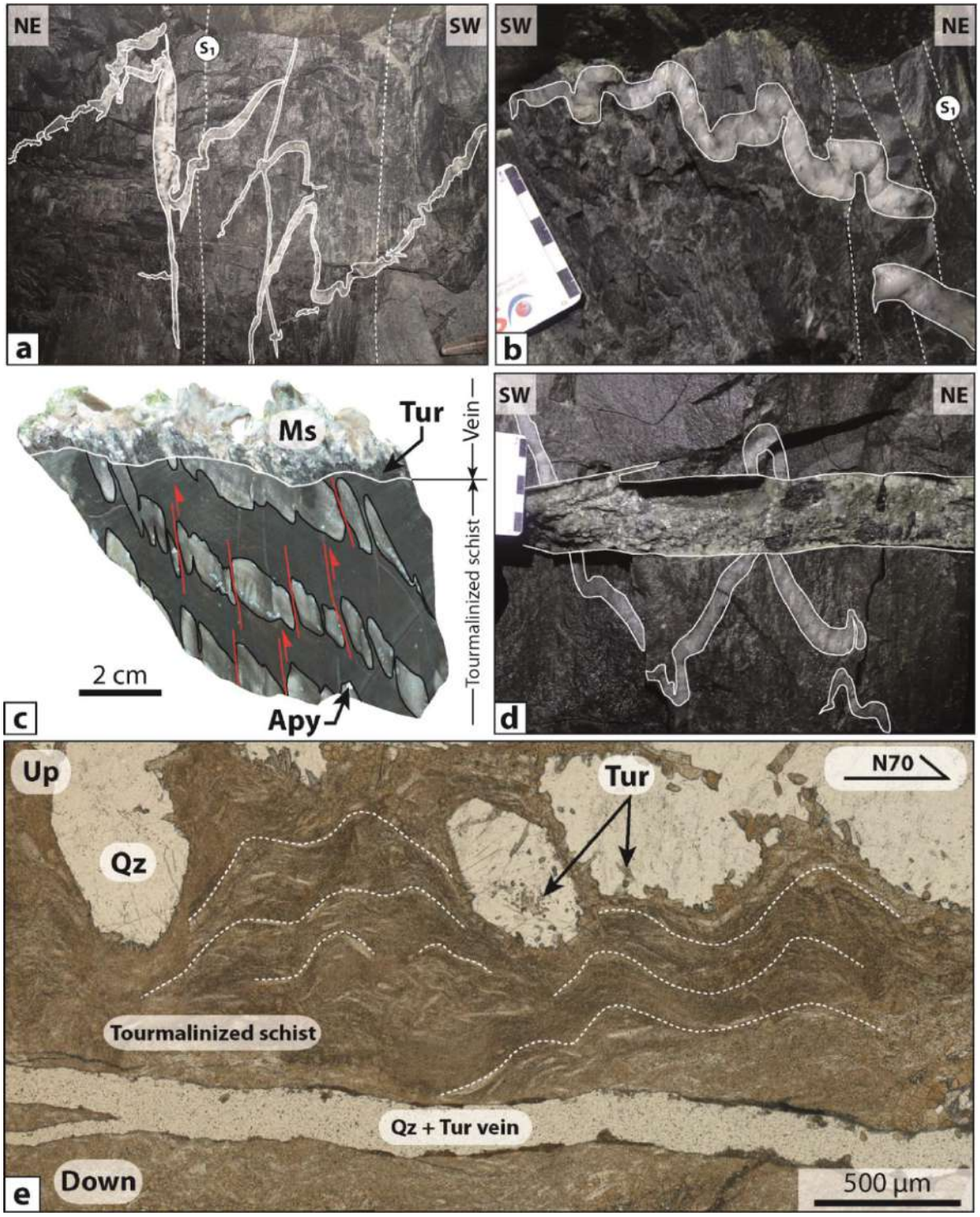

Figure 16 Structural characteristics of the folded sub-horizontal barren quartz veins present in the mine of Panasqueira. (a) and (b) Horizontal barren quartz veins intensively folded (sub-horizontal fold axes). (c) Sample displaying folded barren quartz vein affected by vertical thrusts (sample obtained with courtesy of F. Noronha). (d) Folded barren quartz vein crosscut by horizontal mineralized vein. Note the presence of wolframite in the horizontal mineralized quartz vein. This folded and thrusted barren quartz vein was then crosscut by horizontal mineralized vein. Note the presence of epigenetic arsenopyrite and tourmaline mineralization in the folded barren quartz veins. (e) Photomicrograph displaying folds in tourmalinized schist close to a quartz-tourmaline vein.

2.2.2 The horizontal barren quartz veinlets related to the thermal metamorphism

Additionally to the folded barren quartz veins previously described, and which were probably related to the regional metamorphism, a network of sub-horizontal barren quartz veinlets (of 1 to 5 cm thick) is also exposed in the Panasqueira deposit (Fig. 17). These horizontal barren quartz veinlets are generally roughly parallel to the flat ore-bearing veins and can be easily confounded with them (Fig. 17a). These veinlets are usually mainly composed of quartz and biotite, which occurs preferentially along the vein selvages (Fig. 17b and 17c). The composition of this biotite selvage is close to those of biotite composing the spotted schist and that was formed during the thermal metamorphism induced by the emplacement of the Panasqueira granite (Fig. 17d). The crystallization temperatures estimated for these quartz-biotite veinlets (from the geothermometer of Henry et *al*. (2005)) range between 500 and 600°C and are similar to those obtained for biotite composing the spotted schist (Fig. 17e). These temperatures are close to those previously estimated from the paragenesis of spotted schist. Furthermore, fluid inclusions study performed by Noronha et *al*. (1992) on quartz composing these veinlets suggest that they were formed from metamorphic fluids rich in CH_4, CO_2 and N_2 at temperature ranging between 290 and 420 °C. Accordingly, the formation of these quartz-biotite veinlets was probably related to the thermal metamorphism induced by the emplacement of the Panasqueira granite. These veinlets are generally crosscut or reopened during the formation of the ore-bearing veins. Consequently, the formation of these veinlets predates the hydrothermal activity of Panasqueira. This early event is referred to as quartz biotite stage (QBS) in the following of this chapter.

Figure 17 Petro-structural characteristics of the sub-horizontal barren quartz veinlets parallel to mineralized veins swarm. (a) Dense network of barren quartz veinlets, which are roughly parallel to a thick mineralized vein. (b) and (c) Zoom and photomicrograph of a barren horizontal quartz veinlet showing the presence of biotite along the veinlet selvage. (d) Chemical characteristics of biotite composing the spotted schist and the horizontal barren quartz veinlets. For comparison the chemical composition of biotite composing the two-mica granite of Panasqueira are also plotted in this diagram. (e) Application of the Henry et *al*. (2005) biotite geothermometer on biotite composing the spotted schist, the horizontal barren veinlets and the two-mica granite of Panasqueira.

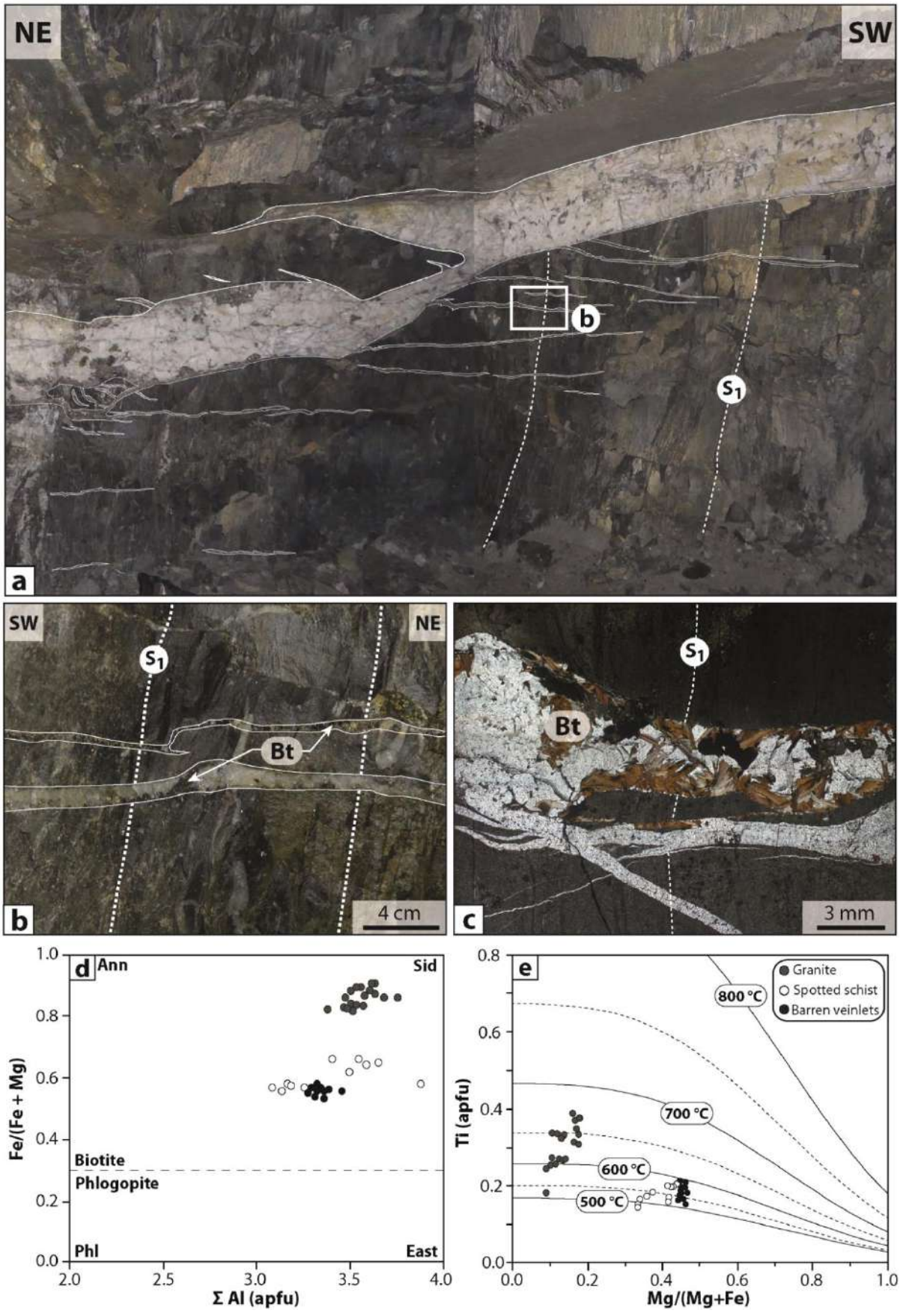
NE
SW
b
S1
a
SW
NE
S1
Bt
4 cm
b
S1
Bt
3 mm
c
d
Ann
Sid
Biotite
Phlogopite
Phl
East
Fe/(Fe + Mg)
Σ Al (apfu)
e
Granite
Spotted schist
Barren veinlets
800 °C
700 °C
600 °C
500 °C
Ti (apfu)
Mg/(Mg+Fe)

2.2.3 Geometric and structural characteristics of the ore-bearing vein swarm

As already described in numerous studies (Thadeu, 1951; Kelly and Rye, 1979; Polya, 1989; Foxford et *al*., 1991; Foxford et *al*., 2000; Jacques et *al*., 2017) the W-Sn-(Cu) mineralization of Panasqueira is hosted by a dense network of stacked shallow-dipping extensional veins crosscutting both the regional vertical foliation and the vertical Seixo bravo veins network (Fig. 18a and 18b). This dense network of flat veins defines an ore zone of approximately 2500 m in length for width ranging between 400 to 2200 m and for maximum vertical extension of about 300 m. These flat veins have generally an average dip of 8 to 10° SW (Fig. 18b) and thickness ranging between 0.1 to more than 1 m. Vein walls are generally sharp and planar and match perfectly with the opposite walls. Accordingly, mineralized veins were vertically opened and dilated suggesting a vertical stretching during the vein formation. Vein lodes are generally interconnected by subvertical bridges, which transfer dilation between overlapping and separated veins (Fig. 18c and 18d). As described by Thadeu (1951) and Kelly and Rye (1979), these bridges are generally rich in wolframite (Fig. 18d). The pre-ore horizontal veins (quartz-biotite and quartz tourmaline veinlets) are generally preserved along one or both vein walls (Fig. 18c, 18 and 18f) and were probably preferentially reopened and exploited during the W-Sn mineralization stage.

Although mineralized veins were generally opened without significant shear displacements, some veins exhibit (i) pull-apart structures, (ii) en echelon-arranged veins and (iii) thrust associated to flat lying veins. These structures define top to the NE or SW shearing (Fig. 18g to 18j) and emphasize that the formation of the flat-lying extensional mineralized veins of Panasqueira was related to a NE-SW horizontal shortening and vertical stretching. During the circulation of mineralizing fluids through the vein network, fluid-rock interactions produced extensive alteration halos of tourmalinized and muscovitized schist around veins (see **Chapter III**).

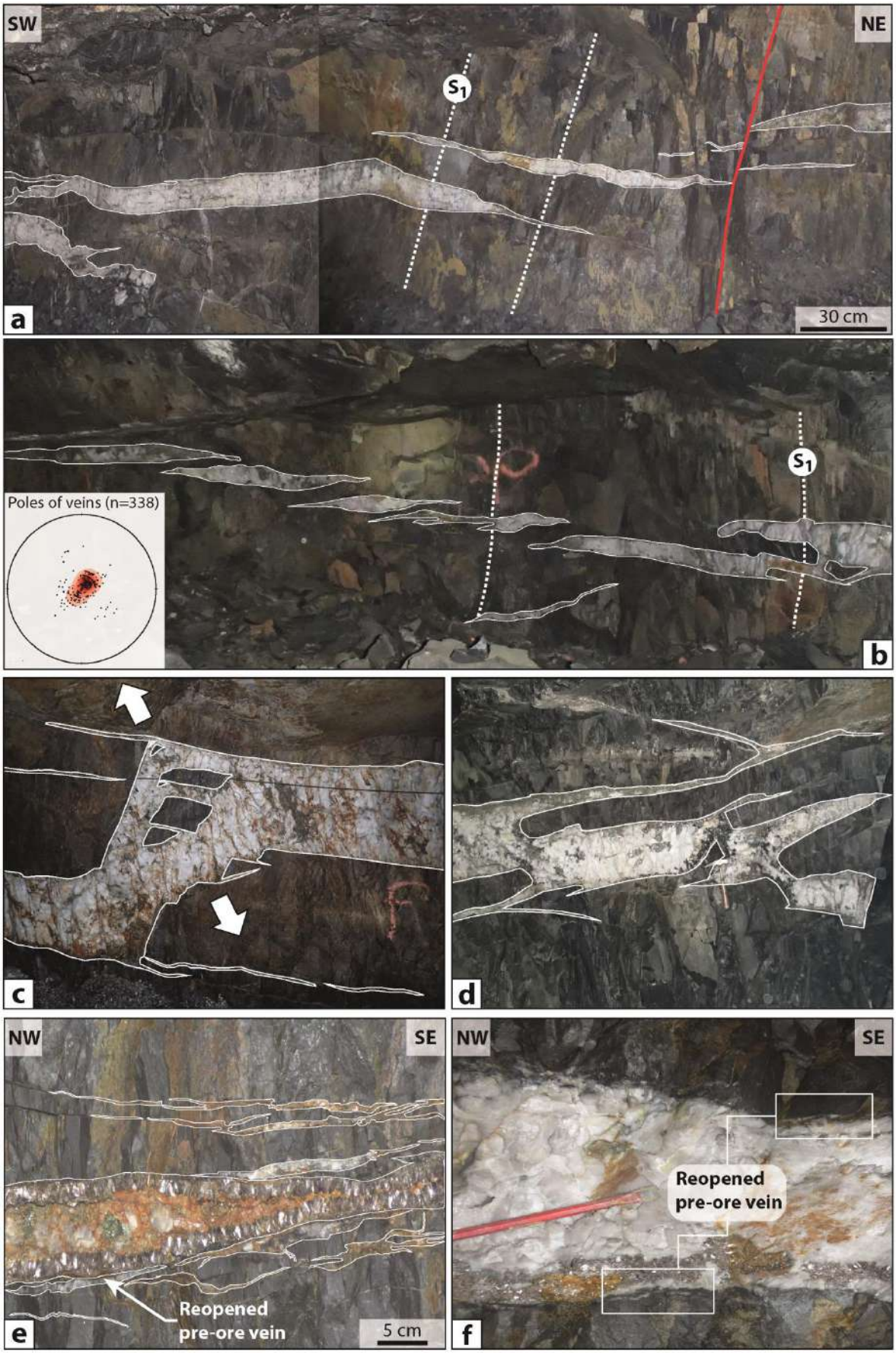
SW
NE
S1
30 cm
a
Poles of veins (n=338)
S1
b
c
d
NW
SE
Reopened
pre-ore vein
5 cm
e
NW
SE
Reopened
pre-ore vein
f

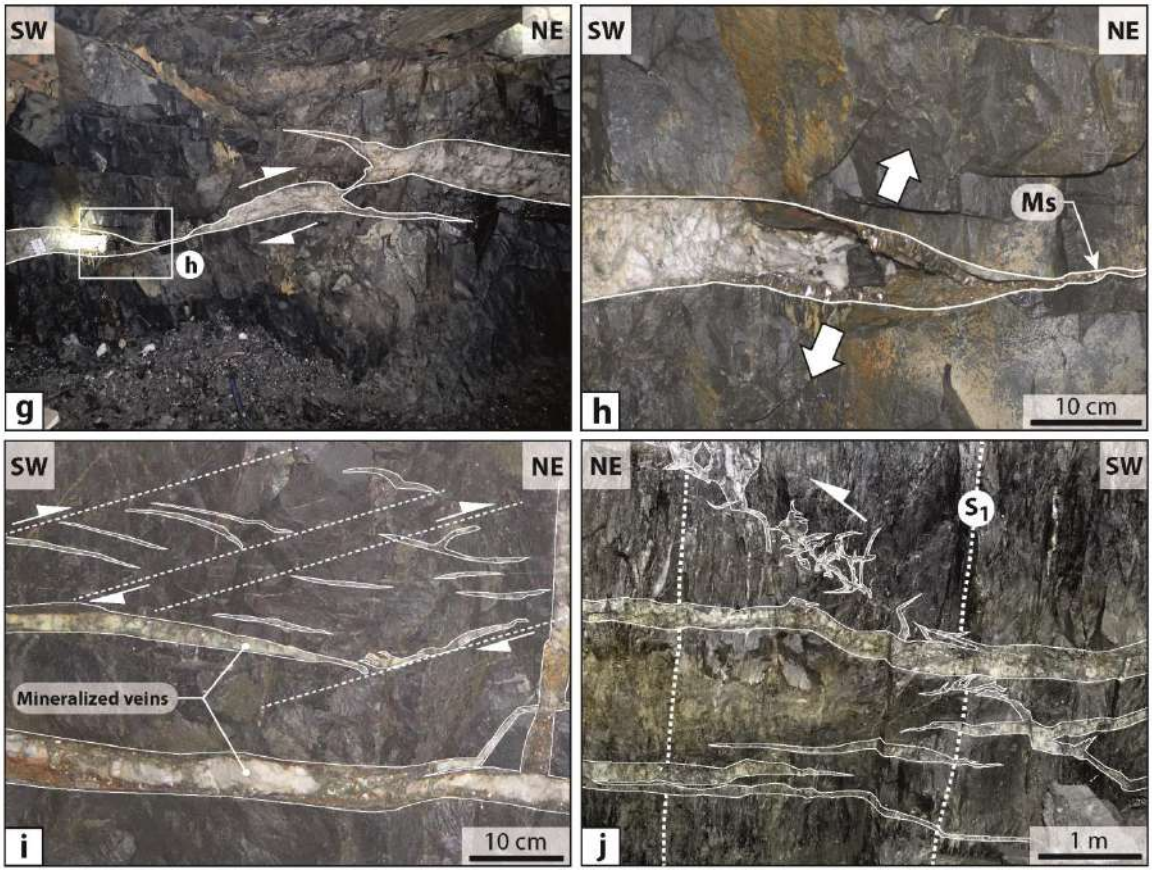

Figure 18 Structural characteristics of the sub-horizontal ore-bearing quartz vein swarm of Panasqueira. (a) and (b) typical horizontal mineralized extensional veins defining en-echelon segments. These ore-bearing veins are perpendicular to the vertical regional foliation and crosscut the barren vertical quartz veins. The lower-hemisphere equal-area stereoplot shows the poles of extensional mineralized veins. (c) and (d) Mineralized veins composed of several linked en-echelon segments, which were connected by sub-vertical bridge structures. (e) and (f) Sub-horizontal pre-ore barren quartz veins reopened during the mineralization stages of Panasqueira (g) Linked flat extensional veins exhibiting pull-apart structure compatible with NE-SW horizontal shortening and vertical opening and dilation of veins. (h) Zoom on the vein displayed in image g. (i) En echelon-arranged extensional mineralized veins defining top to the NE shear band. (j) Relationships between en-echelon arranged tension gashes, thrust and flat mineralized extensional veins. All of these structures seem to be formed in response to a horizontal shortening and vertical stretching.

Although the ore-bearing veins are generally flat and not affected by shear displacement, some veins exhibit slight to moderate deformation occurring as folding and thrusting of the mineralized veins (Fig. 19). Indeed, some veins were slightly folded with vertical NW-SE-trending axial planes, which are parallel to the regional foliation previously described (Fig. 19a to 19c). In some occurrences of folded veins, a rough vertical foliation was developed in veins during their folding. This intra-vein foliation is generally refracted compared to the foliation planes observed in the Beira schist (Fig. 19b). Accordingly, mineralized veins were partially affected by the regional NE-SW horizontal shortening. This horizontal compression led also to the formation of sub-vertical brittle thrusts striking NW-SE that displaced vertically the flat mineralized veins for short distances (Fig. 19e to 19g). These thrusts are generally sub-parallel to the regional foliation and are usually cemented by clay minerals, either by sulfides (galena and pyrite) or carbonate (siderite and calcite) assemblages (Fig. 19e). These faults, which postdate the vein formation have no influence on tungsten grade and have not controlled the circulation of the ore-bearing fluids.

Figure 19 Sub-horizontal ore-bearing quartz veins affected by compressive deformation induced by the regional NE-SW horizontal shortening. (a) Folded quartz veins crosscut by sub-horizontal mineralized flat vein. (b) and (c) Sub-horizontal mineralized veins slightly folded during the NE-SW horizontal shortening. Note the formation and the refraction of rough vertical foliation in the folded mineralized veins displayed in b. (d) Folded barren quartz veins crosscut by horizontal mineralized vein, in which the vertical foliation can be observed. (e) to (g) Sub-horizontal mineralized veins affected and displaced by sub-vertical thrusts in response to the NE-SW horizontal shortening.

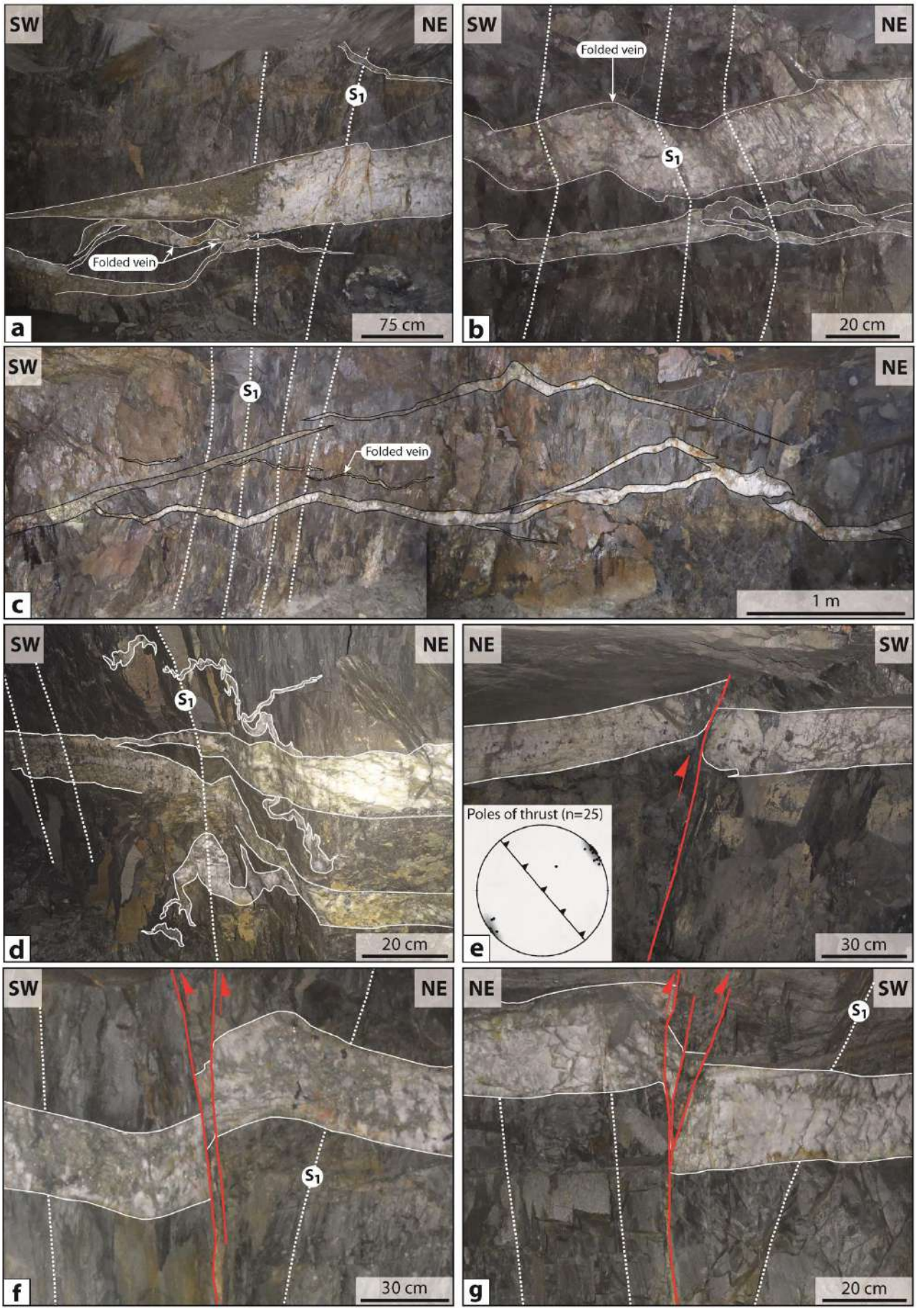
SW
NE
S1
Folded vein
75 cm
a
SW
NE
Folded vein
S1
20 cm
b
SW
NE
S1
Folded vein
1 m
c
SW
NE
S1
20 cm
d
NE
SW
Poles of thrust (n=25)
30 cm
e
SW
NE
S1
30 cm
f
NE
SW
S1
20 cm
g

2.2.4 The strike-slip faults

A late NNW-SSE and ENE-WSW sub-vertical fault system crosscut and postdate the sub-horizontal mineralized veins of Panasqueira (Fig. 20). These two set of conjugate faults were initiated with strike-slip movements during the Variscan orogeny, with dextral displacement for the NNW-SSE trending faults and sinistral displacement for the ENE-WSW trending faults (Fig. 20f). Then, these faults were reactivated with vertical displacements (mainly normal) during the Alpine orogeny. These faults are never mineralized in wolframite. However, they could contain breccia with elements coming from the mineralized veins and are generally cemented by carbonates and sulfides assemblages (galena and pyrite) (Fig. 20). These late faults are similar to those present in the Beira Baixa region and are compatible with the regional NE-SW regional shortening highlighted from structures observed in the Beira Baixa province and in the Panasqueira ore deposit.

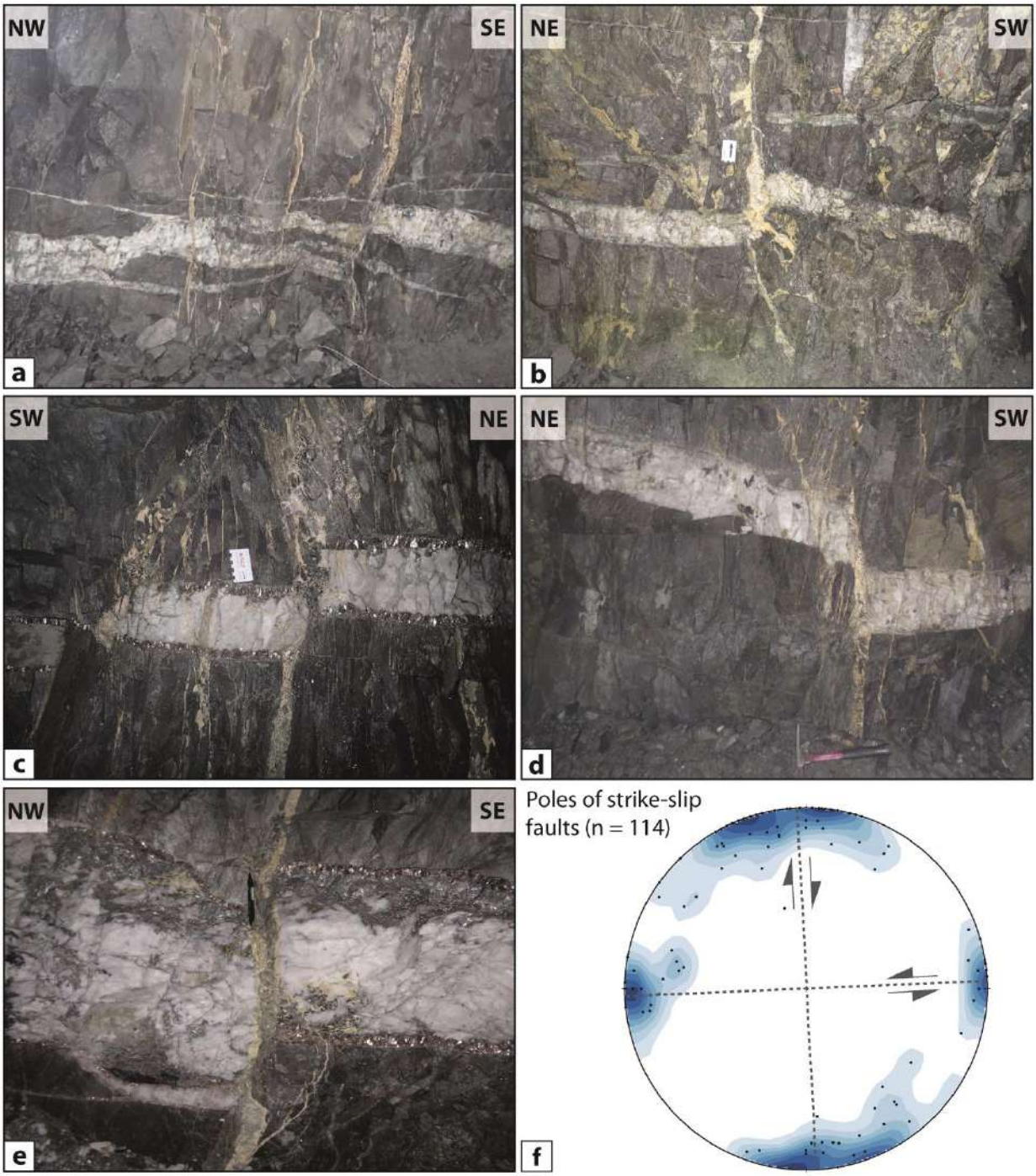

Figure 20 (a) to (e) Sub-vertical strike slip faults crosscutting the flat mineralized veins of Panasqueira. These faults were reactivated during the Alpine orogeny and cemented by carbonate and sulfides assemblages. (f) Lower-hemisphere equal-area stereoplot showing the orientation of poles of the strike-slip faults present in the mine of Panasqueira.

2.2.5 Microstructures of mineralized veins and metasedimentary host rocks

The microstructural characteristics of (i) the metasedimentary host rocks close to the vein lodes and (ii) the mineralized veins of Panasqueira are displayed in Figure 21 and 22. The vertical conjugate strike-slip C-S shear bands observed in the Beira Baixa provinces can also be observed in the metasedimentary host rocks of Panasqueira at the microscopic scale (Fig. 21). This conjugate C-S shear bands system is composed of a series of sinistral E-W trending shear bands (Fig. 21a, 21c and 21e) and a series of dextral N-S trending shear bands (Fig. 2b and 21d). This lateral shearing is accompanied by (i) the transposition of the regional foliation (S_1) into the micro-shear bands and (ii) the formation of pull-apart structures (Fig. 21). Biotite composing spotted schist is generally not deformed and has preferentially crystallized along the shear bands. Accordingly, the thermal metamorphism responsible of the formation of spotted schist occurred likely after the transpressional deformation event, during which C-S shear bands were formed. These macroscopic and micro C-S shear bands could promote the heat transfer by fluid flow induced by the emplacement of the Panasqueira granite, explaining the preferential crystallization of biotite along these micro C-S shear bands.

The sub-horizontal mineralized veins are filled by elongated blocky and fibrous quartz, which have grown vertically from the vein walls toward the center part of veins (Fig. 22a). These veins exhibit typical banded textures characterized by fluid and mineral inclusions trails (tourmaline and sulfides) that form horizontal bands parallel to the vein walls (Fig. 22a, 22b and 22e). These bands emphasize implication of crack-seal mechanism, during which a process of repeated cracking and sealing was involved during the formation of mineralized veins. Accordingly, the mineralized veins of Panasqueira correspond to mode I extensional veins (Pollard and Segall, 1987; Scholz, 2002; Foxford et *al*., 2000; Bons et *al*., 2012), which were preferentially opened vertically and perpendicular to the vein planes without significant shearing. This repetitive vertical opening and dilation of veins is compatible with the regional NE-SW horizontal shortening. However, rare occurrences of horizontal shearing parallel to the vein walls can be locally observed especially within muscovite and biotite selvages, which were sheared with top to the NE or SW displacements (Fig. 22c). This micro-shearing led also to the formation of micro-pull-apart infilled by sulfide minerals (chalcopyrite and pyrite) during the late hydrothermal stages. The vertical C-S shear bands previously described are

crosscut by the horizontal mineralized veins (Fig. 22d) and hence predate the formation of quartz-biotite and mineralized veins of Panasqueira. As observed at the macroscopic scale, the pre-ore horizontal veins (quartz-biotite (QB) and quartz tourmaline veinlets) were preferentially reopened and exploited during the W-Sn mineralization stage (QTS and MOSS) and during the late sulfide stage (MSS).

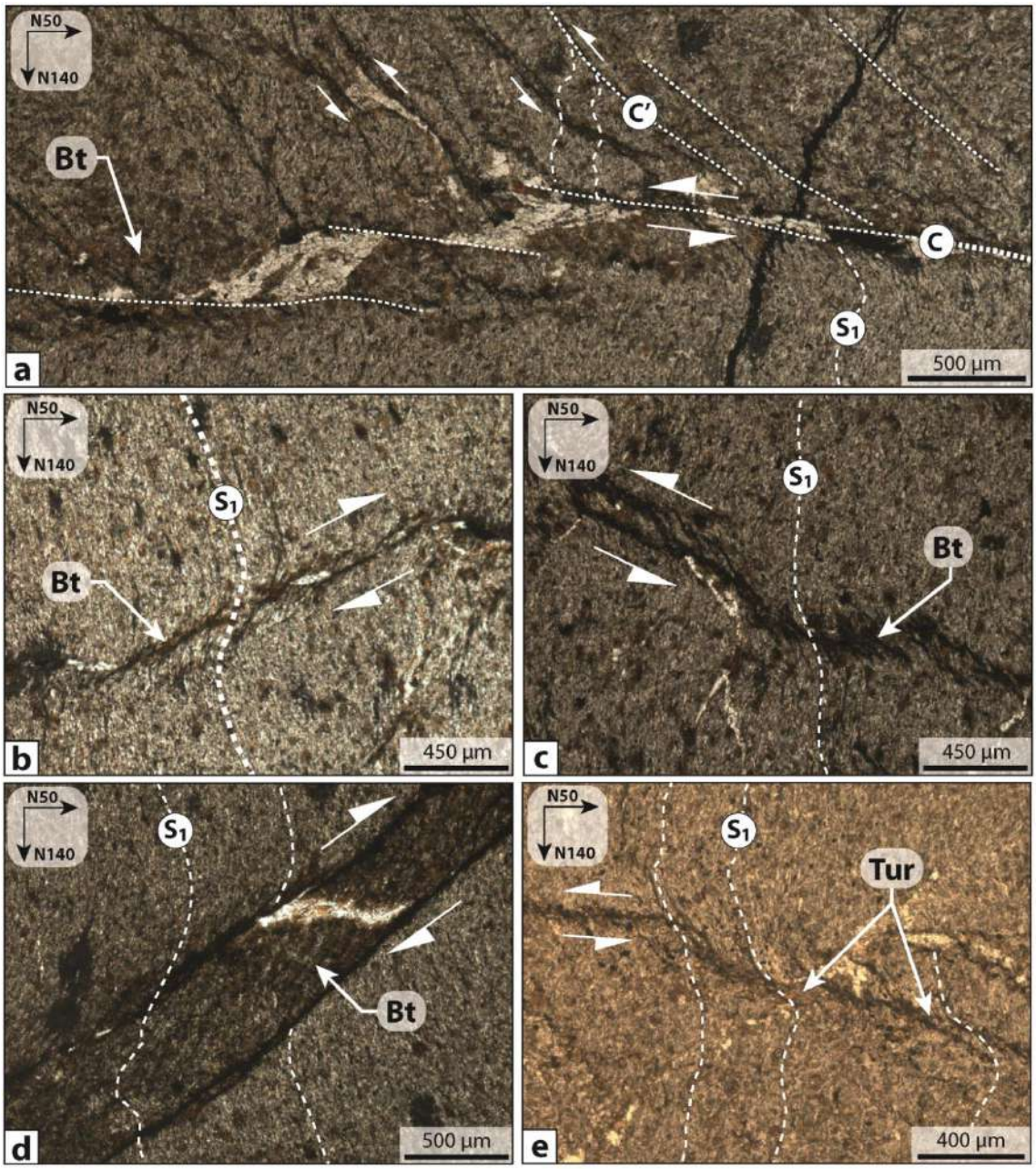

Figure 21 Microphotograph displaying micro-shear bands observed in the metasedimentary host rocks close to sub-horizontal mineralized veins composing the Panasqueira deposit. This set of shear bands comprises dextral shear bands striking N-S (b and d) and conjugate sinistral E-W trending shear bands (a, c and e). Note the preferential crystallization of biotite related to the thermal metamorphism along these shear bands. Pull-apart shown in (a) and (b) are filling by quartz.

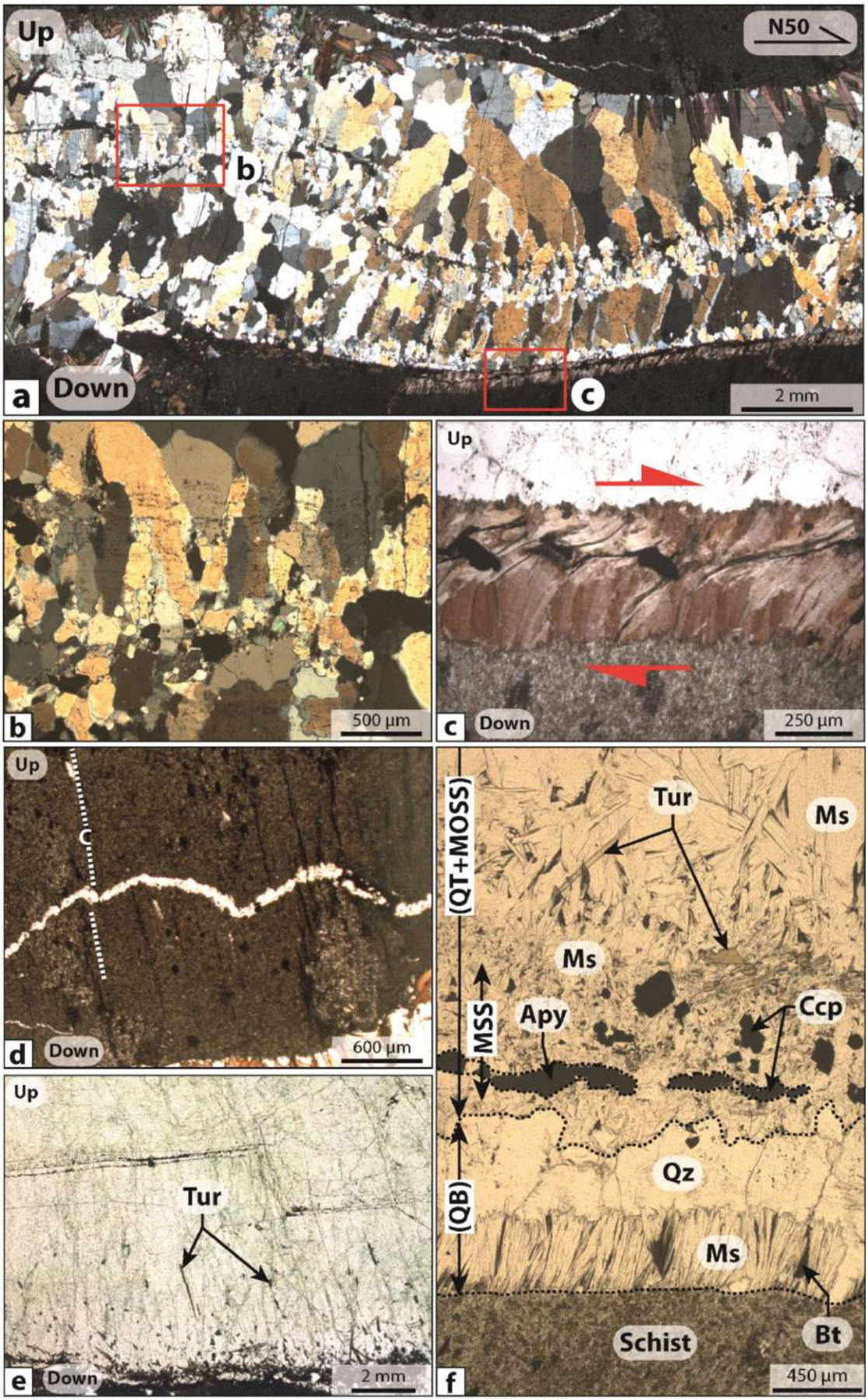
Up
N50
b
a
Down
c
2 mm
b
500 µm
Up
c
Down
250 µm
Up
C
d
Down
600 µm
Up
Tur
e
Down
2 mm
(QT+MOSS)
Tur
Ms
Ms
MSS
Apy
Ccp
Qz
(QB)
Ms
Schist
Bt
f
450 µm

Figure 22 Microstructural characteristics of the flat mineralized veins of Panasqueira. Quartz-biotite vein exhibiting typical crack-and seal structure. Note the shearing of the biotite selvage of the lower vein wall. (b) Zoom on quartz showing horizontal inclusions bands typical of extensional vein. (c) Zoom on the lower vein wall, in which the biotite selvage was sheared with top to the NE displacement. (d) Vertical shear bands displayed in Fig. 21 crosscut by the sub-horizontal mineralized veins of Panasqueira. (e) Typical sub-horizontal quartz-tourmaline vein characterized by crack-and seal texture. (f) Quartz-biotite vein (QB), which was reopened during the mineralization stages (QTS and MOSS).

2.2.6 Structural control of the W-Sn-(Cu) mineralization of Barroca Grande

The structural characteristics and the structural evolution of the Panasqueira deposit (sector of Barroca Grande) are displayed in Figure 23. All of these structurers are similar to those observed in the Beira Baixa network region and compatible with the regional NE-SW horizontal shortening (Z) previously constrained. This compressive deformation led to the formation of sub-horizontal barren quartz veins, which were then folded with varying degrees of intensity to form the Seixo Bravo observed in mine. This horizontal shortening can be locally accommodated by transpressional deformation, during which vertical conjugate C-S shear bands with lateral displacements (dextral and sinistral) were formed. These shear bands could promote the heat transfer induced by the emplacement of the Panasqueira granite that triggered the preferential crystallization of biotite along these shear bands during the thermal metamorphism. The vertical regional foliation, the Seixo bravo veins network and the vertical C-S shear bands were crosscut by (i) the sub-horizontal quartz-biotite pre-ore veins probably formed during the thermal metamorphism and (ii) the horizontal mineralized veins swarm. The opening of mineralized veins can be locally accompanied by the formation of en-echelon-arranged extensional veins, pull-apart and thrusts with top to the NE or SW displacements consistent with NE-SW horizontal shortening and vertical stretching (X).

As suggested by Foxford et *al*. (2000) the opening of these mode I sub-horizontal extensional veins could result from hydraulic fracturing, which involved injection of fluids at supralithostatic pressure conditions ($P_f \geq \sigma_3$) in a compressive crustal regime consistent with the regional stress field. The re-opening of the pre-ore veins, the banded and crack-seal textures observed in the mineralized veins emphasize multistage of opening and infilling that suggest fluctuations of fluid pressure conditions during the hydrothermal activity of Panasqueira. After their formation, the mineralized veins of Panasqueira were locally slightly folded (with sub-horizontal NE-SW fold axes) and crosscut by both

vertical NW-SE trending thrust and the strike-slip fault network observed in the Beira Baixa region Accordingly, the formation of the sub-horizontal mineralized veins of Panasqueira was bracketed by different structures formed over the same regional NE-SW horizontal shortening, and which was again active after the vein formation. Consequently, the mineralized vein network of Panasqueira was likely formed over a same continuum of deformation compatible with the regional compression related to the Variscan orogeny. The occurrence of both compressive and transpressive structures, which were formed closely during the same regional shortening event suggest that strains along the X and Y axes were close and may reverse in response to fluid pressure conditions related to the hydrothermal activity of Panasqueira.

According to these structural characteristics, the formation of the unusual sub-horizontal mineralized veins of Panasqueira does not result from the exploitation of pre-existing structures as suggested in numerous studies (Kelly and Rye, 1979; Derre et *al*., 1986; Jacques et *al*., 2017) but rather from conjunction of high fluid pressure conditions and the regional tectonic activity.

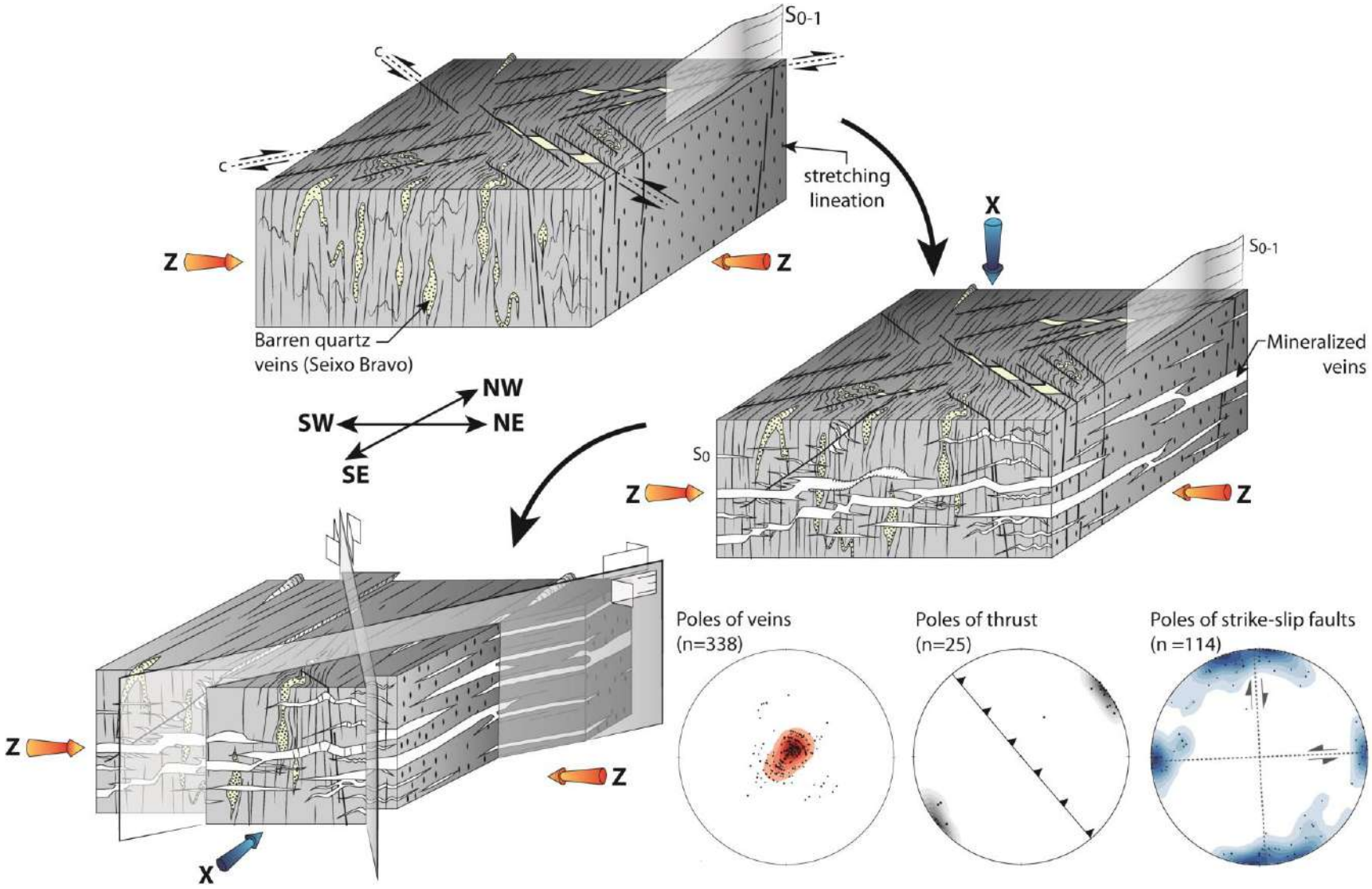

Figure 23 Synthesis of structural data and structures observed in the sector of Barroca Grande of the W-Sn-(Cu) Panasqueira deposit. All of these structures and the formation of mineralized veins were likely formed during the regional NE-SW horizontal shortening (Z).

2.3 Sector of Cabeço do Pião

A second mineralized system is present in the sector of Cabeco do Pião in the southeastern part of the Panasqueira district (Fig. 24). In this sector mineralization occurs as more or less inclined NE-SW veins lodes. This sector is also marked by the occurrences of numerous strike-slip faults that belong to the conjugate dextral N-S trending and sinistral E-W trending shearing system observed in the region of Beira Baixa. Structural data and cartographic relationships between veins and these strike-slip faults suggest that mineralized veins could correspond to tension gashes opened in response to the regional NE-SW horizontal shortening (Fig. 24).

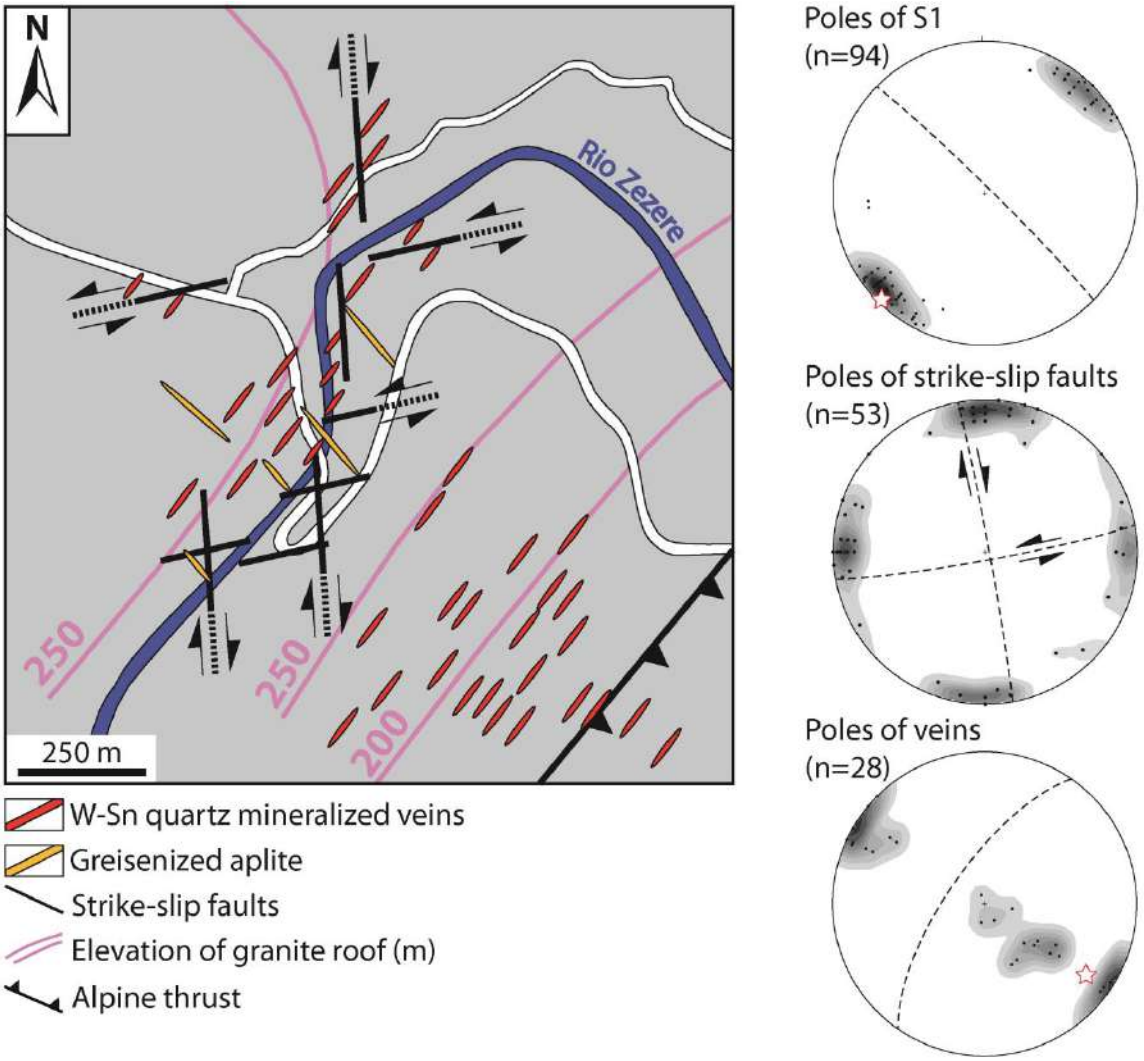

Figure 24 Structural map of the sector of Cabeço do Pião showing relationship between the mineralized tension gashes veins and the conjugate strike-slip faults formed during the regional NE-SW horizontal shortening. The lower-hemisphere equal-area stereoplots show the orientation of poles of the regional foliation (S1), the strike-slip faults and the mineralized quartz veins present in the sector of Cabeço do Pião. (modified from Thadeu, 1951 and Conde et *al*., 1971).

Structural characteristics of the mineralized veins exposed in the sector of Cabeço do Pião are displayed in Figure 25. Dextral N-S striking C-S shear bands can be locally observed and are marked by the transposition of the NW-SE striking foliation into the shear bands (Fig. 25a).Veins can be locally arranged as en-echelon tension gashes defining dextral N-S and sinistral E-W striking shear bands compatible with lateral displacements observed on the strike-slip faults (Fig. 25b and 25c). Some veins occurrences show direct structural relationships between strike-slip faults and inclined quartz veins (Fig. 25d to 25g). These veins are generally infilled by quartz-muscovite assemblage and can also exhibit wolframite (Fig. 25h to 25j), cassiterite and sulfides mineralization suggesting that these extensional tension gashes have drained W-bearing fluids during the mineralization event. The circulation of mineralizing fluids through these tension gashes triggered fluid-rock interactions, which produced extensive alteration halos of tourmalinized and muscovitized schist around inclined veins.

Like ore-bearing structures composing the sector of Barroca Grande, these inclined mineralized veins are compatible with the regional stress field involving NE-SW horizontal shortening.

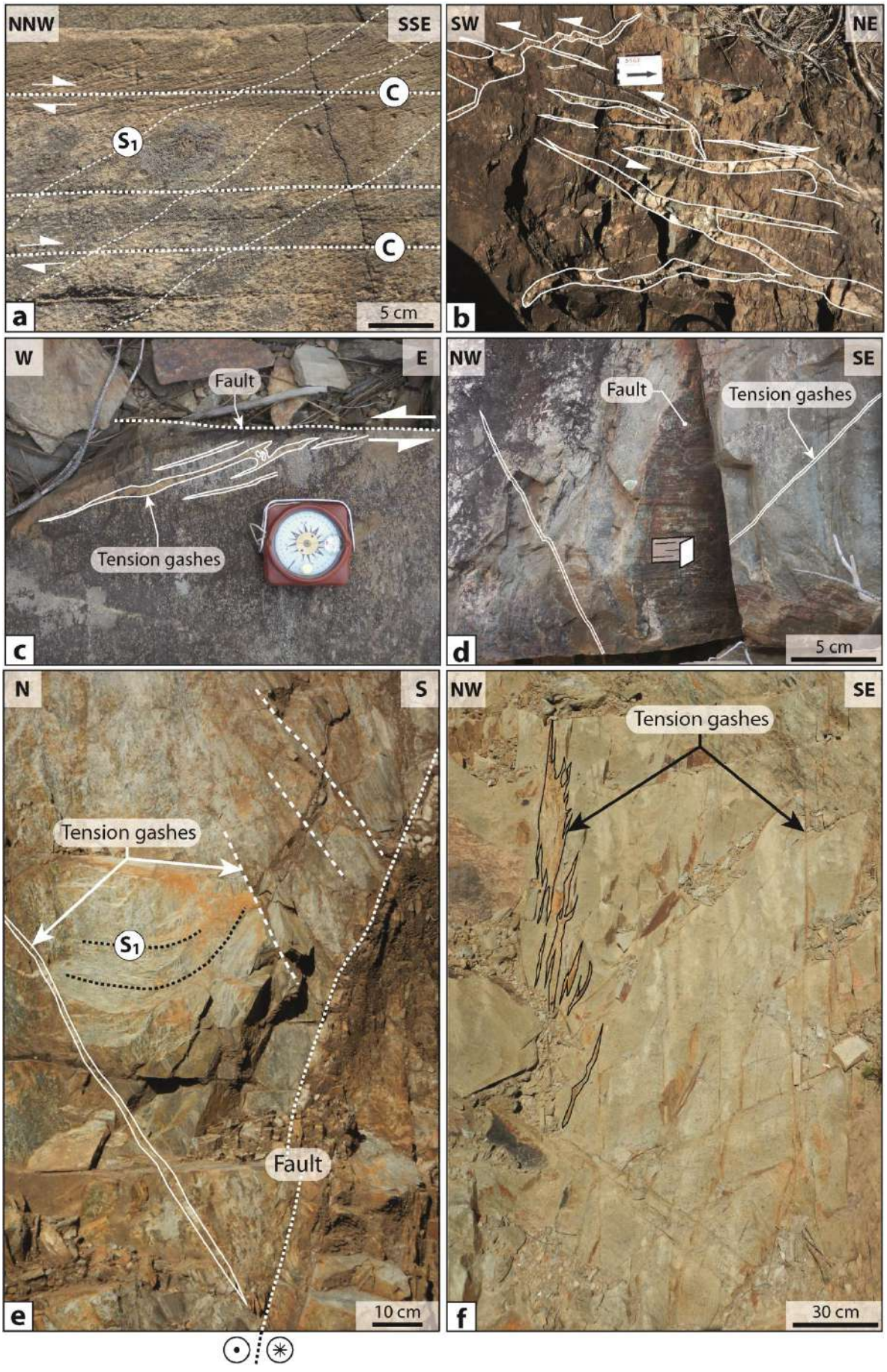
NNW
SSE
C
S1
C
5 cm
a
SW
NE
b
W
E
Fault
Tension gashes
c
NW
SE
Fault
Tension gashes
5 cm
d
N
S
Tension gashes
S1
Fault
10 cm
e
NW
SE
Tension gashes
30 cm
f

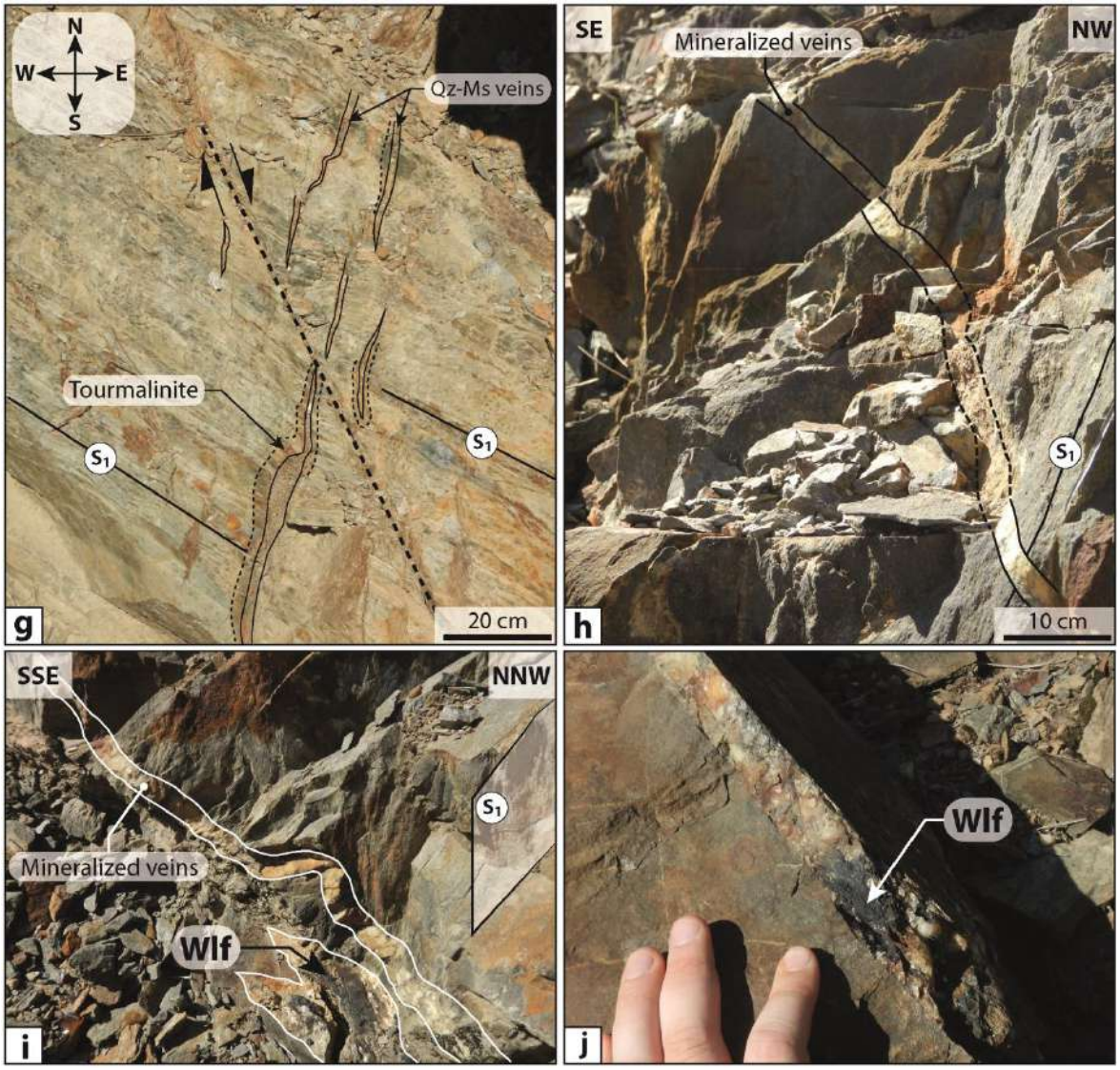

Figure 25 Structural characteristics of the W-Sn-(Cu) mineralization present in the sector of Cabeço do Pião (southeastern part of the Panasqueira district). (a) Dextral N-S trending shear zone with typical C-S structure marked by the transposition of the regional foliation into the shear bands. (b) En echelon-arranged tension gashes defining sinistral E-W trending shear band. (c) to (e) Photographs showing relationship between strike-slip faults and the sub-vertical tension gashes quartz veins. (f) Sub-vertical tension gashes mainly filled by quartz and muscovite. (g) Photograph displaying relationship between mineralized subvertical tension gashes and dextral N-S striking fault. (h) to (j) Sub-vertical quartz veins mineralized in wolframite.

3. Structural model of formation of the Panasqueira deposit

Based on structures observed at the regional scale in the Beira Baixa province and structural controls of the mineralization in the sector of Barroca Grande and Cabeço do Pião, we propose a synthetic structural model of formation of the W-Sn-(Cu) Panasqueira deposit (Fig. 26). In this model we consider that the emplacement of both the granite and the mineralized veins of Panasqueira occurred over a same continuum of deformation compatible with the regional compression related to the Variscan orogeny, which induced a strong NE-SW horizontal shortening.

During this compressive deformation the quartzite and the Beira schist were extremely folded leading to the formation of tight and upright folds with horizontal NW-SE fold axes. This deformation was so intense that the vertical stretching led to the boudinage of fold hinges, which were separated by subvertical thrusts. The extreme vertical stretching caused also the transposition of bedding parallel to the regional vertical foliation. This vertical stretching and horizontal shortening triggered the formation of horizontal extensional barren quartz vein, which were then folded with varying degree of intensity. Moreover, this regional horizontal shortening was locally accommodated by the formation of dextral N-S trending and conjugate sinistral E-W trending brittle-ductile shear bands.

During the late stage of the Variscan orogeny, the Panasqueira granite was emplaced with an elongated shape along the NW-SE direction compatible with the regional NE-SW shortening. The shear zones formed by transpressional deformation could locally promote the emplacement of the cupola of Barroca Grande and the emplacement of the granite apophysis present at depth in the sector of Cabeço do Pião. The conjunction of (i) the regional compressive stress field and (ii) elevated fluid pressure conditions (probably supralithostatic) related to the hydrothermal activity of Panasqueira triggered the opening and the vertical dilation of sub-horizontal extensional (mode I) mineralized veins in the sector of Barroca Grande. The formation of these veins was polyphased and involved several stages of opening and infilling suggesting (i) fluctuations of fluid pressure conditions and (ii) active tectonic during the hydrothermal activity of Panasqueira. The slight folding of these veins and the formation of sub-vertical thrusts and strike slip faults that postdate and crosscut mineralized veins provide evidence of continuous compressive deformation (with NE-SW horizontal shortening) before, during and after the formation of the Panasqueira deposit.

The hydrothermal activity of Panasqueira occurred also in the sector of Cabeço do Pião, in which ore-bearing fluids were drained by inclined structures that likely correspond to extensional tension gashes aligned in the direction of the regional NE-SW shortening. This strong difference of structural control between mineralized veins of Barroca Grande and Cabeço do Pião can be related to difference of fluid pressure conditions involved during the formation of these two distinguished systems. Indeed, high fluid pressure conditions in the sector of Barroca Grande could locally change the stress state and promote the opening of sub-horizontal extensional veins (Sibson et *al*., 1988; Cox, 1995; Foxford et *al*., 2000; Sibson, 2001; Bons et *al*., 2012).

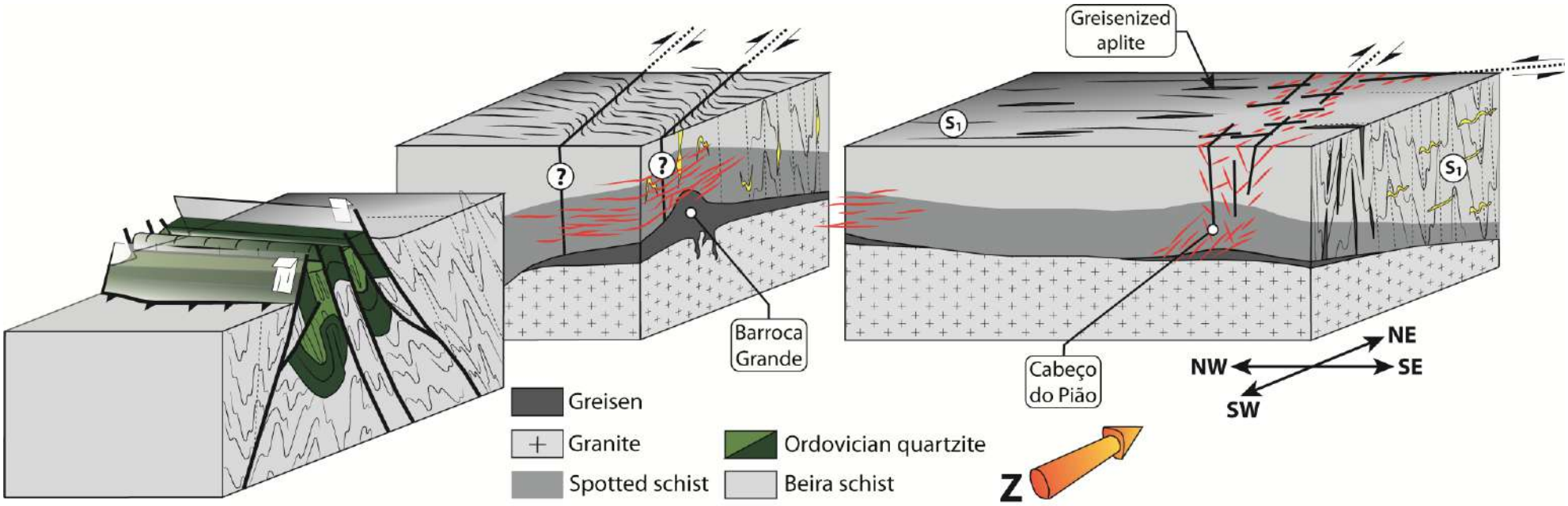

Figure 26 Structural model of formation of the W-Sn-(Cu) Panasqueira ore deposit integrating structures exposed in the Beira Baixa region and in the sector of Barroca Grande and Cabeço do Pião. In this model we assume that the mineralized veins of Barroca Grande and Cabeço do Pião were formed over the same continuum of deformation involving regional NE-SW horizontal shortening (Z).

III- The W-Sn-(Cu) mineralization of Panasqueira

As previously mentioned, the W-Sn mineralization of Panasqueira is hosted by a dense network of low-dipping quartz veins. These veins are clearly polyphased and have recorded a complex history involving different type of mineralization: W-Sn and sulfide (Cu) mineralization. The mineralization of Panasqueira is renowned in the world for the extraordinary quality and the size of some minerals like apatite, wolframite, arsenopyrite and quartz that occur in geodes within the quartz veins. The description of the paragenetic sequence of the mineralized vein system of Panasqueira is relatively complex due to (i) the succession of numerous events of vein opening and infilling (ii) the random reopening of veins, (iii) the precipitation of several generations of the same mineral like quartz, muscovite, apatite and pyrite, (iv) the rare occurrence of veins exhibiting the complete paragenetic sequence, (v) the fact that veins have generally recorded some stages, which are not necessarily consecutive, (vi) the fact that the earliest stages are generally overlapped and partially dissolved during the latest mineralizing stages and (vii) the presence of mineral zoning at the deposit scale like muscovite-topaz.

Despite these different complexities, which make difficult the spatial and the temporal correlation of the different hydrothermal events observed in the mineralized veins of Panasqueira, a simplified paragenetic sequence was proposed by Kelly and Rye (1979) and improved by Polya et *al*., (2000). At least five mineralization stages were recognized in the veins from oldest to youngest: the Quartz-Tourmaline stage (QTS), the Main Oxide Silicate Stage (MOSS), the Main Sulfide Stage (MSS), the Pyrrhotite Alteration Stage (PAS) and the Late Carbonate Stage (LCS). In this study we have recognized one more pre-ore stage occurring before the quartz-tourmaline stage. In the following, we present the textural and the mineralogical characteristics of the main mineralization stages according to the chronological order.

1. The quartz-biotite stage (QBS)

The textural and the mineralogical characteristics of the quartz-biotite stage (QBS) are displayed in Figure 27. This stage, which corresponds to the earliest event formed thin quartz-biotite horizontal veins (2-4 cm of thickness) that are sporadically present in the mine (Fig. 27a and 27b). These veins are generally barren and composed of fibrous quartz and biotite, which form selvage along the schist vein contact (Fig. 27c and 27d). These pre-ore veins are usually re-opened and overlapped during the later hydrothermal events (QTS, MOSS and MSS) (Fig. 27e). This re-opening is random and is mainly marked by crack-seal texture in quartz. The Figure 27e displays an example of fractured and reopened quartz-biotite vein, in which tourmaline and muscovite related to the QTS and the MOSS have crystallized. During these later hydrothermal events, biotite was partially replaced by muscovite (Fig. 27f), which can potentially be confounded with muscovite formed later during the MOSS. In some cases, biotite selvages can be sheared and crosscut by chalcopyrite and pyrite related to the main sulfide stage (MSS) (Fig. 27g).

The QBS is probably related to the thermal metamorphism of the Beira schist induced by the emplacement of the Panasqueira granite. This contact metamorphism is marked by the crystallization of andalusite, cordierite and biotite in the metasedimentary host rocks. During this recrystallization of the Beira schist, the quartz-biotite veins could be opened in response to the releasing of metamorphic fluids during the heating caused by the granite emplacement (Yardley and Cleverley, 2013).

Figure 27 Macroscopic and microscopic characteristics of the quartz-biotite stage (QBS) of the mineralized system of Panasqueira. (a) to (d) veins with biotite along the schist vein-contact. These veins are often crosscut by late sulfide stage (e) Quartz-biotite vein, which was reopened during the main oxide silicate stage (MOSS). Biotite present along the schist-vein contact is partially replaced by muscovite. The muscovite selvage formed during the MOSS and the biotite are both crosscut by the chalcopyrite of the late sulfide stage (MSS). (f) Zoom on grains of biotite partially replaced by muscovite, which is associated with tourmaline. (g) Zoom on biotite selvage crosscut by chalcopyrite

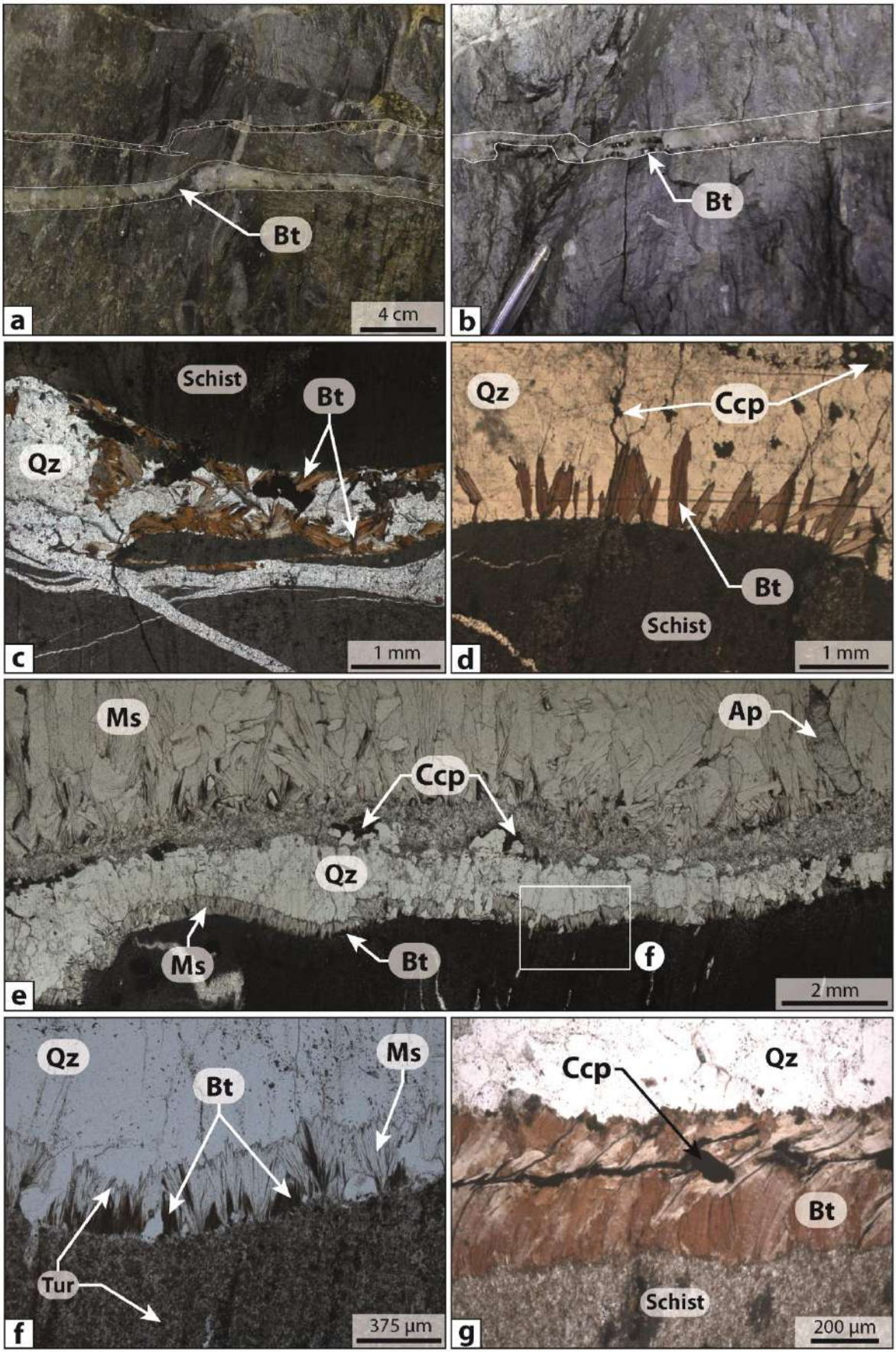
Bt
a
4 cm
Bt
b
Schist
Bt
Qz
c
1 mm
Qz
Ccp
Bt
Schist
d
1 mm
Ms
Ap
Ccp
Qz
Ms
Bt
f
e
2 mm
Qz
Ms
Bt
Tur
f
375 µm
Ccp
Qz
Bt
Schist
g
200 µm

2. The quartz-tourmaline stage (QTS)

The textural and the mineralogical characteristics of the quartz-tourmaline stage (QTS) are displayed in the Figure 28 and 29. In the mineralized system of Panasqueira, tourmaline is common, especially as alteration halos in the metasedimentary host rock surrounding the mineralized veins (Fig. 28a to 28c). These halos result from metasomatic reactions (tourmalinization) induced by fluid–rock interactions during the hydrothermal fluid flow in the veins. Locally, it is possible to observe the preferential crystallization of tourmaline within the foliation planes of the metasedimentary host rocks (Fig. 28d). Tourmaline is also present in pre-ore quartz veins along schist-vein contacts (Fig. 28b, 28c and 28h). It forms fine acicular crystals (1-3 mm), which have crystallized vertically and perpendicular to the vein edge (Fig. 29a). The QTS is associated to crack-seal mechanism as evidenced by the presence of multiple mineralization sheets, fibrous textures and horizontal fluid inclusions trails (Foxford et al., 1991; Foxford et al., 2000). The opening of the quartz-tourmaline veins show a modest shear displacement and hence can be interpreted as mode I opening fractures. The QTS is generally directly followed by the later mineralizing stages (MOSS). Indeed, during the MOSS, tourmaline is often overgrown by fibrous muscovite highlighting a continuum between the QTS and the MOSS (Fig. 29b, 29d and 29e). These tourmalines grains are commonly associated with muscovite, apatite, W-rich rutile and with the ore minerals (wolframite and cassiterite) in some cases. As a result, the QTS corresponds to an early precursor of the MOSS.

The QTS observed in the mineralized system of Panasqueira corresponds to the tourmalinization event commonly described in W-Sn ore deposits and marks the magmatic-hydrothermal transition in this type of deposit. As a result, tourmaline represents a good candidate to track and to study the magmatic-hydrothermal transition in the vein system of Panasqueira (**Chapter III**).

Figure 28 Macroscopic characteristics of the quartz-tourmaline stage (QTS) of the mineralized system of Panasqueira. (a) to (c) veins with tourmalines along the schist vein-contact. (d) Field evidence of the preferential crystallization of tourmaline in the vertical foliation planes. (e) and (f) examples of tourmalinite haloes developed around veins. (g) Example of mineralized vein in mine with tourmaline along the vein edge, (h) zoom on the schist vein contact showing the vertical growth of tourmaline.

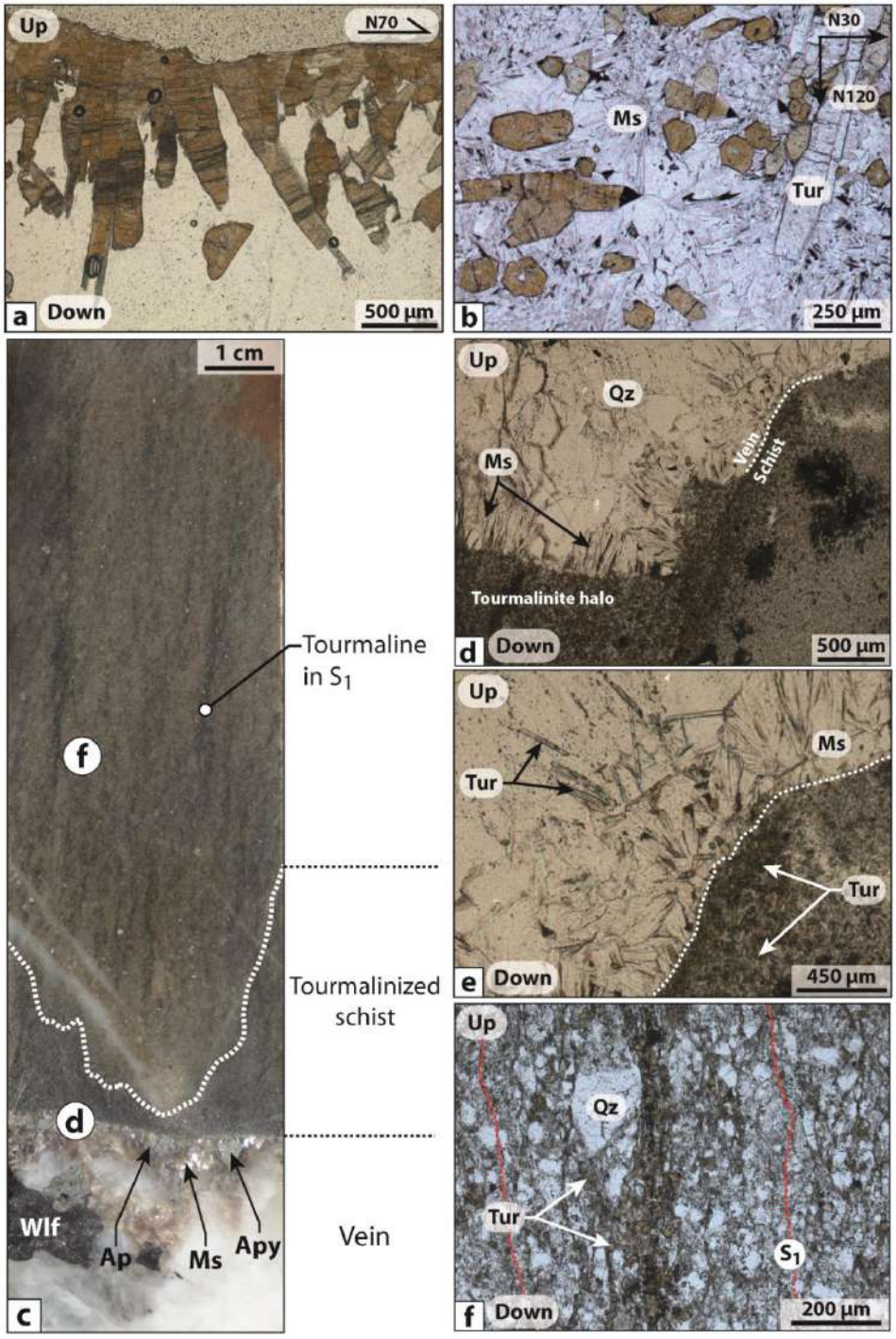

Figure 29 Microscopic characteristics of the quartz-tourmaline (QTS) of the mineralized systems of Panasqueira. Sections of veins tourmaline (a) parallel and (b) perpendicular to the trigonal axis of tourmaline. (c) Sample showing the relationship between a mineralized vein and the tourmalinization of the wall-rock, d and f give the location of the thin sections (d) and (f). In this sample, the vein selvage is composed of muscovite and apatite related to the MOSS (note the preferential crystallization of tourmaline in the foliation planes). (d) Photomicrograph showing the contact between mineralized vein and tourmalinized wall-rocks. (e) Zoom on tourmalines present in the altered schist. Note the preferential crystallization of tourmaline in an inherited more pelitic layer. (f) Zoom on tourmaline, which has preferentially crystallized in the foliation planes.

3. The main oxide silicate stage (MOSS)

The textural and the mineralogical characteristics of the main oxide silicate stage (MOSS) are displayed in the Figure 30, 31 and 32. The MOSS carries the W-Sn mineralization and constitutes the most volumetrically important stage (≈ 60% of the vein volume) (Kelly and Rye, 1979; Polya et al., 2000). The MOSS can be subdivided in two sub-stages:

- (i) An early event marked by the crystallization of quartz-muscovite-apatite rich selvages along the schist vein contacts (Fig. 30a). This sub-stage is usually in direct continuity with tourmaline of the QTS (Fig. 29b and 29e, 31b and 31e). These selvages exhibit a fibrous texture due to the vertical growth of muscovite. In the southwestern part of the deposit, muscovite is less abundant and the selvages are mainly composed of topaz (Fig. 30e to 30h). Cassiterite can be found within these selvages as intergrown with tourmaline muscovite and topaz (Fig. 31d).
- (ii) The sequence continued with a typical syntaxial overgrowth of the vein selvages marked by the crystallization of large euhedral crystals of quartz (Fig. 30c and 31c). This quartz crystallized preferentially vertically and perpendicularly to the schist-vein contact. During this sub-stage the veins exhibit geodic texture characterized by the presence of large void spaces between the crystals of quartz (like “fente Alpine”). This texture emphasizes that the MOSS was related to high fluid pressure conditions that caused the opening and the vertical dilation of veins (Foxford et *al*., 1991; Foxford et *al*., 2000). The quartz crystallization was followed by the cavity-filling with muscovite, apatite, wolframite, and cassiterite (Fig. 31). The wolframite occurs as large nugget-like aggregates that explain the extreme heterogeneous spatial distribution of wolframite in veins. In thin section, wolframite and cassiterite can be found directly in contact with the muscovite selvages (Fig. 32). The presence of muscovite inclusions in wolframite (Fig. 32b and 32d) and the crystallization of wolframite in the cleavage planes of muscovite (Fig. 32) emphasize that the apparition of muscovite predates the wolframite crystallization. Quartz and muscovite selvages related to the MOSS are generally crosscut, overlapped and partially corroded by the late sulfide stage (MSS) (Fig. 31a and 33). The muscovite represents an important tracer of the hydrothermal process related to the W-Sn mineralization. Furthermore, muscovite is ubiquitous both in the mineralized vein system and in the greisen of Panasqueira. Consequently, muscovite constitutes an important mineral to study

relationships between the greisenization of the Panasqueira granite and the W-Sn mineralization related to the MOSS (**Chapter IV**).

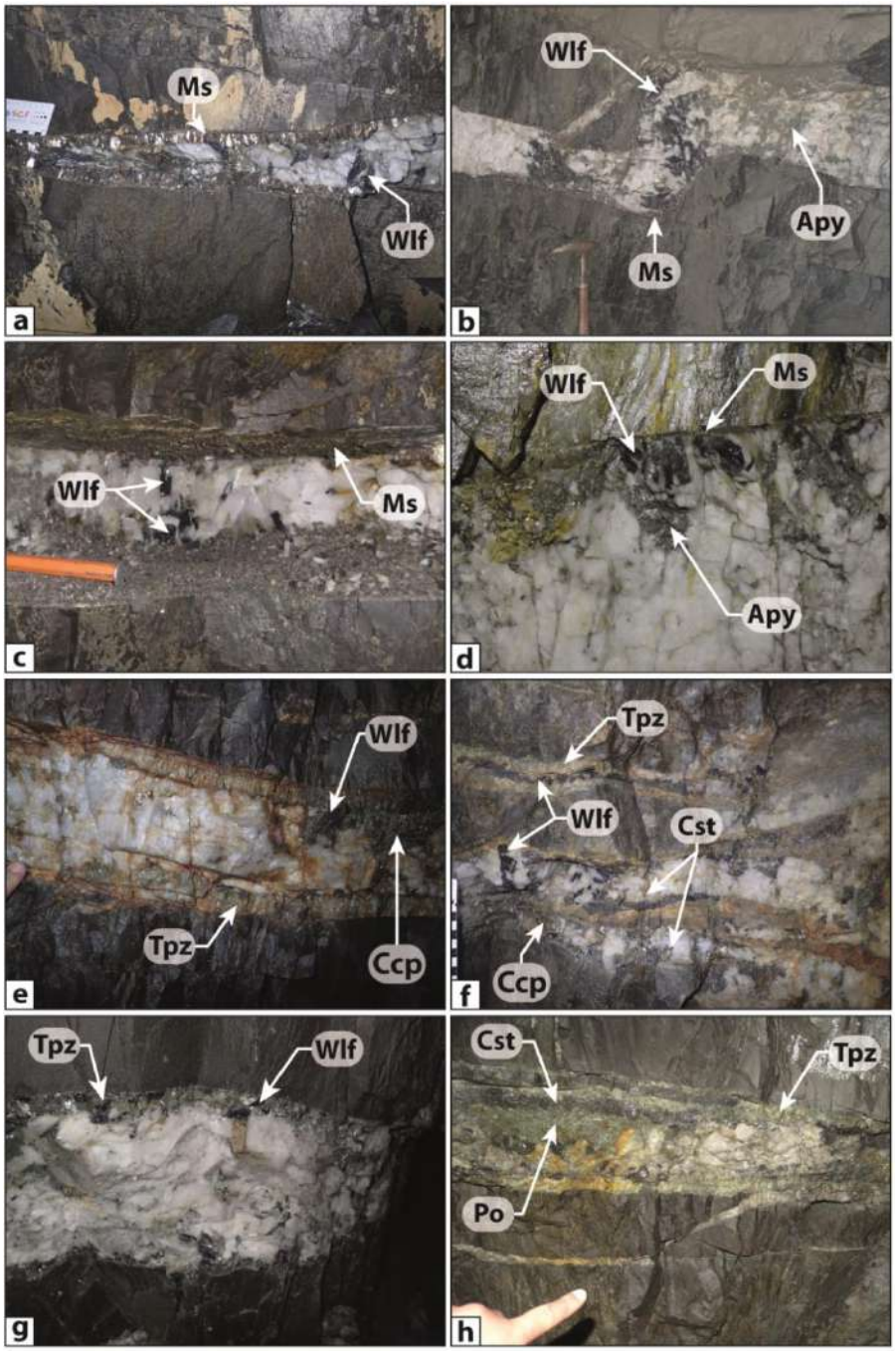

Figure 30 Macroscopic characteristics of the main oxide silicate stage (MOSS) of the mineralized systems of Panasqueira. (a) to (c) typical quartz-muscovite veins mineralized in wolframite. The muscovite is generally located along the schist-vein contacts as selvage and can be also present within the veins. Quartz can exhibit geodic texture as displayed in (c). (d) Zoom on a schist-vein contact showing the relationship between the muscovite selvage and the wolframite. (e) to (h) examples of quartz-topaz veins present in the southwestern part of the mine. In these veins, the muscovite is rare and the vein selvage is composed of topaz.

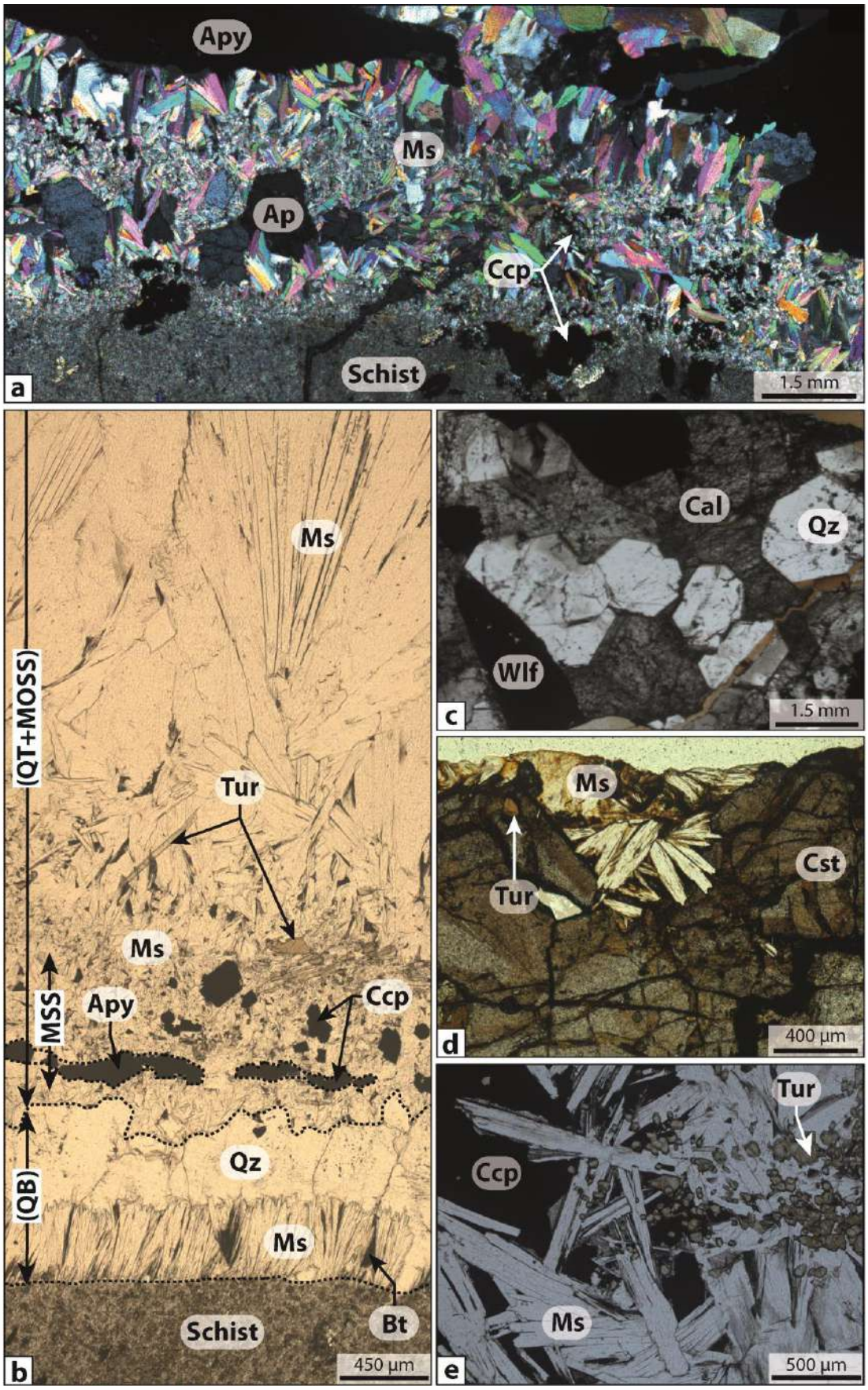
Apy
Ms
Ap
Ccp
Schist
a
1.5 mm
(QT+MOSS)
Ms
Tur
Ms
MSS
Apy
Ccp
Qz
(QB)
Ms
Schist
Bt
b
450 µm
Cal
Qz
Wlf
c
1.5 mm
Ms
Tur
Cst
d
400 µm
Tur
Ccp
Ms
e
500 µm

Figure 31 Microscopic characteristics of the main oxide silicate stage (MOSS) of the mineralized systems of Panasqueira. (a) Muscovite selvage associated to apatite. This selvage is crosscut by arsenopyrite and chalcopyrite related to the sulfide stage (MSS). (b) Sample of vein exhibiting relationship between the quartz-biotite (QB) stage, the quartz-tourmaline stage (QT), the main oxide silicate stage (MOSS) and the main sulfide stage (MSS). This photomicrograph shows clearly that the quartz-biotite vein was reopened during the quartz-tourmaline stage and then during the main oxide silicate stage. The muscovite selvage is then crosscut by arsenopyrite and chalcopyrite during the sulfide stage (MSS). (c) Section of quartz-wolframite vein cut perpendicular to the c-axis of quartz and parallel the vein plane. This section exhibits euhedral quartz with geodic texture, which was then infilled by the late carbonate stage (LCS). (d) Relationship between muscovite and cassiterite along the vein selvage. (e) Section of vein cut perpendicular to the c-axis of tourmaline and parallel to the vein. This section displays the relationship between the tourmaline stage (QT), the muscovite stage (MOSS) and the sulfide stage (MSS).

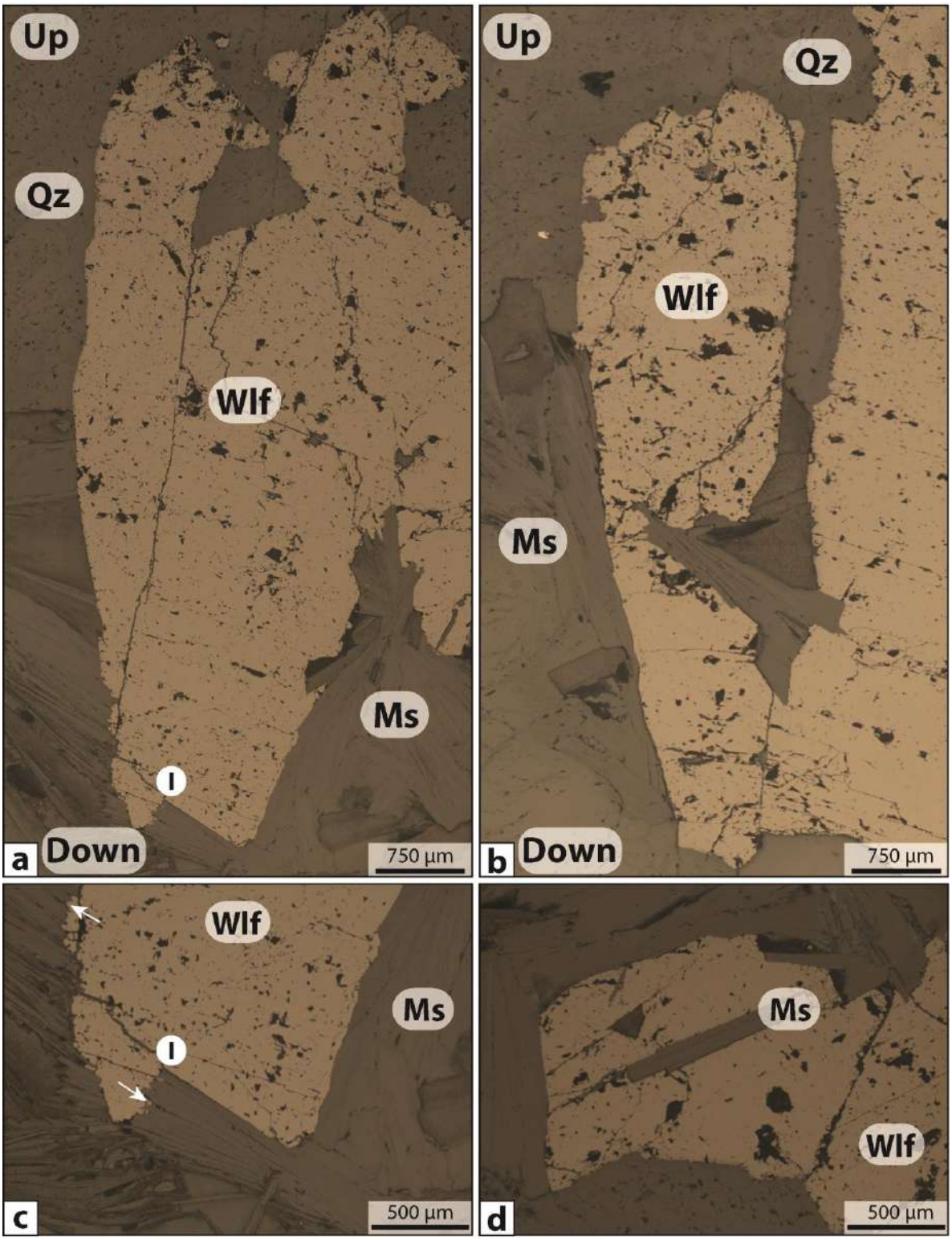

Figure 32 (a) and (b) Photomicrographs showing the relationship between the muscovite selvage and wolframite of the MOSS. (c) Zoom on muscovite-wolframite contact showing the crystallization of wolframite in some cleavage planes of muscovite (indicated by the white arrow). (d) Inclusion of muscovite in wolframite. These photomicrographs suggest that the crystallization of muscovite constituting the vein selvage predates the apparition of wolframite.

4. The main sulfide stage (MSS) and the pyrrhotite alteration stage (PAS)

The textural and the mineralogical characteristics of the main sulfide stage (MSS) are displayed in Figures 33, 34 and 35. The MSS carries the Cu mineralization and represents volumetrically the second largest stage (≈ 16% the vein volume) (Kelly and Rye, 1979; Polya et al., 2000). Field and thin section observations show that the MSS postdates clearly the MOSS (Fig. 33, 34 and 35). The MSS is mainly composed of As-Cu-Zn-Fe-bearing sulfides (arsenopyrite, chalcopyrite, sphalerite, pyrrhotite and pyrite) associated to a lesser extent with quartz, muscovite and apatite. The sulfides related to the MSS occurs mainly: (i) as filling the open-spaces of the geodes formed during the MOSS (Fig. 33e and 33f), (ii) as corrosion and replacement of preceding minerals related to the QTS and the MOSS like quartz, wolframite and cassiterite (Fig. 33b, 33c and 35) and (iii) within fractures that crosscut the vein selvages and minerals related to the previous mineralizing stages like quartz, wolframite and apatite (Fig. 33a and 34a). The fracturing related to the MSS is random, thus explaining the complex texture observed in the vein system of Panasqueira. The MSS is initiated by the crystallization of löllingite and arsenopyrite, which were then followed and crosscut by the apparition of chalcopyrite, pyrrhotite, pyrite and sphalerite (Fig. 34d and 34g).

The MSS is followed by a pyrrhotite alteration event (PAS) mainly hosted by numerous sub-vertical veins and veinlets. The intersection of these veinlets with the horizontal mineralized veins has triggered an extensive replacement of the pyrrhotite related to the MSS by pyrite and marcasite. The PAS is associated with minor sulfide phases like galena, bismuthinite and Pb-Ag-sulfosalts (freibergite, pyargyrite, stephanite) that are present in small amounts.

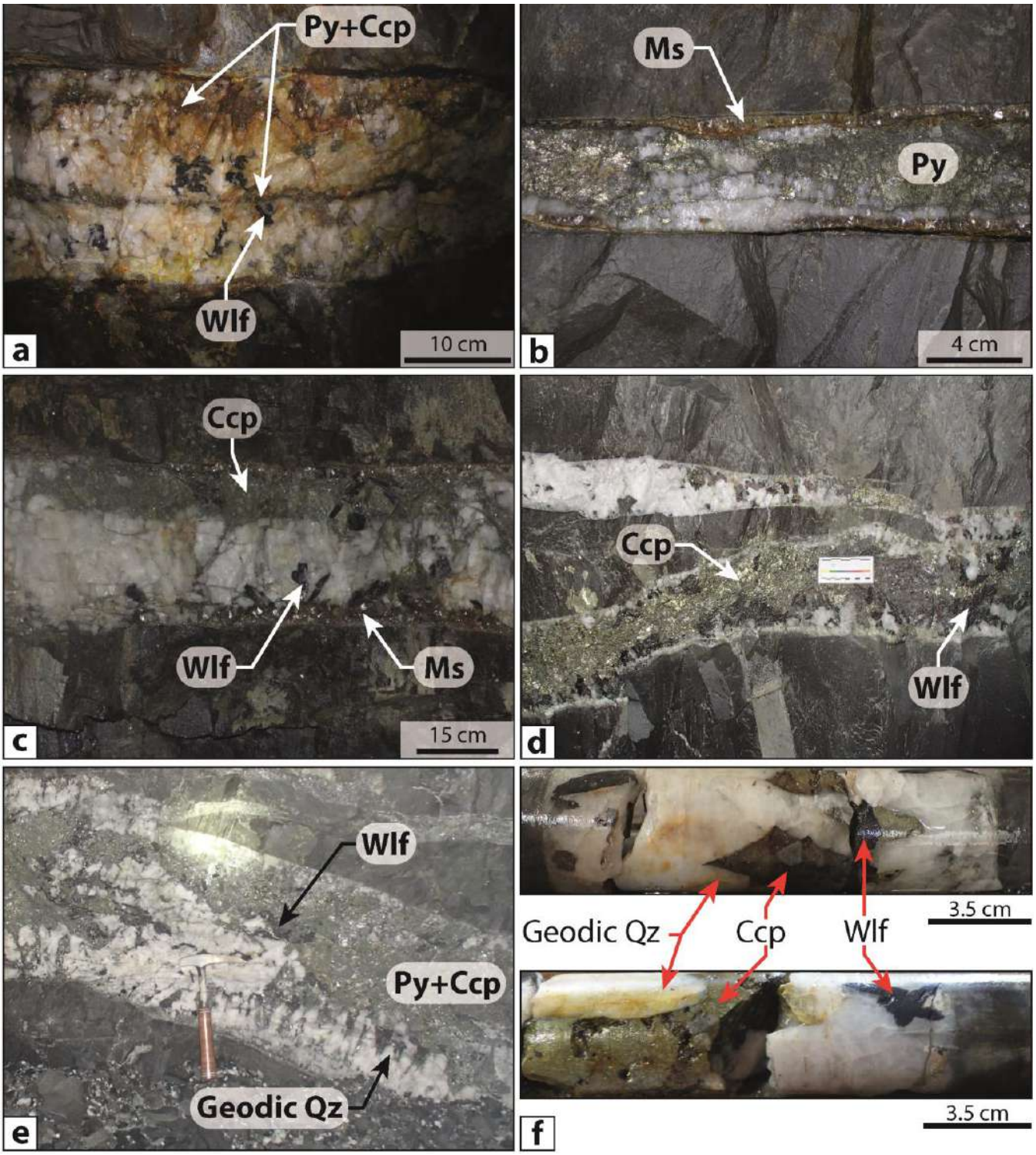

Figure 33 Macroscopic characteristics of the main sulfide stage (MSS) of the mineralized system of Panasqueira. (a) Quartz-muscovite-wolframite vein crosscut by pyrite-chalcopyrite assemblage during the sulfide stage. This picture emphasizes that veins were formed by several stages of opening and infilling (crack-and-seal texture).(b) Quartz-muscovite and quartz-muscovite-wolframite veins, in which the quartz was partially dissolved and corroded during the sulfide stage.(d) to (f) Examples of quartz-wolframite veins exhibiting euhedral quartz and geodic texture, which was infilled by arsenopyrite, chalcopyrite and pyrite during the sulfide stage.

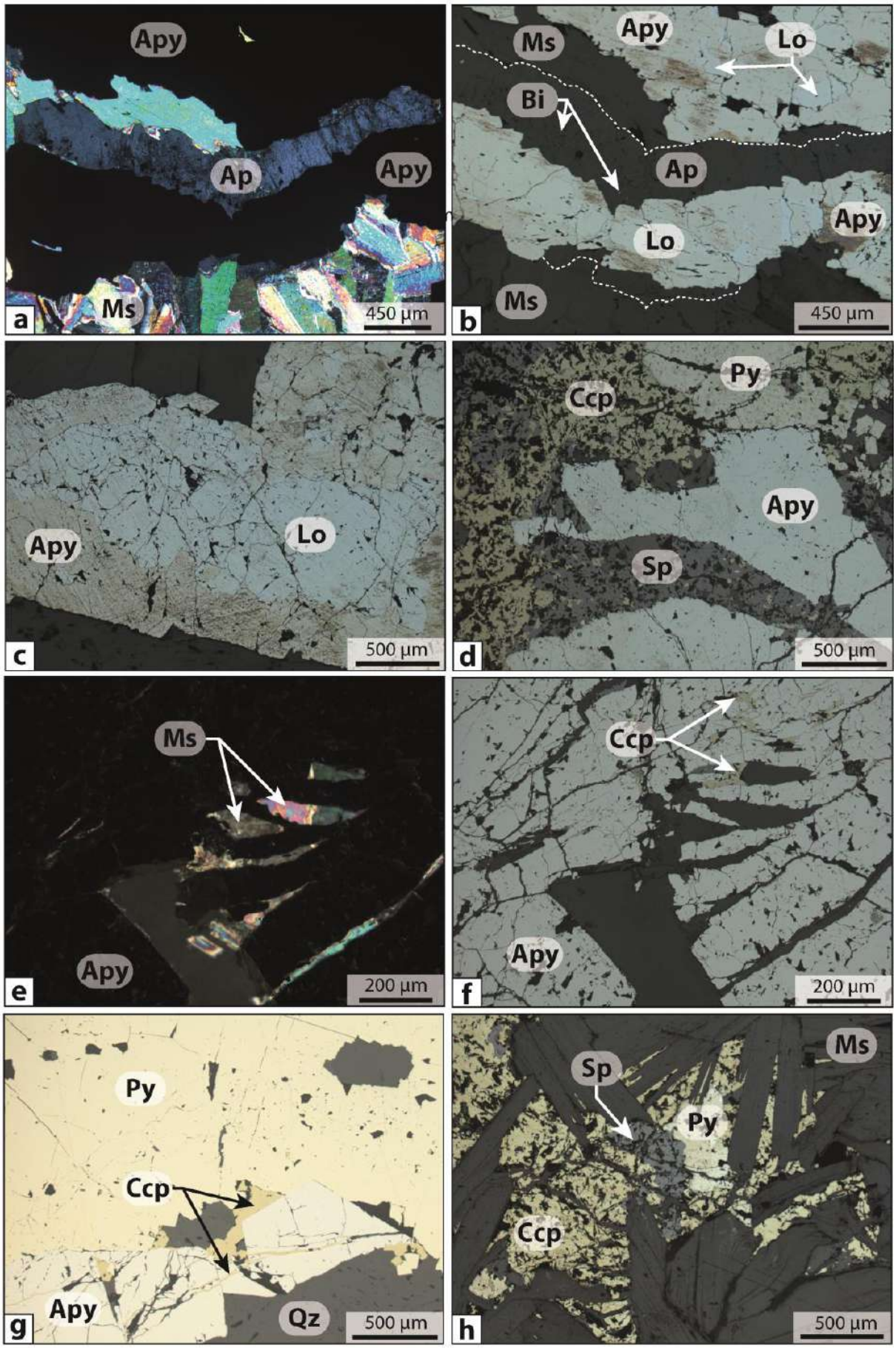
Apy
Ap
Apy
Ms
a
450 µm
Ms
Apy
Lo
Bi
Ap
Apy
Lo
Ms
b
450 µm
Apy
Lo
c
500 µm
Py
Ccp
Apy
Sp
d
500 µm
Ms
Apy
e
200 µm
Ccp
Apy
f
200 µm
Py
Ccp
Apy
Qz
g
500 µm
Ms
Sp
Py
Ccp
h
500 µm

Figure 34 Microscopic characteristics of the main sulfide stage (MSS) of the mineralized system of Panasqueira. (a) and (b) Muscovite-apatite selvage formed during the MOSS and crosscut by löllingite and arsenopyrite formed during the MSS. (c) Textural evidences showing that the crystallization of löllingite predates the apparition of arsenopyrite. (d) and (g) Textural relationship between arsenopyrite, pyrite and sphalerite showing that arsenopyrite is crosscut by the other sulfides related to the MSS. (e) and (f) Textural evidences emphasizing that muscovite related to the MSS predates the crystallization of arsenopyrite. (h) Textural relationship between the muscovite selvages related to the MOSS and the chalcopyrite, sphalerite and pyrite related to the MSS. Sulfides of the MSS infill the cleavage planes of muscovite and the open space between muscovite grains.

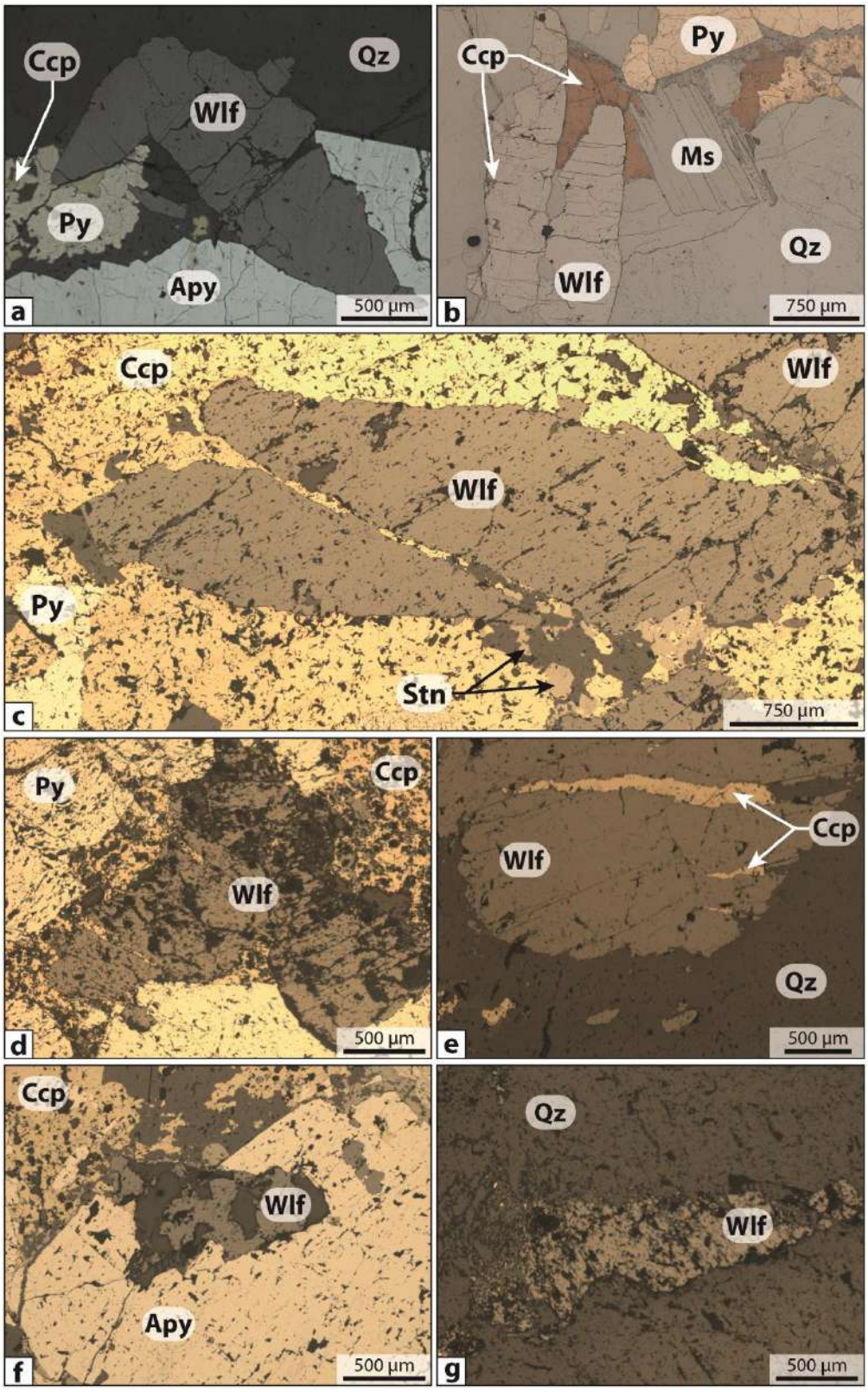

Figure 35 Photomicrographs showing the relationship between the W mineralization and the main sulfide stage (MSS). (a) Section of wolframite crosscut by chalcopyrite. (b) Section of wolframite partially altered and dissolved during the sulfide stage. (c) Section of wolframite crosscut by chalcopyrite. (d) Inclusion of partially altered section of wolframite in grain of arsenopyrite. (e) Section of wolframite altered during the sulfide stage.

5. The late carbonate stage (LCS)

The textural and the mineralogical characteristics of the late carbonate stage (LCS) are displayed in the Figure 36 and 37. This latest stage that post-dates all other mineralized stages is mainly hosted by sub-vertical fracture planes and faults that crosscut and displace the horizontal mineralized veins (Fig. 36a and 36b). The LCS is mainly composed of dolomite, calcite, siderite and chlorite that have also partly infilled the remaining cavities present in the horizontal mineralized veins (Fig. 36c, 36d and 37). These carbonates can be also associated with a small amount of galena and pyrite (Fig. 36b, 36d and 37). These veins were interpreted as equivalent to the late Alpine veins, which were formed during post-ore reheating events (Kelly and Rye, 1979; Lourenço et Noronha, 2000). Pinto et *al*., (2015) have described rare occurrences of cassiterite associated with these vertical carbonates veins (Fig. 36e, 36f, 36g and 37h). This suggests that the hydrothermal activity related to the LCS has dissolved and remobilized a part of the Sn mineralization from the horizontal mineralized veins.

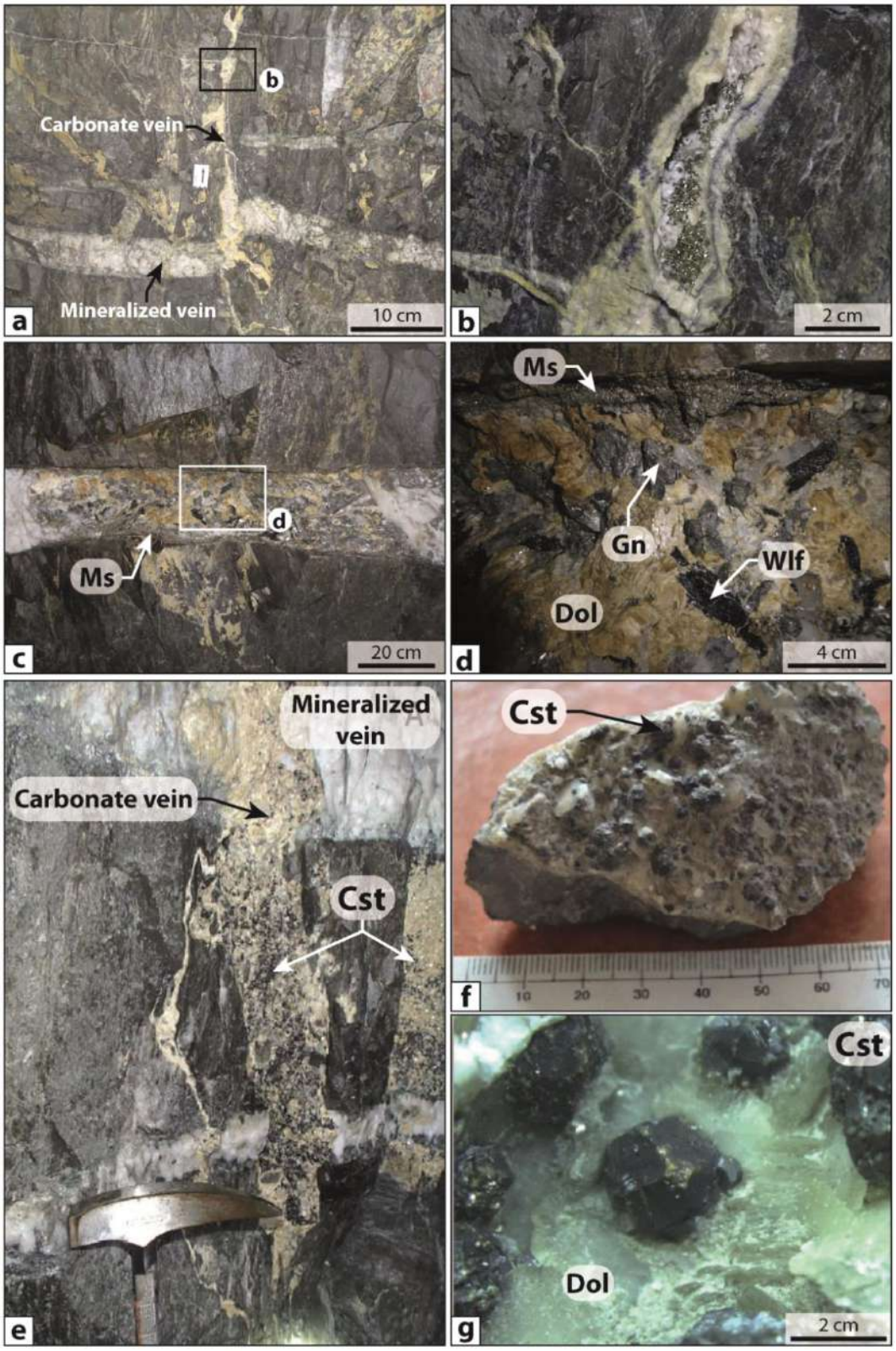

Figure 36 Macroscopic characteristics of the late carbonate stage (LCS) of the mineralized system of Panasqueira. (a) and (b) Vertical fault infilled by dolomite, calcite and pyrite assemblage. (c) and (d) Open voids in horizontal mineralized veins partially infilled by dolomite, galena and calcite. (e) to (g) Vertical fault infilled by the LCS assemblage exhibiting a late generation of cassiterite (photo from Pinto et *al*., 2015).

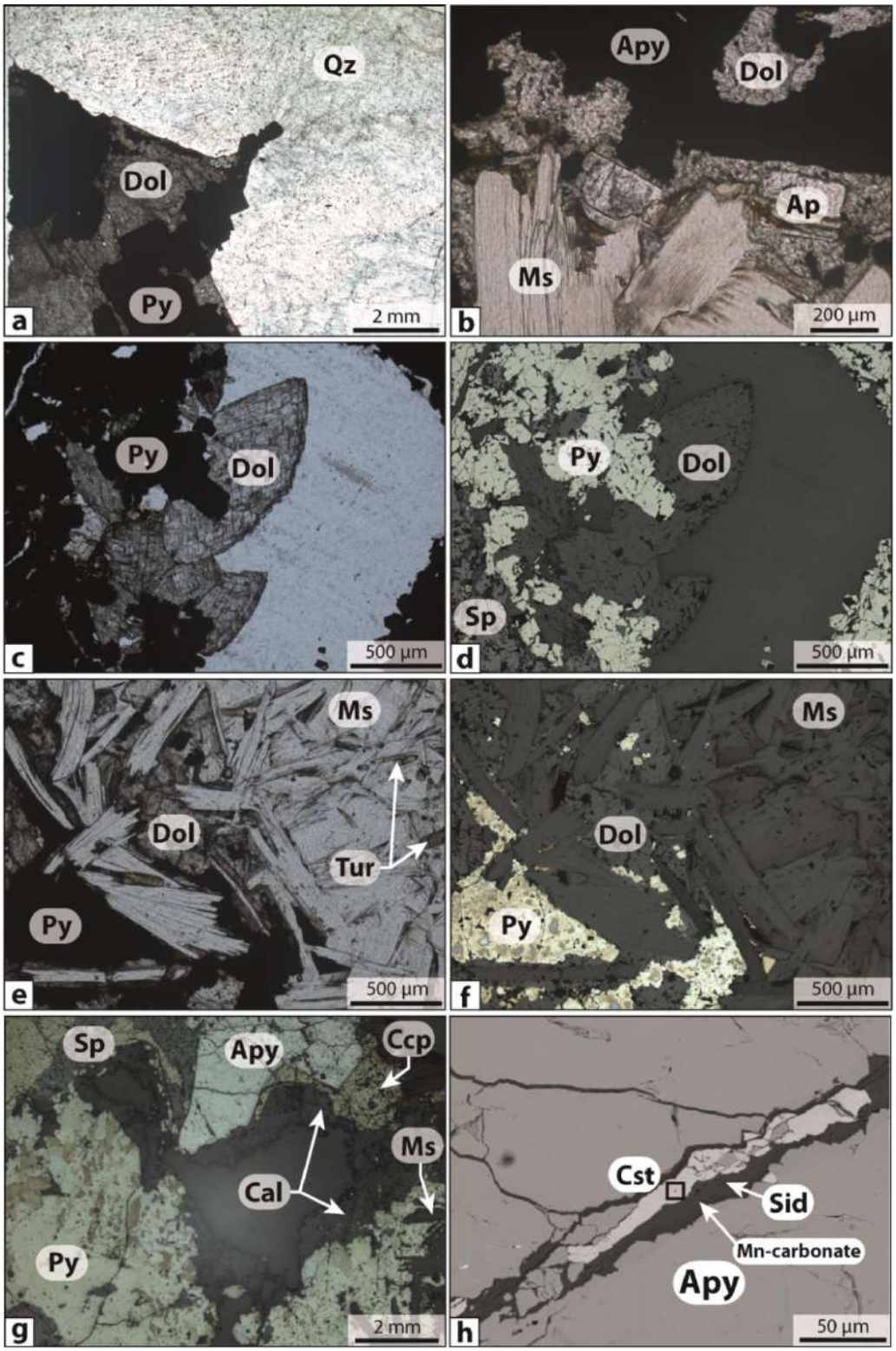

Figure 37 Microscopic characteristics of the late carbonate stage (LCS) of the mineralized system of Panasqueira. (a) to (f) Infilling of the remaining open spaces present in the horizontal mineralized veins by dolomite, pyrite and calcite assemblage related to the LCS. (g) Relationship between the sulfides of the MSS and the carbonates related to the LCS. (h) SEM photomicrograph showing the occurrence of late cassiterite within fracture crosscutting a grain of arsenopyrite. The late generation of cassiterite is associated with siderite (Photomicrograph from Pinto et *al*., 2015).

6. The simplified paragenetic sequence of the mineralized vein system of Panasqueira

On the basis of the previous studies (Kelly and Rye, 1979; Polya et al., 2000) and the textural and mineralogical description of the different mineralization stages realized in this study, a simplified paragenetic sequence is proposed in Figure 38. The MOSS and the MSS are the most economically relevant ore stages that are respectively exploited for the W-Sn and the Cu mineralization. The QBS constitutes a pre-ore stage probably related to the thermal metamorphism induced by the emplacement of the Panasqueira granite. This earliest stage is associated with a first fracturing event, which has led to the generation of barren horizontal quartz-biotite veins. The QBS is followed by the two earliest mineralization stages (QTS and MOSS) that constitute a continuous sequence. The QTS and the MOSS involved opening and reopening of mode I fractures as highlighted by textural evidences. The vertical dilation of the veins during these two stages suggests high fluid pressure conditions. The MSS that postdates the previous mineralization stages is characterized by changes both in the dynamics of vein opening and in the type of mineralization (sulfides). The respective ages of the MOSS and the MSS were constrained by $^{40}Ar/^{39}Ar$ dating technique on muscovite that gives 296.3 to 292.9 Ma for the MOSS and 295.8 to 293.5 Ma for the MSS (Snee et *al*., 1988). These ages suggest that the MOSS and the MSS occurred over a short period of time and probably throughout the same hydrothermal continuum. The two latest stages are clearly posterior and belong to another hydrothermal event. During these stages, the permeable structures, which drained fluids switched from horizontal structures to sub-vertical fractures and faults. This change emphasizes a time evolution of the structural and the tectonic setting.

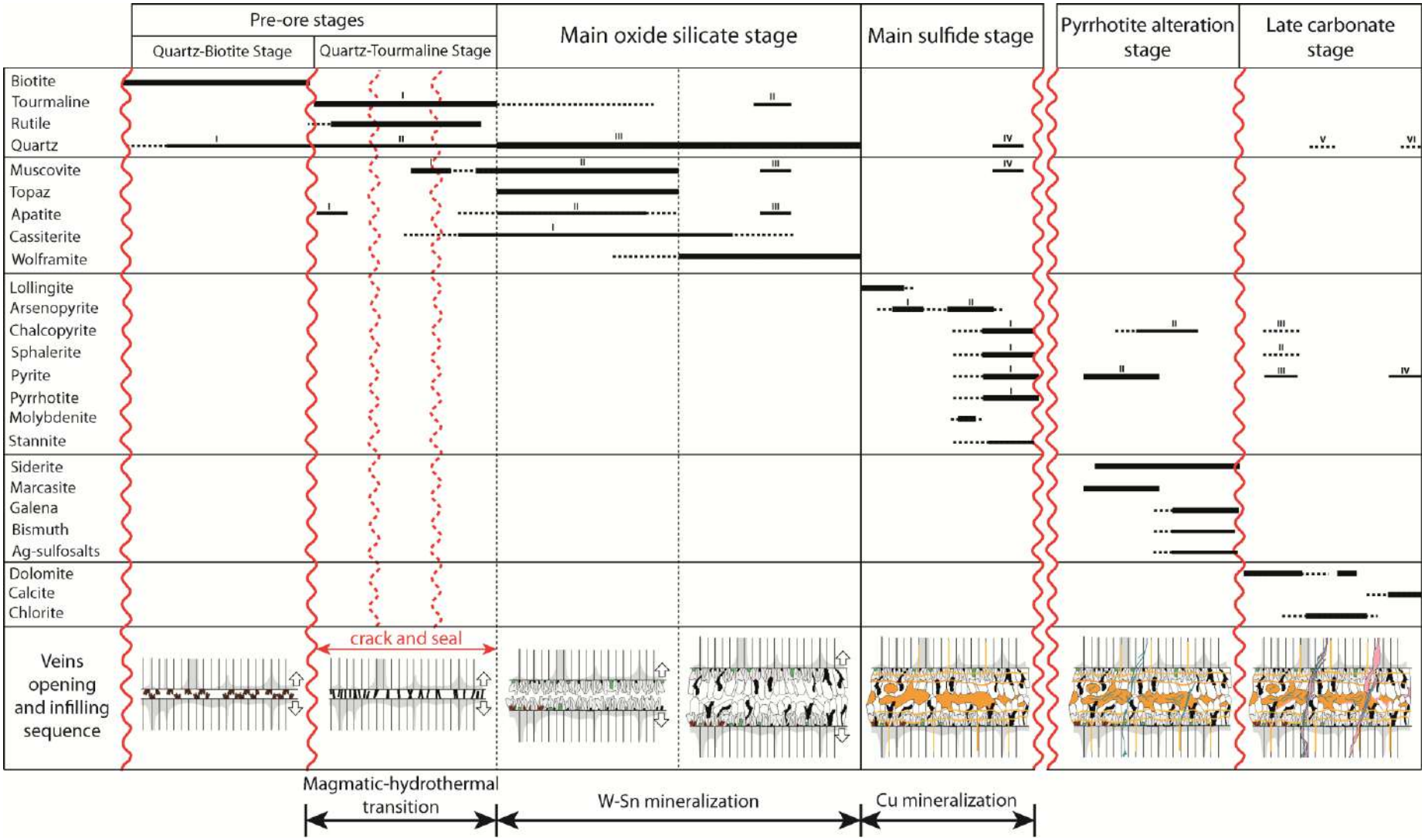

Figure 38 Simplified paragenetic sequence of the W-Sn-(Cu) mineralized veins system of Panasqueira (modified from the paragenetic sequence of Kelly and Rye, 1979 and Polya et *al*., 2000) The red lines correspond to main fracturing events and the red dashed lines correspond to crack and seal events.

References

A

Ábalos, B., Carreras, J., Druguet, E., Escuder Viruete, J., Gómez Pugnaire, M. T., Lorenzo Alavarez, S., Quesada, C., Rodríguez Fernández, L. R. & Gil Ibarguchi, J. I. 2002. Variscan and Pre-Variscan Tectonics. In: The Geology of Spain (edited by Gibbons, W. & Moreno, M. T.). Geological Society, London, 155-183.

Andeweg, B., 2002. Cenozoic tectonic evolution of the Iberian Peninsula, the effects and causes of changing stress fields, Ph.D. thesis, 178 pp., Vrije Univ., Amsterdam.

Arenas, R., et al. ., 2016, Allochthonous terranes involved in the Variscan suture of NW Iberia: A review of their origin and tectonothermal evolution: Earth-Science Reviews , v. 161, p. 140–178, doi:10.1016/j.earscirev.2016.08.010.

Azor, A., Lodeiro, F.G., Simancas, J.F., 1994b. Tectonic evolution of the boundary between the Central Iberian and Ossa-Morena zones (Variscan belt, southwest Spain). Tectonics 13, 45–61.

B

Ballèvre, M., et al., 2014. Correlation of the nappe stack in the Ibero-Armorican arc across the Bay of Biscay: a joint French–Spanish project. In: Schulmann, K.,Martínez Catalán, J.R., Lardeaux, J.M., Oggiano, G. (Eds.), The Variscan Orogeny: Extent, Timescale and the Formation of the European Crust. Geological Society, London, Special Publications, pp. 77–113.

Bea, F., Montero, P., Molina, J.F., 1999. Mafic precursors, peraluminous granitoids, and late lamprophyres in the Avila batholith; a model for the generation of Variscan batholiths in Iberia. Journal of Geology, 107, 399-419.

Blattler, A., 1985, Structural analysis of the fault pattern in the tungsten-tin mine of Panasqueira, Portugal Unpub. Thesis Univ .Geneva, 71 p.

Bons, P.D., Elburg, M.A., Gomez-Rivas, E. 2012. A review of the formation of tectonic veins and their microstructures. Journal of Structural Geology 43: 33-62.

Burg, J.P.I GLESIAMS, LAURENPTH, MATE, P.H. & RIBEIROA,. 1981. Variscan intracontinental deformation: the Coimbra-Cordoba shear zone (SW Iberian peninsula). *Tectonophysics*, 78, 161-177.

Bussink, R.W. 1984. Geochemistry of the Panasqueira Tungsten-Tin Deposit, Portugal. Geol. Ultraiectina.

C

Castro, A., Patiño Douce, A.E., Corretgé, L.G., de la Rosa, J.D., El-Biad, M., El-Hmidi, H., 1999. Origin of peraluminous granites and granodiorites, Iberian Massif, Spain. An experimental test to granite petrogenesis. Contributions to Mineralogy and Petrology, 135, 255-276.

Clark, A. H. 1964. Preliminary study of the temperatures and confining pressures of granite emplacement and mineralization, Panasqueira, Portugal: Inst. Mining MetallurgyTrans., 73, 813-824.

Clark, A. H. 1969. Sulphurization of cordierite, Minas da Panasqueira, Portugal: Geol. Soc. Finland Bull., v. 41, p. 231-234.

Cloetingh, S., Burov, E., Beekman, F., Andeweg, B., Andriessen, P. A. M., Garcia-Castellanos, D., de Vicente, G., Vegas, R. 2002. Lithospheric folding in Iberia. TECTONICS, VOL. 21, NO. 5, 1041.

Cocks, L. R. M. and Fortey, R. A. 1982. Faunal evidence for oceanic separations in the Palaeozoic of Britain. Journal of the Geological Society of London 139: 465-478.

Cocks, L. R. M. & Torsvik, T. H. 2002. Earth geography from 500 to 400 million years ago: a faunal and palaeomagnetic review. Journal of the Geological Society, London, 159, 631– 644.

Conde, L. N., Pereira, V., Ribeiro, A. & Thadeu, D. 1971. Jazigos Hipogénicos de Estanho e volfrâmio. I Congresso Hispano-Luso-Americano de Geologia Económica. Direção Geral de Minas e Serviços Geológicos. Lisboa. 81 pp.

Cox, S.F. 1995. Faulting processes at high fluid pressures: an example of fault valve behavior from the Wattle Gully Fault, Victoria, Australia. J Geophys Res 100:12841–12859.

D

Derré, C. 1982. Caractéristiques de la distribution des gisements à étain-tungstène dans l'ouest de l'Europe. Mineral. Deposita 17:55-77.

Derre, C., Lecolle, M., Roger, G., Tavares de Freitas Carvalho, J. 1986. Tectonics, magmatism, hydrothermalism and sets of flat joints locally filled by Sn-W aplite-pegmatite and quartz veins; southeastern border of the serra de estrela grnaitic massif (Beira Baixa, Portugal). Ore Geology Reviews, 1 : 43-56.

Dias da Silva, Í., GONZÁLEZ CLAVIJO, E., MARTÍNEZ CATALÁN, J.R. 2010. Tectono-thermal evolution of a Central Iberian Zone sector in the Palaçoulo region (east of Morais Massif, NE Portugal). e –Terra http://e-terra.geopor.pt ISSN 1645-0388 Volume 11 – nº 14.

Dias da Silva, Í., 2014. Geología de las Zonas Centro Ibérica y Galicia – Trás-os-Montes en la parte oriental del Complejo de Morais, Portugal/España. Instituto Universitario de Geología "Isidro Parga Pondal" - Área de Xeoloxía e Minería do Seminario de Estudos Galegos, A Coruña, Spain, Serie Nova Terra. 45 (424 pp).

Dias, G., Leterrier, J., Ferreira, N., Lopes Nunes, J.E., 1992. Les granitoıdes biotitiques syn-a tardi-hercyniens de la region de Braga _Nord Portugal.. Typologie chimico–mineralogique et implications petrogenetiques. C. R. Acad. Sci. Paris 314,675–681, serie II.

Dias, G., Leterrier, J., Mendes, A., Simões, P., Bertrand, J.M. 1998. U-Pb zircon and monazite geochronology of syn- to post-tectonic Hercynian granitoids from the central Iberian Zone (northern Portugal). Lithos 45, 349–369.

Dias, R. & Ribeiro, A. 1995. The Ibero Armorican Arc: a collision effect against an irregular continent? Tectonophysics, 246: 113-128

Dias R, Mateus A, Ribeiro A. 2003. Strain partitioning in transpressive shears zones in the southern branch of the Variscan Ibero-Armorican arc. Geodinamica Acta 16 (2-6):119-129. doi:doi: 10.1016/j.geoact.2003.04.001

Dias, R., Ribeiro, A., Coke, C., Pereira, E., Rodrigues, J.F., Castro, P., Moreira, N., Rebelo, J.A., 2013. Evolução estructural dos sectores setentrionais do Autóctone da Zona Centro-Ibérica. In:

Dias, R., Araújo, A., Terrinha, P., Kullberg, J.C. (Eds.), Geologia de Portugal:pp. 73–147.

Dias da Silva, I., Gómez-Barreiro, J., Martínez Catalán, J.R., Ayarza, P., Pohl, J., Martínez, E. 2017. Structural and microstructural analysis of the Retortillo Syncline (Variscan belt, Central Iberia). Implications for the Central Iberian Orocline. Tectonophysics 717 (2017) 99–115.

Diez Balda, M.A., Martinez Catalan, J.R. et Ayarza, P. 1995. Syncollisional extensional collapse parallel to the orogenic trend in a domain of steep tectonics : theSalamanca detachment zone (Central Iberian Zone, Spain) Journal of Structural Geology, 17, 163-182.

Díez Fernández, R., Arenas, R., 2015. The Late Devonian Variscan suture of the Iberian Massif: A correlation of highpressure belts in NW and SW Iberia. Tectonophysics, 654, 96-100, DOI: 10.1016/j.tecto.2015.05.001.

Díez Fernández, R., Pereira,M.F., 2016. Extensional orogenic collapse captured by strike-slip tectonics: Constraints fromstructural geology and UPb geochronology of the Pinhel shear zone (Variscan orogen, Iberian Massif). Tectonophysics 691 (Part B):290–310.

Díez-Montes, A., 2007. La geología del Dominio "aOllo de Sapo" en las comarcas de Sanabria y Terra do Bolo, 2007. Instituto Universitario de Geología "Isidro Parga

Pondal" - Área de Xeoloxía e Minería do Seminario de Estudos Galegos, A Coruña, Spain, Serie Nova Terra. 34 (494 pp.).

Díez Montes, A., and Gallastegui, G., 1992, Geología del plutón granítico de Ciperez-Garcirrey (Prov. Salamanca, España): Cuadernos do Laboratorio Xeolóxico de Laxe , v. 17, p. 279–292.

E

Escuder Viruete, J., Arenas, R. et Martinez Catalan, J.R. 1994. Tectonothermal evolution associated with Variscan crustal extension in the Tormes Gneiss dome (NW Salamenca, Iberian Massif, Spain) Tectonophysics, 238, 117-138.

F

Faure, M., Lardeaux, J.-M., and Ledru, P., 2009, A review of the pre-Permian geology of the Variscan French Massif Central: Comptes Rendus Geoscience , v. 341, p. 202–213, doi:10.1016/j.crte.2008.12.001.

Ferreira, N., Iglesias, M., Noronha, F., Pereira, E., Ribeiro, A., Ribeiro, M.L., 1987a. Granito´ides da Zona Centro Ibe´rica e seu enquadramento geodinˆamico. In: Bea, F., Carnicero, A., Gonzalo, J.C., Lo´pez Plaza, M., Rodriguez Alonso, M.D. _Eds.., Geologia de los Granitoides y Rocas Asociadas del Macizo Hespe´rico. Ed. Rueda, Madrid, pp. 37–51.

Foxford, K.A., Nicholson, R., Polya, D.A., 1991a. Textural evolution of W-Cu-Sn bearing hydrothermal quartz veins at Minas da Panasqueira, Portugal. Mineralogical Magazine 55, 435-445.

Foxford, K.A., Nicholson, R., Polya, D.A., Hebblethwaite, R.P.B. 2000. Extensional failure and hydraulic valving at Minas da Panasqueira, Portugal: Evidence from vein spatial distributions, displacements and geometries. J. Struct. Geol. 22, 1065–1086.

G

Gutiérrez-Alonso, G., Collins, A.S., Fernández-Suárez, J., Pastor-Galán, D., González-Clavijo, E., Jourdan, F., Weil, A.B., Johnston, S.T., 2015. Dating of lithospheric buckling: 40Ar/39Ar ages of syn-orocline strike–slip shear zones in northwestern Iberia. Tectonophysics 643:44–54.

Gutiérrez-Alonso G, Fernández-Suárez J, López-Carmona A, Gärtner A. 2018. Exhuming a cold case: The early granodiorites of the northwest Iberian Variscan belt—A Visean magmatic flare-up? Lithosphere. doi:doi.org/10.1130/L706.1

H

Hebblethwaite, R. P. B., and Antao, A.M. 1982. A report on the study of dilation patterns within the Panasqueira ore body: Barroca Grande, Beralt Tin Wolfram (Portugal), unpub. rept.15p.

Henry, D.J., Guidotti, C.V., Thomson, J.A., 2005. The Ti-saturation surface for low-to medium pressure metapelitic biotites: implications for geothermometry and Ti substitution mechanisms. Am. Mineral. 90, 316–328.

I

Iglesias Ponce de León, M., Ribeiro, A., 1981. La zone de cisaillement ductile de Juzbado (Salamanca) Penalva do Castelo (Viseu): Un linéament ancien reactivé pendant l'orogenese Hercynienne. Comunicações dos Serviços Geológicos de Portugal. 67, pp. 89–93.

J

Jacques, D., Vieira, R., Muchez, P., Sintubin, M., 2017. Transpressional folding and associated cross-fold jointing controlling the geometry of post-orogenic vein-type W-Sn mineralization: examples from Minas da Panasqueira, Portugal. Mineralium Deposita,1-24.

Janssen, M. E., M. Torne, S. Cloetingh, and E. Banda. 1993. Pliocene uplift of the eastern Iberian margin: Inferences from quantitative modeling of the Valencia Trough, Earth Planet. Sci. Lett., 119, 585–597.

Julivert, M., Fontboté, J.M., Ribeiro, A., Conde, L. 1972. Mapa Tectonico de la Peninsula Iberica y Baleares E. 1:1.000.000. Inst. Geol. Min. España, Madrid.

K-L

Kelly, W.C., Rye, R.O. 1979. Geologic, fluid inclusion and stable isotope studies of the tin-tungsten deposits of Panasqueira, Portugal. Econ Geol 74:1721

Kroner, U., and Romer, R.L., 2013. Two plates - many subduction zones: the Variscan orogeny reconsidered. Gondwana Research 24, 298-329.

Lotze, F., 1945. Zur Gliederung der Varisziden der Iberischen Meseta. Geotekt. Forsch. 6, 78–82.

Lourenço, A., Noronha, F. 2000. Post-variscan hydrothermal activity. The case of lead mineralization associated to faults of the Panasqueira Mine, (Portugal). Cadernos Lab. Xeolóxico de Laxe Coruña.. Vol. 25, pp. 293-295.

M

Martínez-Catalán, J.R., Arenas, R., Diaz Garcia, F., et al. 2007. Space and time in the tectonic evolution of the northwestern Iberian Massif: Implications for the Variscan belt. In: Hatcher RD, Carlson MP, McBride JH, Martínez Catalán JR (eds) 4-D Framework of continental crust: Geological Society of America Memoir 200.Geological Society of America, 403–423

Martínez Catalán, J.R., Arenas, R., Abati, J., Sánchez Martínez, S., Díaz García, F., Fernández-Suárez, J., González Cuadra, P., Castiñeiras, P., Gómez Barreiro, J., Díez Montes, A., González Clavijo, E., Rubio Pascual, F., Andonaegui, P., Jeffries, T.E., Alcock, J.E., Díez Fernández, R., López Carmona, A., 2009. A rootless suture and the loss of the roots of a mountain chain: the Variscan Belt of NW Iberia. Compt. Rendus Geosci. 341:114–126. http://dx.doi.org/10.1016/j.crte.2008.11.004.

Martínez Catalán, J.R., Rubio Pascual, F.J., Montes, A.D., Fernández, R.D., Barreiro, J.G., Dias Da Silva, Í., Clavijo, E.G., Ayarza, P., Alcock, J.E., 2014. The late Variscan HT/LP metamorphic event in NWand Central Iberia: relationships to crustal thickening, extension, orocline development and crustal evolution. London, Special Publications] Geol. Soc. Lond., Spec. Publ. 405:225–247.

Martínez Poyatos, D., Nieto, F., Azor, A., Simancas, J.F., 2001. Relationships between very lowgrademetamorphismand tectonic deformation: examples fromthe southern Central Iberian Zone (Iberian Massif, Variscan Belt). J. Geol. Soc. 158:953–968.

Martínez Poyatos, D., Carbonell, R., Palomeras, I., Simancas, J. F., Ayarza, P., Martí, D., Azor, A., Jabaloy, A., González Cuadra, P., Tejero, R., Martín Parra, L.M., Matas, J., González Lodeiro, F., Pérez-Estaún, A., García Lobón, J.L., Mansilla, L. 2012. Imaging the crustal structure of the Central Iberian Zone (Variscan Belt): The ALCUDIA deep seismic reflection transect. TECTONICS, VOL. 31, TC3017.

Mateus A, Dias R, Coke C. 2001. Mecanismos e regimes de deformação em rochas metassedimentares detríticas do Ordovícico inferior e médio da Zona Centro.Ibérica (Portugal). Comunicações do Instituto Geológico e Mineiro 88:79-98.

Mateus, A., Noronha, F., 2010. Sistemas mineralizantes epigenéticos na Zona Centro-Ibérica; expressão da estruturação orogénica Meso- a Tardi-Varisca, In: Cotelo Neiva, J. M., Ribeiro, A., Victor, M., Noronha, F. e Ramalho, M., (Ed.), Ciências Geológicas: Ensino, Investigação e sua História, Geologia Aplicada, II: 47-61.

Matte, Ph., 1986. La chaıne varisque parmi les chaınes plaeozoıques peri atlantiques, modele d'evolution et position des grands blocs continentaux au Permo Carbonifere. Bull. Soc. Geol. France 2, 9–24.

Matte, P. 2001 - The Variscan collage and orogeny (480-290 Ma) and the tectonic definition of the Armorica microplate: a review - Terra Nova, 13, pp.122-128.

Meireles, C., Sequeira, A.J.D., Castro, P. and Ferreira, N. 2013. New data on the lithostratigraphy of Beiras Group (Schist Greywacke Complex) in the region of Góis-Arganil-Pampilhosa da Serra (Central Portugal). Cadernos Lab. Xeolóxico de Laxe Coruña. 2013. Vol. 37, pp. 105-124.

Mendes, A.C., Pupin, J.P., Dias, G., 1997. Petrogenese do macico subalcalino de Peneda Geres NW Penınsula Iberica.:evidencias a partir da estrutura interna e geoquımica de elementos traco de zircoes. X Semana de Geoquımica e IV Congresso de Geoquımica dos Paıses de Lıngua Portuguesa.Braga, Portugal, pp. 99–102.

N-O

Nance, R.D., Gutiérrez-Alonso, G., Keppie, J.D., Linnemann, U., Murphy, J.B., Quesada, C., Strachan, R.A.,. Woodcock, N.H. 2012. A brief history of the Rheic Ocean, Geoscience Frontiers, Volume 3, Issue 2, Pages 125-135, ISSN 1674-9871.

Noronha, F., Doria, A., Dubessy, J., Charoy, B., 1992. Characterization and timing of the different types of fluids present in the barren and ore-veins of the W-Sn deposit of Panasqueira, Central Portugal. Mineralium Deposita, Vol. 27, Issue 1, 72-79.

Noronha, F. 1999. Fluids related to tungsten ore deposits in Northern Portugal and Spanish Central System: a comparative review. Revista Sociedade Geologica de Espana.

Orejana, D., Villaseca, C., Valverde-Vaquero, P., Belousova, E.A., Armstrong, R.A., 2012. U-Pb geochronology and zircon composition of late Variscan S- and I-type granitoids from the Spanish Central System. International Journal of Earth Sciences, 101, 1789-1815.

P

Paris F., Robardet M. (1990). Early Paleozoic paleobiogeography of the Variscan regions.*Tectonophysics* 177, 192–213.

Paris F., Robardet M. (1994). Paleogeographic Synthesis. In: Chantraine, J., Rolet, J., Santallier, D.S., Piqué, A., and Keppie, J.D. (eds.), Pre-Mesozoic Geology in France and Related Areas, IGCP Project 233, Springer Berlin Heidelberg, p. 172–176.

Pereira, E., Ribeiro, A., Meireles, C., 1993. Cisalhamentos herc´ınicos e controlo das mineralizac¸o˜es de Sn–W, Au e U na Zona Centro-Ibe´rica, em Portugal. Cuad. Lab. Xeol. Laxe 18, 89–119.

Pereira I, Dias R, Bento dos Santos T, Mata J. 2017. Exhumation of a migmatite complex along a transpressive shear zone: inferences from the Variscan Juzbado–Penalva do Castelo Shear Zone (Central Iberian Zone). Journal of the Geological Society 174 (6):1004-1018. doi:10.1144/jgs2016-159.

Perroud H. (1985) Synthèse des résultats paléomagnétiques sur le Massif Armoricain *Hercynica* 1, 65–71.

Pinto, F., Vieira, R., Noronha, F. 2015. Different cassiterite generations at the Panasqueira deposit (Portugal): Implications for the metal zonation model. Proceedings, conference 13th SGA Biennial Meeting, Nancy, France.

Pollard, D.D., Segall, P., 1987. Theoretical displacements and stresses near fractures in rocks: with applications to faults, joints, dikes and solution surfaces. In: Atkinson, B.K. (Ed.), Fracture Mechanics of Rock. Academic Press, London, pp. 277-348.

Polya, D.A. 1989. Chemistry of the main-stage ore-forming fluids of the Panasqueira W-Cu-(Ag)-Sn deposit, Portugal: implications for models of ore genesis. Econ. Geol. 84, 1134–1152.

Polya, D.A., Foxford, K.A., Stuart, F., Boyce, A., Fallick, A.E. 2000. Evolution and paragenetic context of low δD hydrothermal fluids from the Panasqueira W-Sn deposit, Portugal: New evidence from microthermometric, stable isotope, noble gas and halogen analyses of primary fluid inclusions. Geochim. Cosmochim. Acta 64, 3357–3371.

R

Ribeiro, A. & Pereira, E. 1982. Controles paleogeográficos, petrológicos e estruturais na génese dos jazigos portugueses de estanho e volfrâmio. *Geonovas*, 1/3: 23-31.

Ribeiro, A., Pereira, E. & Dias, R. 1990a - Central-Iberian Zone, Allochthonous sequences. Structure in the Northwest of the Iberian Peninsula, in Dallmeyer, R. D., and Martínez García, E., (eds.), in Pre-Mesozoic Geology of Iberia - Springer-Verlag, Berlin Heidelberg, 220-236.

Ribeiro, R. 2018. Gravimetric modelling and geological interpretation of Argemela-Panasqueira area. Master thesis, University of Porto.

Rodríguez Alonso, M.D., Díez Balda, M.A., Perejón, A., Pieren, A., Liñán, E., López Díaz, F., Moreno, F., Gámez Vintaned, J.A., González Lodeiro, F., Martínez Poyatos, D., Vegas, R., 2004. La secuencia litoestratigráfica del Neoproterozoico-Cámbrico Inferior. In: Vera, J.A. (Ed.). Geología de España. SGEIGME, Madrid, pp.78-81.

Romer, R.L., and Kroner, U., 2016. Phanerozoic tin and tungsten mineralization – tectonic controls on the distribution of enriched protoliths and heat sources for crustal melting. Gondwana Research 31, 60-95.

Rubio Pascual FJ, Arenas R,Martínez Catalán JR et al 2013. Thickening and exhumation of the Variscan roots in the Iberian Central System: Tectonothermal processes and 40Ar/39Ar ages. Tectonophysics 587:207–221.

S

Sanderson, D.J., Roberts, S., McGowan, J.A., Gumiel, P. 1991. Hercynian transpressional tectonics at the southern margin of the Central Iberian Zone, west Spain. Journal of the Geological Society, London, Vol. 148, 1991, pp. 893-898.

Schermerhorn, L.J.G. 1955. The age of the Beira schists (Portugal). Geological InslituteUniversity of Amslerdam.

Schermerhorn, L.J.G. 1956. Igneous, metamorphic and ore geology of the Castro Daire-Sâo Pedro do Sul-Sátao region (northern Portugal). Com. Serv.Geol. Portugal. 37, 617 pp.

Schermerhorn, L.J.G. 1981. Framework and evolution of Hercynian mineralization in the Iberian Meseta. LEIDSE GEOLOGISCHE MEDEDELINGEN, Deel 52, Aflevering 1, pp. 23-56, 1-7-1981.

Scholz, C.H., 2002. The Mechanics of Earthquakes and Faulting, second ed. Cambridge University Press, Cambridge.

Stampfli, G. M. & Borel, G. D. 2002 - A plate tectonic model for the Paleozoic and Mesozoic constrained by dynamic plate boundaries and restored synthetic oceanic isochrons - Earth and Planetary Science Letters, 196, pp.17-33.

Scotese, C.R., 1997. Continental Drift, 7th edition, PALEOMAP Project, Arlington, Texas, 79 pp.

Sibson R.H., Robert F., Poulsen K.H. 1988. High-angle reverse faults, fluid-pressure cycling, and mesothermal gold-quartz deposits. Geology, 16, 551–5.

Sibson, R. H. 2001, Seismogenic framework for hydrothermal transport and ore deposition: Reviews in Economic Geology, v. 14, p. 25−50.

Simancas, J. F., et al. 2003. The crustal structure of the transpressional Variscan Orogen of the SW Iberia: The IBERSEIS Deep Seismic Reflection Profile, Tectonics, 22(6), 1062.

Simoes, P.P., Dias, G., Leterrier, J., 1997a. Petrogenese de granitoides hercınicos biotıticos associados ao cisalhamento Vigo-Re´gua _Norte de Portugal.. I Congresso Iberico de Geoqu´ımica e VII Congresso de Geoqu´ımica de Espanha, Soria, Spain, pp. 528–534.

Snee, L.W., Sutter, J.F., Kelly, W.C. 1988. Thermochronology of economic mineral deposits; dating the stages of mineralization at Panasqueira, Portugal, by high-precision 40Ar/39Ar age spectrum techniques on muscovite. Econ Geol 83:335–354.

T

Thadeu, D. 1949. A Cordilheira Central entre as serras da Guqrdunha e de Silo Pedro do Afor. Bol. da Soc. Oeol. de Portugal, vol. VIII,pags. 7 a 20, Porto.

Thadeu, D. 1951. Geologia do couto mineiro da Panasqueira. Comunic Serv Geol Port 32:5–64.

Thadeu, D. 1965b. Características da mineralizaçâo hipogénica estanovolframítica portuguesa. Bol. Ordem dos Engenheiros (Lisboa),10. pp. 63 81.

Thadeu, D. 1979. Le gisement stannowolframifere de Panasqueira (portugal). Chronique de la Recherche Miniere 450,35-42.

V

Van Der Voo, R. 1983. Paleomagnetic constraints on the assembly of the old red continent. *Tectonophysics* 91, 273–283.

Villar Alonso, P.M., Escuder Viruete, J.E., and Martínez Catalán, J.R., 1992, La zona de cizalla de Juzbado-Peñalba do Castelo en el sector español: III Congreso Geológico de Españay VIII Congreso Latinoamericano de Geología, Volume 2, p. 446–458.

Villaseca, C., Barbero, L, Rogers, G., 1998b. Crustal origin of Hercynian peraluminous granitic batholiths of Central Spain: petrological, geochemical and isotopic (Sr, Nd) constraints. Lithos 43, 55-79.

Y-Z

Yardley, B., Cleverley, J. 2013. The role of metamorphic fluids in the formation of ore deposits. Geological Society, London, special publications. 393. 10. 1144/SP393.5.

Zeck, H. P., P. Monie, I. M. Villa, and B. T. Hansen, 1992. Very high rates of cooling and uplift in the Alpine belt of the Betic Cordilleras, southern Spain, Geology, 20, 79 – 82.

Chapter III: Deciphering fluid flow at the magmatic-hydrothermal transition: a case study from the world-class Panasqueira W-Sn-(Cu) ore deposit (Portugal)

Objectives of this chapter:

The textural analysis of crystal shape can be a powerful tool providing precious information about the conditions of formation of hydrothermal deposits, such as the dynamic of fluid flow. It is well known that the crystal shape depends directly on (i) the intrinsic crystallographic properties and (ii) the influence of external factors that affect the crystal morphology by differences of growth rate of the equivalent crystalline faces (Curie, 1908). Indeed, when the crystallization is not affected by external environmental factors (isotropic media), the crystal morphology is strictly controlled by the crystallographic properties and the crystal symmetry is conserved. Conversely, when the crystallization is affected by external factors such as fluid flow, the crystal shape is marked by a symmetry breakdown due to the influence of direction and velocity of fluid flow.

In this chapter we exploit these relationships between the symmetry breakdown of the crystal shape and the hydrodynamic to constrain the direction and velocity of fluid flow at the magmatic-hydrothermal transition of Panasqueira. In the following we first present succinctly field observations, experimental and numerical studies illustrating the relationships between the anisotropic growth of minerals and the hydrodynamic. The second part corresponds to an article published at Earth Planetary Science Letters, in which we present results obtained from tourmaline growth bands in the case of Panasqueira that permit to propose a model of fluid flow at the magmatic-hydrothermal transition.

I- Mineral growth bands: a powerful tool to constrain fluid flow in hydrothermal systems

1. Field evidence of the symmetry breakdown of crystal shape in hydrothermal systems

Asymmetric growth of minerals induced by fluid flow has been observed for a long time in numerous hydrothermal systems (Newhouse, 1941; Engel, 1946 and 1948; Kessler, 1972; Sizaret et *al*., 2009) (Fig. 1). These authors have observed that equivalent crystalline faces can be characterized by difference of growth bands thickness interpreted as difference of growth rate in response to the directional fluid flow, from which minerals have crystallized (Fig. 1). From these observations, authors have deduced that the growth rate of the upstream crystalline faces is higher than the downstream faces, and hence that

the textural analysis of mineral growth bands can be a powerful tool to constrain the paleo-fluid flow in hydrothermal systems (Fig. 1c) (Engel, 1948; Kessler, 1972; Sizaret et *al*., 2006, Sizaret et *al*., 2009).

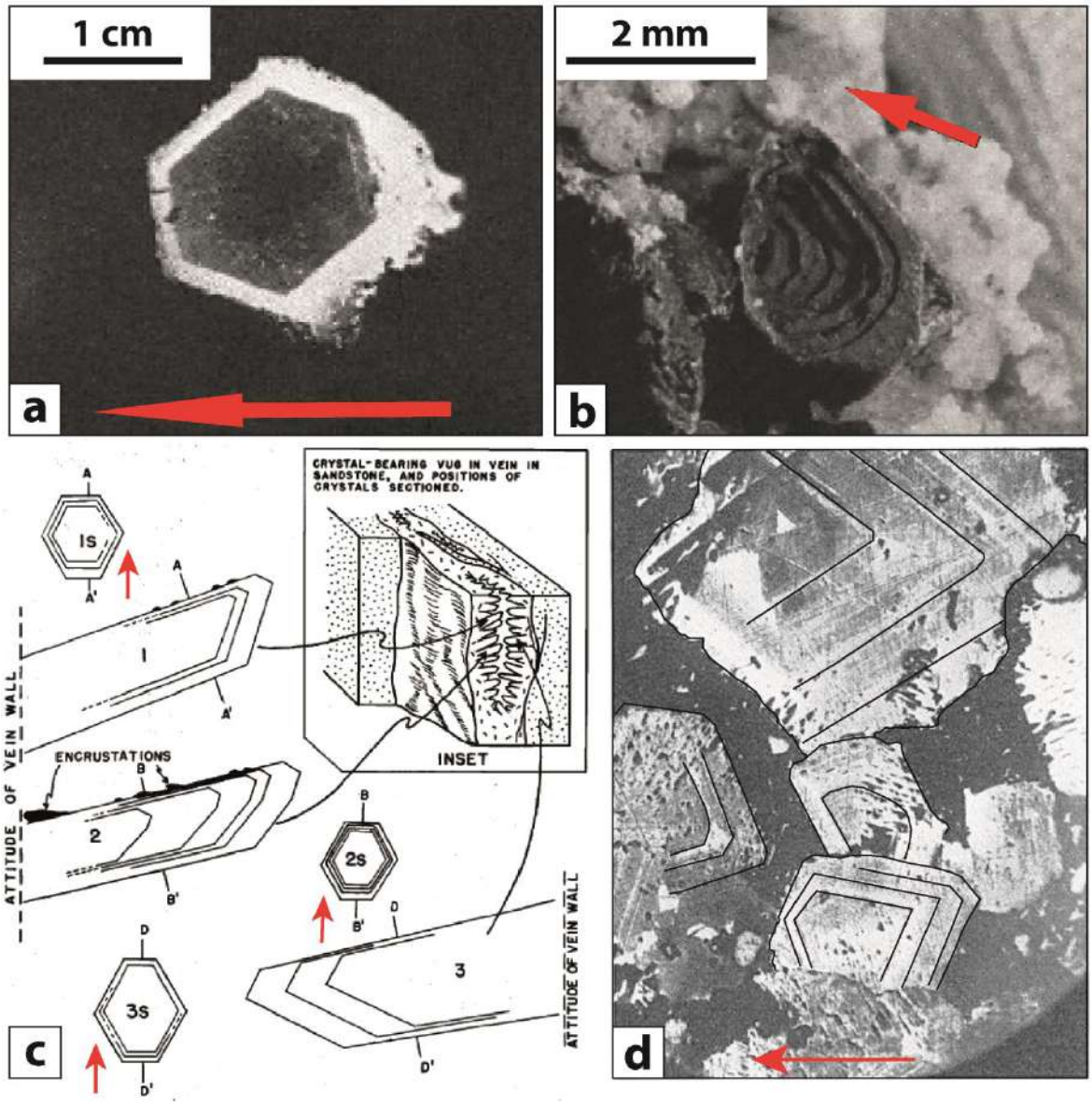

Figure 1 Natural examples of asymmetric growth of minerals, which have crystallized from a flowing solution in hydrothermal systems. (a) Section of quartz cut perpendicular to the <c> axis showing transparent (dark) quartz in the center surrounded by translucent (white) quartz exhibiting an anisotropic overgrowth (Newhouse, 1941). (b) Crystal of galena characterized by an asymmetric shape due to crystallization from a flowing solution (Pine Point, Kessler, 1972). (c) Example of fluid flow reconstruction in a vertical quartz vein, in which sections cut perpendicular to the <c> axis of quartz permit to determine direction of fluid flow from the study of the asymmetric shape of quartz (Engel, 1948). (d) Polished section of galena parallel to the sedimentary bedding showing growth bands or compositional zoning (Southeastern Missouri lead deposits from Newhouse, 1941). The red arrows give the approximate sense of fluid flow deduced by the authors from the asymmetric shape of minerals.

2. Experimental study of the influence of fluid flow on the mineral growth

Relationships between fluid flow (direction and velocity) and the symmetry breakdown of mineral have been experimentally investigated in numerous studies (Garside, 1975; Prieto and Amoros, 1981; Rodriguez-Clemente, 1976; Essalhi, 2009; Sizaret et *al*., 2017). Experiments performed by Garside, (1975) have emphasized that the volumetric growth rate of crystal is directly proportional to (i) the fluid velocity from which crystal has crystalized and (ii) the oversaturation state of fluid (Fig. 2).

Figure 3a shows qualitatively effects of a flowing solution on the shape of crystals of alun. When the crystal grows from a static solution, the equivalent crystal faces (separated by 120°) exhibit the same thickness ($d_1=d_2=d_3$) and the crystal symmetry is conserved. Conversely, a crystal exposed to a directional fluid flow is characterized by an asymmetric shape emphasizing an anisotropic growth with crystal face exposed to the fluid flow marked by a greater thickness than the downstream crystal face ($d_1>d_2\geq d_3$). This emphasizes a symmetry breakdown of the crystal induced by the directional fluid flow.

The effects of a directional fluid flow and its velocity on the symmetry breakdown of the crystal shape were experimentally quantified by Prieto and Amoros, (1981) (Fig. 3b). These experiences performed on crystals of KDP (Potassium Dihydrogen Phosphate) with an unidirectional fluid flow show that at low fluid flow velocity and laminar flow (< 3cm.s^{-1}), the growth rate of the crystal faces exposed to fluid flow is higher than the downstream faces. For high fluid flow velocities (> 3cm.s^{-1}) and turbulent flow, the crystal growth is isotropic and the symmetry of the crystal shape is conserved.

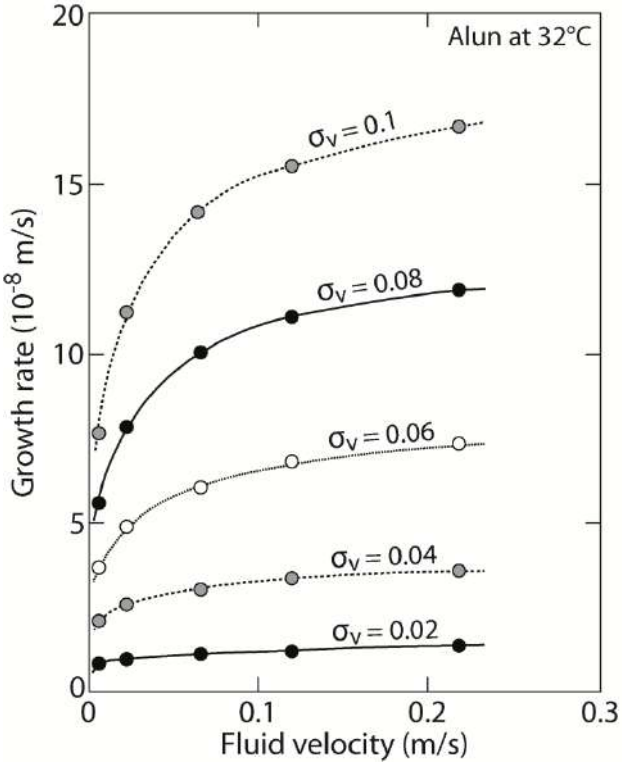

Figure 2 Effect of the fluid velocity on the growth rate of crystals of alun at 32°C. Effects of the fluid oversaturation are also plotted (σ_v) (Experimental data from Garside, 1975).

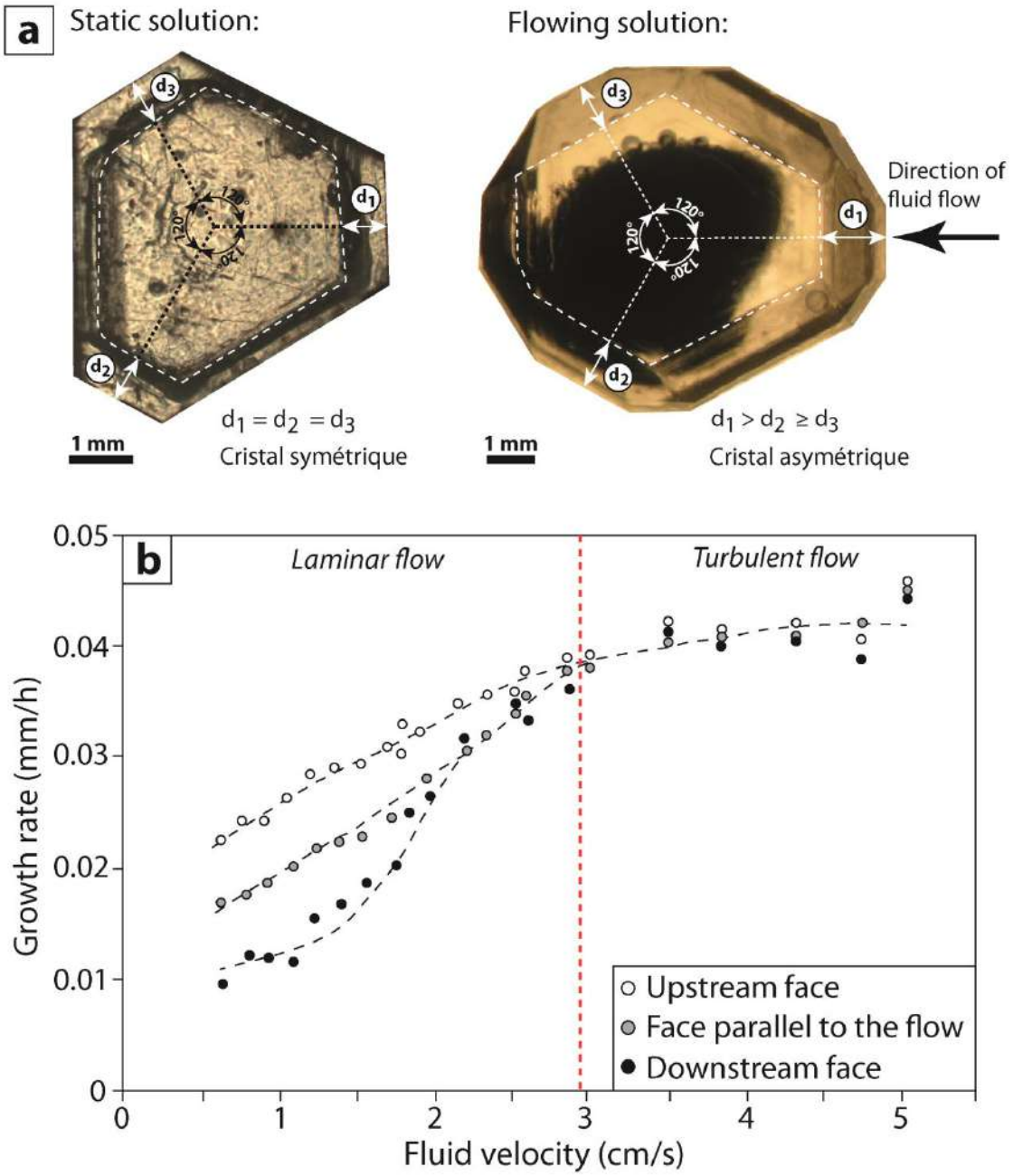

Figure 3 (a) Experimental results obtained for crystals of alun which have grown from a statistic solution (photo on the left) and from a flowing solution (photo on the right) (Experiments performed by Essalhi, 2009). (b) Experimental results obtained by Prieto and Amoros, (1981) for crystal of KDP showing the growth rate of the crystal faces exposed, parallel and opposed to the fluid flow as a function of the fluid velocity. For a laminar fluid flow (v_f < 3 cm.s^{-1}) the upstream face is characterized by a growth rate higher than the downstream face. For turbulent fluid flow (v_f > 3 cm.s^{-1}) the crystal growth is isotropic and the symmetry of the crystal shape is conserved.

3. Numerical modeling of mineral growth under laminar fluid flow

In order to establish a method allowing to constrain the direction and the velocity of fluid flow from the measurement of the growth bands thickness, Sizaret et *al*., (2006 and 2009) have performed numerical modelling coupling the Navier-Stockes and the chemical transport equations. To illustrate this method, we have followed the same numerical method to establish a relationship between the fluid velocity and the ratio of the growth bands thickness between the upstream and downstream crystalline faces (Fig. 4). The complete method is described in the part II in section *4.1*.

As described by Sizaret et *al*., (2009) results show that the variation of the concentration around the crystal is increasingly heterogeneous with the increase of the fluid velocity (Fig. 4a). For low fluid flow velocity (10^{-6} $m.s^{-1}$) the concentration profile realized across the crystal exhibits a symmetric shape with similar chemical gradient in front of and behind the crystal (Fig. 4b). Conversely, the concentration profile realized for high fluid velocity (10^{-3} $m.s^{-1}$) is characterized by an asymmetric shape with a stronger chemical gradient in the upstream part of the profile. This emphasizes that the upstream and the downstream chemical fluxes are different. This hypothesis is confirmed by the chemical flux recorded by the crystalline faces that emphasize an asymmetric repartition of flux around the crystal (Fig. 4a). Furthermore, results show that the difference of flux between the upstream and downstream face is increasingly important with the increase of the fluid velocity. Consequently, the growth rate of the upstream crystalline faces is higher than the downstream faces and the degree of asymmetry of a crystal shape is directly proportional to the fluid velocity. Accordingly, measurement of growth bands thickness can be applied to determine the direction and the velocity of fluid flow in hydrothermal systems. However, the application of this method require some precautionary, indeed the variation of concertation around the crystal can also influence the chemical gradient of the neighboring crystals and hence their growth rate. Consequently, only crystals sufficiently distant from each other can be considered to perform measurements.

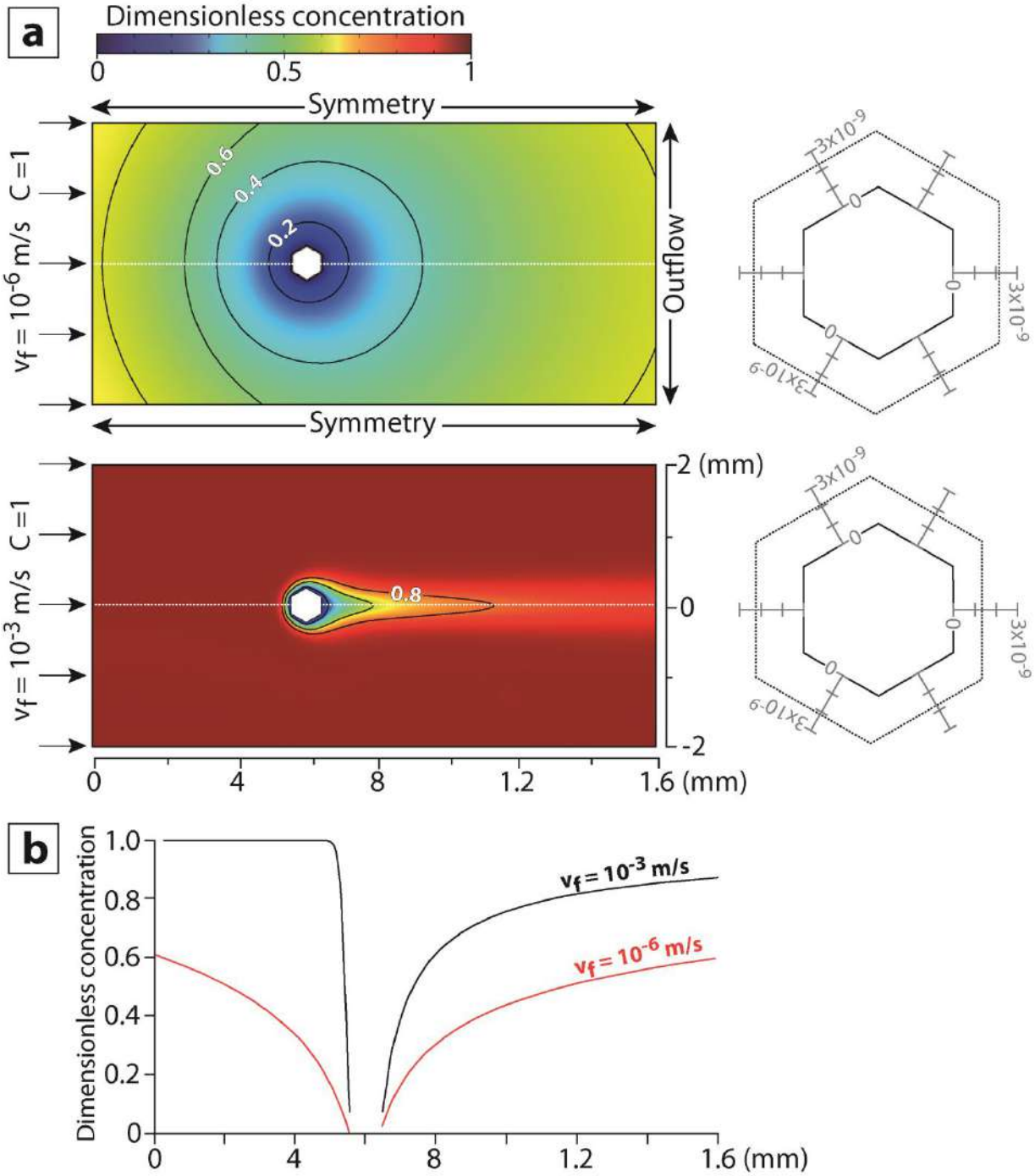

Figure 4 Numerical modeling of crystal growth in a flowing solution performed with the method proposed by Sizaret et *al.*, 2009. This model was performed using a hexagonal crystal deduced from the geometric properties of tourmaline of Panasqueira (edge size of 50 µm). The symmetry condition is applied for boundaries parallel to the fluid flow. A dimensionless concentration of 1 and a fixed velocity (v_f) are used for the left boundary. Along the crystal edges, the dimensionless concentration is fixed at 0. (a) Variation of the dimensionless concentration around the crystal of tourmaline and chemical flux recorded by each crystal faces for fluid velocity of 10^{-6} and 10^{-3} m.s^{-1}. (b) Concentration profiles parallel to the fluid flow passing through the crystal of tourmaline for fluid velocity of 10^{-6} and 10^{-3} m.s^{-1}.

II- Article published in Earth and Planetary Science Letters

Abstract: Deciphering the behavior of fluid flow at the magmatic-hydrothermal transition is crucial to understanding the physical processes leading to the formation of intrusion-related ore deposits and hence to predicting the locations of mineralized bodies. However, the hydrodynamics (direction and velocity) of the hydrothermal fluid flows related to this transitional stage remains poorly constrained. Here we present a coupled textural and chemical study performed on tourmaline growth bands to constrain fluid flow during the initiation of the hydrothermal system of the Panasqueira W-Sn-(Cu) deposit. This exceptional deposit consists of a dense network of flat wolframite and cassiterite-bearing quartz veins intensely developed above a well-known but hidden greisen cupola. The W-Sn mineralization is preceded by a tourmalinization stage occurring as metasomatic halos around veins and as selvages developed along the vein-wall-rocks contacts. Results emphasize the key role of the greisen cupola in fluid focusing and the role of fluid overpressure during vein opening. Velocity values highlight an efficient transport of metals in veins largely dominated by advective processes (10^{-4} to 10^{-3} $m.s^{-1}$), whereas fluid flow in the altered wall-rocks is slow and pervasive (10^{-6} to 10^{-5} $m.s^{-1}$), suggesting that element transport through the metasedimentary host rock was low and limited to the alteration haloes. LA-ICP-MS analyses of tourmaline growth bands reveal that fluids coming from the cupola are enriched in Na, K, Li, Sr and Sn, emphasizing the contribution of magmatic fluids during vein formation and the metasomatic alteration of the wall-rocks. More generally, this study demonstrates that the apical portions of granite bodies act as emanative centers of mineralizing fluids, and highlights the usefulness of mineral growth band analysis in the search for intrusion-related mineralization.

Keywords: magmatic-hydrothermal activity, Panasqueira, tourmaline, growth bands, flow direction, flow velocity

1. Introduction

The formation of hydrothermal ore deposits and the development of alteration halos in rocks involve the transfer of large quantities of fluids through permeable rocks during several episodic pulses integrated over a long period of time (Barnes, 1997; Robb, 2005). To form a high-grade deposit, the flow of metal bearing fluids must be focused in a restricted space and coupled with an efficient precipitation and trapping mechanism. Hence, understanding hydrothermal fluxes constitutes a major issue in metallogeny and requires the resolution of some fundamental questions related to: (i) the driving force behind fluid flow and (ii) the direction and velocity of fluid flow. The search for answers to these issues involves a combination of approaches including recognition of permeable pathways (Sibson, 1992; Cox 2005), mineralogical and geochemical analysis (Cartwright and Buick, 1996; Ferry et *al*., 2002) and fluid hydrodynamics (Ingebritsen and Appold, 2012).

Among hydrothermal ore deposits, those triggered and driven by felsic magmatic intrusions represent a main primary source of economically important metals, including copper (Cu), tungsten (W), tin (Sn), molybdenum (Mo) and gold (Au) (Hedenquist and Lowenstern, 1994; Černý et *al*., 2005). There is general agreement that these magmatic-related deposits are partly formed by the releasing and expulsion of metal-bearing fluids during the emplacement and cooling of magmatic intrusions (Hedenquist and Lowenstern, 1994; Černý et *al*., 2005). Another important process for metal transport in magmatic-hydrothermal systems is the development of large convective cells around plutons driven by the thermal contrast between intrusive bodies and their host rocks. This convective fluid flow is able to mobilize a large volume of fluids from the surrounding host rock and has a marked effect on the fluid-flow patterns (Norton and Cathles, 1979; Eldursi et *al*., 2009). More specifically, it has commonly been observed that mineralized systems are usually centered on small plutons, apices or feeder zones (Dines, 1956; Dilles and Proffett, 1995; Gloaguen et *al*., 2014) suggesting a strong control by the pluton roof geometry on mineralizing fluid flow. Indeed, some numerical models have demonstrated that fluid flow is optimal above the apical part of intrusions and predict the formation of ore deposits in these areas (Sams and Thomas-Betts, 1988; Eldursi et *al*. 2009; Weis et *al*. 2015). Despite these elegant numerical results, the expected fluid flow pattern (flow direction and velocity) needs to be verified by field investigations.

Moreover, it is widely recognized that magmatic-hydrothermal systems are the products of complex histories encompassing episodic stages of fluid flow related to polyphase intrusion emplacement, which have had important effects on the geometry of hydrothermal systems. In this scheme, the magmatic-hydrothermal transition is a key event that marks the initiation of the hydrothermal system and defines the future behavior of fluid flow. It is usually during this transitional stage that permeable structures open and channel mineralized fluids. However, fluid flow related to this specific hydrothermal stage is difficult to access and thus remains poorly constrained owing to the lack of recognized methods to implement in the field.

The textural analysis of mineral growth bands has provided significant information about the direction and velocity of fluid flow involved in the formation of hydrothermal ore deposits (Kessler et *al*. 1972) and during metasomatic processes (Sizaret et *al*., 2009; Mahjoubi et *al*., 2016). This direct approach constitutes a powerful tool for constraining fluid flow related to a specific hydrothermal event such as the magmatic-hydrothermal transition. In the present study, we perform a textural analysis of tourmaline growth bands to decipher fluid flow at the initiation of the magmatic-hydrothermal stage at Panasqueira (Portugal). This textural analysis is combined with trace element analysis of tourmaline growth bands to constrain the chemical characteristics of the fluids from which the tourmalines crystallized. Panasqueira is an historic world-class tungsten vein deposit characterized by a well-preserved magmatic-hydrothermal plumbing system. The deposit is one of the best-documented and characterized in the world and represents a reference site for the study of magmatic-hydrothermal processes leading to the formation of an Sn-W ore deposit (Thadeu, 1951; Kelly and Rye 1979; Polya, 1989; Polya et *al*., 2000; Foxford et *al*., 2000; Lecumberri-Sanchez et *al*., 2017; Codeço et *al*., 2017). Based on the results of estimated fluid flow directions and velocities, we discuss the key parameters controlling the behavior of fluid flow at various scales, such as: (i) the role of granitic cupolas in the localization of mineralized areas by fluid-flow focusing, (ii) the effects of fluid overpressure conditions on vein opening and the propagation of alteration halos in wall-rocks, and (iii) the required duration of fluid flow during the W-Sn mineralization stage.

2. Geological and metallogenic framework

2.1 Regional geology

The Panasqueira W-Sn-(Cu) ore deposit is located in the Central Iberian Zone (CIZ), which constitutes the axial zone of the Iberian Variscan belt (Fig. 5a) (Julivert et *al*., 1972). The CIZ is composed of the Schist-Greywacke-Complex (SGC) intruded by a large volume of granitoid intrusions resulting from an extensive magmatic event during the latest stages of the Variscan orogeny (Dias et *al.*, 1998). The SGC consists of a thick (8-11 km) sequence of late Neoproterozoic schists and graywackes affected by a regional greenschist metamorphism (Martínez-Catalán et *al*., 2007). Deformation of the SGC consists of tight upright folds with NW-SE sub-vertical axial planes produced by a NE-SW shortening related to the earliest compressive stage of the Variscan orogeny (Dias and Ribeiro, 1995 and Martínez-Catalán et *al*., 2007). This folding is associated with a regional sub-vertical penetrative axial planar cleavage (S1) (Fig. 5a and 5b). The CIZ hosts numerous Sn-W ore deposits and occurrences related to granitic intrusions and formed by magmatic-hydrothermal processes (Derré, 1982).

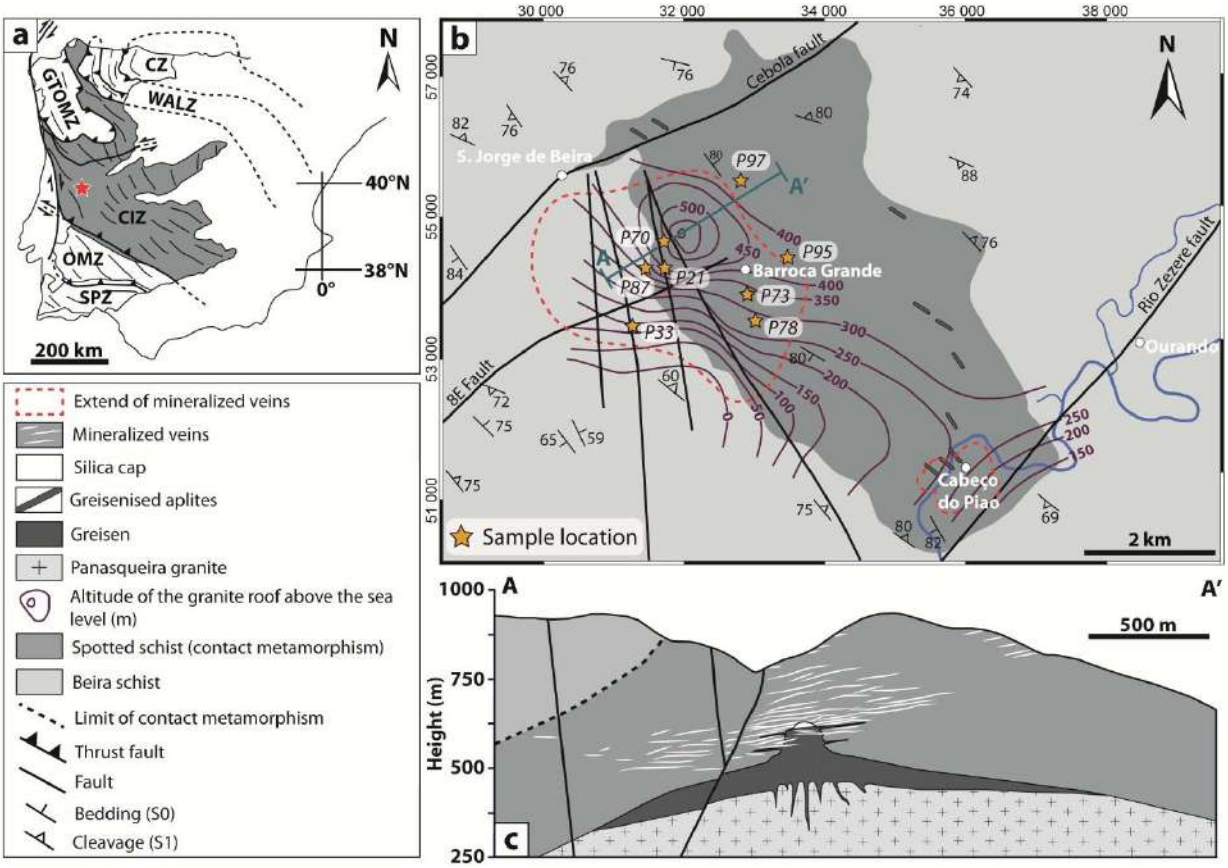

Figure 5 (a) Tectonic map of the Variscan Iberian massif showing the main tectonostratigraphic domains defined by Julivert et *al.*, (1972). The location of the Panasqueira deposit is marked by a red star. CZ: Cantabrian Zone, WALZ: West Asturian-Leonese Zone, GTOMZ: Galicia Tràs-os-Montes Zone, CIZ: Central Iberian Zone, OMZ: Ossa-Morena Zone and SPZ: South Portuguese Zone (b) Geological map of the Panasqueira ore deposit showing the altitude of the granite roof. (c) Geological cross section (A-A') displaying the spatial relationship between mineralized veins and the greisen cupola (data source Beralt Tin & Wolfram S.A.).

2.2 The Panasqueira W-Sn-(Cu) ore deposit

The Panasqueira ore deposit is located in the Beira Baixa province on the southern flank of the Serra da Estrela massif constituted by late- to post-tectonic granitic intrusions. In this region the late Neoproterozoic folded and metamorphosed SGC is locally called the Beira Schist. At Panasqueira, spotted schists mark the presence of a thermal metamorphic aureole related to an underlying S-type granite (Thadeu, 1951; Clark, 1964). The intrusive body is limited by the Cebola fault to the north and the Rio Zêzere fault to the south (Fig. 5b) (Clark, 1964). As exposed in underground mine works and drill cores, the upper part of this granite includes a quartz-muscovite greisen cupola formed by interaction between granitic rocks and acidic F-B and Li-rich fluids (Shcherba, 1970; Bishop, 1989) (Fig. 5c and 6a).

The W-Sn mineralization is hosted by a dense network of shallow-dipping veins crosscutting the vertical foliation of the Beira Schist and the greisen cupola (Fig. 6a). The vein system is centered above the greisen cupola and extends over an area of 6 km² for a depth extension of about 200-300 meters (Fig. 5b and 5c) (Kelly and Rye 1979; Polya et *al*., 2000). This unusual shallow-dipping orientation of mineralized veins is compatible with the regional stress field, which involved NE-SW shortening with a vertical σ_3 leading to the formation of tight upright folds accompanied by the development of the regional NW-SE sub-vertical foliation (Dias and Ribeiro, 1995; Martínez-Catalán et *al*., 2007) (photos in supplementary materials ESM 1). Based on textural and structural analysis of the vein swarms, Foxford et *al*., (2000) proposed a crack-and-seal model involving episodic vein dilation and filling induced by injections of fluids at supralithostatic pressure conditions in a compressive crustal regime. Although this mechanism is quite appealing, these conditions of fluid overpressure in veins remain unproven. The structural control of the vein formation has probably induced permeability anisotropy with a strong horizontal component that could affect the pattern of fluid flow at the time of mineralization. Late NNW-SSE and ENE-WSW sub-vertical fault system crosscuts the veins and the granite intrusion (Fig. 5c) (Thadeu 1951, Kelly and Rye 1979, Foxford et *al*., 2000). As evidenced in the field, these faults postdate the mineralization event and did not control fluid flow during the W-(Sn) mineralization (Thadeu, 1951).

The complex paragenetic sequence of veins was described in detail by Kelly and Rye (1979) and improved by Polya et *al*., (2000). At least five mineralization stages are recognized in the veins from oldest to youngest: the Quartz-Tourmaline (QTS) stage, the Main Oxide Silicate Stage (MOSS), the Main Sulfide Stage (MSS), the Pyrrhotite Alteration Stage (PAS) and the Late Carbonate Stage (LCS). The MOSS (Fig. 6b) and the MSS (Fig. 6c) are the most economically relevant ore stages. The MOSS carries the W-Sn mineralization and consists of muscovite and quartz accompanied by wolframite and cassiterite. The two earliest mineralization stages (QTS and MOSS) constitute a continuous sequence that is then superimposed and/or cross-cut by the late sulfide stage (MSS). The MSS, which carries the Cu mineralization, is mainly composed of arsenopyrite, chalcopyrite, sphalerite pyrite and pyrrhotite (Thadeu 1951, Kelly and Rye 1979, Polya et *al*. 2000). Based on fluid inclusions analyses, Kelly and Rye (1979) and Bussink (1984) have reported that fluids related to the MOSS and the QTS were trapped at temperatures between 300 and 350°C. Although the tourmaline stage (QTS) is

volumetrically of minor importance (mm to cm in thickness), it marks the initiation of the Panasqueira hydrothermal system (Polya et *al*., 2000).

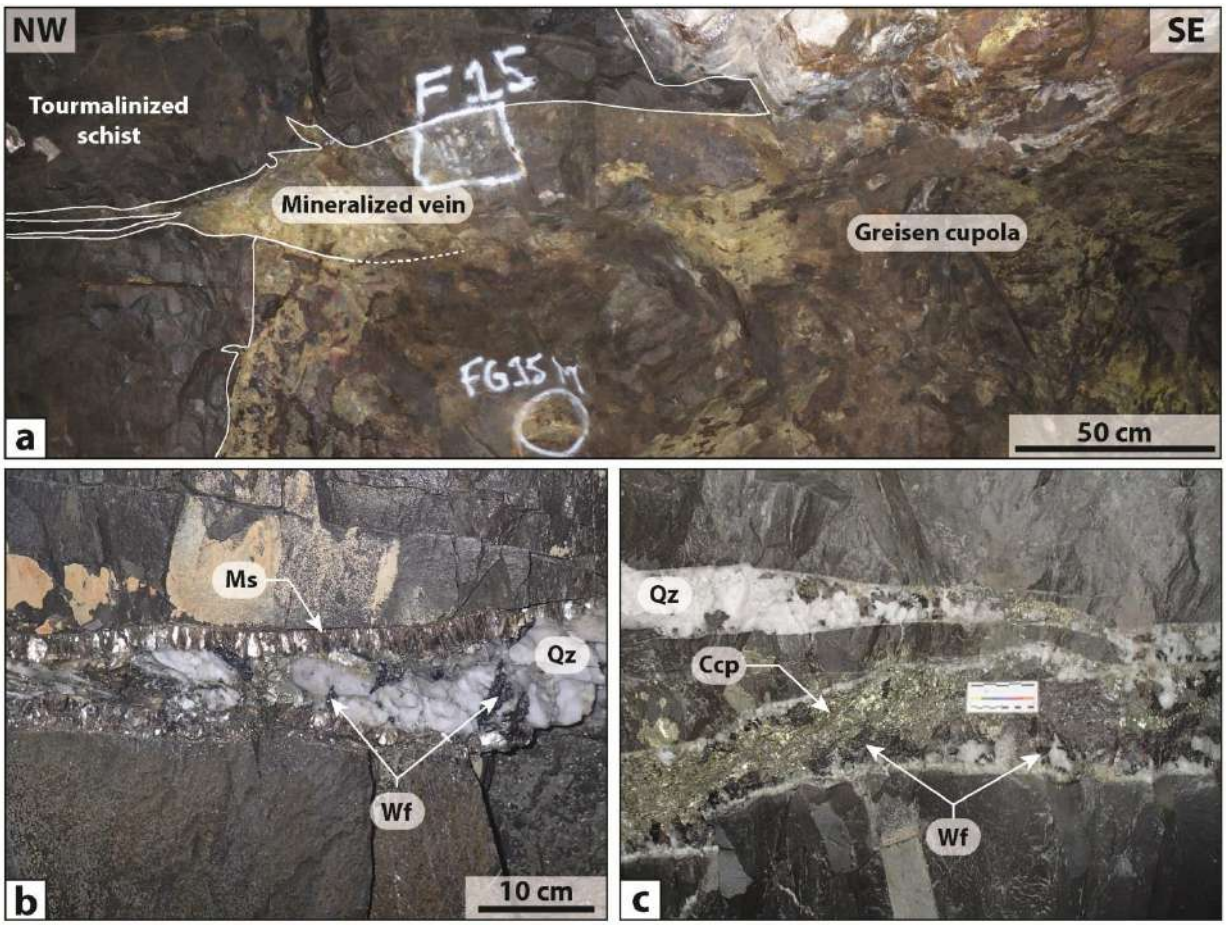

Figure 6 The mineralized system at the Panasqueira W-Sn-(Cu) deposit. (a) Contact between the greisen cupola and the tourmalinized metasedimentary host rock on Level 1 of the mine. Note the presence of mineralized veins that crosscut this contact. (b) Typical Quartz-Wolframite veins corresponding to the main oxide stage. (c) Quartz-Wolframite veins intersected by the late sulfide stage carrying the Cu mineralization. Abbreviations from Whitney and Evans (2010) Ccp: Chalcopyrite, Ms: Muscovite, Qz: Quartz, Wf: Wolframite.

3. Tourmaline occurrence

At Panasqueira, tourmaline is common, especially in metasedimentary host rock surrounding mineralized veins (Fig. 7a). Tourmaline is present within alteration halos, which are developed along schist-vein contacts within the lower and the upper wall-rocks. These halos result from metasomatic reactions induced by fluid–rock interactions during hydrothermal fluid flow in the veins. Locally, it is possible to observe alternation of quartz-rich and tourmaline-muscovite rich layers inherited from lithological heterogeneities in the Beira Schist. These tourmalines are fine-grained and their <c> axes are randomly oriented in the vertical cleavage planes of the schist.

Tourmaline is also present in veins along schist-vein contacts (Fig. 7b and 7c). It forms fine acicular crystals (1-3 mm) with <c> axes vertical and perpendicular to the vein edge and consequently to the inferred plane of fluid flow (Fig. 7c). These tourmalines grains are commonly associated with apatite, rutile and muscovite (Fig. 7d), but their relationships with the ore minerals (wolframite and cassiterite) are difficult to observe. However, in some veins tourmaline appears to slightly predate wolframite and may be texturally associated with cassiterite (Fig. 7e). Consequently, tourmaline represents a good candidate for tracking W-Sn mineralized fluid flow related to the QTS and MOSS in the Panasqueira vein system.

For both types of tourmaline, the sections normal to the <c> axis are characterized by growth band zonation with a core and well-defined rims (Fig. 7d and Fig. 7f). These bands emphasize an anisotropic growth and highlight a symmetry breakdown caused by a directional fluid flow (Fig. 8a and 8b).

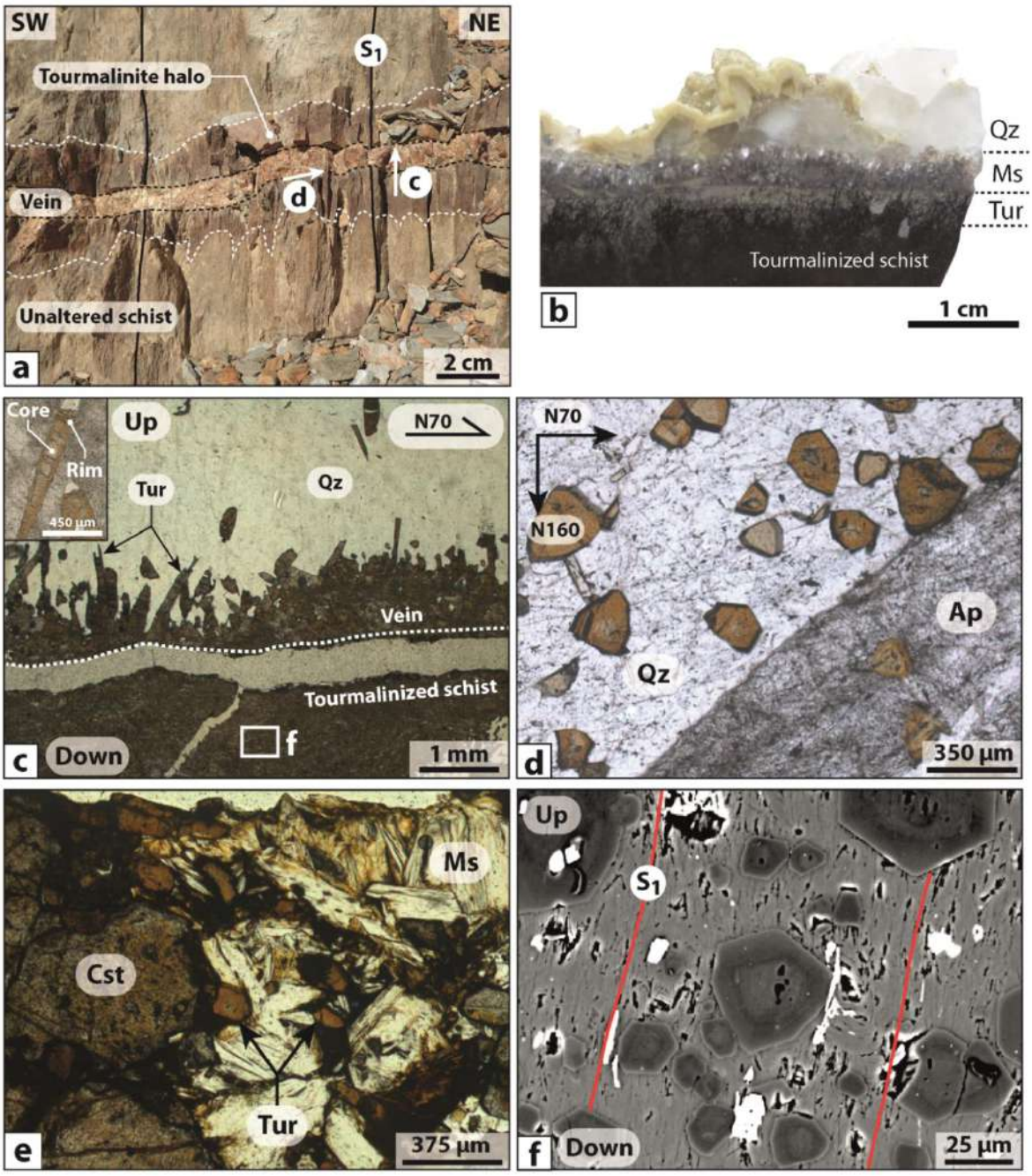

Figure 7 Textural and petrographic characteristics of tourmalines present in the mineralized system of Panasqueira. (a) Quartz-tourmaline vein with tourmalinization of the metasedimentary wall-rocks. The white dashed line indicates the tourmalinization front in the metasedimentary host rock. Arrows c and d indicate the orientation of thin sections c and d. Note the preferential migration of the tourmalinization front in the vertical foliation planes S_1 (b) Sample of mineralized veins showing the vertical growth of acicular tourmalines along the schist-vein contact. (c) and (d) photomicrographs of vein tourmaline showing sections parallel (c) and normal (d) to the <c> axis of tourmaline. (e) Photomicrograph of mineralized vein showing tourmaline grains associated with cassiterite. (f) SEM photomicrograph of altered schist perpendicular to the foliations planes showing growth band zoning in tourmaline basal sections. Abbreviations from Whitney and Evans (2010) Ap: Apatite, Cst: Cassiterite, Ms: Muscovite, Qz: Quartz, Tur: Tourmaline.

4. Sampling and methodology

Owing to its remarkable mechanical and chemical stability, tourmaline is able to record significant information about its host environment (Henry and Dutrow, 1996; Van Hinsberg et *al*. 2011a). In particular, tourmaline provides a powerful tool for constraining the hydrodynamics (direction and velocity of fluid flow) of geological processes involving fluid flow (Sizaret et *al*., 2009; Mahjoubi et *al*., 2015). Moreover, tourmaline incorporates a diversity of traces elements and constitutes a geochemical monitor of fluid compositions (Marks et al., 2013; Van Hinsberg et *al*., 2017). In this study, tourmaline growth bands were used to track both the flow and chemical composition of hydrothermal fluids involved during the earliest stages of vein formation at Panasqueira.

Oriented vein samples containing tourmaline were collected in the mine and at the surface, at various places around the cupola, both horizontally and vertically, so as to have a full spatial distribution, and to establish a paleo-fluid flow map around the granitic intrusion (Fig. 5b). Unfortunately, no samples were available from the northwestern part of the studied area.

The vertical migration of the alteration front (tourmalinization) within the metasedimentary host rocks appears to be driven by the sub-vertical foliation planes (S1). To study the vertical fluid flow related to the alteration of the wall-rocks, samples of alteration halos have been collected above and below veins perpendicularly to the vertical foliation planes (NE-SW section). The orthogonal NW-SE sections are parallel to the foliation planes and hence do not permit fluid flow reconstruction in the wall rock, owing to the preferential crystallization of tourmaline, which itself follows the foliation planes.

4.1 Fluid flow reconstruction by growth band measurement

In hydrothermal systems, a crystal's shape is controlled by its intrinsic symmetry and the effects of external forces, such as fluid flow, that induce anisotropic growth (Curie 1908). The method used for the reconstruction of local fluxes is based on the notion that crystal faces exposed to the chemical flux (i.e. the upstream faces) grow faster than downstream faces (Kessler et *al*. 1972 and Sizaret et *al*., 2006 and 2009). The relationship between flow velocity and the relative growth rate of upstream and downstream faces can be modelled and quantified (Sizaret et *al*. 2006 and 2009). From this postulate, it is possible to deduce local fluid flow directions and velocities within the hydrothermal system. Oriented thin sections were cut parallel to the expected stream-line, i.e. parallel to

veins, within the vein, and vertically and perpendicular to foliation planes in altered host rocks. Tourmaline crystals were examined on polished thin sections using optical transmitted light and scanning electron microscope. Then, on basal tourmaline section (i.e., perpendicular to the <c> axis) the growth band thicknesses of equivalent crystal faces (d_1, d_2 and d_3) and their respective directions (α_1, α_2 and α_3) were measured (Fig. 8c). The three normalized thicknesses d_{max}, d_{int} (intermediate) and d_{min} were determined. Assuming that the thickest band (d_{max}) received the largest chemical flux, the orientation of d_{max} gives the direction of the paleo-fluid flow recorded by the crystal (Fig. 8c).

The relationship between fluid velocity and growth ratios (d_{max}/d_{min}) was established by solving the coupled Navier-Stokes and chemical transport equations with the Comsol Multiphysics finite element code (Sizaret et *al*., 2009). In this modeling the edge size of tourmaline is 50 µm and the fluid (water) viscosity is chosen at realistic mineralizing conditions, taken here at 350°C and 500 bars ($8.3.10^{-5}$ Pa.s source NIST WebBook, 2017, https://webbook.nist.gov/). Varying flow velocity provides a relationship between chemical flux ratio (upstream/downstream) and fluid velocity (Fig. 8d). The growth band thicknesses measured on minerals can be considered as chemical fluxes integrated over a given period of time. Consequently, the fluid velocity can be determined via the inverse method by plotting the measured d_{max}/d_{min} ratio on the flux ratio (upstream/downstream) vs velocity curve (Fig. 8d) (Sizaret et *al*. 2006 and 2009).

To obtain representative measurements, basal sections of tourmaline were chosen using the following criteria: absence of contact with another crystal of tourmaline, absence of recrystallization and corrosion and easily identifiable equivalent faces. For each site, flow directions and velocities deduced from each tourmaline section were obtained and treated with the free meteorological software WRPLOT View™ (Lake Environmental, 2016) in order to establish “wind roses” of local paleo-fluid flow. These rose diagrams were then reported on the map.

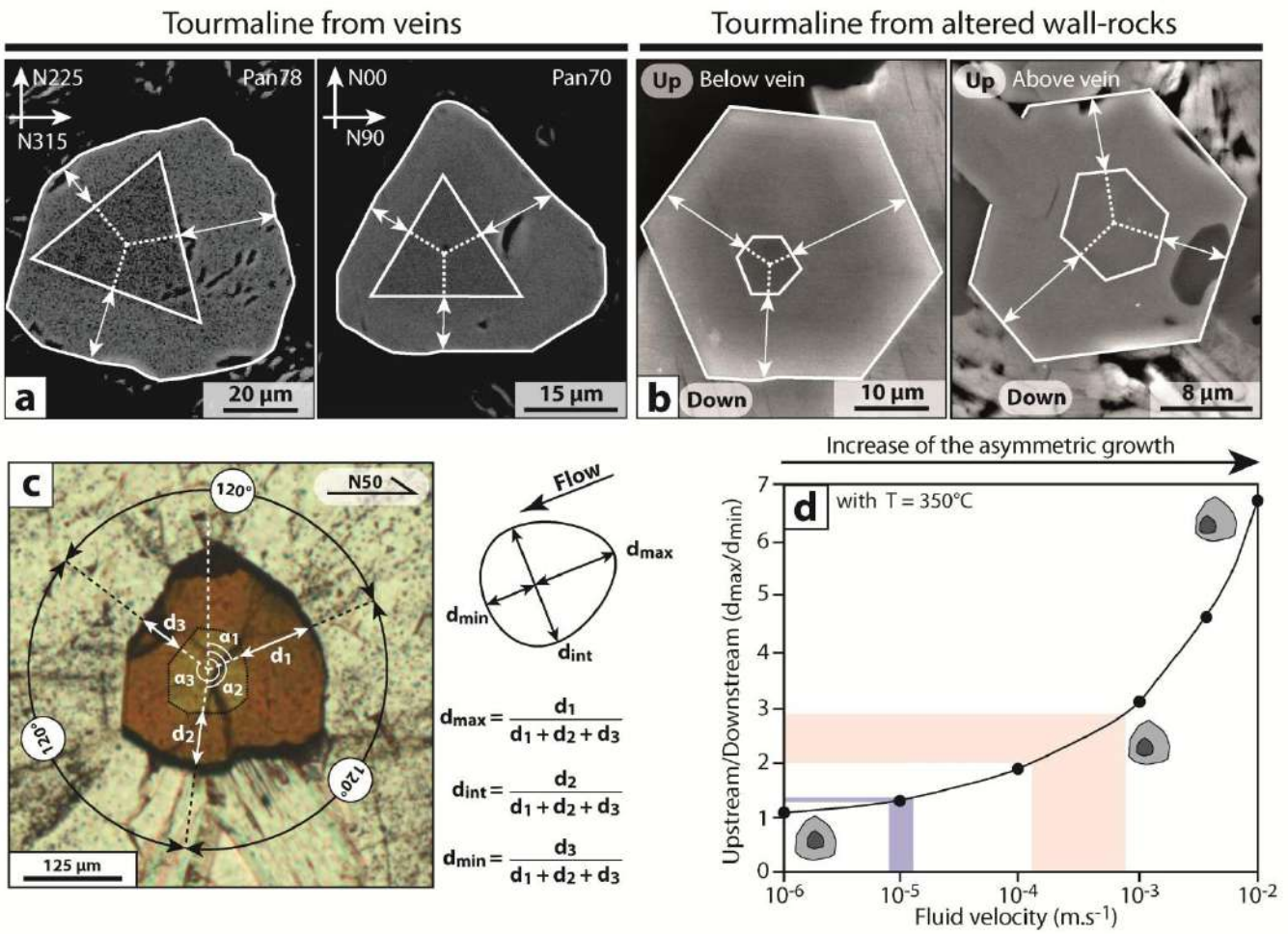

Figure 8 Examples of basal sections of tourmaline from veins (a) and altered wall-rocks (b) displaying an asymmetric shape caused by an anisotropic growth (c) Measurements of growth bands thickness and orientation on a basal section of tourmaline. (d) Curve deduced from numerical modeling showing relationship between fluid velocity and flux ratio (see text for details). The filled boxes indicate range of averages of fluid velocities derived from d_{max}/d_{min} ratio measured on tourmalines from altered wall-rocks (blue) and veins (red).

4.2 Tourmaline growth band chemistry

4.2.1 Major and minor element analysis

The major and minor element compositions of tourmaline were determined on polished thin sections using a Cameca SX-Five electron probe micro-analyzers (EPMA) at the Institut des Sciences de la Terre d'Orléans (ISTO). Analyses were performed using an accelerating voltage of 15 kV, a beam current of 6 nA and a diameter of 2 µm. The elements analyzed were Si, Ti, Al, Fe, Mn, Mg, Ca, Na, K, F and Cl. For calculation of the structural formulae and site allocation in tourmaline, the analyses were normalized to 15 cations (T + Z + Y-sites) and B_2O_3 and H_2O contents were calculated by stoichiometry,

taking B = 3 apfu and OH + F + Cl = 4 apfu. Analytical conditions and calibration are detailed in the electronic supplementary materials (ESM 2).

4.2.2 Trace element analysis

Trace element concentrations in tourmaline were determined by laser ablation inductively coupled plasma-mass-spectrometry (LA-ICP-MS). These analyses were performed at BRGM (French Geological Survey) using a ThermoScientific X series II quadrupole ICP-MS coupled with a Cetac Excite 193 nm laser ablation system. Ablations were performed with a repetition rate of 8Hz and laser energy of 3.5 J/cm² with a beam size of 40 μm. Analyses comprise 20 seconds of gas blank measurement following by 60 seconds of ablation. Elements analyzed were ^{7}Li, ^{23}Na, ^{24}Mg, ^{27}Al, ^{29}Si, ^{47}Ti, ^{51}V, ^{55}Mn, ^{66}Zn, ^{88}Sr and ^{118}Sn. Data reduction was performed with the Glitter 4.0 software using the NIST SRM-612 glass standard for external standardization and ^{29}Si as the internal standard. Concentrations of Mg and Al obtained by LA-ICP-MS data reduction were compared with EPMA analyses to check the accuracy of the results. Analyses of certified standard NIST-612 SRM show a good accuracy with a relative standard deviation (RSD) below 10%. Detection limits for most elements range between 0.2 and 5 ppm. Higher detection limits were obtained for Zn, Ti and Na (respectively 5.5 ppm, 15.4 ppm and 37.4 ppm).

5. Results

5.1 Large scale fluid flow

Fluid flow directions and velocities are summarized in Table 1 (complete measurements in electronic supplementary materials ESM 3) and illustrated in Figure 9. For veins-hosted tourmaline, an average ratio of d_{max}/d_{min} was determined for each of the 8 sample sites. These average ratios range from 2.0 to 2.9 implying a fluid velocity varying from 10^{-4} to 10^{-3} m.s^{-1} in veins (Table 1 and Fig. 9d). Figure 9c shows the histogram representation of all velocity values, which are characterized by an asymmetric distribution centered on 10^{-4} - 5.10^{-4} m.s^{-1}. This wide variable distribution is probably due to the sinuous nature of the fluid flow path. Indeed, a narrowing of the pathway may be responsible for the local high velocity values recorded by some tourmalines. For each sample of veins, the flow directions are dispersed with a significant mean direction (Fig. 9a). In the “rose” diagrams, these directions generally host the highest velocity

values (10^{-4} to 10^{-3} $m.s^{-1}$). Conversely, the lowest fluid velocity values are not aligned with these mean directions of fluid flow (Fig. 9a). Considering all the sites, the mean orientations of flow depict a large-scale streamline structure with radial directions coming from a center located on the greisen cupola (Fig. 9a and 9b). The vertical fault system crosscutting the veins does not influence flow direction in the veins (Fig. 9b). The pitch of flow direction vectors on the vein plane is not aligned to the dip direction of veins (Table 1). Consequently, flow directions are not influenced by veins orientation.

5.2 Fluid flow in host rock

In altered schist, tourmaline growth bands show a fluid flow escaping sub-vertically from veins toward the host rock, with an averaged angle of 55° above and 60° below the vein (Fig. 10).

This symmetrical behavior may be related to the horizontal component of fluid flow within the vein, as suggested by measurements on sample P21. Mean velocities obtained in altered wall-rocks are 1 to 2 orders of magnitude lower than fluid velocities obtained in the veins (Fig. 8d and Fig. 10). In addition, it would appear that velocities are higher above (10^{-5}- 5.10^{-5} $m.s^{-1}$) than below veins (5.10^{-6} to 10^{-5} $m.s^{-1}$) (Fig. 10).

	Coordinates (ETR S89/Portugal TM06)			Veins orientation		d_{max}/d_{min}			Fluid flow		
Veins:	X (m)	Y (m)	Z (m)	Strike	Dip	N	Mean	SD	Mean direction	Mean velocity ($m.s^{-1}$)	Pitch
Pan70	31675.9	54649.3	620	N136	7°	30	2.06	0.66	N28	2.76E-04	77°
Pan87	31410.9	54261.6	620	N300	5°	41	2.50	0.95	N64	6.65E-04	60°
Pan21	31675.1	54253	560	N200	5°	31	2.06	1.06	N27	5.53E-04	10°
Pan33	31217.9	53385.2	470	N130	15°	24	2.24	0.39	N40	3.33E-04	90°
Pan78	33043.4	53490.3	618	N138	7°	31	2.29	1.13	N331	6.66E-04	26°
Pan73	32933.2	53875.3	662	N127	10°	25	2.75	1.10	N321	9.46E-04	24°
Pan95	33058.4	54287	741	N127	5°	18	2.92	1.27	N300	1.38E-03	8°
Pan97	32833.3	55559.5	732	N160	10°	25	2.74	0.96	N201	9.47E-04	42°
Altered wall-rocks :											
P20 Up	31675.1	54253	560	-	-	28	1.36	0.18	55	1.44E-05	-
P20 Down	31675.1	54253	560	-	-	28	1.29	0.11	60	6.95E-06	-

Table 1 Directions and velocities of fluid flow deduced from measurements on tourmaline growth bands in veins and in altered wall-rocks (SD: Standard Deviation and N: number of measurement).

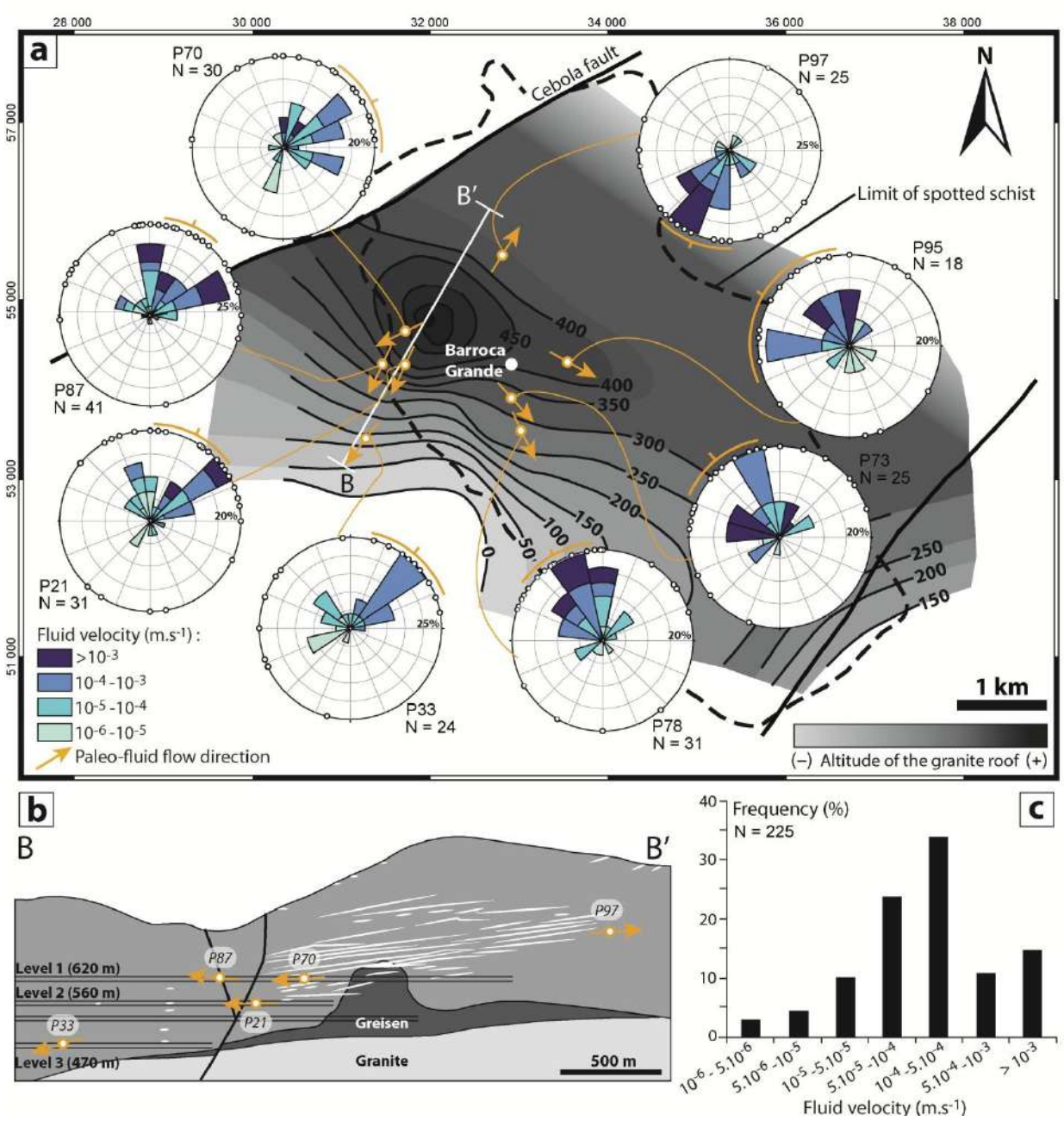

Figure 9 Fluid flow at the ore deposit scale deduced from tourmaline growth bands in mineralized veins. (a) Large scale map of paleo-fluid flow around the hidden granite of Panasqueira. Local fluid flow direction and velocities are represented by "rose" diagrams, which give the direction of tourmaline faces exposed to the fluid flow (d_{max}) and the directional distribution of fluid velocities. The orange arcs indicate the 95% interval of confidence regarding the direction from which the fluid comes. The orange arrows on the map correspond to the mean directions of flow determined for each sample site. N corresponds to the number of measurements performed for each sample sites. (b) Results of fluid flow directions projected onto the geological cross section (B-B') showing flows moving away from the cupola. (c) Histogram showing distribution of all fluid velocity values.

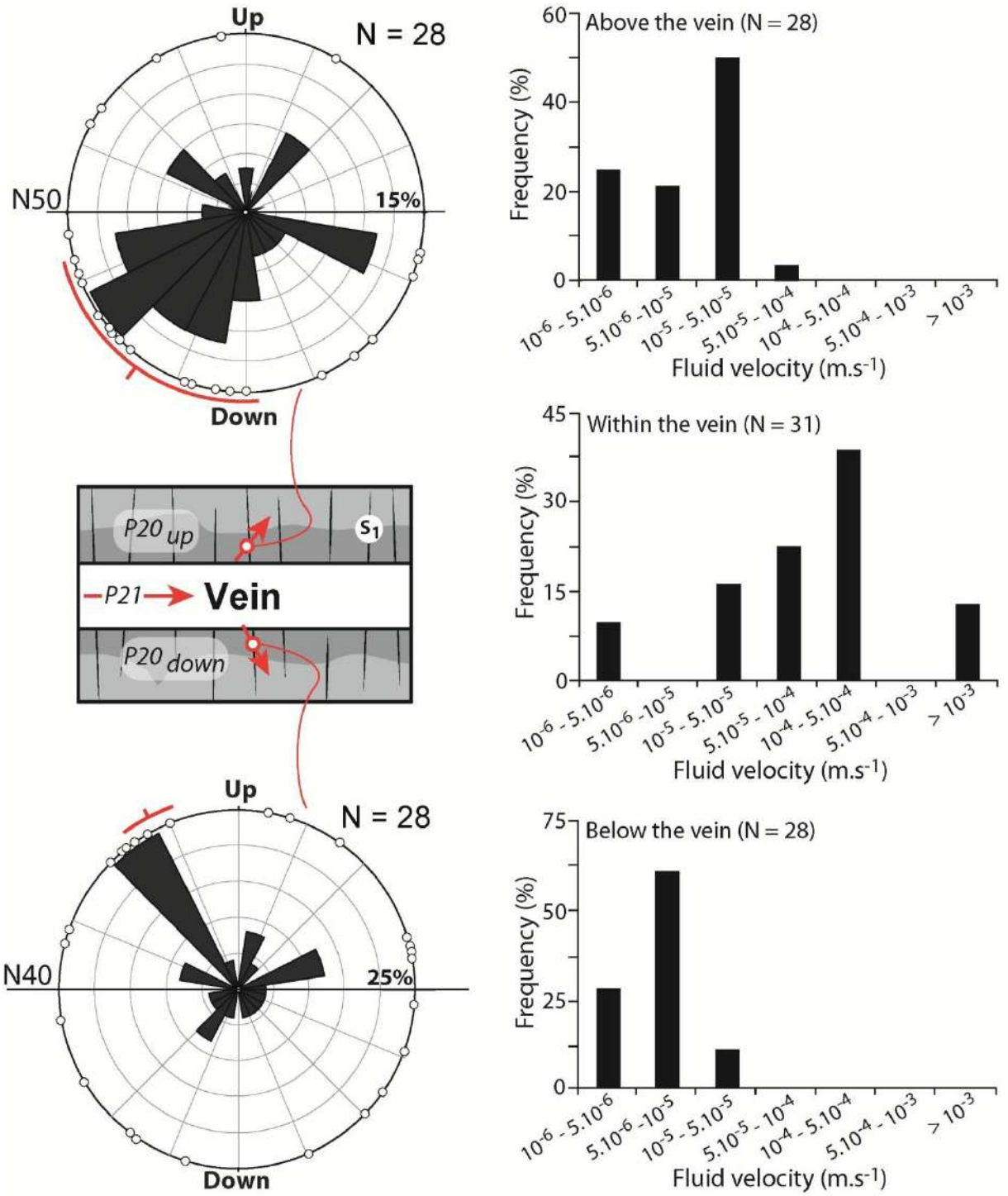

Figure 10 Sketch showing vertical paleo-fluid flow deduced from tourmaline in altered wall-rocks. Fluid flow directions are represented by rose diagrams giving the direction of faces exposed to fluid flow. The red arcs indicate the 95% interval of confidence, regarding the direction from which the fluid comes. Velocity values obtained above, below and within the vein are presented in histogram diagrams. N corresponds to the number of measurement performed for each sample.

5.3 Tourmaline growth band compositions

Chemical compositions of tourmalines are summarized in Table 2 (complete analyses in electronic supplementary materials ESM 4 and ESM 5). The general features and classification of Panasqueira tourmalines have already been described by Codeço et *al*., (2017). Here, we focus on the compositional differences in minor and trace elements between core and growth band used for fluid flow reconstruction. It appears that this growth band zoning is systematically associated with chemical variations in major, minor and trace elements (Table 2). In the veins, the cores and rims of tourmaline crystals exhibit compositions that suggest equilibration with Li-depleted granitic rocks (Fig. 11a). However, rims are richer in Fe and poorer in Mg and Al than cores. In altered wall-rocks, cores are characterized by a wide range of compositions suggesting equilibration with metasedimentary host rocks and Li-depleted granitic rocks, whereas rims exhibit a more restricted composition identical to the rims of vein-tourmalines. This suggests equilibration with Li-depleted granitic rocks (Fig. 11a). The range of core compositions in altered wall-rocks reflects the contribution of hydrothermal fluids and metasedimentary host rocks during the crystallization of tourmaline cores.

It is generally accepted that magmatic fluids contain significant amounts of Na, K and Cl. We therefore plotted the trace element concentrations in cores and rims of tourmaline as function of the Na concentration, to show the possible evolution of the magmatic contribution during tourmaline crystallization. Cores of tourmalines from veins and from altered wall-rocks are characterized by the same compositional ranges. This observation is also valid for rims (Table 2 and Fig. 11b). Consequently, crystallization of tourmalines in the veins is probably contemporaneous with the development of tourmalines in the altered wall-rocks. In addition, the results show strong compositional differences between the cores and rims of tourmalines (Fig. 11b). Indeed, the core to rim enrichment in Na is positively correlated with core to rim enrichments in K, Ti, Li, Mn, Sn, and Sr (Fig. 11b). Average concentrations in rims display high contents of Li, K, Mn, Ti and Zn (several hundreds to thousands of ppm) and moderate concentrations of Sn and Sr (several tens of ppm). In contrast, cores are characterized by lower trace element abundances (< 100 ppm for most elements).

These compositional differences between cores and rims, which are similar in the veins and in the wall-rocks, suggest that tourmalines were formed during two distinct

stages. The first stage is related to core crystallization (both in veins and in wall-rocks) whereas the second stage is related to the rim overgrowths.

The absence of experimental partitioning coefficients between tourmaline and hydrothermal fluids does not allow us to quantify the chemical signature of the hydrothermal fluid from which the tourmaline has crystallized. Nevertheless, according to Van Hinsberg et *al*., (2011a; 2017), the compositional changes between cores and growth bands provide a robust tool for tracking external changes in the trace-element budget of fluids from which tourmalines have crystallized. The present study suggests that rims have crystallized from a fluid richer in Na-K-Sn-Li-F-Zn than the fluid from which cores crystallized.

	Tourmaline from veins				Tourmaline from altered wall-rocks			
	Core		Rim		Core		Rim	
wt%	Ave (n= 20)	Stdev	Ave (n= 20)	Stdev	Ave (n = 20)	Stdev	Ave (n = 20)	Stdev
SiO_2	35.74	0.54	35.14	0.53	34.94	1.43	35.34	0.46
TiO_2	0.18	0.04	0.48	0.08	0.19	0.07	0.46	0.08
Al_2O_3	33.79	0.56	31.10	0.82	34.40	1.07	30.18	0.47
FeO	10.86	0.70	14.23	0.59	8.89	0.83	13.29	0.95
MnO	0.05	0.05	0.11	0.08	0.04	0.06	0.08	0.06
MgO	2.60	0.62	1.31	0.36	3.82	0.54	2.62	0.63
CaO	0.04	0.05	0.08	0.04	0.09	0.05	0.03	0.05
Na_2O	1.39	0.10	2.07	0.20	1.69	0.14	2.26	0.13
K_2O	0.02	0.00	0.05	0.01	0.02	0.01	0.06	0.01
F	0.00	0.01	0.00	0.00	0.00	0.00	0.00	0.00
Cl	0.00	0.00	0.01	0.01	0.01	0.01	0.01	0.01
Total	84.68		84.57		84.09		84.34	
ppm	Ave (n= 16)	Stdev	Ave (n= 17)	Stdev	Ave (n= 11)	Stdev	Ave (n= 14)	Stdev
Li	28	9.6	175	82	43	24	211	33
Na	8399	1049	17190	1739	6843	1887	14514	1463
Ti	1146	211	2465	390	2096	660	3318	269
V	84	29	98	27	61	63	55	16
Mn	413	42	698	125	171	63	542	43
Zn	545	80	908	181	302	105	853	78
Sr	14	6.3	40	9.3	29	18	41	5.5
Sn	9.6	2.9	18	6.1	9.1	6.0	14	3.8

Table 2 Summary of EPMA and LA-ICP-MS results for cores and rims of tourmalines from veins and altered wall-rocks

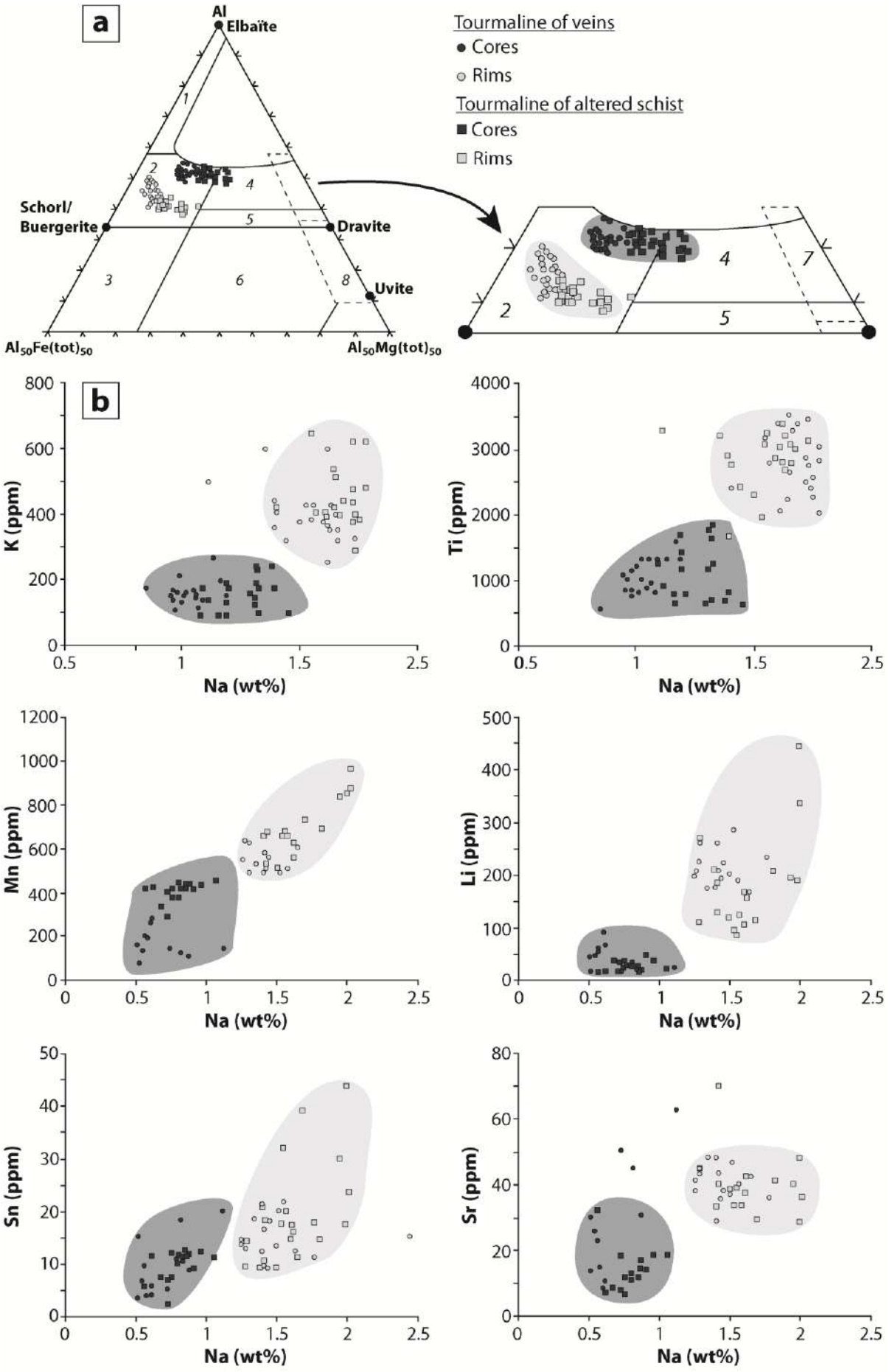
a
Al
Elbaïte
Schorl/
Buergerite
Dravite
Uvite
Al50Fe(tot)50
Al50Mg(tot)50
Tourmaline of veins
Cores
Rims
Tourmaline of altered schist
Cores
Rims
b
K (ppm)
Ti (ppm)
Mn (ppm)
Li (ppm)
Sn (ppm)
Sr (ppm)
Na (wt%)

Figure 11 Geochemical characteristics of tourmalines used for fluid flow reconstruction in veins and altered wall-rocks. (a) $Al_{50}Fe_{50}$-$Al_{50}Mg_{50}$ ternary diagram showing relation between tourmaline compositions and crystallization environment (from Henry and Guidotti, 1985). (1) Li-rich granitoids, pegmatites and aplites; (2) Li-depleted granitoids, pegmatites and aplites; (3) Fe^{3+}-rich hydrothermally altered granitoids; (4) Metapelites and metapsammites with Al-saturating phase; (5) Metapelites and metapsammites without Al-saturating phase; (6) Fe^{3+}-rich metapelites and calc-silicate rocks with quartz and tourmaline; (7) Cr-V-rich metapelites and Ca-depleted meta-ultramafic rocks (8) Meta-carbonates and meta-pyroxenites. (b) Element variation diagrams showing chemical core-rim evolution of tourmalines in minor (Na, K and Ti) and trace (Li, Mn, Sn and Sr) elements.

6. Discussion

6.1 Role of the granitic cupola in focusing fluid flow

In hydrothermal systems, fluid velocity is proportional to pressure gradient and its average direction is parallel to this gradient. Here, our spatial distribution and orientations of flow velocities suggest a high-pressure zone centered on the greisen cupola with a lateral pressure gradient triggering fluid flow in veins. Accordingly, hydrothermal fluids have probably been injected into the vein system from the cupola, which, consequently, represents the emanative center from which mineralizing fluids arose and spread laterally in veins. Moreover, the ΣNa/ΣK ratio determined by Polya et *al*., (1989) for the ore-forming fluids (W-Sn stage) suggests an extensive interaction of these fluids with the underlying granite at 350-400 °C and 1 kbar. The rim compositions of tourmaline confirm an equilibration of fluids with granitic rocks. Furthermore, the extensive greisenization in the apical portion of the granite provides evidence of this equilibration and corroborates our interpretation of a fluid flow focused by the cupola.

This fluid flow pattern can explain the spatial correlation commonly observed between localization of mineralized systems and emplacement of granitic cupolas (Dines, 1956; Dilles and Proffett, 1995). Indeed, it has been proposed that magmatic fluids are preferentially expelled from cupolas, and this can disturb the pattern of convective fluid flow around intrusions by relocating convective cells and discharge zones (Norton and Cathles, 1979; Eldursi et *al*., 2009). Hydrothermal fluxes determined in this study provide direct evidence of the role of cupolas in focusing mineralizing fluids. This fluid flow behavior can be explained by a preferential localization of thermo-mechanical instabilities around apices (Guillou-Frottier and Burov, 2003), which, when coupled with a

preferential accumulation of fluids, leads to the opening of permeable structures into which mineralizing fluids are then discharged.

Thus, the apical parts of plutonic intrusions represent loci of convergence for hydrothermal fluids and form favorable zones for the deposition of high grade mineralization. As a result, the approach applied in this study could be useful for mining exploration as a pathfinder to discovering hidden granitic cupolas and thus for locating emanative centers of mineralizing fluids.

6.2 Fluid escape in wall-rocks and the role of fluid in vein opening

The vertical escape of fluids from veins toward metasedimentary host rock involves a vertical pressure gradient with overpressured fluid conditions in veins, causing pervasive fluid flow in the wall-rocks. This interpretation is consistent with the presence of alteration fronts observed around veins (Fig. 7a). Besides, Lecumberri-Sanchez et *al*., (2017) have demonstrated that schists proximal to the veins are systematically enriched in K, B, Sn and W. The rims of tourmalines present in altered wall-rocks are also enriched in some of these elements (K and Sn). This is consistent with extensive fluid–rock interaction triggered by fluids coming from veins.

According to the rim compositions of vein-and schist-tourmalines, fluid flow in veins can be considered contemporaneous with pervasive fluid flow in altered wall-rocks. As shown above, fluid flow in wall-rocks is related to overpressured conditions in veins. Thus, our results suggest that vein opening and dilation have been induced by the injection of fluids under supralithostatic conditions, as proposed by Foxford et *al*., (2000). The low velocity values (not exceeding 5.10^{-5} $m.s^{-1}$) obtained in altered wall-rocks imply a low permeability in the host rocks. As a result, element transport through the host rock was probably low and limited to the alteration haloes.

Based on the removal of iron (Fe) from the wall-rocks during fluid-rock interactions, Lecumberri-Sanchez et *al*., (2017) suggest that some elements such as Fe have migrated from the host rocks toward veins. At first sight, this chemical flux seems to be incompatible with the direction of fluid flow discussed above. However, iron migration through the host rocks was probably driven by diffusion following a strong chemical gradient between fluid in veins and metasedimentary host rocks, whereas fluid flow was driven by a pressure gradient. These two processes did not involve the same driving force,

and it is, therefore, possible to observe a chemical flux that is characterized by a vector that is opposed to the fluid flow direction.

6.3 Velocity analysis and estimation of fluid flow duration during the QTS-MOSS

In this study, the mean fluid flow velocity deduced from vein tourmalines (10^{-4} m.s^{-1}) is high and close to values obtained by Sizaret et *al*., (2009) and Mahjoubi et *al*., (2016) using the same method in the same type of deposit, and suggests an efficient metal transport in veins. For a porous medium with an average porosity of 1%, the conversion of this mean velocity to a Darcy velocity (V_{Darcy} = V*porosity) gives a value of 10^{-6} m.s^{-1}. Darcy velocities obtained in contact metamorphic aureoles from mineral reactions and by numerical modeling range respectively from 10^{-9} to 10^{-11} m.s^{-1} (Ferry et *al*., 2002), and from 10^{-8} to 10^{-11} m.s^{-1} (Eldursi et *al*., 2009). It appears that velocities obtained in this study are 2 to 5 order of magnitude higher than those deduced from mineral reactions and numerical modeling. This difference may be due to the fact that velocities obtained from mineral growth bands are valid for a specific hydrothermal stage occurring over a short period of time, while those deduced from other methods are integrated over a larger scale and for the total duration of the hydrothermal system (Ingebritsen and Manning, 1999).

It is widely agreed that the overall time span of hydrothermal activity encompasses multiple fluid pulses, each of them occurring over only a short period of time. Although geochronological methods enable the dating of hydrothermal activity, the uncertainties of these analytical methods do not always permit the estimation of the fluid flow duration for a specific stage. As in most cases, the Panasqueira deposit was formed over a long period of time lasting about 4.2 Myr (Snee et *al*., 1988) but subdivided into several pulses. Here we propose the use of the mean fluid velocity value obtained from veins-tourmaline to estimate the fluid flow duration required for the vein formation during QTS and MOSS. To do this, we assume that the QTS and the MOSS were formed during the same continuous hydrothermal event with a constant fluid flow velocity. According to Polya et *al*., (1989) the total volume of fluid that flowed through the vein system during the MOSS is about 1000 km^3 with 0.2 ppm of dissolved WO_3. Considering a total volume of vein of about 0.003 to 0.006 km^3 extending over an area of 6 km² (Hebblethwaite and Antao, 1982) and characterized by an elliptical shape, we can calculate the surface of the vertical section of fluid flow. From this surface and the mean fluid flow velocity (10^{-4} m.s^{-1}) we obtain a fluid flow duration ranging from 35,000 to 70,000 years. This is consistent with

the short time duration of mineralization emplacement estimated for a single magmatic-hydrothermal event (spanning only about 10,000 to 200,000 years) from numerical modeling (Cathles et *al*., 1997; Chelle-Michou et *al*., 2017) and radiometric dating (Parnell, 1998).

6.4 Hydrodynamic model of the Panasqueira deposit

Our results must be considered as a 'snapshot' of the fluid flow at the incipient phase of the Panasqueira hydrothermal system, corresponding to the magmatic-hydrothermal transition. In the light of the chemical characteristics of tourmalines and our fluid flow reconstruction, a hydrodynamic model subdivided into two stages is here proposed for the early hydrothermal event preceding the main stage of W-Sn mineralization (Fig. 12). The first stage is related to the core crystallization of tourmalines and involves an initial flow of boron-rich fluids. These fluids are partly buffered for Al, Mg and Fe by the metasedimentary host rocks during the crystallization of tourmaline in the wall-rocks (Fig. 11a). This first pulse does not seem to be associated with any W-Sn mineralization. This is consistent with the low trace element contents in the cores of tourmaline. We have no information about the directions of fluid flow related to this first pulse. However, the chemical equilibration of cores of vein-tourmalines with Li-depleted granitic rocks suggests that the first stage may be related to a first expulsion of magmatic fluid during granite crystallization.

The second stage is recorded by tourmaline growth bands and is related to the flow of the mineralized (Li-K-Na-Sn)-rich fluid in the veins system. During this second stage, the external convecting fluids and magmatic fluids released by granite crystallization are both focused by the cupola, which causes the greisenization in the apical portion of the granite (Fig. 12). This focused fluid flow is injected into the vein system, whose significant horizontal permeability anisotropy induces a horizontal fluid flow along the vein planes. The low permeability of the metasedimentary host rock promotes fluid pressure increase culminating in vein opening when fluid pressure reaches supralithostatic levels (Fig. 12). The velocity contrast between veins (10^{-4} to 10^{-3}m.s^{-1}) and altered wall-rocks (10^{-6} to 10^{-5} m.s^{-1}) emphasizes this strong permeability contrast and suggests that fluid flow was mainly channeled into the vein system. This channelization of mineralizing fluids in veins could contribute to forming a high grade deposit by an efficient metal transport into structural traps. The overpressured conditions in the veins enhance fluid-rock interaction

and trigger a pervasive fluid migration into the wall-rocks (Fig. 12). According to Lecumberri-Sanchez et *al*., (2017), the metasedimentary host rock is mainly affected by tourmalinization and muscovitization reactions, which are crucial for wolframite deposition by releasing iron into the fluid. Finally, the escape of fluids toward the wall-rocks observed in this study may constitute a crucial mechanism for wolframite deposition by promoting fluid-rock interactions.

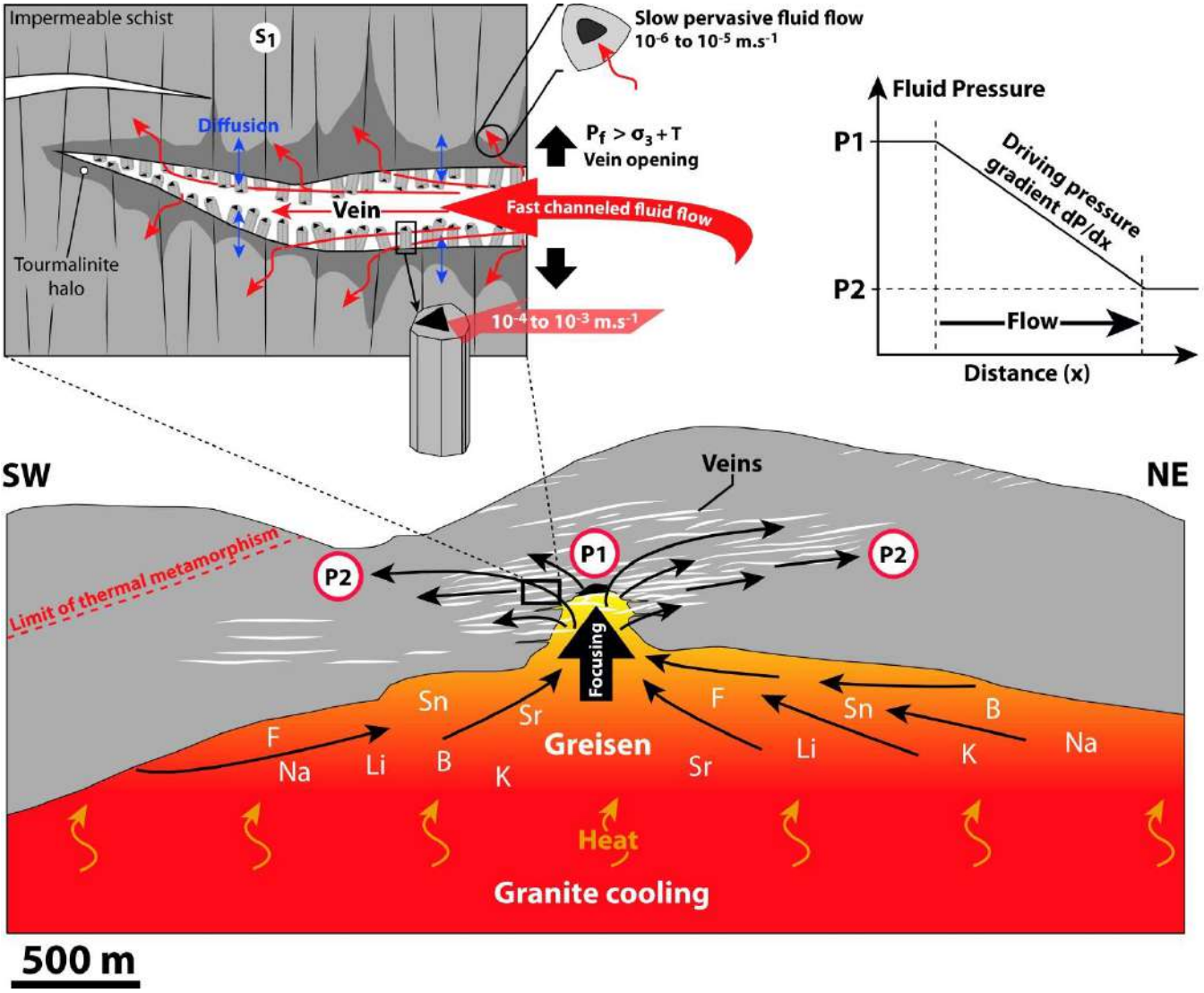

Figure 12 Hydrodynamic model of fluid flow at the magmatic-hydrothermal transition of the Panasqueira W-Sn-(Cu) deposit (after a simplified cross section from Thadeu, 1951). P_f: the fluid pressure condition, σ_3: the vertical stress and T: the tensile strength.

References

B

Barnes, H.L. 1997. Geochemistry of Hydrothermal Ore Deposits, third ed. John Willey and Sons, New York.

Bishop, A.C. 1989. Greisen. In: Petrology. Encyclopedia of Earth Science. Springer, Boston, MA.

Bussink, R.W. 1984. Geochemistry of the Panasqueira Tungsten-Tin Deposit, Portugal. Geol. Ultraiectina.

C

Cartwright, I., Buick, I.S. 1996. Determining the direction of contact metamorphic fluid flow: an assessment of mineralogical and stable isotope criteria. J. Metamorph.Geol. 14, 289–305.

Cathles, L.M., Erendi, A.H.J. & Barrie, T. 1997. How long can a hydrothermal system be sustained by a single intrusive event? Econ. Geol., 92: 766-771.

Černý, P., Blevin, P.L., Cuney, M. and London, D. 2005. Granite-Related Ore Deposits. In: J.W. Hedenquist, J.F.H. Thompson, R.J. Goldfarb, and J.R. Richards (eds.). Economic Geology - One Hundredth Anniversary Volume, 337–370.

Chelle-Michou, C., Rottier, B., Caricchi, L. and Simpson, G. 2017. Tempo of magma degassing and the genesis of porphyry copper deposits. Nature Scientific Reports 7, Article number: 40566.

Clark, A. H. 1964. Preliminary study of the temperatures and confining pressures of granite emplacement and mineralization, Panasqueira, Portugal: Inst. Mining MetallurgyTrans., 73, 813-824.

Codeço, M., Weis, P., Trumbull, R., Pinto, F., Lecumberri-Sanchez, P., Wilke, F. 2017. Chemical and boron isotopic composition of hydrothermal tourmaline from the Panasqueira W-Sn-Cu deposit, Portugal. - Chemical Geology (online).

Cox, S.J. 2005. Coupling between Deformation, Fluid Pressures, and Fluid Flow in Ore-Producing Hydrothermal Systems at Depth in the Crust. In: J.W. Hedenquist, J.F.H. Thompson, R.J. Goldfarb, and J.R. Richards (eds.). Economic Geology - One Hundredth Anniversary Volume, 39–75.

Curie P. 1908. Œuvres, 118p. Gautier-Villars, Paris, Société Française de Physique. Reprinted: Archives contemporaines, Paris 1984.

D

Derré, C. 1982. Caractéristiques de la distribution des gisements à étain-tungstène dans l'ouest de l'Europe. Mineral. Deposita 17:55-77.

Dias, R. & Ribeiro, A. 1995. The Ibero Armorican Arc: a collision effect against an irregular continent? Tectonophysics, 246: 113-128

Dias, G., Leterrier, J., Mendes, A., Simões, P., Bertrand, J.M. 1998. U-Pb zircon and monazite geochronology of syn- to post-tectonic Hercynian granitoids from the central Iberian Zone (northern Portugal). Lithos 45, 349–369.

Dilles, J.H., Profett, J.M. 1995. Metallogenesis of the Yerington batholith, Nevada, in: F.W. Pierce, J.G. Bolm (Eds.), Porphyry Copper Deposits of the American Cordillera, American Geological Society Digest 20, , pp. 306-315.

Dines, H.G. 1956. The metalliferous mining region of South-West England. 2 volumes, HMSO, London.

Eldursi, K., Branquet, Y., Guillou-Frottier, L., Marcoux, E. 2009. Numerical investigation of transient hydrothermal processes around intrusions: Heat-transfer and fluid-circulation controlled mineralization patterns. Earth and Planetary Science Letters 288, 70-83.

Engel, A.E.J. 1946. The quartz crystals deposits of western Arkansas. Economic Geology, v. 41, pp. 598-618.

Engel, A.E.J. 1948. The direction of flow of mineralizing solutions. Economic Geology, v. 43, pp. 655-660.

Essalhi M., 2009. Application de l'étude du magnétisme des roches à la compréhension des gisements : Traçage des paléocirculations (expérimentation et cas des minéralisations de La Florida, Espagne). Structuration et histoire de l'altération des amas sulfurés (cas des chapeaux de fer de la Province Pyriteuse Sud Ibérique, Espagne). Thèse de l'Université d'Orléans.

F

Ferry, J., Wing, B., Penniston-Dorland, S., Rumble, D. 2002. The direction of fluid flow during contact metamorphism of siliceous carbonate rocks: new data for the Monzoni and Predazzo aureoles, northern Italy, and a global review. Contrib. Mineral. Petr. 142,679-699.

Foxford, K.A., Nicholson, R., Polya, D.A., Hebblethwaite, R.P.B. 2000. Extensional failure and hydraulic valving at Minas da Panasqueira, Portugal: Evidence from vein spatial distributions, displacements and geometries. J. Struct. Geol. 22, 1065–1086.

G

Garside, J., Janssen-van Rosmalen, R., Bennema, P., 1975. Verification of crystal growth rate equations, J. Cryst. Growth, 29, 353-366.

Gloaguen, E., Branquet, Y., Chauvet, A., Bouchot, V., Barbanson, L. and Vigneresse, J.L. 2014. Tracing the Magmatic/Hydrothermal Transition in Regional Low-Strain Zones: The Role of Magma Dynamics in Strain Localization at Pluton Roof, Implications for Intrusion-Related Gold Deposits. Journal of Structural Geology 58: 108–121.

Guillou-Frottier, L., Burov, E. 2003. The development and fracturing of plutonic apexes: implications for porphyry ore deposits. Earth & Planetary Science Letters, 214, 341-356.

H

Hebblethwaite, R. P. B., and Antao, A.M. 1982. A report on the study of dilation patterns within the Panasqueira ore body: Barroca Grande, Beralt Tin Wolfram (Portugal), unpub. rept.15p.

Hedenquist, J.W., Lowenstern, J.B. 1994. The role of magma in the formation of hydrothermal ore deposits. Nature Vol. 370: 519-526.

Henry, D.J., Guidotti, C.V. 1985. Tourmaline as a petrogenetic indicator mineral: an example from the staurolite-grade metapelites of NW Maine. Am. Mineral. 70,1–15.

Henry, D.H., Dutrow B. L. 1996. Metamorphic tourmaline and its petrologic applications. Reviews in Mineralogy and Geochemistry 33 (1): 503-557.

I

Ingebritsen, S.E., Manning, C.E. 1999. Geologic implications of a permeability–depth curve for continental crust. Geology 27, 1107–1110.

Ingebritsen, S.E., Appold, M.S. 2012. The physical hydrogeology for ore deposits. Econ Geol 107:559–584

J

Julivert, M., Fontboté, J.M., Ribeiro, A., Conde, L. 1972. Mapa Tectonico de la Peninsula Iberica y Baleares E. 1:1.000.000. Inst. Geol. Min. España, Madrid.

K

Kelly, W.C., Rye, R.O. 1979. Geologic, fluid inclusion and stable isotope studies of the tin-tungsten deposits of Panasqueira, Portugal. Econ Geol 74:1721–1822

Kessler, S.E., Stoiber, R.E. & Billings, G.K. 1972. Direction of flow mineralizing solutions at Pine Point, N.W. T., Econ. Geol., 67, 19–24.

L

Lecumberri-Sanchez, P., Vieira, R., Heinrich, C.A., Pinto, F., Wälle, M. 2017. Fluid-rock interaction is decisive for the formation of tungsten deposits. Geology 45, 579–582.

M

Mahjoubi, E.M., Chauvet, A., Badra, L., Sizaret, S., Barbanson, L., El Maz1, A., Chen, Y., and Amann, M. 2016. Structural, mineralogical, and paleoflow velocity constraints on Hercynian tin mineralization: the Achmmach prospect of the Moroccan Central Massif. Miner. Deposita 51: 431.

Marks, M. A. W., Schühle, P., Guth, A., Wenzel, T. and Markl, G. 2013. Trace element systematics of tourmaline in pegmatitic and hydrothermal systems from the Variscan Schwarzwald (Germany) : the importance of major element composition, sector zoning, and fluid or melt composition. Chemical geology, Vol. 344, p.73-90.

Martínez-Catalán, J.R., Arenas, R., Diaz Garcia, F., et al. 2007. Space and time in the tectonic evolution of the northwestern Iberian Massif: Implications for the Variscan belt. In: Hatcher RD, Carlson MP, McBride JH, Martínez Catalán JR (eds) 4-D Framework of continental crust: Geological Society of America Memoir 200.Geological Society of America, 403–423

N

Newhouse, W. H., 1941. The direction of flow of mineralizing solutions. Society of Economic geologists, Economic geology. 36, 612-629.

Norton, D., Cathles, L.M. 1979. Thermal aspects of ore deposition. In: Barnes, H.L. (Ed.), Geochemistry of Hydrothermal Ore Deposits, second ed. John Wiley and Sons, New York, pp. 611e631.

P

Parnell, J. 1998. Dating and Duration of Fluid Flow and Fluid–Rock Interaction.: Geological Society Special Publication, 144, 284 pp

Prieto M. et Amoros J.-L., 1981. On the influence of hydrodynamic environment on crystal growth. Bull. Minéral., 104, 114-119.

Polya, D.A. 1989. Chemistry of the main-stage ore-forming fluids of the Panasqueira WCu(Ag)-Sn deposit, Portugal: implications for models of ore genesis. Econ. Geol. 84, 1134–1152.

Polya, D.A., Foxford, K.A., Stuart, F., Boyce, A., Fallick, A.E. 2000. Evolution and paragenetic context of low δD hydrothermal fluids from the Panasqueira W-Sn deposit, Portugal: New evidence from microthermometric, stable isotope, noble gas and halogen analyses of primary fluid inclusions. Geochim. Cosmochim. Acta 64, 3357–3371.

R

Robb, L. 2005. Introduction to Ore-forming Processes. Blackwell Publishing, Malden, MA, 373 p.

Rodriguez-Clemente R., 1976. Sobre la dependencia del hàbito cristalino respecto de la hidrodinàmica del medio en que crece el cristal, referido al caso del NaCl. Geologica Hispanica, XI, 4, 93-95.

S

Sams, M. S. & Thomas-Betts, A. 1988. Models of convective fluid flow and mineralization in Southwest England. Journal of the Geological Society. 145, 809-817.

Shcherba, G. N. 1970. Greisens. Int Geol Rev 12: 114–255

Sibson, R.H. 1992. Implications of fault-valve behaviour for rupture nucleation and recurrence. Tectonophysics, 211, 283–93.

Sizaret, S., Fedioun, I., Barbanson, L., Chen, Y. 2006. Crystallization in flow part II: modelling crystal growth kinetics controlled by boundary layer thickness. Geophys J Int 167:1027–1034

Sizaret, S., Branquet, Y., Gloaguen, E., Chauvet, A., Barbanson, L., Chen, Y. 2009. Estimating the local paleo-fluid flow velocity: new textural method and application to metasomatism. Earth Planet Sci Lett 280:71–82.

Sizaret, S., Xiang, L., Huang, X., Lu, J., Wang, R.C. 2017. Hydrothermal flows: A direct approach. Abstract for the Goldschmidt conference, Paris, 2017.

Snee, L.W., Sutter, J.F., Kelly, W.C. 1988. Thermochronology of economic mineral deposits; dating the stages of mineralization at Panasqueira, Portugal, by high-precision 40Ar/39Ar age spectrum techniques on muscovite. Econ Geol 83:335–354

T

Thadeu, D. 1951. Geologia do couto mineiro da Panasqueira. Comunic Serv Geol Port 32:5–64.

V

Van Hinsberg, V.J., Henry, D.J., Dutrow, B.L. 2011a. Tourmaline as a Petrologic Forensic Mineral: A Unique Recorder of Its Geologic Past. Elements 7, 327–332.

Van Hinsberg, V.J., Franz, G. and Wood, B.J. 2017. Determining subduction-zone fluid composition using a tourmaline mineral probe. Geochemical Perspectives Letters v3, n1.

W

Weis, P. 2015. The dynamic interplay between saline fluid flow and rock permeability in magmatic-hydrothermal systems. Geofluids, 15, 350-371.

Whitney, D.L, Evans, B.W. 2010. Abbreviations for names of rock-forming minerals. Am. Mineral 95:185-187.

Chapter IV: Relationships between the greisenization and the mineralized veins of Panasqueira: petrological and geochemical constrains

Objectives of this chapter:

Results obtained from the textural analysis of tourmaline growth bands of Panasqueira emphasize that the greisen cupola could act as emanative center of mineralizing fluids during the incipient stage of the hydrothermal activity (**Chapter III**). Furthermore, the chemical compositions of these tourmalines suggest a potential contribution of magmatic fluids (rich in Na, K, Li, Sr and Sn) during the vein formation. This fluid focusing by the apical portion of the granite intrusion can be responsible of the extensive greisenization of the cupola and the upper part of the granite intrusion observed in mine and from drill-holes. However, the genetic link between the greisenization and the vein formation remains unproven.

In this chapter we investigate genetic and chronological relationships between the greisenization of the Panasqueira granite and the formation of the mineralized veins system. To do this, we have performed a complete petrological and geochemical study dealing with (i) petrographic characterization of the massive greisen and its parental two-mica granite, (ii) whole-rock geochemistry, (iii) in-situ chemical analyses of major and trace elements in muscovite and quartz that are ubiquitous both in the granite, the greisen and within the mineralized veins and (iv) U-Pb dating of magmatic and hydrothermal apatite to constrain the chronology between the granite cooling, the greisenization and the formation of mineralized veins.

Then these data will discuss and compared with those obtained from tourmaline to constrain the relationships between the greisenization and the W-Sn mineralization stage observed in the vein system.

I- Macroscopic and petrographic characteristics of the Panasqueira greisen

1. Field observations of the greisen system of Panasqueira

As mentioned previously (**Chapter II and III**) the vein swarm of Panasqueira is spatially associated to a non-outcropping granite intrusion, whose the presence was highlighted from a contact metamorphism aureole (spotted schist) mapped on the field (Fig. 1a). The detailed morphology of the granite's roof was inferred from the drill-holes distributed over the Panasqueira district and from the underground mining works, which have crosscut a greisen cupola (Fig .1b). The granite's roof dips gently to the NE in the northeastern part and steeply to the SW in the southwestern part of the intrusion (Fig. 1a and 1b). A gravimetric survey recently performed by our partners of the University of Porto permits to better constrain the general geometry and the lateral extent of the intrusive body present at depth. This small intrusive body is characterized by a laccolith shape elongated in the NW-SE direction (7.5 x 4.5 km) for thickness that can locally reaches 2 km. This elongated shape can be related to the regional NE-SW horizontal shortening, which occurred during the vein formation and therefore probably during the granite emplacement. As exposed in the underground mine works and drill-cores, the upper part of this granite intrusion was affected by an intense greisenization resulting from fluid-rock interactions. The mineralogical and textural characteristics of the granite and greisenisation are detailed in the following from observations performed on (i) greisenized aplites present on the field, (ii) the drill-hole SCB2 and (ii) the greisen cupola intersected by the mining works.

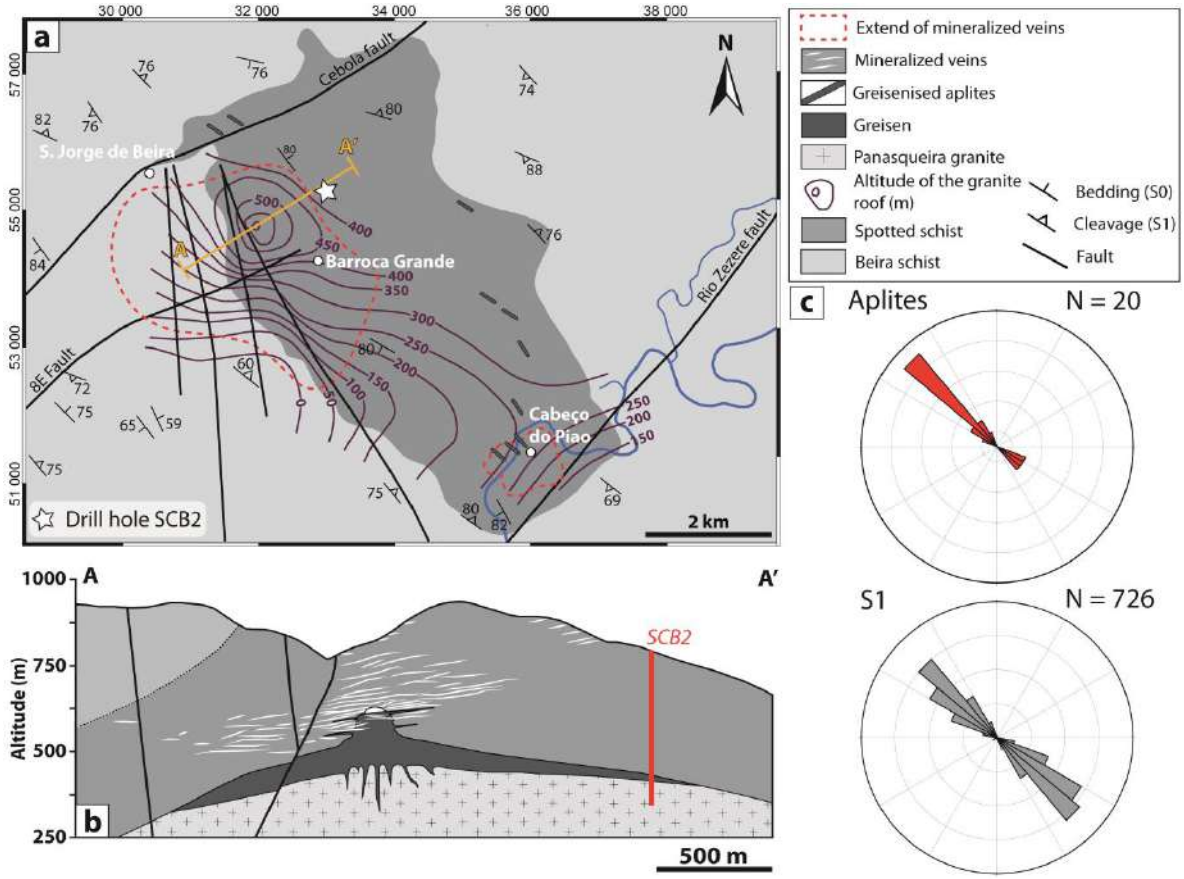

Figure 1 (a) Geological map of the Panasqueira district showing the spatial relationships between the non-outcropping granite intrusion and the mineralized vein system of Panasqueira. (b) Cross section (A-A') displaying the spatial relationship between the greisen cupola and the mineralized veins. The emplacement of the SCB2 drill-hole is also indicated by a white star. (c) Rose diagrams showing the strike directions of the greisenized aplites present over the Panasqueira district and the regional schistosity (S1).

1.1 The greisenized aplites

Despite the absence of granite outcrops at the surface, the Panasqueira district is marked by the occurrences of aplites, which were mainly emplaced in the spotted schist aureole formed during the contact metamorphism induced by the granite emplacement (Fig. 1). As evidenced by their NW-SE strike directions and their sub-vertical dipping, the emplacement of these aplites was controlled by the vertical planes of the regional schistosity (S1) (Fig. 1c, 2a and 2b). These aplites were strongly altered during the hydrothermal activity of Panasqueira and were completely transformed into a quartz-muscovite greisen (Fig. 2c). This greisenization of aplites was accompanied by a strong tourmalinization of the metasedimentary host rock that mainly occurred along the schist-aplite contacts (Fig. 2b). This intense metasomatism observed close to the aplites suggests that they may act as a plumbing system for fluids. The porous texture observed in greisen samples not affected by late silicification (Fig. 2c) seems to confirm this hypothesis and suggests that greisen could be permeable pathways compared to the metasedimentary host rock. Furthermore, the presence of (i) disseminated cassiterite and sulfides mineralization (Fig. 2c) and (ii) quartz-wolframite pockets (Fig. 2d and 2e) in some greisenized aplites suggest that mineralized fluids related to the Sn-W and sulfides stages have preferentially flowed through the greisenized aplites. These field observations seem also to suggest that the greisenization of aplites and the Sn-W mineralization were sub-contemporaneous and related to the same hydrothermal event. However, the absence of field evidence does not permit to establish the relative chronology between greisenised aplite and the sub-horizontal mineralized veins.

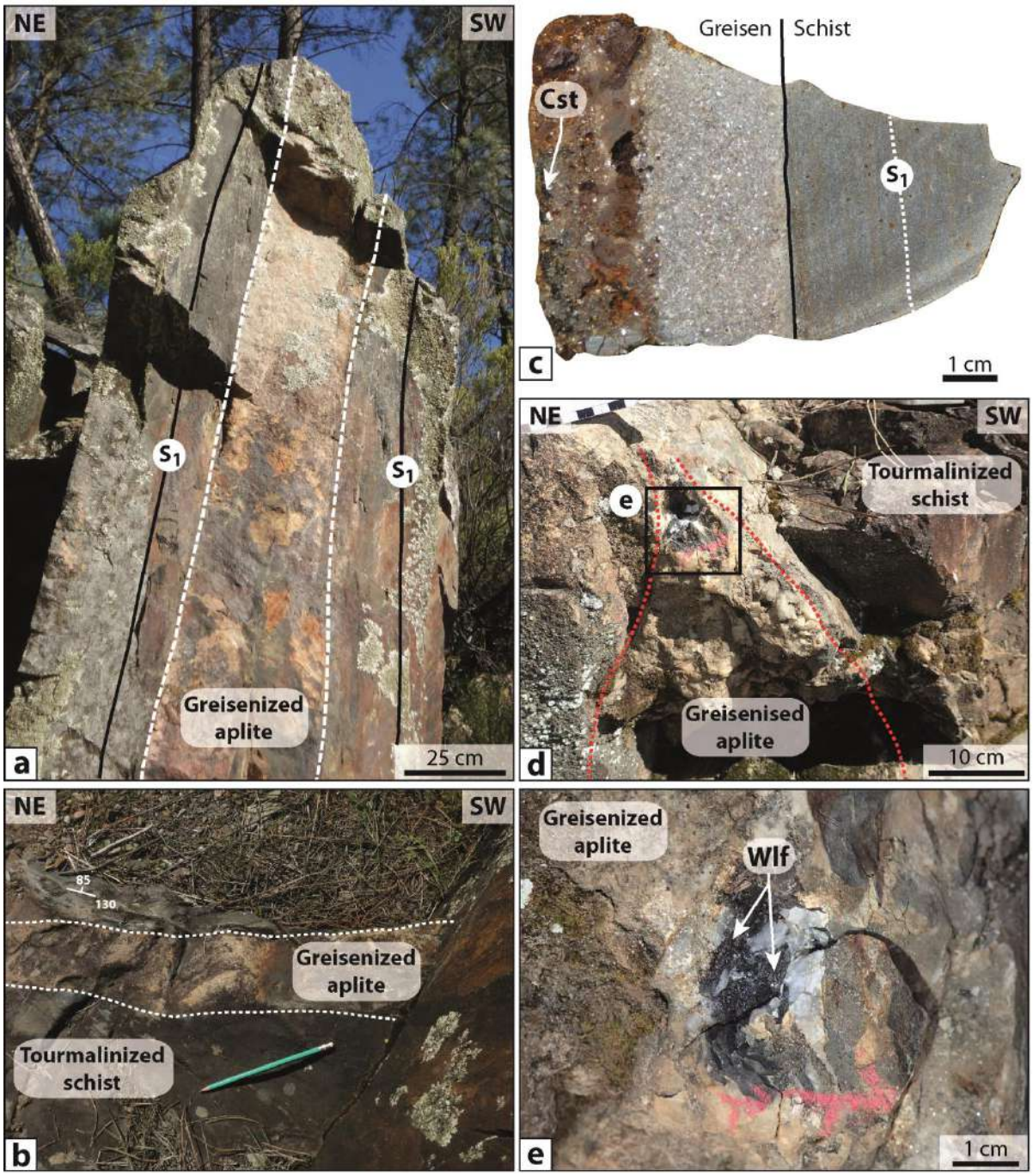

Figure 2 Macroscopic characteristics of the greisenized aplites present over the Panasqueira district. (a) and (b) Sub-vertical greisenized aplites preferentially emplaced within the regional vertical foliation planes. Note the intense tourmalinization of the metasedimentary host rocks around the greisenized aplites. (c) and (d) Greisenized aplite mineralized in wolframite. (e) Contact between a mineralized greisenized aplite and the tourmalinized metasedimentary host rock. The greisen is characterized by a porous texture and exhibits a disseminated cassiterite mineralization.

1.2 The SCB2 drill hole

The SCB2 drill-hole was drilled vertically down to a depth of 400 m in the northeast of the greisen cupola (Fig. 1). The drill-cores recovered from this drill-hole permit to observe different granite facies and the vertical evolution of the greisenization. Based on textural and mineralogical characteristics, at least two distinguished granitoids can be observed in this drill-hole: a porphyritic two-mica granite composing the upper part of the intrusive body (Fig. 3b-4) and a leucogranite, which composes the deeper part of the intrusion (Fig. 3b-5). The two-mica granite exhibits a porphyritic texture with large phenocrysts of k-feldspars (up to 4 cm) and snowball quartz (up to 0.5 cm) embedded in a quartz, albite, k-feldspars, muscovite and biotite coarse matrix. The leucogranite is characterized by an equigranular texture and is composed of feldspars, quartz and muscovite. The contact between these two types of granite is not sharp and corresponds to a transitional zone, in which the two-mica granite evolved progressively to the leucogranite.

The upper part of the two-mica granite exhibits a thick massive greisen that reaches ~30 m of thickness in the SCB2 drill-hole (Fig. 3) and that can reach several hundred meters of thickness in the cupola (Fig. 1). The greisenization of the two-mica granite is marked by the complete breakdown of feldspars and biotite that were replaced by an equigranular quartz-muscovite assemblage (Fig. 3b-1 and 3b-2). This intense greisenization increases progressively up to the granite roof and can be followed from the gradual breakdown of biotite and k-feldspars followed by the breakdown of albite. The two-mica granite is completely converted into greisen along the granite-schist contact (Fig. 3b-1). This massive greisen exhibits a porous texture described in details in the **Chapter V** (Fig. 3b-2). Above the granite-schist contact, the metasedimentary host rock was affected by a strong tourmalinization probably related to the incipient stage of the hydrothermal activity of Panasqueira (**Chapter III**). In the unaltered part of the two-mica granite, the greisenization can be locally observed as narrow halos (1-30 cm) along fractures planes and along mineralized quartz veins (Fig. 3a and 3b-3). The leucogranite does not seem to be affected by greisenization.

The vertical evolution of the Sn (red line) and W (blue line) concentrations in the whole-rock shows a correlation between the Sn and W content in rocks and the greisenisation of granite (Fig. 3a). Indeed, the presence of greisenized halos adjacent to fractures and veins are associated to higher concentrations in Sn and W in the whole-rock.

Furthermore, the progressive increase of greisenization observed in the upper part of the drill-hole appears to be associated to an increase of the Sn and W concentrations with maximum values (Sn = 134 ppm; W = 40 ppm) along the granite roof. This suggests that greisenization could be related to the circulation of Sn-W mineralizing fluids through the granite intrusion and hence that greisenization could record the incipient stage of the hydrothermal activity of Panasqueira.

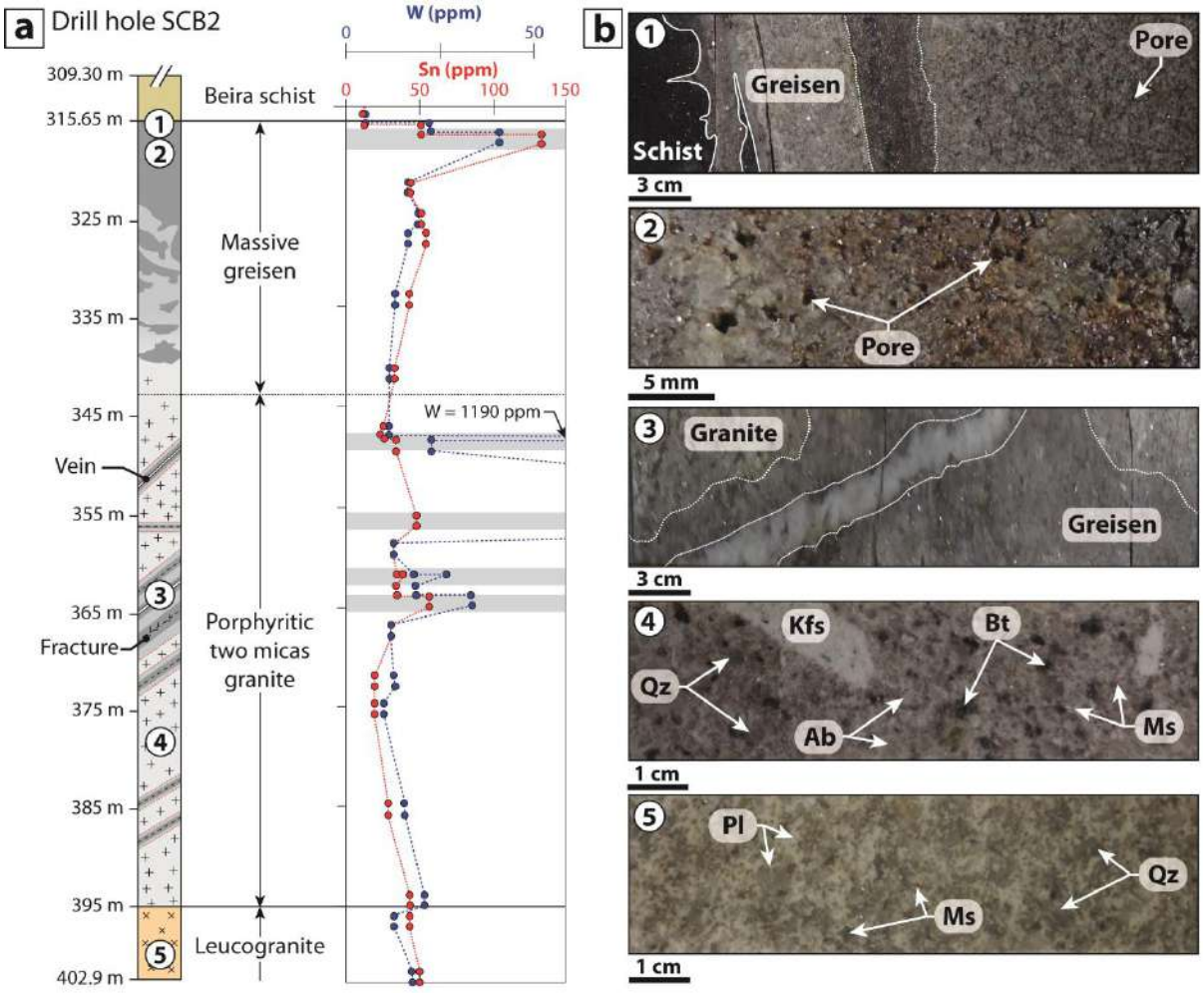

Figure 3 (a) General views of the different facies of granite and greisen observed in the drill hole SCB2. The vertical evolution of the whole rock concentrations in Sn and W along the drill hole is also reported (data source Beralt Tin & Wolfram S.A.). (b) Textural characteristics of 1: Contact between the greisen and the metasedimentary host rock strongly tourmalinized, 2: facies of the most altered greisen (quartz-muscovite greisen) displaying a well-developed porosity, 3: propagation of greisenization around a mineralized vein present in the deeper part of the drill hole, 4: unaltered porphyritic two-mica granite and 5: more evolved leucogranite. Mineral abbreviation from Whitney and Evans (2010) Ab: albite, Bt: biotite, Kfs: K-feldspar, Ms: muscovite, Pl: plagioclase, Qz: quartz.

1.3 The greisen cupola and its relationship with the mineralized veins

The greisenization of the two-mica granite was particularly intense in the cupola exposed in the underground mining works (Level 1 and Level 530). In this cupola, the granite was completely transformed into a massive quartz-muscovite greisen characterized by the same mineralogical and textural features than those observed in the greisenized aplites and the SCB2 drill-hole (Fig. 4). The contact between the cupola and the metasedimentary host rock is sharp (Fig. 4a and 4c) and crosscut by the flat-dipping mineralized veins (Fig. 4a). Greisenized aplite coming from the cupola can be also observed close to this contact (Fig. 4b). This aplite crosscut the vertical barren quartz veins locally named "Seixo Bravo". Mineralized veins are also present within the massive greisen composing the cupola and exhibit the same paragenesis (i.e. muscovite, quartz wolframite and sulfides) than mineralized veins present in the metasedimentary host rocks (Fig. 4c and 4d). In these veins the presence of greisen enclaves ripped from the vein edge suggests that greisenization could occur before the vein opening.

The massive greisen is characterized by a disseminated mineralization (Fig. 4e and 4f) composed of sulfides (chalcopyrite, sphalerite, pyrite and arsenopyrite) and cassiterite to a lesser extent. These metal-bearing minerals infilled partially the pores observed in the greisen and can be associated with apatite and euhedral quartz in large pockets (Fig. 4f). This disseminated mineralization suggests that the massive greisen was a permeable pathway for the different mineralizing fluids. Finally, the greisen cupola was affected by a late extensive silicification stage, which has finished to infill the pores present in greisen. From these field observations, the greisenization appears to be slightly anterior to the formation of mineralized veins.

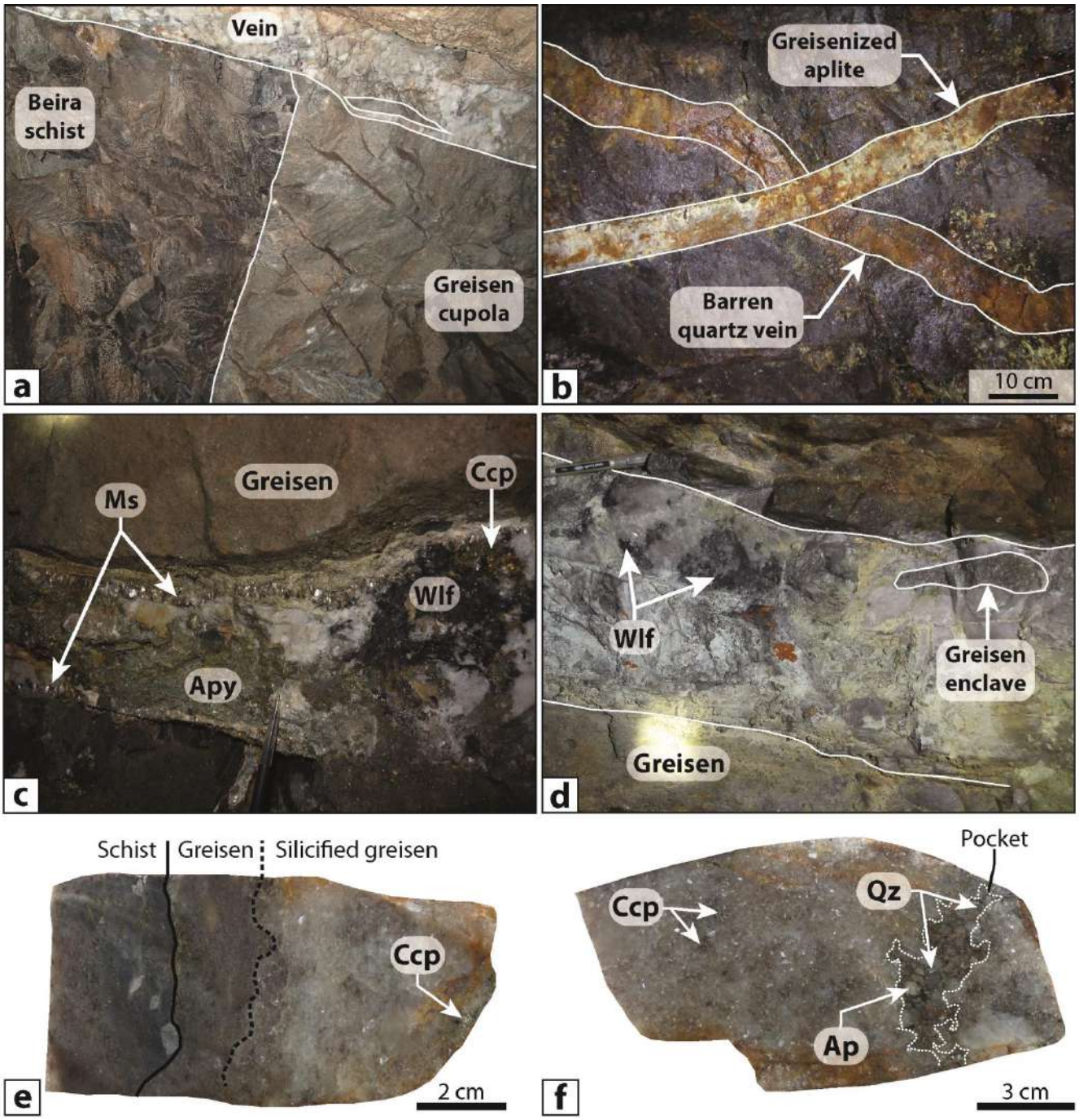

Figure 4 Macroscopic characteristics of the greisen cupola observed in the underground mining works (Level 1) (a) Contact between the massive greisen cupola and the tourmalinized metasedimentary host rock. This contact is crosscut by a mineralized quartz vein (b) Greisenized aplite crosscutting a vertical barren quartz vein (Seixo bravo) (c) Typical flat mineralized (quartz, muscovite, wolframite and sulfides) vein hosted by the massive greisen cupola. (d) Quartz mineralized vein hosted by the greisen cupola in which we can observe a greisen enclave (e) Sample showing the contact between the greisen cupola and the tourmalinized metasedimentary host rock. The greisen is intensively silicified and exhibits a disseminated chalcopyrite mineralization. (f) Sample of massive greisen collected in the cupola showing an intense silicification and a disseminated sulfide mineralization (chalcopyrite, pyrrhotite and sphalerite). This sample exhibits a large pore (pocket) completely infilled by euhedral quartz, apatite and sulfides. Abbreviations from Whitney and Evans (2010) Ap: Apatite, Apy: Arsenopyrite, Ccp: Chalcopyrite, Ms: Muscovite, Qz: Quartz, Wf: Wolframite.

2. Petrographic characteristics

2.1 Petrographic characteristics of the two-mica granite

The mineralogical and the textural characteristics of the two-mica granite of Panasqueira are displayed in Figure 5. As described previously, this two-mica granite exhibits a porphyritic, coarse grained texture (Fig. 5a). The mineralogy consists mainly of quartz (39 %), albite (28 %), k-feldspar (17 %), biotite (8 %), muscovite (7 %) and apatite (1 %) (Mineral abundances were estimated from XRD data, more information are given in **Chapter V**). Accessory minerals include zircon, monazite, rutile and ilmenite.

K-feldspar occurs as large euhedral phenocryst (up to several centimeters) and as small grains in the rock matrix (Fig. 5b). The k-feldspar phenocrysts are characterized by perthitic texture resulting of the exsolution of albite lamellae and poikilitic textures comprising numerous inclusions of quartz, albite, biotite and apatite (Fig. 5b).

Quartz occurs as large euhedral grains (up to 0.5 cm) characterized by snowball texture (Fig. 5a and 5c). This texture is particularly common in highly evolved granitic systems related to rare-metal mineralization (Sn-W-Nb-Ta) (Charoy and Noronha, 1991; Müller, 1999; Müller et *al*., 2002; Müller et *al*., 2018). These snowball quartz can contain small inclusions of albite and muscovite. The extinction of this quartz is homogeneous suggesting the absence of plastic deformation in quartz. However, the presence of fluid inclusions trails attest that snowball quartz were affected by fracturing and healing mechanism that probably occurred after the granite cooling (Fig. 5c). Quartz is also present as small grains in the rock matrix.

Albite is mainly present as numerous small euhedral grains characterized by size ranging from 1 to 5 mm (Fig. 5d). This albite is characterized by a typical polysynthetic twining texture and by poikilitic texture marked by inclusions of quartz and apatite (Fig. 5d). The presence of albite inclusions within k-feldspars phenocrysts suggests that albite crystallized before k-feldspar during the granite crystallization.

Biotite is common and forms large sub-euhedral flakes (up to 2 mm) containing numerous inclusions of accessory minerals like apatite, zircon (outlined by the occurrence of disintegration halos), monazite, rutile and ilmenite (Fig. 5e). The occurrences of biotite inclusions in k-feldspar suggest that the crystallization of biotite precedes the crystallization of k-feldspar.

Muscovite forms individual large sub-euhedral flakes (up to 1-2 mm) consistent with a primary magmatic origin according to the textural criteria given by Miller et *al*. (1981) (Fig. 5f). These flakes of muscovite occur as interstitial grains in the rock matrix and as micaceous aggregates (Fig. 5f). Although the main part of muscovite appears to be igneous origin, some little flakes of muscovite can be observed along grain boundaries of biotite and feldspars and could result from hydrothermal alteration of these minerals.

Apatite represents the most abundant accessory mineral and occurs as small (up to 1 mm) euhedral grains mostly included in feldspars and biotite (Fig. 5d and 5e) suggesting an early formation of apatite during the granite crystallization. Apatite can contain inclusions of monazite and zircon suggesting that the crystallization of apatite occurred after the crystallization of zircon (Fig. 5g).

Zircon, rutile and ilmenite are very scarce and occur mainly as inclusions in biotite and feldspars. Rutile forms generally small needle elongated parallel to the cleavage planes of biotite and is often partially replaced by ilmenite.

Figure 5 Photomicrographs showing the mineralogical and the textural characteristics of the two-mica granite of Panasqueira. (a) General view of the two-micas granite (b) Phenocryst of k-feldspar marked by perthitic and poikilitic textures (c) Typical snowball quartz displaying a fluid inclusions trail (d) Grain of albite comprising inclusion of apatite (e) Grain of biotite comprising numerous inclusions of zircons and apatite (f) Igneous muscovite aggregate. (g) Zoom on the apatite inclusion presents in figure 5e. A grain of zircon is included in this grain of apatite. Abbreviations from Whitney and Evans (2010) Ab: Albite, Ap: Apatite, Bt: Biotite, Kfs: k-feldspar, Ms: Muscovite, Qz: Quartz, Zrn: Zircon.

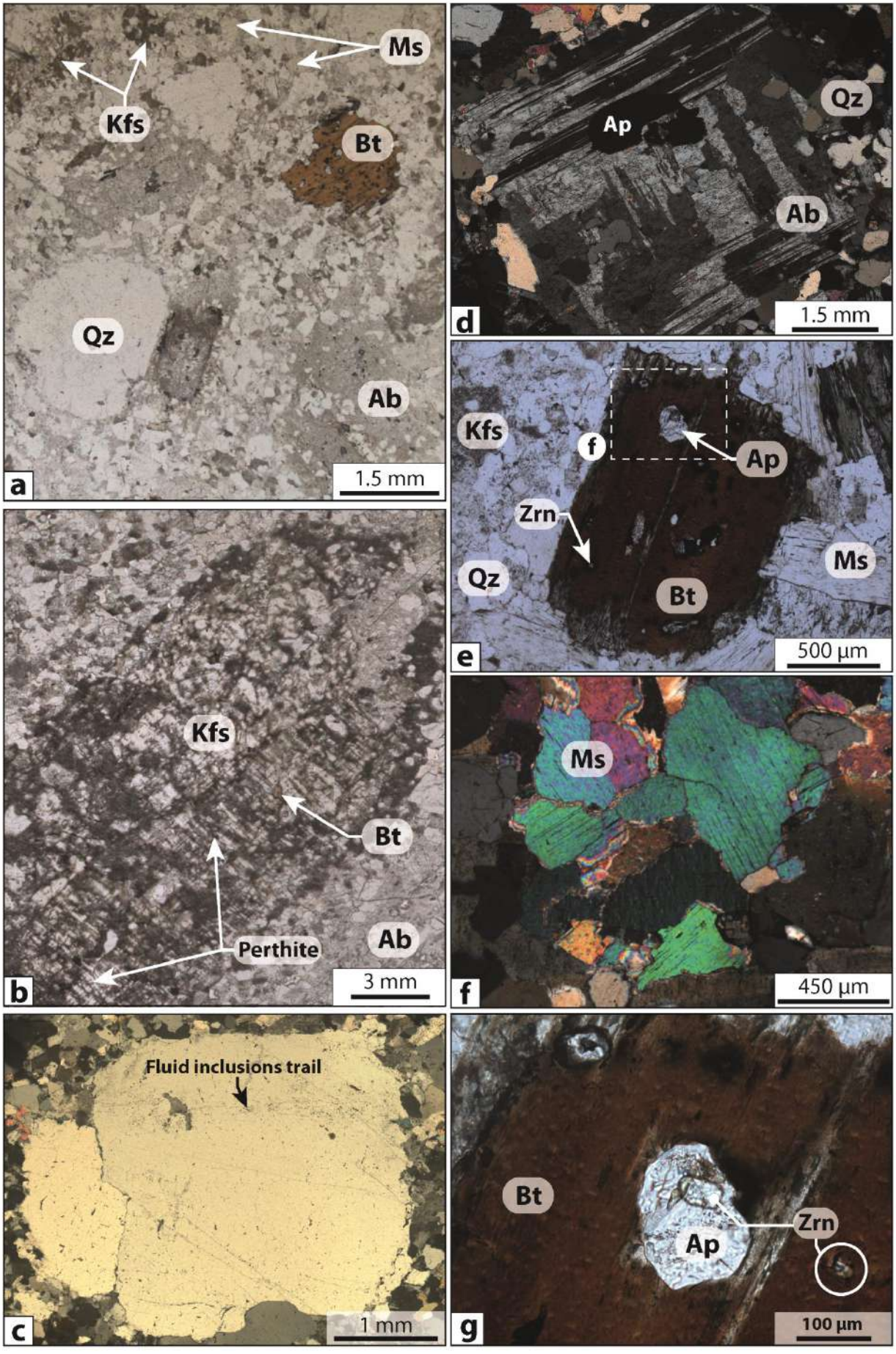
Ms
Kfs
Bt
Qz
Ab
a
1.5 mm
Kfs
Bt
Perthite
Ab
b
3 mm
Fluid inclusions trail
c
1 mm
Ap
Qz
Ab
d
1.5 mm
Kfs
f
Ap
Zrn
Ms
Qz
Bt
e
500 µm
Ms
f
450 µm
Bt
Ap
Zrn
g
100 µm

2.2 Petrographic characteristics of greisen

The mineralogical and the textural characteristics of the quartz-muscovite greisen of Panasqueira are displayed in Figure 6. As evidenced by field observations and petrographic study, the greisenization of the two-mica granite is marked by the total breakdown of feldspars and biotite, which were replaced by the crystallization of a large amount of muscovite and quartz (Fig. 6a). The greisenization is also accompanied by the development of a porous texture (Fig. 6b) partially infilled by the disseminated mineralization observed in the massive greisen (Fig. 7). The origin of this porosity generation and its implications on fluid flow are discussed in **Chapter V**. During this intense metasomatic alteration the primary magmatic texture was completely obliterated. However, relics of snowball quartz and albite composing the initial two-mica granite can be locally observed in greisen.

In partially greisenized facies, the replacement of the primary magmatic minerals is partial and permits to define the replacement reactions involved during the greisenization (Fig. 6c to 6e). In Figure 6c and 6d k-feldspars and albite are partially and unevenly replaced by small flakes of muscovite. In the most greisenized facies, these small flakes of muscovite were progressively agglomerated to form the large flakes observed in the massive greisen (Fig. 6a and 6b).

Biotite alteration is marked by the bleaching of biotite grains and by the formation of coronitic texture composed of residual irregular grains of biotite surrounded by neoformed muscovite (Fig. 6e). The replacement of biotite by muscovite can also occur along the cleavage planes of biotite. The presence of rutile and ilmenite disseminated throughout the neoformed muscovite emphasizes that Fe and Ti released by the biotite alteration have crystallized to form these oxides. Zircons initially included within the biotite were conserved in the neoformed muscovite and can be observed in large flake of muscovite composing the massive greisen (Fig. 6e and 7f).

When snowball quartz was conserved during the greisenization, they exhibit irregular shape due to overgrowth that could be related to the releasing of silica during the feldspars replacement (Fig. 7g). In these overgrowths it is possible to observe some relics of albite, which were probably trapped in during the quartz crystallization (Fig. 7g).

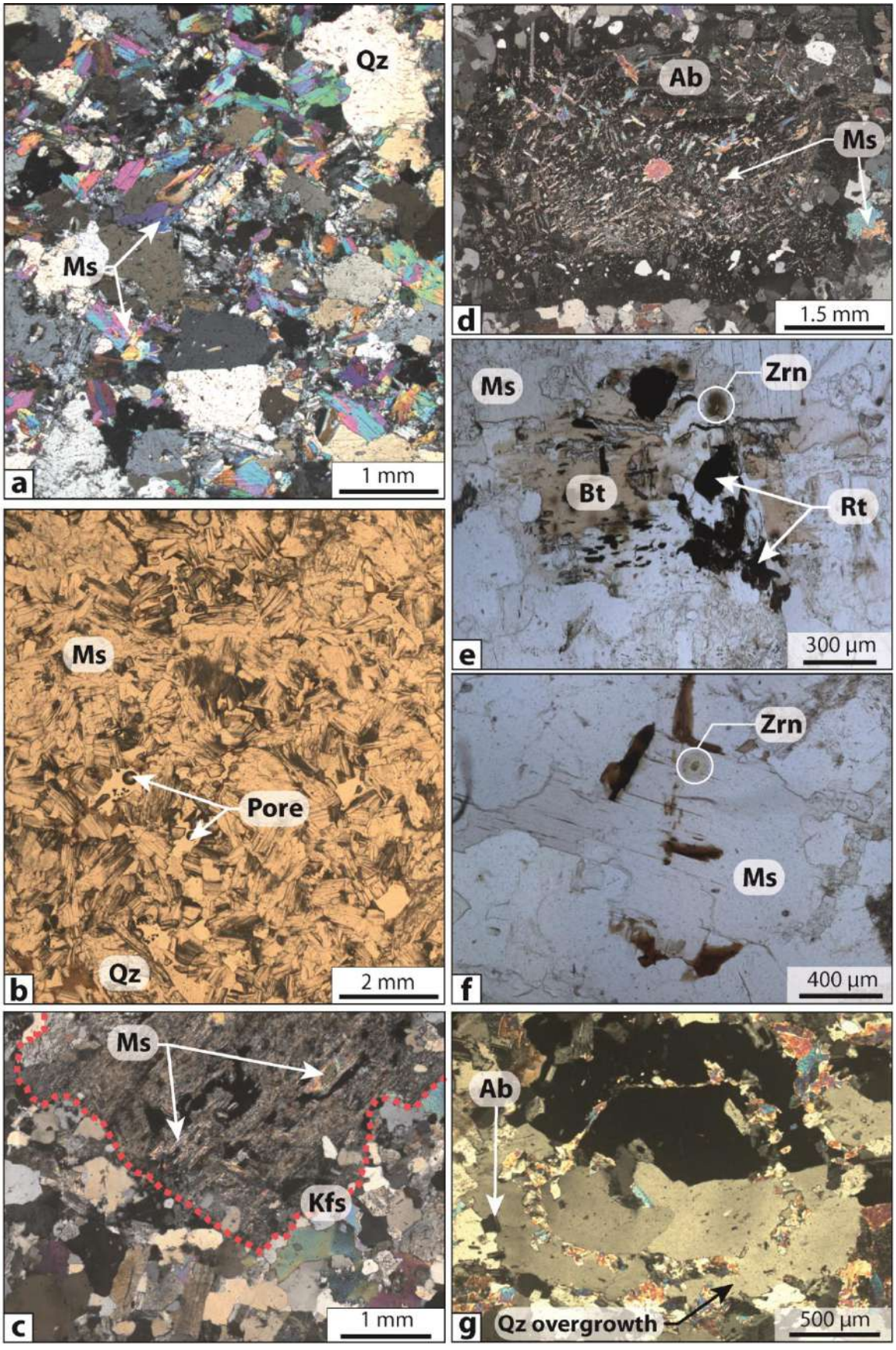
Qz
Ms
a
1 mm
Ab
Ms
d
1.5 mm
Ms
Zrn
Bt
Rt
e
300 µm
Ms
Pore
Qz
b
2 mm
Zrn
Ms
f
400 µm
Ms
Kfs
c
1 mm
Ab
g
Qz overgrowth
500 µm

Figure 6 Photomicrographs showing the mineralogical and the textural characteristics of the massive greisen of Panasqueira. (a) General view of the quartz-muscovite greisen (b) General view of a highly porous quartz-muscovite greisen (sample collected within a greisenized aplite) (c) Grain of k-feldspar completely replaced by muscovite in greisenized granite (d) Grain of albite partially replaced by muscovite during the greisenization (e) Crystal of biotite partially bleached and replaced by muscovite. Note the exsolution of rutile during the replacement of biotite. (f) Large flake of neoformed muscovite resulting from the total replacement of a biotite crystal. Note that zircon initially included in biotite was conserved in the neoformed muscovite. (g) Snowball quartz conserved in greisen during the greisenization. This quartz is marked by overgrowth in which we can observe relics of albite and grains of muscovite. Abbreviations from Whitney and Evans (2010) Ab: Albite, Bt: Biotite, Kfs: k-feldspar, Ms: Muscovite, Qz: Quartz, Zrn: Zircon.

The textural and the petrographic characteristics of the disseminated mineralization observed in the massive greisen of Panasqueira are displayed in Figure 7. During the greisenization, the magmatic apatite initially present within the two-mica granite was conserved in greisen (Fig. 7a). As observed in macroscopic samples, the greisen porosity was partially infilled by metal-bearing minerals during the same mineralization stages described in veins (Fig. 7) (**Chapter II, Part III**). Large void spaces are commonly fringed by euhedral quartz indicating that adjacent crystals were growing into open space until the complete filling of the void by ore-bearing minerals (cassiterite and sulfides) (Fig. 7b).

The main oxide silicate stage (MOSS) that corresponds to the Sn-W mineralization event can be also observed in the massive greisen as cassiterite grains, which have preferentially crystallized within the pore spaces of greisen (Fig. 7a and 7c). However, only very rare occurrence of wolframite has been found within the greisen itself. This suggests that conditions required for wolframite deposition were probably not achieved during the greisenization (**see Chapter V, Part II**). The greisenization is also accompanied by the formation of hydrothermal rutile, which forms small crystals exhibiting complex sector zoning (Fig. 7d and 7e). The formation of this hydrothermal rutile could be related to the releasing of Ti in fluids during the alteration of biotite.

The large pores that can be observed in the massive greisen were mainly infilled during the main sulfide stage (MSS) by chalcopyrite, sphalerite, pyrite and pyrrhotite (Fig. 7b, 7c, 7g and 7h). The interaction between chalcopyrite and sphalerite formed during the sulfide stage and the cassiterite related the Sn-W mineralization stage leads to the formation of a coronitic texture composed of stannite mainly observed along the pore edges (Fig. 7g and 7h). During this alteration of cassiterite a part of Sn was probably remobilized by fluids explaining the rare occurrences of cassiterite within the massive

greisen of Panasqueira. This process was ever been described by Novàk et *al*. (1962) in the case of the polymetallic mesothermal-hydrothermal veins of the Kutnà Hora ore deposit.

The late mineralization stages (PAS and LCS) observed in mineralized veins (**see Chapter II**) can be also found in the disseminated mineralization of the massive greisen. Indeed, pyrrhotite formed during the sulfide stage (MSS) appears to be locally altered and replaced pyrite according to the same type of replacement textures observed in veins (Fig. 7i). This pyrrhotite alteration is accompanied by precipitation of galena which crosscut clearly chalcopyrite related to the sulfide stage (MSS) (Fig. 7j). Finally, pores observed in massive greisen can be completely infilled by carbonate minerals (calcite and dolomite) related to the late carbonate stage (Fig. 7k).

Figure 7 Photomicrographs displaying the mineralogical and the textural characteristics of the disseminated mineralization observed in the massive greisen of Panasqueira. (a) Magmatic apatite conserved in greisen and grain of cassiterite, which has crystallized within a pore space. (b) Large pore completely infilled by euhedral quartz and sulfides (chalcopyrite, sphalerite and pyrite). (c) Grain of cassiterite infilling the porosity observed in the massive greisen. (d) Chalcopyrite associated with hydrothermal rutile. (e) SEM photomicrograph displaying a complex sector zoning in the hydrothermal rutile observed in the massive greisen. (f) Greisen porosity infilled by sphalerite and pyrite. (g) and (h) Coronitic texture composed of stannite displaying interaction between cassiterite related to the MOSS and chalcopyrite related to the MSS. (i) Partial replacement of pyrrhotite by pyrite during the pyrrhotite alteration stage (PAS). (j) Galena related to the PAS that crosscuts chalcopyrite formed during the sulfide stage (MSS). (k) Large pocket completely infilled by sulfides and carbonate minerals during the late carbonate stage (LCS). Note the crystallization of euhedral quartz along the pore edges. Abbreviations from Whitney and Evans (2010) Ap: Apatite, Cal: Calcite, Ccp: Chalcopyrite, Cst: Cassiterite, Gn: Galena, Ms: Muscovite, Po: Pyrrhotite, Py: Pyrite, Qz: Quartz, Rt: Rutile, Stn: Stannite, Zrn: Zircon.

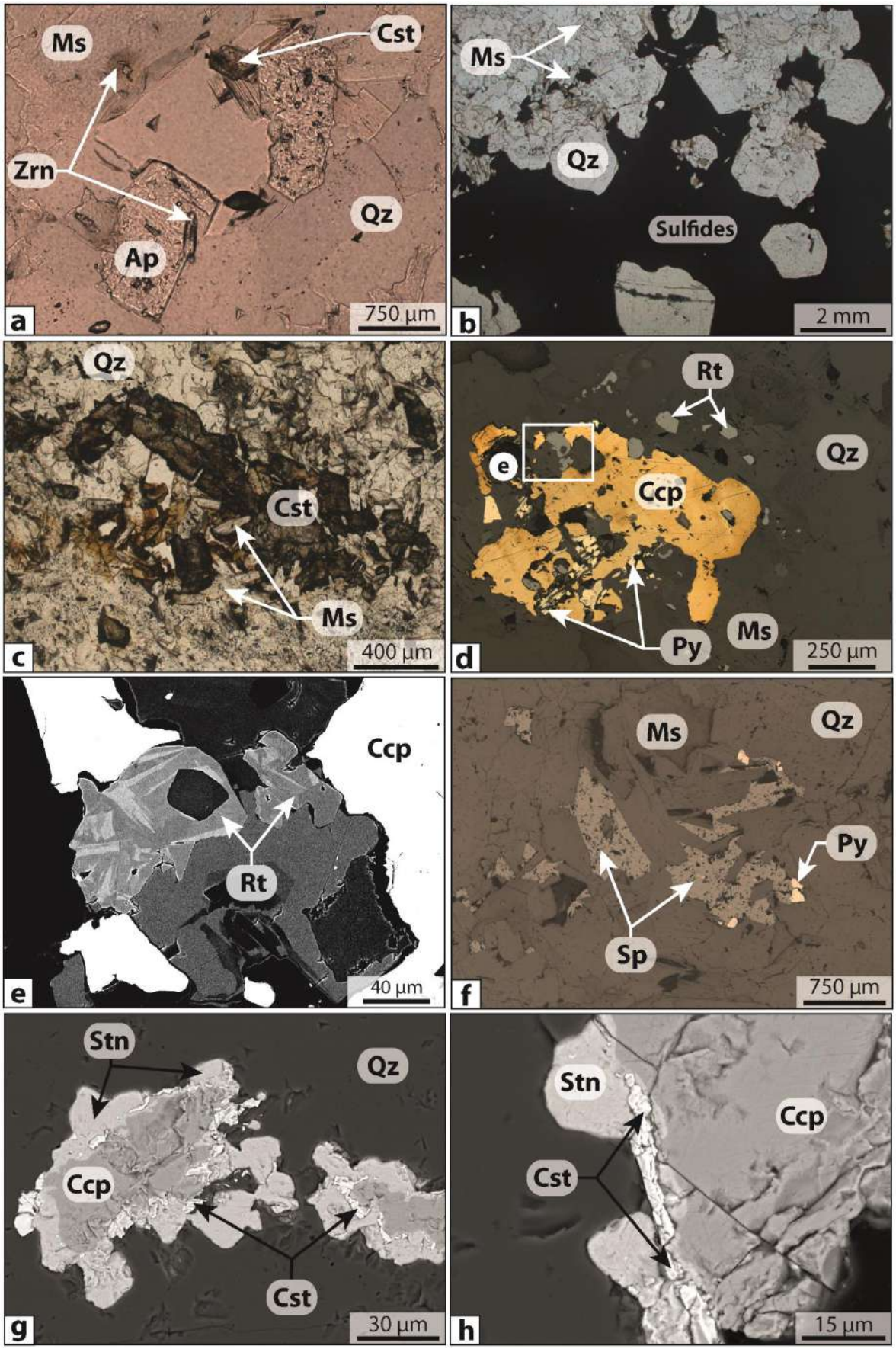
Ms
Cst
Zrn
Qz
Ap
750 µm
a
Ms
Qz
Sulfides
2 mm
b
Qz
Cst
Ms
400 µm
c
Rt
e
Qz
Ccp
Py
Ms
250 µm
d
Ccp
Rt
40 µm
e
Ms
Qz
Py
Sp
750 µm
f
Stn
Qz
Ccp
Cst
30 µm
g
Stn
Ccp
Cst
15 µm
h

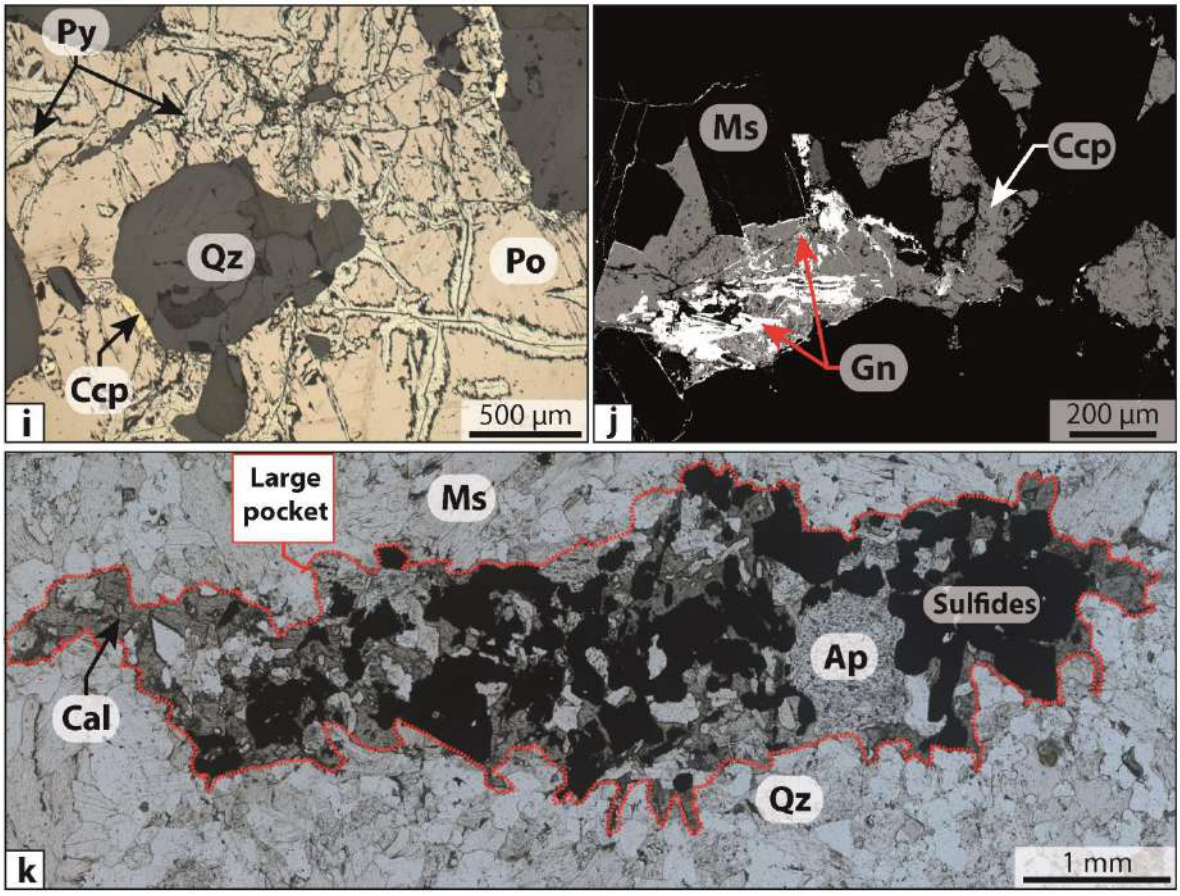

2.3 Simplified parametric sequence of the massive greisen system of Panasqueira

On the basis of our macroscopic and petrographic observations, a simplified paragenetic sequence of the greisen system of Panasqueira is proposed in Figure 8. The different stages observed in the disseminated mineralization of the massive greisen appear to be equivalent than those described in the mineralized veins and are characterized by the same temporal succession (**Chapter II, Part III**). The greisenization seems to be contemporaneous or slightly earlier to the Sn-W mineralization stage. The presence of cassiterite within the greisen porosity and the occurrences of greisen enclaves within mineralized veins observed in the greisen cupola support this relative chronology. The expression of the Sn-W event in the massive greisen is mainly marked by the crystallization of cassiterite and rutile. The absence of wolframite in the massive greisen suggests that physicochemical conditions were not propitious to the wolframite deposition in the greisen. The mineralization observed within the massive greisen is largely dominated by the sulfide stage (MSS and PAS in veins) that infill the porosity developed during the greisenization. During this stage, the cassiterite formed during the Sn-W event

was altered and replaced by stannite. This cassiterite breakdown can be a potential cause of the rare occurrences of cassiterite in the greisen of Panasqueira.

The preferential crystallization of metal-bearing minerals within the porosity developed during greisenization suggest that greisen could constitute permeable pathways for mineralizing fluids related to the different mineralizations stages observed both in veins and within the massive greisen. These considerations are discussed in details in **Chapter V**.

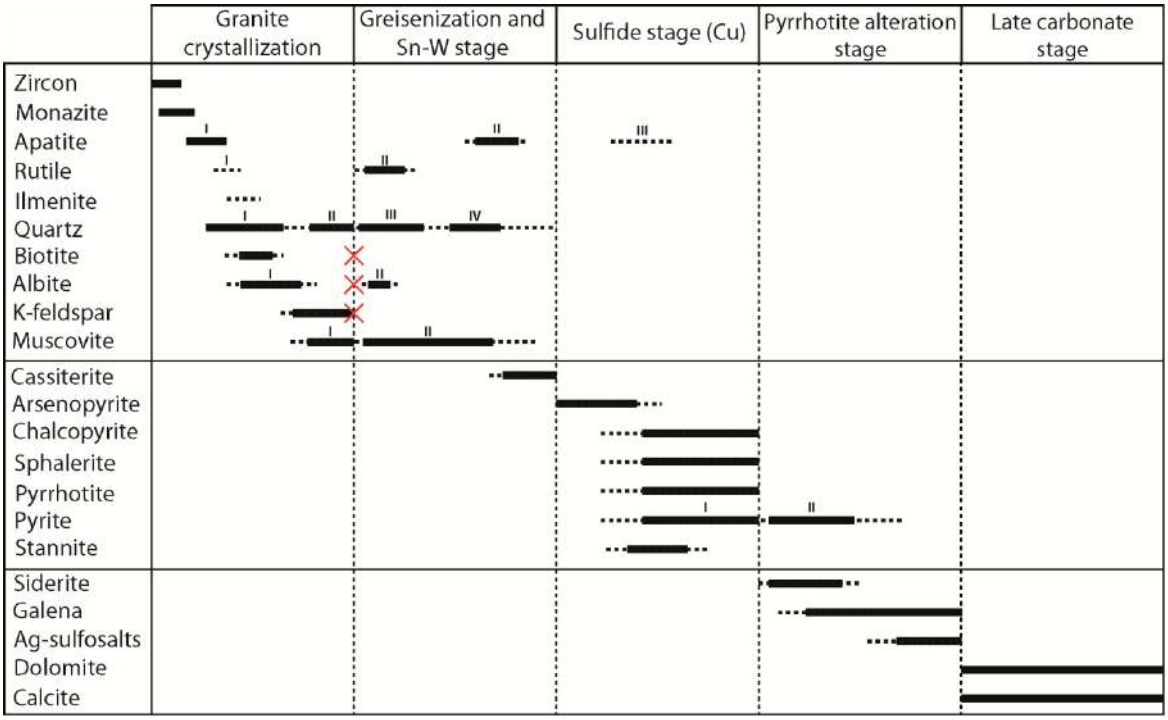

Figure 8 Simplified paragenetic sequence proposed for the massive greisen of Panasqueira. This sequence includes magmatic, greisenization and mineralization stages observed in the massive greisen. The red crosses indicate the breakdown of magmatic minerals induced by the greisenization processes.

II- Materials and methods

In the light of our petrographic observations, several generations of quartz, muscovite and apatite can be observed both in granite, greisen and within the mineralized vein systems of Panasqueira. Furthermore, muscovite and quartz constitute ubiquitous minerals recording (i) magmatic processes related to the granite crystallization, (ii) greisenization processes and (iii) the incipient stages of vein formation (QTS and MOSS). The geochemical characterization of these muscovite and quartz could provide significant information about magmatic-hydrothermal processes involved during the formation of the Panasqueira deposit.

Indeed, muscovite incorporates a large amount of trace elements that can be used as indicators of the evolution of magmatic-hydrothermal systems (Miller et al., 1981; Speer, 1984; Monier et *al*., 1984; Neiva, 1987; Tischendorff et *al*., 1997; Gomes and Neiva, 2000; Legros et *al*., 2016). From the compositional variations potentially observed between the different generations of muscovite, magmatic and hydrothermal processes involved in these systems can be distinguished and identified (Alfonso et *al*., 2003; Hulsbosch et *al*., 2014; Legros et *al*., 2016). Furthermore, the trace elements content in muscovite can also provide information about fluid source(s) involved during the different hydrothermal stages.

Quartz is a generic pathfinder ubiquitous in hydrothermal and magmatic environments. Moreover, quartz is able to incorporate a wide range of trace elements that can be used as pathfinder to track magmatic and hydrothermal processes. The concentrations of these trace elements are generally controlled by (i) their abundances in the parental melt and hydrothermal fluids, (ii) partitioning of these elements between co-genetic minerals, (iii) physicochemical conditions and (iv) pressure and temperature conditions (Gurbanov et al., 1999; Larsen et al., 2004; Jacamon and Larsen, 2009; Thomas et *al*., 2010). Recent studies have demonstrated that Ti content in quartz is generally correlated to the temperature conditions (Huang and Audétat, 2012), while the evolution of the Al, Ge and Li permit generally to highlight the melt differentiation induced by fractionated crystallization (Jacamon and Larsen, 2009). Trace element content in quartz was recently used to track the magmatic-hydrothermal processes in cases of deposits related to magmatic intrusions (Müller et *al*., 2002, 2005; Breiter et *al*., 2012; Rusk, 2012; Müller et *al*., 2018; Monnier et *al*., 2018).

In the following we couple geochemical information obtained from muscovite and quartz to discuss the genetic relationships between the greisenisation processes and the earliest stages of vein formation. These geochemical constrains are completed by U-Pb dating of magmatic and hydrothermal apatite from granite, greisen and veins.

1. Starting materials

To constrain petrological and geochemical characteristics of the magmatic-hydrothermal system of Panasqueira, samples representative of the different facies of granite, greisenized granite and greisen were collected in (i) the drill hole SCB2, (ii) within the greisen cupola observed in mine (Level 1) and (iii) within greisenized aplites observed on the field. Samples of veins representative of the first mineralization stages (MSS and MOSS) were also collected to compare the geochemical characteristics of muscovite and quartz present in veins with those composing the granite and the greisenized facies. A part of these samples were used to prepare polished thin (~ 30 μm) and thick (~100 μm) sections at the laboratory of the Institut des Sciences de la Terre d'Orléans (ISTO).

2. Whole rock geochemistry

The whole rock major and trace element compositions of the selected samples were determined following the analytical procedure of ALS laboratories. Samples were first crushed and pulverized and the finer faction was recovered (75 μm) for analyses. From these powders, the major element composition of samples was determined by inductively coupled plasma atomic emission spectroscopy (ICP-AES).

For trace element analyses, a lithium borate fusion of each sample powder was performed. The melt produced by this method was then completely dissolved by acid digestion and trace element analyses were carried out by inductively coupled plasma mass spectrometry (ICP-MS). More information about the procedure and the accuracy of the analytical methods used for whole rock analyses can be found on the website of ALS laboratories (alsglobal.com/geochemistry).

3. Scanning electronic microscopy and cathodoluminescence imaging

Mineralogical and micro-textural characteristics of samples were examined on polished thin sections by optical microscopy (reflected and transmitted light) and by scanning electron microscopy (SEM) using a Merlin compact Zeiss high resolution scanning

electronic microscope equipped with a Gemini I detector (BRGM, University of Orléans). To display chemical zoning present in some minerals (like muscovite and apatite), element mapping was performed by SEM using an acceleration voltage of 15 kV.

The cathodoluminescence (Cl) images of quartz and apatite were collected at the BRGM (French Geological Survey) using a TESCAN MIRA 3 Scanning Electronic Microscope (SEM) equipped with a single channel panchromatic detector. This detector has a spectral range from 350 to 650 nm providing greyscale images of the Cl emissivity. Polished thick and thin sections were examined for a working distance of 16 mm with an accelerating voltage of 20 kV and a current of 15 nA. For the textural analysis of quartz, the image acquisition has been performed with a scanning speed ranging from 100 to 500 µs/pixel depending on the presence of highly luminescent minerals (apatite, carbonate) associated with quartz.

4. Major elements analyses in minerals

The major and minor elements compositions of mineral phases were determined on polished thin sections using a Cameca SX-Five electron probe micro-analyzers (EPMA) at the Institut des Sciences de la Terre d'Orléans (ISTO). Analyses were performed using an accelerating voltage of 15 kV, an electron beam current of 6 nA and a beam diameter of 2 µm. Elemental mapping of muscovite have been performed using an accelerating voltage of 20 kv. Analytical conditions and calibration used for each mineral phases are given in appendix. For calculation of structural formulae of the mineral phases, the analyses were normalized to the total number of oxygens in the considered mineral. Analytical conditions and calibration used for analyses are detailed in the supplementary materials.

5. Trace elements analyses in minerals

5.1 Trace elements analyses in muscovite

Concentrations of Li, V, Fe, Ni, Cu, Zn, Rb, Sr, Nb, Sn, Cs, Ba, Ta, W and Pb in muscovite from granite, greisen and veins were determined on thin sections by laser ablation inductively coupled plasma-mass-spectrometry (LA-ICP-MS). These analyses were performed at the Laboratoire Géoscience Océan of Brest using a Thermo Element 2 ICP-MS coupled with a Compex Pro 102 Coherent 193 nm laser ablation system. Ablations were performed with a laser shot frequency of 10 Hz and beam size of 50 and 75 µm. Analyses comprise 15 seconds of gas blank measurement following by 30 seconds of ablation. The gas used to carry the ablated material to the ICP-MS was a He and Ar

mixture. Concentrations were obtained with the Glitter 4.0 software using the NIST SRM-612 glass standard for external standardization, while BCR2 and BIR1 were used as supplementary control standards. Then, analyses of muscovite were normalized to ^{29}Si using concentrations obtained by EPMA (more details in appendix).

5.2 Trace element analyses in quartz

The content of Li, Be, B, Na, Al, Si, S, Ti, Ge, As, Rb, Sr, Nb, Sn, Sb, Ta and W in quartz were determined by LA-ICP-MS. These analyses were performed at BRGM (French Geological Survey) using a ThermoScientific X series II quadrupole ICP-MS coupled with a Cetac Excite 193 nm laser ablation system. Ablations were performed on thick sections with a repetition rate of 8Hz and laser energy of 10 J/cm² with a beam size of 85 μm. The ablated material was transported from the laser ablation cell by a He gas with a flow rate of 250 mL/min. Analyses comprise 20 seconds of gas blank measurement following by 60 seconds of ablation. Data reduction was performed with the software Glitter 4.0 (http://www.glittergemoc.com/) using the NIST SRM-612 glass standard for external standardization and the ^{29}Si isotope as internal standard assuming a SiO_2 content of 99 wt% in quartz. The relative standard deviation (RSD) between the measured and reference concentrations of the certified standard NIST-612 SRM (Pearce et *al.*, 1997) are below 10% for all elements (more details in appendix).

6. U-Pb dating of apatite by LA-ICP-MS

U-Pb dating of apatite (magmatic and hydrothermal) was conducted by in-situ LA-ICP-MS analyses at Géosciences Rennes using a quadripole Agilent 7700x ICP-MS coupled to ESI NWR193UC excimer laser. Apatite was ablated with a constant spot diameter of 50 μm for an ablation rate of 5 Hz. The ablated material was then carried to ICP-MS by He mixed with N_2 and Ar. Analyses were performed according to the analytical procedure described by Pochon et *al*. (2016) and detailed in appendix. Analyses of apatite were bracketed by analyses of different apatite standards comprising (i) the Madagascar apatite standard (ID-TIMS age of 473.5 ± 0.7 Ma; Cochrane et *al*., 2014) used as the primary apatite reference and (ii) the Durango (31.44 ± 0.18 Ma; McDowell et *al*., 2005) and the McClure (523.51 ± 2.09 Ma; Schoene and Bowring 2006) apatite standards used to control the reproducibility and accuracy of measurements. Data reduction was performed following the procedure described by Pochon et *al*. (2016) using

VizualAgeUcomPbine (Chew et *al*., 2014) and ages were calculated from the ISOPLOT software (Ludwig, 2012) that provides ages with 2σ error.

III- Results and discussion

1. Microtextural characteristics of minerals

1.1 Microtextural features of muscovite (SEM images)

1.1.1 Muscovite of the two-mica granite

The microtextural characteristics of muscovites composing the two-mica granite are displayed in Figure 9. Backscattered electron images show that these muscovites are generally unzoned and characterized by a homogeneous dark color suggesting homogeneous chemical composition (Fig. 9). This is confirmed be the chemical maps of Al, Fe and Na that exhibit homogeneous concentrations in muscovite grains (Fig. 9). However, a slight depletion in Al can be locally observed along some grain boundaries that could be related to a moderate alteration.

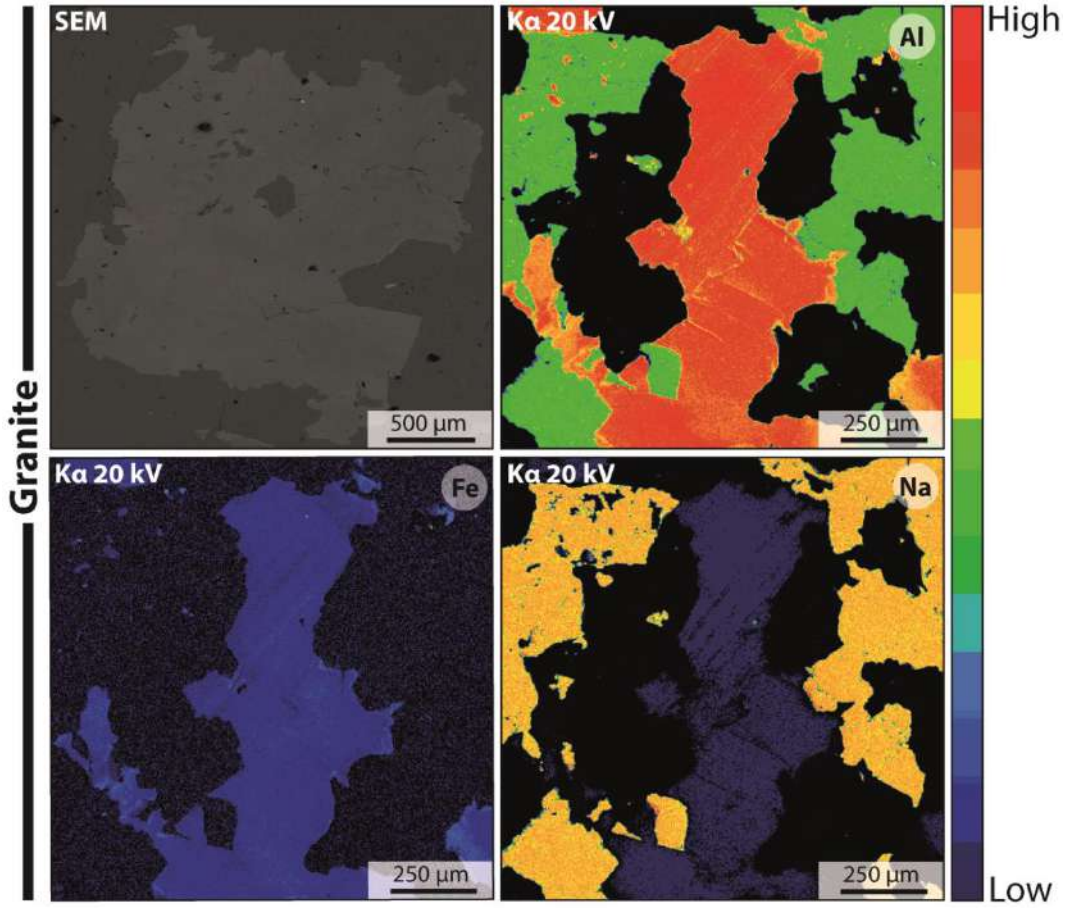

Figure 9 SEM and chemical maps of Al, Fe and Na of primary magmatic muscovite composing the unaltered two mica granite of Panasqueira. These magmatic muscovites are unzoned and exhibit homogeneous composition.

1.1.2 Muscovite of the massive greisen

The microtextural characteristics of muscovites composing the massive greisen of Panasqueira are displayed in Figure 10. These muscovites form large sub-euhedral flakes characterized by a well-developed growth zoning marked by dark cores and light rims (Fig. 10). The contact between core and rim is well defined and the thickness of rims ranges between 50 and 300 µm. These zoning can be also observed from the chemical maps of Al, Fe and Na that display (i) core to rim depletion in Al and Na and (ii) core to rim enrichment in Fe. These chemical and textural zoning can be interpreted as hydrothermal overgrowths of the primary magmatic muscovite during the greisenization. This zoning pattern has ever been described in the hydrothermally altered Sn-bearing granite of Ervedosa (northern Portugal) and interpreted as marker of the hydrothermal alteration related to the Sn mineralization stage (Gomes and Neiva, 2000).

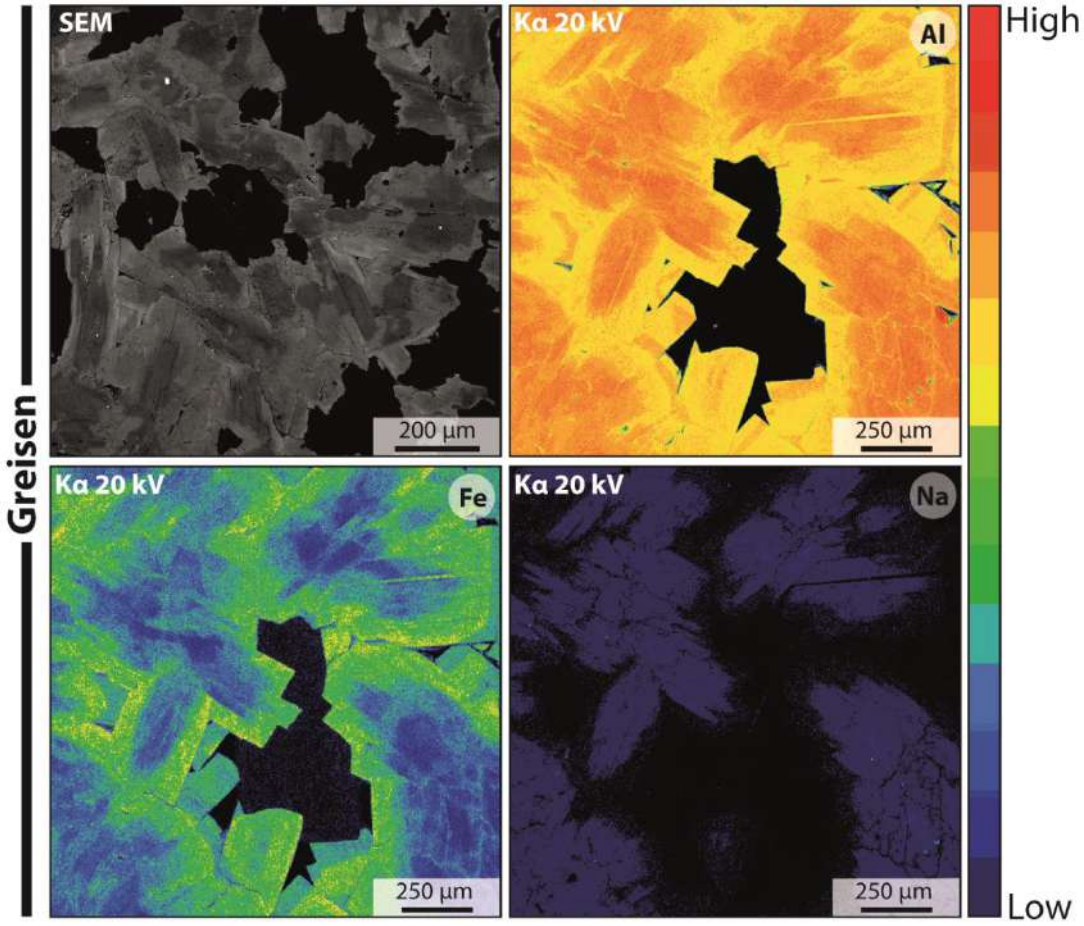

Figure 10 SEM and chemical maps of Al, Fe and Na of muscovites composing the massive greisen of Panasqueira. These muscovites exhibit a strong zoning corresponding to growth and chemical zoning.

1.1.3 Muscovite selvages of the mineralized vein

The microtextural characteristics of the muscovite selvage present along the schist-vein contacts are displayed in Figure 11. These muscovite selvages exhibit a fibrous texture composed of large euhedral flakes (that can reach 3 cm of height) characterized by a vertical growth related to the vertical opening of veins (Fig. 11a). Muscovite is generally found in direct continuity with tourmaline formed during the quartz tourmaline stage (QTS) and can be associated with apatite, cassiterite and wolframite (Fig. 11a, 11b and 11d) (more detailed are given in **Chapter II, Part III**).These muscovites are generally unzoned but brighter-luminescent overgrowth can be locally observed (Fig. 11c).

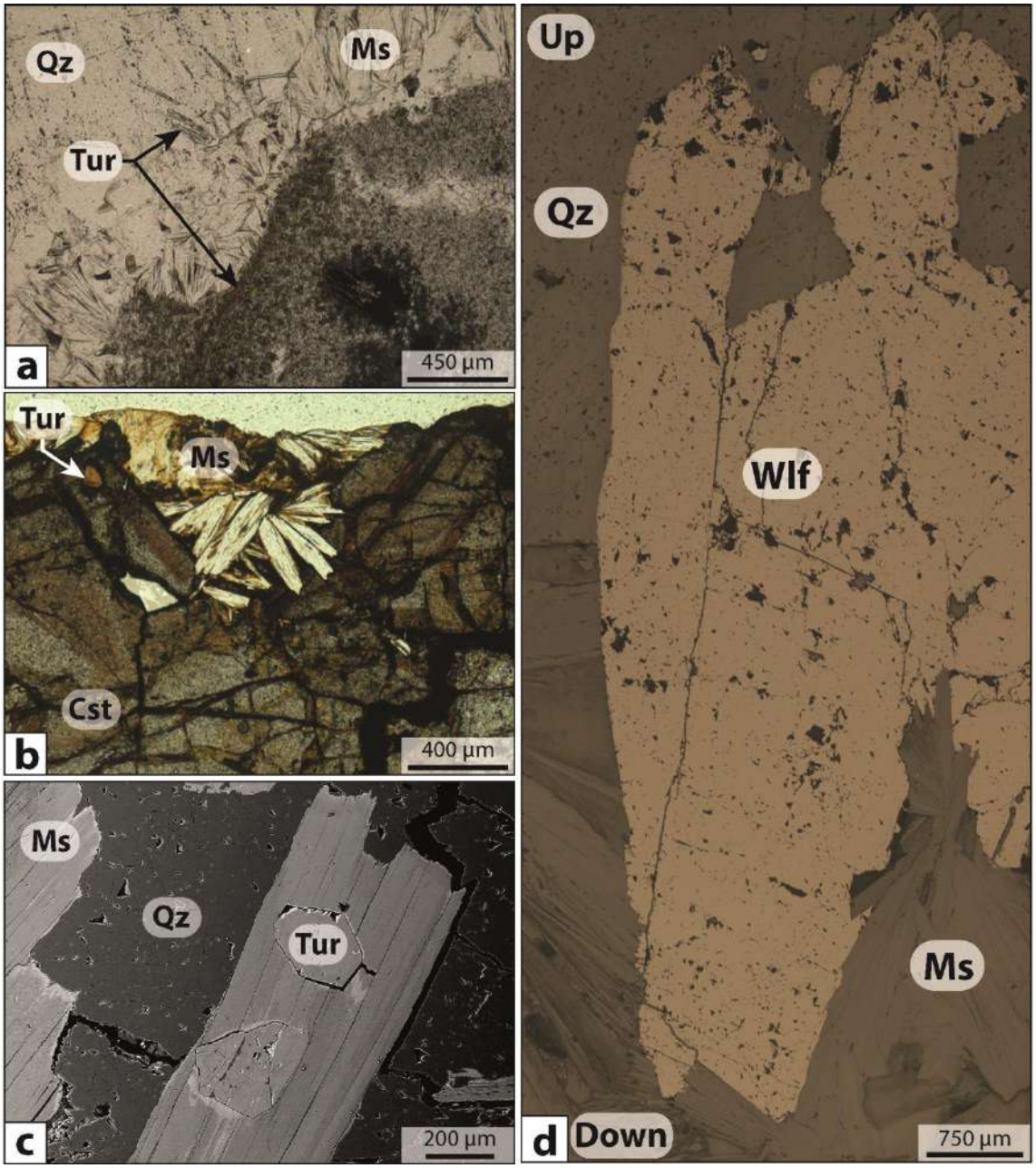

Figure 11 Photomicrographs displaying the textural characteristics of the muscovite selvage observed along the schist-vein contacts. (a) Relationships between muscovite and tourmaline formed during the QTS. (b) Relationship between muscovite and cassiterite along the vein selvage. (c) SEM photomicrograph showing that muscovite is generally homogeneous. (d) Relationship between the muscovite selvage and wolframite.

1.2 Microtextural features of quartz (SEM-CL images)

1.2.1 Quartz of the two-mica granite

As described previously, the two-mica granite of Panasqueira is characterized by the occurrences of snowball-textured quartz that exhibit euhedral shape with straight and sharp boundaries (Fig. 12a and 12b). As evidenced by cathodoluminescence images (CL), these snowball quartz show weakly contrasted, oscillatory growth zoning (Fig. 12c and 12d). Cores are generally marked by higher luminescence intensity than rims. The fluid inclusions trails observed in transmitted light correspond to Cl-dark structures defining healed vein-like structures that result from the precipitation of non-luminescent quartz within fractures planes (Rusk and Reed, 2002). Matrix quartz is usually characterized by low CL and displays the same luminescence intensity than rims of snowball quartz (Fig. 12c and 12d).

Figure 12 Transmitted light (a to b) and SEM-cathodoluminescence images (c to d) of magmatic quartz phenocryst composing the two-mica granite of Panasqueira. These quartz exhibit snowball texture with weakly contrasting growth zoning. These concentric growth zoning are locally overprinted by a dense network of healed fractures infilled by non-luminescent quartz (CL-dark structures).

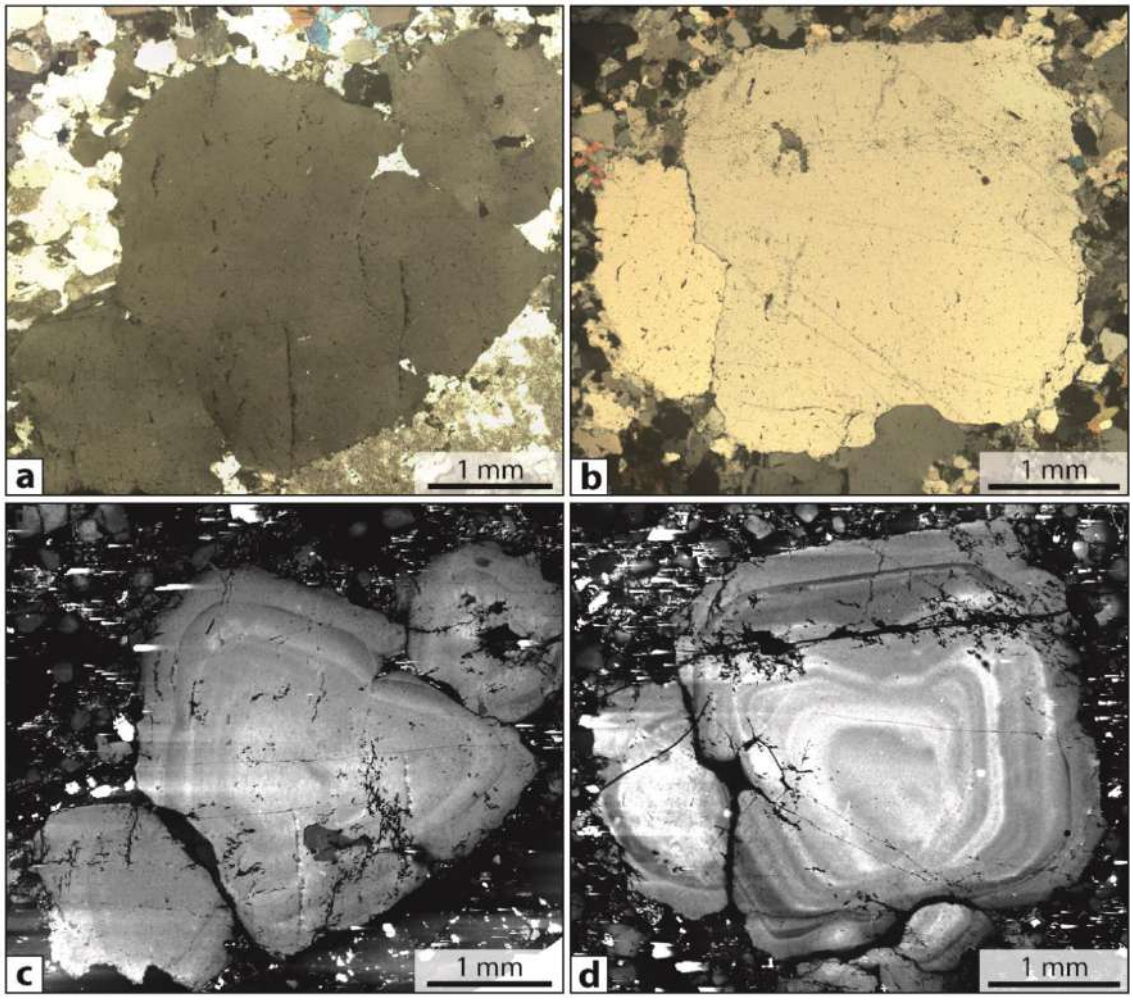

1.2.2 Quartz of the massive greisen

The massive greisen can exhibit remnants of primary magmatic snowball quartz that were partially altered during the greisenization (Fig. 13). These grains are generally characterized by irregular shape marked by the presence of hydrothermal overgrowths that were probably formed during the greisenization (Fig. 13a). Inclusions of albite and muscovite were trapped in these hydrothermal overgrowths (Fig. 13a and 13d). In cathodoluminescence images, these grains exhibit irregularly shape CL-light cores (primary magmatic snowball quartz) surrounded by very weak luminescent quartz (hydrothermal overgrowth), which was probably formed from the greisenizing fluids (Fig. 13b, 13c and 13d). Quartz formed during the greisenization by feldspars and biotite replacement is xenomorphic and characterized by low luminescence intensity (Fig. 13b). The euhedral quartz observed in the greisen porosity is marked by very weak CL equivalent to those observed in the matrix quartz. Secondary structures like healed fractures are common in all quartz composing the massive greisen.

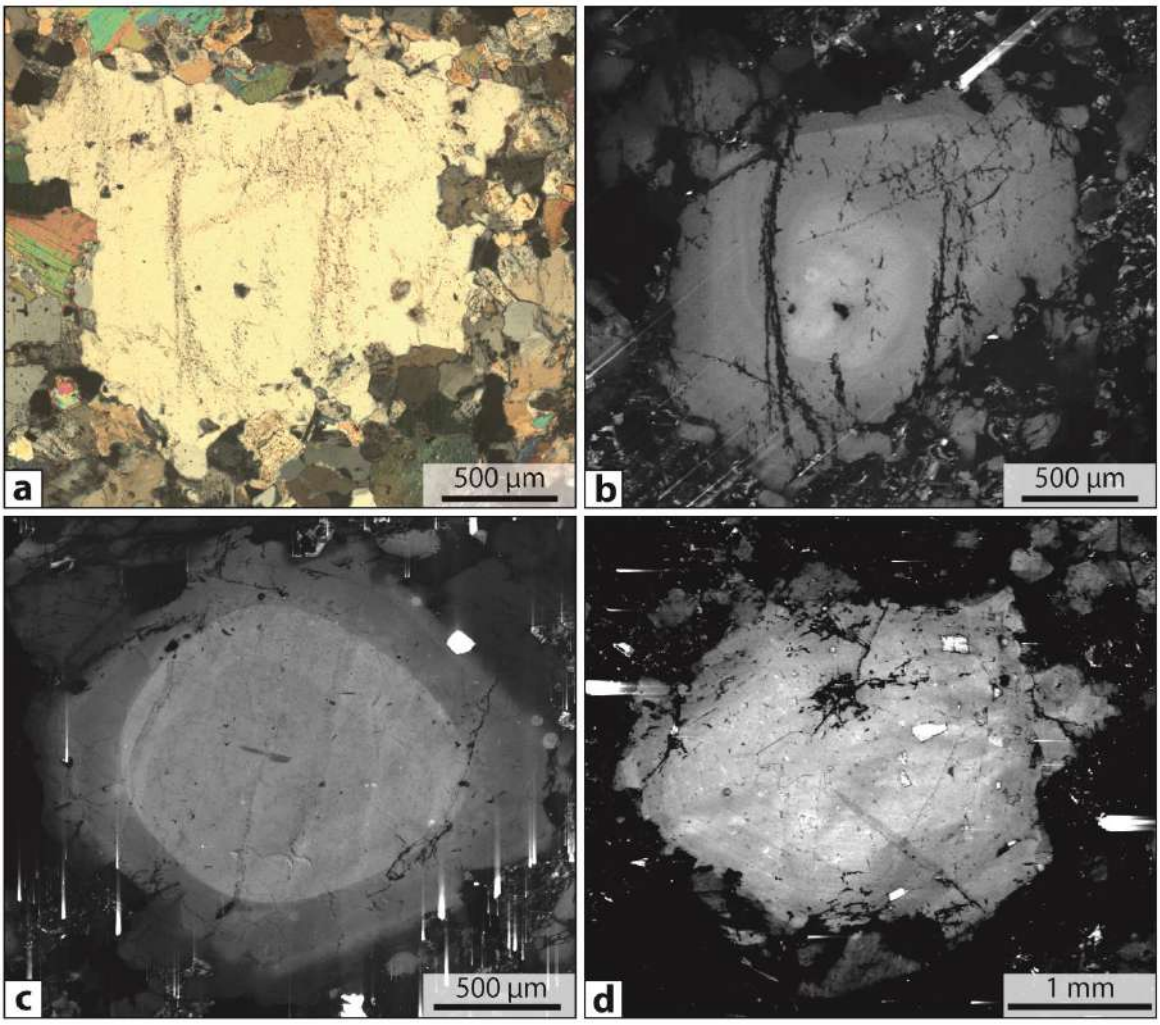

Figure 13 Transmitted light (a) and SEM-cathodoluminescence images (b to d) of remnants of primary magmatic snowball quartz partially altered during the greisenisation. These quartz grains exhibit hydrothermal overgrowth characterized by lower luminescence intensity than the primary snowball cores. In some cases the primary concentric growth zoning are conserved. The CL-dark structures correspond to healed fractures underlined by fluid inclusions trails in transmitted light.

1.2.3 Quartz of the hydrothermal mineralized veins

Quartz of the hydrothermal veins forms generally prismatic megacryst that can reach ~20 cm of length. Several generations of quartz can be distinguished, here we focus our intention on quartz formed during the quartz tourmaline stage (QTS) and during the main oxide silicate stage (MOSS) that mark the incipience of the hydrothermal activity of Panasqueira. In general, quartz grew vertically and perpendicular to the vein edge (see **Chapter II, Part III**). These crystals of quartz form geodes, which were then infilled by wolframite, cassiterite and by minerals related to the late hydrothermal stages (Fig. 14). On sections perpendicular to their <c> axis, quartz exhibit typical euhedral shape surrounded by large cavities, in which cassiterite and wolframite have then crystallized

(Fig. 14a and 14c). Tourmaline is generally anterior and included within these crystals of quartz (Fig. 14a). As evidenced by CL images these quartz are characterized by thin, contrasted, oscillatory growth zoning (Fig. 14b and 14d). Sector zoning emphasize implication of corrosion processes during which quartz could be partially dissolved and re-crystallized (Fig. 14d). Hydrothermal quartz are also characterized by a dense network of secondary structures composed of fractures healed by non-luminescent quartz (Fig. 14b and 14d). This dense network of micro-fractures is consistent with an intense tectonic activity during the vein formation and can be also related to important fluid pressure fluctuations between lithostatic and hydrostatic conditions (Rusk and Reed, 2002).

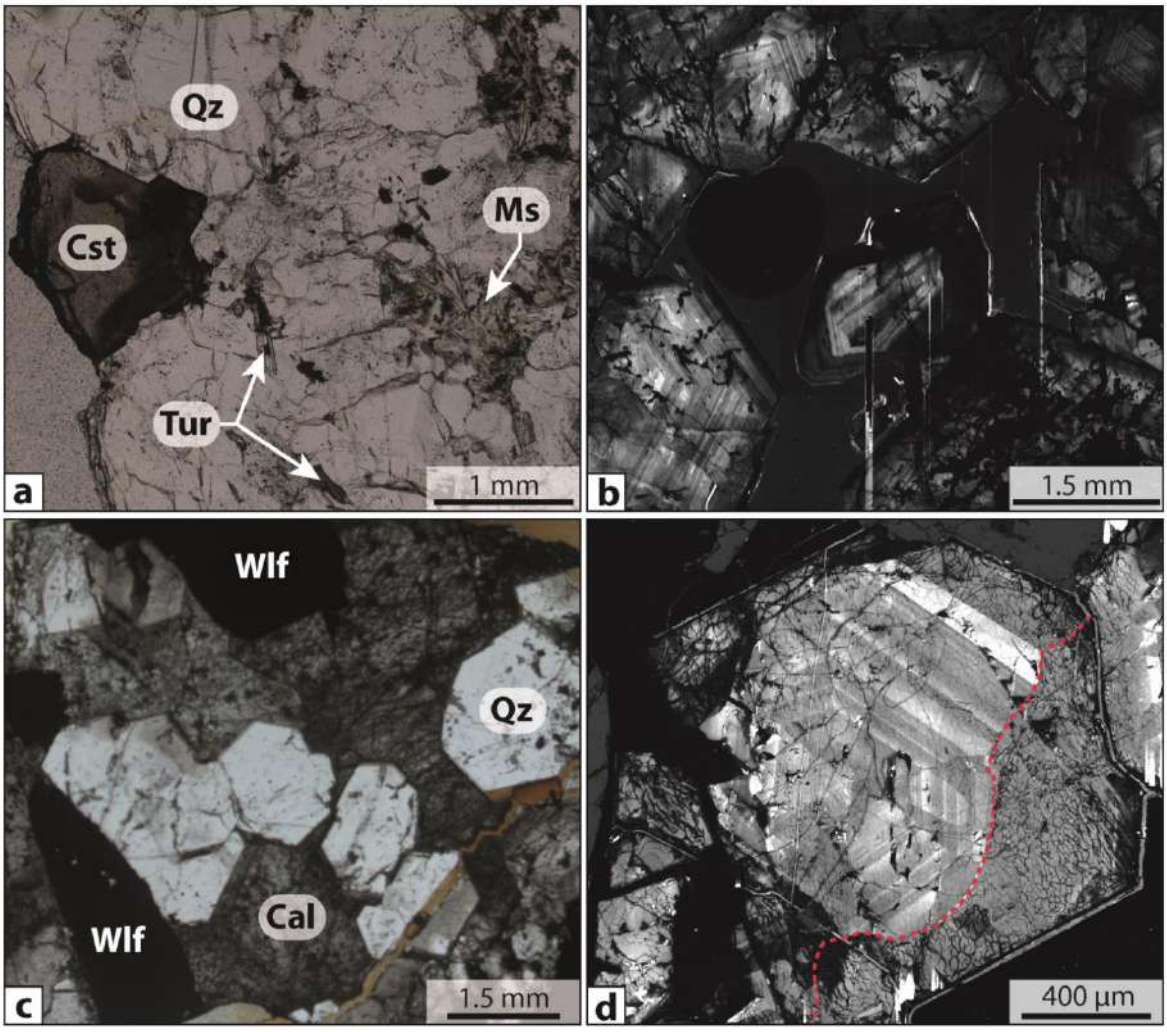

Figure 14 Transmitted light and SEM-cathodoluminescence images of hydrothermal quartz formed during to the quartz tourmaline stage (QTS) (a to b) and during the main oxide silicate stage (MOSS) (c to d). These sections were cut horizontally and perpendicular to the <c> axis of quartz. These two generations of quartz exhibit thin, contrasted, oscillatory growth zoning. The dense network of CL-dark structures corresponds to fractures healed by non-luminescent quartz. Quartz can be partially corroded (red dashed line in d) and marked by sector zoning. Abbreviations from Whitney and Evans (2010) Cal: Calcite, Cst: Cassiterite, Ms: Muscovite, Qz: Quartz, Tur: Tourmaline, Wlf: Wolframite.

1.3 Microtextural features of apatite (SEM-CL images)

1.3.1 Apatite in the unaltered two-mica granite

As previously described magmatic apatite in the unaltered two-mica granite occurs as regular euhedral grains (100 to 1000 μm) generally included within phenocryst of albite and biotite. Numerous of smaller grains (1 to 10 μm) can be also observed in the granite matrix. In cathodoluminescence images these primary magmatic apatites commonly display homogeneous dark-grey luminescence (Fig. 15). However, some grains were slightly altered along the grain boundaries and exhibit a secondary light-grey-luminescent apatite (Fig. 5a, 5c and 5d). Thus, only the unaltered parts of apatite grains were considered during U-Pb dating of magmatic apatites.

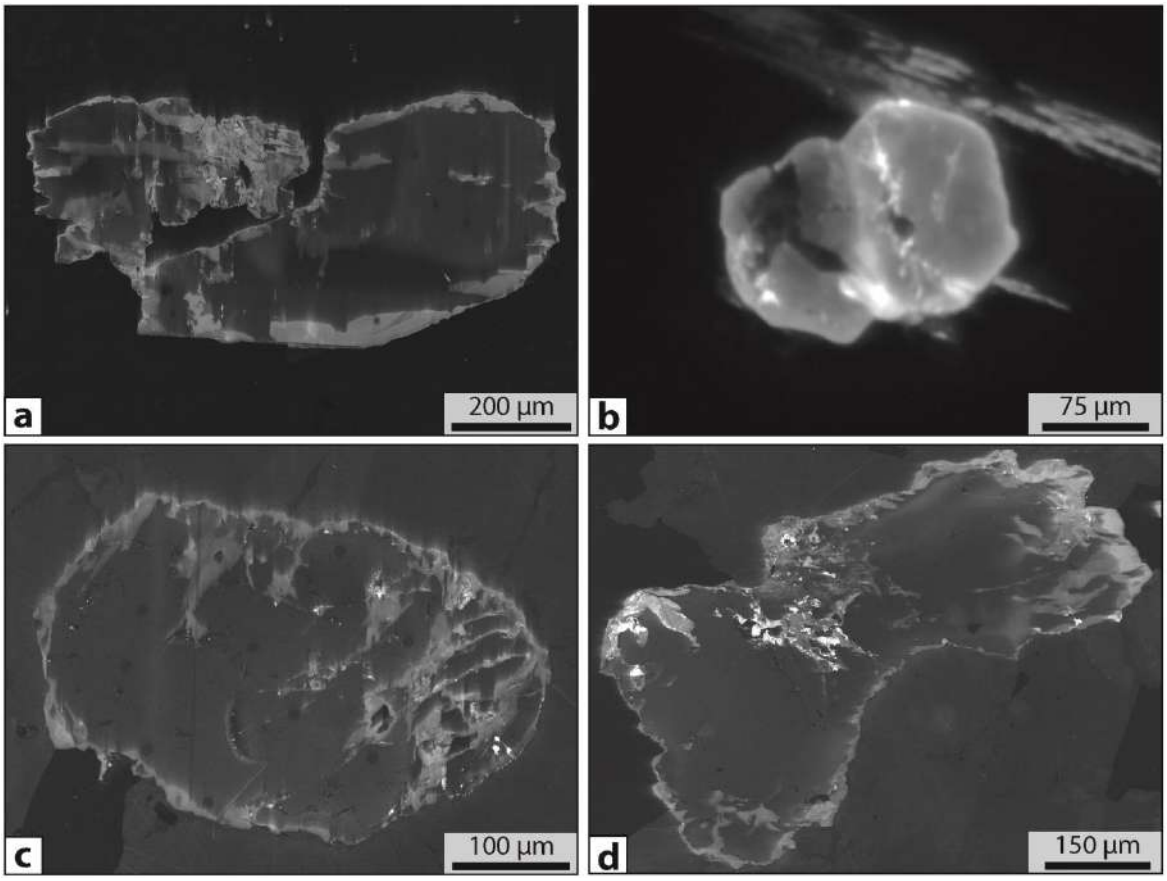

Figure 15 Cathodoluminescence images (CL) of magmatic apatites from the unaltered two-mica granite of Panasqueira. (a) Grain of magmatic apatite included within a phenocryst of albite. This grain was slightly altered along the grain boundaries (lighter zones). (b) Two grains of magmatic apatite with uniform luminescence included within biotite. (c) and (d) Grains of magmatic apatite partially altered along their boundaries (zones with higher luminescence intensity).

1.3.2 Apatite of the massive greisen

During the greisenization of the two-mica granite, the primary magmatic apatites were partially conserved within the massive greisen. Cathodoluminescence images permit to follow the progressive alteration and replacement of these apatites (Fig. 16). When the alteration of these apatites is partial, the primary dark-grey-luminescent apatite was replaced by brighter luminescent secondary apatite along the grain margins and along micro-fracture planes (Fig. 16a). Magmatic apatites most affected by hydrothermal alteration exhibit complex patchy-zoning textures consistent with a strong pervasive alteration (Fig. 16b, 16c and 16d). In these grains, the primary dark-grey-luminescent apatite is practically entirely replaced by the secondary brighter-luminescent apatite. These altered grains were probably re-equilibrated with the greisenizing fluids and thus constitute a good tool to date the greisenization stage. The occurrences of thin oscillatory zoning (hydrothermal overgrowth) that surrounded some altered grains emphasized that a second generation of hydrothermal apatite was formed during the hydrothermal stages (Fig. 16c and 16d). Unfortunately, the U-Pb dating of this second generation of apatite is impossible due to their high content in non-radiogenic lead.

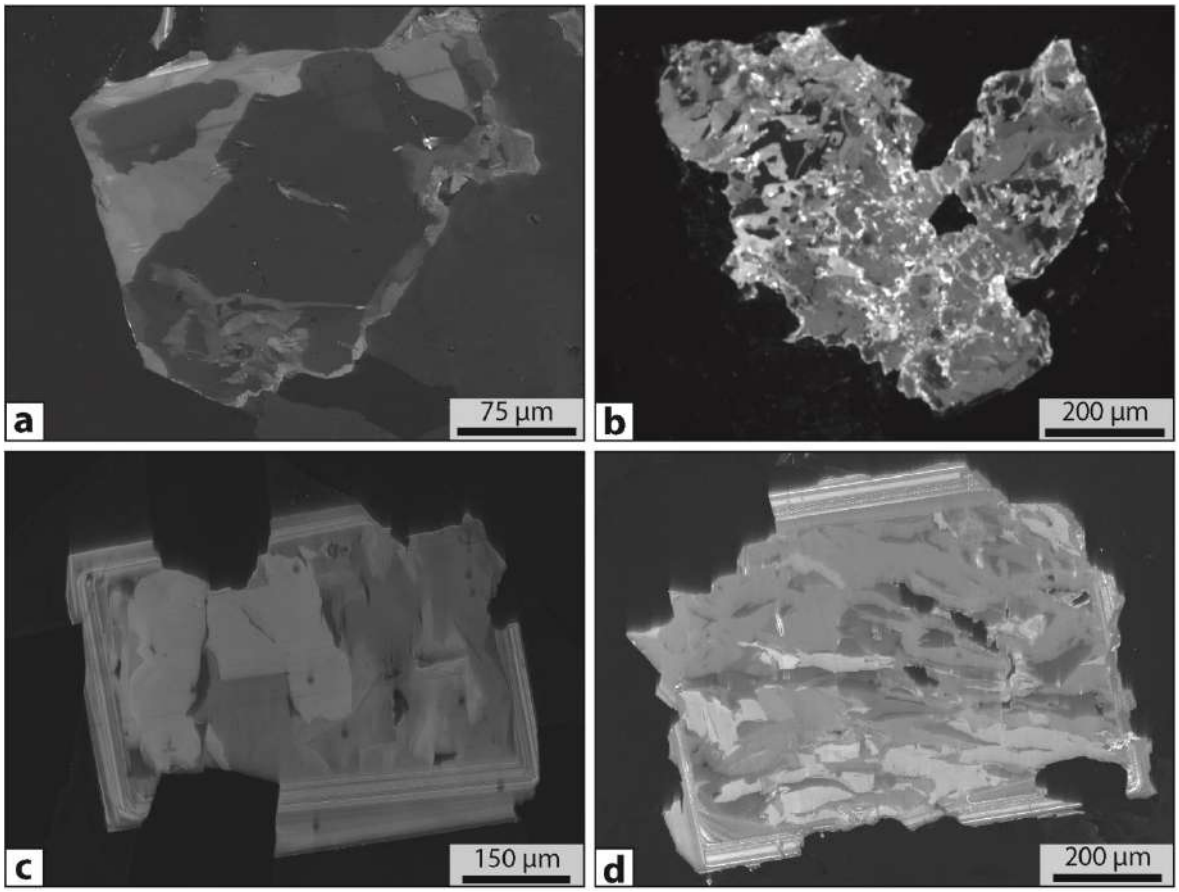

Figure 16 Cathodoluminescence images (CL) of altered magmatic apatites from the massive greisen of Panasqueira. These grains of apatite were altered during the greisenization of the two-mica granite. (a) Grain of magmatic apatite partially altered during the greisenization showing that the dark-luminescent magmatic apatite was replaced by a light-grey luminescent apatite along the grain boundaries. (b) Grain of magmatic apatite strongly and pervasively altered during the greisenization. This grain exhibits typical patchy zoning texture. The dark-luminescent primary apatite is practically entirely replaced by white and dark-grey luminescent secondary apatite. (c) and (d) Grains of primary magmatic apatite altered and replaced by a secondary light-grey-luminescent apatite. These grains are also marked by hydrothermal overgrowths (thin oscillatory zoning) along the grain boundaries.

1.3.3 Apatite of the hydrothermal mineralized veins

As mentioned in **Chapter II; Part III** several generations of apatite can be distinguished in the mineralized veins of Panasqueira. Here we focus our intention on the first generation of apatite whose the crystallization accompanied the formation of the muscovite selvage and marks the early stages of vein formation (MOSS). These hydrothermal apatites occur generally as large euhedral crystals whose the <c> axes have preferentially grew in the vertical direction (Fig. 17a). Cathodoluminescence images of these hydrothermal apatite display oscillatory zoning corresponding to growth bands (Fig. 17b and 17c). In some cases, apatite can be crosscut by sulfide minerals related to the main sulfide stage (MSS) (Fig. 17a). These apatites exhibit patchy zoning textures indicating that apatite was partially or entirely altered and re-equilibrated during the sulfide stage. Consequently, these grains were not considered for the U-Pb dating of hydrothermal apatite.

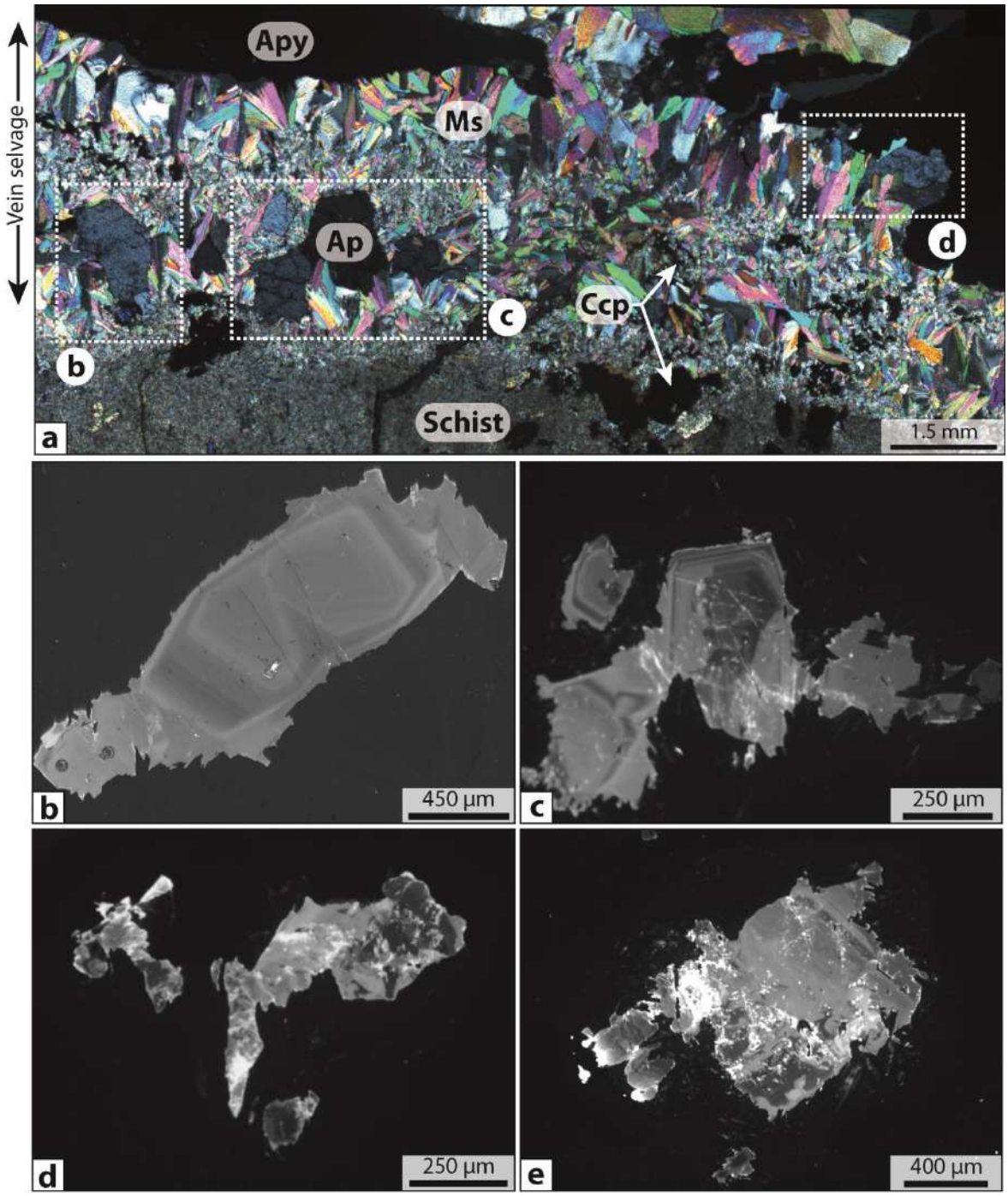

Figure 17 Cathodoluminescence images (CL) of hydrothermal apatites associated to muscovite selvage from mineralized veins of Panasqueira. (a) Photomicrograph (transmitted light) showing textural relationships between apatite and muscovite selvage present along the schist-vein contacts. Some apatites were crosscut by arsenopyrite during the main sulfide stage (MSS). Dashed white rectangles give emplacement of apatite grains displayed in b, c and d. (b) and (c) typical grains of euhedral hydrothermal apatite present within the muscovite selvage. These apatites exhibit growth oscillatory zoning. (d) and (e) Grains of hydrothermal apatite altered during the late mineralization stages (sulfide stage).

2. Whole-rock geochemistry

The whole-rock geochemical characteristics of the two-mica granite, the leucogranite and the massive greisen of Panasqueira are summarized in appendix and plotted in different discriminating diagrams displayed in Figure 18. The entire whole-rock compositions dataset (major and trace element) are given in appendix. The two granite facies belong to rich-phosphorus granites (0.35 to 0.44 wt% in the two-mica granite and 0.2 to 0.76 wt% in the leucogranite) and both exhibit peraluminous compositions, with A/CNK ratio ranging from 1.16 to 1.32 in the two-mica granite and from 1.31 to 1.40 in the leucogranite (Fig. 18a). They exhibit almost the same chondrite-normalized REE patterns marked by (i) enrichment from HREE to LREE and (ii) negative Eu anomalies emphasizing the occurrence of residual feldspars in the rock source, from which granitic melts were produced (Fig. 18b). Accordingly, these granites were probably derived from crustal melting of a rich quartz-feldspar source (like meta-arkoses and par-orthogneiss) containing probably a large amount of phosphorus nodules. The REE pattern of the leucogranite is characterized by lower content in REE than the two-mica granite and by positive anomalies in Tb and Yb that could be related to the occurrences of HREE-bearing phosphate minerals.

The leucogranite seems to be more differentiated than the two-mica granite with higher peraluminosity and lower contents in Fe, Mg, Ti and REE (Fig. 18a to 18d). This suggests a potential magmatic differentiation trend, during which the more evolved leucogranite could derive from the two-mica granite by fractionated crystallization processes. This differentiation trend is consistent with the mineralogical and the textural transition observed from the two-mica granite to the leucogranite in the deeper part of the SCB2 drill-hole. The enrichment of the leucogranite in Sn (65 %), W (36 %), Nb (44 %), Ta (40 %) and Rb (65 %) relative to the two-mica granite (Fig. 18e) is compatible with a progressive magmatic differentiation during which rare metals and incompatible elements were concentrated in the more evolved granite facies. This is confirmed by positive correlation between the whole-rock enrichments in Sn-W and increase of the peraluminosity index (A/CNK) from the two-mica granite to the leucogranite (Fig. 18f and 18g).

The greisenization is accompanied by an evolution trend marked by (i) an increase of the peraluminosity with A/CNK ranging from 1.44 to 2.38, (ii) a relative enrichment in

Al, K, Si, Cs, Rb, Li, Sn, W, Nb and Ta and (iii) a relative depletion in Mg, Ca, Na, Ba, Sr and Eu compared to the unaltered two-mica granite (Fig. 18a, 18c, 18d and 18e). This evolution is consistent with the breakdown of feldspar and biotite composing the two-mica granite and the crystallization of large amount of muscovite during the greisenization. Indeed, the alteration of feldspar has probably released Na, K, Ba, Sr and Eu in fluids, whereas the crystallization of a large amount of muscovite was probably responsible of the enrichment in Li, Rb and Cs, which are efficiently incorporated by muscovite. Consequently, the increase of peraluminosity index (A/CNK) observed during the greisenization reflects directly the progressive replacement of feldspars by muscovite (Fig. 18f and 18g). This increase of peraluminosity is positively correlated with a significant enrichment of the whole-rock in Sn and W suggesting that greisenization of the two-mica granite was probably induced by the circulation of the Sn-W-bearing fluids through the granite roof (Fig. 18f and 18g). The massive greisen exhibits chondrite-normalized REE pattern parallel to those of the original two-mica granite with typical lower REE content than the parental granite (Fig. 18d). This depletion in REE during greisenization processes is commonly described in massive greisen system (Štemprok et *al*., 2005; Müller et *al*., 2018) and can be attributed to the breakdown of accessory minerals hosting REE (like zircon, apatite and monazite).

Figure 18 Whole-rock geochemical characteristics of the two-mica granite, the leucogranite and the massive greisen of Panasqueira. (a) Diagram of aluminous saturation index (A/NK vs. A/CNK) of the different granite facies and the massive greisen of Panasqueira. (b) Chondrite-normalized REE pattern of the two-mica granite, the leucogranite and the massive greisen. (c) and (d) Multicationic discriminating diagrams of Debon & LeFort (1983). (e) Relative mass changes in the leucogranite and the massive greisen compared to the porphyritic two-mica granite (calculated from average values). (f) and (g) Evolution of concentrations in W and Sn in whole-rock as a function of the aluminosity index ratio A/CNK.

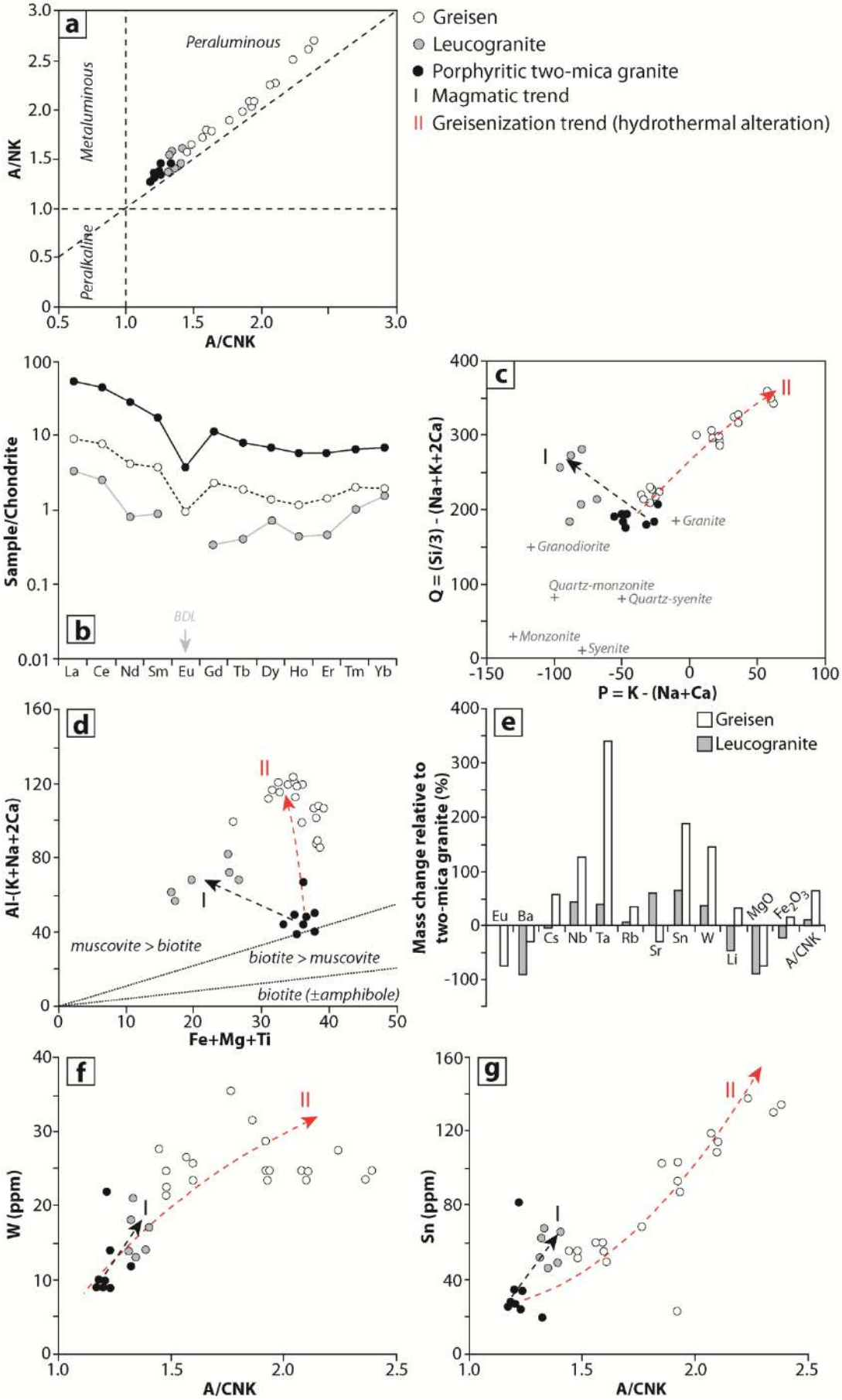
a
Peraluminous
Metaluminous
Peralkaline
A/NK
A/CNK
Greisen
Leucogranite
Porphyritic two-mica granite
I Magmatic trend
II Greisenization trend (hydrothermal alteration)
b
Sample/Chondrite
BDL
La Ce Nd Sm Eu Gd Tb Dy Ho Er Tm Yb
c
Q = (Si/3) - (Na+K+2Ca)
P = K - (Na+Ca)
+ Granite
+ Granodiorite
Quartz-monzonite
+ Quartz-syenite
+ Monzonite
+ Syenite
d
Al-(K+Na+2Ca)
Fe+Mg+Ti
muscovite > biotite
biotite > muscovite
biotite (±amphibole)
e
Greisen
Leucogranite
Mass change relative to two-mica granite (%)
Eu Ba Cs Nb Ta Rb Sr Sn W Li MgO Fe2O3 A/CNK
f
W (ppm)
A/CNK
g
Sn (ppm)
A/CNK

3. Mineral geochemistry

3.1 Muscovite geochemistry

Major and trace elements compositions of muscovite composing the unaltered two-mica granite, the greisenized granite, the massive greisen and the selvages of mineralized veins of Panasqueira are summarized in Table 1 (the entire dataset is available in appendix).

3.1.1 Major element composition of muscovite and thermometric considerations

All white-mica described previously are classified according to the discriminating diagrams of Miller et *al*. (1981) and Monier & Robert (1986) (Fig. 19a and 19b). White-mica composing the unaltered two-mica granite falls in the primary muscovite field (Fig. 18a) and is characterized by compositions close to theoretical muscovite according to the classification of Monier & Robert (1986) (Fig. 18b). Hydrothermal muscovite formed during the greisenization and composing the massive greisen fall in the secondary muscovite field (Fig. 18a) and are characterized by compositions ranging from muscovite to Zinnwaldite (Fig. 18b). As mentioned previously, some muscovite composing greisenized granite and massive greisen are marked by well-developed growth zoning textures. The cores of these muscovites fall in the primary muscovite field and are characterized by compositions close to the primary magmatic muscovite of the two-mica granite, while rims fall in the secondary muscovite field and exhibit almost the same compositions than the secondary hydrothermal muscovite formed during the greisenization by replacement of feldspars and biotite (Fig. 18a and 18b). Accordingly, the rims of this zoned muscovite correspond likely to hydrothermal overgrowth of the primary magmatic muscovite. Like secondary hydrothermal muscovite composing the massive greisen, this overgrowth was formed during the greisenization and hence was equilibrated with greisenizing fluids. Hydrothermal white-mica composing the selvages along the schist-vein contacts are characterized by compositions ranging from muscovite to Zinnwaldite (Fig. 18b).

Binary diagrams displaying the concentrations in Ti, Na, Fe and F as a function of the concentration in Al for the different generation of muscovite show that the primary magmatic muscovite (from the two-mica granite and cores of zoned muscovite) is richer in Al, Ti and Na and poorer in Fe and F than secondary hydrothermal muscovite composing the massive greisen (rims of zoned muscovite and muscovite formed by

replacement of feldspars) (Fig. 18c). This transition from Ti-rich magmatic muscovite to Ti-poor hydrothermal muscovite is consistent with chemical and thermic evolution of magmatic-hydrothermal system, during which muscovite composition was first controlled by hot magmatic processes and then by hydrothermal processes (Luhr et *al*., 1984; Miller et *al*., 1981; White et *al*., 2007; Tartèse et *al*., 2011). This decrease in Ti content in muscovite during the greisenization has been balanced by the addition of Fe and Mg in the octahedral site by the exchange vector (Mg, Fe)-Ti explaining the higher Fe and Mg concentrations in muscovite composing the massive greisen (Table 1 and Fig. 18a and 18b). The higher F content in muscovite composing the massive greisen is consistent with fluid-rock interactions between granitic rocks and acidic F-rich magmatic fluids commonly observed and described in greisen systems (Shcherba, 1970; Ŝtemprok, 1987; Bishop, 1989). Hydrothermal muscovite composing the vein selvages exhibits intermediate compositions between the primary magmatic muscovite of the two-mica granite and the secondary hydrothermal muscovite of the massive greisen (Fig. 18c).

The muscovite geothermometer of Monier & Robert (1986) is based on the phengitic substitution in the solid-solution of dioctahedral micas for temperatures ranging from 300 to 650°C and pressure from 50 to 300 MPa. The primary magmatic muscovite (from the two-mica granite and cores of zoned muscovite) compositions fall mainly in the domain between 600 to 650°C (Fig. 18d). Secondary hydrothermal muscovite formed during the greisenization (rims of zoned muscovite and muscovite formed by replacement of feldspars) provides temperatures mainly bracketed between 400 and 500°C, similar to temperature ranges obtained for muscovite composing the vein selvages (Fig. 18d). This temperature evolution between magmatic and hydrothermal muscovite emphasizes that (i) greisenization processes could occurred during the magmatic-hydrothermal transition, (ii) the formation of the muscovite vein selvages is related to an early stage marked by high temperature conditions (close to magmatic temperature conditions) and (iii) the formations of the muscovite vein selvages was probably sub-contemporaneous to the greisenization.

Figure 19 Geochemical characteristics of muscovite composing the unaltered two-mica granite, the greisenized granite, the massive greisen and the selvages of mineralized veins of Panasqueira. (a) Ternary Ti-Na-Mg diagram displaying the fields of primary and secondary muscovite (after Miller et *al*., 1981). (b) Compositions of muscovite plotted in the mineralochemical phase diagrams (Al-(Fe+Mg+Mn)-Si) of Monier and Robert (1986). (c) Binary diagrams displaying the content in Ti, Na, Fe and F (in apfu) as a function of the content in Al (in apfu) for the different studied muscovite (d) Application of the Monier and Robert (1986) thermometer on the magmatic and hydrothermal muscovite present in the system of Panasqueira.

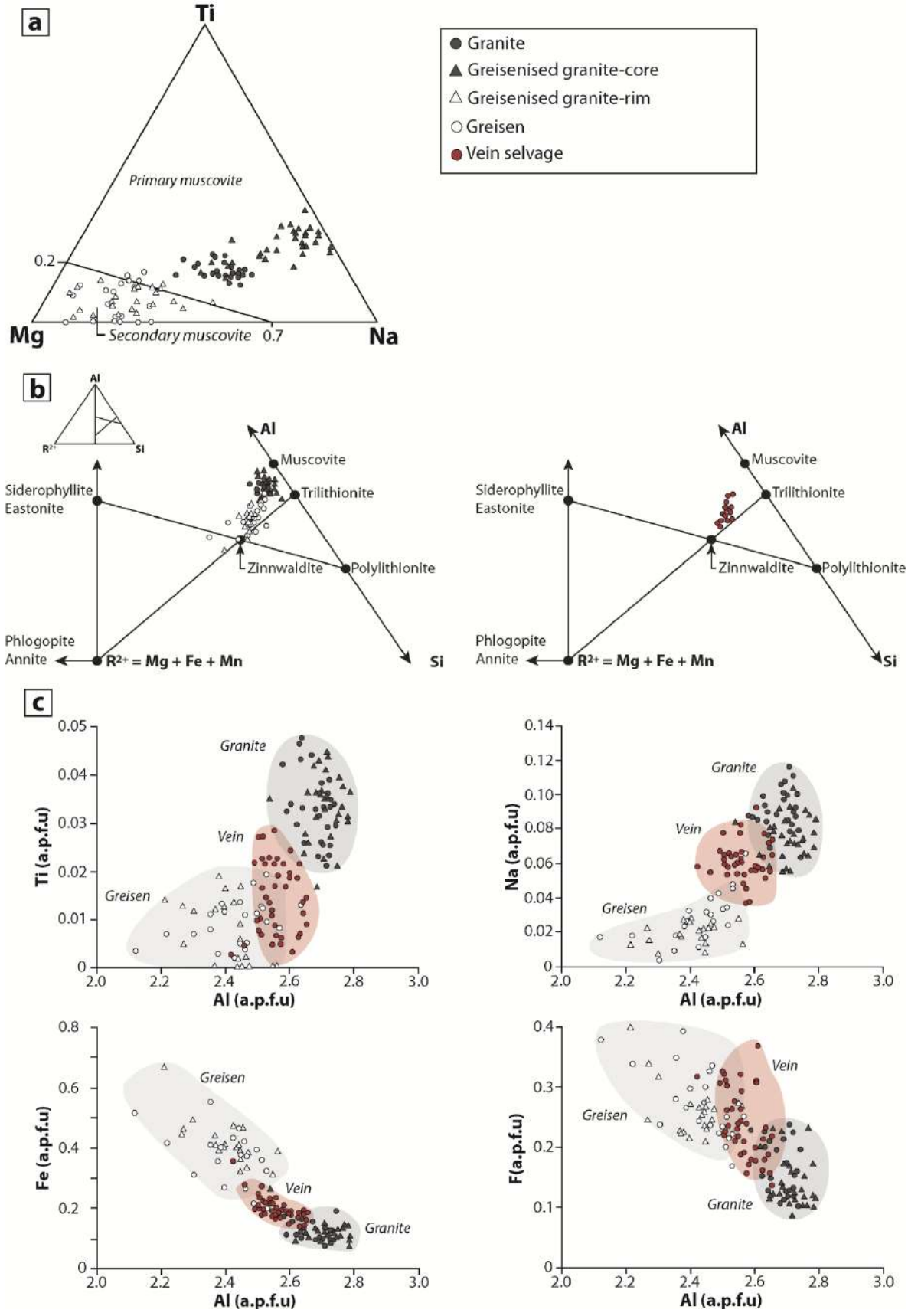
a
Ti
Mg
Na
Primary muscovite
Secondary muscovite
0.2
0.7
Granite
Greisenised granite-core
Greisenised granite-rim
Greisen
Vein selvage
b
Al
R²⁺
Si
Muscovite
Trilithionite
Siderophyllite
Eastonite
Zinnwaldite
Polylithionite
Phlogopite
Annite
R²⁺ = Mg + Fe + Mn
c
Ti (a.p.f.u)
Na (a.p.f.u)
Fe (a.p.f.u)
F(a.p.f.u)
Al (a.p.f.u)
Granite
Vein
Greisen

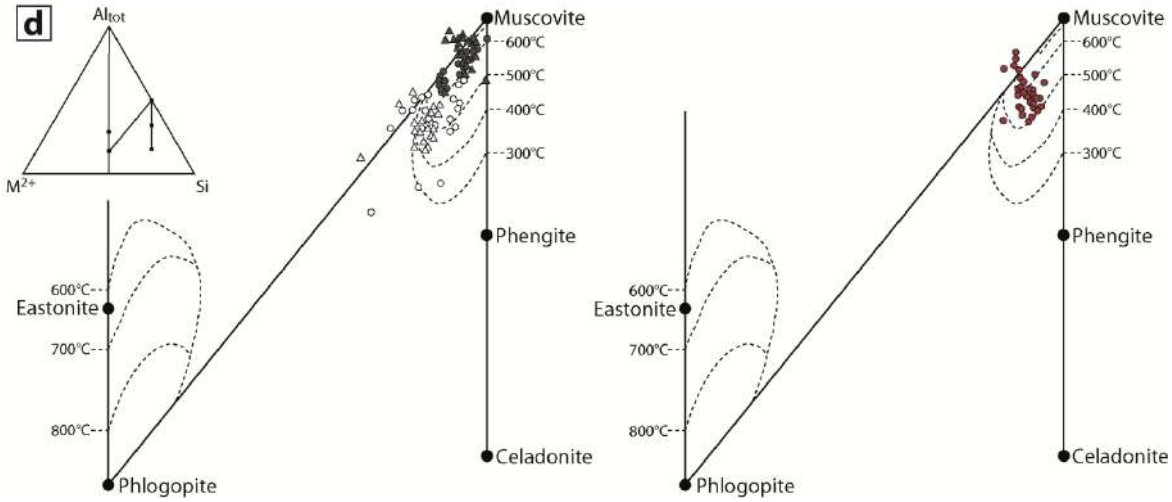
d
Altot
M2+
Si
Muscovite
600°C
500°C
400°C
300°C
Phengite
Celadonite
600°C
Eastonite
700°C
800°C
Phlogopite
Muscovite
600°C
500°C
400°C
300°C
Phengite
Celadonite
600°C
Eastonite
700°C
800°C
Phlogopite

	Magmatic muscovite (two-mica granite)		Muscovite from greisenized granite				Hydrothermal muscovite (massive greisen)		Hydrothermal muscovite (vein selvages)	
			core		rim					
wt%	**Ave (n =28)**	**Stdev**	**Ave (n =31)**	**Stdev**	**Ave (n =21)**	**Stdev**	**Ave (n =24)**	**Stdev**	**Ave (n =41)**	**Stdev**
SiO_2	45.64	0.69	45.56	0.68	44.36	1.42	45.64	1.44	45.17	1.83
TiO_2	0.66	0.14	0.66	0.13	0.14	0.13	0.20	0.10	0.28	0.14
Al_2O_3	33.92	0.79	34.17	0.85	29.14	0.88	29.89	1.88	31.65	1.18
FeO	2.15	0.49	2.24	0.60	7.28	1.35	6.35	2.29	3.57	0.69
MnO	0.05	0.05	0.04	0.05	0.14	0.09	0.18	0.09	0.08	0.06
MgO	0.69	0.14	0.18	0.15	0.67	0.17	0.79	0.27	0.83	0.17
CaO	0.00	0.01	0.01	0.02	0.01	0.02	0.02	0.04	0.00	0.01
Na_2O	0.70	0.10	0.58	0.09	0.15	0.05	0.24	0.15	0.46	0.08
K_2O	10.22	0.28	10.03	0.32	9.86	0.36	9.93	0.47	9.71	0.85
P_2O_5	0.05	0.06	0.13	0.25	0.01	0.03	0.04	0.06	0.03	0.04
Cl	0.18	0.39	0.01	0.01	0.01	0.01	0.01	0.02	0.01	0.01
F	0.64	0.37	0.69	0.2	1.19	0.21	1.28	0.30	1.11	0.26
OH	4.12	0.08	4.13	0.1	3.71	0.12	3.76	0.16	3.84	0.18
Total	99.02		98.42		96.67		98.10		96.75	
ppm	**Ave (n =16)**	**Stdev**	**Ave (n =14)**	**Stdev**	**Ave (n =16)**	**Stdev**	**Ave (n =16)**	**Stdev**	**Ave (n =15)**	**Stdev**
Li	672	395	754	277	1853	853	2705	540	1715	144
Cs	49	20	80	20	190	35	223	50	138	14
Rb	981	456	1720	278	3155	287	3836	741	2677	257
Zn	108	35	115	19	262	36	321	115	196	24
Ba	28	14	33	23	321	88	168	52	396	76
Nb	18	14	112	34	44	16	117	64	63	15
Ta	5	5	82	28	43	16	32	26	21	8
Sn	60	28	62	17	346	112	332	103	292	35
W	11	10	28	4	31	10	48	19	99	18

Table 1 Average compositions in major (wt%) and trace elements (ppm) of muscovite composing the unaltered two-mica granite, the greisenized granite, the massive greisen and the selvages of mineralized veins of Panasqueira.

3.1.2 Trace element composition of muscovite

It has been proposed that trace element variations in muscovite permit to track the chemical evolution of melt and fluids from which muscovite have crystallized (Alfonso et *al*., 2003; Hulsbosch et *al*., 2014; Legros et *al*., 2016). Accordingly, processes of magmatic differentiation and magmatic-hydrothermal transition can be track from trace element compositions of muscovite. Due to its incompatible behavior and its mobility in fluids, Rb concentration in muscovite was chosen as the reference parameter to (i) plot the trace element concentrations in muscovite and (ii) characterize behavior of trace elements during the magmatic-hydrothermal evolution of Panasqueira (Fig. 20).

Figure 20 shows that Rb concentrations in muscovite increase significantly during the greisenization, with average concentration increasing from 981 ppm in primary magmatic muscovite to 3835 ppm in hydrothermal muscovite of the massive greisen. This muscovite enrichment in Rb during greisenization is accompanied by significant increase in Cs (from 49 to 223 ppm), Li (from 671 to 2705 ppm), Zn (107 to 321 ppm) and Sn (from 60 to 332 ppm) concentrations and, to a lesser extent, by increase in W concentration (from 11 to 48 ppm) (Fig. 20). The crystallization of a large amount of muscovite enriched in Li, Cs, Rb, Sn and W in the massive greisen explains the progressive whole-rock enrichment in these elements during the greisenization. Accordingly, the greisenization was probably related to fluid-rock interactions between the two-mica granite and mineralizing fluids rich in metals (Sn, W and Zn) and granitophils elements (Cs, Rb and Li). Furthermore, these results suggest potential implication of magmatic fluids, in which incompatible elements and metals were accumulated during the granite crystallization triggering the greisenization of the granite roof.

Hydrothermal muscovite composing the vein selvages exhibits (i) intermediate concentrations in Li, Cs, Zn and Rb between the primary magmatic muscovite and the secondary hydrothermal muscovite of the massive greisen, (ii) the same compositional ranges in Sn than hydrothermal muscovite of the massive greisen and (ii) higher concentrations in W (between 56 and 136 ppm) than hydrothermal muscovite composing the massive greisen (Fig. 20). At the light of these results, the formation of muscovite selvage observed in veins could be related to fluid mixing between (i) a magmatic fluids rich in metals (Sn, W and Zn) and granitophil elements (Rb, Cs, Li) responsible of the greisenization and (ii) an external fluids poor in metals and incompatible elements leading

to the dilution of magmatic fluids explaining the intermediate compositions of these muscovite.

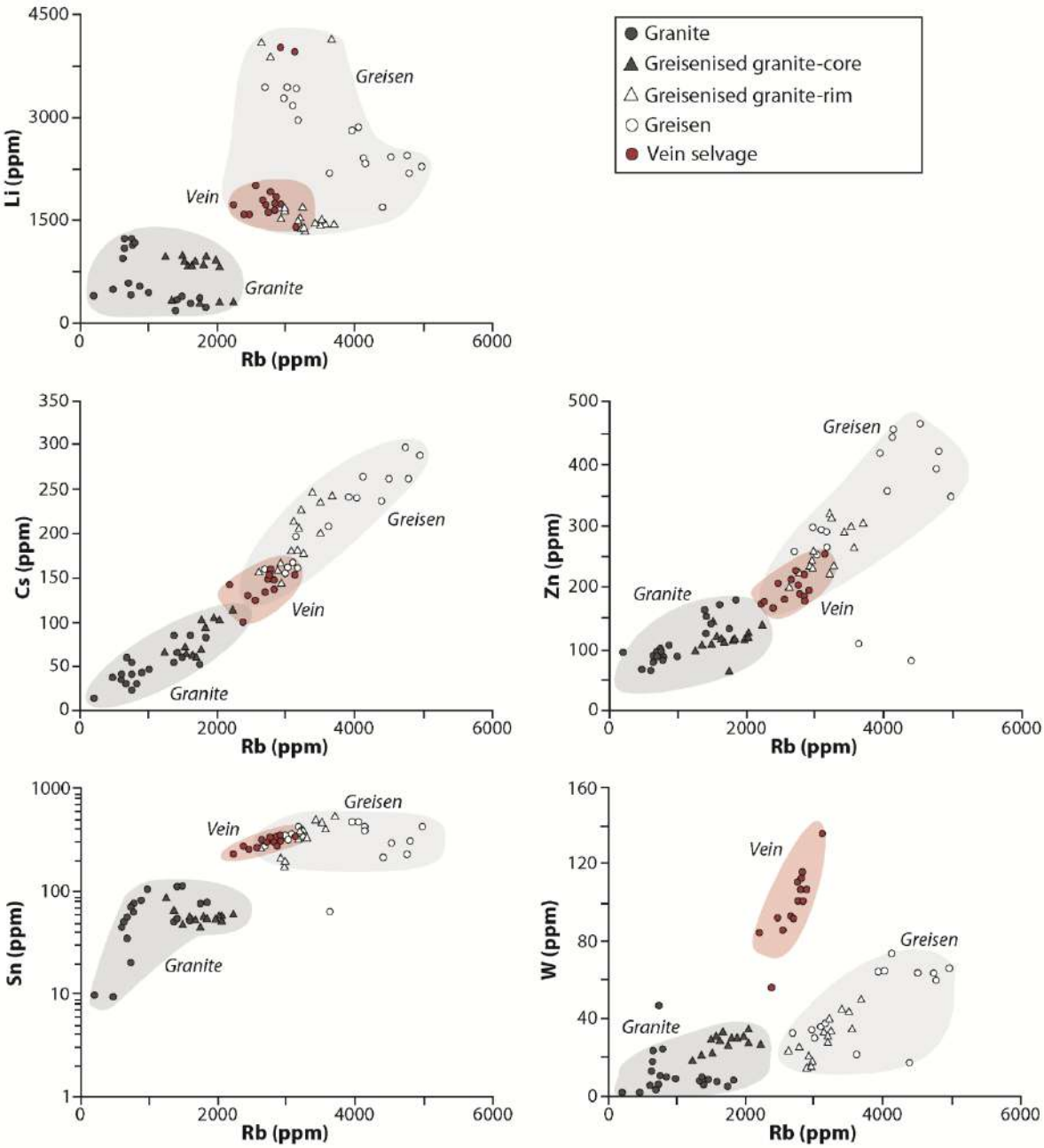

Figure 20 Binary diagrams displaying the trace element content for the different generations of muscovite considered in this study. The concentration (in ppm) of Li, Cs, Zn, Sn and W are plotted as a function of the concentration in Rb.

3.2 Rutile compositions

Due to its structure that can accommodate substitutions with a wide variety of elements (HFSE, Fe, Mn, Cr, V, Sb, U, Sn, Nb, Ta and W), rutile can provide significant information about processes involved during the formation of magmatic-hydrothermal ore deposits (Smith and Perseil, 1997; Rice et *al*., 1998; Zack et *al*., 2002; Clark and Williams-Jones, 2004; Triebold et *al*., 2007; Meinhold, 2010). As previously described, a first generation of rutile can be observed in the unaltered two-mica granite and a second in the massive greisen. To constrain the geochemical characteristics of fluids involved during the greisenization, these different generations of rutile were analyzed by EPMA. The compositions of rutile are summarized in Table 2 and displayed in Figure 21 (the complete dataset of rutile analyses is available in appendix).

SEM image displayed in Figure 21a shows that rutiles formed during the greisenization are characterized by complex sector zoning marked by black and white zones. In the chemical map of W these white zones are characterized by higher concentrations in W than black zones (Fig. 21b). Compositions of rutile from the unaltered two-mica granite, the greisenized granite and the massive greisen of Panasqueira are plotted in ternary Fe-Ti-Sn and Fe-Ti-W diagrams displayed in Figure 21c. Magmatic rutile of the two-mica granite displays low content in Sn, W, Nb and Ta and relatively high content in Fe (up to 3.7 wt%) (Table 2). Conversely, rutiles formed during the greisenization are marked by a progressive enrichment in Sn (up to 0.3 wt%), W (up to 4 wt%), Nb (up to 2.5 wt%) and Ta (up to 1 wt%) that define evolution trends in the ternary diagrams (Fig. 21c). Except for W and Fe there is little compositional difference between the sectors zones observed in SEM images (Table 2). Overall our results suggest that rutile formed during the greisenization were equilibrated with Sn-W rich fluids and hence that greisenization could be related to the circulation of mineralizing fluids through the apical portion of the two-mica granite. This is consistent with mineralogical observations and chemical evolution of muscovite described previously.

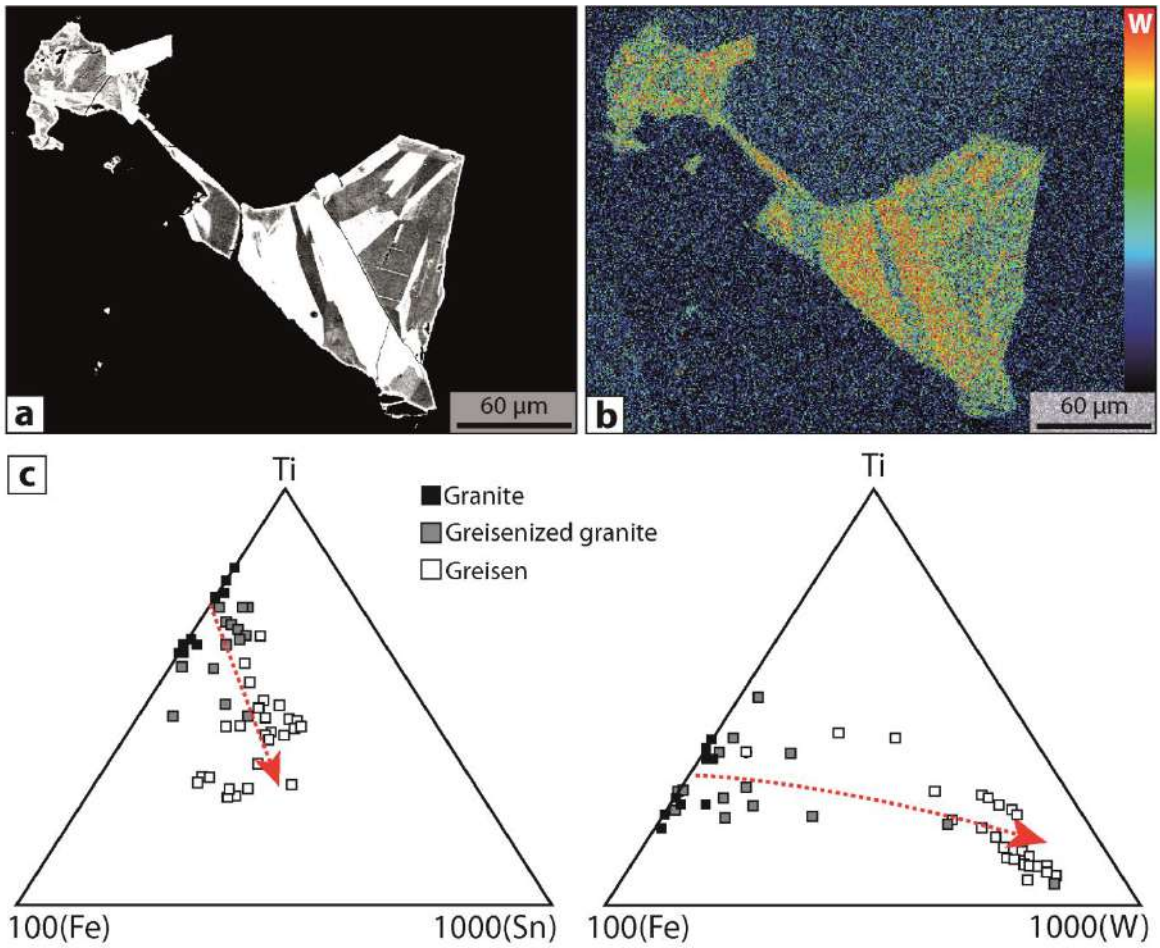

Figure 21 Evolution of the chemical characteristics of rutile during greisenization. (a) SEM photomicrograph of rutile formed during the greisenization. (b) Chemical map of W in the grain of rutile displayed in b. (c) Ternary diagrams displaying the content in Fe, Ti, Sn and W in rutile composing the unaltered two-mica granite, the greisenized granite and the massive greisen of Panasqueira.

	Unaltered two-mica granite		Greisenized granite		Massive greisen			
					Black zones		White zones	
wt%	Ave (n = 11)	Stdev	Ave (n = 15)	Stdev	Ave (n = 14)	Stdev	Ave (n = 13)	Stdev
TiO_2	96.86	0.78	96.11	1.58	98.22	0.87	95.45	0.97
MnO	0.25	0.47	0.01	0.01	0.01	0.01	0.01	0.02
FeO	2.10	0.82	1.91	0.61	0.78	0.29	1.48	0.34
Nb_2O_5	0.17	0.05	0.91	0.65	0.53	0.24	0.96	0.17
SnO_2	0.00	0.00	0.05	0.03	0.12	0.04	0.16	0.04
Ta_2O_5	0.02	0.02	0.18	0.13	0.17	0.26	0.39	0.20
WO_3	0.01	0.02	0.68	1.41	0.69	0.36	2.35	0.63

Table 2 Average compositions (wt%) of rutile composing the unaltered two mica granite, the greisenized granite and the massive greisen of Panasqueira.

3.3 Quartz chemistry

3.3.1 Chemical zoning in magmatic snowball quartz

As described previously, snowball quartz grains present in the unaltered two-mica granite of Panasqueira are characterized by typical growth zoning (Fig. 22). These zones can be also highlighted from chemical maps of Ti, Li and B that depict (i) core to rim depletion in Ti and Li and (ii) core to rim enrichment in B (Fig. 22). This type of chemical zoning in snowball quartz has been described in detail in late Variscan granites of central and Western Europe by Müller et *al*. (2010) and is coherent with a progressive differentiation of the granite intrusion. Indeed, it is generally admitted that Ti content in quartz depends directly on temperature conditions (Müller et *al*., 2002; Larsen et *al*., 2009; Müller et *al*., 2010; Thomas et *al*., 2010; Breiter et *al*., 2017). Accordingly, the core to rim depletion in Ti observed in our study suggest that snowball quartz have recorded the progressive cooling and differentiation of the granite intrusion. Conversely, B is incompatible and preferentially accumulated in residual melt and magmatic fluids leading to enrichment of quartz in B during the late magmatic stages explaining the core to rim enrichment in B observed in Figure 22 (Müller et *al*., 2010). The Li evolution trend in quartz is more difficult to discuss due to the occurrence of a large amount of mica that may incorporate a large amount of Li and affect directly the Li content in quartz. Here, the core to rim depletion in Li observed in snowball quartz can be related to the crystallization of a large amount of muscovite and biotite that buffered the Li content in quartz. Finally, these qualitative results emphasize that the chemical evolution of magmatic snowball quartz can permit to track the cooling and the differentiation processes of the granite intrusion.

Figure 22 SEM-CL image and chemical maps of Ti, Li and B of a snowball quartz grain composing the unaltered two-mica granite. The chemical maps were performed by LA-ICP-MS following the same analytical procedure described in the subsection *5.2*.

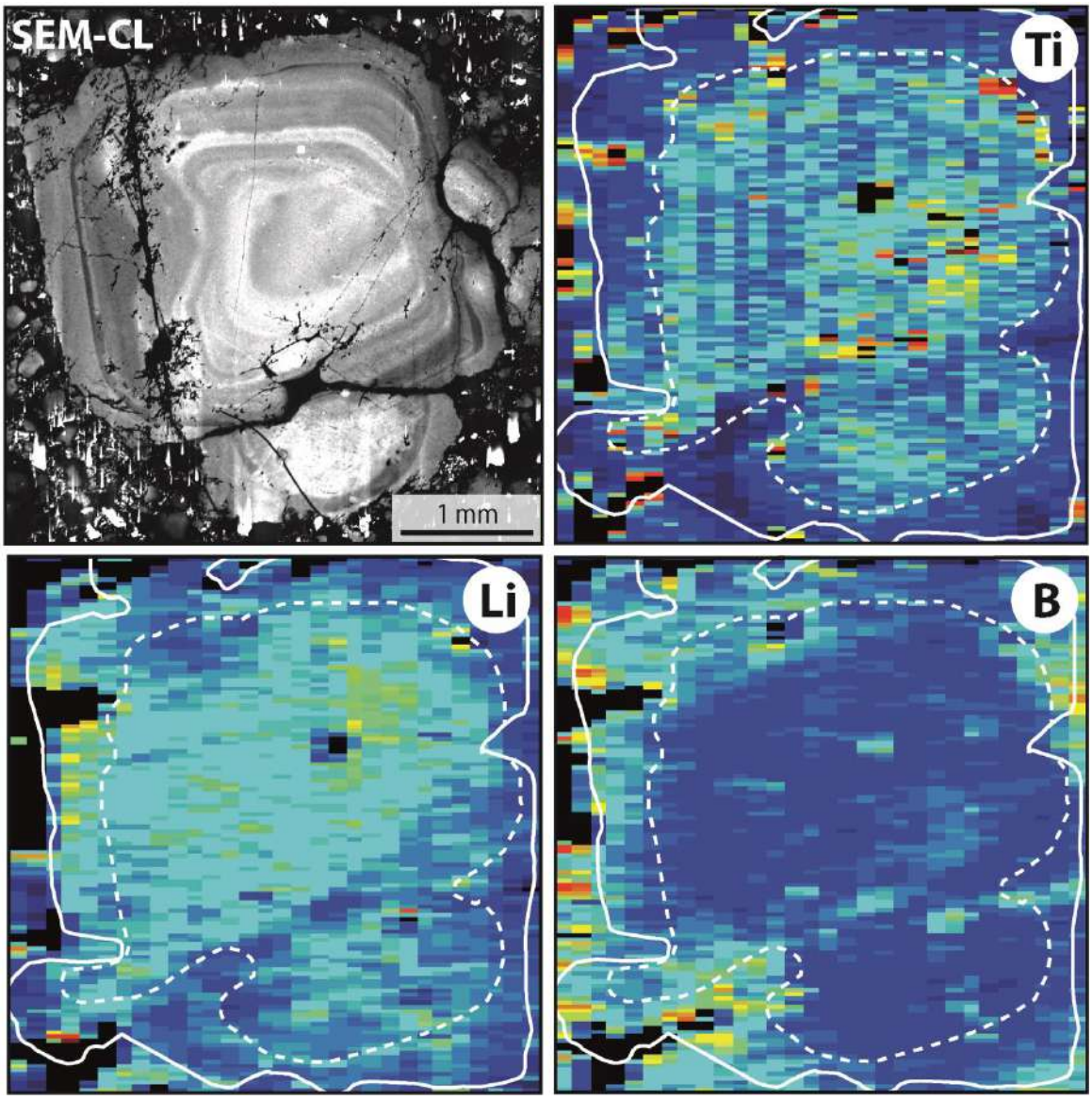

3.3.2 Chemical zoning in snowball quartz affected by greisenization

Despite the greisenization, snowball quartz grains of the two-mica granite can be conserved in greisenized facies and within the massive greisen of Panasqueira. To determine potential chemical evolution between the primary magmatic snowball quartz and the hydrothermal overgrowth (related to greisenization processes) described previously, we have performed compositional profiles (Ti, Al, Na, Li, B and Ge). These profiles and the CL image of the analyzed grain are displayed in Figure 23. These profiles exhibit clearly depletion in Ti, Al, Li and enrichment in Na, B and Ge from the magmatic snowball quartz grain toward the hydrothermal overgrowth (Fig. 23). As shown before, the magmatic snowball quartz exhibits also chemical zoning that can be also observed in compositional profiles (Fig. 23). Indeed, the snowball quartz grain displays slight core to rim depletion in Ti and Li and core to rim enrichment in B. The progressive depletion in Ti, Li and Al from core of snowball quartz to hydrothermal overgrowth is consistent with magmatic-hydrothermal evolution, in which composition of quartz was first controlled by magmatic processes (like cooling and differentiation) and then by hydrothermal processes like greisenization. The enrichment in Na, B and Ge from snowball quartz to hydrothermal overgrowth suggests that the greisenization could be induced by the releasing and the circulation of magmatic fluids enriched in incompatible elements (Ge and B) and expelled during the final stage of the granite crystallization. As a result the compositional evolution of quartz during the greisenization can permit to follow and track the magmatic-hydrothermal transition within the granite intrusion.

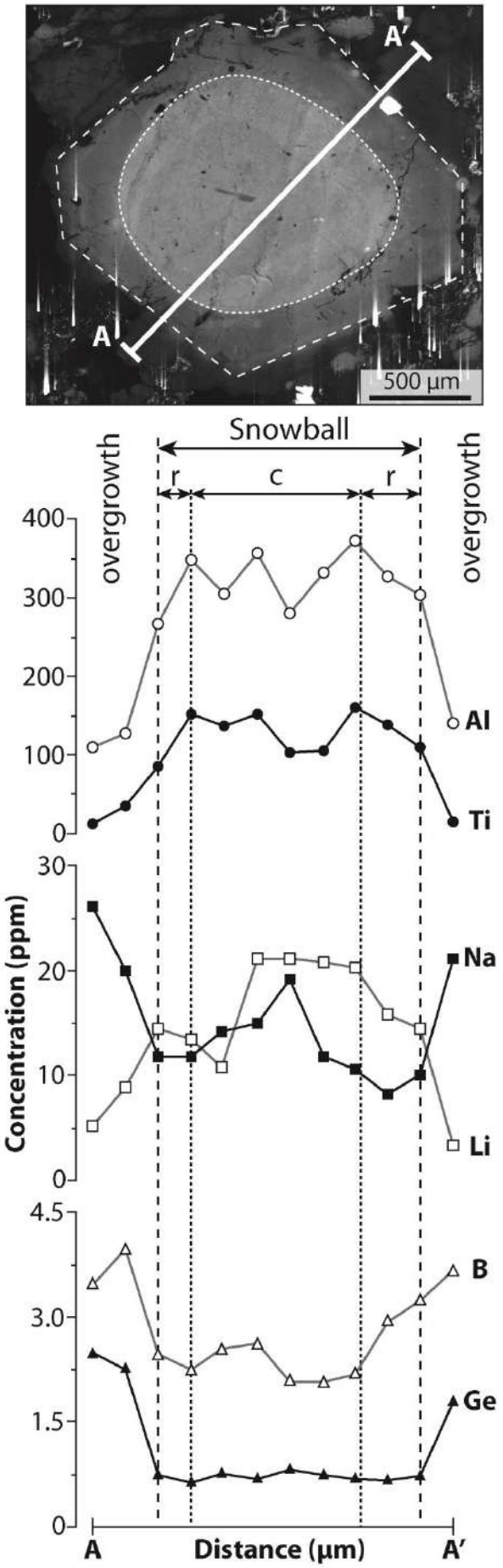

Figure 23 SEM-CL image and compositional profiles (Al, Ti, Na, Li, B and Ge) performed across a representative grain of snowball quartz overprinted by the greisenization (overgrowth). Abbreviations, c: core and r: rim.

3.3.3 Chemical characteristics of the different generations of quartz

Li, Be, B, Na, Al, S, Ti, Ge, As, Rb, Sr, Nb, Sn, Sb, Ta and W were analyzed for the different quartz generations considered in this study. Trace elements contents in these quartz are summarized in Table 3 and 4 and reported as spider diagrams (Fig. 24) (the complete dataset is available in appendix). Although the main part of analyzed elements was generally detected for all quartz, the concentrations in Be, Nb, Ta, Sn and W were often close to their detection limits (0.05 ppm for Be and 0.01 ppm for the other). Al, Li, Ti, Na and S are the most abundant elements (several tens to several hundred of ppm) in all quartz generations. Light elements like Ge and B were also significantly detected (up to several tens of ppm) in all quartz, whereas heavy elements contents (from As to W) are generally lower and more scattered. This is probably due to the fact that concentrations of these elements are generally close to detection limits (Fig. 24). Nb and Ta were generally not detected and hence are not considered to discriminate the different quartz generations. Al, Ti and Rb depict peaks specific of magmatic quartz, while Ge, B, As and W are generally enriched in hydrothermal quartz composing both greisen and mineralized veins (Fig. 24).

Quartz from the unaltered two-mica granite: Cores of magmatic snowball quartz are characterized by high contents in Ti (> 136 ppm), Al (> 295 ppm) and Li (> 10 ppm) and low content in B (< 3.4 ppm) and Ge (< 0.9 ppm). As previously highlighted from chemical maps and compositional profiles, snowball quartz are generally marked by slight core to rim enrichments in Ge (from 0.6 to 1.1 ppm), B (from 2.1 to 4.2 ppm) and Na (from 14 to 22 ppm) and by slight core to rim depletion in Ti (from 183 to 64 ppm), Li (from 23 to 13 ppm), Al (from 408 to 263 ppm) and Rb (from 2.2 to 1 ppm) (values refer to median values for cores and rims). These rims exhibit also highly variable concentrations in Be, As, Rb, Sr, Nb, Sn, Sb and W. Quartz composing the granite matrix are characterized by the same median concentrations in trace elements than rims of snowball quartz (Table 3). Accordingly, these two populations of quartz have probably crystallized sub-contemporaneously and later than cores of snowball quartz.

Quartz from the massive greisen: Snowball quartz conserved in greisen exhibit the same spider diagram pattern and are characterized by the same compositional ranges than snowball quartz of the unaltered two-mica granite (Fig. 24). Indeed they exhibit the same typical peaks in Ti, Al and Rb previously described in magmatic quartz with almost the

same median values of concentrations. This suggests that despite the strong fluid-rock interactions related to the greisenization, the primary magmatic signature of snowball quartz was conserved in greisen, in which a large amount of secondary and recrystallized quartz were formed during the greisenization. Hydrothermal overgrowth of these snowball quartz are characterized by a spider diagram pattern significantly different than magmatic snowball quartz, with lower content in Ti (< 36 ppm), Al (< 140 ppm) and Rb (< 1.2 ppm) and higher content in Ge (> 1.8 ppm), B (> 3.1 ppm) and Na (> 20 ppm). Euhedral quartz from the greisen porosity exhibits the same signature than (i) neoformed quartz composing the greisen matrix and (ii) hydrothermal overgrowth of snowball quartz (Fig. 24). Indeed, these different generations of quartz are marked by (i) the absence of peaks in Ti and Rb, (ii) highly variable concentrations in As, Rb, Sr, Nb, Sn, Sb and W and (iii) higher contents in B, Na and Ge compared to magmatic quartz. Accordingly, quartz formed during the greisenization by (i) feldspars and biotite replacement, (ii) overgrowth of snowball quartz and (iii) porosity infilling were formed and equilibrated with the same hydrothermal fluid.

Quartz from the mineralized veins: Hydrothermal quartz from mineralized veins related to the quartz-tourmaline (QTS) and the W-Sn mineralization stages exhibit signatures clearly different than those of magmatic quartz and close to signatures of hydrothermal quartz from greisen, with (i) absence of Ti and Rb peaks, (ii) lower contents in Al, Ti and Li and (iii) higher contents in Ge, B and Na than magmatic quartz. However, median As and B concentrations in hydrothermal quartz from veins (from 1.6 to 2.5 ppm for As and from 4.9 to 6.6 ppm for B) are significantly higher than those of hydrothermal quartz from greisen (from 0.08 to 0.29 ppm for As and from 3.8 to 4.2 ppm for B). Although quartz formed during the W-Sn mineralization stage has globally similar chemistry to quartz formed during the QTS, they are characterized by lower median concentrations in B, Al and Ti and higher median concentrations in Na than quartz of the QTS. Despite highly variable concentrations, W content in hydrothermal quartz from veins (up to 5.8 ppm) and greisen (up to 3.5 ppm) seem to be higher than in magmatic quartz (up to 1.7 ppm).

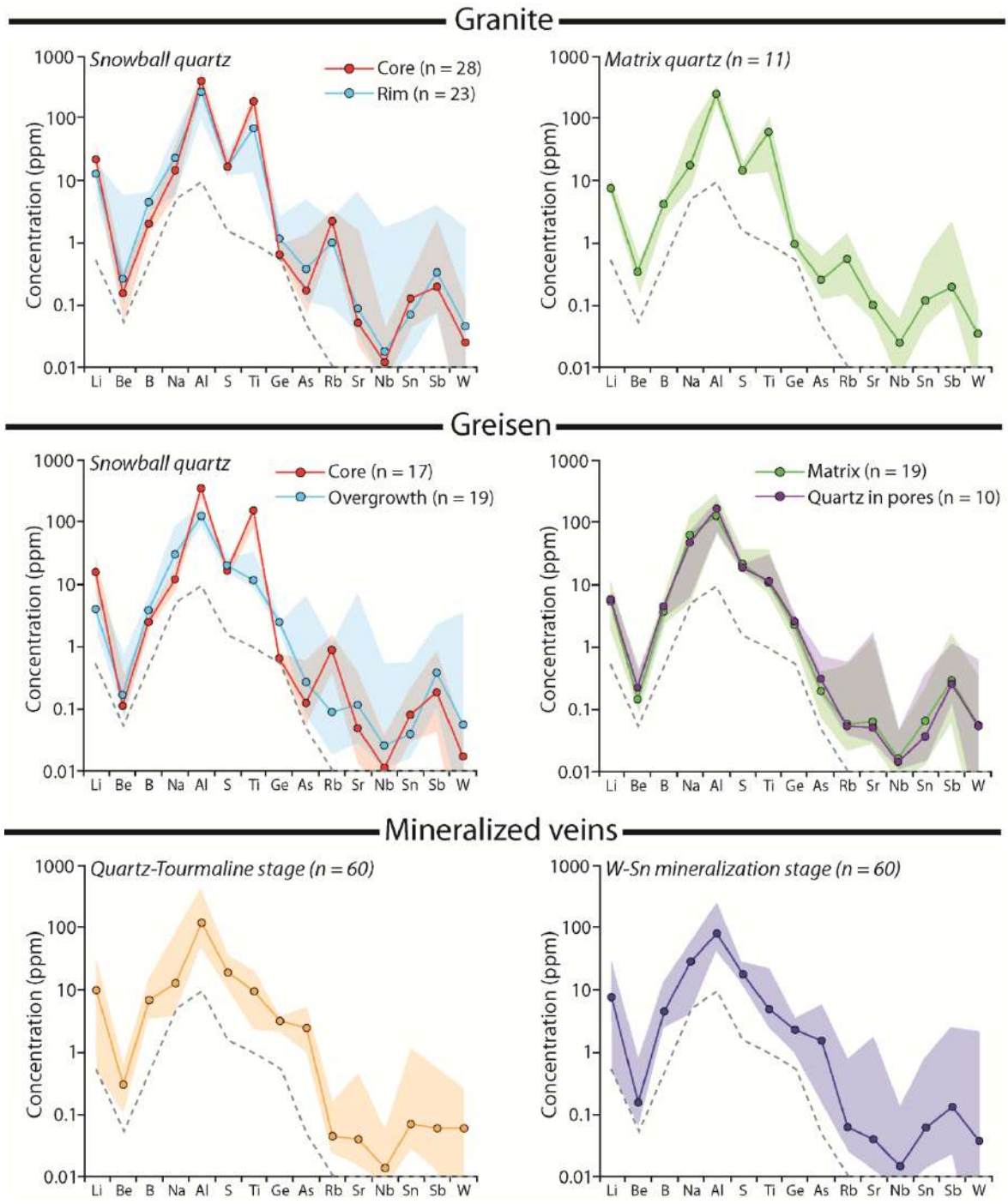

Figure 24 Spider diagrams displaying trace element contents in the different generations of quartz considered in this study. The grey dashed line corresponds to the detection limit. Color lines correspond to median values for each quartz generation. Color domains were defined from maximal and minimal concentrations for each element.

	Unaltered two-mica granite									Massive greisen											
	Snowball quartz						Quartz from granite matrix (n = 11)			Snowball quartz conserved in greisen						Quartz from greisen matrix (n = 19)			Quartz from greisen porosity (n = 10)		
	Core (n = 28)			Rim (n = 23)						Core (n = 17)			Overgrowth (n = 19)								
	Med	Min	Max	Med	Min	Max	Med	Min	Max	Med	Min	Max	Med	Min	Max	Med	Min	Max	Med	Min	Max
Li	23.3	10	32.8	12.6	4.8	17.9	7.6	6.1	10.1	15.2	8.2	24.1	4.0	1.7	9	5.8	1.7	11.4	5.6	3.3	7.3
Be	0.15	0.1	0.3	0.25	0.1	5.6	0.35	0.16	0.50	0.11	0.08	0.32	0.16	0.08	0.76	0.14	0.09	0.35	0.22	0.13	0.4
B	2.1	1.5	3.4	4.2	3.2	6.6	4.3	2.7	5.5	2.4	2	3.2	3.9	3.1	7.5	3.8	2.5	7.5	4.2	2.9	5.3
Na	14.1	6.1	33.9	22	5.7	57.6	18.6	8.9	71.8	11.9	8.2	19.3	30.8	20.3	91.9	66.6	5.5	138.2	47.8	6.1	75.7
Al	408.7	295.6	557.5	263.5	102.5	386.7	253.5	194.9	356.9	352	254.9	384.6	127.7	98	193.5	137.7	70.9	300.1	159.9	71.9	216.5
S	16.5	11.5	22.1	15.7	12.2	27.8	15.1	13.2	20.3	15.1	12.5	18.4	19.3	16.3	27.1	21.3	16.2	38.5	18.5	16.4	20.8
Ti	183.3	136.2	278.5	64.5	13.3	122.7	64.3	15.1	112.7	138.5	82.9	170.1	11.7	9.2	35.9	10.9	7.5	38.9	11.1	9.2	29.9
Ge	0.6	0.5	0.9	1.1	0.77	2.5	0.96	0.76	1.6	0.69	0.56	0.80	2.5	1.8	2.7	2.3	1.2	2.8	2.5	1.5	2.8
As	0.2	0.1	1.3	0.35	0.12	4.9	0.25	0.13	0.62	0.12	0.06	0.59	0.27	0.08	6.8	0.19	0.07	0.4	0.29	0.15	0.68
Rb	2.2	1.1	3.3	1.03	0.09	2.3	0.57	0.15	1.5	0.89	0.38	1.5	0.08	0.02	1.2	0.06	0.02	0.5	0.05	0.04	0.56
Sr	0.05	0.02	1.5	0.09	0.4	6.5	0.10	0.06	0.19	0.05	0.01	0.36	0.11	0.03	7.5	0.06	0.03	1.4	0.05	0.03	1.6
Nb	0.01	0.01	0.04	0.02	<0.01	1.7	0.03	<0.01	0.06	0.01	<0.01	0.04	0.03	0.01	0.55	0.02	<0.01	0.04	0.01	0.01	0.05
Sn	0.12	0.04	0.3	0.06	0.01	2.4	0.12	0.05	0.63	0.08	0.03	0.20	0.04	0.02	0.56	0.07	0.01	0.22	0.04	0.01	0.39
Sb	0.20	0.08	2.4	0.32	0.07	4.0	0.19	0.12	2.4	0.18	0.04	0.84	0.39	0.11	2.4	0.29	0.06	1.7	0.24	0.13	1.17
Ta	<0.01	<0.01	0.01	<0.01	<0.01	1.3	0.01	<0.01	0.04	<0.01	<0.01	<0.01	<0.01	<0.01	0.16	<0.01	<0.01	0.03	<0.01	<0.01	<0.01
W	0.03	0.01	0.12	0.04	<0.01	1.7	0.04	0.01	0.09	0.02	<0.01	0.04	0.35	0.07	3.5	0.05	<0.01	0.31	0.05	0.01	0.61

Table 3 Summary of trace elements composition for quartz composing the unaltered two-mica granite and the massive greisen of Panasqueira

	Quartz-Tourmaline stage (n = 60)			W-Sn mineralization stage (n = 60)		
	Med	**Min**	**Max**	**Med**	**Min**	**Max**
Li	9.9	11.1	31.5	7.8	0.15	28.1
Be	0.30	0.3	0.6	0.14	0.06	0.74
B	6.6	6.7	13.8	4.9	2.5	13.4
Na	12.2	16.5	84.1	27.2	4.3	64.2
Al	130.5	178.8	453.1	88.9	43.6	258.2
S	18.5	20.1	36.7	17.9	12.8	29.7
Ti	9.6	9.9	20.5	4.7	2.7	21.9
Ge	2.9	2.9	3.6	2.4	0.99	3.4
As	2.5	2.3	5.6	1.6	0.16	6.0
Rb	0.04	0.03	0.15	0.06	0.03	0.72
Sr	0.04	0.02	0.45	0.04	0.01	1.7
Nb	0.01	<0.01	0.05	0.01	<0.01	0.13
Sn	0.07	0.03	1.2	0.06	0.01	0.88
Sb	0.06	0.01	0.23	0.12	0.02	2.5
Ta	<0.01	<0.01	0.05	<0.01	<0.01	0.03
W	<0.01	<0.01	0.25	0.04	<0.01	5.8

Table 4 Summary of trace elements composition for quartz composing the quartz tourmaline stage and the W-Sn mineralization stage of the mineralized veins of Panasqueira

3.3.4 Chemical evolution trends

To highlight (i) the behavior of trace elements during magmatic-hydrothermal transition and (ii) the genetic link between greisenization processes and the formation of mineralized veins, the chemical compositions of the different generation of magmatic and hydrothermal quartz are plotted in discriminating binary diagrams (Fig. 25).

Li and Al (Fig. 25a) show positive linear correlation for both magmatic quartz and the different generation of hydrothermal quartz. This correlation commonly described in magmatic-hydrothermal systems (Breiter et *al*., 2017; Müller et *al*., 2018; Monnier et *al*., 2018) is due to the coupled substitution Al^{3+}- Li → Si^{4+} (Weil, 1984; Heaney et *al*., 1994; Götze et *al*., 2004). The chemical trend depicted in the Li vs. Al diagram exhibit a progressive depletion in Al and Li from magmatic quartz of the two-mica granite to hydrothermal quartz of greisen and mineralized veins (Fig. 25a).

The Ge vs Ti diagram (Fig. 25b) displays a negative correlation marked by progressive Ti depletion and progressive Ge enrichment from magmatic quartz to hydrothermal quartz of greisen and mineralized veins. This negative correlation is typical in granites and marks the progressive differentiation of melts occurring in polyphased granitic systems (Larsen et *al*., 2004; Müller et *al*., 2010; Breiter et *al*., 2017; Monnier et *al*., 2018). Accordingly,

this trend is attributed to the compatible behavior of Ti, whose the incorporation in quartz is easier at high magmatic temperature than at low hydrothermal temperature conditions, while Ge is incompatible and preferentially concentrated in residual melt and fluids explaining the higher Ge contents observed in quartz from evolved granites and hydrothermal veins. Here, given the consistent behavior of Ge and Ti, we therefore conclude that evolution of Ge and Ti content in quartz can be used as indicator of magmatic-hydrothermal evolution. Thus, the Ge/Ti ratio provides a reliable index to track and unravel magmatic-hydrothermal transition in the mineralized system of Panasqueira. This ratio permits to constrain conditions (temperature and fluid chemistry) of quartz crystallization during magmatic and hydrothermal processes and is applied to plot the evolution of the other trace elements significantly detected in quartz to constrain their behavior during magmatic-hydrothermal transition.

The Al, Li and Rb vs Ge/Ti diagrams (Fig. 25c to 25e) show that the magmatic-hydrothermal evolution of Panasqueira defined by increase of Ge/Ti ratio in quartz, is marked by a progressive depletion in Al, Li and Rb from the magmatic quartz of the two-mica granite to hydrothermal quartz of greisen and mineralized veins. Li and Rb are generally considered as incompatible elements, which were preferentially concentrated in residual melt and magmatic fluids. Accordingly, hydrothermal quartz from greisen and mineralized should be richer in Li and Rb than magmatic quartz, but compositional evolutions of quartz presented above show the opposite trend. This contradiction can be attributed to (i) the crystallization of a large amount of muscovite both in greisen and within the mineralized veins that incorporate preferentially these elements and (ii) a limited incorporation of Al in hydrothermal quartz that consequently inhibits the incorporation of Li according to the coupled substitution described previously. Although, the high Rb and Li contents in hydrothermal muscovite of greisen and veins support the first hypothesis, the low Al contents in hydrothermal quartz and the Li-Al correlation described previously seem to confirm the second one.

The B vs Ge/Ti diagram shows that the magmatic-hydrothermal evolution of Panasqueira is accompanied by B enrichment from magmatic quartz to hydrothermal quartz of veins. This evolution is consistent with the incompatible behavior of B that is preferentially concentrated in residual melt and tends to be expelled with magmatic fluids (Pichavant, 1981; London et *al.*, 1988; Helvig et *al.*, 2002).

In these different chemical trends, quartz composing the greisen exhibits intermediate compositions that overlap both compositions of magmatic quartz from the two-mica granite and hydrothermal quartz from veins. This overlap is probably caused by the occurrences of remains magmatic quartz in the greisen (like snowball quartz) and the crystallization of neoformed quartz equilibrated with hydrothermal mineralizing fluids during greisenization. This suggests a continual transition between magmatic and hydrothermal processes, during which magmatic fluids enriched in incompatible elements (B and Ge) were released and caused the greisenization of the two-mica granite before triggering the vein formation. Consequently, the greisenization of the two-mica granite probably occurred during the magmatic-hydrothermal transition and was contemporary to the formation of mineralized veins (i.e. quartz-tourmaline and W-Sn mineralization stages). On the other hand, quartz formed during the greisenization of the granite roof has probably recorded the expulsion of magmatic fluids enriched in incompatible elements (Ge and B) and that were responsible of the formation of mineralized veins. These fluids were probably released and expelled from the deeper part of the granite intrusion, which was not yet crystallized.

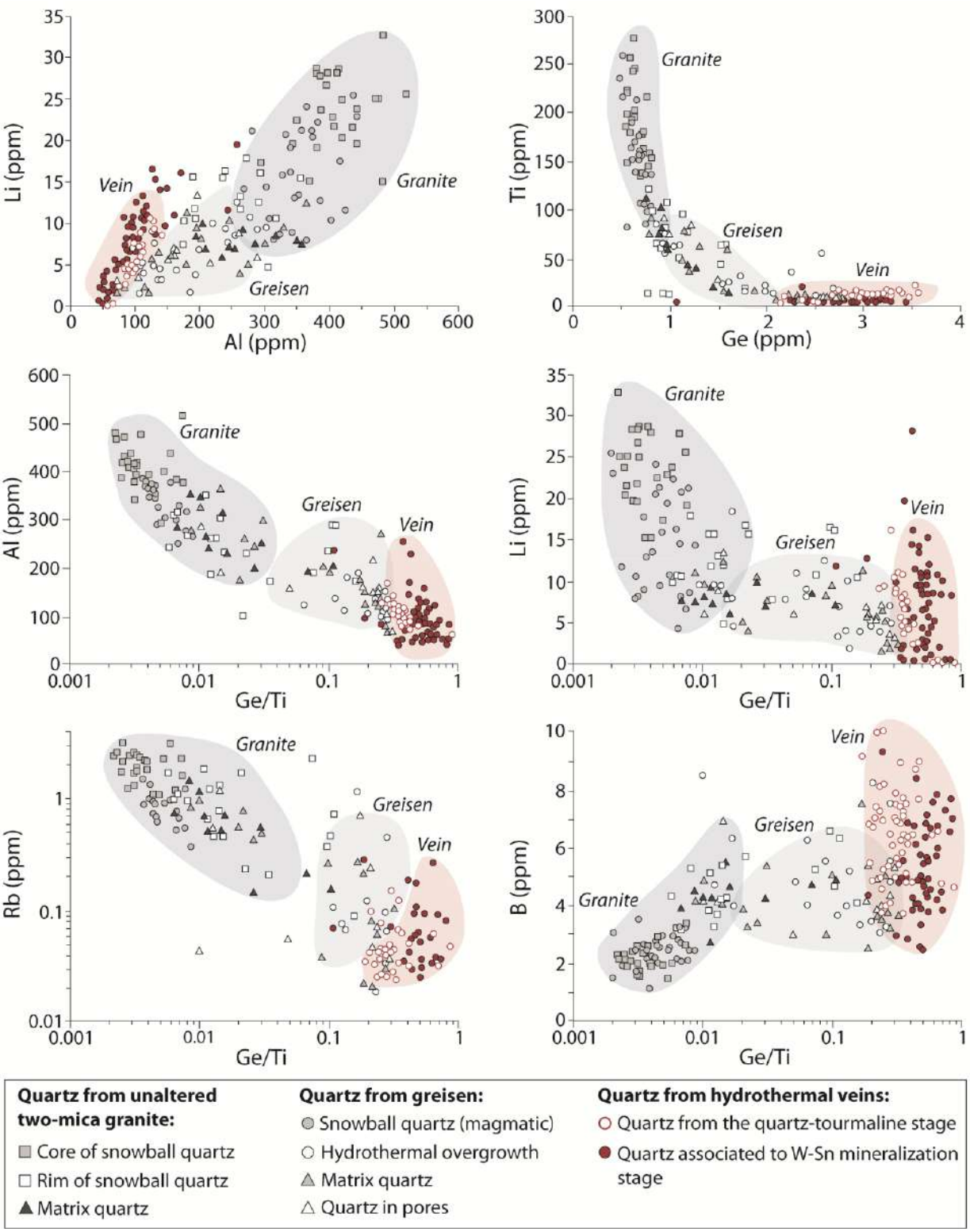

Figure 25 Chemical evolution trends from magmatic to hydrothermal quartz displaying the behavior of Ti, Al, Ge, Li, Rb and B during magmatic-hydrothermal evolution of the Panasqueira ore deposit.

3.3.5 Thermometric considerations by the TitaniQ method

It is largely admitted that incorporation of Ti in quartz depends strongly on (i) its activity in the melt-fluids, (ii) pressure conditions and (iii) on temperature conditions (Thomas et *al*., 2010). From experimental data and thermodynamic studies, several calibrations permitting to estimate temperature of quartz crystallization from Ti concentration were proposed (Wark and Watson, 2006; Thomas et *al*., 2010; Huang and Audétat, 2012). Here, we apply the equation defined by Thomas et *al*. (2010) to estimate temperatures of crystallization for the different generations of quartz analyzed. For this calculation we consider a pressure of 1 and 2 kbar close to values estimated by Bussink (1984) from fluid inclusions. Petrographic study provided evidence of occurrences of rutile in the unaltered two-mica granite, in greisen and within mineralized veins associated to tourmaline. However, due to the difficulty to determine if these different generations of quartz and rutile are cogenetic, we consider values of a_{TiO2} ranging from 0.2 to 1 for calculations.

Calculations performed with Ti activity (a_{TiO_2}) of 0.2 give relatively high crystallization temperatures for both magmatic quartz (800 and 850 °C, at respectively 1 and 2 kbar) and hydrothermal quartz from mineralized veins (in the range 450-500 °C) (Fig. 26a and 26b). These temperatures are inconsistent with (i) temperatures previously estimated from magmatic and hydrothermal muscovite, (ii) classical crystallization temperatures of granitic melts and (iii) with temperatures obtained from fluid inclusions for the earliest hydrothermal stages (QTS and MOSS) estimated between 250 and 360 °C (Kelly and Rye, 1979; Bussink, 1984; Noronha et *al*., 1992; Lüders, 1996). Conversely, calculations performed with Ti activity of 0.5 and 1 give temperatures (350-450 °C for hydrothermal veins and 600-650 °C for magmatic snowball quartz) more consistent with the magmatic-hydrothermal system of Panasqueira.

Ranges of crystallization temperatures calculated for rims of snowball quartz and for the granite matrix quartz are similar. Accordingly, these two generations of quartz crystallized contemporaneously and later than cores of snowball quartz. Hydrothermal quartz formed during the greisenization and quartz-tourmaline stage (i.e the earliest stage of veins formation) exhibit the same temperature ranges suggesting that greisenization and vein formation were probably contemporaneous. These crystallization temperatures are compatible with those estimated in greisen systems worldwide (Smith et *al*., 1996; Conliffe and Feely, 2006; Audétat et *al*., 2008).

Finally, temperatures depict a cooling trend from magmatic quartz of granite to hydrothermal quartz of greisen and veins. This cooling trend is consistent with the expected thermic evolution of magmatic-hydrothermal systems and seems to confirm hypothesis of a continual transition between magmatic and hydrothermal processes, in which greisenization occurred during the magmatic-hydrothermal transition.

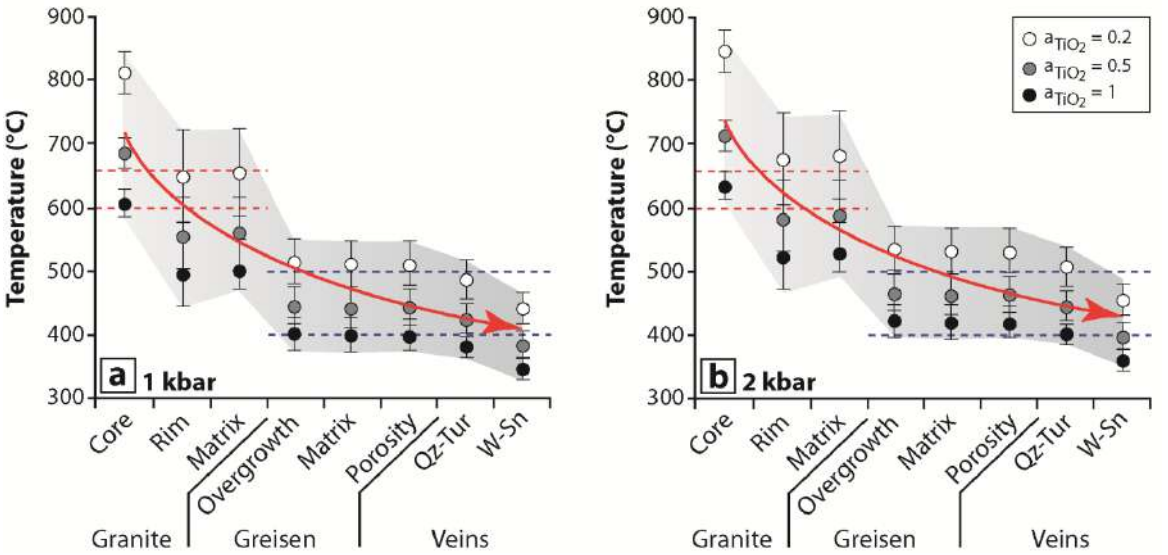

Figure 26 Temperatures of quartz crystallization obtained for the different generations of magmatic and hydrothermal quartz of the unaltered two-mica granite, greisen and mineralized veins. Temperatures were obtained by applying the TitaniQ geothermometer defined by Thomas et *al*. (2010) at (a) 1 and (b) 2 kbar for Ti activity ranging from 0.2 to 1. Red and blue dashed lines give respectively the ranges of temperatures obtained from primary magmatic muscovite and from hydrothermal muscovite of greisen and veins.

3.3.6 Comparison with other magmatic and magmatic-hydrothermal systems

In Figure 27, we compare the chemical evolution of quartz from Panasqueira (magmatic to hydrothermal quartz) with different other magmatic-hydrothermal systems well documented from the Bohemian Massif (compilation from Breiter et *al*., 2017) and the French Massif Central (Monnier et *al*., 2018). This comparison shows that the progressive differentiation of granites and the transition between magmatic to hydrothermal processes can be significantly highlighted from relative Al and Ge enrichments in quartz. Indeed the Al/Ti and Ge/Ti values are lower in less evolved granite (like two-mica granite and I-type granite) than in strongly evolved granite (like rare-metal granites of Beauvoir and Cinovec). Furthermore, in complete magmatic-hydrothermal systems (i.e. systems with granite(s), greisen and mineralized veins), greisens and mineralized veins are generally characterized by the highest values of Al/Ti and Ge/Ti. Additionally, these systems (like Panasqueira, Beauvoir and Cinovec) are generally

marked by magmatic-hydrothermal evolution trends, in which values of Al/Ti and Ge/Ti increase progressively first from the less evolved granite to the more evolved and then from this evolved granite to greisens and mineralized veins. Accordingly, greisenization could result from interactions between granitic rocks and evolved fluids that could be released and expelled during the final stages of granite differentiation and crystallization. Consequently, greisenization can constitute a good marker of the magmatic-hydrothermal transition and hence of the incipience of hydrothermal activity related to the formation Sn-W deposits. The systematic occurrence of Al/Ti and Ge/Ti evolution trends in Sn-W mineralized magmatic-hydrothermal systems and the fact that mineralized bodies (veins and greisens) are generally associated to quartz marked by the highest values of Al/Ti and Ge/Ti demonstrate that these elemental ratios could be useful for mining exploration as a pathfinder to track mineralized bodies.

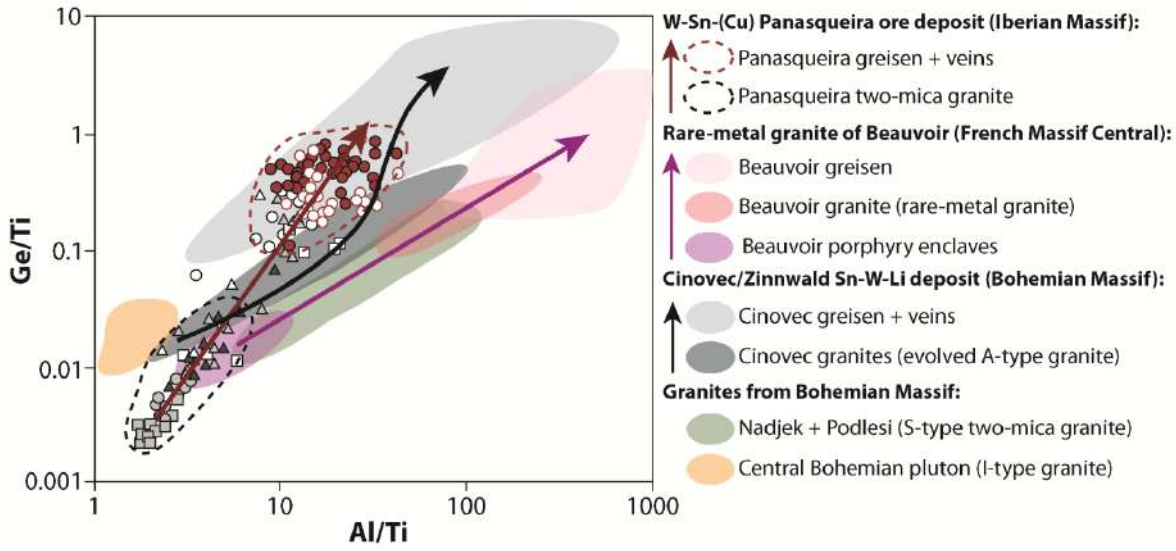

Figure 27 Compilation of chemical signatures (Ge/Ti vs Al/Ti) of quartz from different magmatic and magmatic-hydrothermal systems. Data were compiled from the synthesis of Breiter et *al*., (2017) and from data of Monnier et *al*., (2018) for the rare-metal granite of Beauvoir.

4. Geochronology

4.1 Apatite U-Pb dating

U-Pb analyses of magmatic apatite from the unaltered two-mica granite, altered magmatic apatite from greisen and hydrothermal apatites from mineralized veins are given in appendix and are reported in Terra-Wasserburg diagrams (Fig. 28). The ages are provided with 2σ errors and are calculated with unforced discordias (i.e. initial common Pb values are unforced). All ages presented in the following were obtained from discordant data (Fig. 28).

Due to the thin thickness of altered rims observed by CL images (light-grey-luminescent apatite) in magmatic apatites from unaltered two-mica granite, analyses were exclusively performed on the unaltered grains cores (dark-grey luminescent apatite). A total of 23 analyses performed on a dozen grains give a well-defined discordia with $^{207}Pb/^{206}Pb$ ratios ranging from 0.262 to 0.839 and with a well-defined lower intercept date of 296.3 ± 4.2 Ma (MSWD = 0.6) (Fig. 28a).

For altered magmatic apatite observed in greisen, we performed 31 analyses distributed over 15 grains. Analyses display high contents in common Pb compared to magmatic apatite with $^{207}Pb/^{206}Pb$ ratios ranging from 0.533 to 0.839. The unforced discordia yields a lower intercept date of 292 ± 10 Ma (MSWD = 1.7) (Fig. 28b). The hydrothermal overgrowths (oscillatory zoning) surrounding the altered magmatic apatite grains are only composed of common Pb (red ellipses) and therefore do not permit to determine a lower intercept date (Fig. 28b).

For hydrothermal apatite composing the veins selvages, we performed 22 analyses out of 12 grains. These analyses display $^{207}Pb/^{206}Pb$ ratios ranging from 0.353 to 0.650 and give an unforced intercept date of 294.5 ± 5.3 Ma (MSWD = 2.2) (Fig. 28c).

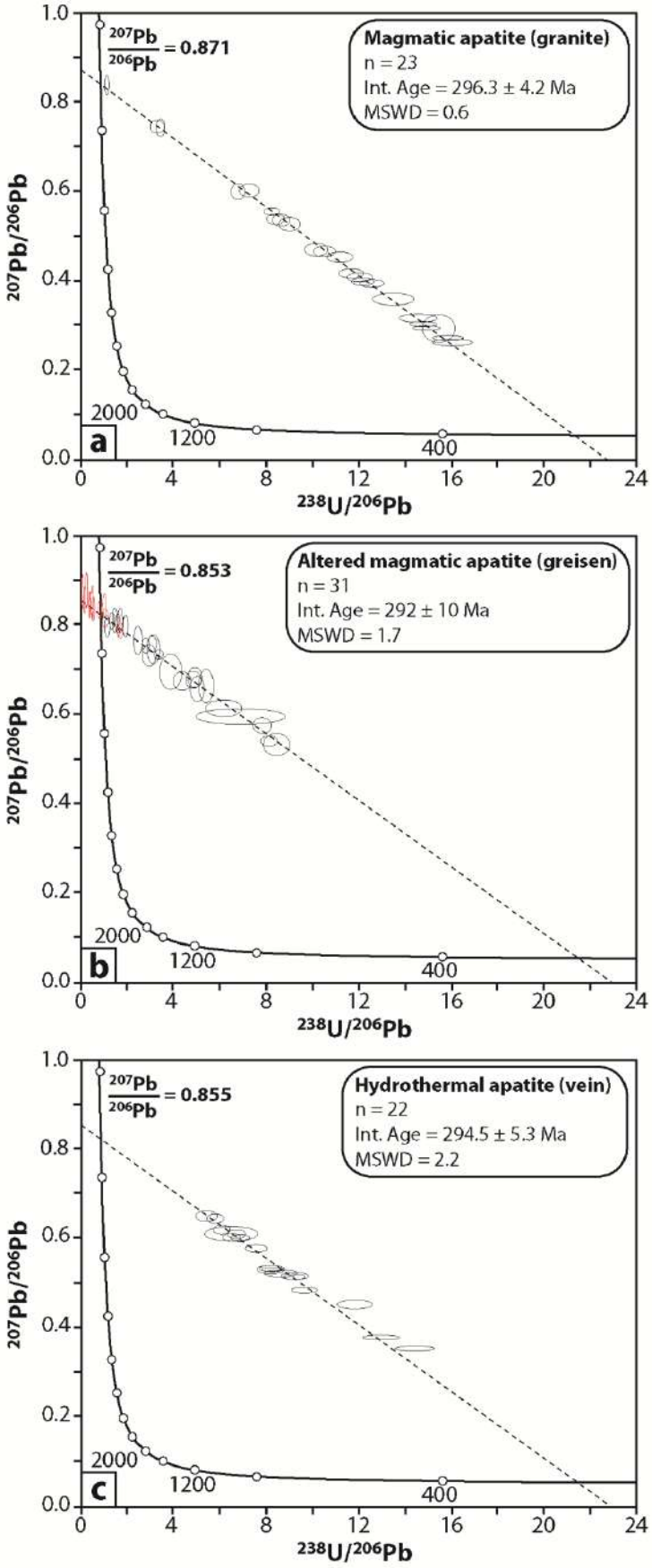

Figure 28 Tera-Wasserburg concordia diagrams, in which apatite analyses were reported to define lower intercept date. (a) Results obtained for magmatic apatite from the unaltered two-mica granite. (b) Results obtained for altered magmatic apatite from greisen. Black ellipses correspond to analyses of altered magmatic apatite and red ellipses correspond to hydrothermal oscillatory zoning overgrowth (c) Results obtained for hydrothermal apatite from mineralized veins (veins selvages). The black dashed lines represent the unforced discordias used for age determination, the $^{207}Pb/^{206}Pb$ values obtained from the upper intersect of discordias are also indicated. Ellipses and errors on ages are reported at 2σ.

4.2 Timing between the different magmatic-hydrothermal events of Panasqueira

Experimental and empirical studies have demonstrated that the closure temperature of apatite range from 375 to 550°C (Chamberlain and Bowring, 2001; Schoene and Bowring, 2006; Cochrane et *al*., 2014). Consequently, the U-Pb dating of apatite could represents a good tool to determine ages of cooling for large and polyphased intrusive bodies and ages of emplacement for small intrusive bodies like dyke and aplite (Pochon et *al*., 2016). As observed by cathodoluminescence images of altered apatites present in greisen, apatite is highly reactive during fluid flow (Harlov, 2015; Bouzari et *al*., 2016) and hence can constitute a good candidate to date hydrothermal events and metasomatic processes. Thus, we use ages obtained from the different generations of apatite to constrain the timing between the magmatic and hydrothermal processes involved during the formation of the Panasqueira deposit. We compare our apatite ages with ages published by Snee et *al*., (1981) obtained by $^{40}Ar/^{39}Ar$ method on the different generations of muscovite present in veins and within the massive greisen.

The compilation of is displayed in Figure 29 and show that the magmatic and hydrothermal processes involved during the formation of the mineralized system of Panasqueira occurred over a relative short span of time (from 301 to 289 Ma considering the error bars) that define a continuum without interruption between the different magmatic and hydrothermal stages. The granite cooling stage (550-375 °C) estimated from the ages of magmatic apatite is contemporaneous with the formation of vein selvages (muscovite + apatite), which mark the vein opening and the W-Sn mineralization stage (MOSS). Accordingly, the W-Sn mineralization of Panasqueira was probably related to the crystallization and the cooling of the granite intrusion present at depth.

Ages obtained by Snee et *al*. (1981) on muscovites associated to the main sulfide stage (MSS) are in direct continuity with the W-Sn and granite cooling events. Accordingly, the different hydrothermal stages observed in the mineralized veins of Panasqueira were probably related to the same thermic event, which is the cooling of the granite intrusion.

Greisenization is characterized by younger ages (from both apatite and muscovite) than granite cooling stage, MOSS and MSS (Fig. 29). Although the relative chronology between the granite cooling and the greisenization is compatible with observations and data described previously, the relative chronology between the greisenization and the main mineralization stages (MOSS and MSS) is inconsistent with structural, textural and mineralogical observation described in the first part (Part I) of this chapter. Indeed, the

presence of greisen enclave within mineralized veins that crosscut the greisen cupola demonstrate that greisenization predate or is sub-contemporaneous of the hydrothermal stages related to the W-Sn mineralization. Furthermore, the occurrences of W-rich rutile, cassiterite and sulfides within the porosity of greisen provide evidence that greisenization occurred before/contemporaneously the different mineralization stages (MOSS and MSS). According to Snee et *al*. (1981) primary ages of muscovite composing the greisen were probably resetting during the latest hydrothermal stages. The occurrences of pyrite and carbonates in greisen that are respectively related to the pyrrhotite alteration (PAS) and late carbonates (LCS) stages confirm that greisen was affected by the latest hydrothermal stages that could trigger the resetting of muscovite ages. Accordingly, greisen was a preferential pathway for the different fluids related to the different hydrothermal stages observed in the mineralized vein system. This suggests that greisen was a permeable facies which drain the mineralized fluids leading the formation of disseminated mineralization observed in the massive greisen.

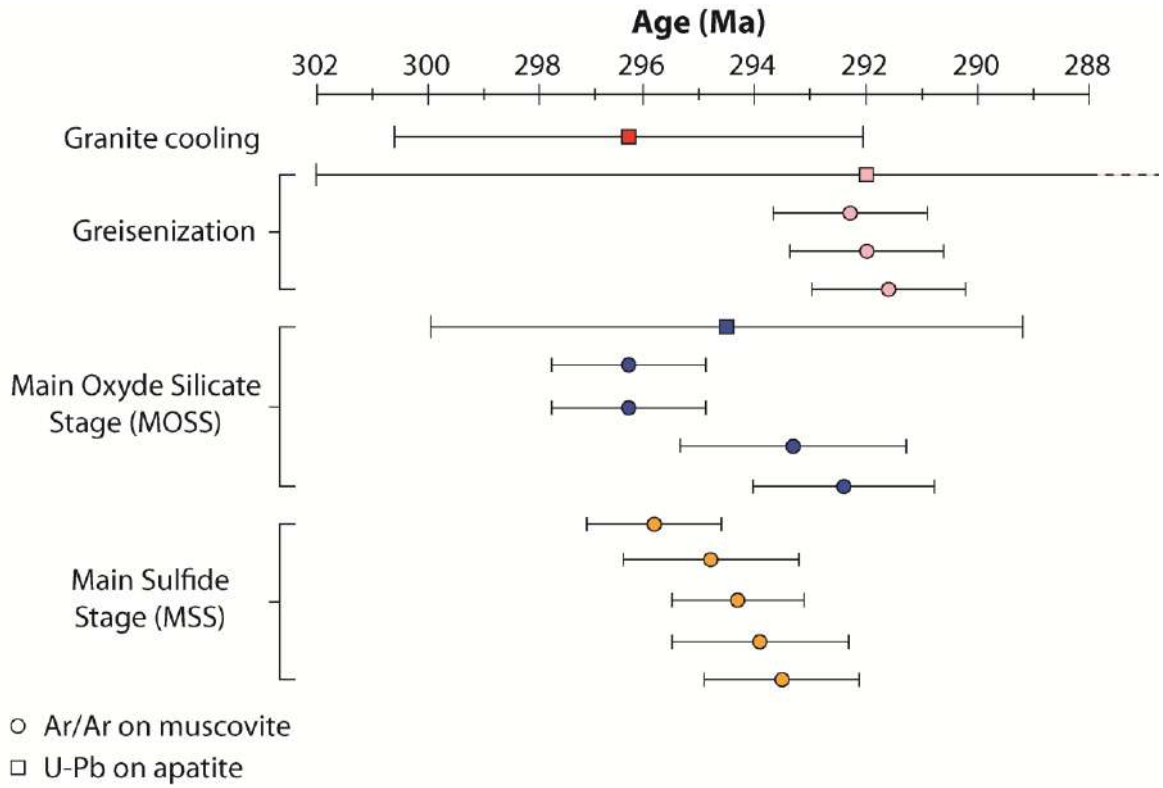

Figure 29 Comparison and compilation of dating data from this study (U-Pb on apatite) and from Snee et al. (1981) (Ar/Ar on muscovite) on the magmatic-hydrothermal system of Panasqueira. The Ar/Ar ages were reported here with 2σ error bars.

IV- Integrated discussion

1. Chemical characteristics of fluids responsible of greisenization

As highlighted from compositions of muscovite, quartz, rutile and tourmaline (**Chapter III**) formed during the earliest hydrothermal stages, fluids responsible of the greisenization and the formation of vein selvages were rich in incompatible granitophil elements like K, Na, F, Li, Rb, Cs and B and in metals W, Sn and Zn.

Analyses of fluid inclusions performed by Lecumberri-Sanchez et *al*. (2017) have demonstrated that fluids related to the MOSS (W-Sn event) are systematically and significantly enriched in (i) incompatible elements like, B, Li, Cs and Rb (from hundred to several thousand of ppm), (ii) in granitophil elements like Na and K (from several thousand to several tens of thousands of ppm) and (iii) in metals W, Cu and Zn (several tens or hundreds of ppm) (Fig. 30). On other hand, the mineralizing fluids related to the W-Sn event are characterized by the same signature than those inferred from trace element compositions in muscovite, quartz and tourmaline. From these fluids compositions, Lecumberri-Sanchez et *al*. (2017) suggests that mineralizing fluids responsible of the W-Sn mineralization of Panasqueira derived from an evolved granitic melt.

Accordingly, greisenization and the earliest stages of vein formation were related to the circulation of the same hydrothermal fluids that could be magmatic origin. Consequently, greisenization constitutes a potential monitor of the magmatic-hydrothermal transition, during which mineralizing fluids released during the granite crystallization were expelled to form the vein system of Panasqueira.

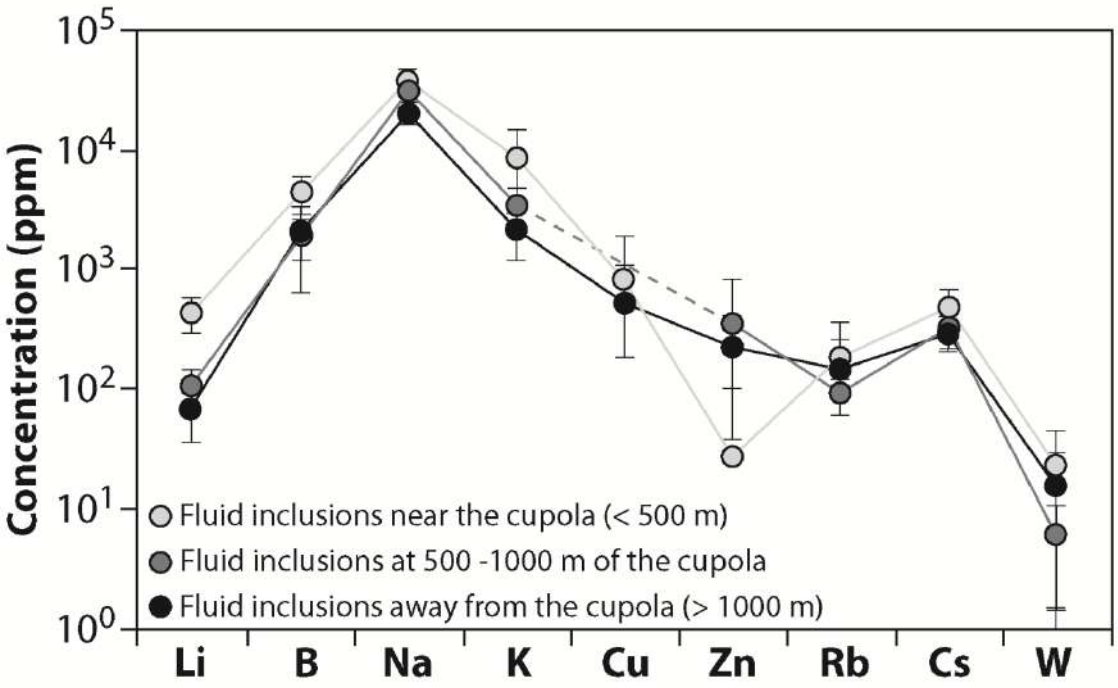

Figure 30 Average concentrations and standard deviations of elements detected in fluid inclusions associated with the main oxide silicate stage (MOSS, W-Sn mineralization event) in veins. Data from Lecumberri-Sanchez et *al.* (2017). Fluid inclusions were analyzed at different distance of the cupola.

2. Genetic relationships between the greisenization and the formation of mineralized veins of Panasqueira

Greisenization is commonly associated to strong fluid rock interactions between granitic rocks and hot acidic fluids (Shcherba, 1970; Ŝtemprok, 1987; Taylor and Pollard, 1988; Bishop, 1989; Zaraisky et *al.*, 1995). Here, we suggest from the chemical signatures of quartz, muscovite and rutile that fluids involved during greisenization of Panasqueira are enriched in incompatible granitophil elements (Li, F, B, Rb, Ge, Cs…) and metals (Sn, W and Zn). Accordingly, greisenization seems to be induced by the releasing and the expulsion of magmatic fluids during the final stages of the granite crystallization.

From our mineralogical, textural and geochemical data and from mineral reactions involved during greisenization (replacement of feldspars by muscovite), we propose a conceptual model to illustrate the formation of greisen based on the disequilibrium between hot fluids released at high temperature and cooler crystallized part of the granite intrusion (Fig. 31). If we consider that albite, k-feldspar and muscovite are equilibrated during the final stages of the granite crystallization (eutectic), the compositions of

magmatic fluids in $\log(a_{Na^+}/a_{H^+})$ and $\log(a_{K^+}/a_{H^+})$ produced and released by the granite are constrained by the triple point at high temperature conditions (red star at 600°C in Fig. 31). The expulsion and the circulation of these fluids through the cooler and crystallized part of the granites intrusion trigger the replacement of feldspars (k-feldspar and albite) by muscovite due to disequilibrium induced by the temperature differences between hot magmatic fluids (600°C in Fig. 31) and crystallized granite (400 °C in Fig. 31).

During the replacement of feldspars and biotite, the neoformed muscovite, quartz and rutile record the chemical signature of magmatic fluids that were enriched in granitophil elements and metals, whereas elements hosted by feldspars (Na, Ba, Sr, Eu…) were released in fluids. The crystallization of a large amount of muscovite and quartz and chemical exchanges between these mineral phases and fluids explain the enrichment in Cs, Rb, Li, Sn, W and depletion in Na, Ba, Sr and Eu observed in the whole-rock composition during the greisenization. The differentiation between the two-mica granite composing the upper part of the intrusive body to the more evolved leucogranite present at depth emphasizes that magmatic fluids were probably released during the progressive crystallization and differentiation of the granite system of Panasqueira.

As highlighted from tourmaline growth bands, these fluids were then preferentially expelled from the cupola (**Chapter III**), which served as suitable sites for focusing hydrothermal fluids that produced alterations (greisenization) sub-sequent to granite crystallization (Fig. 31). This fluid focusing lead to the vein opening, in which greisen enclaves were trapped during the earliest mineralization stages. Muscovite and quartz formed during the quartz-tourmaline and the W-Sn stages exhibit almost the same compositions than those composing the greisen. Consequently, the greisenization of the two-mica granite occurred likely during the magmatic-hydrothermal transition and was contemporary to the earliest mineralization stages of veins (quartz-tourmaline and main oxide silicate stages).

Finally the presence of disseminated cassiterite and sulfides mineralization in greisen that infill porosity emphasizes that massive greisen could constitute a permeable pathway for the different mineralizing fluids involved during the hydrothermal activity of Panasqueira. This hypothesis is investigated in details in the next chapter (**Chapter V**).

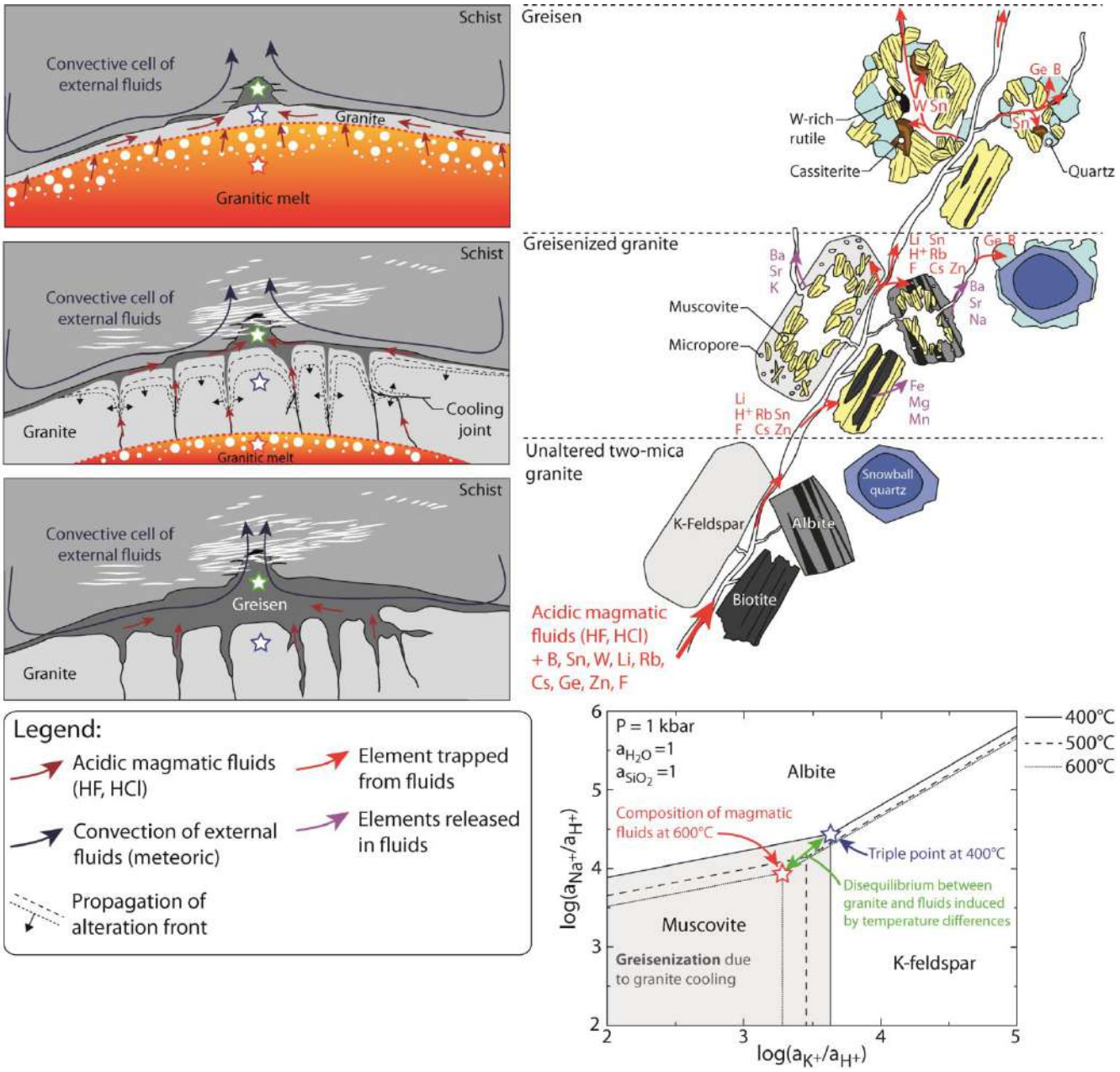

Figure 31 Conceptual model of greisen formation during the magmatic-hydrothermal transition of Panasqueira. In this model are displayed (i) the schematic time evolution of fluid flow during the granite crystallization and cooling, (ii) the textural and the mineralogical evolution of granite with the behavior of some elements considered in this study and (iii) $log(a_{Na^+}/a_{H^+})$ **vs.** $log(a_{K^+}/a_{H^+})$ **phases diagram at 1 kbar illustrating effect of temperatures (from 600 to 400 °C) on equilibria between K-feldspar, albite and muscovite. Triple point corresponds to hypothetic eutectic of the two-mica granite of Panasqueira. During granite cooling, fluid produced at high magmatic temperature (red star) is imbalance with the cooler crystallized part of the granite intrusion that potentially trigger greisenization. This diagram was built from thermodynamic database of SUPCRTBL (Johnson et *al.*, 1992; Zimmer et *al.*, 2016).**

References

A-B

Alfonso, P., Melgarejo, J.C., Yusta, I., Velasco, F., 2003. Geochemistry of feldspars and muscovite in granitic pegmatite from the Cap de Creus field, Catalonia, Spain. The Canadian Mineralogist 41, 103-116.

Audétat, A., Pettke, T., Heinrich, C.A., Bodnar, R.J. 2008. Magmatic-hydrothermal evolution in a fractionating granite: a microchemical study of the Sn-W-F mineralized Mole granite (Australia). Geochim Cosmochim Acta 64:3373-3393.

Bishop, A.C. 1989. Greisen. In: Petrology. Encyclopedia of Earth Science. Springer, Boston, MA.

Bouzari, F., Hart, C.J.R., Bissig, T., Barker, S. 2016. Hydrothermal Alteration Revealed by Apatite Luminescence and Chemistry: A Potential Indicator Mineral for Exploring Covered Porphyry Copper Deposits. Economic Geology, v. 111, pp. 1397–1410.

Breiter, K., Svojtka, M., Ackerman, L., Švecová, K., 2012. Trace element composition of quartz from the Variscan Altenberg–Teplice caldera (Krušné hory/Erzgebirge Mts, Czech Republic/Germany): insights into the volcano-plutonic complex evolution. Chem. Geol. 326–327, 36–50.

Breiter, K., Ďurišová, J., Dosbaba, M., 2017a. Quartz chemistry –A step to understanding magmatic-hydrothermal processes in ore-bearing granites: Cínovec/Zinnwald Sn-W-Li deposit, Central Europe. Ore Geology Rewiews 90, 25–35.

Breiter, K., Ďurišová, J., Hrstka, T., Korbelová, Z., Vaňková, M.H., Galiová, M.V., Dosbaba, M., 2017b. Assessment of magmatic vs. metasomatic processes in rare-metal granites: a case study of the Cínovec/Zinnwald Sn–W–Li deposit, Central Europe. Lithos 292, 198–217.

Bussink, R.W. 1984. Geochemistry of the Panasqueira Tungsten-Tin Deposit, Portugal. Geol. Ultraiectina.

C-D

Chamberlain, K.R., and Bowring, S.A. (2001) Apatite–feldspar U–Pb thermochronometer: a reliable, mid-range (~450°C), diffusion controlled system. Chemical Geology, 172, 173–200.

Charoy, B, Noronha, F. 1991. The Argemela granite-porphyry (Central Portugal): The subvolcanic expression of a high-fluorine, rare-element pegmatite magma. Source, Transport and Deposition of Metals, Pagel & Leroy (eds) Balkema. Rotterdam. ISBN 90 54100206.

Chew, D.M, Petrus, J.A., Kamber, B.S. 2014. U–Pb LA–ICPMS dating using accessory mineral standards with variable common Pb. Chem Geol 363:185–199.

Clark, J.R., Williams-Jones, A.E., 2004. Rutile as a potential indicator mineral for metamorphosed metallic ore deposits. Rapport Final de DIVEX, Sous-projet SC2, Montréal, Canada. 17 pp.

Cochrane, R., Spikings, R.A., Chew, D., Wotzlaw, J.-F., Chiaradia, M., Tyrrell, S., Schaltegger, U., and Van der Lelij, R. (2014) High temperature (>350 °C) thermochronology and mechanisms of Pb loss in apatite. Geochimica et Cosmochimica Acta, 127, 39–56.

Conliffe, J., Feely, M. 2006. Microthermometrics characteristics of fluids associated with granite and greisen quartz and vein quartz and beryl from Rosses Granite complex, Donegal, NW Ireland. J Geochem Explor 89:73-77.

Debon, F. & Le Fort, P. 1983. A chemical-mineralogical classification of common plutonic rocks and associations - Transactions of the Royal Society of Edinburgh-Earth Sciences, 73, pp.135-149.

G

Gomes, M., Neiva, A., 2000. Chemical zoning of muscovite from the Ervedosa granite, northern Portugal. Mineralogical Magazine - MINER MAG. 64. 347-358. 10.1180/002646100549247.

Götze, J., Plötze, M., Graupner, T., Hallbauer, D.K., Bray, C.J., 2004. Trace element incorporation into quartz: a combined study by ICP-MS, electron spin resonance, cathodoluminescence, capillary ion analysis, and gas chromatography 1. Geochimica et Cosmochimica Acta 68, 3741–3759.

Gurbanov, A.G., Chernukha, D.G., Koshchug, D.G., Kurasova, S.P., Fedyushchenko, S.V., 1999. EPR spectroscopy and geochemistry of rock-forming quartz as an indicator of the superimposed processes in rocks of igneous associations of various ages in the Greater Caucasus. Geochem. Int. 37, 519–604.

H

Harlov D.E., Wirth R., Förster, H.J. 2005. An experimental study of dissolution–reprecipitation in fluorapatite: fluid infiltration and the formation of monazite. Contrib Mineral Petr 150:268 286.

Heaney, P.J., Veblen, D.R., Post, J.E., 1994. Structural disparities between chalcedony and macrocrystalline quartz. American Mineralogist 79, 452–460.

Huang, R., Audétat, A., 2012. The titanium-in-quartz (TitaniQ) thermobarometer: A critical examination and re-calibration. Geochimica et Cosmochimica Acta 84, 75–89.

Hulsbosch, N., Hertogen, J., Dewaele, S., André, L., Muchez, P., 2014. Alkali metal and rare earth element evolution of rock-forming minerals from the Gatumba area pegmatites (Rwanda): quantitative assessment of crystal-melt fractionation in the regional zonation of pegmatite groups. Geochim. Cosmochim. Acta 132, 349–374.

J- K

Jacamon, F., Larsen, R.B., 2009. Trace element evolution of quartz in the charnockitic Kleivan granite, SW-Norway: the Ge/Ti ratio of quartz as an index of igneous differentiation. Lithos 107, 281–291.

Kelly, W.C., Rye, R.O. 1979. Geologic, fluid inclusion and stable isotope studies of the tin-tungsten deposits of Panasqueira, Portugal. Econ Geol 74:1721–1822.

L

Larsen, R.B., Henderson, H., Ihlen, P.M., Jacamon, F., 2004. Distribution and petrogenetic behaviour of trace elements in granitic pegmatite quartz from granite from South Norway. Contributions to Mineralogy and Petrology 147, 615–628.

Lecumberri-Sanchez, P., Vieira, R., Heinrich, C.A., Pinto, F., Wälle, M. 2017. Fluid-rock interaction is decisive for the formation of tungsten deposits. Geology 45, 579–582.

Legros, H., Marignac, C., Mercadier, J., Cuney, M., Richard, A., Wang, R-C., Charles, N., and Lespinasse, M-Y. (2016) Detailed paragenesis and Li-mica compositions as recorders of the magmatic-hydrothermal evolution of the Maoping W-Sn deposit (Jiangxi, China). Lithos, 264, 108-124.

London, D., Hervig, R.L., Morgan VI, G.B. 1988. Melt – vapor solubilities and elemental partitioning in peraluminous granite – pegmatite systems: experimental results with Macusani glass at 200 MPa. Contrib. Mineral. Petrol. 99, 360– 373.

Lüders, V., 1996. Contribution of infrared microscopy to fluid inclusion studies in some opaque minerals (Wolframite, Stibnite, Bournonite) : Metallogenic implications. Economic Geology, Vol. 91, 8, 1462-1468.

Ludwig, K.R. 2012. User's Manual for Isoplot 3.75. A geochronological toolkit for Microsoft Excel. Berkeley Geochronological Center, 1–75.

Luhr, J.F., Carmichael, I.S.E., Varecamp, J.C. 1984. The 1982 eruptions of El Chichon volcano, Chiapas, Mexico: mineralogy and petrology of the anhydrite-bearing pumices. Journal of Volcanology and Geothermal Research 76, 83-109.

M

McDowell, F.W., McIntosh, W.C., and Farley, K.A. (2005) A precise 40Ar–39Ar reference age for the Durango apatite (U–Th)/He and fission-track dating standard. Chemical Geology, 214, 249–263.

Meinhold, G., 2010. Rutile and its applications in earth sciences. Earth Sci. Rev. 102, 1-28.

Miller, C.F., Stoddard, E.F., Bradfish, L.J. and Dollase, W.A., 1981. Composition of plutonic muscovite: genetic implications. Can. Mineral., 19, 25–34.

Monier, G., Merggoil-Daniel, J. and LabernardieÁre, H. 1984. GeÂneÂrations successives de muscovites et feldspaths potassiques dans les leucogranites du massif de Millevaches (Massif Central Francais). Bull. Mineral., 107, 55-68.

Monier, G. & Robert, J.L. 1986. Muscovite solid solutions in the system K_2O-MgO-FeO-Al_2O_3-SiO_2-H_2O: an experimental study at 2 kbar PH_2O and comparison with natural Li-free white micas. Mineralogical Magazine, 50, pp. 257-266.

Monnier, L., Lach, P., Salvi, S., Melleton, J., Bailly, L., Béziat, D., Monnier, Y., Gouy, S. 2018. Quartz trace-element composition by LA-ICP-MS as proxy for granite differentiation, hydrothermal episodes, and related mineralization: The Beauvoir Granite (Echassières district), France. Lithos 320–321 : 355–377.

Müller, A., Seltmann, R., 1999. The genetic significance of snowball quartz in high fractionated tin granites of the Krušné Hory/Erzgebirge. In: Stanley, C. (Ed.), Mineral Deposits: Processes to Processing. Proceedings of the 5th Biennial SGA Meeting London. vol. 1. Balkema, Rotterdam, pp. 409–412.

Müller, A., Kronz, A., Breiter, K., 2002. Trace elements and growth patterns in quartz: a fingerprint of the evolution of the subvolcanic Podlesí Granite System (Krušné Hory, Czech Republic). Bulletin of the Czech Geological Survey 77, 135–145.

Müller, A., Breiter, K., Seltmann, R., Pécskay, Z., 2005. Quartz and feldspar zoning in the eastern Erzgebirge volcano-plutonic complex (Germany, Czech Republic): evidence of multiple magma mixing. Lithos 80, 201–227.

Müller, A., van den Kerkhof, A.M., Behr, H.-J., Kronz, A., Koch-Müller, M., 2010a. The evolution of late-Hercynian granites and rhyolites documented by quartz—a review. Geol. Soc. Am. Spec. Pap. 472, 185–204.

Müller, A., Herrington, R., Armstrong, R., Seltmann, R., Kirwin, D.J., Stenina, N.G., Kronz, A., 2010b. Trace elements and cathodoluminescence of quartz in stockwork veins of Mongolian porphyry-style deposits. Mineral. Deposita 45, 707–727.

Müller, A., Herklotz, G., Giegling, H. 2018. Chemistry of quartz related to the Zinnwald/Cínovec Sn-W-Li greisen-type deposit, Eastern Erzgebirge, Germany. Journal of Geochemical Exploration 190 : 357–373.

N

Neiva, A.M.R. 1987. Geochemistry of greisenized granites and metasomatic schists of tungsten-tin deposits in Portugal. In: Helgeson, H.C. (ed.) Chemical Transport in Metasomatic Processes. NATO ASI Series C218, 681–700.

Noronha, F., Doria, A., Dubessy, J., Charoy, B., 1992. Characterization and timing of the different types of fluids present in the barren and ore-veins of the W-Sn deposit of Panasqueira, Central Portugal. Mineralium Deposita 27, 72-79. doi:10.1007/BF00196084.

Novak, F. 1964. F. The origine of stannite by replacement of cassiterite in the Tukank zone of the Kutna Hora ore deposit.

P

Pichavant, M., 1981. An experimental study of the effect of boron on a water-saturated haplogranite at 1 Kbar vapour pressure. Contributions to Mineralogy and Petrology 76, 430-439.

Pochon, A., Poujol, M., Gloaguen, E., Branquet, Y., Cagnard, F., Gumiaux, C., Gapais, D., 2016b. U-Pb LA-ICP-MS dating of apatite in mafic rocks: Evidence for a major magmatic event at the Devonian-Carboniferous boundary in the Armorican Massif (France). Am. Mineral. 101, 2430–2442.

Pirajno, F. and Schlögl, H.U. 1987. The alteration-mineralization of the Krantzberg tungsten deposit, South West Africa/Namibia. S. Afr. J. Geol, 90, 239-255.

R

Rice, C., Darke, K., Still, J., 1998. Tungsten-bearing rutile from the Kori Kollo gold mine Bolívia. Mineral. Mag. 62, 421–429.

Rusk, B., 2012. Cathodoluminescent textures and trace elements in hydrothermal quartz. In: Götze, J., Möckel, R. (Eds.), Quartz: Deposits, Mineralogy and Analytics. Springer, Heidelberg, New York, pp. 307–329.

Rusk, B., Reed, M., 2002. Scanning electron microscope-cathodoluminescence analysis of quartz reveals complex growth histories in veins from the Butte porphyry copper deposit, Montana. Geology; v. 30; no. 8; p. 727–730.

S

Shcherba, G. N. 1970. Greisens. Int Geol Rev 12: 114–255.

Schoene, B., and Bowring, S.A. (2006) U–Pb systematics of the McClure Mountain syenite: Thermochronological constraints on the age of the 40Ar/39Ar standard MMhb. Contributions to Mineralogy and Petrology, 151, 615–630.

Smith, M.P., Banks, D.A., Yardley, B.W.D. 1996. Fluid inclusion and stable isotope constraints on the genesis of the Cligga Head Sn-W deposit, SW England. Eur J mineral 8:961-974.

Smith, D.C., Perseil, E.A., 1997. Sb-rich rutile in the manganese concentrations at St. Marcel-Praborna, Aosta Valley, Italy; petrology and crystal-chemistry. Mineral. Mag. 61, 655–669.

Snee, L.W., Sutter, J.F., Kelly, W.C. 1988. Thermochronology of economic mineral deposits; dating the stages of mineralization at Panasqueira, Portugal, by high-precision 40Ar/39Ar age spectrum techniques on muscovite. Econ Geol 83:335–354

Speer, J.A. 1984. Micas in igneous rocks. Pp. 299-356 in: Micas (S.W. Bailey, editor). Reviews in Mineralogy, 13, Mineralogical Society of America, Washington D.C.

Stemprok, M. 1987. Greisenization (a review). Geol Rundsch , Springer-Verlag 76: 169.

Stemprok, M., Pivec, E., Langrova, A. 2005. The petrogenesis of a wolframite-bearing greisen in the Vykmanov granite stock, Western Krušné hory pluton (Czech Republic). Bulletin of Geosciences, Vol 80, No 3, pages 163 – 184.

T

Tartèse, R., Ruffet, G., Poujol, M., Boulvais, P., Ireland, T.R., 2011b. Simultaneous resetting of the muscovite K–Ar and monazite U–Pb geochronometers: a story of fluids. Terra Nova 23, 390–398.

Taylor, R.G., Pollard, P.J. 1988. Pervasive hydrothermal alteration in tin-bearing granite and implications for the evolution of ore-bearing magmatic fluids. Canadian Institute of Mining and Metallurgy Special Volume 39, p. 86.95.

Thomas, J.B., Watson, E.B., Spear, F.S., Shemella, P.T., Nayak, S.K., Lanzirotti, A., 2010. TitaniQ under pressure: the effect of pressure and temperature on the solubility of Ti in quartz. Contributions to Mineralogy and Petrology 160, 743–759.

Tischendorf, G., Gottesmann, B., Förster, H.-J., Trumbull, R.B., 1997. On Li-bearing micas: estimating Li from electron microprobe analyses and an improved diagram for graphical representation. Mineral. Mag. 61, 809–834. https://doi.org/10.1180/minmag.1997.061.409.05.

Triebold, S., von Eynatten, H., Luvizotto, G.L., Zack, T., 2007. Deducing source rock lithology from detrital rutile geochemistry: an example from the Erzgebirge, Germany. Chem. Geol. 244, 421–436.

W

Wark, D.A., Watson, E.B., 2006. TitaniQ: a titanium-in-quartz geothermometer. Contributions to Mineralogy and Petrology 152, 743–754.

Weil, J.A., 1984. A review of electron spin spectroscopy and its application to the study of paramagnetic defects in crystalline quartz. Physics and Chemistry of Minerals 10,149–165.

White, R. W., Powell, R. & Holland, T. J. B., 2007. Progress relating to calculation of partial melting equilibria for metapelites. Journal of Metamorphic Geology, 25, 511–527.

Whitney, D.L, Evans, B.W. 2010. Abbreviations for names of rock-forming minerals. Am. Mineral 95:185-187.

Z

Zack, T., Kronz, A., Foley, S.F., Rivers, T., 2002. Trace element abundances in rutiles from eclogites and associated garnet mica schists. Chem. Geol. 184, 97–122.

Zaraisky, G.P., Stoyanovskaya, F.M. 1995. Experimental modeling of gain and loss of rare metals (W, Mo, Sn) during greisenization and alkalic metasomatism of leucocratic granite. Experiment in Geosciences, No. 4, pp 19-21.

Chapter V: Dynamic permeability related to greisenization reactions in Sn-W ore deposits: Quantitative petrophysical and experimental evidence

Objectives of this chapter:

From textural, mineralogical and geochemical data (**Chapter IV**) we have demonstrated that greisenization of the Panasqueira granite occurred likely during the magmatic-hydrothermal transition and during the earliest stages of vein formation. According to chemical characteristics of muscovite and quartz composing the massive greisen, greisenization was induced by the releasing and the expulsion of orthomagmatic fluids during the final stages of the granite crystallization. During this metasomatic alteration, feldspars and biotite composing the two-mica granite of Panasqueira were completely replaced by a quartz-muscovite assemblage. During this mineralogical transformation, the rock texture was drastically affected and marked by the development of porous texture both in greisenized aplites and within the massive greisen of Panasqueira. This porosity generation during greisenization is commonly described in other worldwide greisen systems and can constitute a key process to enhance circulation of mineralizing fluids during the magmatic-hydrothermal transition. Furthermore, these fluid-rock interactions and replacement reactions can significantly affect the physicochemical characteristics of fluids (like pH and fO_2) and hence can promote precipitation of ore-bearing mineral like cassiterite and wolframite (Halter et *al*., 1996; Heinrich, 1990).

In this chapter we investigate effects of fluid-rock interaction related to greisenization on (i) rock porosity and permeability (**Part I**) and (ii) on chemical changes in fluid composition (**Part II**). To do this we perform a complete study combing mineralogical and microtextural analysis with experimental approaches.

I- Article submitted to Geofluids

Abstract: Massive greisens are commonly associated with Sn-W mineralization and constitute low-grade high-tonnage deposits. The formation of this type of deposit results from an intense pervasive metasomatic alteration involving a major fluid and mass transfer through a nominally impermeable parental granite. A decrease in the volume of the solid phases associated with the mineral replacement reactions may be a potential process for creating pathways to enhance fluid flow. Here, we explore the effects of the replacement reactions related to greisenization on the granite's mineralogy and petrophysical properties (density, porosity and permeability), as well as their potential implications for fluid flow in the case of the world-class W-Sn-(Cu) Panasqueira deposit, Portugal. Mineralogical and microtextural analysis of greisenized facies show that the total replacement of feldspars by muscovite is associated with a volume decrease of the solid phases that induces a significant porosity generation in greisen (~8.5%). Greisenization experiment coupled with permeability measurement show that the replacement of feldspars by muscovite permits new pathways at the crystal scale that significantly enhance the transient permeability. Moreover, permeability measurements performed on representative samples with different degrees of greisenization show that permeability increases progressively with the level of alteration from -10^{-20} m² in less granite to 10^{-17} m² in greisen. The correlation between the permeability and porosity evolutions demonstrate that the porous texture developed during replacement reactions create new pathways that enhance significantly the permeability in greisen systems. The occurrences of mineral-bearing metals such as cassiterite in the newly formed porosity of greisen provides evidence that greisenization can be a decisive process for enhancing fluid flow and promoting transport of metals in Sn-W deposits. Finally, we present a model involving a positive feedback between greisenization and permeability, in which mineralizing fluids are able to generate their own pathways in initially impermeable granite via replacement reactions, which in turn promote further hydrothermal alteration and mass transport.

Keywords: Greisenization, replacement reactions, porosity, reaction-enhanced permeability, fluid flow, Sn-W deposits

1. Introduction

Greisenization is a common hydrothermal alteration associated with Sn-W and rare metals deposits that are usually spatially and genetically associated with fractionated crustal granitic intrusions (Stemprok, 1987; Pollard et *al*., 1988; Pirajno, 1992; Černý et *al*., 2005). This post-crystallization alteration, marked by the breakdown of feldspars and biotite, occurs generally on the tops of intrusions during the cooling stage of the granitic intrusions and the first stages of hydrothermal activity. Numerous studies have established that greisenization results from strong interactions between granitic rocks and acidic fluids at temperatures ranging from 250°C to 450°C (Shcherba, 1970; Ŝtemprok, 1987; Taylor and Pollard, 1988; Bishop, 1989; Zaraisky et *al*., 1995). These intense fluid-rock interactions lead to complete mineralogical transformation of the granitic rocks by coupled dissolution-precipitation (CDP) reactions (Kontak and Clark, 2002; Plümper and Putnis, 2009; Dostal et *al*., 2014 and 2015 Jonas et *al*., 2014; Putnis, 2015). Field observations have shown that greisen can form (i) at local scale adjacent to veins or fractures present in granite, as at Cligga Head (Hall, 1971), and (ii) on a broad scale as massive greisens that are mainly present in the apical portions of granite, as at Cinovec, East Kemptville and Panasqueira (Ŝtemprok, 1987 and 2005; Halter et *al*., 1996 and 1998; Thadeu, 1951; Kelly and Rye, 1979). These massive greisens may extend to depth of 200-300 meters and can constitute low grade, high tonnage deposits marked by a disseminated mineralization (Taylor, 1979; Ŝtemprok, 1987; Pollard et *al*., 1988). Accordingly, the formation of these massive greisens requires the mass transfer of a large amount of fluid through the initially impermeable granitic rock. This apparent contradiction emphasizes that the permeability of granite intrusions must evolve significantly during the greisenization event to enable an efficient fluid flow.

Recent advances have recognized permeability as a dynamic parameter evolving in response to tectonism, fluid production, and mineralogical reactions (Ingebritsen and Appold, 2012; Ingebritsen and Gleeson, 2015). Depending on the reaction's stoichiometry and on the pressure and temperature conditions, replacement reactions may cause significant negative or positive changes in the total solid volume that can affect significantly fluid flow by changing the permeability (Putnis, 2002; Putnis and Austrheim, 2010; Pollok et *al*., 2011; Booden and Simpson, 2011; Putnis and John, 2010; Jonas et *al*., 2014; Putnis, 2015). Replacement reactions associated with a volumetric increase of the solid phases may lead to the self-sealing of the fluid pathways causing a permeability

decrease and hence an inhibition of fluid flow that prevents further hydrothermal alteration. However, in some extreme cases such as serpentinization (hydration of ultramafic rocks), the drastic expansion of the solid phases induced by replacement reactions can generate stress perturbations that trigger micro-fracturing significantly enhancing the permeability (Jamtveit et *al.*, 2000; Iyer et *al.*, 2008; Jamtveit et *al.*, 2009). Conversely, replacement reactions involving a volumetric decrease of the solid phases may be accompanied by porosity and permeability increases that enhance fluid flow. This in turn could enhance mass transport that promotes further hydrothermal alteration, leading to the pervasive transformation of rocks. Consequently, a change in volume occurring during the replacement reactions can become an efficient process for enhancing the permeability of hydrothermal systems as well as by favoring fracturing and deformation processes. However, the implications of this process for metal transport and hence for the formation of large ore deposits remain poorly constrained.

The process of greisenization has mostly been investigated from the geochemical and mineralogical standpoints. Nevertheless, greisens appear to be generally more porous than the parental granites from which they formed (Halter et *al.*, 1996 and 1998, Ŝtemprok, 2005; Kontak et *al.*, 2011; Ŝtemprok et *al.*, 2014). This emphasizes that greisenization can be associated with a significant volumetric decrease of the solid phases. However, the effects of these replacement reactions on the permeability, which can ultimately enhance fluid flow and promote the transport of metals in granitic rocks, need to be investigated and quantified. In the following, we present a complete study that combines mineralogical and microtextural analysis with porosity and density measurements for representative samples of different degrees of greisenization from the world-class W-Sn-(Cu) Panasqueira ore deposit. These measurements of the rocks' petrophysical properties were supplemented by the experimental determination of permeability under realistic hydrothermal conditions representative of their degree of greisenization. Additionally, experimental greisenization coupled with permeability measurement has been performed to establish relationships between the rock-volume decrease induced by the replacement reactions identified by mineralogical study, and the evolution of permeability.

The analysis of these various results provides evidence that greisenization can be a decisive process in enhancing the permeability of granitic rock and thereby promoting metal transport in Sn-W deposits, in the absence of external stress. Accordingly, this may

explain the formation of large greisen deposits as well as the efficient transport of metals toward structural traps, as in the lode vein deposits of Panasqueira.

2. Geological setting

2.1 The Panasqueira W-Sn-(Cu) ore deposit

The W-Sn-(Cu) Panasqueira ore deposit is located in Portugal's Beira Baixa province in the Central Iberian Zone (CIZ), which belongs to the Iberian Variscan belt (Julivert et *al*., 1972) (Fig.1a). This region is mainly underlain by Neoproterozoic schist (Schist-Greywacke-Complex) constituting the Beira schist formation, into which a large volume of granitoids was emplaced during the latest stage of the Variscan orogeny (300 to 280 Ma) (Dias et *al*., 1998; Castro et *al*., 2002; Pereira et *al*., 2015).

In the Panasqueira district, the Beira schist was affected by thermal metamorphism (Spotted schist) related to an underlying S-type granite (Fig. 1band 1c) (Clark, 1964; Bussink 1984). Although this granite does not outcrop, its lateral extent is inferred from the surface distribution of spotted schist and from drill holes distributed across the Panasqueira district (Fig.1b). This small intrusive body is characterized by an elliptical shape elongated NW-SE (7.5 x 4.5 km) limited by the Cebola fault to the north-west and the Rio Zêzere fault to the south-east (Fig.1b) (Hebblethwaite and Antao, 1982; Thadeu, 1951; Kelly and Rye 1979; Clark, 1964). The granite's roof geometry is marked by the presence of a cupola observable only in the underground mine (Fig.1b and 1c). This cupola and the upper part of the Panasqueira granite have been converted into a massive greisen by an intense metasomatic alteration (Thadeu, 1951; Clark, 1964; Kelly and Rye, 1979; Bussink, 1984) (Fig.1b and 1c). This greisen is extensively mineralized by sulfides (arsenopyrite, chalcopyrite, sphalerite, pyrite and pyrrhotite) and to a lesser extent by cassiterite and wolframite.

The economic W-Sn mineralization is mainly hosted by a dense network of flat-lying quartz veins, which crosscuts the vertical foliation of the metasedimentary host rock (Beira schist). This ore zone is connected at depth to the greisen cupola and extends over an area of 6 km² for a depth extension of about 200-300 meters (Fig.1b and 1c) (Kelly and Rye 1979; Polya et *al*., 2000).

The paragenetic sequence of the vein system at Panasqueira may be grouped into two main stages (Thadeu 1951; Kelly and Rye 1979; Polya et *al*. 2000). The first stage carries the W-Sn mineralization and is composed of muscovite and quartz accompanied by

wolframite and cassiterite. The second stage, which postdates the Sn-W stage carries the Cu mineralization and consists of arsenopyrite, chalcopyrite, sphalerite pyrite and pyrrhotite. Based on the geological setting and the analyses of fluid inclusions from the Panasqueira mineralized vein system, the conditions related to the W-Sn mineralization stage were estimated at between 300 and 350°C and pressures ranging between 20 and 50 MPa (Kelly and Rye, 1979; Bussink 1984; Noronha et *al*., 1992; Lüders, 1996; Polya et *al*., 2000).

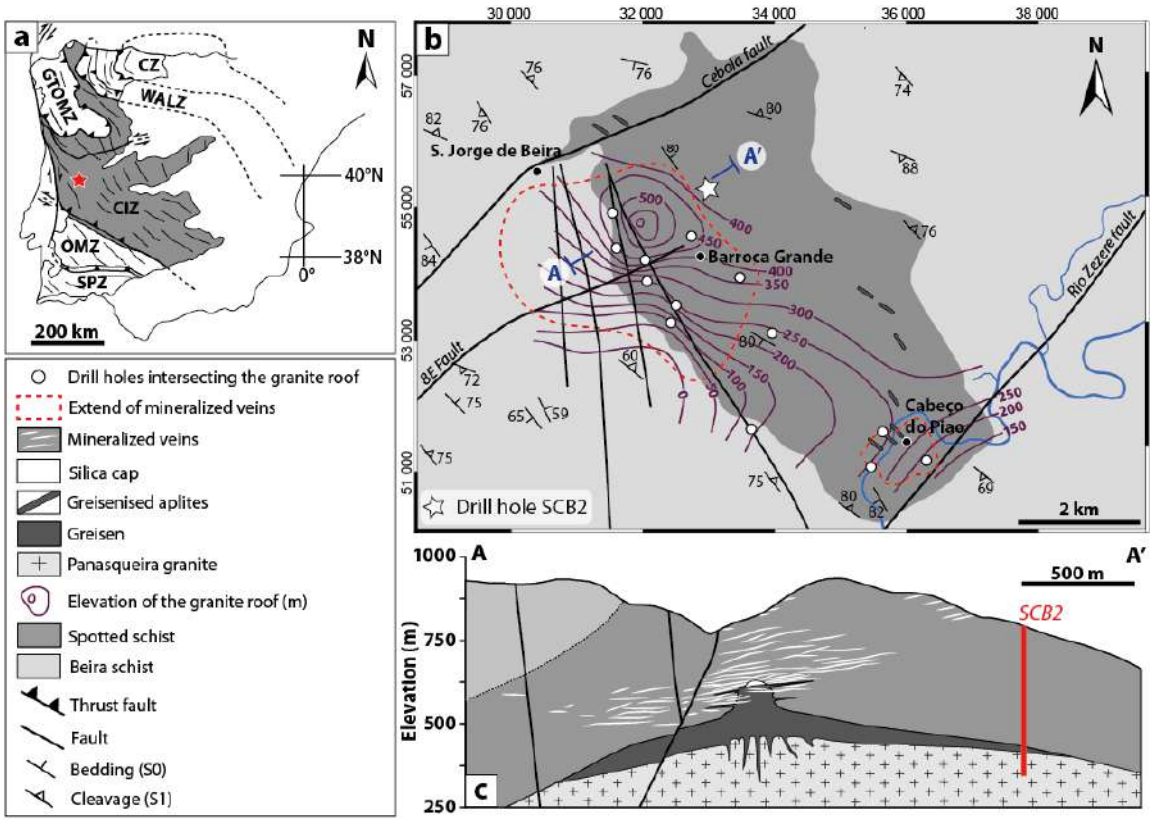

Figure 1 (a) Location of the Panasqueira ore deposit in the Iberian Variscan belt (red star) (b) Geological map of the Panasqueira W-Sn-(Cu) ore deposit including the location of the drill hole SCB2 (white star) used in this study. (c) The (A-A') geological cross section displays the spatial relationship between the mineralized veins and the massive greisen constituting the top of the granite intrusion (data source Beralt Tin & Wolfram S.A.) (modified from Launay et *al*., 2018). Abbreviations, CZ: Cantabrian Zone, WALZ: West Asturian-Leonese Zone, GTOMZ: Galicia Tràs-os-Montes Zone, CIZ: Central Iberian Zone, OMZ: Ossa-Morena Zone and SPZ: South Portuguese Zone.

2.2 The greisen alteration of the Panasqueira granite

The SCB2 borehole was drilled in the NE flank of the intrusive body (Fig.1b and 1c) down to a depth of 400 m. The drill cores display a strong vertical mineral zoning of the granite-greisen assemblages that reflects the progressive transformation of the Panasqueira granite into greisen (Fig.2a).

The deeper part of the intrusion exhibits a porphyritic two-mica granite mainly composed of K-feldspar phenocrysts (up to 4 cm) and snowball quartz embedded in a coarse (millimeter grains) matrix of albite, quartz, biotite and muscovite (Fig.2b photo 4). Accessory minerals include apatite, zircon and Fe-Ti oxides. In this granite, the greisen alteration is present only at local scale as narrow halos (1-30 cm) developed along each side of fracture or mineralized veins (Fig.2a and 2b photo 4).

The upper part of the intrusion consists of a broad massive greisen (≈ 30 m thick in drill hole SCB2), which can become several hundred meters thick in the cupola (Fig.1c). In drill hole SCB2, the greisenization increases progressively up to the granite roof, as evidenced by changes in the rock's mineralogical composition (Fig.2a). The granite is completely altered and converted into greisen along the granite-schist contact. The presence of granite relics embedded in the massive greisen marks the migration front of this pervasive alteration (Fig.2b Photos 2 and 3). During this intense hydrothermal alteration, the primary magmatic texture of the Panasqueira granite was completely obliterated by replacement minerals. Feldspars and biotite are totally replaced by an equi-granular, medium grained quartz-muscovite assemblage characterized by a porous texture suggesting the development of porosity during the greisen alteration (Fig.2b Photo1).

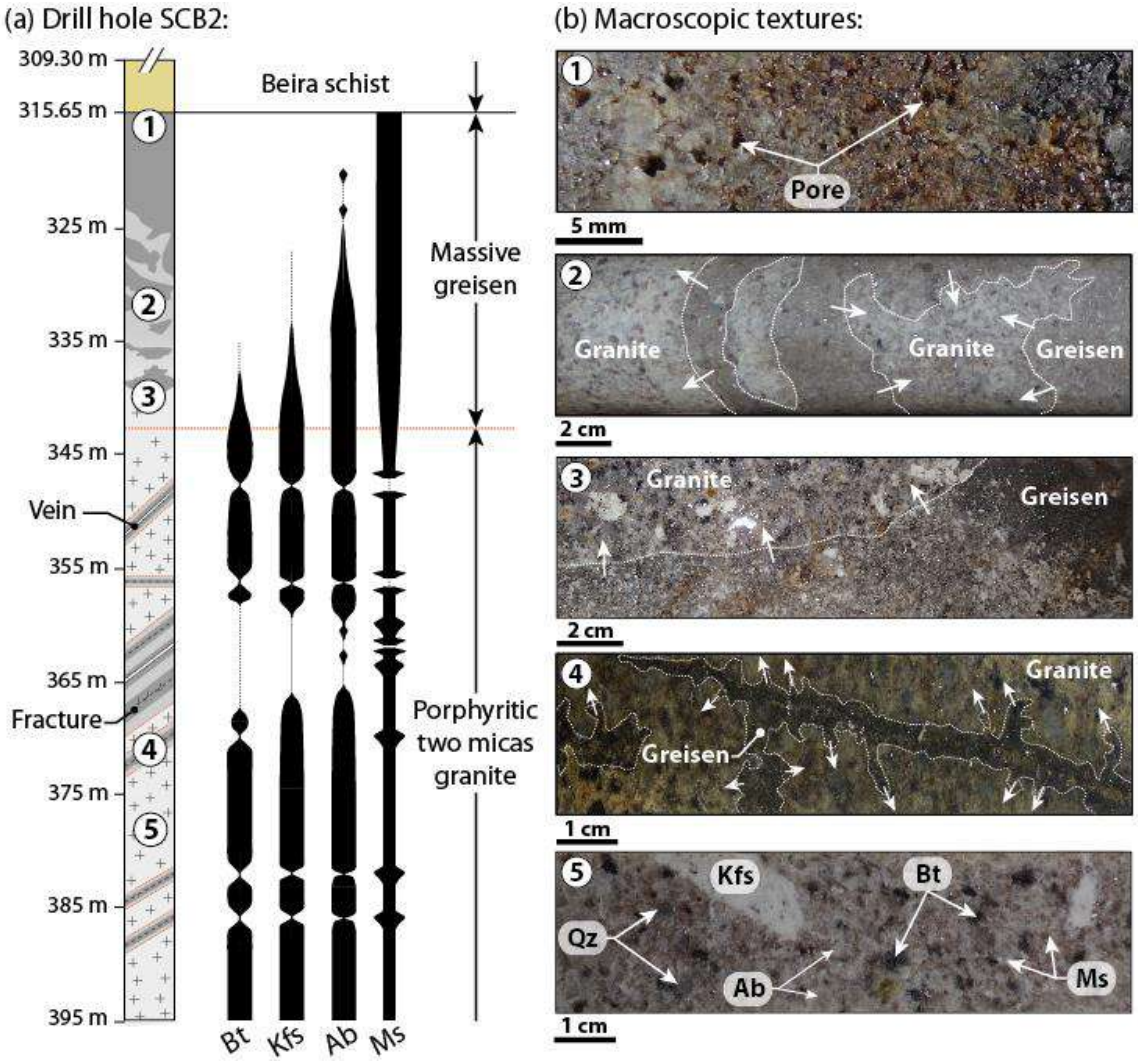

Figure 2 (a) Drill hole SCB2 showing the vertical mineral zoning of the greisen alteration (b) Macroscopic textural characteristics of 1:facies of the most altered greisen displaying a well-developed porosity, 2: quartz-muscovite greisen in which it is possible to observe pieces of less altered granite (white dashed lines correspond to the alteration front and white arrows to the expected direction of propagation), 3: propagation of the pervasive greisenization toward the Panasqueira granite, 4: propagation of alteration from fracture in deeper part of the drill hole and 5: the porphyritic two-mica granite of Panasqueira. Mineral abbreviations from Whitney and Evans (2010) Ab: albite, Bt: biotite, Kfs: K-feldspar, Ms: muscovite, Qz: quartz.

3. Materials and methods

3.1 Starting materials

To investigate the influence of the greisen alteration on the petrophysical properties, especially on permeability, five samples of the least altered granite, three samples of the most altered greisen and eleven samples of greisenized granite with various alteration levels were collected from drill hole SCB2 and within the greisen cupola. To compare the greisen's permeability with the background permeability of the metasedimentary host rock and to assess the potential role of greisen as possible and preferential pathway for mineralized fluids, we collected one additional sample of schist above the granite-schist contact in drill hole SCB2.

3.2 Mineralogical and micro-textural analysis

The micro-textures and micro-structures of samples were examined on polished thin sections by optical microscopy (reflected and transmitted light) and by scanning electron microscopy (SEM) using a Zeiss Merlin compact high resolution scanning electronic microscope equipped with a Gemini I detector (BRGM, University of Orléans). To display alteration textures in natural samples and in experimental alteration products, element mapping was performed by SEM using an acceleration voltage of 15 kV.

3.3 Whole rock geochemical analysis

The whole rock major and trace element compositions of the selected samples were determined by inductively coupled plasma atomic emission spectroscopy (ICP-AES) and mass spectrometry (ICP-MS) following the standard analytical procedure of ALS laboratories (alsglobal.com/geochemistry).

From these analyses, the relative mobility of elements during the greisen alteration has been used (i) to discuss the mass/volume changes of rocks induced by alteration reactions, and (ii) to define a chemical alteration index characterizing the degree of alteration of each sample. This alteration index was then applied to determine the evolution of the petrophysical properties (density, porosity and permeability) as a function of the greisen's degree of alteration.

3.4 Greisenization experiment coupled with permeability measurement

To determine whether replacement reactions involved during the greisen alteration can enhance permeability during the first stage of the alteration and develop new pathways at the mineral scale, we performed a greisenization experiment coupled with permeability measurements. This experiment was conducted in an external heated pressure vessel for which the maximum allowable confining pressure and temperature conditions are 30 MPa and 300°C. This experimental system includes two metering pumps, which can work at constant fluid pressure condition during the experiment (precision of ±0.01 MPa) (Fig. 3a). The fluid flow across the sample was induced by a differential fluid pressure gradient imposed by the two metering pumps, which were also used to record the volume of fluid injected/collected through the core sample over the experimental period. These metering pumps (upstream and downstream) were connected to a gold jacket that contained the granite core (diameter 0.5 cm, length 2 cm) (Fig. 3b). The ductile nature of gold at the applied pressure and temperature conditions ensures a perfect coupling between the side of the core and the jacket and prevents fluid flow along the sample surface. Permeable ceramic spacers were placed on each end of the core sample to act in the place of spreader plates, ensuring that the fluid impinged on the entire sample area.

The greisenization experiment was conducted for a duration of 20 days at 300°C for a confining pressure of 30 MPa and with a differential fluid pressure gradient (ΔP) of 10 MPa (upstream pump = 27 MPa, downstream pump = 17 MPa). The fluid used for the experiment was characterized by a log(mKCl/mHCl) of 2.5 and a log(mNaCl/mHCl) of 2.0 for an initial pH of 2.0. This fluid chemical composition was chosen to promote the replacement of feldspars (albite and K-feldspars) by muscovite under the applied experimental conditions, according to the phases diagram shown in Figure 3c. Once experimental conditions were stabilized, the sample remained for 24hr under the imposed temperature, confining and pore fluid pressure conditions without fluid flow, to couple the jacket with the granite core and to equilibrate sample with the experimental conditions. The differential fluid pressure gradient of 10 MPa was then applied to initiate fluid flow across the core sample. The volume of fluid which passed through the sample was recorded continuously by the downstream metering pump. From this recorded volume, the flow rate (Q) was calculated for each day of the experiment and at each significant change of the volume over time. Permeability (k in m^2) was then calculated using Darcy's law and assuming a steady state flow:

$$k = \frac{\mu L Q}{A \Delta P} \quad (1)$$

where Q ($m^3.s^{-1}$) is the flow rate across the sample, μ is the fluid viscosity under the experimental conditions (6.7 x 10^{-5} Pa.s), L (m) and A (m^2) are respectively the length and cross-sectional area of the core sample, ΔP (Pa) is the imposed differential fluid pressure across the core sample ($P_{up} - P_{down}$).

At the end of the experiment, the sample core was recovered and a polished thin section was prepared to study the alteration products and micro-textures produced during the experiment using the analytical procedure described in section *3.2*.

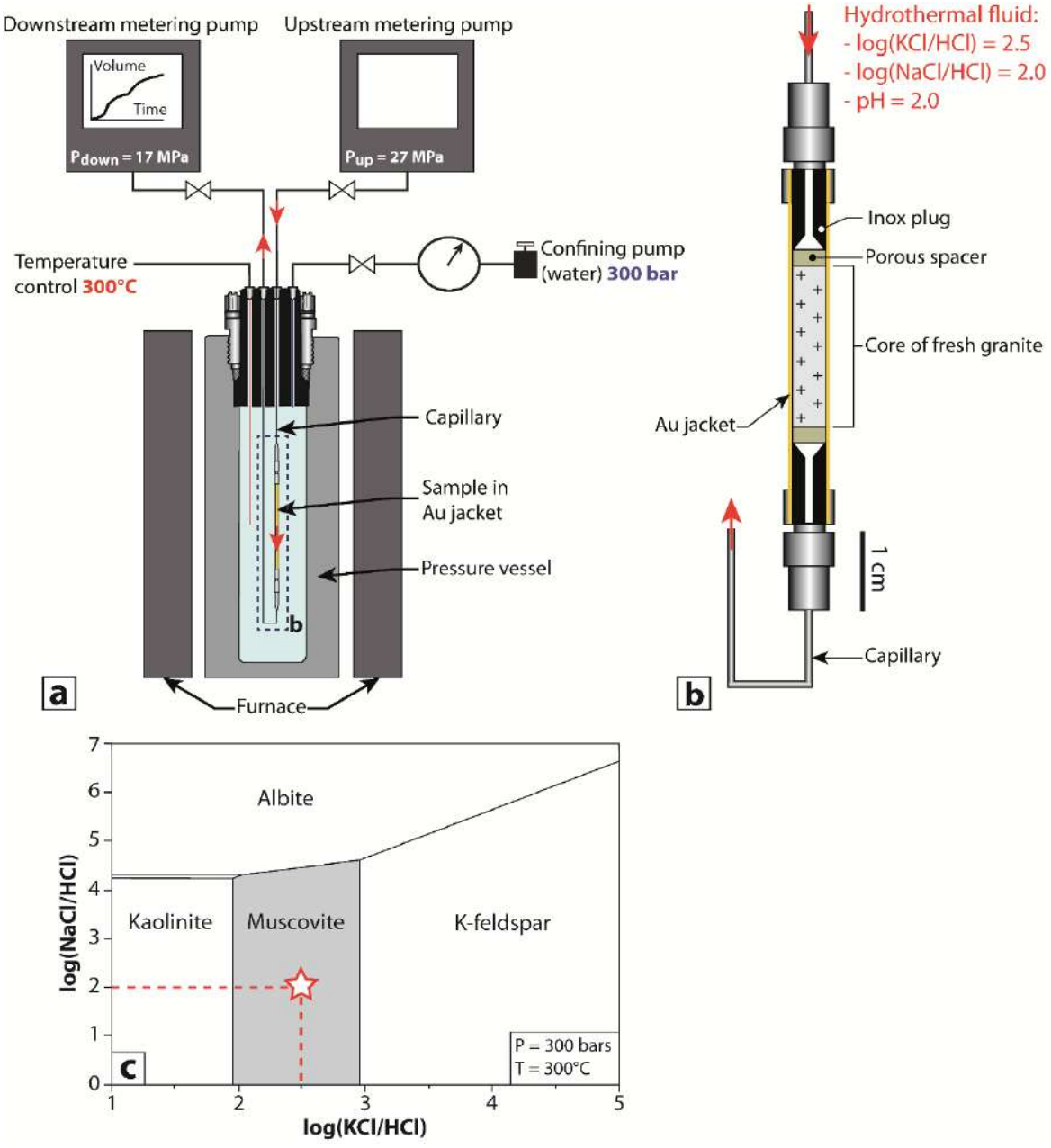

Figure 3 Apparatus used for the greisenization experiment coupled with permeability measurement (a) External heated pressure vessel equipped with two metering pumps used for the pore fluid system and the permeability measurement (b) Connection between the granite core (encapsulated in the Au jacket) and the pore fluid system. Red arrows give the sense of fluid flow in the pore fluid system. (c) log(NaCl/HCl) vs. log(KCl/HCl diagram showing the stability fields of albite, muscovite and K-feldspars under the experimental conditions used for the greisenization experiment (300°C and 300 bar). The white star indicates the composition of the starting solution used for the experiment. This diagram was established from the SUPCRTLB thermodynamic database (Zimmer et *al.*, 2016 and Johnson et *al.*, 1992).

3.5 Porosity and density measurements

The connected water porosity (φ) and the matrix density of samples were determined using the double weight water saturation (or imbibition) method at the BRGM laboratory (French Geological Survey). Before measurements, samples were cleaned and dried in a vacuum for at least 24h. Dry samples were weighted (m_d) and were then immerged for 24h to ensure the total saturation of pores. After the full saturation of samples, the weight of the immerged samples (m_b) was determined by hydrostatic weighing. Then, the weight of the saturated samples (m_w) was determined after the excess of water from the surface of samples was removed. For each sample φ was calculated from:

$$\varphi\ (\%) = 100 \text{ x } \frac{m_w - m_d}{m_w - m_b} \tag{2}$$

and the matrix density (ρ_s) of samples was determined from the following expression:

$$\rho_s = \frac{m_d}{m_d - m_b} \tag{3}$$

This method provides good accuracy with precisions of ±0.01 g.cm^{-3} for the density and ±0.02% for the connected porosity.

3.6 Permeability measurements at hydrothermal conditions

The permeability of natural samples collected at Panasqueira was measured in an internally heated Paterson apparatus equipped with a pore fluid pressure system enabling measurement of the permeability under realistic temperature and pressure conditions (Tenthorey et *al.*, 2006; Cox and Tenthorey 2003; Coelho et *al.*, 2015). This apparatus allows independent control of the argon confining pressure (P_c), the temperature, and the

pore fluid pressure (P_f), and can be configured to deform samples both coaxially (compression) and non-coaxially (torsion) (Paterson and Olgaard, 2000) (ESM 1).

Six cylindrical samples (15 mm diameter, 35 mm in length) were prepared from rock specimens representative of different levels of greisenization, for which the connected porosity and density had been previously measured. Pore fluid pressure and core samples were separated from the confining medium by a copper jacket, whose ductile nature ensures a complete sealing between the sample's sides and the jacket.

Based on hydrothermal conditions estimated from fluid inclusion studies performed on greisen systems worldwide and on the Panasqueira deposit, we imposed a temperature of 400°C, a confining pressure of 100 MPa and a pore fluid pressure of 50 MPa so as to determine the permeability at realistic and representative conditions for greisen systems. In all experiments, the procedure consisted of first raising P_c up to the target level of 100 MPa. The temperature was then raised to 400°C; P_c and P_f were adjusted to remain fixed at the conditions initially selected. Once the experimental conditions were stabilized, permeability was measured with de-ionized water as pore fluid using the steady-state flow method for a Darcian flow (1). In all experiments, ΔP was fixed at 5 MPa, representing approximately10% of the total pore fluid pressure. For this purpose, the upstream pressure (P_{up}) was automatically kept at 50 MPa using a servo-controlled volumometer, while the downstream pressure (P_{down}) was maintained at 45 MPa by a micrometering needle valve. The volumometer that imposes P_{up} was also used to measure the volume of fluid that flowed through the sample over the experimental period, enabling the calculate of Q by linear regression (dV/dt) (for more information in the electronic supplementary materials see ESM 1). Greisenization reactions and microtextural evolution

4. Greisenization reactions and microtextural evolution

4.1 Least altered two-mica granite: mineralogical and textural characteristics

The mineralogical and microtextural characteristics of the least altered two-mica Panasqueira granite of are displayed in Figure 4 (more photomicrographs are presented in electronic supplementary materials ESM 2). This granite exhibits a porphyritic texture marked by a lack of visible pores (Fig. 4a).

K-feldspar forms large euhedral phenocryst (up to several centimeters) and small grains in the rock matrix (Figs. 4a to 4d). The K-feldspar may display perthitic texture resulting from the exsolution of albite lamellae, and poikilitic textures comprising numerous inclusions of quartz, albite, biotite and apatite (Figs. 4b and 4c). In cathodoluminescence image, K-feldspar is marked by a complex texture with prominant blue and red luminescent zones (Fig. 4d). Microprobe analyses (EPMA) of these zones indicate that the blue luminescent feldspars are characterized by compositions ranging between Or84 to Or93, while the red zones are characterized by compositions ranging between Or97 to Or98 (Fig. 4d) (complete analyses of feldspars are provided in electronic supplementary materials ESM 3). Evidently, the original magmatic alkali feldspars (blue luminescent zones) were affected by K-metasomatism, during which they were converted to nearly pure orthoclase (red luminescent zones). These observations are consistent with numerous studies describing the relationships between the cathodoluminescence characteristics of alkali feldspars and the level of K-metasomatism induced by hydrothermal fluids (Smith and Stenstrom, 1965; Mariano, 1976; Finch and Walker, 1991; Lee et *al.*, 2007).

Biotite is common, forming large sub-euhedral flakes (up to 2 mm) containing numerous inclusions of accessory minerals such as apatite, zircon (outlined by the occurrence of disintegration halos), monazite, rutile and ilmenite (Fig. 4e). The occurrences of biotite inclusions in K-feldspar suggest that the crystallization of biotite precedes the crystallization of K-feldspar.

Albite is mainly present as numerous small euhedral grains and also as large phenocrysts with sizes ranging from 1 to 5 mm (Figs. 4a and 4f). This albite is characterized by a typical polysynthetic twining texture and by poikilitic texture marked by inclusions of quartz and apatite (Fig. 4f). Microprobe analyses show that the plagioclase has nearly pure albite compositions (Ab93 to Ab100) (Fig. 4f). These

compositions suggest that primary magmatic plagioclase were completely replaced by albite during an early albitization event commonly observed in greisen systems, which predates greisenization (Shcherba 1970; Pirajno, 2009). This pseudomorphic replacement of plagioclase is accompanied by the development of a pervasive network of micropores (pitted textures) within the albite grains (Figs. 4g and 4h). This porosity generation is commonly described from magmatic-hydrothermal systems affected by K-metasomatism and albitization (Kontak, 1990; Kontak and Clark, 2002; Kontak, 2006; Pandur et *al*., 2016; Dostal et *al*., 2014, 2015) and results from coupled dissolution-precipitation reactions (CDP) discussed in detail by Putnis (2002), Engvik et *al*. (2008) and Putnis and Austrheim, (2010). The development of pitted textures during albitization could contribute to the enhancement of subsequent greisenization by promoting pervasive fluid flow through feldspars.

These textural and mineralogical observations provide evidence that greisenization of the two-mica Panasqueira granite was preceded by high temperature alkali metasomatism (K-metasomatism and albitization), during which primary magmatic plagioclase and alkali feldspars were respectively converted into nearly pure albite and orthoclase. Consequently, samples used as reference for the initial rock properties before greisenization are referred as to the "least altered granite" in the following sections.

Figure 4 Mineralogical and microtextural characteristics of the two-mica Panasqueira granite. (a) Photomicrograph displaying a general view of the two-mica granite (transmitted light). (b) Photomicrograph of matrix K-feldspars exhibiting typical perthitic textures (polarized transmitted light). (c) Phenocryst of K-feldspar marked by poikilitic textures (inclusions of biotite, albite and apatite) (transmitted light). (d) Cathodoluminescence image of the same k-feldspar phenocryst displayed in c. This grain exhibits blue and red luminescent zones corresponding to different chemical compositions (indicated on image) that are related to K-metasomatism of primary magmatic alkali feldspars (blue luminescent zones). (e) Large euhedral flake of biotite containing numerous zircon and apatite inclusions (transmitted light). (f) Phenocryst of albite with quartz and apatite inclusions. The chemical composition of albite is indicated on the photomicrograph (polarized transmitted light). (g) and (h) SEM-BSE images of albite displaying typical pitted textures marked by the occurrence of a dense network of micropores. Abbreviations from Whitney and Evans (2010) Ab: Albite, Ap: Apatite, Bt: Biotite, Kfs: K-feldspar, Ms: Muscovite, Or: Orthoclase; Qz: Quartz, Zrn: Zircon.

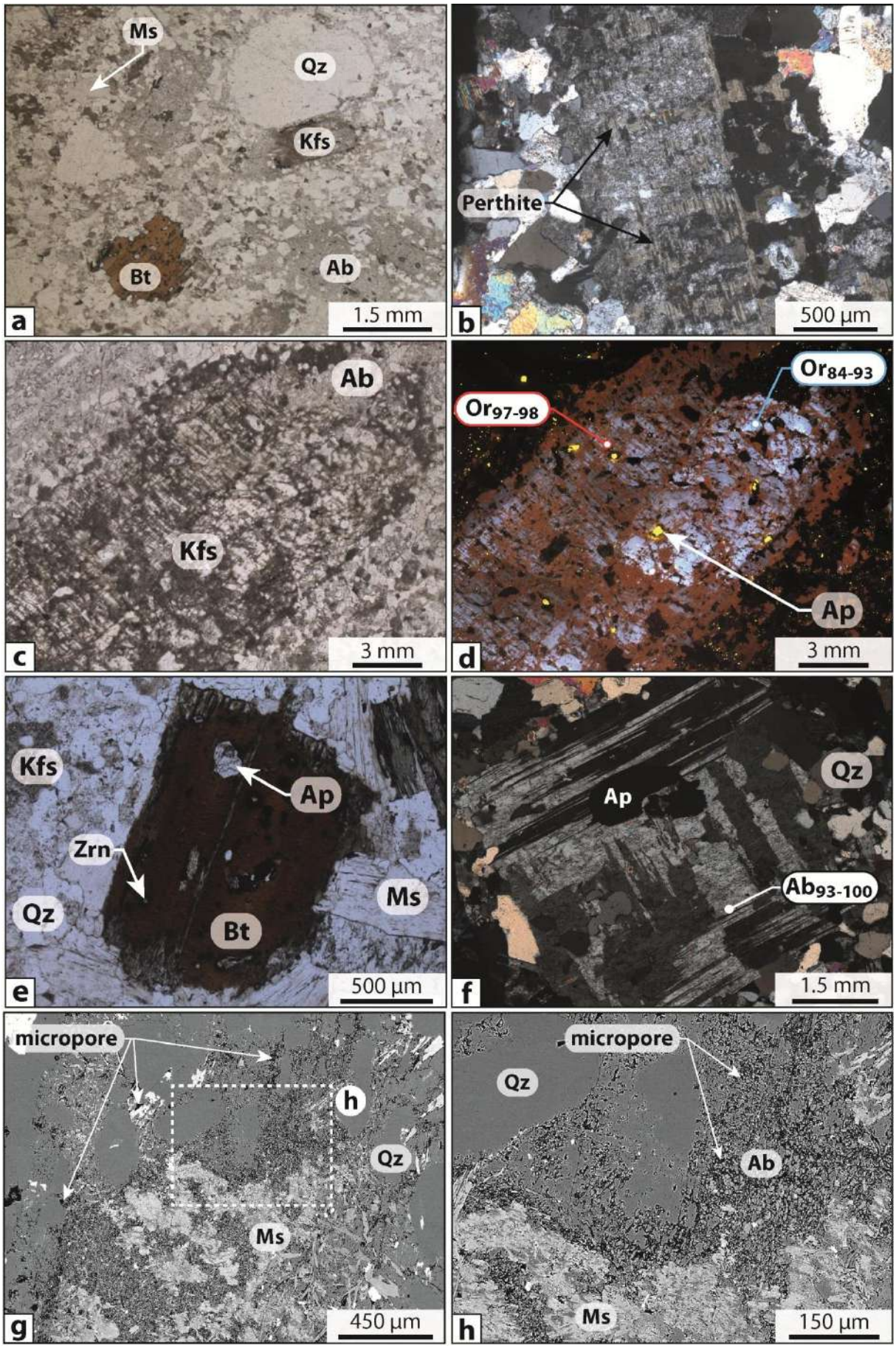
Ms
Qz
Kfs
Bt
Ab
1.5 mm
a
Perthite
500 µm
b
Ab
Kfs
3 mm
c
Or84-93
Or97-98
Ap
3 mm
d
Kfs
Ap
Zrn
Qz
Ms
Bt
500 µm
e
Ap
Qz
Ab93-100
1.5 mm
f
micropore
h
Qz
Ms
450 µm
g
micropore
Qz
Ab
Ms
150 µm
h

4.2 Mineral replacement textures

Partially greisenized facies enable observation of the progressive breakdown of albite (Fig.5a), K-feldspar (Fig.5b) and biotite (Fig.5c) induced by the greisen alteration.

K-feldspars and albite are partially and unevenly replaced by a fine-grained quartz-muscovite assemblage. In the most altered portions of feldspars, the small flakes of muscovite have progressively recrystallized and become agglomerated to form large flakes. As illustrated by Na and K mapping, small portions of the parental feldspars have survived along grain edges and may still occur as intergrowth between muscovite crystals.

Alteration of biotite creates coronitic textures composed of irregular residual grains of biotite surrounded by neoformed muscovite. The replacement of biotite by muscovite can also occur along the cleavage planes of biotite that were probable pathways for fluids. The presence of ilmenite disseminated throughout the neoformed muscovite indicates that Fe and Ti released by the biotite alteration have crystallized to form these oxide minerals.

These alteration textures show that the greisenization involves coupled dissolution-precipitation (CDP) mechanisms, during which primary magmatic minerals were gradually dissolved and simultaneously replaced by newly crystallized muscovite and quartz. The micropore network observed in altered sections of K-feldspars and albite developed during the early alkali metasomatism could promote the circulation of greisenizing fluids through feldspars and enhance their replacement by muscovite during the greisenization.

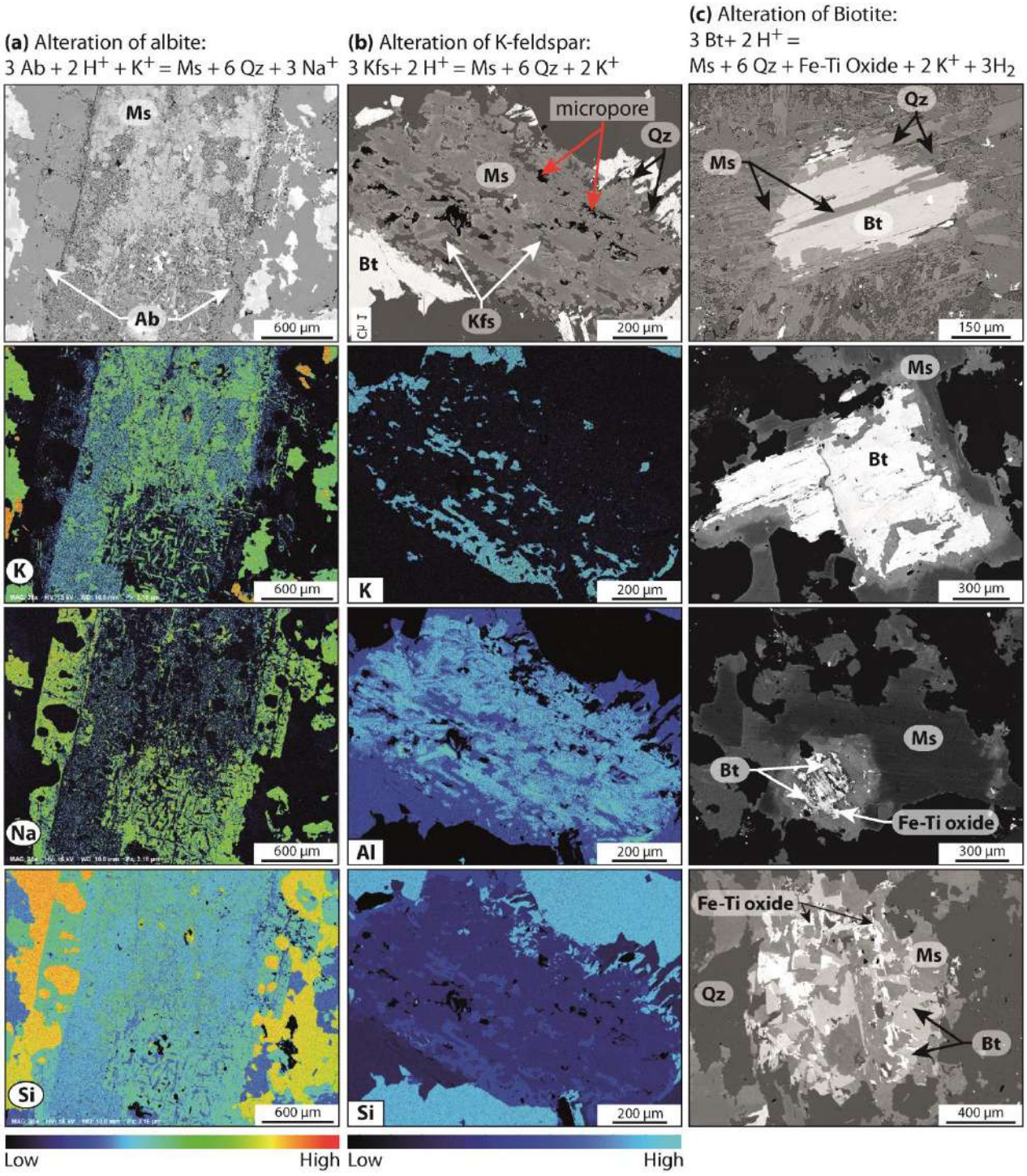

Figure 5 SEM microphotographs and element mapping of Na, K and Al showing the replacement textures of (a) albite, (b) K-feldspar and (c) biotite involved during the greisen alteration. Note the development of micro-porosity in the altered sections of K-feldspar and albite. Abbreviations from Whitney and Evans (2010) Ab: Albite, Bt: Biotite, Kfs: k-feldspar, Ms: Muscovite, Qz: Quartz.

4.3 Microtextural evolution related to the greisenization

The microtextural evolution induced by the greisenization is displayed from SEM-BSE images in Figure 6 (more SEM-BSE images are displayed in electronic supplementary materials ESM 4). As evidenced in the SEM-BSE images, the greisenization is accompanied by the development of a porous texture. In greisenized granite, albite is still present in the rock matrix and the porosity comprises a combination of pores and microcracks connecting individual pores. Spaces between muscovite grains provide a network of intergranular pores (Fig. 6a). These pores are unevenly distributed in the rock matrix and organized into pockets (Figs. 6a and 6b). This heterogeneous distribution may result from the uneven distribution of feldspars from which pores could be formed during the replacement reactions.

As in greisenized granite, the porosity within the greisen comprises a combination of pores and microcraks preferentially opened in quartz (Figs. 6c and 6d). These microcraks seem to connect the isolated pores unevenly distributed throughout the rock matrix. The intergranular spaces between muscovite represent a large part of the porosity (Fig. 6d). The abundance and size of the pores seem to increase between greisenized granite and the most altered greisen, with pore size ranging from few microns to tens of microns in greisenized granite and from several hundred micrometers to several millimeters in greisen. In the most porous facies, porosity forms a dense intergranular network, in which hydrothermal minerals such as euhedral apatite have crystallized (Figs. 6d and 6f). Large voids (up to 5 mm) can also be observed in greisen and show the development of porosity during greisenization (Fig. 6e). These voids are commonly fringed by euhedral quartz indicating that adjacent crystals were growing into open space.

Muscovite composing the greisen forms large euhedral flakes characterized by well-developed growth zoning marked by dark cores and light rims in SEM-BSE images (Figs. 6a and 6f). These zonings correspond to core to rim enrichment in Fe and core to rim depletion in Al (Figs. 6g and 6h). This chemical and textural zoning can be interpreted as hydrothermal overgrowths on primary magmatic muscovite during greisenization. This zoning pattern has previously been described in the hydrothermally altered Sn-bearing granite of Ervedosa (northern Portugal) and interpreted as a marker of the hydrothermal alteration related to the Sn mineralization stage (Gomes and Neiva, 2000). As shown by chemical mapping, these hydrothermal overgrowths on muscovite have grown preferentially in the open pore spaces developed during the greisenization.

The extensive development of pores and micropores in greisen may be a response to the mineralogical transformation induced by the replacement of primary minerals in the Panasqueira granite during greisenization. This suggests that replacement reactions related to the greisenization are probably associated with a volume decrease of the solid phase that may constitute an efficient mechanism for enhancing porosity.

Figure 6: SEM-BSE images displaying the microtextural evolution induced by the greisenization of the Panasqueira granite. (a) Porous texture in a greisenized granite sample showing the heterogeneous distribution of the porosity. A microporous pocket and a microcrack are labeled. (b) Enlargement of a microporous pocket showing the intergranular porosity corresponding to spaces around muscovite grains. (c) Porous texture in greisen showing large pores corresponding to spaces around muscovite grains (this section was made from the sample shown in Figure 2b-1). (d) Porous greisen, in which a large amount of hydrothermal apatite has crystallized during the late hydrothermal stages. (e) Large void space fringed by euhedral quartz, which has crystallized from the pore's edge. (f) SEM-BSE image showing hydrothermal overgrowth of muscovite forming greisen and pore space partially infilled by hydrothermal apatite. (g) Fe and (h) Al chemical maps prepared from section shown in (f). Abbreviations from Whitney and Evans (2010) Ab: Albite, Ap: Apatite, Ms: Muscovite, Qz: Quartz.

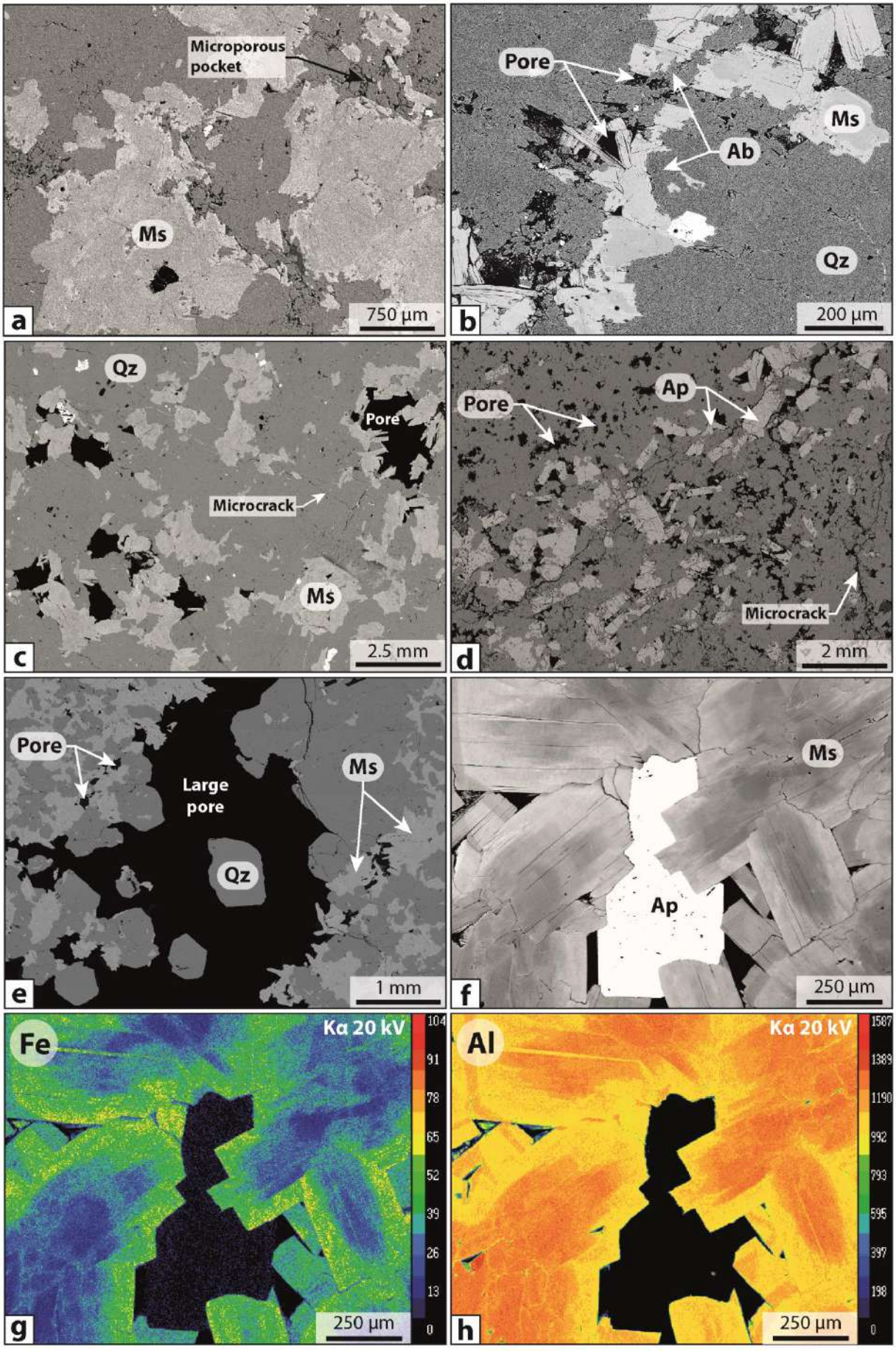
Microporous pocket
Ms
750 µm
a
Pore
Ab
Ms
Qz
200 µm
b
Qz
Pore
Microcrack
Ms
2.5 mm
c
Pore
Ap
Microcrack
2 mm
d
Pore
Large pore
Ms
Qz
1 mm
e
Ms
Ap
250 µm
f
Fe
Kα 20 kV
104
91
78
65
52
39
26
13
0
250 µm
g
Al
Kα 20 kV
1587
1389
1190
992
793
595
397
198
0
250 µm
h

4.4 Chemical changes and chemical alteration index (AI)

The mineralogical transformations described above cause significant changes in the whole rock composition. To account for element mobility during the greisen alteration, the whole rock composition of samples representative of different degrees of greisenization are reported as a function of the least altered granite composition in an isocon diagram (Fig. 7) (Grant, 1986 and 2005). We define the best fit isocon (blue line in Fig. 7) for the most altered granite (greisen) by using the least scattered of all elements: Al, P, Mn and Fe and assuming that these elements were immobile during the greisenization. The aluminum immobility is a reasonable assumption considering that feldspars are replaced by muscovite which is a major aluminum-bearing-mineral. Figure 7 shows that the greisen alteration encompasses a complex history leading to a progressive mass loss in Na, K, Si, Ca, Sr, Ba, Eu, Mg and Ti and mass gain in Li, Rb, Cs, Sn, W, Cu, Zn and As.

This evolution is consistent with the breakdown of feldspar and biotite and the crystallization of large amount of muscovite during the greisen alteration. Destructions of K-feldspar and albite have respectively released K, Ba and Na, K, Ba, Sr, Eu into the fluids, while the formation of muscovite was probably responsible of the enrichment in Li, Rb and Cs, all these elements having a strong affinity with muscovite. This enrichment in granitophile elements (Li, Rb and Cs) is also probably related to the ingress of orthomagmatic fluids, which are commonly enriched in these elements.

Although Ti-rich oxides were formed during the transformation of biotite into muscovite, the mass loss in Ti suggests that the Ti constituting biotite was partially released into the fluids. The significant mass gain in Sn, W and Cu, Zn and As highlights that greisen facies have also recorded the various mineralization stages occurring in the vein system at Panasqueira. The presence of a disseminated mineralization of cassiterite and sulfides in greisen is consistent with these mass gains and suggests that the various mineralized fluids flowed through the greisen during the time that the mineralization stages occurred.

According to the best-fit isocon, the greisenization of the Panasqueira granite is characterized by an overall volume loss of ~12.4% consistent with the porosity developed in the greisen facies.

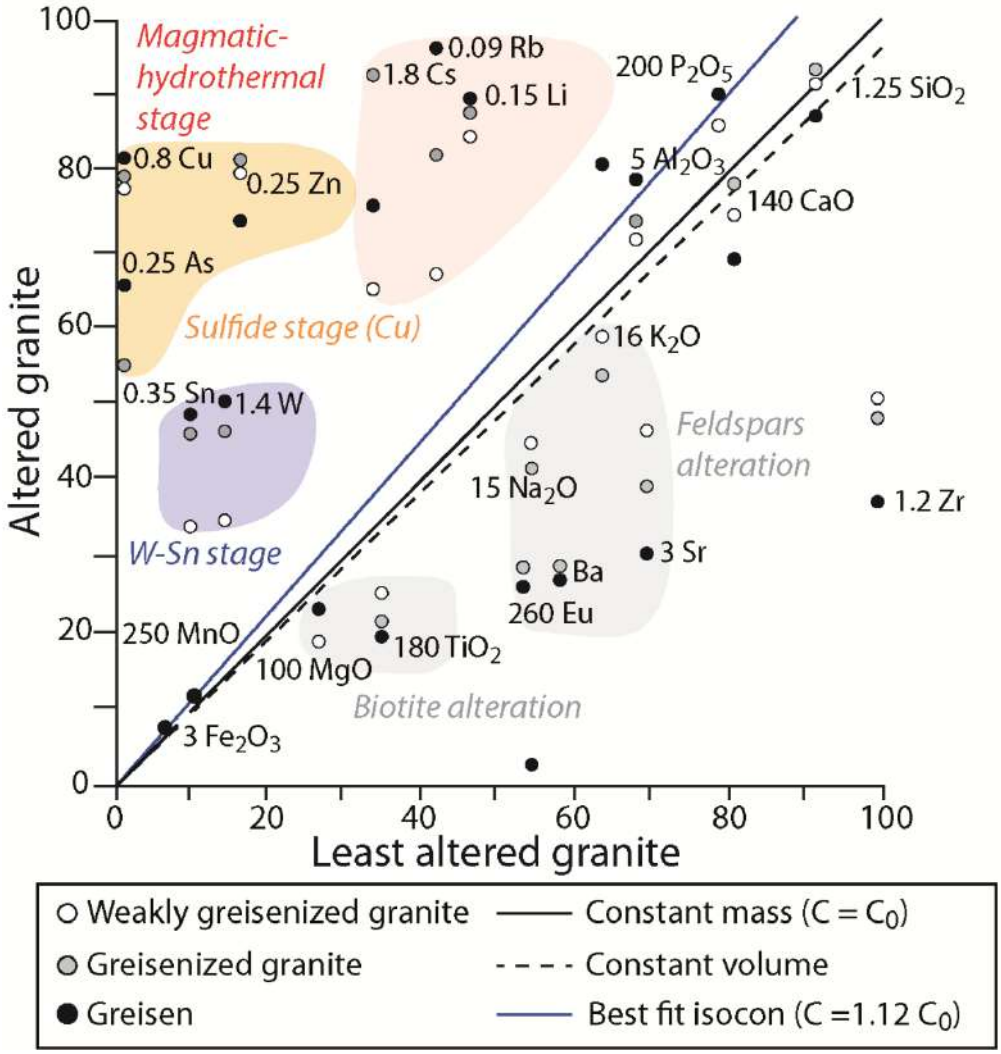

Figure 7 Isocon diagram comparing the chemical composition of the least altered granite and the Panasqueira greisen. Granite composition is an average of 5 analyses. Oxides analyses are in wt% and trace elements in ppm, values are scaled with the factors indicated for each element. The best fit isocon (blue line) defined from P_2O_5, Al_2O_3, MnO and Fe_2O_3 is compatible with an immobile alumina during the greisen alteration. This best fit is characterized by a slope of 1.12 corresponding to a volume decrease of about 12.4 %. For comparison isocon based on hypotheses of constant mass (black line) and constant volume (dashed line) are also plotted.

Based on the assumption that the whole rock compositional change in greisen facies is controlled by the degree of alteration, we can define a chemical alteration index (AI) from the changes in Al, Na and K concentrations (in wt%):

$$AI = 100 \text{ x } \frac{Al_2O_3}{Al_2O_3 + CaO + Na_2O + K_2O} \quad (4)$$

This chemical alteration index, which increases with greisen alteration, is based on the ratio of immobile (Al) to mobile (Ca, Na and K) elements during greisen alteration and reflects the progressive breakdown of feldspars. This index provides a useful approach for

estimating the degree of greisen alteration of the samples investigated and was used to follow the evolution of the rock's petrophysical properties as a function of the level of greisenization. Moreover, this chemical alteration index is commonly applied in the literature to characterize the degree of alteration in diverse geological environments involving the breakdown of feldspars (Nesbitt and Young, 1982; Pola et *al*., 2012; Mayer et *al*., 2016).

4.5 Mineral replacement reactions and changes in rock volume

Based on the mineral replacement textures and the whole-rock geochemical changes related to the greisen alteration, replacement reactions involved during the greisenization may be written as summarized in Table 1. These reactions are based on the assumption that Al was immobile and conserved among the solid phases during the alteration. As previously mentioned, primary magmatic feldspars had already been metasomatised as to form albite and orthoclase, so the reactions were defined considering feldspars with pure albite and orthoclase compositions. During these reactions, a large amount of H^+ was consumed from fluids, whereas Na^+ and K^+ were released into the fluids, as expected from the whole-rock compositional changes described earlier. This is consistent with the extreme leaching of alkali cations by acidic fluids commonly observed in greisen systems (Shcherba 1970; Bishop 1989).

The relative volume change ΔV (%) induced by these reactions can be calculated from the stoichiometric coefficients and molar volumes of the solid phases (Pollok et *al*., 2011). Calculations were performed using the molar volumes of minerals in the thermodynamic database SUPCRTBL (Zimmer et *al*., 2016; Johnson et *al*., 1992) under realistic hydrothermal conditions (400°C and 100 MPa) (Polya, 1989) and applying the following expression:

$$\Delta V(\%) = 100.\left(\frac{\Sigma x_i^p.V_i - \Sigma x_i^r.V_i}{\Sigma x_i^r.V_i}\right) \quad (5)$$

with x_i^p and x_i^r the stoichiometric coefficients of the product and reactant minerals and V_i (cm^3/mol) the molar volumes of associated minerals. Volume changes induced by each alteration reaction are summarized in Table 1.

Replacement reaction		ΔV (cm^3/mol)	ΔV (%)
(R1)	$3\ KAlSi_3O_8 + 2\ H^+_{(aq)} = KAl_3Si_3O_{10}(OH)_2 + 6\ SiO_2 + 2\ K^+_{(aq)}$	-35.3	-10.8
(R2)	$3\ NaAlSi_3O_8 + 2\ H^+_{(aq)} + K^+_{(aq)} = KAl_3Si_3O_{10}(OH)_2 + 6\ SiO_2 + 3\ Na^+_{(aq)}$	-44.4	-14.3
(R3)	$3\ KFe_3AlSi_3O_{10}(OH)_2 + 2\ H^+_{(aq)} = KAl_3Si_3O_{10}(OH)_2 + 6\ SiO_2 + Fe_3O_4 + 2\ K^+_{(aq)} + 3\ H_{2(aq)}$	-38.1	-8.2

Table 1 Molar volume changes (ΔV) induced by the replacement reactions related to the greisen alteration of the least altered Panasqueira granite. ΔV (cm^3/mol) are calculated at 400°C and 100 MPa using the thermodynamic database SUPCRTBL. ΔV (%) is the molar volume change relative to the molar volume of the reactant minerals.

Reactions R1, R2 and R3 are characterized by volume decreases of 10.8%, 14.3% and 8.2% respectively, compatible with the presence of micropores on altered sections of feldspars (Figs.4a and 4b). This suggests that open spaces were created during these replacement reactions and hence that porosity could increase during the greisenization. In the case of the Panasqueira greisen, feldspars and biotite are completely replaced by muscovite and the replacement reactions may therefore be considered as total. Consequently, the porosity potentially developed during these reactions can be estimated assuming volumetric mineral abundances of 17% for K-feldspar, 28% for albite and 8% for biotite (mineral abundances estimated from XRD data in the electronic supplementary materials ESM 5). In light of this estimation, the process of mineral replacement could be accompanied by a porosity increase of ~6.2%, which is consistent with the overall volume decrease predicted by the isocon diagram. This predicted porosity increase is compatible with the development of the porous textures observed in greisen and greisenized facies.

5. Relationships between textural evolution and permeability during greisenization

Replacements reactions involved during the greisenisation result in a volume decrease of the solid phases that could induce porosity generation in greisenized facies. This raises the question of the effect of these replacement reactions on rock permeability. In this section we discuss the results obtained from the greisenization experiment to determine whether alteration reactions can generate new fluid pathways by the development and maintenance of neoformed porosity at the start of the greisen alteration event.

5.1 Evolution of permeability over time during the greisenization experiment

The time evolution of permeability during the greisenization experiment is shown in Figure 8. The initial permeability of the unaltered granite is about 2.0 x 10^{-20} m², a value similar to the permeability values usually obtained in intact granite samples (Moore 1983; Selvadurai et *al*., 2005; Tenthorey and Fitz Gerald, 2006; Ingebritsen and Appold, 2012). The permeability changes measured over the experimental period are normalized to this initial permeability value. After three days of experiment, the permeability increases rapidly with a factor growth of 14 up to 3.0 x 10^{-19} m². Afterwards, the permeability decreases progressively for five days and returns to its initial value following an exponential law. Then, after eleven days of experiment, the permeability increases a second time up to 1.3 x 10^{-19} m² (factor growth of 6). This second increase is also followed by an exponential permeability decrease down to 3.3 x 10^{-20} m².

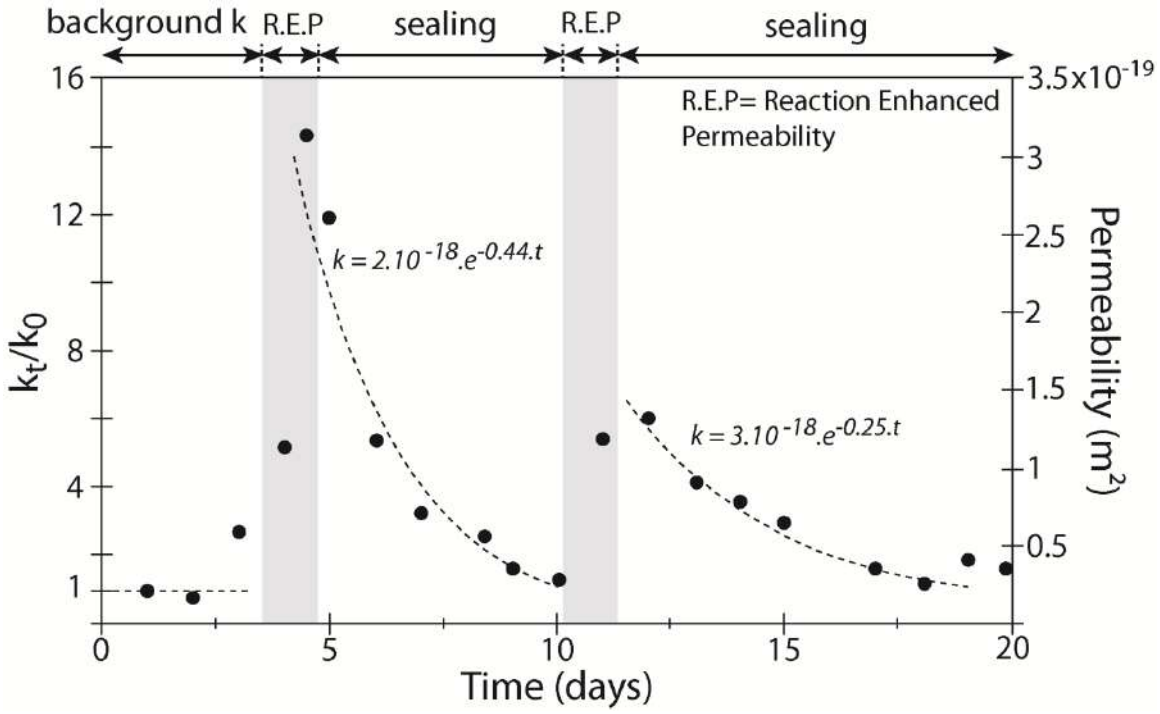

Figure 8 Evolution of permeability over time during the greisenization experiment. This time evolution depicts cycles of permeability increase followed by stages of gradual decrease that may respectively be attributed to porosity generation during the replacement reactions and sealing by closing of the neoformed pathways. The stages of permeability decrease fit with exponential functions commonly observed in experimental studies.

5.2 Replacement products and interpretation of the permeability's evolution

SEM photomicrographs and chemical maps of the alteration products and microtextures developed during the greisenization experiment are shown in Figure 9 (more SEM-BSE images are displayed in electronic supplementary materials ESM 6 and ESM 7). As evidenced by Na, K and Fe chemical maps (Figs. 9b to 9d), alteration has progressed from the upper edge of the granite core in which relics of residual albite can be observed in the neoformed muscovite. During this alteration, feldspars (albite) were replaced by muscovite enriched in Fe compared to the primary muscovite constituting the initial granite. This replacement has occurred preferentially along the grain boundaries and cleavage planes that probably played the role of preferential pathways for elements dissolved in fluid. These interfaces have enhanced the fluid-mineral interactions and initiated the replacement reactions. SEM images show that the replacement of feldspar by muscovite is marked by the development of a microporous texture in altered products (Figs. 9e and 9f). Partially altered sections of albite (Fig. 9f) are characterized by the presence of numerous micropores that are partially fringed by muscovite and euhedral

quartz (Fig. 9g). This suggests that fluids have flowed through the newly formed porosity to promote further alteration.

The creation of porosity seen in the alteration products can be related to the molar volume decrease induced by coupled dissolution-precipitation (CDP) reactions involving the dissolution of albite and the precipitation of muscovite (Pollok et *al*., 2011; Putnis, 2002; Plümper and Putnis, 2009; Putnis and Austrheim, 2010). These CDP reactions were mainly controlled by the pH of the fluid that has triggered and driven the dissolution of albite. This development of porosity in the reaction products has probably provided new fluid pathways that may explain the two permeability increases observed during the experiment (at 5 and 11 days). The permeability reductions observed after each permeability increases are characterized by the same type of reduction rate (exponential decrease) observed in experiments performed on fractured granite samples (Moore et *al*., 1983; Morrow et *al*., 2001 and Tenthorey and Fitz Gerald, 2006). In these studies, the permeability decrease is commonly interpreted as the result of the gradual chemical equilibration of the fluid with the rock sample during fluid-rock interactions. This equilibration could lead to the fluid becoming saturated in product phases such as SiO_2 that could induce the precipitation of quartz in the neoformed porosity, thereby triggering the sealing of the pathways and hence the permeability decrease observed in our experiment. This suggests a potential competition between replacement reactions, which promote and enhance fluid flow by the generation of porosity, and the solubility of product phases released into fluids that could induce the sealing of fluid pathways by mineral precipitation (Putnis 2010; Pollok et *al*., 2011). The cycles of permeability increase and reduction observed during our experiment may be interpreted as the results of the successive generation of pathways by alteration, and the closing of those pathways in response to the processes described above.

Thus, ultimately, this experiment suggests that greisen alteration is able to increase the permeability by the same order of magnitude as those observed during fracturing experiments by Tenthorey and Fitz Gerald, (2006). This emphasizes that replacement reactions related to greisenization are able to generate new pathways for fluids and that this mechanism can be as efficient as fracturing for improving fluid flow in granitic systems. However, this feedback between replacement reactions and permeability requires an efficient fluid renewal and element transport with high water/rock ratios, so as to keep

open the neoformed pathways and to limit the process of sealing caused by the saturation and precipitation of product phases such as SiO_2.

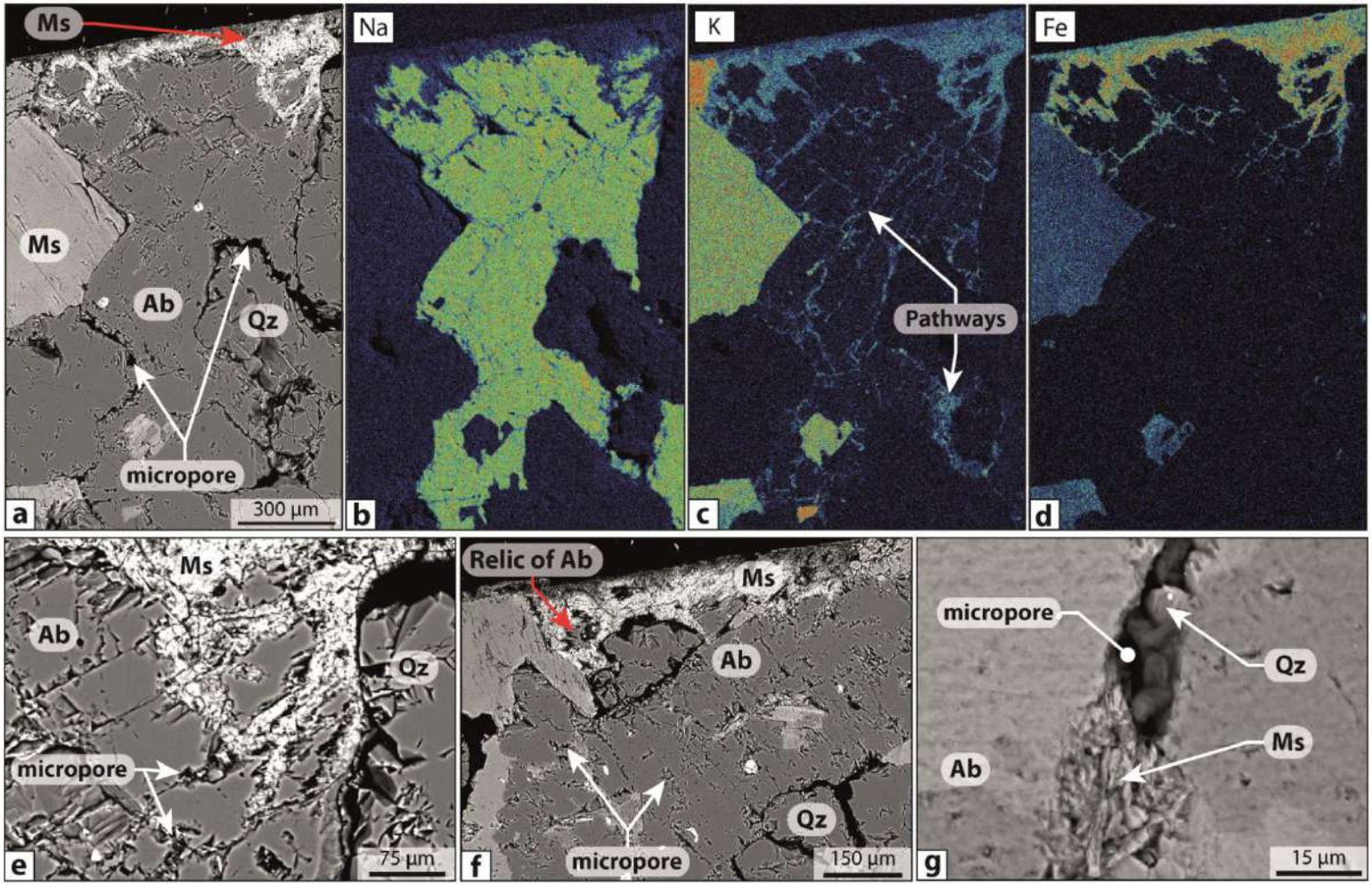

Figure 9 Texture of the alteration products obtained during the greisenization experiment. (a-d) SEM-BSE images and element maps showing the distribution of Na, K and Fe in a partially altered part of the granite core. These maps display the pathways along which fluids have preferentially flowed and altered albite into muscovite during the experiment. (e) SEM photomicrograph showing the dissolution and enlargement of pathway along the grain boundary between quartz and albite and the development of micropore along the cleavage planes of albite. (f) SEM photomicrograph showing the microporous texture of a partially altered albite. (g) Zoom on a micropore developed during the experiment that was partially coated by euhedral quartz and muscovite. Abbreviations from Whitney and Evans (2010) Ab: Albite, Ms: Muscovite, Qz: Quartz.

6. Effects of the greisenization on rock petrophysical properties

The replacement reactions related to the greisen alteration may generate porosity and enhance permeability. In the following, we present the results of petrophysical measurements carried out on natural samples representative of various degrees of greisenization to determine (i) to what extent the porosity and permeability can increase during greisen alteration, (ii) relationships between the evolution of porosity and permeability and the rock alteration index (AI), and (iii) the role of mineral replacement on changes in the rock's petrophysical properties.

6.1 Evolution of density, porosity and permeability during greisen alteration

The evolution of rock matrix density, connected porosity and permeability are summarized in Table 2 and plotted as a function of the chemical alteration index (AI) in Figure 10. Permeabilities measured at 25°C are also included in Figure 10c to show the effect of room temperature on permeability. The unaltered granite is characterized by a matrix density ranging from 2.66 to 2.69 $g.cm^{-3}$, a low connected porosity ranging from 0.54 to 0.71 % and a permeability that lies between 1.9×10^{-20} and 6.3×10^{-20} m^2. These relatively low porosity and permeability are comparable with values commonly observed in granitic rocks (Ingebritsen and Appold, 2012) and emphasize that granite is not favorable for fluid flow. The matrix density (Fig. 10a), the connected porosity (Fig. 10b) and the permeability (Fig. 10c) increase progressively with the chemical alteration index (AI) and hence with the degree of greisenization. Greisen is characterized by a matrix density ranging from 2.87 to 2.93 $g.cm^{-3}$, a connected porosity ranging from 5.86 to 8.97 % and a permeability of 1.24×10^{-17} m^2. These results show that, the mineralogical changes induced by greisen alteration have significant effects on the rock's petrophysical properties and especially on permeability, which increases by three orders of magnitude. This suggests that greisenization probably exerts a strong control on fluid flow, as also do the fracturing and deformation processes (Zhang et al., 1994; Tenthorey and Fitz Gerald, 2006).

	Location	AI	ρ_s (g.cm^{-3})	φ (%)	$k_{25°C}$ (m²)	$k_{400°C}$ (m²)
Granite						
E2	SCB2	61.9	2.68	0.54	3.53×10^{-20}	1.89×10^{-20}
D3	SCB2	62.2	2.66	0.59	-	-
D1	SCB2	62.1	2.69	0.6	-	-
D2	SCB2	64.3	2.69	0.70	-	-
D4	SCB2	62.6	2.68	0.71	-	6.27×10^{-20}
Greisenized granite						
C1	SCB2	66.4	2.70	1.08	6.5×10^{-19}	2.20×10^{-19}
O4	SCB2	66.1	2.72	0.99	-	-
P3D	Mine	67.0	2.71	1.37	-	-
P3C	Mine	68.1	2.76	1.8	4.45×10^{-18}	1.52×10^{-18}
P3E	Mine	66.9	2.75	1.53	-	-
O1	SCB2	68.6	2.72	1.64	-	-
O3	SCB2	66.1	2.73	1.58	-	-
O5	SCB2	70.3	2.73	3.26	5.36×10^{-18}	2.97×10^{-18}
P4-2	Mine	72.3	2.79	3.34	-	-
P4-3	Mine	69.8	2.73	2.04	-	-
P4-4	Mine	71.4	2.73	2.04	-	-
Greisen						
B2	SCB2	72.9	2.9	5.91	1.26×10^{-17}	1.24×10^{-17}
B1	SCB2	72.8	2.87	5.86	-	-
P57-A	Mine	73.9	2.93	8.97	-	-
Host rock (Beira schist)						
A1	SCB2	-	-	-	-	1.52×10^{-20}

Table 2 Rock petrophysical properties measured in samples of granite, greisenized granite and greisen from Panasqueira. AI corresponds to the chemical alteration index defined in section *4.3*

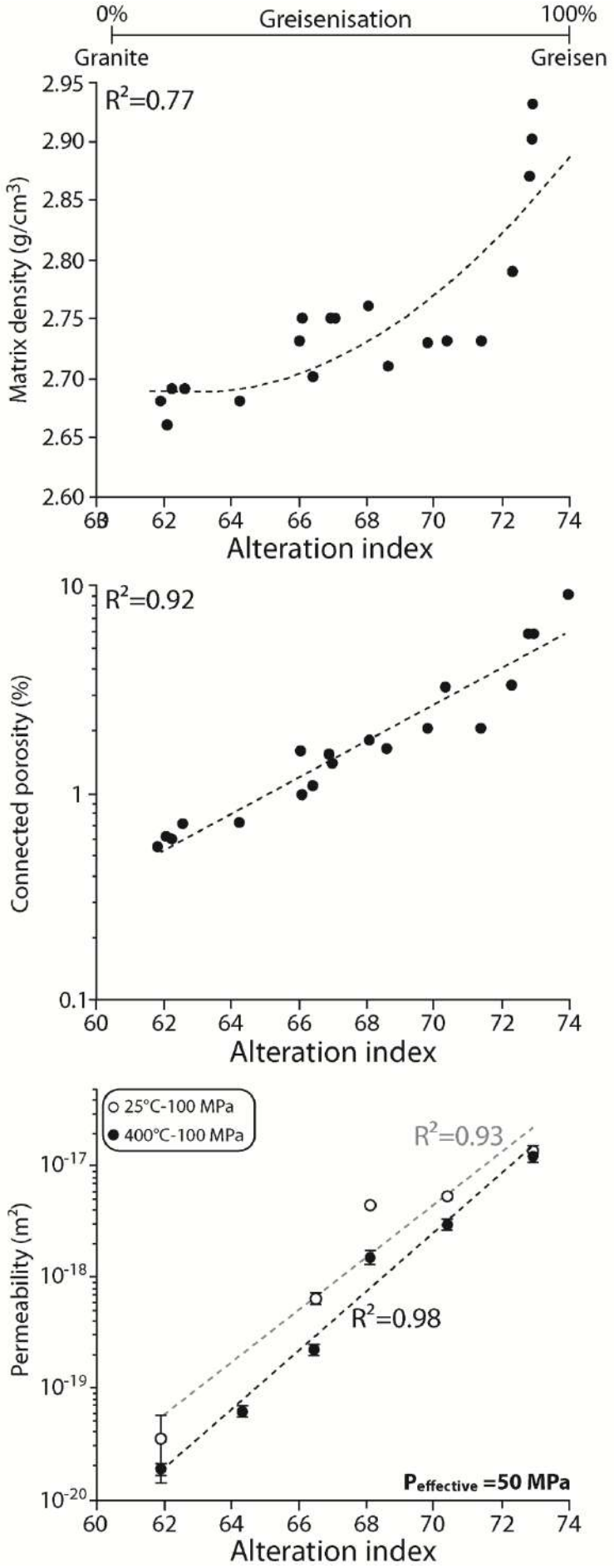

Figure 10 Evolution of (a) matrix density, (b) connected porosity and (c) permeability as a function of the chemical alteration index (AI). The AI increases upon greisen alteration (see the top horizontal qualitative axis and section *4.3* for explanation).

6.2 Porosity-density relationship and dynamic permeability

The rock's petrophysical properties appear to be strongly affected by the advance of greisen alteration. Here, we discuss the relationships between the replacement reactions and changes in the rock's petrophysical properties. In Figure 11a the evolution of porosity is positively correlated with rock matrix density, which depends directly on the density of minerals constituting the rocks. Accordingly, the metasomatic replacement of less dense minerals (albite 2.61-2.63 $g.cm^{-3}$ and K-feldspars 2.54-2.57 $g.cm^{-3}$) by a large amount of denser muscovite (2.77-2.88 $g.cm^{-3}$) is certainly responsible for the overall increase in rock matrix density observed during the greisenization. Consequently, the correlation observed between the porosity and the matrix density emphasizes that the increase in porosity during greisenization was probably caused by replacement reactions related to the greisen alteration described in section *4*. Furthermore, the range of porosity increase (~8.43 %) indicated by our measurements matches the theoretical porosity estimated from (i) the molar volume decrease (9.7 %) induced by replacement reactions related to greisenization and (ii) the best isocon (12.4 %) deduced from changes in the whole-rock composition. We conclude that, the mineralogical transformations induced by greisen alteration can be an efficient process for generating porosity and hence potential pathways for fluid flow. Finally, the high matrix density values observed in the most altered and porous greisen are certainly due to the presence of dense metal-bearing minerals such as sulfides (pyrite 5.01 $g.cm^{-3}$;chalcopyrite 4.2 $g.cm^{-3}$) and cassiterite (6.9 $g.cm^{-3}$) and suggest that greisen was a potential pathway and trap for mineralized fluids.

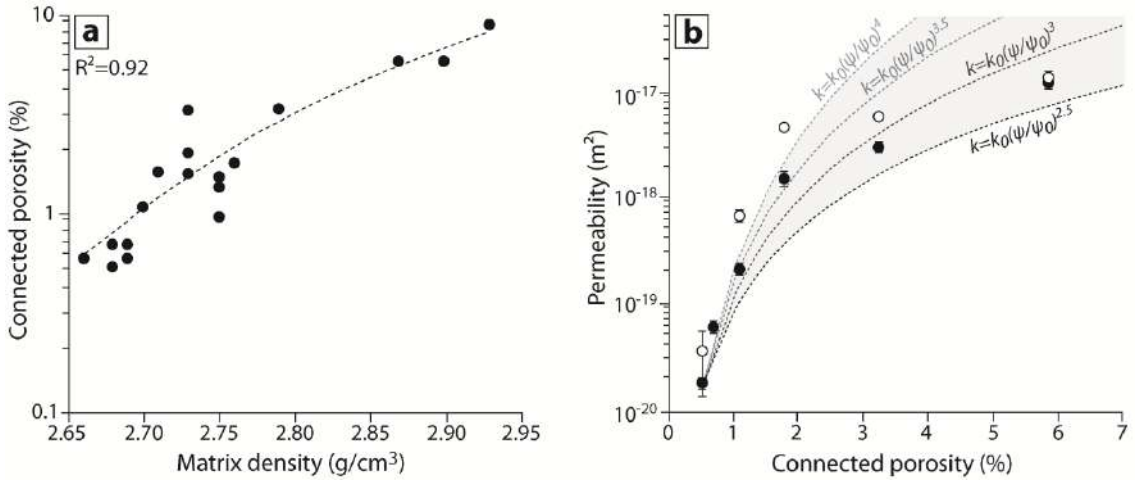

Figure 11 (a) Relationship between matrix density and connected porosity deduced from measurements performed on the Panasqueira granite-greisen samples. (b) Relationship between connected porosity and permeability deduced from granite greisen samples in which porosity and permeability were measured. Black and white dots correspond respectively to permeability values obtained at 25°C and 400°C. The dashed lined corresponds to modeled evolutions of permeability as a function of rock porosity using power law equations (see text for explanations).

The development of a porous texture and porosity during the greisen alteration seems to be directly related to the replacement reactions involved during the greisenization. To highlight the effect of this porosity generation on permeability, we have plotted the permeability evolution as a function of the rock porosity in Figure 11b. We observe that permeability varies strongly as a function of the porosity following an empirical power-law relationship between permeability (k) and porosity (φ):

$$k = k_0 . \left(\frac{\varphi}{\varphi_0}\right)^n \quad (6)$$

Where (k_0) and (φ_0) are respectively the initial permeability and porosity of the unaltered granite and (n) a coefficient depending on pore geometry and the material's grain size. In this study, permeability and porosity values fit the power law for n ranging from 3 to 4. This cubic dependence relationship has been used and adopted in several studies to define permeability evolution in natural systems (Norton and Knapp, 1977; Gavrilenko and Gueguen, 1993; Zhang et *al.*, 1994a; Mezri et *al.*, 2015).

This strong interdependence between greisen porosity and permeability emphasizes that the porosity generated by the replacement reactions is responsible for the strong increase in permeability observed during greisenization. Accordingly, greisenization is probably an example of the 'reaction-enhanced permeability' process described by Putnis

(2002) and also seen elsewhere (Putnis and Austrheim, 2010). Greisen alteration is evidently able to generate permeable pathways that could enhance fluid flow and promote further alteration. This positive feedback between alteration and permeability may constitute a potential explanation for the development of massive greisens found in numerous Sn-W deposits.

7. Permeability change during greisenization: implications for fluid flow

7.1 Massive greisen: a potential pathway for mineralized fluids?

The transient porosity-permeability developed during greisenization can affect large scale mass transport and propagation of the alteration in a granite massif. To discuss the implications of the permeability change during greisenization, permeability values were plotted on the vertical profile of the SCB2 drill hole (Fig. 12a). Additionally, the whole-rock composition in Sn, W and Cu was added to this profile to establish a potential link between the rock permeability and metal content. As expected, the permeability increases up to the granite's roof and is highest along the granite-schist contact, where granite was totally converted to greisen. In contrast, the low permeability of the metasedimentary host rock (1.52×10^{-21} m²) suggests that fluid flow was probably controlled by the permeable greisen that forms the apical portion of the granite intrusion. Moreover, the impermeable nature of the overlying metasedimentary host rocks could promote the greisenization of the granite by inhibiting the expulsion of fluid from the granite's roof. The correlation between permeability and concentration of Sn, W and Cu provides evidence that fluids related to the Sn-W and sulfide stages in the mineralized Panasqueira vein system have flowed through the greisen. The occurrences of euhedral quartz (Fig. 5e), metal-bearing minerals such as cassiterite (Fig. 12b), and sulfides (chalcopyrite, sphalerite and pyrite) (Fig. 12c and 12d) that partially fill the neoformed porosity corroborate this interpretation. In addition, the presence of sulfides in the cleavage planes of muscovite (Fig. 12e) shows that the formation of large amounts of muscovite during the greisenization provides another type of pathway that connects the intergranular pores and could enhance fluid flow. In light of these observations, greisen appears to be a preferential pathway for mineralized fluids; hence increased permeability related to greisenization may provide an important mechanism for enhancing fluid flow and forming Sn-W deposits.

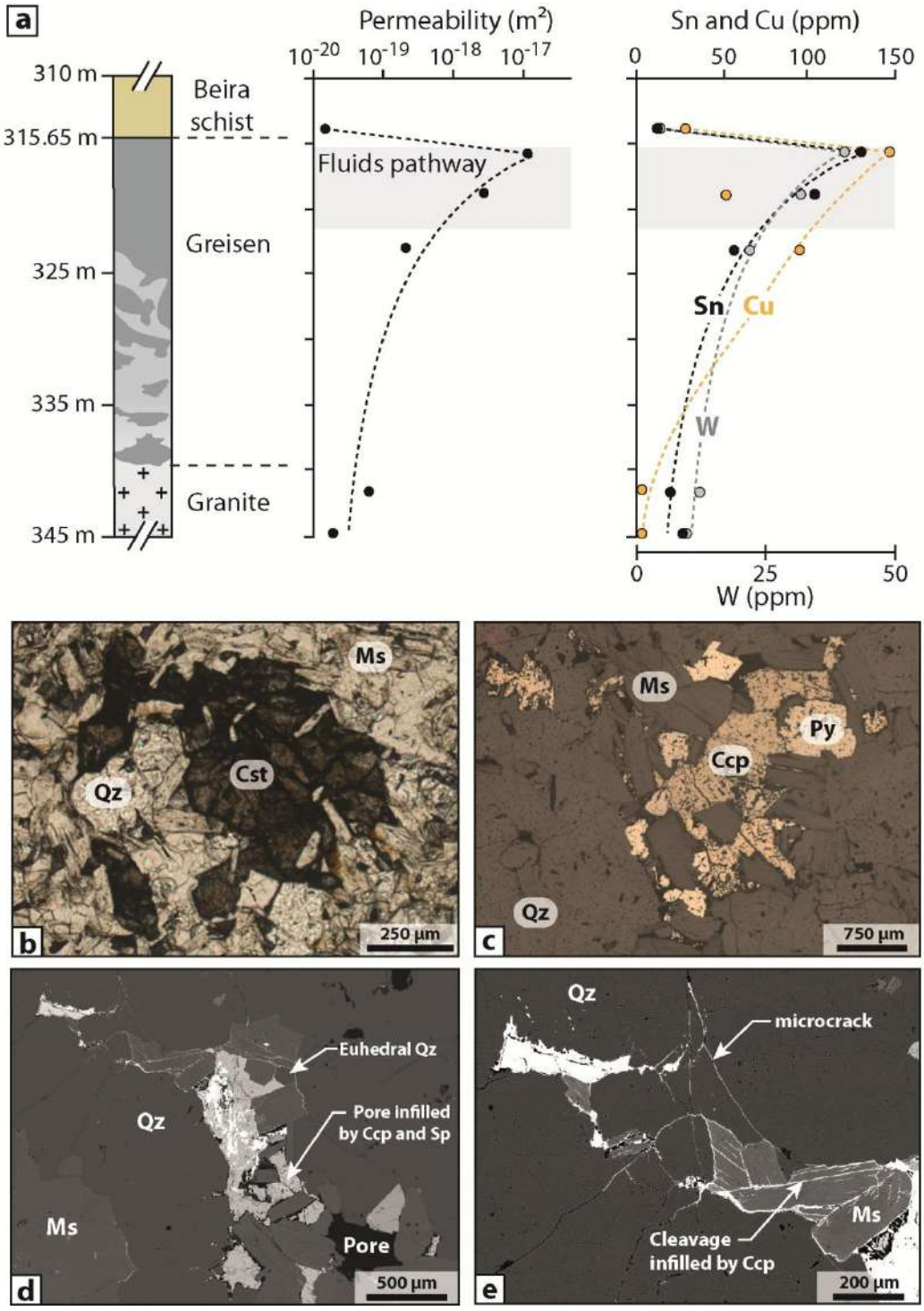

Figure 12 (a) Vertical evolution of the permeability and whole-rock Sn, W and Cu contents in drill hole SCB2. The spatial correlation between rock permeability and in metal contents suggests that greisen was probably a preferential pathway for fluids related to the main mineralization stages occurring in the Panasqueira vein system. Greisen pores infilled by ore-bearing minerals (b) cassiterite (transmitted light) (b) chalcopyrite (reflected light) and (d-e) chalcopyrite and sphalerite (SEM-BSE images). Note the presence of sulfides within the cleavage planes of muscovite suggesting that these weakness planes may be potential pathways for fluids. Abbreviations from Whitney and Evans (2010) Ccp: Chalcopyrite, Cst: Cassiterite, Ms: Muscovite, Py: Pyrite, Qz: Quartz, Sp: Sphalerite.

7.2 Application to other greisen systems

As shown previously, the evolution of matrix density constitutes a useful monitor for following the progressive mineralogical transformation of the granitic rocks during greisenization (replacement of less dense minerals by denser ones). Owing to the lack of permeability data on greisen systems, and given the relationship between porosity and permeability, we have plotted the evolution of porosity as a function of matrix density to discuss the effect of greisen alteration on metal transport for several greisen systems associated with Sn-W mineralization (Fig. 13a). The positive correlation between matrix density and porosity described in the Panasqueira greisen system can also be observed in other greisen systems, as shown in Figure 13a. Additionally, the range of porosity increase usually appears to be similar from one greisen system to another (maximum porosity of about 10%). Accordingly, the process of porosity generation induced by the replacement reactions (monitored by the rock's matrix density) is evidently a common process in greisen systems. It follows that the permeability increase triggered by porosity generation may be a crucial mechanism for enhancing fluid flow and thereby metal transport in granitic intrusions related to Sn-W deposits. Figure 13b indicates that greisen can form low grade (0.1 to 0.4 wt%) and high tonnage (100 to 500 kt) Sn deposits such as Sn-porphyry and skarn (Taylor 1979; Mlynarczyk et *al.*, 2002). This emphasizes that despite the initial low permeability of the parental granite, greisens becomes porous and permeable enough to permit fluid flow and to trap metals. The process of reaction-enhanced permeability related to greisenization may be required to enhance Sn-W metal transport and hence to form this type of deposit. Moreover, deposits such as the Panasqueira, greisens are frequently associated with a network of mineralized veins or lodes (Taylor, 1979; Taylor and Pollard, 1988; Černý et *al.*, 2005).

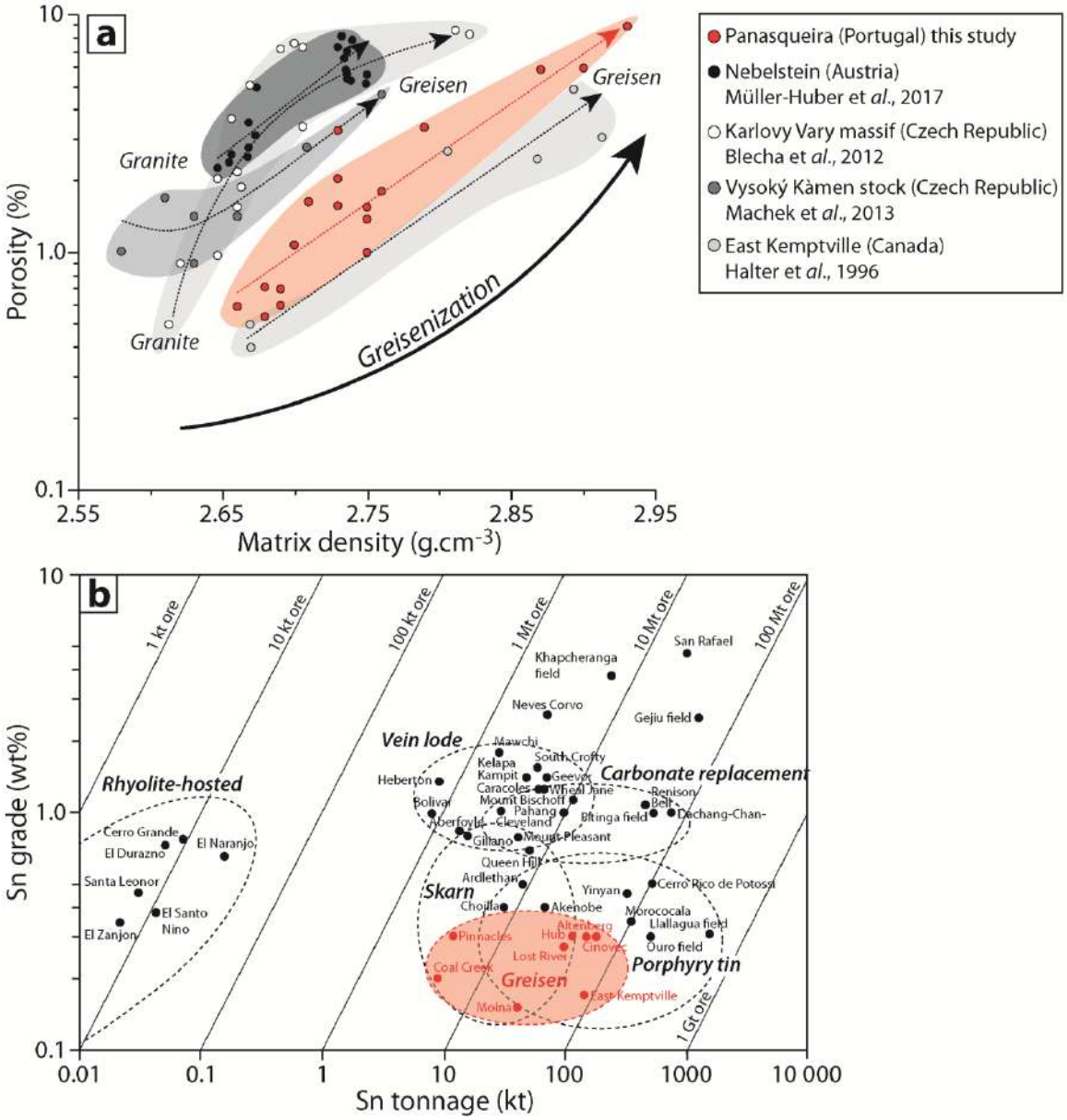

Figure 13 (a) Compilation of matrix density and porosity data measured in various granite-greisen systems. This compilation shows that increases in matrix density and porosity are common in greisen systems. It also suggests that feedback between greisen alteration and permeability may be a common process in this type of deposit. (b) Grade versus metal content for several types of large, high-grade, primary tin deposits (modified from Mlynarczyk et al., 2003). Note that greisen systems can form high tonnage low grade tin deposits.

8. Summary and conclusion

We have investigated the effects of the mineralogical changes produced by greisenization on rock porosity and permeability by coupling experimental and petrophysical approaches. To summarize our results, we propose a conceptual model of greisenization and fluid flow, in which the evolution of permeability is considered (Fig. 14). In this model, we assume that greisenization take place during the granite's cooling phase, just after the magmatic-hydrothermal transition and after the alkali metasomatism (K-metasomatism and albitization) responsible of the conversion of alkali feldspars and plagioclase into orthoclase and albite. At the initiation of this model (Fig. 14a) the granite-schist interface was probably a permeable one, in which fluids preferentially flowed and initiate the greisenization of the granite's roof. This is consistent with the vertical zoning of the greisen alteration observed at Panasqueira and in several other greisen systems associated with Sn-W deposits. This alteration triggers the replacement feldspars and biotite that starts along grain boundaries, along the cleavage planes of feldspars and from micropores developed in albite by CDP reactions during the early albitization stage. The decrease in molar volume caused by these replacement reactions progressively generates porosity and thereby increases the permeability of the greisen. A positive feedback between greisenization and permeability is proposed, to explain the propagation of the alteration front toward the deeper portion of the granite intrusion and the formation of the massive greisen commonly observed in Sn-W deposits (Fig. 14b). As a consequence, this enhancement of permeability would promote fluid flow and metal transport thought the massive greisen leading to the deposition of metal-bearing minerals (cassiterite and sulfides) in the newly formed greisen porosity. This may be a process of greater importance than previously assumed in the formation of large greisen deposits (Fig. 14c). Furthermore, the permeable greisen could also constitute a significant drain into which fluids released by the underlying granite and the surrounding convecting fluids could be focused and directed towards structural traps to form vein deposits.

Finally, this study emphasizes that mineralizing fluids are able to generate their own pathways in an initially impermeable granite by means of the replacement reactions related to greisenisation. This reaction-enhanced permeability process is rarely discussed in hydrothermal systems associated with ore deposits. Here, we demonstrate in the case of greisenization that replacement reactions involved in numerous hydrothermal alterations can provide an efficient process for creating the high-permeability pathways required for

vigorous fluid flow and for the self-propagating of pervasive alterations. All these experimentally-deduced fluid flow processes should be tested by numerical models of hydrothermal processes surrounding cooling granite intrusions, including dynamic permeability during greisenization. Such a numerical approach would provide quantitative information about the effects of permeability change on the fluid flow pattern and thus on metal transport and deposition in Sn-W deposits.

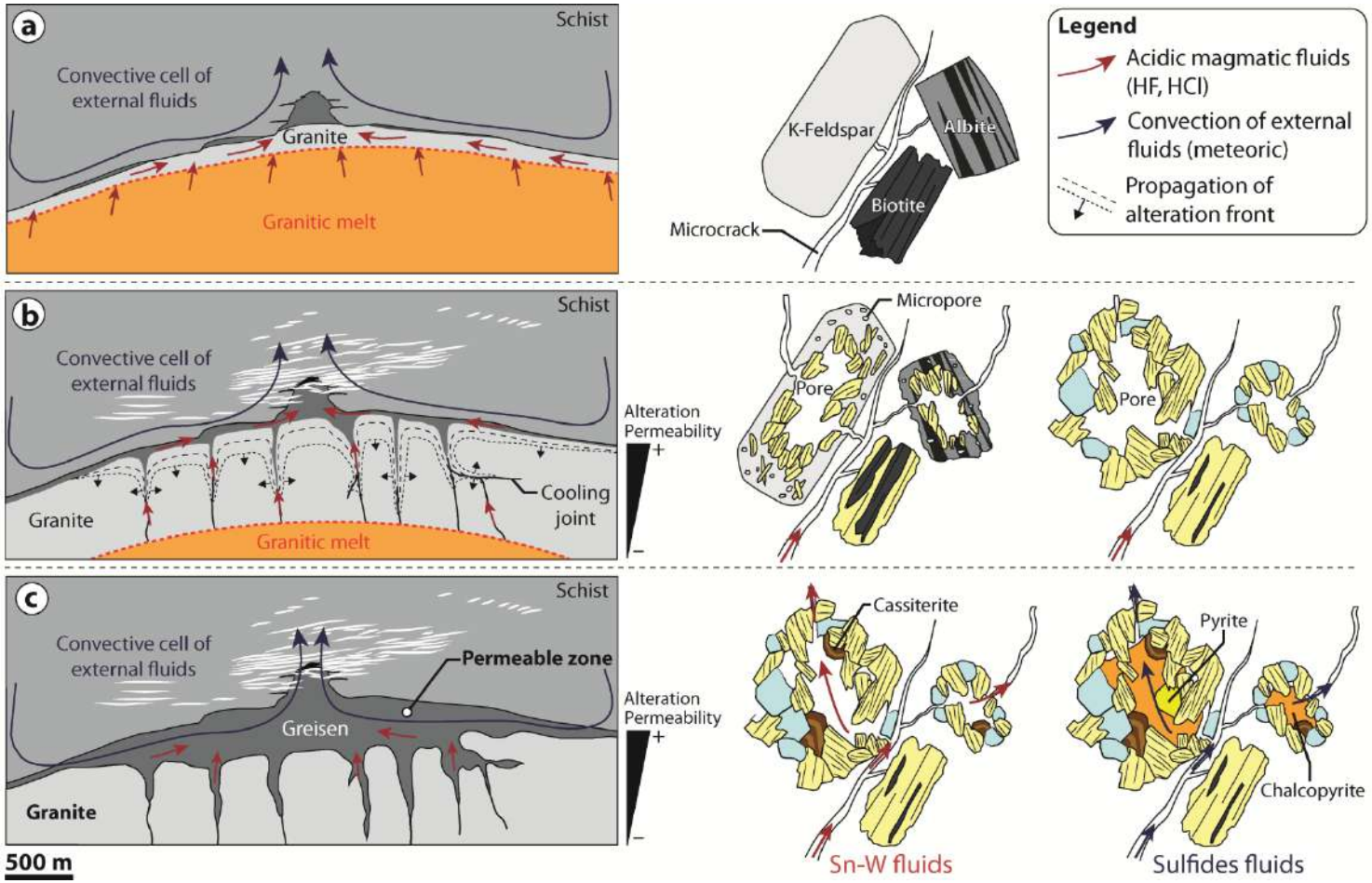

Figure 14 Conceptual model incorporating the evolution of permeability over time induced by replacement reactions related to greisenization of the Panasqueira granite. (a) Initiation of granite cooling and fluid flow, which trigger the greisenization of the granite along the granite-schist contact (permeable interface). (b) Alteration of the granite leading to the progressive replacement of feldspars and biotite by muscovite. This mineralogical transformation is accompanied by the generation of porosity resulting from the decrease in molar volume associated with the replacement reactions. A positive feedback between greisen alteration and permeability is assumed here to explain the propagation of the greisenization front and the development of massive greisen (c) The porosity generated by the greisen alteration enhances permeability and creates a potential permeable zone that can enhance fluid flow and metal transport. The presence of metal bearing-minerals (cassiterite and sulfides) in the newly formed greisen's porosity seems to confirm the role of massive greisen as a drain for mineralizing fluids and to explain the formation of this type of deposit.

II- Evolution of the fluid composition during the replacement reactions related to greisenization

1. Experimental and analytical methods

1.1 Experimental setup

In order to investigate effects of the greisenization on chemical evolution of hydrothermal fluids, an experiment of greisenization was conducted using Dixon-Seyfried hydrothermal apparatus (Seyfried et *al*., 1987) (Fig. 15). This experiment was performed at 400°C and 500 bars for a water/rock ratio of about 1 and for a duration of 20 days. This experiment was performed using powder of the Panasqueira granite and a starting solution characterized by a log(mKCl/mHCl) of 2.2 and a log(mNaCl/mHCl) of 1.6 for an initial pH of 1.7. This chemical composition of fluid was chosen to promote feldspars (Albite and K-feldspars) replacement by muscovite under the chosen experimental conditions. The granite powder and the solution were introduced in Ti-reaction cell system, which permits to sample experimental solution and follow the reaction progress over the experiment time (Fig. 15). The sampling process involves attachment of a small Ti-syringe connecting to the reaction cell sampling valve (Fig. 15). For each sampling time, two aliquots of fluid (2 mL) were extracted from the reaction cell. The first aliquots served only to flush the exit tube, whereas the second aliquots were analyzed to monitor the chemical evolution of fluid during the greisenization. The pH of the solution at the sampling time was determined using accurate pH test strips (0.2 pH unit). Samples of hydrothermal solution were then diluted with de-ionized water to inhibit mineral precipitation. At the end of the experiment, the alteration products were recovered, washed and dried at 45°C during a few days. Then the powder was embedded in resin and polished for micro-textural analysis.

1.2 Analysis of hydrothermal solutions

Chemical composition of hydrothermal solutions were determined by HR-ICP-MS at the University of Bretagne Occidental (UBO, Brest) using a high resolution Thermo Element2 (Thermo Fisher). Solutions with elemental concentrations close to the expected concentrations of the experimental fluids were produced and used as standard reference.

1.3 Microtextural analysis of the alteration products

Micro-textures of the alteration products developed during the experimental greisenization were analyzed by scanning electron microscopy (SEM) using a Merlin compact Zeiss high resolution scanning electronic microscope equipped with a Gemini I detector (BRGM, University of Orléans). The SEM images were acquired using an acceleration voltage of 15 kV.

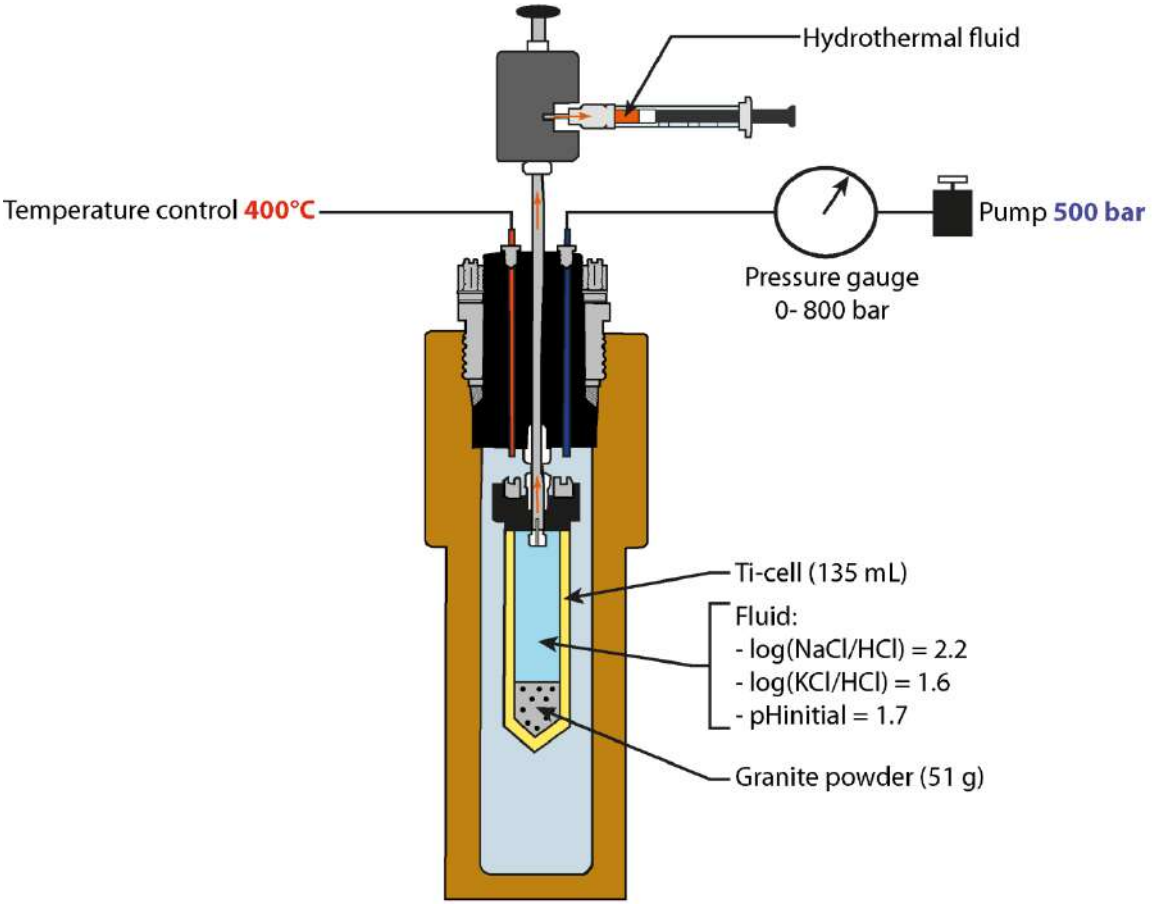

Figure 15: Schematic illustration of the experimental apparatus used for the experiment of greisenization (modified from Seyfried et *al.*, 1987). Note the connection between the syringe used for the sampling of solutions and the Ti-reaction cell.

2. Results

2.1 Time evolution of the fluid compositions

The pH and the chemical composition evolutions of the hydrothermal solutions sampled during the greisenization experiment are summarized in Table 3 and plotted as a function of time in Figure 16. The pH increases quickly from 1.7 to 4 during the first 150 hours of the experiment. Dissolved Ba, Ca, Sr, Mn and Si increase significantly and attained steady-state after 200-300 hours of experiment (Fig. 16) with maximum concentrations of 2218.6 ppb for Ba, 311.6 ppm for Ca, 1658.8 ppb for Sr, 91.7 ppm for Mn and 1094 ppm for Si. Concentrations in Mg and Fe increase slowly and attained maximum concentrations after 300 hours of experiment with 23.7 ppm for Mg and 28.5 ppm for Fe. This chemical evolution of the hydrothermal solution indicates that fluid has reacted with the mineral phases composing the Panasqueira granite and hence that fluid was probably buffered by the granite powder through mineralogical transformations.

Time (hours)	pH	Ba (ppb)	Ca (ppm)	Sr (ppb)	Mn (ppm)	Mg (ppm)	Fe (ppm)	Si (ppm)
0	1.7	0	0	0	0	0	0	0
20	3	1018	215	1008	75.3	8.6	7.5	464
60	3	1306	306	1173	89	12.2	2.1	840
160	4	1004	196	924	91.7	6.2	1.5	1020
234	4	1905	311	1296	80.6	19.2	12.5	953
323	4	2108	311	1658	81.5	23.7	26.6	1094
496	4.5	2218	229	1554	90.5	12.9	28.5	1055

Table 3: Time evolution of concentrations of selected dissolved species and pH obtained during the greisenization experiment.

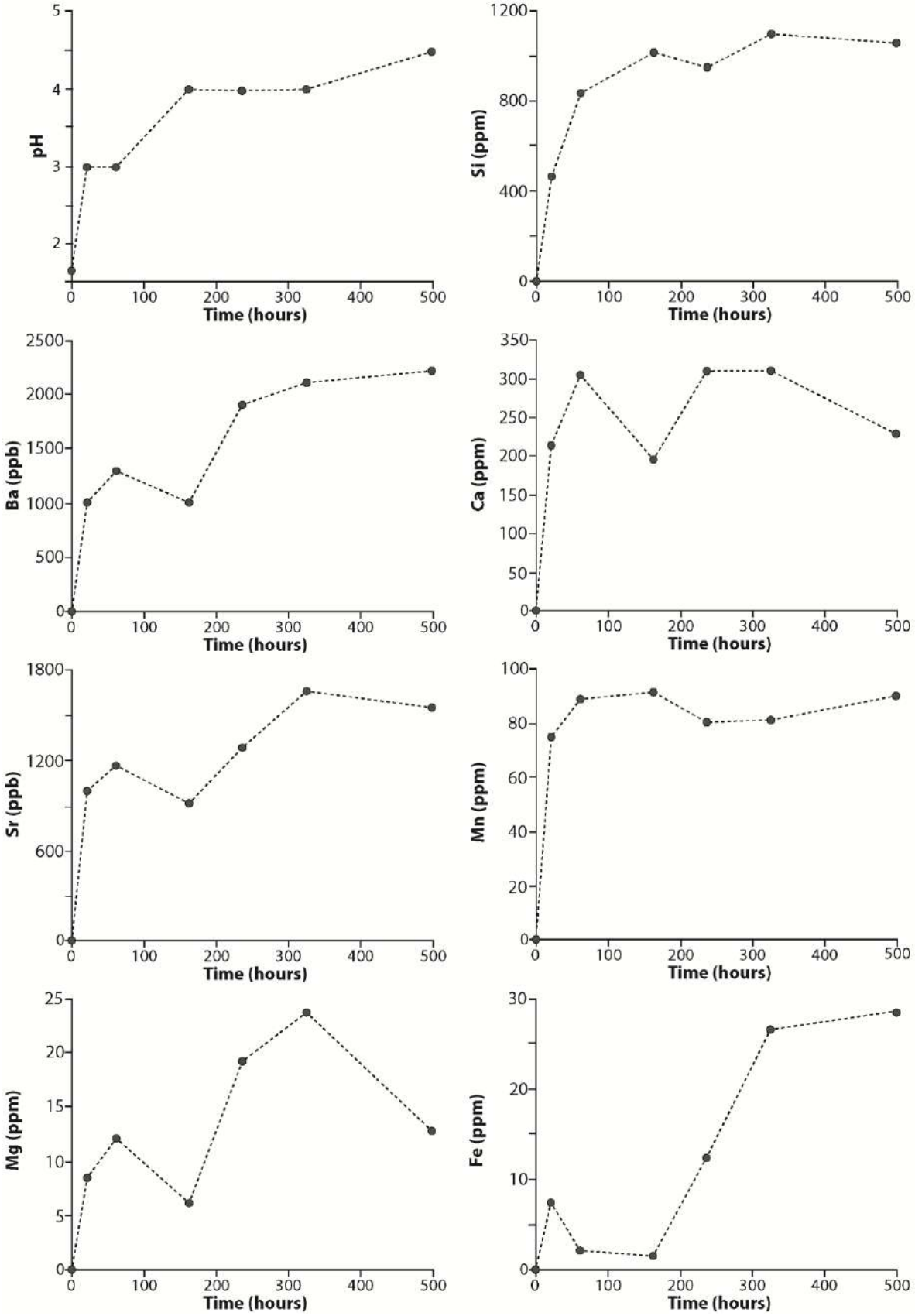

Figure 16: Evolution of pH and the concentrations (ppm and ppb) in Si, Ba, Ca, Sr, Mn, Mg and Fe with time. The data suggest that equilibrium between fluid and granite powder was attained at the end of the experiment.

2.2 Microtexture of the alteration products

SEM-BSE images showing the alteration products formed during the greisenization experiment are displayed in Figure 17. During this experiment, albite and k-feldspar were partially replaced by muscovite (Fig. 17a to 17d). This replacement occurred mainly along the grain edges of feldspars (Fig. 17a, 17b and 17c) and along fracture planes present in some grains (Fig. 17d). SEM images show also that muscovite replacing feldspars exhibit a more porous texture compared to the parental feldspars**.** Consequently, the replacement of feldspar by muscovite is marked by the development of a microporous texture in the altered products that could be related to the molar volume decrease induced by the transformation of feldspars into muscovite.

Some grains of albite appear to be partially replaced by k-feldspar (Fig. 17e and 17f). This conversion emphasizes a K^+ and Na^+ exchange between albite and the hydrothermal solution. This feldspar transformation can be due to changes of the pH and fluid composition caused by the replacement of feldspars by muscovite. We can infer that fluid was buffered by the muscovite → k-feldspar mineralogical equilibrium that could trigger the albite transformation into k-feldspar.

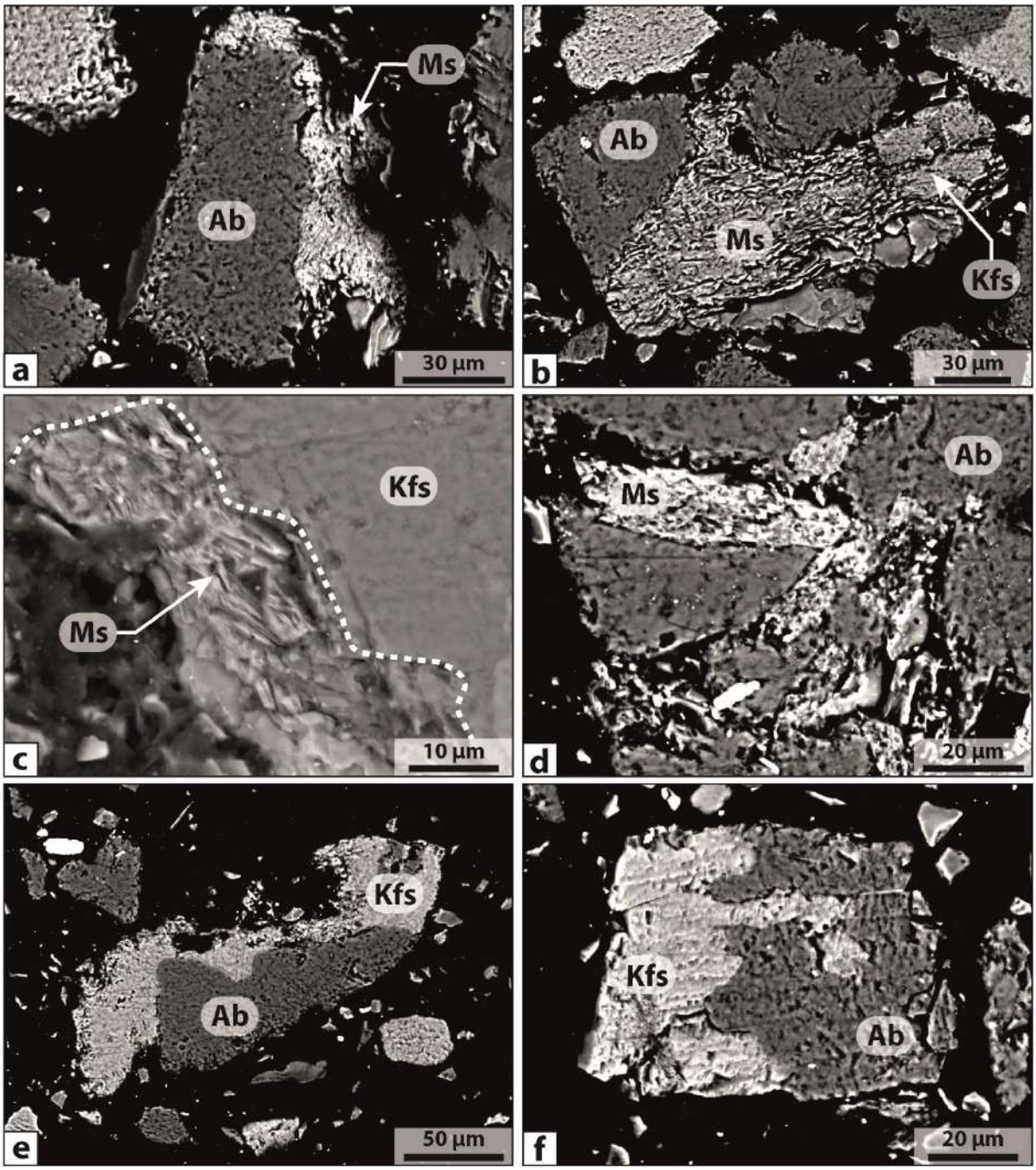

Figure 17: SEM photomicrographs displaying the alteration products obtained during the greisenization experiment. (a) to (c) grains of albite and k-feldspar partially replaced by muscovite. (e) and (f) grains of albite partially replaced by k-feldspar. Abbreviations from Whitney and Evans 2010, Ab: albite, Kfs: k-feldspar and Ms: muscovite. Muscovite replacing feldspars exhibit a microporous texture compared to the parental feldspars.

3. Discussion

3.1 Replacement reactions controlling pH and composition of the hydrothermal solution

The quick compositional change observed during the experiment was probably due to the relatively high abundance of reactive feldspars that buffer the hydrothermal solution. Ba, Ca and Sr are generally hosted by feldspars, the replacement of albite and k-feldspar by muscovite is certainly responsible of the releasing of these elements into fluid during the experiment. Mn, Mg and Fe are mainly hosted by biotite, thus the releasing of these elements into fluids was probably due to the biotite alteration. The mineral replacement occurring during the greisenization experiment can be summarized by the following reactions:

(R1) $3\ KAlSi_3O_8 + 2\ \mathbf{HCl} = KAl_3Si3O_{10}(OH)_2 + 2\ KCl + 6\ SiO_2$

(R2) $3\ NaAlSi_3O_8 + KCl + 2\ \mathbf{HCl} = KAl_3Si_3O_{10}(OH)_2 + 3\ NaCl + 6\ SiO_2$

(R3) $3\ KFe_3AlSi_3O_{10}(OH)_2 + 2\ \mathbf{HCl} = KAl_3Si_3O_{10}(OH)_2 + 2\ KCl + 3\ Fe_3O_4 + 6\ SiO_2 + 3\ H_2$

These replacement reactions have important implications for pH. Indeed, the transformation of feldspars and biotite into muscovite consume a large amount of HCl explaining the pH increase observed during the experiment. The solubility of numerous metals are directly affected by the pH of the hydrothermal fluids (Crerar et *al*., 1985; Seward and Barnes, 1997; Migdisov and Williams-Jones, 2005; Williams-Jones and Migdisov, 2014), thus replacement reactions induced by the greisenization can have strong impacts on the precipitation of mineral bearing-metals in greisen.

Our experimental results provide also explanation about the whole rock compositional changes observed in the greisen of Panasqueira. Indeed, the greisenization is marked by important depletions in Na, K, Ba, Ca, Sr, Mg and Mn in greisen (Fig. 7) that appear directly related to the total breakdown of feldspars and biotite constituting the Panasqueira granite. The chemical evolution of the hydrothermal fluid during our experiment emphasizes that these elements are efficiently mobilized from the granite by fluids during the replacement reactions induced by the greisenization.

3.2 Implication for cassiterite and wolframite deposition

Experimental and theoretical studies realized by Eugster and Wilson, 1985; Eugster, 1986 and Heinrich, 1990 have shown that Sn is mainly transported in hydrothermal fluids as $SnCl^+$ complex, which the stability depends on temperature, fO_2 and pH conditions. Accordingly, the cassiterite precipitation can be written as follow:

(R4) $SnCl^+ + H_2O + 0.5\ O_2 + Cl^- = SnO_2 + 2$ **HCl**

This reaction suggests that cassiterite precipitation can be triggered by a fO_2 increase, a variation in Cl^- concentration in fluids and a pH increase induced by HCl concentration decrease. As discussed previously, replacement of feldspars and biotite by muscovite cause an important consumption of HCl that leads to a pH increase in fluid. Assuming a constant fO_2, temperature and Cl^- activity and that pH is the only parameter evolving during the greisenization, the transformation of feldspars in muscovite can buffer significantly the acidity of the Sn-W bearing fluids. This fluid neutralization can induce a Sn solubility decrease and thus cassiterite crystallization in greisen (Fig. 18a) (Migdisov and Williams-Jones, 2005). This process has ever been proposed by Eugster, (1986) and Heinrich, (1990) and Halter et *al.*, (1998) to explain the deposition of cassiterite in greisen systems. Our experimental results seem to confirm that replacement reactions related to greisenization can be a decisive process to form Sn-greisen deposits by neutralization of fluids during fluid-rock interactions.

The wolframite deposition is more complex and depends on the $FeCl_2$ activity in fluids in the case of ferberite crystallization:

(R5) $H_2WO_4 +$ **$FeCl_2$** $= FeWO_4 + 2$ **HCl**

(R6) $Na_2WO_4 +$ **$FeCl_2$** $= FeWO_4 + 2\ NaCl$

These reactions highlight that the wolframite deposition requires a large amount of Fe. In the reaction (R5), the consumption of HCl during the greisenization could lead to the wolframite deposition if Fe is available. In reaction (R6) the wolframite crystallization is not influenced by the HCl activity in fluids, thus replacement reactions related to greisenisation do not affect the tungsten solubility. Furthermore, our results seem to suggest that greisenisation does not affect significantly the Fe content in fluids. Moreover, experimental study realized by Wood, (1992) show that the W solubility in fluids is probably not influenced by the HCl activity (Fig. 18b). Consequently if the $FeCl_2$ content

in fluid is low, the greisenisation does not affect the wolframite deposition despite a strong consumption of HCl during the transformation of feldspars into muscovite. Study realized by Lecumberri-Sanchez et *al*., 2017 on composition of fluid inclusions related to the Sn-W mineralization of Panasqueira has highlighted the absence of Fe in fluids. This study suggests that the wolframite deposition is mainly controlled by fluid-schist reactions (alteration of chlorite) that release efficiently Fe in fluid and hence causes wolframite deposition. In the case of greisen, reactions of alteration do not release enough Fe to permit the wolframite deposition, explaining the rare occurrence of wolframite in greisen.

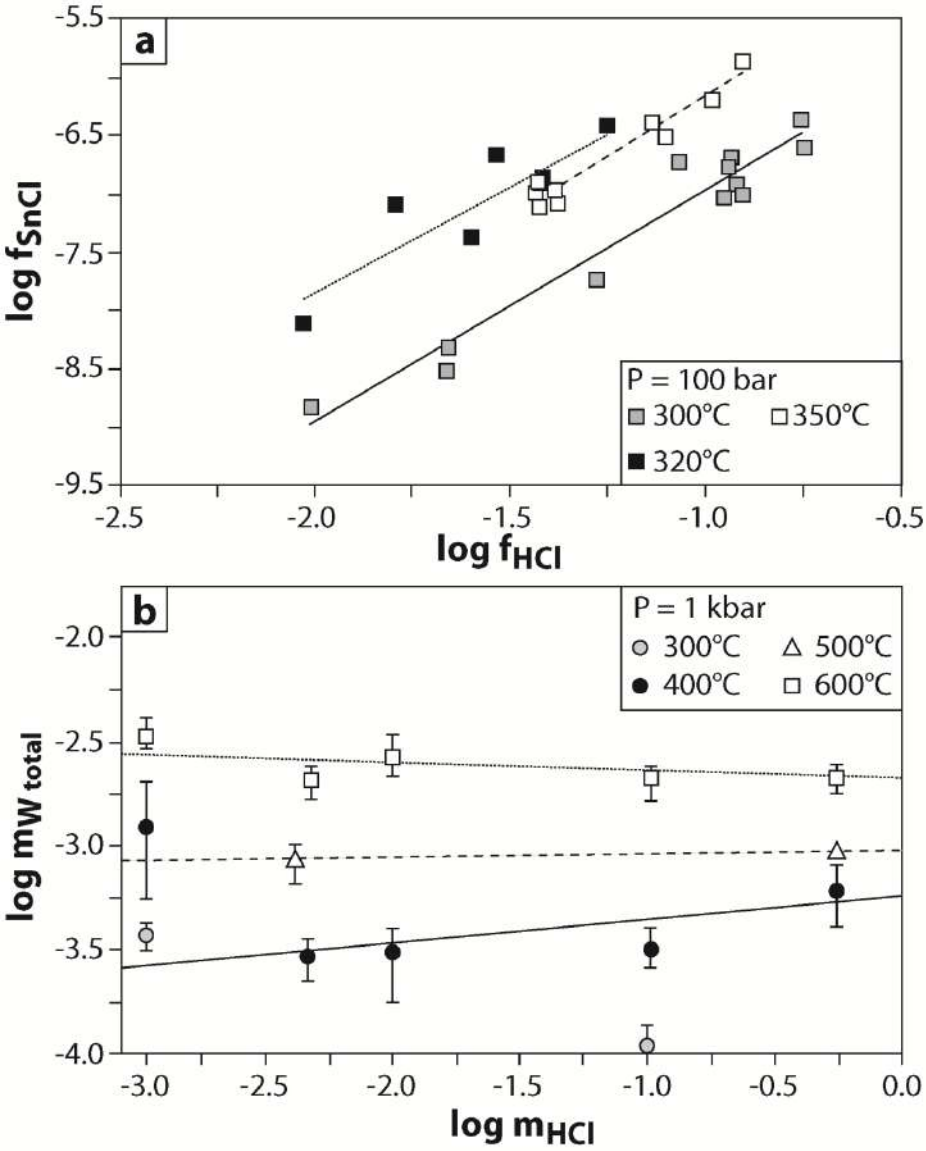

Figure 18: (a) Evolution of the Sn solubility as a function of the HCl fugacity in fluids at 100 bar from 300 to 350°C (Mgdisov and Williams-Jones, 2005). (b) Evolution of the W solubility as a function of the HCl concentration in fluids at 1 kbar and from 300 to 600°C (Wood, 1992).

3.3 Implications for the genetic model of greisen formation

If we consider permeability evolution during the greisenization and the effects of this alteration on the chemical composition of the hydrothermal fluids, it appears that replacement reactions is an important process to (i) enhance circulation of mineralizing fluids in an initially impermeable granite by porosity generation and (ii) promote cassiterite deposition in greisen by neutralization (pH increase) of the mineralizing fluids that triggers a significant decrease of the Sn solubility (Fig. 19). Furthermore, petrographic evidences highlight that cassiterite precipitates preferentially in the newly formed porosity. This suggests that porosity developed during the greisenization constitutes preferential trap for Sn deposition in greisen. Consequently, the mineralizing fluids are able to create their own pathways and trap via the replacement reactions. Fluid rock interaction involved during greisenization could be a key process for the formation of large greisen deposits by petrophysical and geochemical changes.

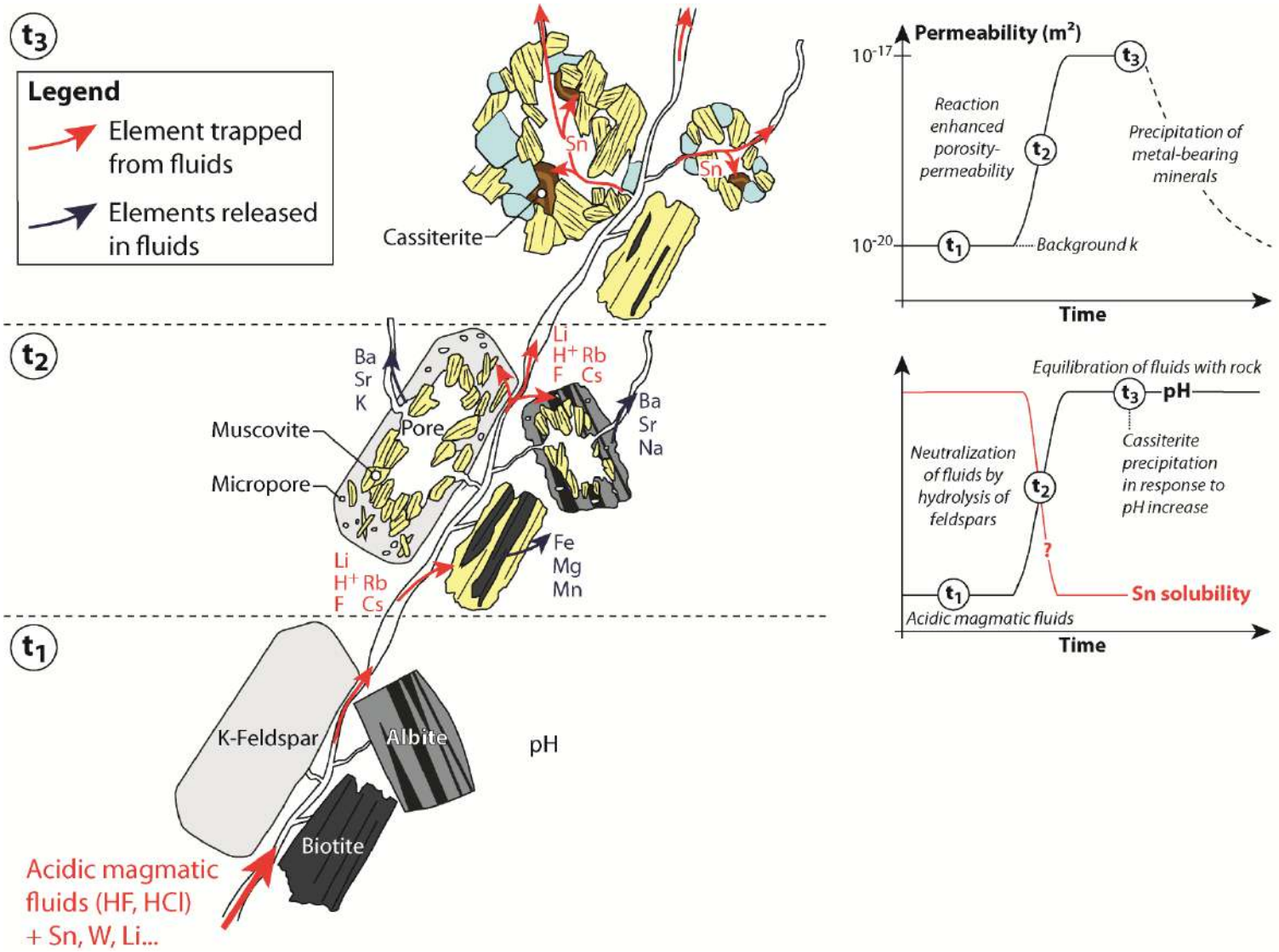

Figure 19: Conceptual model of greisen formation at the mineral scale. This model integrates the time evolution of permeability induced by the replacement reactions and effects of fluid rock interactions on the fluid chemistry. (t_1) Initial texture of the Panasqueira granite. (t_2) Replacement of feldspars and biotite induced by the greisenization. This mineralogical transformation induced permeability increase by porosity generation and the neutralization of the fluid acidity leading to a pH increase. The breakdown of feldspars and biotite releases Ba, Sr Na, K, Fe, Mg and Mn, whereas the crystallization of muscovite traps a part of Li, Cs, Rb and F from fluids. (t_3) The pathways developed by the replacement reactions enhance metal transport, while the fluid neutralization causes the precipitation of cassiterite in the newly formed porosity.

References

B

Blecha, V., Stemprok, M. 2012. Petrophysical and geochemical characteristics of late Variscan granites in the Karlovy Vary Massif (Czech Republic) – implications for gravity and magnetic interpretation at shallow depths. Journal of Geosciences. 65 - 85.

Booden, M.A., Mauk, J.L., Simpson, M.P. 2011. Quantifying Metasomatism in Epithermal Au-Ag Deposits: A Case Study from the Waitekauri Area, New Zealand. Economic Geology ; 106 (6): 999–1030.

Bishop, A.C. 1989. Greisen. In: Petrology. Encyclopedia of Earth Science. Springer, Boston, MA.

Bussink, R.W. 1984. Geochemistry of the Panasqueira Tungsten-Tin Deposit, Portugal. Geol. Ultraiectina.

C

Castro, A., Castañón, Luis & de la Rosa, Jesús D. & Enriqeu, P & Martinez, F & Pascual, Emilio & Lago San José, Marceliano & Arranz Yagüe, Enrique & Gale, Carlos & Fernandez, Carlos & Donaire, T & Lopez-Aparicio, Susana. 2002. Palaeozoic magmatism. 117-153.

Černý, P., Blevin, P.L., Cuney, M. and London, D. 2005. Granite-Related Ore Deposits. In: J.W. Hedenquist, J.F.H. Thompson, R.J. Goldfarb, and J.R. Richards (eds.). Economic Geology - One Hundredth Anniversary Volume, 337–370.

Clark, A. H. 1964. Preliminary study of the temperatures and confining pressures of granite emplacement and mineralization, Panasqueira, Portugal: Inst. Mining MetallurgyTrans., 73, 813-824.

Coelho, G., Branquet, Y., Sizaret, S., Arbaret, L., Champallier, R., Rozenbaum, O. 2015. Permeability of sheeted dykes beneath oceanic ridges: Strain experiments coupled with 3D numerical modeling of the Troodos Ophiolite, Cyprus. Tectonophysics, Elsevier, 2015, 644-645, pp.138-150.

Crerar, D., Wood, S.M., Brantley, S., and Bocarsly, A. 1985, Chemical controls on solubility of ore-forming minerals in hydrothermal solutions. Canadian Mineralogist, v. 23, p. 333-352.

D-E-F

Dias, G., Leterrier, J., Mendes, A., Simões, P., Bertrand, J.M. 1998. U-Pb zircon and monazite geochronology of syn- to post-tectonic Hercynian granitoids from the central Iberian Zone (northern Portugal). Lithos 45, 349–369.

Dostal, J., Kontak, D. J., Karl, S. M., 2014. The Early Jurassic Bokan Mountain peralkaline granitic complex (southeastern Alaska): Geochemistry, petrogenesis and rare-metal mineralization, Lithos,Volumes 202–203, 2014, Pages 395-412.

Dostal, J., Kontak, D.J., Ochir, G., Shellnutt, J., Fayek, M., 2015. Cretaceous ongonites (topaz-bearing albite-rich microleucogranites) from Ongon Khairkhan, Central Mongolia: Products of extreme magmatic fractionation and pervasive metasomatic fluid: Rock interaction. Lithos. 236-237. 173-189.

Engvik, K., Peter, A. & I., Håkon, A., 2014. Characterisation of Na-metasomatism in the Sveconorwegian Bamble Sector of South Norway. Geoscience Frontiers. 5. 10.1016/j.gsf.2014.03.008.

Eugster, H.P., and Wilson, G.A. 1985. Transport and deposition of ore-forming elements in hydrothermal systems with granite. in Halls, C., et al., High heat production granites, hydrothermal circulation and ore genesis: London, England, Institution of Mining and Metallurgy, p. 87-98.

Eugster, H.P. 1986. Minerals in hot water. American Mineralogist. v. 7 1, p. 655-673.

Finch, A. A., Walker, F. D. L., 1991. Cathodoluminescence and Microporosity in Alkali Feldspars from the Blå Måne Sø Perthosite, South Greenland Mineralogical Magazine 55 : 583-589.

G

Gavrilenko, P., Gueguen, Y. 1993. Fluid overpressures and pressure solution in the crust. Tectonophysics. 217. 91-110.

Gomes, M., Neiva, A., 2000. Chemical zoning of muscovite from the Ervedosa granite, northern Portugal. Mineralogical Magazine - MINER MAG. 64. 347-358. 10.1180/002646100549247.

Grant, J.A. 1986. The isocon diagram; a simple solution to Gresens' equation for metasomatic alteration. Economic Geology, 81 (8): 1976–1982.

Grant, J.A. 2005. Isocon analysis: A brief review of the method and applications. Physics and Chemistry of the Earth, Volume 30, Issue 17-18, p. 997-1004.

H-I-J

Hall, A. 1971. Greisenisation in the granite of Cligga Head, Cornwall. Proceedings of the Geologists' Association 82(2).

Halter, W.E., Williams-Jones, A.E., Kontak, D.J. 1996. The role of greisenization in cassiterite precipitation at the East Kemptville tin deposit, Nova Scotia. *Economic Geology*, 91 (2): 368–385.

Halter, W.E., Williams-Jones, A.E., Kontak, D.J. 1998. Origin and evolution of the greisenizing fluid at the East Kemptville tin deposit, Nova Scotia, Canada. *Economic Geology*, 93 (7): 1026–1051

Hebblethwaite, R. P. B., and Antao, A.M. 1982. A report on the study of dilation patterns within the Panasqueira ore body: Barroca Grande, Beralt Tin Wolfram (Portugal), unpub. rept.15p.

Heinrich, C.A., 1990. The chemistry of hydrothermal tin –tungsten ore deposits. Econ. Geol. 85, 457–481.

Ingebritsen, S.E., Appold, M.S. 2012. The physical hydrogeology for ore deposits. Econ Geol 107:559–584.

Ingebritsen, S. E. and Gleeson, T. 2015. Crustal permeability: Introduction to the special issue. Geofluids, 15: 1-10.

Iyer, K., Jamtveit, B., Mathiesen, J., Malthe-Sørenssen, A., Feder, J., 2008. Reaction-assisted hierarchical fracturing during serpentinization. Earth Planet. Sci. Lett. 267, 503–516.

Jamtveit, B., Austrheim, H., Malthe-Sorenssen, A., 2000. Accelerated hydration of the Earth's deep crust induced by stress perturbations. Nature 408, 75–78.

Jamtveit, B., Malthe-Sørenssen, A., Kostenko, O. 2008. Reaction enhanced permeability during retrogressive metamorphism. Earth and Planetary Science Letters. Volume 267, Issues 3–4, 620-627.

Johnson, J.W., Oelkers, E.H. and Helgeson, H.C. 1992. SUPCRT92 - A software package for calculating the standard molal thermodynamic properties of minerals, gases, aqueous species, and reactions from 1-bar to 5000-bar and 0°C to 1000°C. Computer and Geosciences 18:899-947.

Jonas, L., John, T., King, H.E., Geisler, T., Putnis,A. 2014. The role of grain boundaries and transient porosity in rocks as fluid pathways for reaction front propagation. Earth and Planetary Science Letters, Volume 386, 64-74.

Julivert, M., Fontboté, J.M., Ribeiro, A., Conde, L. 1972. Mapa Tectonico de la Peninsula Iberica y Baleares E. 1:1.000.000. Inst. Geol. Min. España, Madrid.

K

Kelly, W.C., Rye, R.O. 1979. Geologic, fluid inclusion and stable isotope studies of the tin-tungsten deposits of Panasqueira, Portugal. Econ Geol 74:1721–1822.

Kontak, D. J., 1990. The East Kemptville muscovite-topaz leucogranite. I. Geological setting and whole rock geochemistry. Can. Mineral. 28, 787-825.

Kontak, D. J., Clark, A. H. 2002. Genesis of the Giant, Bonanza San Rafael Lode Tin Deposit, Peru: Origin and Significance of Pervasive Alteration. Economic Geology, 97 (8): 1741–1777.

Kontak, D.J., 2006. Nature and origin of an LCT-type pegmatite with late-stage sodium enrichment, Brazil Lake, Yarmouth County, Nova Scotia: I. Geological setting and petrology. Canadian Mineralogist, vol. 44, p. 563-598.

Kontak, D.J. & Kyser, K. 2011. A fluid inclusion and isotopic study of an intrusion-related gold deposit (IRGD) setting in the 380 Ma South Mountain Batholith, Nova Scotia, Canada: evidence for multiple fluid reservoirs. Miner. Deposita, Volume 46, Issue 4, pp 337–363.

L

Launay, G., Sizaret, S., Guillou-Frottier, L., Gloaguen, E., Pinto, F. 2018. Deciphering fluid flow at the magmatic-hydrothermal transition: A case study from the world-class Panasqueira W–Sn–(Cu) ore deposit (Portugal). Earth and Planetary Science Letters, Volume 499, 1-12.

Lecumberri-Sanchez, P., Vieira, R., Heinrich, C.A., Pinto, F., Wälle, M. 2017. Fluid-rock interaction is decisive for the formation of tungsten deposits. Geology 45, 579–582.

Lee, M.R., Parsons, I., Edwards, P.R., Martin, R.W., 2007. Identification of cathodoluminescence activators in zoned alkali feldspars by hyperspectral imaging and electron-probe microanalysis. American Mineralogist, 92 (2-3): 243–253.

Lüders, V., 1996. Contribution of infrared microscopy to fluid inclusion studies in some opaque minerals (Wolframite, Stibnite, Bournonite) : Metallogenic implications. Economic Geology, Vol. 91, 8, 1462-1468.

M

Mariano, A. N. (1976) In Simposio lnternacional de Carbonatitos, 1. Pocos de Caldas.

Machek, M., Roxerová, Z., Janoušek, V., Staněk, M., Petrovský, E., René, M. 2013. Petrophysical and geochemical constraints on alteration processes in granites. Stud Geophys. Geod., Volume 57, Issue 4, pp 710–740.

Mayer, K., Scheu, B., Montanaro, Cristian & Yilmaz, Tim & Isaia, Roberto & Aßbichler, Donjá & Dingwell, D. (2016). Hydrothermal alteration of surficial rocks at Solfatara (Campi Flegrei): Petrophysical properties and implications for phreatic eruption processes. Journal of Volcanology and Geothermal Research. 320. 10.1016/j.jvolgeores.2016.04.020.

Mezri, L., Le Pourhiet, L., Wolf, S., Burov, E. 2015. New parametric implementation of metamorphic reactions limited by water content, impact on exhumation along detachment faults. Lithos. 236. 10.1016/j.lithos.2015.08.021.

Migdisov, A.A., Williams-Jones, A.E. 2005. An experimental study of cassiterite solubility in HCl-bearing water vapour at temperatures up to 350°C. Implications for tin ore formation. Chemical Geology, 217, 29– 40

Mlynarczyk, M., Sherlock, R., Williams-Jones, A. 2002. San Rafael, Peru: Geology and structure of the world's richest tin lode. Mineralium Deposita. 38. 555-567.

Moore, D., Morrow, C., Byerlee, J.D. 1983. Chemical reactions accompanying fluid flow through granite held in a temperature gradient. Geochimica et Cosmochimica Acta. 47. 445-453.

Morrow, C.A., Moore, D.E., Lockner, D.A., 2001. Permeability reduction in granite under hydrothermal conditions. J. Geophys. Res. 106, 30551-30560.

Müller-Hubner, E., Börner, F. 2017. Multi-parameter petrophysical charcaterization of Variscan greisen rocks from the Southern Bohemian Batholith (Austria) and the Eastern Erzgebirge Volcano-Plutonic Complex (Germany). Austrian Journal of Earth Sciences, Vol. 110/1, 78-100.

N

Nesbitt, H.W., Young, G.M., 1982. Early Proterozoic climates and plate motions inferred from major element chemistry of lutites. Nature 299, 715–717.

Noronha, F., Doria, A., Dubessy, J., Charoy, B., 1992. Characterization and timing of the different types of fluids present in the barren and ore-veins of the W-Sn deposit of Panasqueira, Central Portugal. Mineralium Deposita, Vol. 27, Issue 1, 72-79.

Norton, D., Knapp, R. 1977. Transport phenomena in hydrothermal systems; the nature of porosity. American Journal of Science, vol. 277, issue 8, pp. 913-936.

P

Pandur, K., Ansdell, K. M., Kontak, D. J., Halpin, K. M., Creighton, S. 2016. Petrographic and Mineral Chemical Characteristics of the Hoidas Lake Deposit, Northern Saskatchewan, Canada: Constraints on the Origin of a Distal Magmatic-Hydrothermal REE System. Economic Geology; 111 (3): 667–694.

Paterson, M. S., Olgaard, D. L. 2000. Rock deformation tests to large shear strains in torsion. Journal of Structural Geology, Volume 22, Issue 9, p. 1341-1358.

Pereira, M.F., Castro, A., Fernandez, C. 2015. The inception of a Paleotethyan magmatic arc in Iberia. Geoscience Frontiers, (6) 297-306.

Pirajno, F. 1992. Greisen systems. In: Hydrothermal Mineral Deposits. Springer, Berlin, Heidelberg, 280-324.

Pirajno, F., 2005. Hydrothermal Processes and Mineral Systems. DOI https://doi.org/10.1007/978-1-4020-8613-7.

Plümper, O., Putnis, A., 2009. The Complex Hydrothermal History of Granitic Rocks: Multiple Feldspar Replacement Reactions under Subsolidus Conditions, Journal of Petrology, Volume 50, Issue 5, Pages 967–987.

Pola, A., Crosta, G., Fusi, N., Barberini, V., Norini, G., 2012.Influence of alteration on physical properties of volcanic rocks. Tectonophysics 566, 67–86.

Pollard, P.J., Taylor, R.G., Cuff, C. 1988. Genetic Modelling of Greisen-Style Tin Systems. In: Hutchison C.S. (eds) Geology of Tin Deposits in Asia and the Pacific. Springer, Berlin, Heidelberg, pp 59-72.

Pollok, K., Putnis, C.V., Putnis, A. 2011. Mineral replacement reactions in solid solution-aqueous solution systems: Volume changes, reactions paths and end-points using the example of model salt systems. Am J Sci March 2011 311:211-236.

Polya, D.A. 1989. Chemistry of the main-stage ore-forming fluids of the Panasqueira W-Cu-(Ag)-Sn deposit, Portugal: implications for models of ore genesis. Econ. Geol. 84, 1134–1152.

Polya, D.A., Foxford, K.A., Stuart, F., Boyce, A., Fallick, A.E. 2000. Evolution and paragenetic context of low δD hydrothermal fluids from the Panasqueira W-Sn deposit, Portugal: New evidence from microthermometric, stable isotope, noble gas and halogen analyses of primary fluid inclusions. Geochim. Cosmochim. Acta 64, 3357–3371.

Putnis, A. 2002. Mineral replacement reactions: from macroscopic observations to microscopic mechanisms. Mineralogical Magazine, 66 (5): 689–708.

Putnis, A., Austrheim, H. 2010. Fluid-induced processes: metasomatism and metamorphism. Geofluids, 10: 254-269.

Putnis, A. and John, T. 2010. Replacement processes in the earth's crust. Elements: an international magazine of mineralogy, geochemistry, and petrology. 6 (3): pp. 159-164.

Putnis, A. 2015. Transient Porosity Resulting from Fluid–Mineral Interaction and its Consequences. Reviews in Mineralogy and Geochemistry, 80 (1): 1–23.

S

Seyfried W. E., JR., Janecky D. R., and Berndr M. E. 1987. Rocking autoclaves for hydrothermal experiments: II. The flexible reaction-cell system. In Hydrothermal Experimental Techniques (ed. H. BARNES and G. ULMER), Chap. 9, pp. 2 16-239. Wiley- Interscience.

Seward, T.M., and Barnes, H.L. 1997, Metal transport by hydrothermal fluids *in* Geochemistry of Hydrothermal Ore Deposits H.L. Barnes (ed), p. 235-285. John Wiley and Sons Inc.

Shcherba, G. N. 1970. Greisens. Int Geol Rev 12: 114–255

Selvadurai, A., Boulon, M., Nguyen, T. 2005. The Permeability of an Intact Granite. Pure appl. geophys. Volume 162, Issue 2, pp 373–407.

Smith, J. V. and Stenstrom, R. C. (1965) J. Geol., 73, 627-35.

Stemprok, M. 1987. Greisenization (a review). Geol Rundsch , Springer-Verlag 76: 169.

Stemprok, M., Pivec, E., Langrova, A. 2005. The petrogenesis of a wolframite-bearing greisen in the Vykmanov granite stock, Western Krušné hory pluton (Czech Republic). Bulletin of Geosciences, Vol 80, No 3, pages 163 – 184.

Štemprok, M., Dolejš, D., Holub, F.V. 2014. Late Variscan calc-alkaline lamprophyres in the Krupka ore district, Eastern Krušné hory/Erzgebirge: their relationship to Sn-W mineralization. Journal of Geosciences, volume 59, issue 1, 41 – 68.

T

Taylor, R.G. 1979. Geology of tin deposits. Developments in economic geology, Volume 11, Elsevier, 543p.

Taylor, R.G., Pollard, P.J. 1988. Pervasive hydrothermal alteration in tin-bearing granite and implications for the evolution of ore-bearing magmatic fluids. Canadian Institute of Mining and Metallurgy Special Volume 39, p. 86.95.

Tenthorey, E., Cox, S. 2003. Reaction-enhanced permeability during serpentine dehydration. Geology. 31. 10.1130/G19724.1.

Tenthorey, E., Cox, S.F., 2006. Cohesive strengthening of fault zones during the interseismic period: An experimental study. J. Geophys. Res. 111.

Tenthorey, E., Gerald, J.D., 2006. Feedbacks between deformation, hydrothermal reaction and permeability evolution in the crust: Experimental insights. Earth Planet. Sci. Lett. 247, 117-129.

Thadeu, D. 1951. Geologia do couto mineiro da Panasqueira. Comunic Serv Geol Port 32:5–64.

W-Z

Whitney, D.L, Evans, B.W. 2010. Abbreviations for names of rock-forming minerals. Am. Mineral 95:185-187.

Williams-Jones, A.E., and Migdisov, A. 2014. Experimental contraints on . The transport and deposition of metals in ore-forming hydrothermal systems. Society of Economic Geologists, Special Publication 18, pp 77-95.

Wood, S.A. 1992. Experimental determination of the solubility of WO3(s) and the thermodynamic properties of H2WO4(aq) in the range 300–600°C at 1 kbar: Calculation of scheelite solubility, Geochimica et Cosmochimica Acta, Volume 56, Issue 5, Pages 1827-1836.

Zaraisky, G.P., Stoyanovskaya, F.M. 1995. Experimental modeling of gain and loss of rare metals (W, Mo, Sn) during greisenization and alkalic metasomatism of leucocratic granite. Experiment in Geosciences, No. 4, pp 19-21.

Zhang, S., Cox, S.F., Paterson, M.S., 1994a. The influence of room temperature deformation on porosity and permeability in calcite aggregates. J. Geophys. Res. 99, 15761-15775.

Zhang, S., Paterson, M.S., Cox, S.F., 1994b. Porosity and permeability evolution during hot isostatic pressing of calcite aggregates. J. Geophys Res. 99, 15741-15760.

Zimmer, K., Zhang, Y.L., Lu, P., Chen, Y.Y., Zhang, G.R., Dalkilic, M. and Zhu, C. 2016. SUPCRTBL: A revised and extended thermodynamic dataset and software package of SUPCRT92. Computer and Geosciences 90:97-111.

Chapter VI: How greisenization could trigger formation of large vein-and-greisen Sn-W deposits: a numerical investigation

Objectives of this chapter:

In the previous chapter (**Chapter V**) we have highlighted that replacement reactions involved during greisenization lead to porosity generation, which enhances significantly permeability (up to 3 orders of magnitude) of the upper part of granitic intrusion related to Sn-W deposits. As evidenced by the occurrences of ore-bearing minerals within the neoformed porosity of massive greisen, the development of this porosity is favorable to circulation of mineralizing fluids through the intrusive body at the mineral scale. However, effects of this permeability change on (i) large scale pattern of fluid flow, (ii) time evolution of fluid flow and fluxes and (iii) localization of mineralization need to be constrained. Furthermore, textural analysis of tourmaline growth bands and geochemical characteristics of minerals (muscovite and quartz) formed during greisenization emphasize implication and contribution of orthomagmatic fluids both during the greisenization and the formation of mineralized veins. These fluids were produced during the granite crystallization and were preferentially expelled from the greisen cupola that could contribute to ensure high fluid pressure conditions favorable to opening and dilation of the mineralized vein network. Role and implications of this magmatic fluid production on opening of permeable structure (veins) and its conjugate effects with permeability change during greisenization need also to be constrained.

In this chapter we investigate effects of permeability change during greisenization and effects magmatic fluid production on the formation of large Sn-W deposits. To do this we apply numerical modelling that permits to (i) test individually each process to evaluate their respective contributions during fluid flow and (ii) the time evolution of fluid flow and heat and mass transfer.

Abstract: The formation of large tin-tungsten (Sn-W) deposits around granitic intrusions requires the circulation of large amounts of fluids within permeable structures. Half of the world tungsten production originates from highly mineralized veins above granitic intrusions and from the altered part of the granite (the greisen), whose formation results from intense fluid-rock interactions. During greisenization processes, mineral reactions involve a decrease in the rock volume and thus an increase in porosity and permeability. To understand the complex fluid-rock interactions leading to the formation of large Sn-W ore deposits, we consider a numerical modeling approach accounting for magmatic fluid production and realistic permeability changes. The production of magmatic fluids induces a variation of permeability due to overpressure in the hosting rocks. Porosity and permeability changes in the numerical models are constrained by previous measurements on rock samples from the world-class Panasqueira Sn-W ore deposit. The water/rock ratio is computed during granite cooling and applied to constrain the rate of greisenization. The numerical approach consists in a coupled heat and mass transfer modeling involving the inferred dynamic permeability law and a total fluid production of 5 % is assumed at the end of granite crystallization. The interplay between greisenization and fluid production creates zones of overpressure above the granite that could lead to the formation of permeable structures such as veins. Four model results are presented: with and without fluid production, and with and without dynamic permeability. Fluid circulation processes are clearly controlled by fluid production, which is promoted by highly permeable zones. Formation of greisen is reproduced and greisen thickness reaches 200 m for the more sophisticated model. This last model also shows that time integrated fluid flux is maximum within the greisen and within a large zone above the granite. This zone of near lithostatic fluid pressure can be built in a few thousands of years. Dynamic permeability promotes high fluid velocity and intense fluid-rock exchanges that could result in the formation of large ore deposits by enhancing mass transfer within and above granitic intrusions.

Keywords: Greisenization, large magmatic-hydrothermal deposits, dynamic permeability, magmatic fluid production, fluid flux, fluid overpressure conditions, numerical modelling

1. Introduction

The vein, stockwork and greisen Sn-W deposits are magmatic-hydrothermal systems that provide an important part of the world W production (Werner et *al*., 2014) and represent an important source of Sn. These deposits generally include (i) a disseminated mineralization within a massive greisen characterized by low grade and high tonnage and (ii) mineralized quartz veins usually characterized by high grade and low tonnage (Taylor, 1979; Taylor and Pollard, 1988; Mlynarczyk et al., 2002). The formation of veins is strongly controlled by the regional structures and the fluid pressure conditions that promote the opening of the permeable structures. Massive greisens are generally present in the apical portions of granite intrusions and result from strong interactions between granitic rocks and hydrothermal fluids during the magmatic-hydrothermal transition (Stemprok, 1987; Pollard et *al*., 1988; Pirajno, 1992; Černý et *al*., 2005). The formation of vein and greisen deposits implies the transfer and the focusing of a large amount of mineralizing fluids (Dolejs, 2015). Moreover, a recent fluid inclusion study performed by Korges et *al*. (2018) in the vein-and-greisen system of Zinnwald (Erzebirge, in between Czech Republic and Germany) suggests that the formation of mineralized veins and greisen are contemporaneous and result in the boiling of a single magmatic fluid.

The advection constitutes the privileged mode of heat and mass transport, which the efficiency directly depends on rock permeability and on the driving forces involved during fluid flow (Phillips, 1991; Hedenquist & Lowenstern 1994; Cox 2005). According to a recent geochemical study, the mineralization stage around granitic intrusions would occur over a very short time period (less than 35 kyr for large-scale economic porphyry copper deposits; Cernushi et al., 2018). It follows that the formation of large-scale ore deposits around granitic intrusions would require a very efficient heat and mass transfer process.

Magmatic-hydrothermal mineralized systems were investigated in numerous studies involving numerical simulation describing and constraining the organization of fluid in and around granitic intrusions (Norton et Cathles, 1979; Cathles, 1997; Gerdes et al., 1998; Cui et al., 2001; Eldursi et al., 2009; 2018). These models permit to constrain in simplified way the time evolution of the fluid flow patterns and, in some cases, to delineate in time and space the most favorable zones for mineralization to occur. However, these models do not consider the different feedbacks between geological processes and petrophysical properties, like permeability evolution during fluid flow. The non-consideration of these processes in the previous numerical models may explain why

lifespan of mineralization stages is often overestimated (a few hundreds of kyr). Indeed, permeability is a dynamic parameter that is mainly affected by interplays between the stress state, the rock alteration and fluid pressure conditions (Sibson et *al*., 1988; Manning et Ingebritsen, 1999; Cox, 2010; Ingebritsen et Appold, 2012; Ingebritsen et Gleeson, 2015). Effects of rock deformation and fracturing on permeability and hence on fluid flow were investigated in numerous structural and experimental studies (Sibson 1987 and 1988; Zhang et al., 1994; Tenthorey and Fitz Gerald, 2006; Coelho et al., 2015). These studies have demonstrated that deformation transiently enhance permeability of the hydrothermal systems by formation of permeable structures like shear zone and fractures. Fluid overpressure conditions related to fluid injection is another important parameter that promotes the opening of permeable structures enhancing the rock permeability by factors of 100 to 1000 (Zhang et *al*., 1994; Ingebritsen et Gleeson, 2015).

The hydrologic effects of these different feedbacks were investigated by numerical modeling in cases of geothermal reservoirs related to magmatic-hydrothermal ore deposits by Weis et *al*., (2012) and Weis (2015). These numerical studies have highlighted that the combination of dynamic permeability with the stress state and the magmatic fluid production permits to reproduce the geometry of ore shell commonly observed in copper porphyry deposits (Weis et *al*., 2012).

Depending on the spatial organization of fluid flow, the pressure and temperature conditions and the chemical characteristics of fluids, the hydrothermal alteration can trigger dissolution, precipitation and mineralogical transformation of rocks that affect directly the permeability (Putnis, 2002; Jamtveit et al., 2009; Putnis and Austrheim, 2010; Pollok et *al*., 2011; Booden and Simpson, 2011; Putnis and John, 2010; Jonas et *al*., 2014; Putnis, 2015; Scott and Driesner, 2018). According to the volume changes of the solid phase induced by replacement reactions related to hydrothermal alteration, these mineralogical transformations can lead to the self-sealing of the permeable pathways causing the inhibition of fluid flow, or conversely trigger the porosity and permeability increase that enhance fluid flow and promote mass and heat transport. The greisenization responsible of the massive greisen formation is a metasomatic alteration leading to the total replacement of early magmatic feldspars of granite by a late magmatic-hydrothermal quartz muscovite assemblage. A recent experimental and petrophysical study performed by Launay et *al*. (submitted) has demonstrated that the replacement of feldspars by muscovite during the greisenization is accompanied by a volume decrease of the mineral

phases. This volume decrease could trigger porosity generation and hence permeability increase that can reach 3 orders of magnitude.

Massive greisens are common in the upper part of granitic intrusions related to Sn-W mineralized systems and their thickness can reach ~ 200-300 hundred meters like at Cinovec, East Kemptville and Panasqueira (Halter et al., 1998; Jarchovsky, 2006; Laznicka, 2010). The development of this thick permeable pathway during the magmatic-hydrothermal activity responsible of the formation of Sn-W deposits can significantly enhance fluid flow and mass transport. However, effects of this feedback between the greisenization and permeability on fluid flow in vein and greisen deposits need to be constrained. Based on the coupling of physical equations that described the physical hydrology of fluid flow and heat and mass transport in hydrothermal systems, the numerical modelling approach represents a powerful tool to understand and quantify the controlling processes leading to the formation of hydrothermal ore deposits, as well as the development of hydrothermal alteration zones.

As above mentioned, the potential mechanisms susceptible to affect the permeability and fluid flow during the formation of vein and greisen deposits are: (i) the greisenization of granite that can enhance permeability of granite roof, promote fluid flow and facilitate the expulsion of magmatic fluids released during the granite crystallization at depth and (ii) the opening of permeable structures in response to fluid overpressure conditions induced by the expulsion of magmatic fluids. In this study we explore by numerical modelling the interplays between the permeability changes induced by the greisenization, the production of magmatic fluid during granite crystallization, and the opening of permeable structures induced by potential fluid overpressure conditions. The model geometry and parameters are based on geological and petrophysical observations (porosity and permeability measurements) from the world class W-Sn-(Cu) Panasqueira ore deposit that represents a reference system to study magmatic-hydrothermal processes leading to the formation of large vein and greisen deposits. We present results from 2D numerical modelling of time evolution of fluid flow patterns and fluxes to evaluate influence of permeability changes during greisenization processes.

2. The vein and greisen W-Sn-(Cu) world class Panasqueira ore deposit

The W-Sn-(Cu) Panasqueira ore deposit is located in the Central Iberian Zone (CIZ) that covers the middle part of the Iberian Variscan Belt (Fig. 1a) (Julivert et al., 1972). This tectonic domain is marked by the occurrences of numerous granitic intrusions mainly emplaced in a thick (8-11 km) monotonous Neoproterozoic schisto-greywacke sequence during the latest stages of the Variscan orogeny (Dias et *al*., 1998; Castro et *al*., 2002). The CIZ is particularly rich in Sn-W deposits and indices, whose the formation is related to the magmatic-hydrothermal processes induced by the emplacement of this large volume of granitic bodies. These deposits comprise mostly vein and greisen mineralized systems like Regoufe, Gois and Panasqueira, which were/are mainly exploited for the W mineralization.

The world class W-Sn-(Cu) Panasqueira deposit belongs to the Beira Baixa province located in the South of the Serra da Estrela granitic Massif. This region is largely composed of schist greywacke sequence affected by tight and upright folds and by a low grade greenschist metamorphism during the Variscan orogeny. The presence of spotted schist delineates a thermal metamorphism aureole, which betrays the presence of a non-outcropping granitic intrusion at depth (Clark, 1964; Kelly and Rye, 1979; Bussink, 1984). The surface distribution of spotted schist, the drill holes distributed over the Panasqueira district and gravimetric survey show that the granite is characterized by an elongated shape in the NW-SE direction (7.5 x 4.5 km) for a thickness not exceeding 2 km (Fig.1b) (Hebblethwaite and Antao, 1982; Thadeu, 1951; Kelly and Rye 1979; Clark, 1964).

A cupola intersected by the underground mining works and the upper part of this granite was altered into a massive greisen during fluid flow related to the incipient stage of the magmatic hydrothermal activity of Panasqueira (Fig. 1b) (Thadeu, 1951; Clark, 1964; Kelly and Rye, 1979; Bussink, 1984). This massive greisen can be characterized by porous and microporous textures emphasizing the development of porosity during the replacement reactions related to the greisenization processes. Petrophysical measurements performed by Launay et al., (submitted) highlight (i) a significant porosity generation (~8.5%) during the greisenization that can be also observed in other mineralized greisen systems and (ii) a significant permeability increase (more than 3 orders of magnitude) induced by this porosity generation. The occurrences of metals-bearing minerals like cassiterite and chalcopyrite in the porosity generated during the greisenization suggest that

the development of these permeable pathways could promote and enhance fluid flow in greisen systems during the mineralizing events.

The economic W-Sn mineralization consists of a dense swarm of sub-horizontal quartz veins mostly hosted by the metasedimentary host rock (Beira schist). The ore zone is spatially associated with the greisen cupola and extends over an area of 6 km² (Fig. 1b and 1c). The presence of geochemical tungsten anomalies centered on the cupola (Oosterom et al., 1984) suggests an important role of this cupola on fluid flow organization (Fig. 1b), as confirmed by Launay et al. (2018). The Panasqueira district is also marked by the presence of a late NNW-SSE and ENE-WSW sub-vertical strike slip fault system crosscutting and postdating clearly the mineralized vein systems of Panasqueira and that were re-activated during the Alpine orogeny (Fig. 1b) (Thadeu 1951, Kelly and Rye 1979, Foxford et al., 2000). Consequently, these faults were not implicated during fluid flow related to the W-(Sn) mineralization and hence were not considered in the present work.

The vertical distribution of the cumulative vein thickness along the vertical section of drill holes emphasizes that the vein system of Panasqueira form a relatively regular band of about 100-250 m of thickness mainly present at elevation ranging between 650 to 500 m (Fig. 1d, after Foxford et al., 2000). This distribution suggests that fluid responsible of the mineralization of Panasqueira has preferentially flowed through a regular horizontal permeable damage zone. From this observation Foxford et al., (2000) proposed a structural model of vein formation involving extensional failure induced by supralithostatic fluid pressure conditions in a compressive crustal regime ($\sigma_3 = \sigma_v$). Recent results based on the growth bands study of tourmaline are consistent with the implication of fluid overpressure conditions during the incipient stages of the vein opening (Launay et *al*., 2018). However, the expulsion of magmatic fluids at lithostatic pressure conditions during the granite crystallization can constitute an important mechanism during opening of the vein swarm, and need to be explored by numerical modelling. The formation of this dense vein system was related to the circulation of a large amount of fluids estimated at ~1000 km^3 by Polya et *al*., (1989) for the W-Sn mineralization stages. This implies efficient processes of fluid flow and hence sufficient permeable structures and lithological facies to permit the transfer of this volume of fluid.

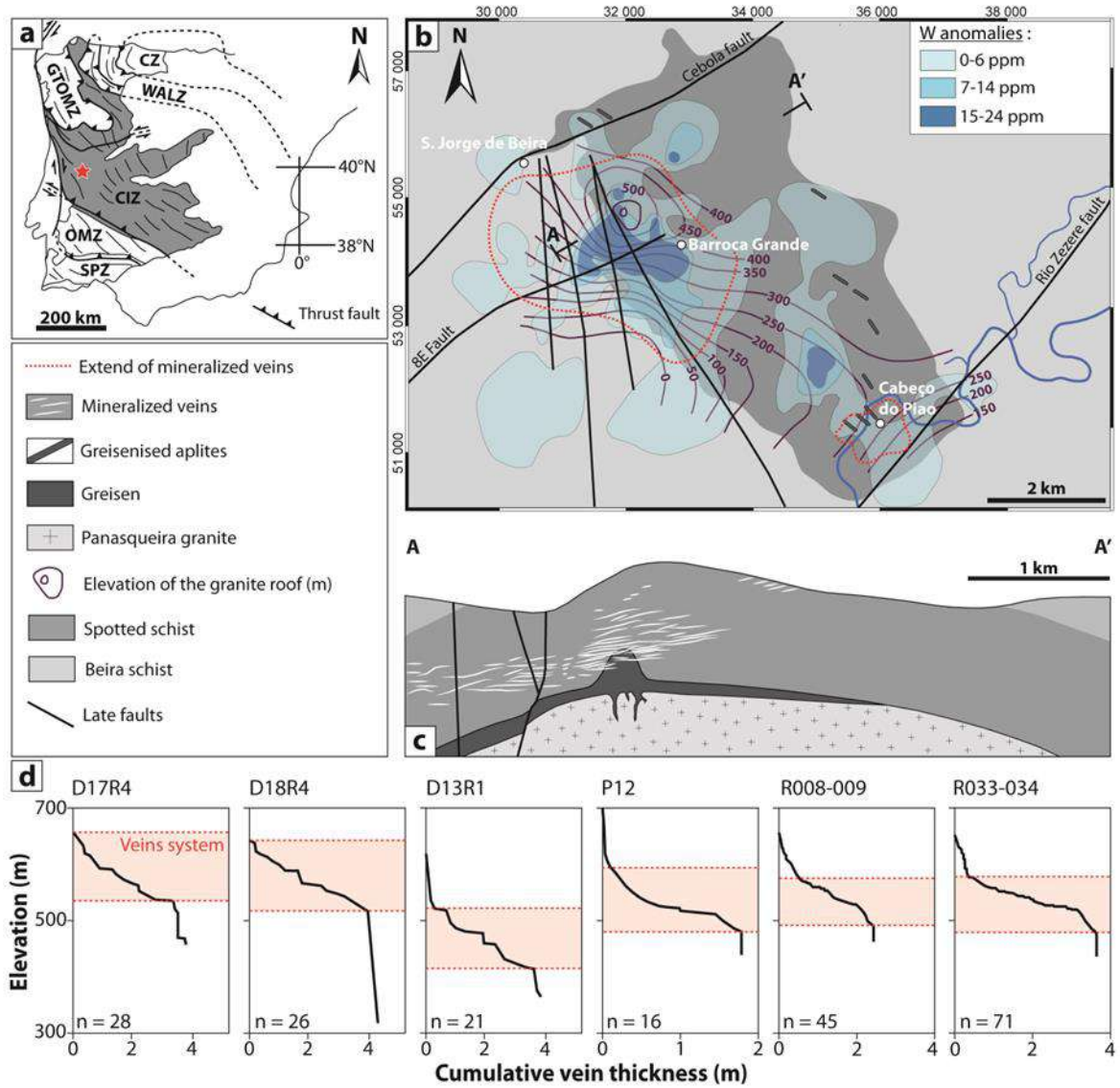

Figure 1 (a) Tectonic map displaying the tectonostratigraphic domains composing the Iberian massif (modified from Julivert et al., 1972). The location of the Panasqueira deposit is marked by a red star. CZ: Cantabrian Zone, WALZ: West Asturian-Leonese Zone, GTOMZ: Galicia Tràs-os-Montes Zone, CIZ: Central Iberian Zone, OMZ: Ossa-Morena Zone and SPZ: South Portuguese Zone. (b) Regional geological map of the W-Sn-(Cu) Panasqueira ore deposit, in which the lithogeochemical anomalies in W are represented (compiled from data of Oosterom et al., 1984). (c) The (A-A') geological cross section displaying the spatial relationships between the mineralized vein system, the greisen and the Panasqueira granite. (d) Cumulative vein thickness along the vertical sections of drill holes showing the vertical distribution of the mineralized vein network of Panasqueira (n refers to the number of veins crosscut by the drill holes) (drill holes data compiled from Foxford et al., 2000 and Wheeler, 2015).

3. Model set-up and time-dependent properties

To investigate the role of greisenization on the formation of W-Sn deposits, we have performed a time-dependent 2D numerical modeling of fluid flow and heat transfer around a granitic intrusion, integrating (i) the depth dependent permeability profile, (ii) effect of fluid overpressure conditions on permeability in response to magmatic fluid expulsion and (iii) effects of feedback between greisenization, porosity and permeability on fluid flow. These models were performed with the finite element code Comsol Multiphysics™. This numerical method has been tested and validated by several benchmarks in cases of fluid flow around hot granite intrusions (Eldursi et al., 2009) and geothermal systems (Garibaldi et al., 2010; Taillefer et *al*., 2017) for which results were compared with those obtained from well-established codes.

3.1 Governing equations

In magmatic-hydrothermal systems, the main driving forces involved during fluid flow are (i) the buoyancy force induced by variation of fluid density due to the change in temperature, pressure and salinity conditions and (ii) production of magmatic fluids that affect the pressure gradient and hence the mass transport by advection. In this study, we consider several physical equations that were usually applied and coupled to describe the behavior of fluid flow in hydrothermal systems. The mass conservation equation is considered for an incompressible fluid with variable density within a saturated porous medium:

$$\frac{\partial(\varphi.\rho)}{\partial t} = 0 = -\nabla.\left(\rho_f.\vec{u}\right) + Q_{H_2O} \quad (1)$$

where φ is the rock porosity, ρ_f the fluid density (kg.m^{-3}), t the time (s), u the fluid velocity (m.s^{-1}) and Q_{H2O} a fluid source term (s^{-1}) in models corresponding to the magmatic fluid production.

Darcy's law was applied to calculate the fluid velocity according the following equation:

$$\vec{u} = -\frac{k}{\mu_f}(\vec{\nabla}P - \rho_f\vec{g}) \quad (2)$$

with k the rock permeability (m²), μ_f the fluid dynamic viscosity (Pa.s) , P the fluid pressure (Pa) and g the gravitational acceleration (m.s^{-2}).

Heat transport is achieved by conduction and advection in a porous medium and is described for single fluid phase by:

$$\rho_r Cp_r \frac{\partial T}{\partial t} = \lambda \Delta T - \rho_f Cp_f . \vec{u} . \vec{\nabla} T + Q_H \quad (3)$$

with ρ_r (kg.m^{-3}) the rock density, Cp_r (J.kg^{-1}.K^{-1}) the heat capacity of rocks, T (K) the temperature, λ (W.m^{-1}.K^{-1}) the thermal conductivity Cp_f (J.kg^{-1}.K^{-1}) the heat capacity of fluid, and Q_H the heat source produced by the granite intrusion (W.m^{-3}).

3.2 Model geometry, boundary conditions and rock properties

Model geometry is based on geological and borehole data acquired at Panasqueira (Hebblethwaite and Antao, 1982; Thadeu, 1951; Kelly and Rye 1979; Wheeler, 2015; Launay et *al*., 2018). The chosen 2D geometry is inferred from the A-A' cross-section shown in Fig. 1c and 2. We assume a granite intrusion characterized by a laccolith shape with a 6 km lateral extent and a height of 2 km. This granitic intrusion is characterized by an asymmetric shape with a cupola in the granite roof at 2.7 km of depth. This granite domain is located at 3 km of depth in a host rock domain of 20 km of width for 10 km of height. We assume an initial granite temperature of 850°C and an initial geothermal gradient of 30°C per kilometer in the host rock domain. Physical properties for the granite and the host rock domains were chosen according to the physical properties of granitic rocks and metasedimentary rocks (schist) commonly described in the literature (Table 1).

For the boundary conditions, we assume a flat surface topography in the upper boundary with a fixed pressure of 1.015×10^5 Pa and a fixed temperature of 20 °C (Fig. 2). A temperature of 320 °C and an impermeable condition are fixed at the bottom boundary. The lateral boundaries are assumed impermeable and thermally insulated (Fig. 2). The mesh comprises 24646 triangular elements with resolution ranging between element side length of 50 m to 200 m. The elements were refined in the granite domain, along the upper boundary and along the contacts between the granite domain and the host rock domain that constitute the most important part of the model.

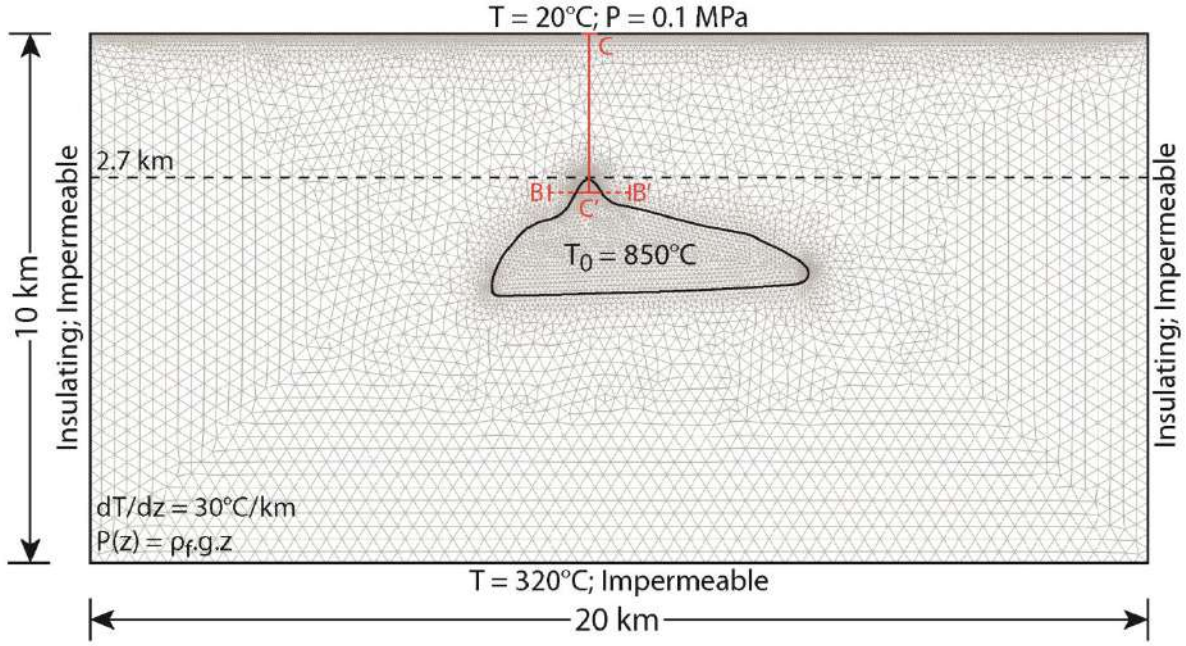

Figure 2 Meshing and model geometry with a laccolith magma chamber of about 6 km of width for 2 km of height and a cupola at 2.7 km of depth. This geometry corresponds to the inferred geometry of the Panasqueira granite. The boundary and the initial conditions used for the modelling are also displayed. Cross-sections B-B' and C-C' refer to horizontal and vertical profiles used in Figures 6 to 9.

Initial rock properties	Symbol	Host rock	Granite	Unit
Specific heat capacity of rock	Cp_r	800	1200	J/(kg.K)
Thermal conductivity	K_P	2	3	W/(m.K)
General heat source	Q_H	0	5.10^{-6}	W/m^3
Rock density	ρ_r	2700	2700	kg/m^3
Initial porosity	φ_0	0.1	0.004	Pore volume fraction
Initial permeability	k_0	Eq. (9)	10^{-20}	m^2
Gravitational acceleration	g	9.81		m/s^2
Initial fluid properties				
Specific heat capacity of fluid	Cp_f	4200		J/(kg.K)
Thermal conductivity	K_L	0.6		W/(m.K)
Dynamic viscosity	μ_f	Equation of state		Pa.s
Fluid density	ρ_f	Equation of state		kg/m^3
Magmatic fluid production	Q_{H2O}	Eq. (8)		m^3 of fluid/m^3 of rock/s (s^{-1})

Table 1 Initial physical properties of rocks and fluid used for models. Eq(n) refers to equations presented in the text

3.3 Fluid properties

For the fluid phase we assume a porous media saturated by a single fluid phase composed of pure water. The fluid density was calculated at each time step as a function of the pressure and the temperature using an interpolated function based on the IAPWS-IFP97 equation of state for pure water defined by the International Association for the Properties of Water and Steam (IAPWS, Wagner et *al*., 2000). From this database, an interpolated function (polynomial with 15 coefficients) was defined from Matlab™ script and then implemented as parameter in Comsol Multiphysics™. Based on the analytical approximation of Kestin et *al*., 1978 and Rabinowicz et *al*., 1998, the dynamic viscosity evolution with temperature is given by:

$$\mu_f = 2.414\ 10^{-5}.10^{\left(\frac{247.8}{T-140}\right)} \quad (4)$$

with *T* the fluid temperature in K. As discussed by Clauser (2006), fluid viscosity is mainly controlled by temperature conditions and effects of pressure can be neglected.

3.4 Water/rock ratio and alteration intensity

To evaluate the rate of greisenization induced by fluid-rock interactions during fluid flow, we have calculated the time-integrated water/rock ratios following the method proposed by Schardt and Large (2009):

$$W/R = \int_0^t \frac{\rho_f.u.\varphi}{\rho_r.(1-\varphi).L}.dt \quad (5)$$

where *W/R* is the time-integrated water/rock ratio, φ is the rock porosity, *u* is the fluid velocity, *dt* is the time difference between successive time step, ρ_f is the fluid density, ρ_r is the rock density and L the length scale of the defined mass rock, taken here as 1 m. Hence, W/R represents the total mass of fluid that has flowed through a defined mass of rock of scale *L*. Accordingly the localization and extent of greisenization is directly controlled by the organization and the patterns of fluid flow and the fluid fluxes.

3.5 Magmatic fluid production

At each time step, the rate of magmatic fluid production is calculated as being proportional to the crystallization rate of the granitic intrusion between the liquidus (T_l) and the solidus (T_s) temperatures. For each element composing the granite domain characterized by temperatures ranging between the solidus and the liquidus, the volume of crystallized granite (V_{cryst}) was calculated from the melt fraction (F) according to the formulation of Caricchi and Blundy (2015):

$$V_{cryst}(t) = (1 - F).A.dy \quad (6)$$

where $V_{cryst}t$ (m^3) is the volume of crystallized granite at the considering time step, F the melt fraction, A (m^2) the surface of the considering element and dy (m) the extension of the element in the third dimension; here we assume dy = 1 m to account for only the mass of fluid produced on the 2D section considered in our modelling. From this volume of crystallized granite we assume that 5 wt% of fluid (pure water) was produced during the crystallization of the granite. The effective mass of fluid (M_W *(t)*) produced at the considering time step was calculated by subtracting the mass of fluid produced during the previous time step:

$$M_W(t) = 0.05.\rho_r.V_{cryst}(t) - M_W(t-1) \quad (7)$$

with $M_W(t)$ (kg) the mass of fluid produced at the considering time step, ρ_r ($kg.m^{-3}$) the density of granite, $V_{cryst}(t)$ the volume of crystallized granite at the considering time step and $M_W(t\text{-}1)$ (kg) the mass of fluid produced during the previous time step. From this mass of produced fluid, we calculate for each element composing the granite domain the rate of fluid production according to the following expression:

$$Q_{H2O}(t) = \frac{M_W(t)}{\rho_f}.\frac{1}{V.dt} \quad (8)$$

where Q_{H2O} (s^{-1}) is the rate of fluid production for the considering element and at the considering time step, $M_W(t)$ (kg) is the mass of fluid produced by the considering element at the considering time step, ρ_f ($kg.m^{-3}$) is the fluid density, V (m^3) is the volume of the considering element and dt (s) is the time difference between successive time steps.

3.6 Dynamic Permeabilities

3.6.1 The background permeability

Compilation of permeability values estimated in tectonically active continental crust permitted to define a depth-dependent profile of the permeability (Manning and Ingebritsen, 1999). Due to the impermeable nature of the metasedimentary host rocks present at Panasqueira (Launay et *al*., submitted), we have defined, for depths exceeding 0.5 km, a function of permeability evolution modified from this depth-dependent function:

$$\log(k) = -16 - 3.2\log(z) \quad (9)$$

where k (m²) is permeability and z (km) is depth. Above 0.5 km, permeability was fixed at 10^{-15} m² (Fig. 3a). This function was applied in our models to define the background permeability values in the host rock domain for hydrostatic fluid pressure conditions.

3.6.2 Feedback between fluid overpressure conditions and permeability

Fluid overpressure conditions ($P_f > P_{hydrostatic}$) constitute a key process to increase temporarily the rock permeability (Sibson 1988; Cox, 2010; ref). Indeed, numerous experimental and field studies have emphasized that permeability can increase by 2 to 3 orders of magnitude under overpressure fluid conditions (Ingebritsen and Manning, 2010; Howald et al., 2016; Ingebritsen and Gleeson, 2015). This feedback is mainly involved in hydraulic fracturing processes and in fault-valve systems, but can also be applied to explain the formation of veins in response to the expulsion of magmatic fluids in magmatic-hydrothermal deposits (ref). At Panasqueira, Foxford et *al*., (2000) proposed a model of vein opening involving episodic vein dilation induced by lithostatic fluid pressure conditions in compressive regime. To account for this feedback between permeability changes in the host rock domain and fluid overpressure conditions potentially induced by the expulsion of magmatic fluids, we evaluate the pore fluid factor at each time step:

$$\lambda_v = \frac{P_f}{\sigma_v} \quad (10)$$

where P_f (Pa) is the fluid pressure condition, σ_v (Pa) is the lithostatic pressure and λ_v is the pore fluid factor, with λ_v = 0.4 for hydrostatic fluid pressure conditions and λ_v = 1 for lithostatic fluid pressure conditions. From values of λ_v a factor of permeability change (f_k) was calculated assuming that it increases linearly with the pore fluid factor, with f_k = 1 for

λ_v = 0.4 and f_k = 100 for λ_v = 1. This maximum f_k value was arbitrarily chosen according to common values found in the literature (e.g. Zhang et *al*., 1994; Ingebritsen and Gleeson, 2015). For values of λ_v > 1 we assume that f_k = 100. From this factor of permeability change, the permeability was calculated at each depth from its initial background value (Fig. 3b):

$$k(t) = k_0 . f_k \tag{11}$$

where $k(t)$ (m²) is the permeability for a given depth and for a given fluid pressure conditions, k_0 (m²) is the background permeability at a given depth and f_k is the factor of permeability change depending on the fluid pressure conditions.

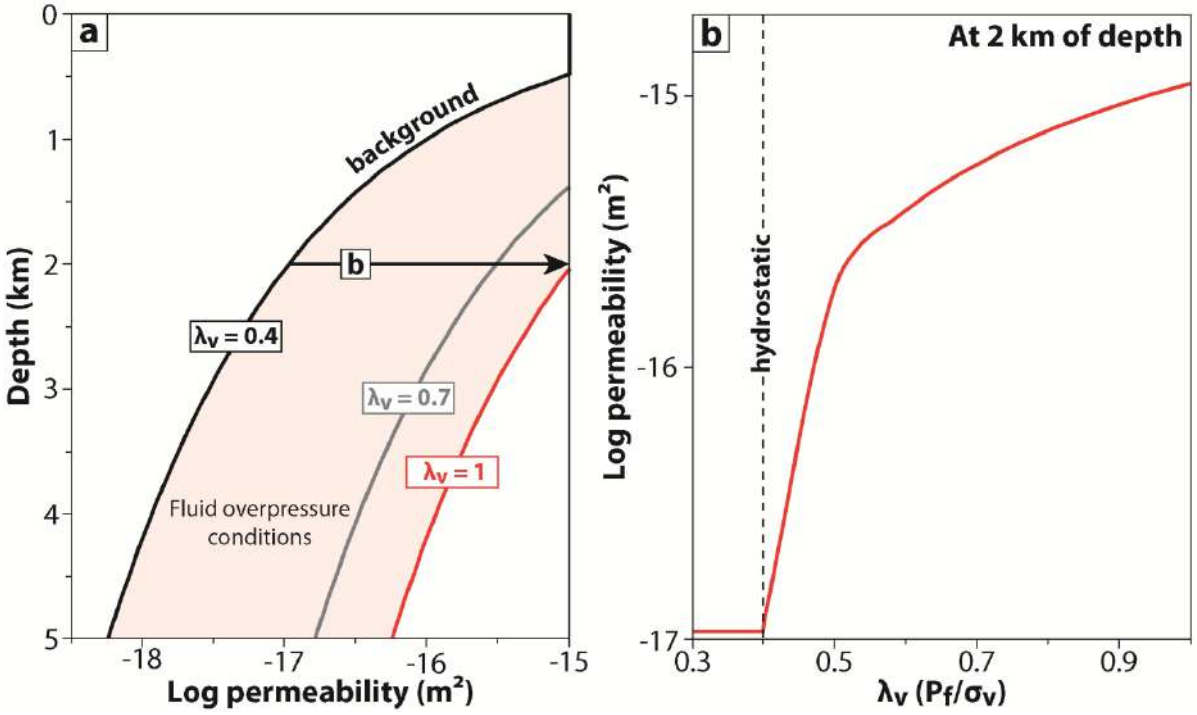

Figure 3 Model of dynamic permeability in the country rocks domain describing the permeability increase induced by fluid overpressure conditions. (a) Permeability profile as function of depth (adapted from Ingebristen and Manning, 1999). Permeability increase induced by fluid overpressure conditions (λ_v > 0.4) are also displayed. For a given depth, the permeability increases by 2 orders of magnitude from the background value when the fluid pressure conditions are lithostatic (λ_v = 1). (b) Permeability evolution at 2 km of depth as function of the pore fluid factor (λ_v), shown here with a logarithmic scale. We assume that the permeability increases linearly with the pore fluid factor until lithostatic pressure conditions (λ_v = 1).

3.6.3 Feedback between greisenization, porosity and permeability

Porosity and permeability measurements performed by Launay et *al*., (submitted) on samples representative of different degree of greisenization have emphasized a positive correlation between the porosity evolution and the alteration degree that follows an exponential law (Fig. 5a). To implement this experimental function of the porosity evolution in our numerical modeling, we have converted the alteration index (AI) in water/rock ratio (W/R) according to the results presented in the thermodynamic study of Reed et *al*., (2013). In this work, the crystallization and the breakdown of minerals composing the Butte granite are mapped for different temperatures as a function of the water/rock ratio and hence as a function of the hydrothermal alteration (Fig. 4). We assume that the complete greisenization of the granite is achieved by the total breakdown of feldspars (albite and k-feldspars) that corresponds to W/R of 2 at 500°C (total alteration of albite).

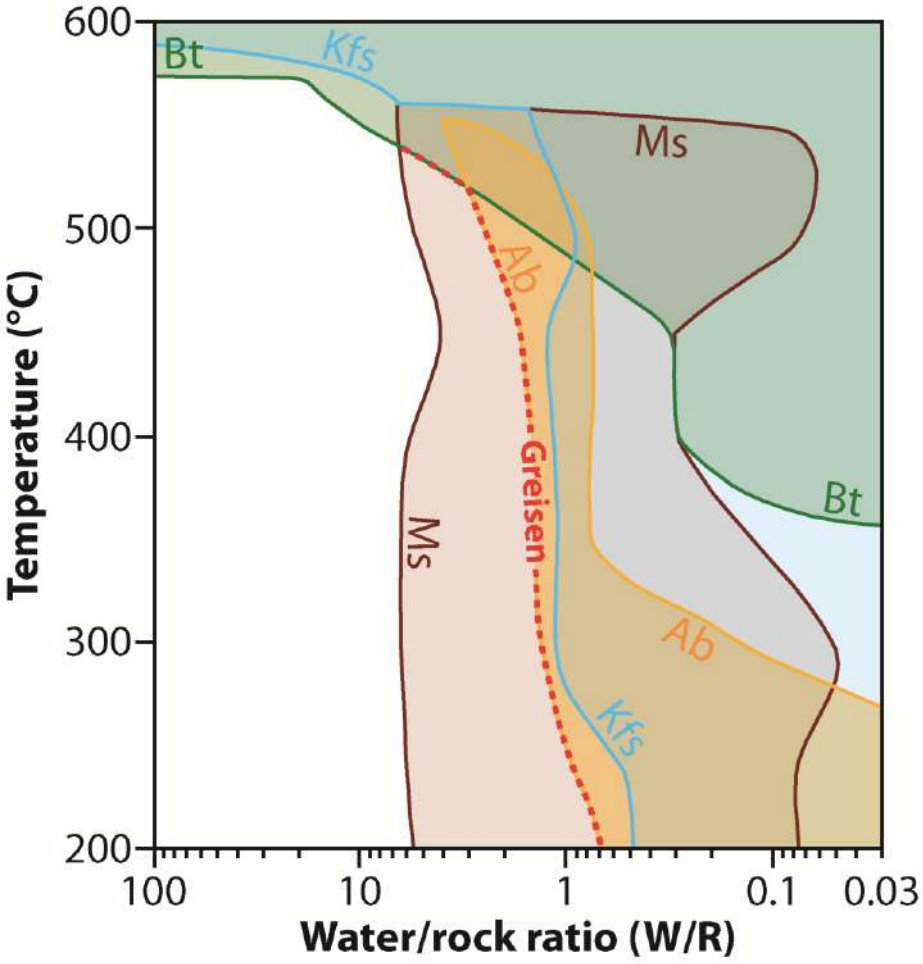

Figure 4 Alteration mineral phase diagram displaying crystallization and breakdown of minerals for the Butte granite as a function of the water/rock ratio and temperature conditions (modified from Reed et *al*., 2013). The red dashed line marks the total breakdown of primary magmatic minerals (albite, k-feldspars and biotite) and corresponds to the total greisenization of granite. Mineral abbreviations: Ab = Albite, Bt= Biotite, Kfs= k-feldspar, Ms= Muscovite.

From this W/R value, which marks the complete greisenization of granite, we define a function describing the porosity evolution as a function of the W/R ratio between 0 and 2. This function conserves the same exponential evolution of the experimental law of Launay et *al.*, (submitted):

$$\varphi\ (\%) = 7.29\ 10^{-7}\ .\ e^{(0.21.W/R)} \tag{12}$$

This function was coupled with the calculated time-integrated W/R ratio described previously. At each time step of calculation, the porosity of granite was calculated from this function for W/R ratio ranging between 0 and 2. For values of W/R ratio exceeding 2, we assume a fixed porosity of 7%. The permeability evolution related to the greisenization was assumed to vary with the porosity according to a cubic power law consistent with the experimental data described by Launay et al., (submitted) (Fig. 5b):

$$k = k_0 \left(\frac{\varphi}{\varphi_0}\right)^3 \tag{13}$$

where k_0 the initial grnaite permeability is 2.10^{-20} m² and φ0 the initial granite porosity is 0.004.

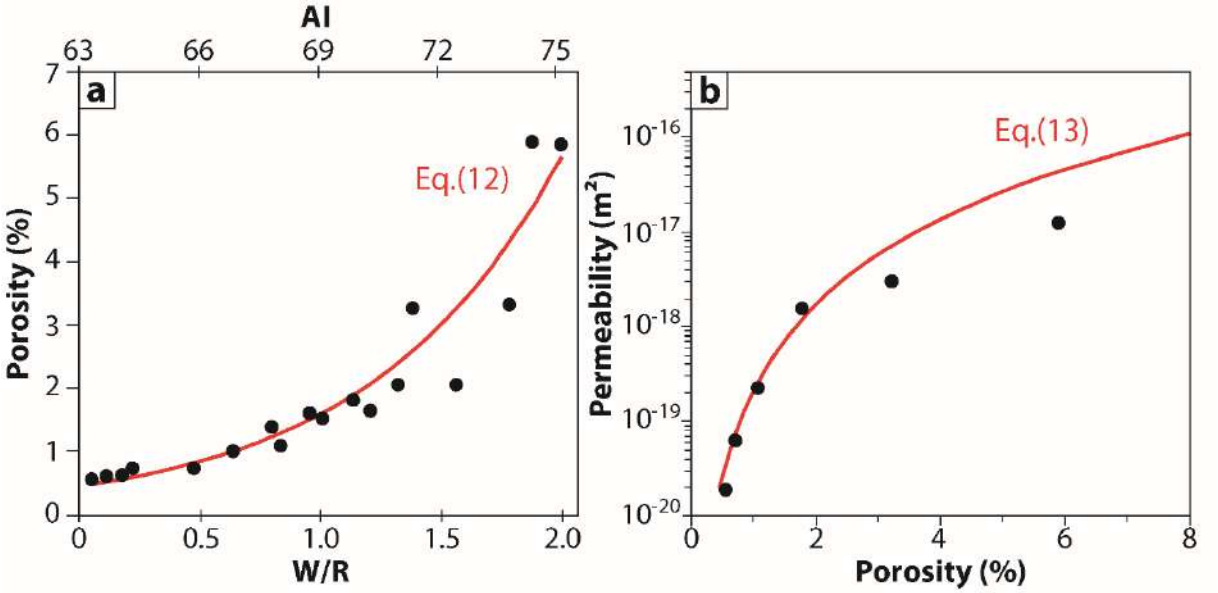

Figure 5 Model of dynamic permeability in the granite intrusion describing the feedback between the greisenization, the porosity and the permeability (Experimental data after Launay et *al.*, (submitted)). (a) Model of porosity evolution in greisen as a function of the water/rock (W/R) ratio and the alteration index (AI = 100.(Al_2O_3/(Al_2O_3+K_2O+Na_2O))). The conversion of the alteration index (AI) in water rock (W/R) ratio is detailed in the text. (b) Model of permeability evolution in greisen as function of the porosity generated during the greisenization. The red curves correspond to functions (Eq.(12) and Eq.(13)) used in numerical modeling to describe the porosity and the permeability evolution during the greisenization.

4. Results

To investigate the specific effects of permeability changes during greisenization and magmatic fluid production, we have performed four different numerical models involving two different types of magmatic-hydrothermal systems: (i) one with a "passive" granitic intrusion without fluid production and where fluid flow is only driven by convective processes and (ii) another one involving magmatic fluid production during granite crystallization and where overpressure fluid conditions constitute an additional driving force. For these two different scenarios, we first describe results obtained with static (constant) granite permeability. Then, permeability changes induced by greisenization are accounted for, following the approach described in section 3.

The numerical modelling results obtained for the four configurations are displayed in Figures 5 to 8 as snapshots of different times illustrating the time evolution of the fluid flow patterns and the key processes involved during fluid flow. For each model, one figure presents three time steps of fluid flow patterns and permeability changes (left column), thermal field and time-integrated fluid flux (middle), and cross sections of some hydrodynamics parameters through the cupola (horizontal B-B' profile) and along the C-C' vertical profile (right column).

4.1 Models with static granite permeability

4.1.1 Without magmatic fluid production (M1)

This first model (Fig. 6) illustrates the development of convective fluid flow pattern around the cooling granite. Despite convection clearly occurs, the small velocity values do not disturb significantly the isotherms, which remain parallel to the granite roof geometry. Temporal evolution shows that fluid loops, firstly focused just above the intrusion, progressively widen and propagates upward (black arrows in left column of Fig. 6). This spatial propagation simply reflects the heat diffusion from granite, whose temperature equals 850°C at the initial time. The two convective cells appear to be centered above the cupola. This spatial control can be explained by strong contrasts induced by the granite geometry, such as large lateral temperature difference and high permeability contrast between the cupola and the host rock domain. The second column of Fig. 6 shows relatively low values of the time-integrated fluid flux. The maximum values are reached at time 50 kyr, and do not exceed $10^{4.8}$ $kg.m^{-2}$. These maximum values appear localized along the granite-host rock contacts and above the cupola, that correspond to zones with

the highest fluid velocities. In the third column, the fluid velocity curves show strong variations between the permeable host rock and the impermeable cupola, with highest values ($1.2\ 10^{-9}$ $m.s^{-1}$) at the incipient stage of the hydrothermal circulation.

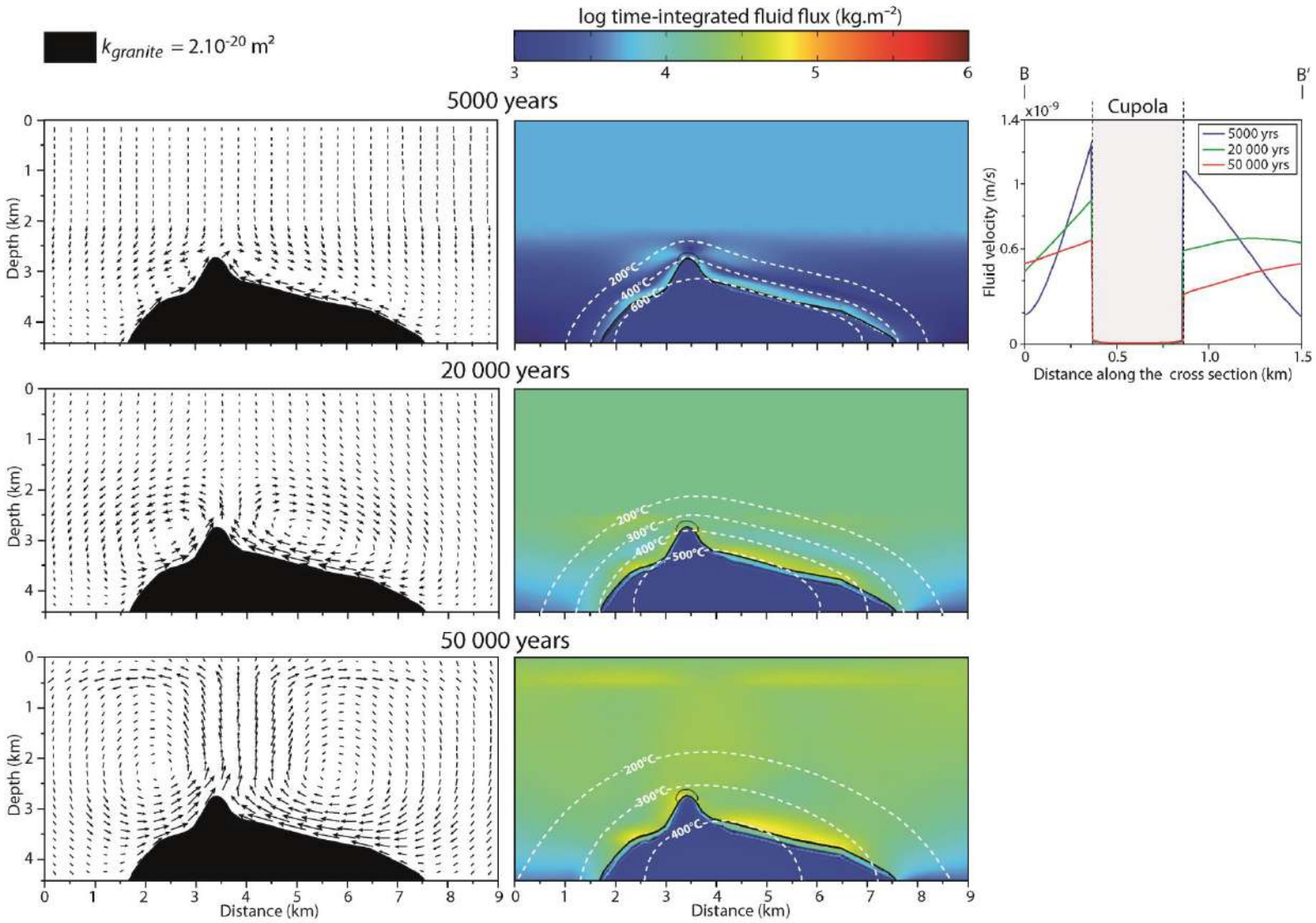

Figure 6 Results of time evolution of the fluid flow patterns and the time integrated fluid flux obtained for modeling with static granite permeability and without magmatic fluid production. After 50 kyrs a near steady state conditions are achieved

4.1.2 With magmatic fluid production (M2)

The heat conduction and convection induced by the emplacement of granite intrusion lead to the progressive cooling of the magma chamber that triggers the production of magmatic fluids within the crystallized part of the magma chamber. This fluid production occurs approximately during the first 10 kyr and leads to the establishment of fluid overpressure conditions in the upper part of the intrusive domain that reach lithostatic values (see white contours in Fig. 7, with λ_v = 1). The distribution of the pressure anomalies appears to be affected by the granite roof geometry. Indeed, the λ_v contours are characterized by the same shape than the granite roof geometry with highest fluid pressure conditions within the cupola. This affects strongly the fluid flow pattern, which is mainly marked by the expulsion of fluids from the upper part of the granitic intrusion toward the external part of the host rocks domain (Fig. 7). In this fluid flow pattern, the cupola appears to be a preferential zone of fluid expulsion. This expulsion of fluids in the host rock domain causes a moderate increase of the fluid pressure that enhances locally (i.e mainly around the cupola) and moderately the permeability of the host rock domain (log of permeability change not exceeding 1.3). This slight permeability change suggests a limited effect of magmatic fluid production on the permeability evolution of the host rock domain. Nevertheless, these zones of higher permeability are marked by fluid focusing and more elevated fluid velocities that locally reach 10^{-8} $m.s^{-1}$. Moreover, extend of the area of permeability change in the host rock domain increase progressively over the first 8000 kyr. After 10 kyr, the granite is entirely crystallized and the fluid production vanishes. However, lithostatic fluid pressure conditions remain within the intrusive body after 50 kyr (Fig. 7). This implies that the fluid produced during the granite crystallization is not efficiently extracted from the intrusive body due to the low permeability of the granite domain. This fluid pressure anomaly affects strongly the convective fluid flow processes that dominate fluid flow pattern at 50 kyr. Indeed, convective cells are marked by an important upward fluid flow above the cupola that is probably induced by the slow and continuous expulsion of fluids from the granite domain.

During the first 10 kyr, the highest values of time integrated fluid flux are mainly localized above the granite roof and the cupola due the expulsion of fluids produced during the granite crystallization. After 50 kyr of fluid flow, the time integrated fluid flux reach values of 10^{-5} $kg.m^{-2}$. These maximum values are mainly concentrated above the cupola that corresponds to zones of fluid focalization and highest fluid velocities in

response to permeability increase observed during the first 10 kyr. The presence of a ~200 m thick zone with relatively high time-integrated fluid flux (light blue zone at 50 kyr, $10^{3.75}$ $kg.m^{-2}$) in the upper part of the granite is consistent with the preferential release of magmatic fluid from the granite roof.

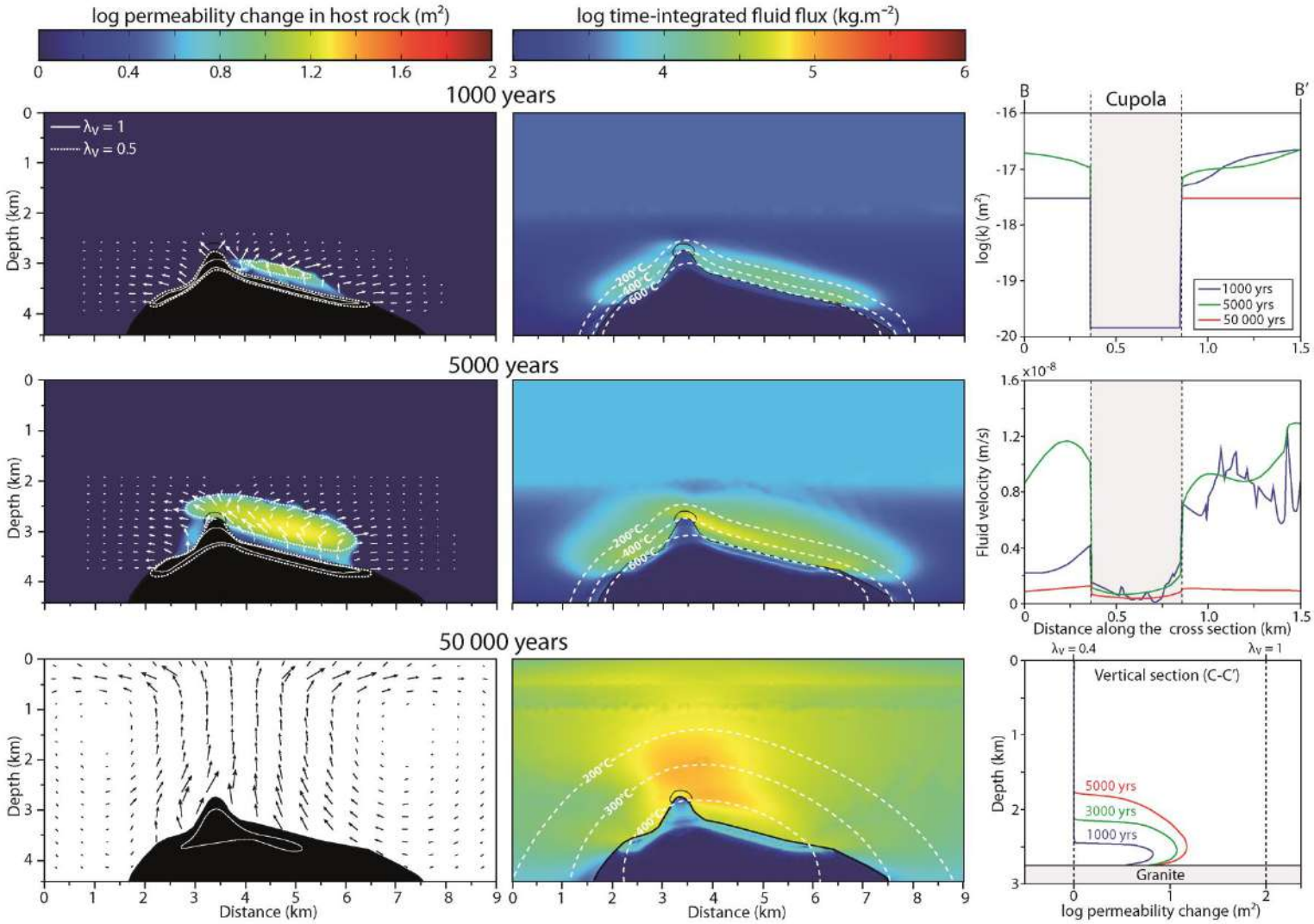

Figure 7 Results of time evolution of the fluid flow patterns and the time integrated fluid flux obtained for modeling with static granite permeability considering magmatic fluid production during the granite crystallization. Fluid flow is mainly controlled by expulsion processes during the first 10 kyrs and by convective circulation after 50 kyrs. (the localization of the vertical and the horizontal profiles are given in Figure 2).

4.2 Models considering dynamic permeability during the greisenization

Although the results described previously provide a useful reference framework for heat and fluid flow during the cooling stage of a granitic intrusion with a constant permeability, effect of the metasomatic alteration on the granite permeability cannot be ignored. Here, the two following models include a time-varying permeability, induced by greisenization processes. In other words, equation (12) and (13) are implemented in the computation of the granite permeability for the two t types of magmatic-hydrothermal systems presented previously.

4.2.1 Without magmatic fluid production (M3)

Left column of Figure 8 shows the same convective pattern as that observed in the case of constant granite permeability (Figure 6), with small convective cells centered near the cupola and expanding with time. The main difference consists in the progressive increase of the granite roof permeability. Indeed, as in the case of Figure 6, fluid velocity is highest along the granite roof but in this case, permeability is increased (see grey zones in the left column) in the zones where W/R ratio is high.

As a result, the greisenization front (red line in Figure 8) continuously deepens through the granite until fluid velocity is not high enough to permit further fluid-rock interactions. Continuous development of this high permeability zone (the greisen) focuses fluid flow, as illustrated by progressive increase of velocity (from 10^{-9} $m.s^{-1}$ at 5 kyr to 10^{-8} at 50 kyr) across the cupola. This also causes elevated values of time-intergrated fluid flux, up to $10^{5.5}$ $kg.m^{-2}$ in the greisen, but also above the cupola over a large area (around 10^{5} $kg.m^{-2}$).

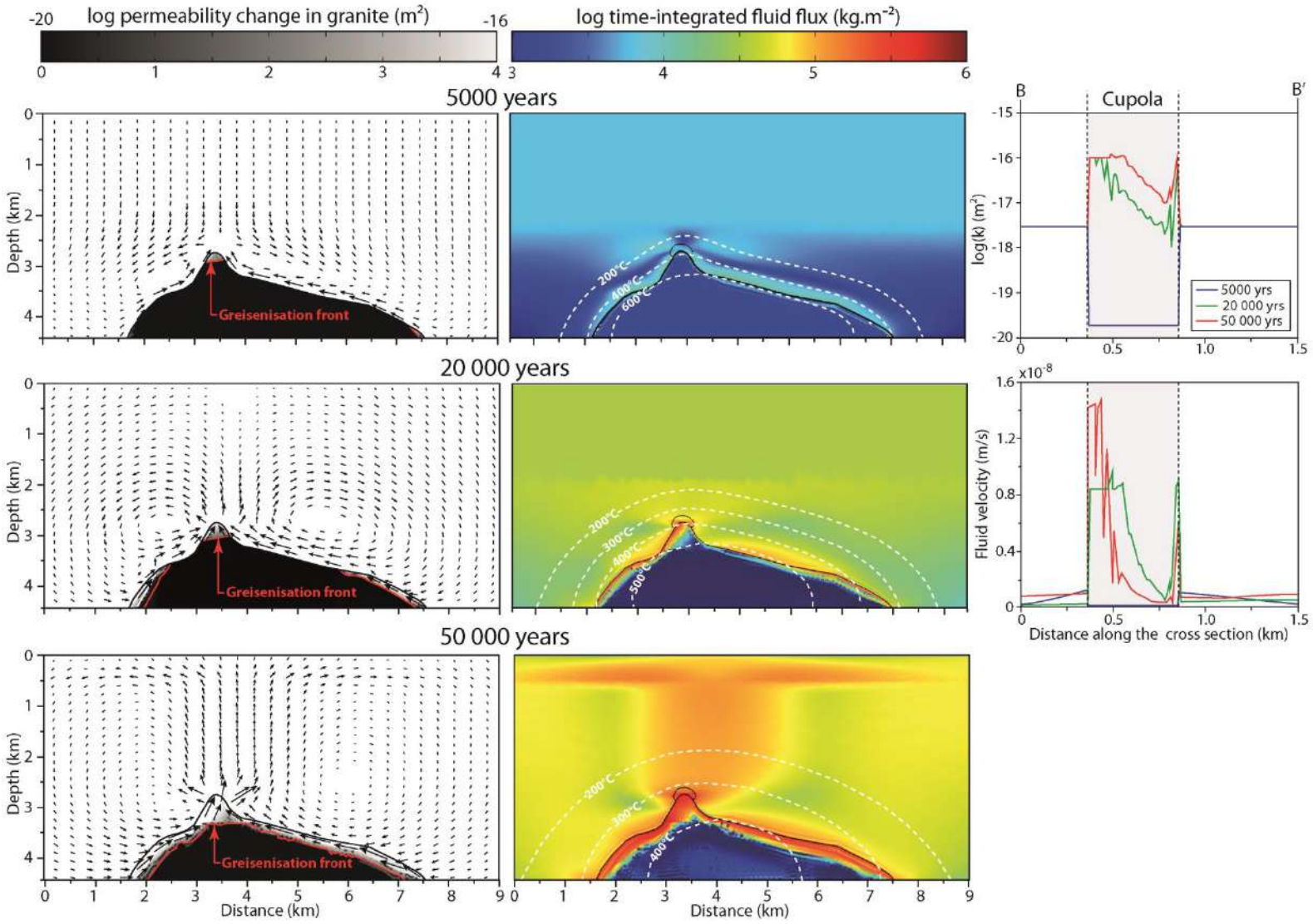

Figure 8 Results of time evolution of the fluid flow patterns and the time integrated fluid flux obtained for modeling with static granite permeability considering dynamic permeability during the greisenization process and without fluid production. Fluid flow is mainly controlled by convective processes.

4.2.2 With magmatic fluid production (M4)

This last model (M4, Figure 9) corresponds to the most elaborated one and includes both magmatic fluid production, permeability changes in the host rock domain due to potential fluid overpressure conditions, and permeability changes within the granite related to greisenization processes.

The fluid flow pattern is firstly controlled by expulsion processes induced by magmatic fluid production during the first 10 kyr (time step not shown in Figure 9). Then, due to complete granite crystallization, fluid production vanishes and convective process takes over expulsion mechanism. As shown in the last time step, shallow convective cells are developed in the permeable upper part of the host rock domain.

Due to fluid production within the granite, the W/R ratio quickly increases in the upper part of the granite, leading to the formation of a permeable pathway along the granite roof (the greisen, shown in white in left column). As in the previous case, the greisenization front deepens with time. It is noteworthy that the greisen thickness is slightly larger than in the previous case (M3).

In response to fluid expulsion, a fluid overpressured zone progressively develops above the granite roof, leading to a large zone of permeability increase that can reach two orders of magnitude. This zone quickly expands in the first 5 kyr, as shown by vertical C-C' profile of permeability changes (right column). When the granite is completely crystallized (after ~ 10 kyr) fluid production ceases and consequently, the fluid pressure anomaly disappears.

The development of permeable zones in both the granite and the host rock is accompanied by high fluid velocity, reaching 10^{-7} $m.s^{-1}$ within and around the cupola (see right column). The isotherms, illustrated in the middle column (dashed white lines), are parallel to the pluton roof geometry in the first stages. In the last stage (50 kyr), the 200 to 400°C isotherms are stretched up by the hot fluids rising quickly above the cupola.

As far as time-integrated fluid flux are concerned, similar description as in the M2 model can be made, but absolute values are one order of magnitude higher. A worthy difference, however, deals with the high value of the time-integrated fluid flux (up to 10^{6} $kg.m^{-2}$) within the upper part of the granite (greisen).

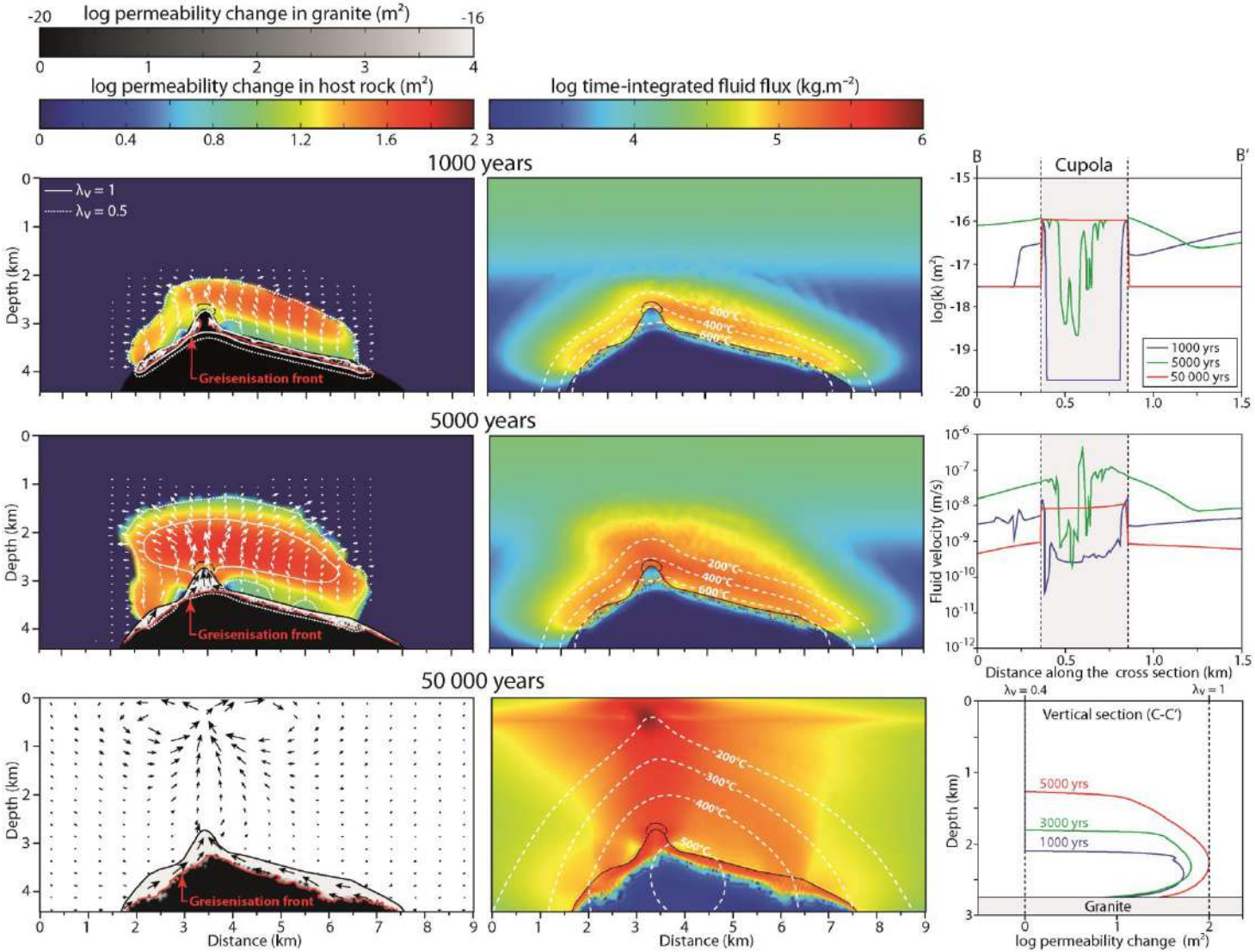

Figure 9 Results of time evolution of the fluid flow patterns and the time integrated fluid flux obtained for modeling considering both dynamic permeability and magmatic fluid production during the granite crystallization. Fluid flow is mainly controlled by expulsion processes during the first 10 kyrs and by convective circulation after 50 kyrs.

5. Discussion

This study deals with 2D numerical models investigating the influences of dynamic permeability related to greisenization processes, magmatic fluid production, and permeability changes in the host rock due to elevated fluid pressure conditions. Although some recent studies already explored the physical interactions between geological processes and permeability changes (Weis et *al*., 2012; Mezri et *al*., 2015; Weis 2015; Scott and Driesner, 2018), our approach is also based on laboratory measurements of the evolution of porosity and permeability during greisenization. In the following, we compare numerical results from the four models M1 to M4 to discuss the effects of permability changes on (i) expulsion of magmatic fluids, (ii) intensity of fluid fluxes and (iii) formation of massive greisens.

5.1 Effect of the cupola

In all cases (M1 to M4), the cupola strongly affects the fluid flow pattern by focusing both the convective upwelling and the expulsion of magmatic fluid. This can be explained by strong physical contrasts (permeability and temperature) between the cupola and its host rock. This result has already been described by Eldursi et *al*. (2009; 2018). This fluid focusing by the cupola (from the cupola towards the host rock) has been independently deduced from growth band study of tourmalines, which mark the incipient stage of the hydrothermal activity at Panasqueira (Launay et *al*., 2018).

Besides focusing fluid expulsion, plutonic apexes also localize thermo-mechanical instabilities (formation of fault and shear zones) (Guillou-Frottier and Burov, 2003; Gloaguen et *al*., 2014). The combination of these processes can favor the formation of hydrothermal systems, thus explaining the observed spatial relationship between cupolas and mineralized systems (e.g. Dilles and Profett, 1995).

5.2 Interactions between dynamic permeability and extraction of magmatic fluids

The comparison between models M2 and M4 emphasizes that the permeability change induced by greisenization processes enhance and facilitate the expulsion of the magmatic fluids produced during granite crystallization. Figure 10 displays time evolution of the pore fluid factor and the fluid flow velocity above and within the cupola. It shows that fluid overpressure conditions remain elevated in the granite (red curves) – even after the end of fluid production – in the model M2 (left column), while they drop quickly when the

permeability change in granite is considered (M4). Moreover, fluid overpressure conditions above the granite (blue curves) are significantly more elevated in the model M4 than in the model M2. This emphasize that the fluid produced during the granite crystallization is more efficiently expelled from the granite when high permeability zone is present at the top of the intrusive body. The highest fluid velocities both in cupola and above the granite in the model M4 are consistent with a more efficient fluid expulsion when the effects of greisenization on permeability are considered. This efficient expulsion of the magmatic fluids promotes the development of a thicker band of high permeability, as observed in Figure 9 at time 5 kyr. This zone of elevated permeability could correspond to the damage zone described by Foxford et *al*., (2000) and illustrated in Figure 1d. Consequently, the greisenization processes can be an important mechanism to form the vein swarm by favoring the establishment of fluid overpressure conditions above the granite roof. Even if the vertical scales of permeable zones observed in the model M4 (2-3 km) and that observed at Panasqueira (200-400 m) differ, the interplay processes between greisenization, expulsion of fluid and formation of overpressured permeable zone can constitute a potential physical mechanism to explain the concomitant formation of mineralized veins and greisen, as recently proposed by Korges et *al*. (2018).

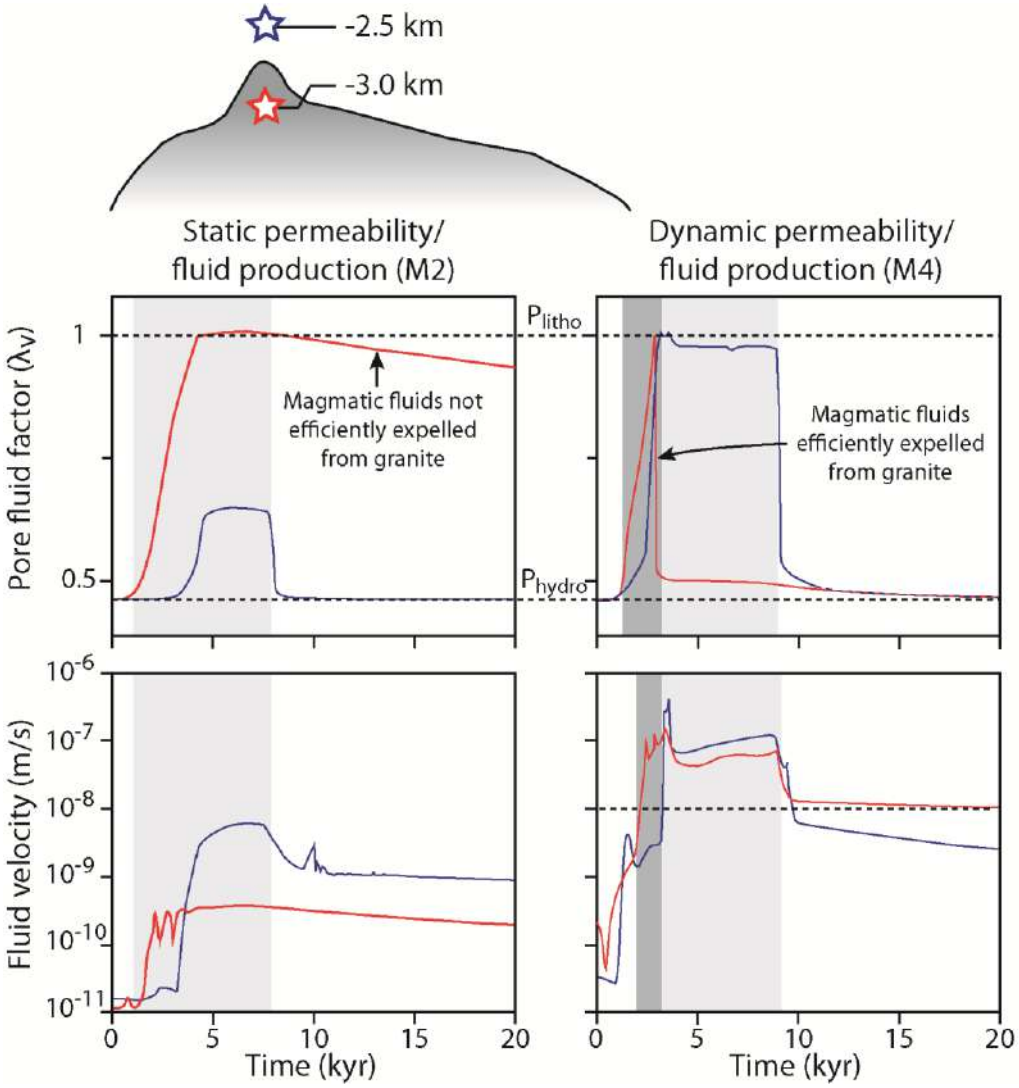

Figure 10 Time evolution of pore fluid factor and fluid flow velocity above and within the cupola (emplacements indicated by the blue and the red stars) in cases of magmatic fluid production without (left) and with (right) dynamic permeability in granite. Light grey areas correspond to the timespan of fluid production and dark grey areas highlight the sharp increase of fluid velocity and overpressure in the M4 model.

5.3 Influence of dynamic permeability on fluid flow and mass transfer

Figure 11 shows the time evolution of fluid fluxes for the four models, computed in a small area above the cupola (red area). Models M1 and M3 (without fluid production) are shown in grey. As expected, the model with dynamic permeability (M3) is marked by a higher fluid flux, with a maximum value of ~10^{-2} kg.s^{-1} reached at 50 kyr. Maximum fluid fluxes are achieved for M2 and M4 (black curves, with fluid production) at the end of the fluid production stage (~10 kyr). After this stage, a regular decrease of the fluid flux illustrates the progressive cooling of the magmatic-hydrothermal system. The account of (i) a dynamic permeability both in the granite and in the host rocks and (ii) a magmatic fluid source, leads to the highest fluid flux (3.10^{-1} kg.s^{-1}, equivalent to ~ 10 Mt.kyr^{-1})

(model M4, dashed black line in Figure 11a). Due to the development of high permeability zones in the upper part of granitic intrusion, the values of time integrated fluid flux in models (M3 and M4) considering the dynamic permeability (Figure 8 and 9) are higher by approximately one order of magnitude than values obtained in their equivalent models considering static granite permeability (Figure 6 and 7). It appears that model M4 is the most favorable for transferring a large amount of fluid. As recently confirmed by Cernuschi et *al*. (2018), a large amount of focused mineralizing fluids is required to form large magmatic-hydrothermal ore deposits. Furthermore, the highest values of time integrated fluid flux obtained in the model M4 (with dynamic permeability and fluid production) are similar to those described in numerical studies involving high values of static permeability (10^{-16} to $10^{-14.5}$ m²) in magmatic-hydrothermal systems where fluid fluxes reaching (10^{6} to10^{7} kg/m²) (Gerdes, 1998; Cui et *al*., 2001). Our results suggest that dynamic permeability and greisenization processes could be important to promote and enhance the transport of a large amount of fluid and hence to form large deposits.

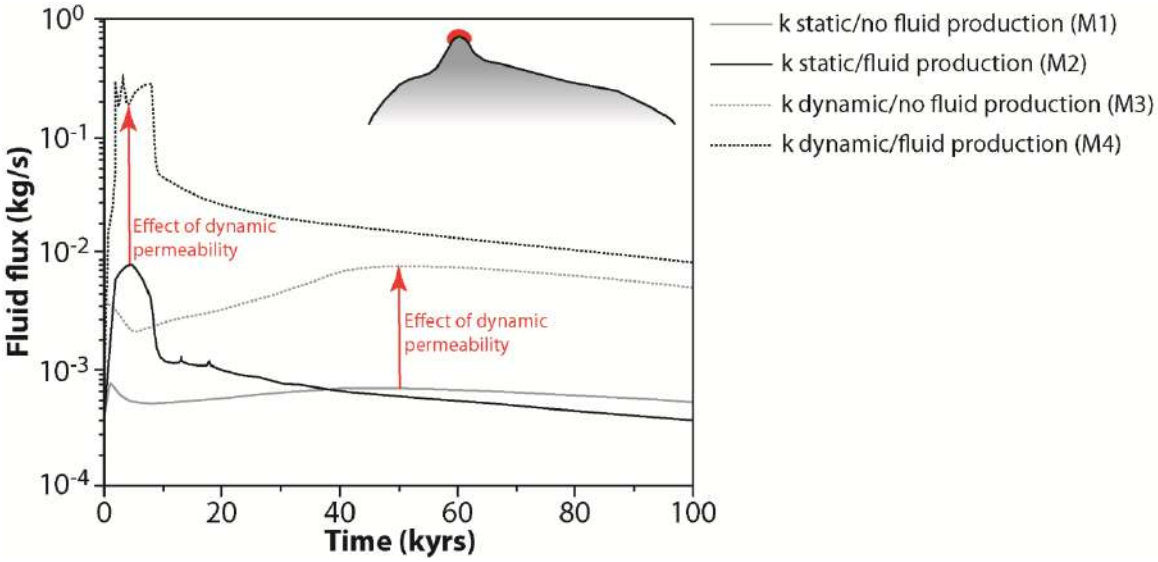

Figure 11 Effects of the dynamic permeability and the magmatic fluid production on the time evolution of fluid flux above the cupola (red area).

.

5.4 Implications for the formation of massive greisen

The interplays between greisenization and permeability have also a strong effect on the propagation of the greisenization front toward the deeper part of the intrusive body. Figure 12 shows that models M3 and M4 considering dynamic permeability during greisenization processes are characterized by a thicker greisen after 50 kyr of fluid flow than models (M1 and M2) with static granite permeability. Accordingly, the dynamic permeability seems to promote significantly the formation of massive greisen with thickness of about 140 m for the model M3 and 200 m for the model M4 (Fig. 12). Conversely, a static low permeability in granite allows only developing a fine greisen with thickness of about 20 m in the model M1 and 50 m in the model M2 (Fig. 12). Furthermore, model (M4) coupling dynamic permeability and magmatic fluid production appears to be the most favorable for the development of massive greisen by vigorous fluid flow and self-propagating of pervasive alteration (greisenization). The positive feedbacks between greisenization and permeability and the magmatic fluid production could be important processes to form large massive greisen deposits (disseminated mineralization) like Cinovec and East Kemptville, in which massive greisen can reach 200 to 300 m (Halter, 1996; Jarchovsky, 2006, Laznicka, 2010).

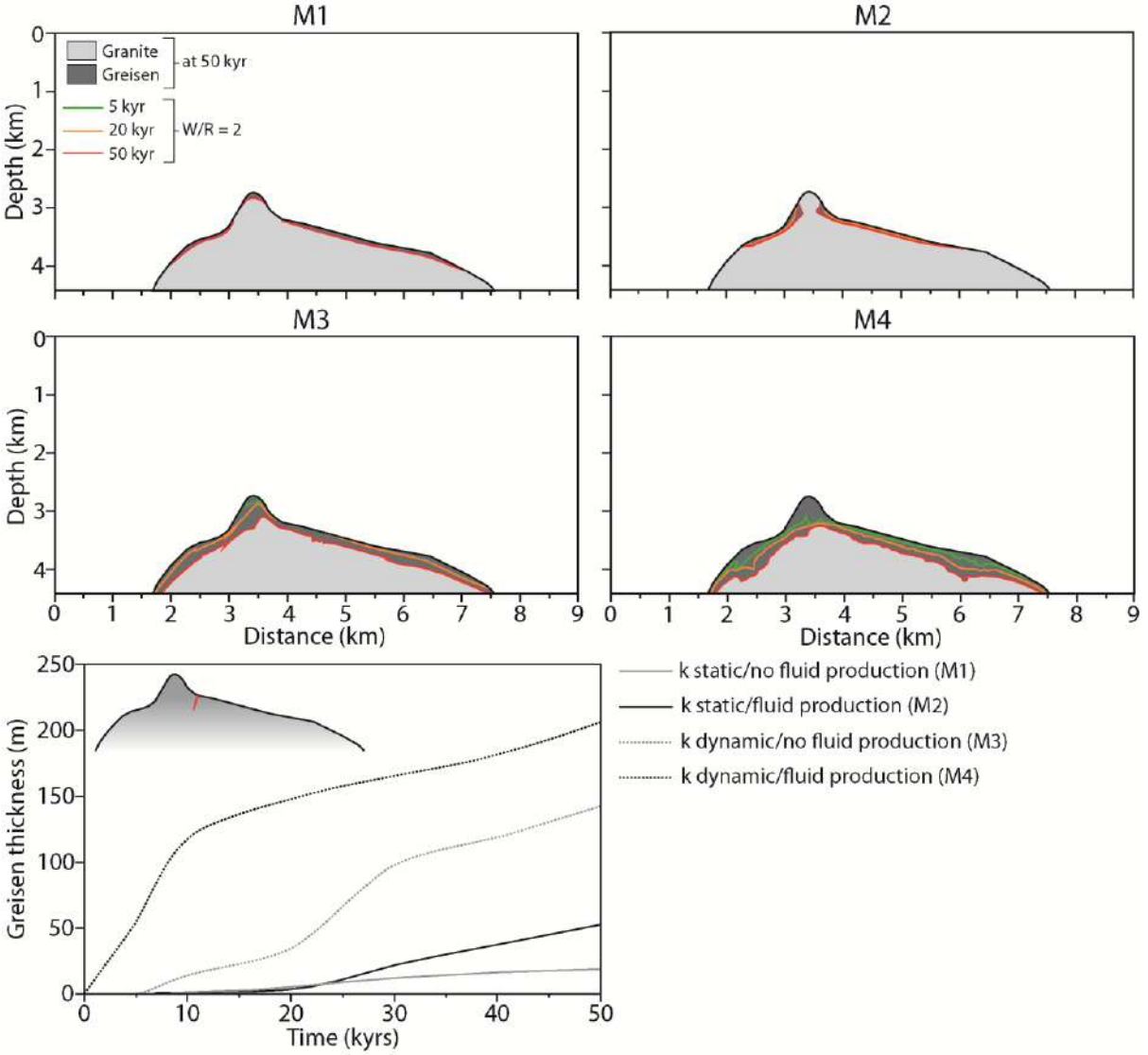

Figure 12 Time evolution of the greisen thickness resulting from fluid-rock interactions during fluid flow (for M1 to M4). We assume that W/R ratio of 2 marks the total breakdown of feldspars present in the granite and corresponds to the complete greisenization of granite (see explanation in section 3.6.3). The red line indicates the emplacement of profile along which, the time evolution of the greisen thickness has been determined.

5.5 Limitations and further perspectives

Although results obtained in this study permit to discuss the potential role of interplays between dynamic permeability and greisenization processes during the formation of vein and greisen deposits, we computed fluid flow on 2D sections with simplified geometries. Instead, 3D models would need to be considered in future works. Indeed, fluid flow patterns and fluxes described in this study should probably be different in 3D, but the interplays (physical processes) between dynamic permeability and greisenization processes and their consequences should not be affected by the geometry.

Furthermore, our models are based on the assumption of a single fluid phase (pure water). Recent studies (Weis et *al*. 2012; Gruen et *al*., 2014; Weis, 2015) have demonstrated that the salinity of fluid affects significantly (i) fluid flow patterns (ii) fluid velocities and especially (iii) fluid pressure conditions. In our models, the effects of greisenization and the opening of permeable zones above the granite should probably be enhanced in the case of a multiphasic fluid. Indeed, the potential increase in fluid volume induced by the separation of a vapor phase can increase drastically fluid pressure conditions favoring the opening of permeable zones (Weis, 2015). The stress state is another parameter not considered in this study and that could also enhance and promote the opening of permeable zones (Zhang et al., 1994; Cox, 2010; Weis, 2015).

Besides, metamorphic reactions related to the thermal metamorphism induced by the granite emplacement can lead to the production of metamorphic fluids (dehydration reactions) that could constitute an additional source of fluids during the incipient stage of the magmatic-hydrothermal systems (Connolly and Thompson, 1989; Hanson, 1992; Cui et *al*., 2001). This additional source of fluids can promote fluid overpressure conditions and enhance the opening of permeable zones above the granite intrusion. Further tests need to be performed to constrain the influence of the thermal metamorphism on fluid flow dynamics. A recent study (Scott and Driesner, 2018) has demonstrated that quartz precipitation and dissolution can lead to significant permeability changes. In our study we have not consider the potential precipitation of quartz in the neoformed porosity of greisen that could partially seal pathways and inhibit the feedback between permeability and greisenization processes.

Additionally, we simplified the magmatic-hydrothermal system by a single stage of pluton emplacement and its subsequent cooling. The concept of incremental emplacement of granitic bodies (Dilles 1987; Sillitoe, 2010; Blundy and Annen, 2016) is thus not

considered but our results show that geological processes investigated in this study occur in a very short time-span. Consequently, our hypothesis can be considered as representative of one pulse of a long time magmatic-hydrothermal history.

Despite these numerous limitations and future perspectives, the present study provides a first contribution describing the effects of interplays between hydrothermal alteration, dynamic permeability, expulsion of fluid and formation of overpressured permeable zones in magmatic-hydrothermal systems. These complex interactions can constitute important mechanisms to enhance and promote mass transfer to form large vein and greisen ore mineralized systems. Finally, this contribution demonstrates that feedbacks between fluid-rock reactions, porosity and permeability changes affect significantly fluid flow and need to be considered in future numerical modelling studies to provide more accurate predictive models.

References

B-C

Blundy, J. D., & Annen, C. J. (2016). Crustal magmatic systems from the perspective of heat transfer. Elements, 12(2), 115-120.

Booden, M.A., Mauk, J.L., Simpson, M.P. 2011. Quantifying Metasomatism in Epithermal Au-Ag Deposits: A Case Study from the Waitekauri Area, New Zealand. Economic Geology ; 106 (6): 999–1030.

Bussink, R.W. 1984. Geochemistry of the Panasqueira Tungsten-Tin Deposit, Portugal. Geol. Ultraiectina.

Caricchi, L.&Blundy, J. D. (eds) 2015.Chemical, Physical and Temporal Evolution of Magmatic Systems. Geological Society, London, Special Publications, 422.

Castro, A., G.L. Corretgé, J. De La Rosa, P. Enrique, F.J. Martínez, E. Pascual, M. Lago, et al. 2002 « Palaeozoic Magmatism ». In The Geology of Spain, édité par W. Gibbons et M.T. Moreno, 117-53. London: Geological Society.

Cathles, L.M., Erendi, A.H.J. & Barrie, T. 1997. How long can a hydrothermal system be sustained by a single intrusive event? Econ. Geol., 92: 766-771.

Černý, P., Blevin, P.L., Cuney, M. and London, D. 2005. Granite-Related Ore Deposits. In: J.W. Hedenquist, J.F.H. Thompson, R.J. Goldfarb, and J.R. Richards (eds.). Economic Geology - One Hundredth Anniversary Volume, 337–370.

Cernuschi, F., Dilles, J. H., Grocke, S.B., Valley, J.W., Kitajima, K., Tepley, F.J. 2018. Rapid formation of porphyry copper deposits evidenced by diffusion of oxygen and titanium in quartz. *Geology* ; 46 (7): 611–614.

Clark, A. H. 1964. Preliminary study of the temperatures and confining pressures of granite emplacement and mineralization, Panasqueira, Portugal: Inst. Mining MetallurgyTrans., 73, 813-824.

Clauser, C., 2006. Geothermal energy. In: Heinloth, K. (Ed.), Landolt-Börnstein, Group VIII: Advanced Material and Technologies. Energy Technologies, Subvol C: Renewable Energies, Vol. 3. Springer Verlag, Heidelberg-Berlin, pp. 493–604.

Coelho, G., Branquet, Y., Sizaret, S., Arbaret, L., Champallier, R., Rozenbaum, O. 2015. Permeability of sheeted dykes beneath oceanic ridges: Strain experiments coupled with 3D numerical modeling of the Troodos Ophiolite, Cyprus. Tectonophysics, Elsevier, 2015, 644-645, pp.138-150.

Connolly, J.A.D. and Thompson, A.B., 1989. Fluid and enthalpy production during regional metamorphism. Contrib. Mineral. Petrol., 102: 347-366.

Cox, S.F., 2010. The application of failure mode diagrams for exploring the roles of fluid pressure and stress states in controlling styles of fracture-controlled permeability enhancement in faults and shear zones Geofluids 10, 217–233.

Cox, S.F., 2005 Coupling between deformation, fluid pressures and fluid flow in ore-producing hydrothermal environments. Economic Geology, 100th Anniversary Volume, 39–75

Cui, X., Nabelek, P.I., Liu, M., 2001. Controls of layered and transient permeability on fluid flow and thermal structure in contact metamorphic aureoles, with application to the Notch Peak aureole Utah. J. Geophys. Res. 106, 6477–6491.

D

Dias, G., Leterrier, J., Mendes, A., Simões, P., Bertrand, J.M. 1998. U-Pb zircon and monazite geochronology of syn- to post-tectonic Hercynian granitoids from the central Iberian Zone (northern Portugal). Lithos 45, 349–369.

Dilles JH (1987) The petrology of the Yerington Batholith, Nevada: evidence for the evolution of porphyry copper ore fluids. Economic Geology, 82, 1750–89.

Dilles, J.H., Profett, J.M. 1995. Metallogenesis of the Yerington batholith, Nevada, in: F.W. Pierce, J.G. Bolm (Eds.), Porphyry Copper Deposits of the American Cordillera, American Geological Society Digest 20, , pp. 306-315.

Dolejs, D., 2015. Quantitative characterization of hydrothermal systems and reconstruction of fluid fluxes: the significance of advection, disequilibrium, and dispersion. SGA proceedings 13th SGA Biennial Meeting.

E-F

Eldursi, K., Branquet, Y., Guillou-Frottier, L., Marcoux, E. 2009. Numerical investigation of transient hydrothermal processes around intrusions: Heat-transfer and fluid-circulation controlled mineralization patterns. Earth and Planetary Science Letters 288, 70-83.

Eldursi, K., Branquet, Y., Guillou-Frottier, L., Martelet, G., Calcagno, P. 2018 Intrusion-Related Gold Deposits: new insights from gravity and hydrothermal integrated 3D modeling applied to the Tighza gold mineralization (Central Morocco) Journal of African Earth Sciences.

Foxford, K.A., Nicholson, R., Polya, D.A., Hebblethwaite, R.P.B. 2000. Extensional failure and hydraulic valving at Minas da Panasqueira, Portugal: Evidence from vein spatial distributions, displacements and geometries. J. Struct. Geol. 22, 1065–1086.

G

Garibaldi, C. Guillou-Frottier, L., Lardeaux, J.M. et al., 2010. Thermal anomalies and geological structures in the Provence basin: Implications for hydrothermal circulations at depth. Bulletin de la Societe Geologique de France ,vol.181,no.4,pp.363–376.

Gerdes, M.L., Baumgartner, L.P., Person, M., 1998. Convective fluid flow through heterogeneous country rocks during contact metamorphism. J. Geophys. Res. 103, 23,983–24,003.

Gloaguen E., Branquet Y., Chauvet A., Bouchot V., Barbanson L., Vigneresse J.L. 2014. Tracing the magmatic/hydrothermal transition in regional low-strain zones: The role of magma dynamics in strain localization at pluton roof, implications for intrusion-related gold deposits. Journal of Structural Geology 58: 108-21.

Guillou-Frottier, L., Burov, E. 2003. The development and fracturing of plutonic apexes: implications for porphyry ore deposits. Earth & Planetary Science Letters, 214, 341-356.

Gruen, G., Weis, P., Driesner, T., Heinrich, C.A., De Ronde, C.E.J. 2014.Hydrodynamic modeling of magmatic–hydrothermal activity at submarine arc volcanoes, with implications for ore formation. Earth and Planetary Science Letters 404 (2014) 307–318.

H

Halter, W.E., Williams-Jones, A.E., Kontak, D.J. 1998. Origin and evolution of the greisenizing fluid at the East Kemptville tin deposit, Nova Scotia, Canada. Economic Geology, 93 (7): 1026–1051.

Hanson RB (1995) The hydrodynamics of contact-metamorphism.Geological Society of America Bulletin, 107, 595–611.

Hebblethwaite, R. P. B., and Antao, A.M. 1982. A report on the study of dilation patterns within the Panasqueira ore body: Barroca Grande, Beralt Tin Wolfram (Portugal), unpub. rept.15p.

Hedenquist, J.W., Lowenstern, J.B. 1994. The role of magma in the formation of hydrothermal ore deposits. Nature Vol. 370: 519-526.

Howald T, Person M, Campbell A, Lueth V, Hofstra A, Sweetkind D,Gable CW, Banerjee A, Luijendijk E, Crossey L, Karlstrom K,Kelley S, Phillips FM (2016) Evidence for long-timescale (>103 years) changes in hydrothermal activity induced by seismic events. In: Crustal permeability. Wiley, Chichester, UK, pp 260–274.

I-J

Ingebritsen SE, Manning CE (2010) Permeability of the continental crust: dynamic variations inferred from seismicity and metamorphism. Geofluids, 10, 193–205.

Ingebritsen, S.E., Appold, M.S. 2012. The physical hydrogeology for ore deposits. Econ Geol 107:559–584

Ingebritsen, S. E., Gleeson, T., 2015 Crustal permeability: Introduction to the special issue. Geofluids, Volume15, Issue1-2

Jamtveit, B., Malthe-Sørenssen, A., Kostenko, O. 2008. Reaction enhanced permeability during retrogressive metamorphism. Earth and Planetary Science Letters. Volume 267, Issues 3–4, 620-627.

Jarchovsky, T. 2006. The nature and genesis of greisen stocks at Krásno, Slavkovský les area western Bohemia, Czech Republic. Journal of the Czech Geological Society 51/3-4.

Jonas, L., John, T., King, H.E., Geisler, T., Putnis,A. 2014. The role of grain boundaries and transient porosity in rocks as fluid pathways for reaction front propagation. Earth and Planetary Science Letters, Volume 386, 64-74.

Julivert, M., Fontboté, J.M., Ribeiro, A., Conde, L. 1972. Mapa Tectonico de la Peninsula Iberica y Baleares E. 1:1.000.000. Inst. Geol. Min. España, Madrid.

K-L

Kelly, W.C., Rye, R.O. 1979. Geologic, fluid inclusion and stable isotope studies of the tin-tungsten deposits of Panasqueira, Portugal. Econ Geol 74:1721–1822.

Kestin, J., Khalifa, H.E., Abe, Y., Grimes, C.E., Sookiazan, H., Wakehan, W.A., 1978. Effect of the pressure on the viscosity of aqueous NaCl solutions in the temperature range 20–150 C. J. Chem. Eng. Data 23, 328–336.

Korges, M., Weis, P., Lüders, V., Laurent, O. 2018. Depressurization and boiling of a single magmatic fluid as a mechanism for tin-tungsten deposit formation. Geology, January 2018; v. 46; no. 1; p. 75–78.

Launay, G., Sizaret, S., Guillou-Frottier, L., Gloaguen, E., Pinto, F. 2018. Deciphering fluid flow at the magmatic-hydrothermal transition: A case study from the world-class Panasqueira W-Sn-(Cu) ore deposit (Portugal). Earth and Planetary Science Letters, Volume 499, p. 1-12.

Laznicka P. 2010. Giant metallic deposits. Future sources of industrial metals. Springer, Berlin, 949 стр., ISBN: 978-3-642-12404-4

M-N

Manning, C.E., Ingebritsen, S.E., 1999. Permeability of the continental crust: implications of geothermal data and metamorphic systems. Rev. Geophys. 37, 127–150.

Mezri, L., Le Pourhiet, L., Wolf, S., Burov, E. 2015. New parametric implementation of metamorphic reactions limited by water content, impact on exhumation along detachment faults. Lithos. 236. 10.1016/j.lithos.2015.08.021.

Mlynarczyk, M., Sherlock, R., Williams-Jones, A. 2002. San Rafael, Peru: Geology and structure of the worlds richest tin lode. Mineralium Deposita. 38. 555-567.

Norton, D., Cathles, L.M. 1979. Thermal aspects of ore deposition. In: Barnes, H.L. (Ed.), Geochemistry of Hydrothermal Ore Deposits, second ed. John Wiley and Sons, New York, pp. 611e631.

O-P

Oosterom, M. G., Bussink, R. W., Vriend, S.P. 1984. Lithogeochemical studies of aureoles around the panasqueira tin-tungsten deposit, Portugal. Mineralium Deposita, Volume 19, Issue 4, pp.283-288

Phillips, O.M., 1991. Flow and reactions in permeable rocks. Cambridge University Press, Cambridge. 285 pp.

Pirajno, F. 1992. Greisen systems. In: Hydrothermal Mineral Deposits. Springer, Berlin, Heidelberg, 280-324.

Pollard, P.J., Taylor, R.G., Cuff, C. 1988. Genetic Modelling of Greisen-Style Tin Systems. In: Hutchison C.S. (eds) Geology of Tin Deposits in Asia and the Pacific. Springer, Berlin, Heidelberg, pp 59-72.

Pollok, K., Putnis, C.V., Putnis, A. 2011. Mineral replacement reactions in solid solution-aqueous solution systems: Volume changes, reactions paths and end-points using the example of model salt systems. Am J Sci March 2011 311:211-236.

Polya, D.A. 1989. Chemistry of the main-stage ore-forming fluids of the Panasqueira W-Cu-(Ag)-Sn deposit, Portugal: implications for models of ore genesis. Econ. Geol. 84, 1134–1152.

Putnis, A. 2002. Mineral replacement reactions: from macroscopic observations to microscopic mechanisms. Mineralogical Magazine, 66 (5): 689–708.

Putnis, A., Austrheim, H. 2010. Fluid-induced processes: metasomatism and metamorphism. Geofluids, 10: 254-269.

Putnis, A. and John, T. 2010. Replacement processes in the earth's crust. Elements: an international magazine of mineralogy, geochemistry, and petrology. 6 (3): pp. 159-164.

Putnis, A. 2015. Transient Porosity Resulting from Fluid–Mineral Interaction and its Consequences. Reviews in Mineralogy and Geochemistry, 80 (1): 1–23.

R-S

Rabinowicz, M., Boulègue, J., Genthon, P., 1998. Two and three-dimensional modelling of hydrothermal convection in the sedimented Middle Valley segment, Juan de Fuca Ridge. J. Geophys. Res. 103, 24045–24065.

Reed, M.H., Rusk, B.G., and Palandri, J., 2013, The Butte magmatic-hydrothermal system: One fluid yields all alteration and veins: Economic Geology, v. 108, p. 1379–1396.

Schardt, C and Large, RR 2009 , 'New insights into the genesis of volcanic-hosted massive sulfide deposits on the seafloor from numerical modeling studies' , *Ore Geology Reviews*, vol. 35, no. 3-4 , pp. 333-351

Scott, S.W. and Driesner, T. 2018. Permeability Changes Resulting from Quartz Precipitation and Dissolution around Upper Crustal Intrusions. Geofluids, Volume 2018, Article ID 6957306, 19 pages.

Sibson RH (1987) Earthquake rupturing as a mineralizing agent in hydrothermal systems. Geology, 15, 701–4.

Sibson RH, Robert F, Poulsen KH (1988) High-angle reverse faults, fluid-pressure cycling, and mesothermal gold-quartz deposits. Geology, 16, 551–5.

Sillitoe RH (2010) Porphyry Copper Systems. Economic Geology, 105, 3–41.

Stemprok, M. 1987. Greisenization (a review). Geol Rundsch , Springer-Verlag 76:169.

T

Taillefer, A., Soliva, R., Guillou-Frottier, L., Le Goff, E., Martin, G., Seranne, M. 2017. Fault-Related Controls on Upward Hydrothermal Flow: An Integrated Geological Study of the Têt Fault System, Eastern Pyrénées (France). Geofluids, Volume 2017, Article ID 8190109, 19 pages

Taylor, R.G. 1979. Geology of tin deposits. Developments in economic geology, Volume 11, Elsevier, 543p.

Taylor, R.G., Pollard, P.J. 1988. Pervasive hydrothermal alteration in tin-bearing granite and implications for the evolution of ore-bearing magmatic fluids. Canadian Institute of Mining and Metallurgy Special Volume 39, p. 86.95.

Tenthorey, E., Gerald, J.D., 2006. Feedbacks between deformation, hydrothermal reaction and permeability evolution in the crust: Experimental insights. Earth Planet. Sci. Lett. 247, 117-129.

Thadeu, D. 1951. Geologia do couto mineiro da Panasqueira. Comunic Serv Geol Port 32:5–64.

W-Z

Wagner,W.,Cooper,J.R.,Dittmann,A.,Kijima,J.,Kretzschmar,H.J.,Kruse,A.,Mares; R., Oguchi,K.,Sato,H.,Stocker,I.,Sifner,O.,Takaishi,Y.,Tanishita,I.,Trubenbach,J.,Willkommen,T.,2000.The IAPWS industrial formulation 1997forth thermodynamic properties of water and steam.Journal of Engineering for Gas Turbines and Power—Transactions of the ASME(American Society of Mechanical Engineers)122,150–182.

Weis P, Driesner T, Heinrich C.A., 2012. Porphyry-copper ore shells form at stable pressure-temperature fronts within dynamic fluid plumes. Science, 338, 1613–6.

Weis, P. 2015. The dynamic interplay between saline fluid flow and rock permeability in magmatic hydrothermal systems. Volume15, Issue1-2

Werner A.B.T., Sinclair W.D., Amey E.B. 2014. International strategic mineral issues summary report—Tungsten (ver. 1.1, November 2014). U.S. Geological Survey Circular 930–O, 74 p.

Wheeler, A. 2015. Technical report on the mineral resources and reserves of the Panasqueira mine, Portugal. Report NI 43-101, Prepared for Almonty Industries.

Zhang, S., Cox, S.F., Paterson, M.S., 1994a. The influence of room temperature deformation on porosity and permeability in calcite aggregates. J. Geophys. Res. 99, 15761-1

Chapter VII: Synthesis, conclusions and scientific outlook

Objectives of this chapter:

The vein, stockwork and greisen Sn-W deposits are magmatic-hydrothermal systems that provide an important part of the world W production and represent an important source of Sn. The purpose of this study was focused on improving understanding of hydrothermal and geological processes involved during the transport and the deposition of metals leading to the formation of this type of deposits. To do this, we have performed a complete study combining (i) field works (structural and geological constrains), (ii) fluid flow reconstruction at the magmatic-hydrothermal transition (based on textural analysis of tourmaline growth bands), (iii) whole-rock and mineral petrology and geochemistry, (iv) experimental determination of permeability change during greisenization and (v) numerical modeling of perigranitic fluid flow accounting for magmatic fluid production and dynamic permeability related to fluid-rock interactions. This methodology was applied in the case of the world-class W-Sn-(Cu) Panasqueira deposit, which exposes a well-preserved magmatic-hydrothermal plumbing system and therefore represents a reference site to study magmatic-hydrothermal processes leading to the formation of large vein and greisen Sn-W deposit.

In this summarizing chapter, we integrate the main results and conclusions discussed in the previous chapters to propose a complete metallogenic model considering hydrodynamic and geological processes involved during the formation of the W-Sn-(Cu) Panasqueira ore deposit. From this metallogenic model we propose outlook for mining exploration and for general understanding of other worldwide hydrothermal Sn-W deposits related to granite intrusions. Furthermore, importance of feedbacks between permeability and hydrothermal alteration is discussed in case of greisen systems and also for others mineralized hydrothermal systems of economic importance, for which hydrothermal alterations can potentially, enhance permeability and fluid flow. Finally, we propose further potential research topics focused on importance of fluid-rock interactions.

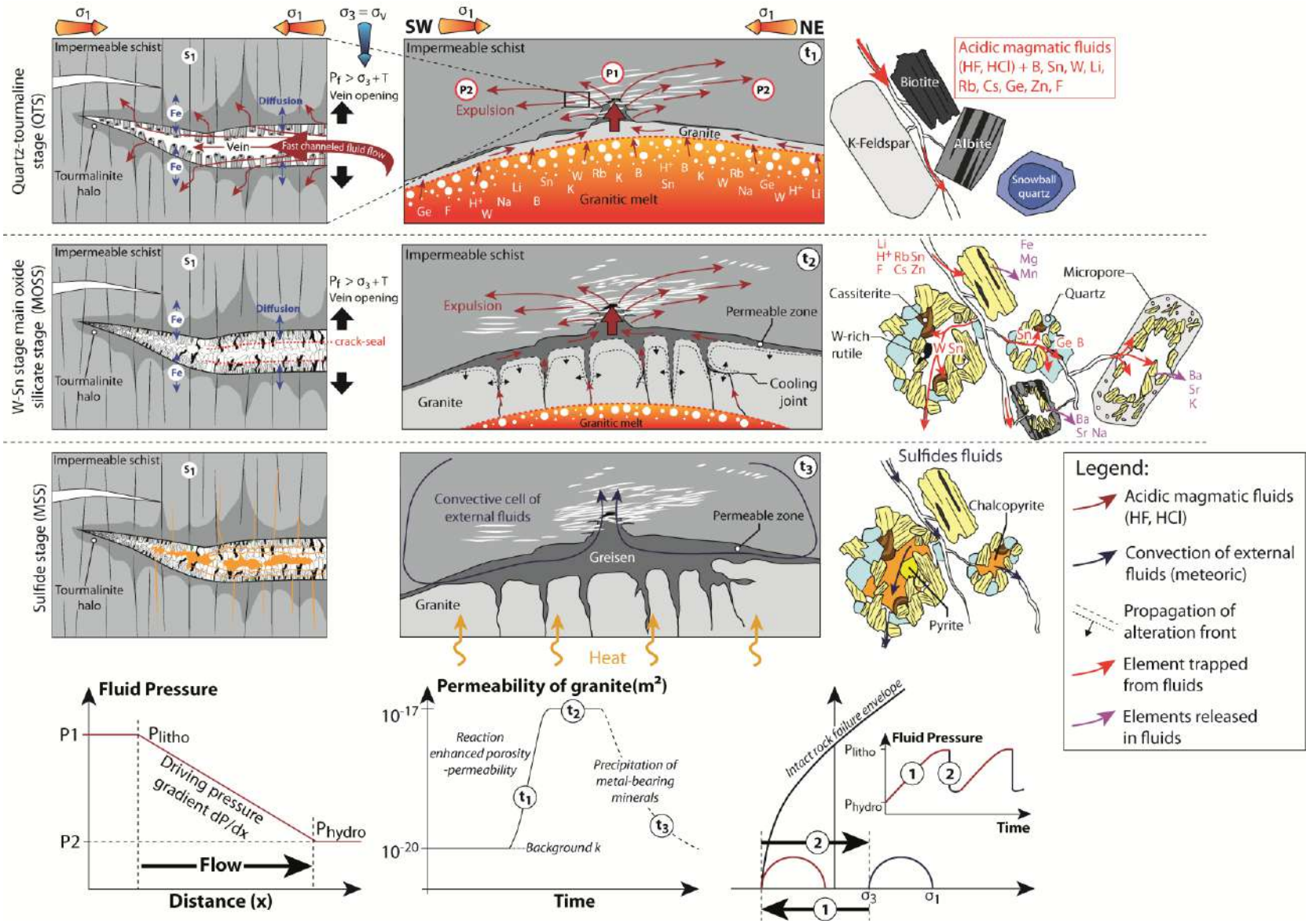

Figure 1 Synthetic metallogenic model of formation of the W-Sn-(Cu) Panasqueira ore deposit integrating hydrodynamic and geological processes highlighted from results obtained in this study. Fluid flow between (t_1) and (t_2) is controlled by expulsion of magmatic ore-bearing fluids released and expelled during the magmatic-hydrothermal transition. Fluid flow related to the later stages (t_3) involved convective processes during which sulfide mineralization was deposed. More details are given in the main text.

I- Model of formation of the W-Sn-(Cu) Panasqueira ore deposit

Figure 1 displays the metallogenic model of formation of the W-Sn-(Cu) Panasqueira ore deposit. This model integrates the main geological and hydrodynamic processes highlighted from results obtained in this study and that were involved during the magmatic hydrothermal activity of Panasqueira.

1. Formation of the mineralized veins swarm of Panasqueira: structural control and role of fluid pressure conditions

As evidenced from the structural analysis performed in this study, the sub-horizontal mineralized veins swarm of Panasqueira corresponds to extensional veins (mode I), whose the formation was likely driven by fluid overpressure conditions at moderate differential stresses (σ_d < 4T) as suggested by Foxford et *al*. (1991) and (2000). These veins were preferentially opened and developed in the metasedimentary host rocks above the greisen cupola suggesting (i) a strong rheological control on the localization of the structural weakness, and (ii) preferential localization of thermo-mechanical instabilities around the cupola. The vein geometry arrangement emphasizes a compressive crustal regime compatible with the regional NE-SW horizontal shortening (σ_1) and vertical stretching (σ_3) constrained from structures observed in the Beira Baixa region and in the Panasqueira district (**Chapter II**). The opening and the formation of these extensional veins involved high fluid pressure conditions that reached or exceeded the lithostatic load (Cox et *al*. 1991, 1995, Robert et *al*. 1995, Sibson et *al*. 1988).

The vertical escape of fluids from veins toward metasedimentary host rocks highlighted from tourmaline growth bands composing the metasomatised wall-rocks is consistent with fluid overpressure conditions in veins during the incipient stages of vein opening (**Chapter III**). This vertical pressure gradient caused (i) the opening and the vertical dilation of the mineralized veins and (ii) pervasive fluid flow in wall rocks triggering the development of the tourmalinization fronts observed around mineralized veins. The sub-vertical crystallization of tourmaline and elongated blocky to fibrous quartz perpendicularly to the vein walls supports implication of supralithostatic fluid pressure conditions. As evidenced by the crack-seal textures observed in mineralized veins, the formation of the veins swarm of Panasqueira was polyphased and involved several stages of opening and filling suggesting (i) fluctuations of fluid pressure

conditions and (ii) active tectonics over the hydrothermal activity of Panasqueira (Ramsay, 1980, Cox, 1987, 1995). Furthermore, it would also appear that the formation of the sub-horizontal mineralized veins of Panasqueira was bracketed by the formation of different structures formed over the same regional NE-SW horizontal shortening. Consequently, the mineralized vein network of Panasqueira was likely formed over a same continuum of deformation compatible with the regional compression related to the Variscan orogeny. The strong fracturing of quartz composing the mineralized veins supports this interpretation.

The geochemical characteristics of tourmaline (**Chapter III**), muscovite and quartz (**Chapter IV**) formed during the earliest mineralization stages indicates that the vein opening was probably related to the production and the expulsion of magmatic fluids (rich in Rb, Li, F, Zn, W, Sn, Cs, Ge and B), which were preferentially expelled from the cupola during the granite crystallization. Numerical modeling (**Chapter VI**) have demonstrated that the production and the releasing of magmatic fluids during the magmatic-hydrothermal transition is indispensable to ensure fluid overpressure conditions above the granite roof and hence to promote the opening of the mineralized vein swarm.

At the light of our results, the formation of the mineralized veins network of Panasqueira likely results from the conjunction of (i) a compressive crustal regime and (ii) the production and expulsion of a large amount of magmatic fluids, which causes the establishment of high fluid pressure conditions that promote the opening of sub-horizontal veins when they reached supralithostatic values (shift to the left of Mohr circle in Fig. 1). The strong fluid velocity contrast observed between veins (10^{-4} to 10^{-3}m.s^{-1}) and altered wall-rocks (10^{-6} to 10^{-5} m.s^{-1}) suggests that metasedimentary host rock could constitute impermeable barrier, which could promote (i) rising of fluid pressure conditions in veins and (ii) channelization of mineralizing fluids in the veins contributing to form a high grade deposit by an efficient metal transport into structural traps. The multistage of opening and filling induced by fluctuation of fluid pressure conditions suggest that the production and the expulsion of magmatic fluids were likely pulsatile and polyphased.

Finally this hydrodynamic-structural model is consistent with the tectono-magmatic events affecting the Central Iberian zone during the Variscan orogeny (Dias da Silva et *al*., 2010; Martínez Catalán et *al*., 2014; Dias da Silva, 2014).

2. Greisenization: a key process to enhance fluid flow and promote formation of large vein and greisen Sn-W deposits

As exposed in the underground mining works and drill cores, the upper part of the Panasqueira granite was affected by an intense greisenization resulting from fluid-rock interactions related to the hydrothermal activity of Panasqueira (**Chapter IV** and **V**). During this metasomatic alteration feldspars and biotite composing the two-mica granite of Panasqueira were completely replaced by the crystallization of a large amount of muscovite and quartz. Chemical composition of feldspars provide evidence that greisenization was preceded by high temperature alkali metasomatism (K-metasomatism and albitization), during which primary magmatic plagioclase and alkali feldspars were respectively converted into nearly pure albite and orthoclase. The albitization of plagioclase is accompanied by the development of pitted textures in albite grains (induced by coupled dissolution precipitation mechanisms), which could promote the pervasive fluid flow through feldspars and their transformation into muscovite during the greisenization.

As highlighted by chemical signatures of muscovite, quartz and rutile formed during the greisenization and the earliest hydrothermal stages of veins, fluids responsible of the greisenization and the vein opening were rich in incompatible granitophile elements like K, Na, F, Li, Rb, Cs, Ge and B and in metals W, Sn and Zn (**Chapter IV**). Accordingly, the greisenization was induced by the releasing and the expulsion of magmatic fluids produced by the progressive crystallization of the deeper part of the granite intrusion, which was not yet entirely crystallized. The expulsion and the circulation of these hot acidic magmatic fluids through the cooler and crystallized upper part of the granite intrusion triggered the greisenization and hence the replacement of feldspars (k-feldspar and albite) and biotite into muscovite. Accordingly, greisenization of the two-mica granite occurred likely during the magmatic-hydrothermal transition and was coeval to the earliest mineralization stages of veins formation (quartz-tourmaline and W-Sn stages).

The molar volume decrease induced by the replacement reactions related to greisenization caused a progressive porosity generation (~8.5%) and therefore a significant permeability increase in greisen (up to 3 orders of magnitude) (**Chapter V**). This positive feedback between the greisenization and permeability can explain the

propagation of the alteration front toward the deeper part of the granite intrusion and the formation of massive greisen commonly observed in Sn-W deposits.

As evidenced from numerical modeling (**Chapter VI**), the permeability increase induced by the greisenization can enhance significantly fluid flux and hence mass transfer of metals that could promote significantly the formation of large Sn-W deposits. Additionally, the development of permeable pathway in the top of granite intrusion that constitutes an important drain seems to enhance the expulsion and the focusing of magmatic fluids produced during the crystallization of the underlying granite. This enhancement of magmatic fluids expulsion could promote and ensure the establishment of high fluid pressure conditions above the granite roof and hence enable the opening of mineralized veins following structural mechanisms described previously. This interplay between magmatic fluid production, greisenization and permeability is also favorable to the development of massive greisen by vigorous fluid flow and self-propagating of the pervasive alteration. Thus, the positive feedback between greisenization and permeability can be a key process to form large massive greisen deposits, which constitute generally low-grade high tonnage Sn-W deposits (disseminated mineralization). In this model, the impermeable nature of the overlying metasedimentary host rocks (10^{-20} m^2) could enable the greisenization of the granite by inhibiting the fluid expulsion from the granite roof. The preferential greisenization of the Panasqueira granite along the granite-schist interface supports this interpretation and suggests that this contact was likely a permeable interface, in which fluids have preferentially flowed and initiate the greisenization of the granite roof.

The occurrences of euhedral quartz and disseminated cassiterite and sulfides (chalcopyrite, pyrite and sphalerite) mineralization that infill the porosity developed during the greisenization provide evidence that massive greisen have acted as plumbing system for the different ore-bearing fluids related to the different mineralization stages composing the mineralized veins (**Chapter IV** and **V**).

The porosity increase induced by greisenization would also appear to be a common process in worldwide greisen systems (**Chapter V**). Consequently, the permeability increase triggered by porosity generation during greisenization can be a crucial and a universal mechanism to enhance fluid flow and hence metal transport to form world class Sn-W deposits.

3. Role of granite cupolas and apophyses on the focusing of mineralizing fluids

As highlighted from paleo-fluid flow reconstruction (**Chapter III**) and numerical modeling (**Chapter VI**), the presence of granite cupolas and apophyses affects strongly fluid flow pattern by focusing (from the cupola towards the host rock) both (i) the expulsion of magmatic fluids released during the magmatic-hydrothermal transition and (ii) upwelling fluids of the external convective cells. This fluid focusing is significantly enhanced by the development of permeable massive greisen in the upper part of granite intrusion that promotes both the expulsion of magmatic fluids and the focusing of the external convecting fluids.

Thus, the apical parts of plutonic intrusions represent loci of convergence for hydrothermal fluids. This could be favorable to establishment of fluid overpressure conditions at the top of cupolas and hence promote the opening and the vertical dilation of the mineralized veins. Besides, thermo-mechanical instabilities are generally preferentially localized around granitic apices (Guillou-Frottier and Burov, 2003; Gloaguen et *al*., 2014) that lead to preferential localization of weakness and damage zone around apical parts of granite intrusions. The combination of this localization of damage zone with a preferential accumulation of fluids could trigger the opening of permeable structures, which then drained mineralizing fluids. This could favor the formation of hydrothermal systems, thus explaining the spatial relationship commonly observed between greisen cupolas and mineralized veins networks (Pirajno and Bentley, 1985; Pollard et *al*., 1988; Taylor and Pollard, 1988).

Accordingly, granite cupola and apophyses represent favorable zones for the deposition of high grade mineralization and constitute emanative centers, from which mineralizing fluids were preferentially expelled and spread laterally toward the country rocks explaining (i) the intense tourmalinization of the host rocks surrounding granite apophysis and (ii) the opening of hydraulic mineralized veins commonly observed above apical parts of granite intrusions (Pirajno et Schlögl, 1987).

4. Evolution of fluid flow pattern and driving forces over time

The evolution of paragenetic sequence over time both in massive greisen (**Chapter IV**) and mineralized veins swarm (**Chapter II**) can be summarized by an oxide silicate stage associated to the W-Sn mineralization (MOSS) followed and overprinted by a sulfides stage (MSS), during which ore-bearing minerals related to the MOSS (cassiterite and wolframite) were partially altered and replaced. Accordingly, the formation of the Panasqueira deposit involved different ore-forming fluids that could be related to different mechanisms of fluid flow involving different driving forces.

As suggested by stable isotopic composition of fluids related to the MOSS (blue dots in Fig. 2), the W-Sn stage of Panasqueira was likely related to mixing and interactions between magmatic ore-bearing fluids and meteoric water, while fluids related to the sulfide stage (MSS) (yellow dots) exhibit signatures suggesting fluid-rock interactions between meteoric water and coal rich metasedimentary host rocks (Fig. 2) (Polya et *al*., 2000). According to these isotopic signatures and numerical modelling results (**Chapter VI**), hydrothermal circulation related to the formation of the W-Sn-(Cu) Panasqueira ore deposit is suggested to be subdivided in two main stages:

- A first magmatic-hydrothermal stage, which corresponds to the magmatic-hydrothermal transition recorded by the tourmalinization of the metasedimentary host rocks and the formation of the quartz-tourmaline veins that occurred during the earliest mineralization stage (QTS). This first stage is marked by the progressive crystallization of the granite intrusion, which released and expelled magmatic fluids enriched in incompatible granitophile elements (B, Li, F, Cs, Rb…) and metals (W, Sn and Zn). This expulsion of magmatic fluids triggered (i) the greisenization of the granite roof and cupola and (ii) the establishment of fluid overpressure conditions above the granite intrusion that coupled with the regional compressive crustal regime caused the opening of the sub-horizontal vein swarm. Owing to the impermeable nature of the metasedimentary host rocks, the magmatic ore-bearing fluids were then channeled into the vein network and may interact both with the metasedimentary host rocks (tourmalinization) and external meteoric water leading to the deposition of wolframite during the W-Sn mineralization stage (MOSS) (Kelly and Rye, 1979; Bussink, 1984; Polya, 1989; Polya et *al*., 2000; Lecumberri-Sanchez et *al*., 2017). During this first stage, the

main driving force involved during fluid flow was the hydraulic potential (Bethke, 1985; Zhao et *al*., 1998a), which represents the excess of fluid pressure and corresponds to difference between fluid pressure conditions and hydrostatic pressure (Chi and Xue, 2011). This excess of fluid pressure was induced by the exsolution of magmatic fluids from the not crystallized part of granite intrusion. Fluids were expelled from high overpressure areas (granite cupolas and apophysis) to low pressure areas (surrounding metasedimentary host rocks) consistent with directions of fluid flow obtained from tourmaline growth bands (**Chapter III**). The several stages of vein opening and filling induced by fluctuation of fluid pressure conditions observed in quartz-tourmaline veins indicates that the expulsion of magmatic ore-bearing fluids was polyphased and pulsatile.

- The second stage corresponds to the convection of meteoric external water, which interacted with the metasedimentary country rocks. During this convective circulation, fluid-rock interactions could trigger (i) the leaching of the sulfides minerals (pyrite) disseminated in the metasedimentary host rocks and (ii) the mobilization of metals (Cu and Zn) hosted by these sulfides. Then, the convecting sulfide-bearing fluids circulate through the permeable massive greisen and within the vein swarm of Panasqueira leading to the deposition of a large amount of sulfides minerals (MSS) that crosscut minerals related to the previous mineralization stages (MOSS). This second stage occurred during the granite's cooling phase after the expulsion of magmatic fluids. Fluid flow was controlled by the buoyancy force induced by change in fluid density in response to the strong thermal contrast between the granite intrusion and the surrounding fluids (Norton and Cathles, 1979; Cathles, 1997).

These two stages were clearly controlled by the emplacement end the cooling of the granite intrusion that represents the main driving force of fluid flow and an important source of ore-bearing fluids indispensable to the formation of the deposit. The paragenetic evolution observed in the Panasqueira ore deposit is common in numerous other vein and greisen Sn-W deposits worldwide. Thus, time evolution of driving forces and fluid pattern discussed above may be also involved during the formation of these other mineralized systems.

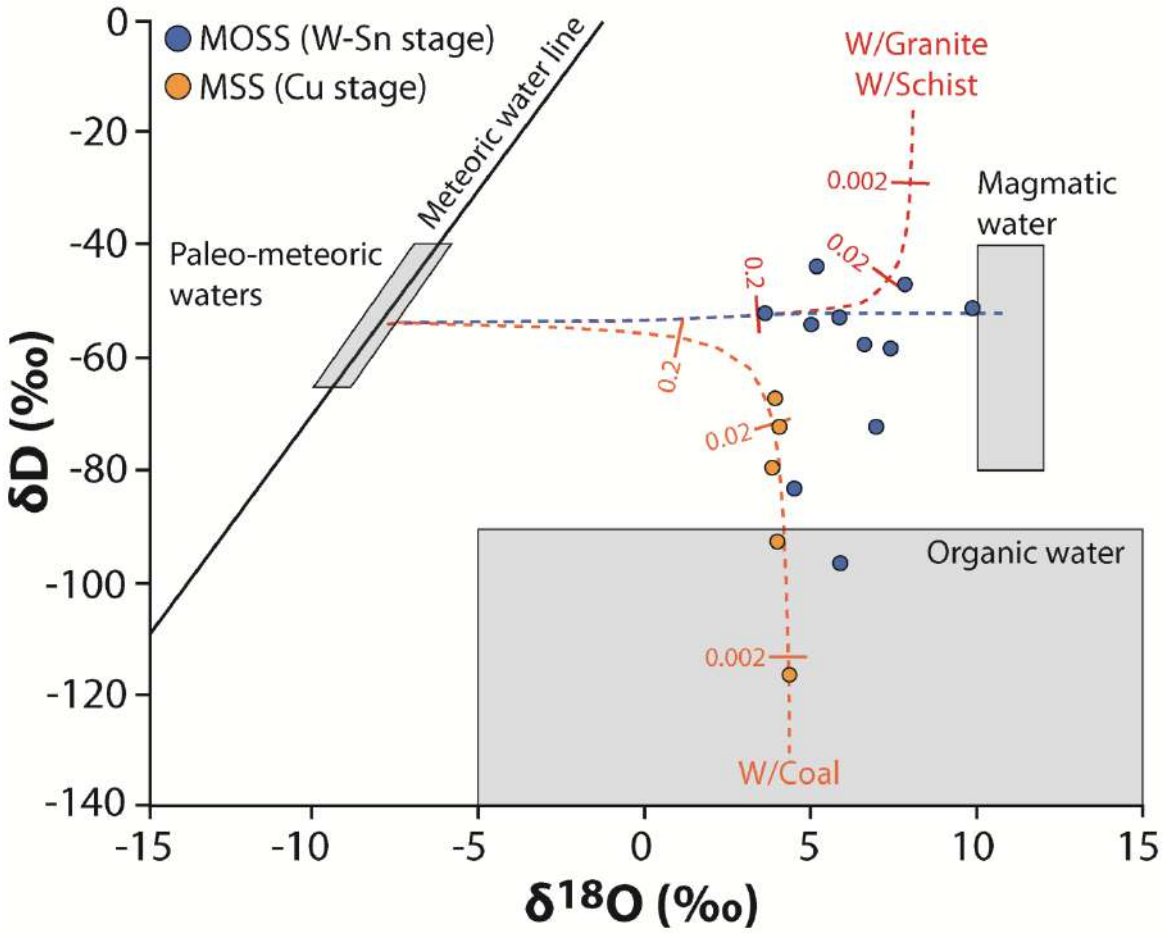

Figure 2 Measured and modelled isotopic compositions of ore forming fluids related to the Main Oxide Silicate Stage (MOSS) and the Main Sulfide Stage (MSS) of the Panasqueira deposit (modified from Polya et *al.*, 2000). Dashed orange and red curves correspond respectively to modelled equilibrium isotopic composition of meteoric water exchanged with coal rich metasediments and granite-schist. Water/Rock exchange ratios of 0.2, 0.02 and 0.002 are also reported.

5. Implication of fluid rock interactions on metal deposition

Fluid-rock interactions involved during hydrothermal activity related to the formation of Sn-W deposits have also strong effects on the evolution of physicochemical characteristics of fluids and hence potentially on metal deposition. Indeed, study performed by Lecumberri-Sanchez et *al.*, (2017) has demonstrated that fluid-rock interactions between ore-bearing fluids and metasedimentary host rocks constitute a key process for the deposition of wolframite in Sn-W deposits. Tourmalinization and muscovitization reactions (alteration of chlorite) triggered by the escape of ore-bearing fluids from veins toward the wall-rocks caused (i) pH neutralization of fluids and (ii) releasing of large amount of Fe in fluids that strongly promote the wolframite deposition in veins.

In the case of greisenization, our experimental results (**Chapter V, Part II**) indicate that the breakdown of feldspars and biotite consume a large amount of H^+ that could buffer the pH of hydrothermal fluids. This fluid neutralization can induce a significant decrease of the Sn solubility, which is partly controlled by the fluid acidity. Accordingly, replacement reactions related to greisenization can be a decisive process to promote cassiterite deposition in greisen. This mechanism can explain the occurrence of cassiterite within the porosity developed during the greisenization and the formation of low-grade, high tonnage Sn-greisen deposits. Despite alteration of biotite may release Fe in fluids, this reaction did not release enough Fe to permit the wolframite deposition, explaining the rare occurrence of wolframite in the Panasqueira greisen.

Finally, fluid-rock interactions involved during greisenization could be a key process for the formation of large vein and greisen Sn-W deposits by (i) enhancing fluid flow and metal transport by permeability increase and (ii) by promoting cassiterite deposition by fluid neutralization (Eugster, 1986; Heinrich, 1990; Halter et *al*., 1998).

6. Implication for mining exploration

In this study, we provide additional evidence that greisen cupola and apophyses constitute emanative centers for mineralizing fluids and thereby favorable zones for the deposition of mineralization. Massive greisen composing the granite roof represents both potential low-grade, high-tonnage Sn deposit and potential pathways for ore-bearing fluids. Accordingly, occurrences of greisen facies may serve as prospecting guide to discover ore bodies.

Tourmalinization observed in metasedimentary host rock appear to be related to the expulsion of magmatic ore-bearing fluids and may be a decisive process promoting the tungsten deposition. Moreover, growth bands of tourmaline composing the tourmalinite appear to be a potential powerful tool to track fluid flow related to incipient stage of magmatic-hydrothermal activity related to Sn-W mineralization. Consequently, tourmalinization zones could constitute a useful pathfinder for mining exploration to discovering not outcropping granite cupolas and hence mineralized bodies associated to these cupolas.

Numerical modeling is a complementary approach permitting to test effects of hydrodynamic and geological processes involved during the formation of hydrothermal

deposits. This approach represents a powerful tool to predict pattern of fluid flow and thereby localization of mineralization. In cases of Sn-W deposits related to granite intrusions, numerical modeling permits to reproduce localization of mineralized bodies observed in natural system. Accordingly, numerical simulation could represent a useful approach for mining exploration by predicting zones favorable for metal deposition, which were not yet discovered.

II- Scientific outlook and further works

1. Implication of permeability change during hydrothermal alteration: other examples

Feedbacks between hydrothermal alteration, porosity and permeability may constitute key mechanisms enhancing (i) fluid flow and metal transport, and (ii) formation of large alteration halos that could promote metal deposition. In the following we present three other ore-bearing hydrothermal systems for which alteration reactions could enhance permeability and promote fluid flow.

1.1 The episyenite

Episyenitization is a common metasomatic alteration of highly differentiated peraluminous leucogranite intrusion related to uranium mineralization (Dahlkamp, 2013). This sub-solidus alteration is generally induced by the expulsion and the circulation of ore-bearing magmatic fluids through the crystallized portions of granite intrusions. This alteration may lead to the formation of pipe-like masses of episyenite, which may exhibit disseminated uranium mineralization (Leroy, 1984; Dahlkamp, 2013). Episyenitization is generally marked by (i) dissolution of quartz, (ii) equilibration of feldspars with hydrothermal fluids (albitization and K-metasomatism), (iii) chloritization of ferromagnesian phases (biotite and amphibole), and (iv) the development of vuggy texture (Fig. 3a to 3d) (Cathelineau, 1986; Scaillet et *al*., 1996; Hecht et *al*., 1999; Dahlkamp, 2013; Nishimoto et *al*., 2010 and 2014).

Precipitation of geodic secondary hydrothermal minerals (calcite, chlorite and illite) (Fig. 3d to 3f) and disseminated pitchblende mineralization in vugs developed during episyenitization indicates that Uranium-bearing fluids likely flowed within the porous network of episyenite (Leroy, 1984; Dahlkamp, 2013). Accordingly, episyenitization seems to be a potential process enhancing permeability and promoting fluid flow during

hydrothermal activity leading to the formation of uranium deposit related to granite intrusions.

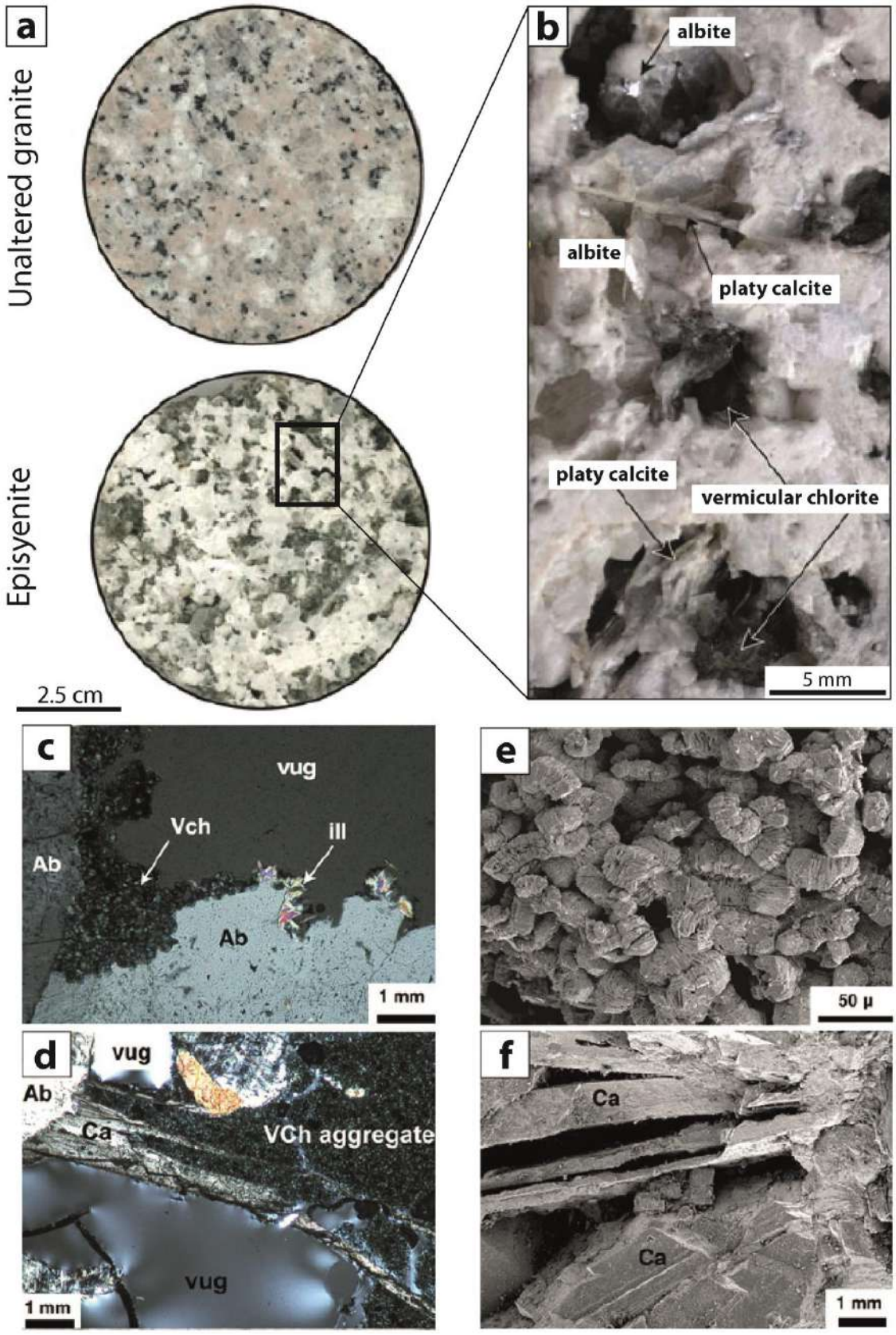

Figure 3 Mineralogical and microtextural characteristics of the episyenitization of the Toki granite (Japan) (Nishimoto et *al*., 2010 and 2014). (a) Macroscopic characteristics of the unaltered Toki granite and the episyenite. (b) Photomicrograph showing porous texture of the episyenite and its mineralogical composition. (c) to (f) Photomicrographs showing occurrences of secondary minerals in vugs formed during the episyenitization.

1.2 The epidosite

Epidosite results from metasomatic alteration of basaltic rocks of the upper oceanic crust induced by the hydrothermal circulation of seawater beneath oceanic ridges (Richardson et *al*., 1987; Alt, 1995). Epidosites are generally depleted in metals and are interpreted as the main sources of metals composing the volcanogenic massive sulfides (VMS) deposits formed by exhalation of ore-bearing hydrothermal fluids on the oceanic seafloor (Richardson et *al*., 1987; Jowitt et *al*., 2012).

This pervasive metasomatic alteration causes the total breakdown of feldspars composing basaltic rocks that were replaced by the crystallization of a large amount of epidote and quartz (Fig. 4). This strong mineralogical transformation is generally accompanied by an overall volume decrease (ΔVr) of about 9 % that trigger significant porosity increase in epidosite (Fig. 4c and 4d) (Harper, 1988; Cann et *al*., 2015; Brett et *al*., 2017). According to studies performed by Coelho et *al*, (2015) and Brett et *al*, (2017) epidotization may lead to increase of connected porosity by 4-10 % and permeability by 1-3 orders of magnitude.

This increase of permeability could enhance the self-propagation of alteration in a large volume of rocks promoting the leaching of a large amount of metals from basaltic rocks. This enhancement of permeability could also promote convective circulation and the discharging of mineralizing fluids through initially impermeable rocks (Brett et *al*., 2017).

Figure 4 (a) and (b) Macroscopic characteristics of partial epidotised pillow lavas composing oceanic crust (photo from Brett et *al*., 2017). (c) and (d) SEM-BSE images showing the development of porosity during epidotization (images from Cann et *al*., 2015). Note the crystallization of euhedral quartz in the void spaces. Mineral abbreviations, C: Chlorite, E: Epidote, Q: Quartz, V: void spaces.

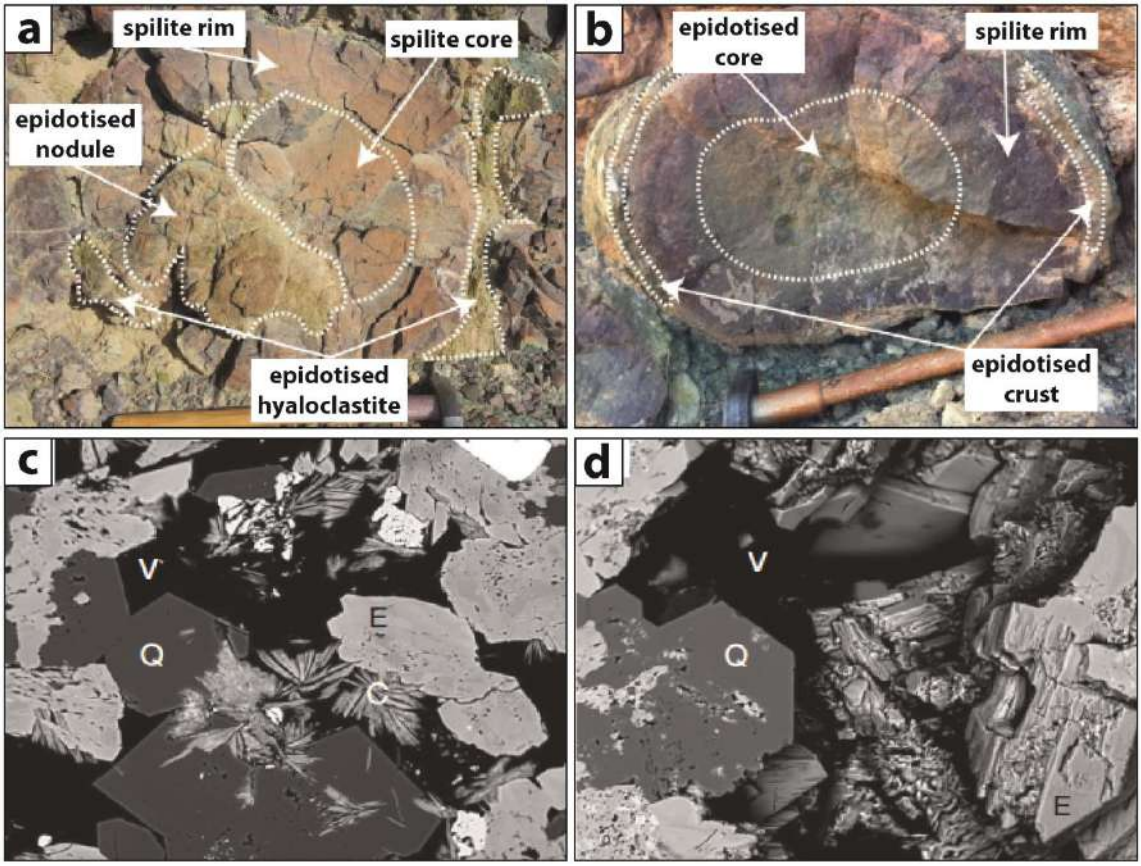

1.3 High sulphidation epithermal deposits

High sulphidation (HS) epithermal deposits are hydrothermal gold, copper and silver deposits spatially related to volcanic centers and diatremes (Jébrak and Marcoux, 2008). Ore-bearing fluids correspond to high-level degassed volcanic vapors enriched in SO_2, H_2S and HCl. The circulation of these acidic fluids up to the surface leads to the extreme alteration of country rocks and the deposition of metals. This hydrothermal alteration is marked by well-developed zoning occurring vertically and laterally (Fig. 5a), which marks the progressive neutralization of fluids by fluid-rock interactions (Henley and Ellis, 1983; Rye et *al*., 1992):

- The central zone consists of an extremely porous and permeable rocks exclusively composed of silica and commonly named vuggy silica (Fig. 5b and 5c). This porous altered rock results from the total leaching of the aluminosilicate minerals (feldspars, micas and amphibole) due to the extreme acidity of hydrothermal fluids (pH < 2). Owing to the occurrence of disseminated gold mineralization in vugs composing the vuggy silica, this permeable zone is generally considered as the main drains of the ore-bearing fluids during the formation of epithermal deposits.

- The vuggy silica is surrounded by a quartz-alunite zone, which is marked by the complete replacement of aluminosilicate minerals by alunite and quartz ($2 < pH < 3$). Like vuggy silica this alteration is accompanied by the development of porous texture that could significantly enhance fluid flow (Fig. 5d).
- The peripheral zone consists of clay alteration leading to the formation of kaolinite ($pH \approx 5$), which marks the progressive neutralization of fluids occurring previously during the formation of the vuggy silica and quartz-alunite zone.

As described by Mayer et *al*, (2016), the development of vuggy silica and quartz-alunite zone are marked by a strong increase of connected porosity, which increases significantly the rock's permeability (up to 3 orders of magnitude). Accordingly, acidic alteration occurring in HS epithermal deposits could enhance significantly fluid flow and promote the transport of metals. The fact that mineralized fluids impregnate the altered and porous zones confirms this hypothesis.

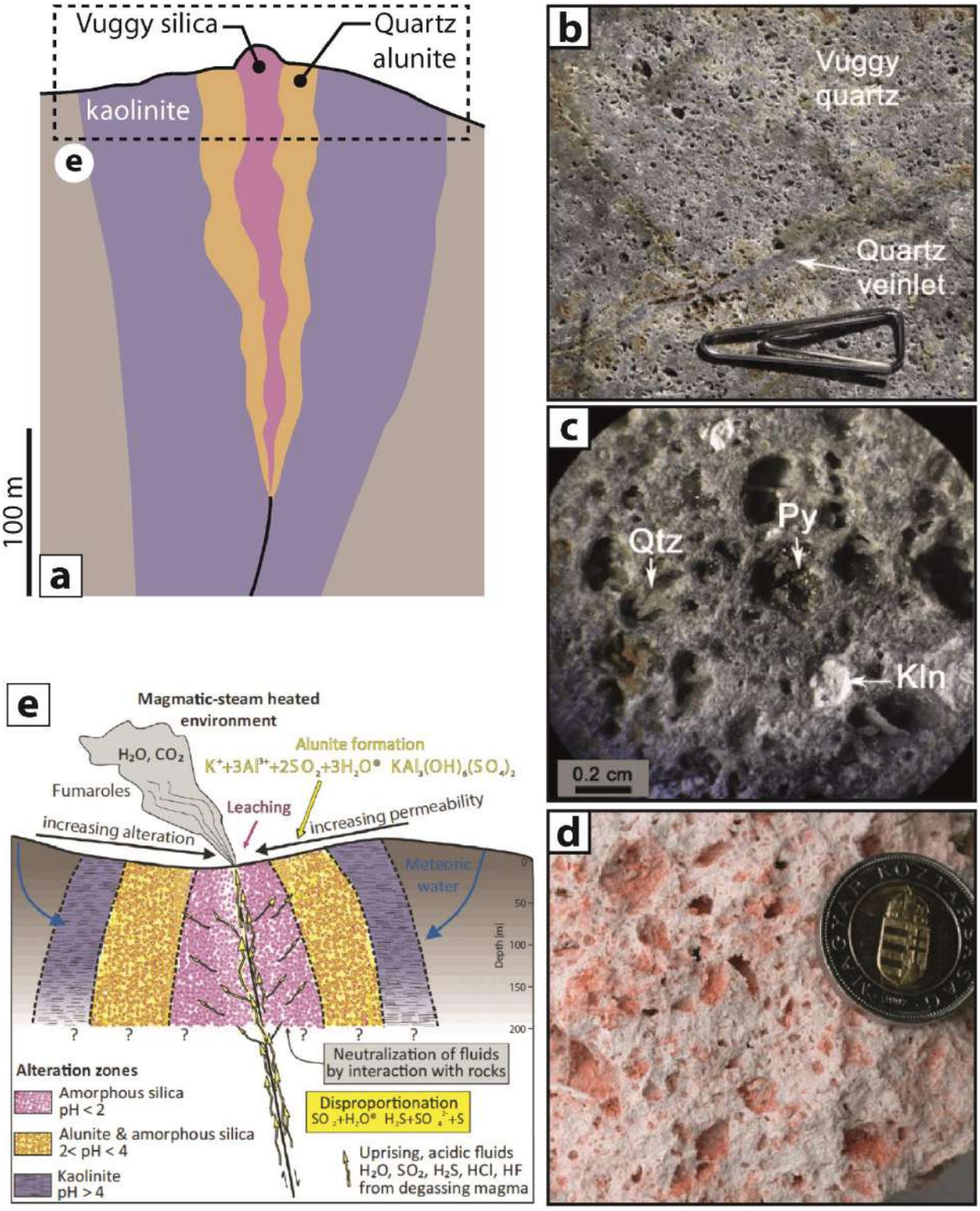

Figure 5 Geological and textural characteristics of hydrothermal alterations involved during the formation of high sulphidation (HS) epithermal deposits. (a) Spatial zoning of hydrothermal alterations commonly observed in epithermal deposits (b) and (c) Textural characteristics of vuggy silica, which exhibits extremely porous texture (photographs from http://www.mininggeologyhq.com/epithermal/). (d) Textural characteristics of quartz-alunite zone whose the formation is accompanied by the development of porosity. (e) Conceptual model proposed by Mayer et *al*, (2016) considering the increase of permeability induced by acidic alterations related to the circulation of ore-bearing fluids. In this model the increase of permeability promotes the circulation of hydrothermal fluids.

1.4 Implications for further works

These different examples emphasize that feedback between hydrothermal alteration and permeability is common in a wide range of mineralized hydrothermal systems. It seems that reactive hydrothermal fluids are able to generate their own pathways in initially impermeable rocks. Combined with permeability related to structures, this process represents an important mechanism to enhance fluid flow and promote the formation of large hydrothermal deposits. Consequently, the methodology used and presented in this study may be applied in future works to investigate effects of this feedback on the formation of economically important hydrothermal systems. Experimental laws describing the evolution of permeability as a function of the degree of alteration could then be implemented in numerical modeling to (i) perform more accurate and realistic model of fluid flow and (ii) predict more precisely favorable zones for the formation of ore bodies.

2. Implications of fluid-rock interactions on metal deposition: further experimental investigations

As shown in this work and study carried out by Lecumberri-Sanchez et *al*., (2017) fluid-rock interactions could be a key process promoting metal deposition in Sn-W deposits. Experimental approaches constitute a powerful tool permitting to reproduce fluid-rock interactions under realistic hydrothermal conditions. Moreover, these supplementary experiments may also help to (i) quantify physicochemical changes of fluids induced by these interactions and (ii) assess whether these interactions may lead to metal deposition. Experiments of greisenization (interactions between granite powder and fluids) and tourmalinization (interactions between schist powder and fluids) should be performed to quantify (i) the amount of iron potentially released during these two types of alteration and (ii) evolution of pH over the experiment time. Secondly, experiments performed with Sn-W-bearing fluids may help to investigate effects of greisenization and tourmalinization on the deposition of metals via the evolution of Sn and W concentrations in fluids over the experiment time.

Obviously, this experimental methodology could be applied in several other mineralized hydrothermal systems for which fluid-rock interactions may trigger the deposition of metals, such as skarn and epithermal deposits. This methodology also permits to simulate the leaching of metal from source rocks and quantify the amount of

metals that could be potentially mobilized during fluid flow under hydrothermal conditions. Finally, experimental simulations could also be applied to determine partitioning between minerals and hydrothermal fluids in order to constrain the chemical signatures of fluids in natural systems from analyses of major and trace elements on common gangue minerals, such as quartz, tourmaline and muscovite.

References

A-B

Alt, J., 1995. Subseafloor processes in mid-ocean ridge hydrothermal systems. In: Humphris, S.E., Zierenberg, R.A., Mullineaux, L.S., Thomson, R.E. (Eds.), Seafloor Hydrothermal Systems: Physical, Chemical, Biological, and Geological Interactions. AGU Monograph Series, No. 91. American Geophysical Union, Washington, DC, pp. 85–114.

Barnes, H.L. 1997. Geochemistry of Hydrothermal Ore Deposits, third ed. John Willey and Sons, New York.

Bethke, C.M., 1985. A numerical model of compaction-driven groundwater flow and heat transfer and its application to paleohydrology of intracratonic sedimentary basins. Journal of Geophysical Research 90,6817-6828.

Brett, A., Diamond, L.W., Gilgen, S.A. 2017. Deep flow paths in VMS systems: Porosity and permeability of epidosite alteration in the Semail ophiolite, Oman. Proceeding Vol. 2, 14th SGA Biennial Meeting Quebec City, Canada

Bussink, R.W. 1984. Geochemistry of the Panasqueira Tungsten-Tin Deposit, Portugal. Geol. Ultraiectina.

C

Cann, J.R., McCaig, A.M., Yardley, B.W.D. 2015. Rapid generation of reaction permeability in the roots of black smoker systems, Troodos ophiolite, Cyprus. Geofluids 15:179–192

Cathelineau, M. 1986. The hydrothermal alkali metasomatism effects on granitic rocks: quartz dissolution and related subsolidus changes. J. Petrol. 27: 945-965.

Cathles L.M. 1977. An analysis of the cooling of intrusives by Ground-Water convection which including boiling. Econo. Geol. 77. 804-826.

Chi, G. Xue, C. 2011. An overview of hydrodynamic studies of mineralization. GEOSCIENCE FRONTIERS 2(3) (2011) 423-438.

Cox, S.F. 1987. Antitaxial crack-seal vein microstructures and their relationships to displacement paths. J Struct Geol 9:79–787.

Cox, S.F., Wall, V.J, Etheridge, M.A., Potter, T.F. 1991. Deformation and metamorphic processes in the formation of mesothermal vein-hosted gold deposits: examples from the Lachlan Fold Belt in central Victoria, Australia. Ore Geol Rev 6:391–423.

Cox, S.F. 1995. Faulting processes at high fluid pressures: an example of fault valve behavior from the Wattle Gully Fault, Victoria, Australia. J Geophys Res 100:12841–12859.

D-E

Dahlkamp**,** F.J., 2013. Uranium Deposits of the World. 10.1007/978-3-540-78554-5

Dias da Silva, Í., GONZÁLEZ CLAVIJO, E., MARTÍNEZ CATALÁN, J.R. 2010. Tectono-thermal evolution of a Central Iberian Zone sector in the Palaçoulo region (east of Morais Massif, NE Portugal). e –Terra http://e-terra.geopor.pt ISSN 1645-0388 Volume 11 – nº 14.

Dias da Silva, Í., 2014. Geología de las Zonas Centro Ibérica y Galicia – Trás-os-Montes en la parte oriental del Complejo de Morais, Portugal/España. Instituto Universitario de Geología "Isidro Parga Pondal" - Área de Xeoloxía e Minería do Seminario de Estudos Galegos, A Coruña, Spain, Serie Nova Terra. 45 (424 pp).

Eugster, H.P. 1986. Minerals in hot water. American Mineralogist. v. 7 1, p. 655-673.

F

Foxford, K.A., Nicholson, R., Polya, D.A., 1991a. Textural evolution of W-Cu-Sn bearing hydrothermal quartz veins at Minas da Panasqueira, Portugal. Mineralogical Magazine 55, 435-445.

Foxford, K.A., Nicholson, R., Polya, D.A., Hebblethwaite, R.P.B. 2000. Extensional failure and hydraulic valving at Minas da Panasqueira, Portugal: Evidence from vein spatial distributions, displacements and geometries. J. Struct. Geol. 22, 1065–1086.

G-H

Gloaguen, E., Branquet, Y., Chauvet, A., Bouchot, V., Barbanson, L. and Vigneresse, J.L. 2014. Tracing the Magmatic/Hydrothermal Transition in Regional Low-Strain Zones: The Role of Magma Dynamics in Strain Localization at Pluton Roof, Implications for Intrusion-Related Gold Deposits. Journal of Structural Geology 58: 108–121.

Guillou-Frottier, L., Burov, E. 2003. The development and fracturing of plutonic apexes: implications for porphyry ore deposits. Earth & Planetary Science Letters, 214, 341-356.

Halter, W.E., Williams-Jones, A.E., Kontak, D.J. 1998. Origin and evolution of the greisenizing fluid at the East Kemptville tin deposit, Nova Scotia, Canada. *Economic Geology*, 93 (7): 1026–1051

Harper, G.D., 1988. Reaction--enhanced Permeability by Formation of Epidosites in Seafloor Hydrothermal Systems. Abstract EOS, 69, 527.

Hecht, L., Thuro, K., Plinninger, R., Cuney, M. 1999. Mineralogical and geochemical characteristics of hydrothermal alteration and episyenitization in the Könighstan granites, northern Bohemian Massif, Germany. Int Journ Earth Science 88: 236-252.

Heinrich, C.A., 1990. The chemistry of hydrothermal tin –tungsten ore deposits. Econ. Geol. 85, 457–481.

Henley, R.W., Ellis, M., 1983. Geothermal system ancient and modern : a geothermal reviews. Earth Science Reviews, 19: 1-50.

J-K

Jébrak M., Marcoux E., 2008. Géologie des ressources minérales. Géologie Québec. 685p.

Jowitt, S.M., Jenkin, G.R.T., Coogan, L.A., Naden, J., 2012. Quantifying the release of base metals from source rocks for volcanogenic massive sulfide deposits: Effects of protolith composition and alteration mineralogy. Journal of Geochemical Exploration 118, 47-59.

Kelly, W.C., Rye, R.O. 1979. Geologic, fluid inclusion and stable isotope studies of the tin-tungsten deposits of Panasqueira, Portugal. Econ Geol 74:1721–1822.

L

Lecumberri-Sanchez, P., Vieira, R., Heinrich, C.A., Pinto, F., Wälle, M. 2017. Fluid-rock interaction is decisive for the formation of tungsten deposits. Geology 45, 579–582.

Leroy, J. 1984. Episyénitisation dans le Gisement d'Uranium du Bernardan (Marche): Comparaison avec des Gisements Similaires du Nord-Ouest du Massif Central Français. Mineral. Deposita Volume 19, Issue 1, pp 26–35.

M-N

Martínez Catalán, J.R., Rubio Pascual, F.J., Montes, A.D., Fernández, R.D., Barreiro, J.G., Dias Da Silva, Í., Clavijo, E.G., Ayarza, P., Alcock, J.E., 2014. The late Variscan HT/LP metamorphic event in NWand Central Iberia: relationships to crustal thickening, extension, orocline development and crustal evolution. London, Special Publications] Geol. Soc. Lond., Spec. Publ. 405:225–247.

Mayer, K., Scheu, B., Montanaro, C., Yilmaz, T.I. Isaia, R., Aßbichler, D., Dingwell, D.B. 2016. Hydrothermal alteration of surficial rocks at Solfatara (Campi Flegrei): Petrophysical properties and implications for phreatic eruption processes. Journal of Volcanology and Geothermal Research 320 : 128–143

Nishimoto, S., Yoshida, H. 2010. Hydrothermal alteration of deep fractured granite: effect of dissolution and precipitation. Lithos 115:153–162.

Nishimoto, S., Yoshida, H., Asahara, Y., Tsuruta, T., Ishibashi, M., Katsuta, N. 2014. Episyenite formation in the Toki granite, central Japan. Contrib Mineral Petrol, 167:960.

Norton, D., Cathles, L.M. 1979. Thermal aspects of ore deposition. In: Barnes, H.L. (Ed.), Geochemistry of Hydrothermal Ore Deposits, second ed. John Wiley and Sons, New York, pp. 611e631.

P

Pirajno, F., Bentley, P.N. 1985. Greisen-related scheelite, gold and sulphide mineralization at Kirwans Hili and Bateman Creek, Reefton district, Westland, New Zealand. New Zealand Journal of Geology and Geophysics 28(1): 97-109.

Pollard, P.J., Taylor, R.G., Cuff, C. 1988. Genetic Modelling of Greisen-Style Tin Systems. In: Hutchison C.S. (eds) Geology of Tin Deposits in Asia and the Pacific. Springer, Berlin, Heidelberg, pp 59-72.

Polya, D.A. 1989. Chemistry of the main-stage ore-forming fluids of the Panasqueira W-Cu-(Ag)-Sn deposit, Portugal: implications for models of ore genesis. Econ. Geol. 84, 1134–1152.

Polya, D.A., Foxford, K.A., Stuart, F., Boyce, A., Fallick, A.E. 2000. Evolution and paragenetic context of low δD hydrothermal fluids from the Panasqueira W-Sn deposit, Portugal: New evidence from microthermometric, stable isotope, noble gas and halogen analyses of primary fluid inclusions. Geochim. Cosmochim. Acta 64, 3357–3371.

R

Ramsay, J.G. 1980. The crack-seal mechanism of rock deformation. Nature 284: 135–139.

Richardson, C.J., Cann, J.R., Richards, H.G., Cowan, J.G., 1987. Metal-depleted root zones of the Troodos ore-forming hydrothermal systems, Cyprus. Earth Planet. Sci. Lett. 84, 243–253.

Robert, F., Boullier, A.M., Firdaous, K. 1995. Gold–quartz veins in metamorphic terranes and their bearing on the role of fluids in fauting. J Geophys Res 100:12841–12859.

Rye, R.O., Bethke, P.M., Wasserman, M.D. 1992. The stable isotope geochemistry of acid sulfate alteration. Economic Geology, 215: 5-36.

S

Scaillet, S., cuney, M., Le Carler de Veslud, C., Cheilletz, A., Royer, J.J. 1996. Cooling pattern and mineralization of the Saint Syvestre and Western Marche leucogranite pluton, French Massif Central : II. Thermal modelling and implications for the mechanism of uranium mineralization. Geochim Cosmochim Acta 60: 4673-4688.

Sibson, R.H. 1985. A note on fault reactivation. J Struct Geol 7:751–754.

T

Taylor, R.G., Pollard, P.J. 1988. Pervasive hydrothermal alteration in tin-bearing granite and implications for the evolution of ore-bearing magmatic fluids. Canadian Institute of Mining and Metallurgy Special Volume 39, p. 86.95.

Zhao, C., Hobbs, B.E., Mühlhaus, H.B., 1999a. Effects of medium thermoelasticity on high Rayleigh number steady-state heat transfer and mineralization in deformable fluid-saturated porous media heated from below. Computer Methods in Applied Mechanics and Engineering 173,41-54.

Liste des tableaux et des figures

Chapitre I

fluide hydrothermal déterminés pour différentes conditions de pression et de température (modifiées d'après Schatz et al., 2004).

Figure 11 Compilation des données microthermométriques (températures et pression) (a), des valeurs de salinité (b) et des données compositionnelles des inclusions fluides (c) analysées au sein des différents types de gisements à W-Sn présent à travers le monde (modifié d'après Naumov, 2011).

Figure 12 Compilation des compositions isotopiques en $\delta^{18}O$ et δD (en ‰) des fluides minéralisateurs responsables de la formation de différents gisements à W-Sn présent dans le monde (modifié d'après Legros, 2017).

Figure 13 (a) Evolution de la solubilité du tungstate dans les fluides hydrothermaux en fonction de la concentration en HCl (Wood, 1992) et (b) de la concentration en NaCl, HCl pour différentes conditions de température (Bryzgalin, 1976a)

Figure 14 Effet de la mise en place d'un apex granitique sur la localisation de la déformation. La ligne en pointillés noir correspond au contact granite-encaissant (d'après Guillou-Frottier et Burov, 2003).

Figure 15 Modèle conceptuel présentant les trois étapes de formation d'un gisement hydrothermal (source-transport-dépôt) (d'après Heinrich, 1996 communication orale).

Figure 16 Répartition des modes de transport par advection et diffusion dans l'espace vitesse-diffusion. Les gammes de vitesses estimées pour les différents types d'environnement géologiques et hydrothermaux sont également représentées. Les lignes en pointillés serrés correspondent aux nombres de Péclet (Pe). Les domaines en gris correspondent aux gammes de vitesses-diffusion pour les veines hydrothermales, les shear zones et le métamorphisme régional (Dolejs, 2015).

Figure 17 Modèles schématiques présentant les différents types de circulation hydrothermale ainsi que les forces motrices associées impliquées en environnement péri-granitique (d'après Chi et Xue, 2011). (a) Expulsion de fluides magmatiques en sommet de coupole granitique provoquant des conditions de surpression fluides. (b) Convection hydrothermale péri-granitique induite par l'anomalie thermique que constitue l'intrusion granitique.

Figure 18 (a) Relation entre porosité et perméabilité au sein de différents réservoirs géothermiques et hydrothermaux (d'après Moeck, 2014). (b) Gammes de perméabilité observées au sein des principales roches composant la croûte terrestre. Les valeurs limites de perméabilités nécessaires au fonctionnement de certains processus de circulation sont également représentées (d'après Ingebritsen et Appold, 2012). Les gammes de perméabilité et de porosité matricielles au sein des roches cristallines et métamorphiques sont en apparences faibles (lignes en pointillés rouges) mais peuvent être améliorées par des processus de fracturation et d'altération hydrothermale (ligne en pointillés verts).

Figure 19 Evolution de la porosité (a) et de la perméabilité (b) en fonction de la profondeur (d'après Manning et Ingebritsen, 1999; Moore et Saffer, 2001).

Figure 20 (a) Effet de la fracturation sur la perméabilité d'un échantillon de granite (d'après Tenthorey et Fitz Gerald, 2006). (b) Effet de la fracturation sur la perméabilité d'un échantillon de métadiabase (d'après Coelho et al., 2015). Après l'augmentation de perméabilité induite par la fracturation, la perméabilité diminue et retourne à sa valeur initiale en raison de la cicatrisation des microcracks. (c) Effet de la déformation ductile sur la perméabilité d'un échantillon de marbre. La pression fluide a également un effet majeur sur l'augmentation de perméabilité induite par la déformation (d'après Zhang et al., 1994a).

Figure 21 (a) Effet de la serpentinisation sur la perméabilité, ces expériences ont été réalisées à partir de différents échantillons de péridotite (d'après Farough et al., 2015). (b) Effet de la rétromorphose de la serpentine en olivine sur la perméabilité. Ces expériences ont été réalisées à différentes températures (d'après Tenthorey et Cox, 2003). (c) Effet de l'altération de type argile sur la perméabilité de roche granitique. Ces expériences ont été réalisées à différentes températures (d'après Tenthorey et Fitz Gerald, 2006).

Figure 22 Exemples de modèles numériques prenant en compte certains processus mécaniques et chimiques ayant un effet significatif sur la perméabilité dynamique en environnement péri-granitique. (a) Effet de conditions de surpression fluide induite par l'expulsion de fluide magmatique sur la perméabilité de l'encaissant en contexte de porphyre cuprifère (d'après Weis et al., 2012). (b) Effet de la précipitation et de la dissolution du quartz sur la perméabilité autour d'intrusions granitiques (d'après Scott et Driesner, 2018).

Figure 23 Gammes de porosité totale et de porosité connectée mesurées dans le greisen composant le complexe de Nebelstein (Autriche) (d'après Müller-Huber et Börner, 2017).

Chapitre II

Figure 1 Paleogeographic reconstructions of the Variscan orogeny (adapted by Nance et al., 2012 from Scotese, 1997; Cocks and Torsvik, 2002; Stampfli and Borel, 2002).

Figure 2 (a) Structural map of the European Variscan belt displaying the different tectonic domains and the main Variscan thrust and shear zones. (b) Reconstruction of the Variscan paleogeography during the Variscan orogeny (330-300 Ma), and simplified cross section showing the general fan-like shape of the Variscan belt (From Díez Fernández and Arenas, 2015).

Figure 3 (a) Tectonic map of the Variscan Iberian massif showing the main tectonostratigraphic domains defined by Julivert et al., (1972). CZ: Cantabrian Zone, WALZ: West Asturian-Leonese Zone, GTMZ: Galicia Tràs-os-Montes Zone, CIZ: Central Iberian Zone, OMZ: Ossa-Morena Zone and SPZ: South Portuguese Zone. (b) Synthetic map displaying the tectono-magmatic and the metallogenic setting of the CIZ. This map exhibits notably the spatial relationships between the main Variscan shear zones (C3) and the granitic intrusions as well as the spatial and the genetic link between the Variscan granites and the Sn-W ore deposits (realized from Pereira et al., 1993; Dias et al., 1998; Diez Fernandez and Pereira, 2016). (c) Synthetic geological cross sections across the southern part of the CIZ displaying the main Variscan structures and the relationships between these structure and the Variscan granitic intrusions (section (A-D) is modified from Diez Fernandez and Pereira, 2016 and the section (E-F) from Poyatos et al., 2012). (d) Detailed map view of the Tomar-Cordoba shear zone displaying the relationship between the ductile shear zone and the domino faults system formed during the C3 deformation event (from Sanderson et al., 1991).

Figure 4 Tectono-magmatic evolution of the Central Iberian zone during the Variscan orogeny. This schematic representation displays the main compressional (C1, C2 and C3) and extensional (E1) stages, as well as the different generations of granitic intrusions. (From Dias et al., 2010).

Figure 5 Structural map of the Iberian peninsula showing the main structures related to general uplift induced by the Alpine orogeny. Number in boxes corresponds to quantitative estimation of the vertical displacement (in meters) of the Pliocene-Quaternary uplift observed in Iberia (modified by Cloetingh et al., 2002 from Janssen et al., 1993; Zeck et al., 1992; Andeweg, 2002).

Figure 6 Geological and structural setting of the Beira Baixa province. (a) Geological map, (b) stratigraphy and (c) cross section of the Beira Baixa province. The cross section (A-A') was realized through the NW-SE cartographic folds (Ordovician quartzite) and the W-Sn-(Cu) Panasqueira ore deposit**.**

Figure 7 Structural characteristics of the Ordovician quartzite syncline of Unhais-o-Velho. (a) Panoramic photograph of the folded Ordovician quartzite outcropping along the "Rio Zêzere" river. The lower-hemisphere equal-area stereoplots show the orientation of stratigraphy (S_0), fold axes and reverse faults observed in the Unhais-o-Velho syncline. (b), (c) and (d) mesoscale folds observed in the Armorican quartzite, and emphasizing a NE-SW shortening. Note the development of a discrete planar axial cleavage (S_1). (e) and (f) reverse faults and fault gouge emphasizing a NE-SW shortening.

Figure 8 Photographs showing relationships between folding, the regional foliation (S_1) and faults affecting the Beira schist formation (outcrops in the sector of Chiqueiro). (a) Panoramic photography displaying mesoscale anticline and syncline. (b) and (c) Zooms on fold limb and fold hinge showing the bedding (S_0) and the axial planar cleavage corresponding to the regional foliation (S_1). The lower-hemisphere equal-area stereoplots show the orientation of stratigraphy (S_0), axial planar cleavage and faults observed in the sector of Chiqueiro.

Figure 9 Vertical stretching lineation observed in the Beira schist formation close to the Panasqueira deposit (sector of Chiqueiro). (a) Photograph showing vertical stretching lineation recorded by chlorite (b) Lower-hemisphere equal-area stereoplot showing trend and plunge of the stretching lineation observed on the field. (c) and (d) Photomicrographs (transmitted light) showing boudinage and pressure shadow microstructures emphasizing a vertical stretching.

Figure 10 Structural characteristics of sub-horizontal barren quartz veins present in the Beira Baixa province close to the Panasqueira deposit (road between Paul and Barco). (a) Sub-horizontal barren quartz veins crosscutting the vertical foliation of Beira schist. (b) Horizontal quartz tension gashes folded during the regional NE-SW shortening. (c) and (d) Zooms on folded horizontal quartz tension gashes showing refraction of the vertical foliation due to the more competent nature of quartz veins. (e) Lower-hemisphere equal-area stereoplots showing the orientation of the regional foliation (S1) and poles of barren quartz veins.

Figure 11 Vertical brittle-ductile thrust faults present in the Beira Baixa province close to the Panasqueira deposit (road between San Jorge de Beira and Barroca Grande). (a) En echelon-arranged extensional veins defining a sub-vertical shear band characterized by a reverse sense of shear (top to the SW). (b) Vertical shear band with reverse sense of shear. This shear band was accompanied by folding and boudinage of quartz exudation. (c) Zoom on the shear band displayed on (b). The lower-hemisphere equal-area stereoplot shows the orientation of poles of the brittle-ductile thrust faults.

Figure 12 Subvertical brittle-ductile strike-slip faults present in the Beira Baixa province close to the Panasqueira deposit. (a) E-W trending sinistral ductile shear band located in the sector of Cabeço do Pilão (Southeastern part of the Panasqueira district). (b) Zoom on the shear band displayed in (a) showing the transposition of the regional foliation (S_1) induced by the shearing. (c) En echelon-arranged extensional veins defining E-W trending sinistral shear band. (d) S-C structure defining N-S trending dextral shear zone. (e) Conjugate brittle strike-slip faults with N-S trending dextral fault and E-W trending sinistral fault. (f) and (g) zooms on fault planes showing orientations of lineation on slip surfaces, with (f) sinistral displacement and (g) dextral displacement.

Figure 13 Synthesis of structural data and structures observed in the Beira Baixa province close to the Panasqueira deposit. All of these structures were formed during the same compressive event involving NE-SW shortening (Z).

Figure 14 Samples of Beira schist and spotted schist from the Panasqueira deposit displaying effect of thermal metamorphism induced by the emplacement of the Panasqueira granite. KFMASH petrogenetic grid showing stability field (P and T conditions) of the paragenesis composing the spotted schist.

Figure 15 Geological and structural setting of the W-Sn-(Cu) Panasqueira ore deposit. (a) Geological map of the Panasqueira ore deposit showing the elevation (above the sea level) of the granite roof. (b) Interpolated foliation trajectories emphasizing occurrences of NNW-SSE trending dextral shear zone close the greisen cupola (data source Beralt Tin & Wolfram S.A.). (c) Geological cross sections (A-A') and (B-B') displaying the spatial relationship between mineralized veins and the underlying granite. The cross section (B-B') displays the vertical motion induced by the Alpine faults (Cebola fault, the Rio Zezêre and the 8E fault).

Figure 16 Structural characteristics of the folded sub-horizontal barren quartz veins present in the mine of Panasqueira. (a) and (b) Horizontal barren quartz veins intensively folded (sub-horizontal fold axes). (c) Sample displaying folded barren quartz vein affected by vertical thrusts (sample obtained with courtesy of F. Noronha). (d) Folded barren quartz vein crosscut by horizontal mineralized vein. Note the presence of wolframite in the horizontal mineralized quartz vein. This folded and thrusted barren quartz vein was then crosscut by horizontal mineralized vein. Note the presence of epigenetic arsenopyrite and tourmaline mineralization in the folded barren quartz veins. (e) Photomicrograph displaying folds in tourmalinized schist close to a quartz-tourmaline vein.

Figure 17 Petro-structural characteristics of the sub-horizontal barren quartz veinlets parallel to mineralized veins swarm. (a) Dense network of barren quartz veinlets, which are roughly parallel to a thick mineralized vein. (b) and (c) Zoom and photomicrograph of a barren horizontal quartz veinlet showing the presence of biotite along the veinlet selvage. (d) Chemical characteristics of biotite composing the spotted schist and the horizontal barren quartz veinlets. For comparison the chemical composition of biotite composing the two-mica granite of Panasqueira are also plotted in this diagram. (e) Application of the Henry et al. (2005) biotite geothermometer on biotite composing the spotted schist, the horizontal barren veinlets and the two-mica granite of Panasqueira.

Figure 18 Structural characteristics of the sub-horizontal ore-bearing quartz vein swarm of Panasqueira. (a) and (b) typical horizontal mineralized extensional veins defining en-echelon segments. These ore-bearing veins are perpendicular to the vertical regional foliation and crosscut the barren vertical quartz veins. The lower-hemisphere equal-area stereoplot shows the poles of extensional mineralized veins. (c) and (d) Mineralized veins composed of several linked en-echelon segments, which were connected by sub-vertical bridge structures. (e) and (f) Sub-horizontal pre-ore barren quartz veins reopened during the mineralization stages of Panasqueira (g) Linked flat extensional veins exhibiting pull-apart structure compatible with NE-SW horizontal shortening and vertical opening and dilation of veins. (h) Zoom on the vein displayed in image g. (i) En echelon-arranged extensional mineralized veins defining top to the NE shear band. (j) Relationships between en-echelon arranged tension gashes, thrust and flat mineralized extensional veins. All of these structures seem to be formed in response to a horizontal shortening and vertical stretching.

Figure 19 Sub-horizontal ore-bearing quartz veins affected by compressive deformation induced by the regional NE-SW horizontal shortening. (a) Folded quartz veins crosscut by sub-horizontal mineralized flat vein. (b) and (c) Sub-horizontal mineralized veins slightly folded during the NE-SW horizontal shortening. Note the formation and the refraction of rough vertical foliation in the folded mineralized veins displayed in b. (d) Folded barren quartz veins crosscut by horizontal mineralized vein, in which the vertical foliation can be observed. (e) to (g) Sub-horizontal mineralized veins affected and displaced by sub-vertical thrusts in response to the NE-SW horizontal shortening.

Figure 20 (a) to (e) Sub-vertical strike slip faults crosscutting the flat mineralized veins of Panasqueira. These faults were reactivated during the Alpine orogeny and cemented by carbonate and sulfides assemblages. (f) Lower-hemisphere equal-area stereoplot showing the orientation of poles of the strike-slip faults present in the mine of Panasqueira.

Figure 21 Microphotograph displaying micro-shear bands observed in the metasedimentary host rocks close to sub-horizontal mineralized veins composing the Panasqueira deposit. This set of shear bands comprises dextral shear bands striking N-S (b and d) and conjugate sinistral E-W trending shear bands (a, c and e). Note the preferential crystallization of biotite related to the thermal metamorphism along these shear bands.

Figure 22 Microstructural characteristics of the flat mineralized veins of Panasqueira. Quartz-biotite vein exhibiting typical crack-and seal structure. Note the shearing of the biotite selvage of the lower vein wall. (b) Zoom on quartz showing horizontal inclusions bands typical of extensional vein. (c) Zoom on the lower vein wall, in which the biotite selvage was sheared with top to the NE displacement. (d) Vertical shear bands displayed in Fig. 21 crosscut by the sub-horizontal mineralized veins of Panasqueira. (e) Typical sub-horizontal quartz-tourmaline vein characterized by crack-and seal texture. (f) Quartz-biotite vein (QB), which was reopened during the mineralization stages (QTS and MOSS).

Figure 23 Synthesis of structural data and structures observed in the sector of Barroca Grande of the W-Sn-(Cu) Panasqueira deposit. All of these structures and the formation of mineralized veins were likely formed during the regional NE-SW horizontal shortening (Z).

Figure 24 Structural map of the sector of Cabeço do Pião showing relationship between the mineralized tension gashes veins and the conjugate strike-slip faults formed during the regional NE-SW horizontal shortening. The lower-hemisphere equal-area stereoplots show the orientation of poles of the regional foliation (S1), the strike-slip faults and the mineralized quartz veins present in the sector of Cabeço do Pião. (modified from Thadeu, 1951 and Conde et al., 1971).

Figure 25 Structural characteristics of the W-Sn-(Cu) mineralization present in the sector of Cabeço do Pião (southeastern part of the Panasqueira district). (a) Dextral N-S trending shear zone with typical C-S structure marked by the transposition of the regional foliation into the shear bands. (b) En echelon-arranged tension gashes defining sinistral E-W trending shear band. (c) to (e) Photographs showing relationship between strike-slip faults and the sub-vertical tension gashes quartz veins. (f) Sub-vertical tension gashes mainly filled by quartz and muscovite. (g) Photograph displaying relationship between mineralized subvertical tension gashes and dextral N-S striking fault. (h) to (j) Sub-vertical quartz veins mineralized in wolframite.

Figure 26 Structural model of formation of the W-Sn-(Cu) Panasqueira ore deposit integrating structures exposed in the Beira Baixa region and in the sector of Barroca Grande and Cabeço do Pião. In this model we assume that the mineralized veins of Barroca Grande and Cabeço do Pião were formed over the same continuum of deformation involving regional NE-SW horizontal shortening (Z).

Figure 27 Macroscopic and microscopic characteristics of the quartz-biotite stage (QBS) of the mineralized system of Panasqueira. (a) to (d) veins with biotite along the schist vein-contact. These veins are often crosscut by late sulfide stage (e) Quartz-biotite vein, which was reopened during the main oxide silicate stage (MOSS). Biotite present along the schist-vein contact is partially replaced by muscovite. The muscovite selvage formed during the MOSS and the biotite are both crosscut by the chalcopyrite of the late sulfide stage (MSS). (f) Zoom on grains of biotite partially replaced by muscovite, which is associated with tourmaline. (g) Zoom on biotite selvage crosscut by chalcopyrite

Figure 28 Macroscopic characteristics of the quartz-tourmaline stage (QTS) of the mineralized system of Panasqueira. (a) to (c) veins with tourmalines along the schist vein-contact. (d) Field evidence of the preferential crystallization of tourmaline in the vertical foliation planes. (e) and (f) examples of tourmalinite haloes developed around veins. (g) Example of mineralized vein in mine with tourmaline along the vein edge, (h) zoom on the schist vein contact showing the vertical growth of tourmaline.

Figure 29 Microscopic characteristics of the quartz-tourmaline (QTS) of the mineralized systems of Panasqueira. Sections of veins tourmaline (a) parallel and (b) perpendicular to the trigonal axis of tourmaline. (c) Sample showing the relationship between a mineralized vein and the tourmalinization of the wall-rock, d and f give the location of the thin sections d and f. In this sample, the vein selvage is composed of muscovite and apatite related to the MOSS (note the preferential crystallization of tourmaline in the foliation planes). (d) Photomicrograph showing the contact between mineralized vein and tourmalinized wall-rocks. (e) Zoom on tourmalines present in the altered schist. Note the preferential crystallization of tourmaline in an inherited more pelitic layer. (f) Zoom on tourmaline, which has preferentially crystallized in the foliation planes.

Figure 30 Macroscopic characteristics of the main oxide silicate stage (MOSS) of the mineralized systems of Panasqueira. (a) to (c) typical quartz-muscovite veins mineralized in wolframite. The muscovite is generally located along the schist-vein contacts as selvage and can be also present within the veins. Quartz can exhibit geodic texture as displayed in (c). (d) Zoom on a schist-vein contact showing the relationship between the muscovite selvage and the wolframite. (e) to (h) examples of quartz-topaz veins present in the southwestern part of the mine. In these veins the muscovite is rare and the vein selvage is composed of topaz.

Figure 31 Microscopic characteristics of the main oxide silicate stage (MOSS) of the mineralized systems of Panasqueira. (a) Muscovite selvage associated to apatite. This selvage is crosscut by arsenopyrite and chalcopyrite related to the sulfide stage (MSS). (b) Sample of vein exhibiting relationship between the quartz-biotite (QB) stage, the quartz-tourmaline stage (QT), the main oxide silicate stage (MOSS) and the main sulfide stage (MSS). This photomicrograph shows clearly that the quartz-biotite vein was reopened during the quartz-tourmaline stage and then during the main oxide silicate stage. The muscovite selvage as then crosscut by arsenopyrite and chalcopyrite during the sulfide stage (MSS). (c) Section of quartz-wolframite vein cut perpendicular to the c-axis of quartz and parallel the vein plane. This section exhibits euhedral quartz with geodic texture, which was then infilled by the late carbonate stage (LCS). (d) Relationship between muscovite and cassiterite along the vein selvage. (e) Section of vein cut perpendicular to the c-axis of tourmaline and parallel to the vein. This section displays the relationship between the tourmaline stage (QT), the muscovite stage (MOSS) and the sulfide stage (MSS).

Figure 32 (a) and (b) Photomicrographs showing the relationship between the muscovite selvage and wolframite of the MOSS. (c) Zoom on muscovite-wolframite contact showing the crystallization of wolframite in some cleavage planes of muscovite (indicated by the white arrow). (d) Inclusion of muscovite in wolframite. These photomicrographs suggest that the crystallization of muscovite constituting the vein selvage predates the apparition of wolframite.

Figure 33 Macroscopic characteristics of the main sulfide stage (MSS) of the mineralized system of Panasqueira. (a) Quartz-muscovite-wolframite vein crosscut by pyrite-chalcopyrite assemblage during the sulfide stage. This picture emphasizes that veins were formed by several stages of opening and infilling (crack-and-seal texture).(b) Quartz-muscovite and quartz-muscovite-wolframite veins, in which the quartz was partially dissolved and corroded during the sulfide stage.(d) to (f) Examples of quartz-wolframite veins exhibiting euhedral quartz and geodic texture, which was infilled by arsenopyrite, chalcopyrite and pyrite during the sulfide stage.

Figure 34 Microscopic characteristics of the main sulfide stage (MSS) of the mineralized system of Panasqueira. (a) and (b) Muscovite-apatite selvage formed during the MOSS and crosscut by löllingite and arsenopyrite formed during the MSS. (c) Textural evidences showing that the crystallization of löllingite predates the apparition of arsenopyrite. (d) and (g) Textural relationship between arsenopyrite, pyrite and sphalerite showing that arsenopyrite is crosscut by the other sulfides related to the MSS. (e) and (f) Textural evidences emphasizing that muscovite related to the MSS predates the crystallization of arsenopyrite. (h) Textural relationship between the muscovite selvages related to the MOSS and the chalcopyrite, sphalerite and pyrite related to the MSS. Sulfides of the MSS infill the cleavage planes of muscovite and the open space between muscovite grains.

Figure 35 Photomicrographs showing the relationship between the W mineralization and the main sulfide stage (MSS). (a) Section of wolframite crosscut by chalcopyrite. (b) Section of wolframite partially altered and dissolved during the sulfide stage. (c) Section of wolframite crosscut by chalcopyrite. (d) Inclusion of partially altered section of wolframite in grain of arsenopyrite. (e) Section of wolframite altered during the sulfide stage.

Figure 36 Macroscopic characteristics of the late carbonate stage (LCS) of the mineralized system of Panasqueira. (a) and (b) Vertical fault infilled by dolomite, calcite and pyrite assemblage. (c) and (d) Open voids in horizontal mineralized veins partially infilled by dolomite, galena and calcite. (e) to (g) Vertical fault infilled by the LCS assemblage exhibiting a late generation of cassiterite (photo from Pinto et al., 2015).

Figure 37 Microscopic characteristics of the late carbonate stage (LCS) of the mineralized system of Panasqueira. (a) to (f) Infilling of the remaining open spaces present in the horizontal mineralized veins by dolomite, pyrite and calcite assemblage related to the LCS. (g) Relationship between the sulfides of the MSS and the carbonates related to the LCS. (h) SEM photomicrograph showing the occurrence of late cassiterite within fracture crosscutting a grain of arsenopyrite. The late generation of cassiterite is associated with siderite (Photomicrograph from Pinto et al., 2015).

Figure 38 Simplified paragenetic sequence of the W-Sn-(Cu) mineralized veins system of Panasqueira (modified from the paragenetic sequence of Kelly and Rye, 1979 and Polya et *al*., 2000) The red lines correspond to main fracturing events and the red dashed lines correspond to crack and seal events.

Chapitre III

Figure 1 Natural examples of asymmetric growth of minerals, which have crystallized from a flowing solution in hydrothermal systems. (a) Section of quartz cut perpendicular to the <c> axis showing transparent (dark) quartz in the center surrounded by translucent (white) quartz exhibiting an anisotropic overgrowth (Newhouse, 1941). (b) Crystal of galena characterized by an asymmetric shape due to crystallization from a flowing solution (Pine Point, Kessler, 1972). (c) Example of fluid flow reconstruction in a vertical quartz vein, in which sections cut perpendicular to the <c> axis of quartz permit to determine direction of fluid flow from the study of the asymmetric shape of quartz (Engel, 1948). (d) Polished section of galena parallel to the sedimentary bedding showing growth bands or compositional zoning (Southeastern Missouri lead deposits from Newhouse, 1941). The red arrows give the approximate sense of fluid flow deduced by the authors from the asymmetric shape of minerals.

Figure 2 Effect of the fluid velocity on the growth rate of crystals of alun at 32°C. Effects of the fluid oversaturation are also plotted (σ_v) (Experimental data from Garside, 1975).

Figure 3 (a) Experimental results obtained for crystals of alun which have grown from a statistic solution (photo on the left) and from a flowing solution (photo on the right) (Experiments performed by Essalhi, 2009). (b) Experimental results obtained by Prieto and Amoros, (1981) for crystal of KDP showing the growth rate of the crystal faces exposed, parallel and opposed to the fluid flow as a function of the fluid velocity. For a laminar fluid flow ($v_f < 3$ cm.s^{-1}) the upstream face is characterized by a growth rate higher than the downstream face. For turbulent fluid flow ($v_f > 3$ cm.s^{-1}) the crystal growth is isotropic and the symmetry of the crystal shape is conserved.

Figure 4 Numerical modeling of crystal growth in a flowing solution performed with the method proposed by Sizaret et al., 2009. This model was performed using a hexagonal crystal deduced from the geometric properties of tourmaline of Panasqueira (edge size of 50 µm). The symmetry condition is applied for boundaries parallel to the fluid flow. A dimensionless concentration of 1 and a fixed velocity (v_f) are used for the left boundary. Along the crystal edges, the dimensionless concentration is fixed at 0. (a) Variation of the dimensionless concentration around the crystal of tourmaline and chemical flux recorded by each crystal faces for fluid velocity of 10^{-6} and 10^{-3} m.s^{-1}. (b) Concentration profiles parallel to the fluid flow passing through the crystal of tourmaline for fluid velocity of 10^{-6} and 10^{-3} m.s^{-1}.

Figure 5 (a) Tectonic map of the Variscan Iberian massif showing the main tectonostratigraphic domains defined by Julivert et al., (1972). The location of the Panasqueira deposit is marked by a red star. CZ: Cantabrian Zone, WALZ: West Asturian-Leonese Zone, GTOMZ: Galicia Tràs-os-Montes Zone, CIZ: Central Iberian Zone, OMZ: Ossa-Morena Zone and SPZ: South Portuguese Zone (b) Geological map of the Panasqueira ore deposit showing the altitude of the granite roof. (c) Geological cross section (A-A') displaying the spatial relationship between mineralized veins and the greisen cupola (data source Beralt Tin & Wolfram S.A.).

Figure 6 The mineralized system at the Panasqueira W-Sn-(Cu) deposit. (a) Contact between the greisen cupola and the tourmalinized metasedimentary host rock on Level 1 of the mine. Note the presence of mineralized veins that crosscut this contact. (b) Typical Quartz-Wolframite veins corresponding to the main oxide stage. (c) Quartz-Wolframite veins intersected by the late sulfide stage carrying the Cu mineralization. Abbreviations from Whitney and Evans (2010) Ccp: Chalcopyrite, Ms: Muscovite, Qz: Quartz, Wf: Wolframite.

Figure 7 Textural and petrographic characteristics of tourmalines present in the mineralized system of Panasqueira. (a) Quartz-tourmaline vein with tourmalinization of the metasedimentary wall-rocks. The white dashed line indicates the tourmalinization front in the metasedimentary host rock. Arrows c and d indicate the orientation of thin sections c and d. Note the preferential migration of the tourmalinization front in the vertical foliation planes S_1 (b) Sample of mineralized veins showing the vertical growth of acicular tourmalines along the schist-vein contact. (c) and (d) photomicrographs of vein tourmaline showing sections parallel (c) and normal (d) to the <c> axis of tourmaline. (e) Photomicrograph of mineralized vein showing tourmaline grains associated with cassiterite. (f) SEM photomicrograph of altered schist perpendicular to the foliations planes showing growth band zoning in tourmaline basal sections. Abbreviations from Whitney and Evans (2010) Ap: Apatite, Cst: Cassiterite, Ms: Muscovite, Qz: Quartz, Tur: Tourmaline.

Figure 8 Examples of basal sections of tourmaline from veins (a) and altered wall-rocks (b) displaying an asymmetric shape caused by an anisotropic growth (c) Measurements of growth bands thickness and orientation on a basal section of tourmaline. (d) Curve deduced from numerical modeling showing relationship between fluid velocity and flux ratio (see text for details). The filled boxes indicate range of averages of fluid velocities derived from d_{max}/d_{min} ratio measured on tourmalines from altered wall-rocks (blue) and veins (red).

Table 1 Directions and velocities of fluid flow deduced from measurements on tourmaline growth bands in veins and in altered wall-rocks (SD: Standard Deviation and N: number of measurement).

Figure 9 Fluid flow at the ore deposit scale deduced from tourmaline growth bands in mineralized veins. (a) Large scale map of paleo-fluid flow around the hidden granite of Panasqueira. Local fluid flow direction and velocities are represented by "rose" diagrams, which give the direction of tourmaline faces exposed to the fluid flow (d_{max}) and the directional distribution of fluid velocities. The orange arcs indicate the 95% interval of confidence regarding the direction from which the fluid comes. The orange arrows on the map correspond to the mean directions of flow determined for each sample site. N corresponds to the number of measurements performed for each sample sites. (b) Results of fluid flow directions projected onto the geological cross section (B-B') showing flows moving away from the cupola. (c) Histogram showing distribution of all fluid velocity values.

Figure 10 Sketch showing vertical paleo-fluid flow deduced from tourmaline in altered wall-rocks. Fluid flow directions are represented by rose diagrams giving the direction of faces exposed to fluid flow. The red arcs indicate the 95% interval of confidence, regarding the direction from which the fluid comes. Velocity values obtained above, below and within the vein are presented in histogram diagrams. N corresponds to the number of measurement performed for each sample.

Table 2 Summary of EPMA and LA-ICP-MS results for cores and rims of tourmalines from veins and altered wall-rocks

Figure 11 Geochemical characteristics of tourmalines used for fluid flow reconstruction in veins and altered wall-rocks. (a) $Al_{50}Fe_{50}$-$Al_{50}Mg_{50}$ ternary diagram showing relation between tourmaline compositions and crystallization environment (from Henry and Guidotti, 1985). (1) Li-rich granitoids, pegmatites and aplites; (2) Li-depleted granitoids, pegmatites and aplites; (3) Fe^{3+}-rich hydrothermally altered granitoids; (4) Metapelites and metapsammites with Al-saturating phase; (5) Metapelites and metapsammites without Al-saturating phase; (6) Fe^{3+}-rich metapelites and calc-silicate rocks with quartz and tourmaline; (7) Cr-V-rich metapelites and Ca-depleted meta-ultramafic rocks (8) Meta-carbonates and meta-pyroxenites. (b) Element variation diagrams showing chemical core-rim evolution of tourmalines in minor (Na, K and Ti) and trace (Li, Mn, Sn and Sr) elements.

Figure 12 Hydrodynamic model of fluid flow at the magmatic-hydrothermal transition of the Panasqueira W-Sn-(Cu) deposit (after a simplified cross section from Thadeu, 1951). P_f: the fluid pressure condition, σ_3: the vertical stress and T: the tensile strength.

Figure 1 (a) Geological map of the Panasqueira district showing the spatial relationships between the non-outcropping granite intrusion and the mineralized vein system of Panasqueira. (b) Cross section (A-A') displaying the spatial relationship between the greisen cupola and the mineralized veins. The emplacement of the SCB2 drill-hole is also indicated. (c) Rose diagrams showing the strike directions of the greisenized aplites present over the Panasqueira district and the regional schistosity (S1).

Figure 2 Macroscopic characteristics of the greisenized aplites present over the Panasqueira district. (a) and (b) Sub-vertical greisenized aplites preferentially emplaced within the regional vertical foliation planes. Note the intense tourmalinization of the metasedimentary host rocks around the greisenized aplites. (c) and (d) Greisenized aplite mineralized in wolframite. (e) Contact between a mineralized greisenized aplite and the tourmalinized metasedimentary host rock. The greisen is characterized by a porous texture and exhibits a disseminated cassiterite mineralization.

Figure 3 (a) General views of the different facies of granite and greisen observed in the drill hole SCB2. The vertical evolution of the whole rock concentrations in Sn and W along the drill hole is also reported (data source Beralt Tin & Wolfram S.A.). (b) Textural characteristics of 1: Contact between the greisen and the metasedimentary host rock strongly tourmalinized, 2: facies of the most altered greisen (quartz-muscovite greisen) displaying a well-developed porosity, 3: propagation of greisenization around a mineralized vein present in the deeper part of the drill hole, 4: unaltered porphyritic two-mica granite and 5: more evolved leucogranite. Mineral abbreviation from Whitney and Evans (2010) Ab: albite, Bt: biotite, Kfs: K-feldspar, Ms: muscovite, Pl: plagioclase, Qz: quartz.

Figure 4 Macroscopic characteristics of the greisen cupola observed in the underground mining works (Level 1) (a) Contact between the massive greisen cupola and the tourmalinized metasedimentary host rock. This contact is crosscut by a mineralized quartz vein (b) Greisenized aplite crosscutting a vertical barren quartz vein (Seixo bravo) (c) Typical flat mineralized (quartz, muscovite, wolframite and sulfides) vein hosted by the massive greisen cupola. (d) Quartz mineralized vein hosted by the greisen cupola in which we can observe a greisen enclave (e) Sample showing the contact between the greisen cupola and the tourmalinized metasedimentary host rock. The greisen is intensively silicified and exhibits a disseminated chalcopyrite mineralization. (f) Sample of massive greisen collected in the cupola showing an intense silicification and a disseminated sulfide mineralization (chalcopyrite, pyrrhotite and sphalerite). This sample exhibits a large pore (pocket) completely infilled by euhedral quartz, apatite and sulfides. Abbreviations from Whitney and Evans (2010) Ap: Apatite, Apy: Arsenopyrite, Ccp: Chalcopyrite, Ms: Muscovite, Qz: Quartz, Wf: Wolframite.

Figure 5 Photomicrographs showing the mineralogical and the textural characteristics of the two-mica granite of Panasqueira. (a) General view of the two-micas granite (b) Phenocryst of k-feldspar marked by perthitic and poikilitic textures (c) Typical snowball quartz displaying a fluid inclusions trail (d) Grain of albite comprising inclusion of apatite (e) Grain of biotite comprising numerous inclusions of zircons and apatite (f) Igneous muscovite aggregate. (g) Zoom on the apatite inclusion presents in figure 5e. A grain of zircon is included in this grain of apatite. Abbreviations from Whitney and Evans (2010) Ab: Albite, Ap: Apatite, Bt: Biotite, Kfs: k-feldspar, Ms: Muscovite, Qz: Quartz, Zrn: Zircon.

Figure 6 Photomicrographs showing the mineralogical and the textural characteristics of the massive greisen of Panasqueira. (a) General view of the quartz-muscovite greisen (b) General view of a highly porous quartz-muscovite greisen (sample collected within a greisenized aplite) (c) Grain of k-feldspar completely replaced by muscovite in greisenized granite (d) Grain of albite partially replaced by muscovite during the greisenization (e) Crystal of biotite partially bleached and replaced by muscovite. Note the exsolution of rutile during the replacement of biotite. (f) Large flake of neoformed muscovite resulting from the total replacement of a biotite crystal. Note that zircon initially included in biotite was conserved in the neoformed muscovite. (g) Snowball quartz conserved in greisen during the greisenization. This quartz is marked by overgrowth in which we can observe relics of albite and grains of muscovite. Abbreviations from Whitney and Evans (2010) Ab: Albite, Bt: Biotite, Kfs: k-feldspar, Ms: Muscovite, Qz: Quartz, Zrn: Zircon.

Figure 7 Photomicrographs displaying the mineralogical and the textural characteristics of the disseminated mineralization observed in the massive greisen of Panasqueira. (a) Magmatic apatite conserved in greisen and grain of cassiterite, which has crystallized within a pore space. (b) Large pore completely infilled by euhedral quartz and sulfides (chalcopyrite, sphalerite and pyrite). (c) Grain of cassiterite infilling the

porosity observed in the massive greisen. (d) Chalcopyrite associated with hydrothermal rutile. (e) SEM photomicrograph displaying a complex sector zoning in the hydrothermal rutile observed in the massive greisen. (f) Greisen porosity infilled by sphalerite and pyrite. (g) and (h) Coronitic texture composed of stannite displaying interaction between cassiterite related to the MOSS and chalcopyrite related to the MSS. (i) Partial replacement of pyrrhotite by pyrite during the pyrrhotite alteration stage (PAS). (j) Galena related to the PAS that crosscuts chalcopyrite formed during the sulfide stage (MSS). (k) Large pocket completely infilled by sulfides and carbonate minerals during the late carbonate stage (LCS). Note the crystallization of euhedral quartz along the pore edges. Abbreviations from Whitney and Evans (2010) Ap: Apatite, Cal: Calcite, Ccp: Chalcopyrite, Cst: Cassiterite, Gn: Galena, Ms: Muscovite, Po: Pyrrhotite, Py: Pyrite, Qz: Quartz, Rt: Rutile, Stn: Stannite, Zrn: Zircon.

Figure 8 Simplified paragenetic sequence proposed for the massive greisen of Panasqueira. This sequence includes magmatic, greisenization and mineralization stages observed in the massive greisen. The red crosses indicate the breakdown of magmatic minerals induced by the greisenization processes.

Figure 9 SEM and chemical maps of Al, Fe and Na of primary magmatic muscovite composing the unaltered two mica granite of Panasqueira. These magmatic muscovites are unzoned and exhibit homogeneous composition.

Figure 10 SEM and chemical maps of Al, Fe and Na of muscovites composing the massive greisen of Panasqueira. These muscovites exhibit a strong zoning corresponding to growth and chemical zoning.

Figure 11 Photomicrographs displaying the textural characteristics of the muscovite selvage observed along the schist-vein contacts. (a) Relationships between muscovite and tourmaline formed during the QTS. (b) Relationship between muscovite and cassiterite along the vein selvage. (c) SEM photomicrograph showing that muscovite is generally homogeneous. (d) Relationship between the muscovite selvage and wolframite.

Figure 12 Transmitted light (a to b) and SEM-cathodoluminescence images (c to d) of magmatic quartz phenocryst composing the two-mica granite of Panasqueira. These quartz exhibit snowball texture with weakly contrasting growth zoning. These concentric growth zoning are locally overprinted by a dense network of healed fractures infilled by non-luminescent quartz (CL-dark structures).

Figure 13 Transmitted light (a) and SEM-cathodoluminescence images (b to d) of remnants of primary magmatic snowball quartz partially altered during the greisenisation. These quartz grains exhibit hydrothermal overgrowth characterized by lower luminescence intensity than the primary snowball cores. In some cases the primary concentric growth zoning are conserved. The CL-dark structures correspond to healed fractures underlined by fluid inclusions trails in transmitted light.

Figure 14 Transmitted light and SEM-cathodoluminescence images of hydrothermal quartz formed during to the quartz tourmaline stage (QTS) (a to b) and during the main oxide silicate stage (MOSS) (c to d). These sections were cut horizontally and perpendicular to the <c> axis of quartz. These two generations of quartz exhibit thin, contrasted, oscillatory growth zoning. The dense network of CL-dark structures corresponds to fractures healed by non-luminescent quartz. Quartz can be partially corroded (red dashed line in d) and marked by sector zoning. Abbreviations from Whitney and Evans (2010) Cal: Calcite, Cst: Cassiterite, Ms: Muscovite, Qz: Quartz, Tur: Tourmaline, Wlf: Wolframite.

Figure 15 Cathodoluminescence images (CL) of magmatic apatites from the unaltered two-mica granite of Panasqueira. (a) Grain of magmatic apatite included within a phenocryst of albite. This grain was slightly altered along the grain boundaries (lighter zones). (b) Two grains of magmatic apatite with uniform luminescence included within biotite. (c) and (d) Grains of magmatic apatite partially altered along their boundaries (zones with higher luminescence intensity).

Figure 16 Cathodoluminescence images (CL) of altered magmatic apatites from the massive greisen of Panasqueira. These grains of apatite were altered during the greisenization of the two-mica granite. (a) Grain of magmatic apatite partially altered during the greisenization showing that the dark-luminescent magmatic apatite was replaced by a light-grey luminescent apatite along the grain boundaries. (b) Grain of magmatic apatite strongly and pervasively altered during the greisenization. This grain exhibits typical patchy zoning texture. The dark-luminescent primary apatite is practically entirely replaced by white and dark-grey luminescent secondary apatite. (c) and (d) Grains of primary magmatic apatite altered and replaced by a secondary light-grey-luminescent apatite. These grains are also marked by hydrothermal overgrowths (thin oscillatory zoning) along the grain boundaries.

Figure 17 Cathodoluminescence images (CL) of hydrothermal apatites associated to muscovite selvage from mineralized veins of Panasqueira. (a) Photomicrograph (transmitted light) showing textural relationships between apatite and muscovite selvage present along the schist-vein contacts. Some apatites were crosscut by arsenopyrite during the main sulfide stage (MSS). Dashed white rectangles give emplacement of apatite grains displayed in b, c and d. (b) and (c) typical grains of euhedral hydrothermal apatite present within the muscovite selvage. These apatites exhibit growth oscillatory zoning. (d) and (e) Grains of hydrothermal apatite altered during the late mineralization stages (sulfide stage).

Figure 18 Whole-rock geochemical characteristics of the two-mica granite, the leucogranite and the massive greisen of Panasqueira. (a) Diagram of aluminous saturation index (A/NK vs. A/CNK) of the different granite facies and the massive greisen of Panasqueira. (b) Chondrite-normalized REE pattern of the two-mica granite, the leucogranite and the massive greisen. (c) and (d) Multicationic discriminating diagrams of Debon & LeFort (1983). (e) Relative mass changes in the leucogranite and the massive greisen compared to the porphyritic two-mica granite (calculated from average values). (f) and (g) Evolution of concentrations in W and Sn in whole-rock as a function of the aluminosity index ratio A/CNK.

Figure 19 Geochemical characteristics of muscovite composing the unaltered two-mica granite, the greisenized granite, the massive greisen and the selvages of mineralized veins of Panasqueira. (a) Ternary Ti-Na-Mg diagram displaying the fields of primary and secondary muscovite (after Miller et al., 1981). (b) Compositions of muscovite plotted in the mineralochemical phase diagrams (Al-(Fe+Mg+Mn)-Si) of Monier and Robert (1986). (c) Binary diagrams displaying the content in Ti, Na, Fe and F (in apfu) as a function of the content in Al (in apfu) for the different studied muscovite (d) Application of the Monier and Robert (1986) thermometer on the magmatic and hydrothermal muscovite present in the system of Panasqueira.

Table 1 Average compositions in major (wt%) and trace elements (ppm) of muscovite composing the unaltered two-mica granite, the greisenized granite, the massive greisen and the selvages of mineralized veins of Panasqueira.

Figure 20 Binary diagrams displaying the trace element content for the different generations of muscovite considered in this study. The concentration (in ppm) of Li, Cs, Zn, Sn and W are plotted as a function of the concentration in Rb.

Figure 21 Evolution of the chemical characteristics of rutile during greisenization. (a) SEM photomicrograph of rutile formed during the greisenization. (b) Chemical map of W in the grain of rutile displayed in b. (c) Ternary diagrams displaying the content in Fe, Ti, Sn and W in rutile composing the unaltered two-mica granite, the greisenized granite and the massive greisen of Panasqueira.

Table 2 Average compositions (wt%) of rutile composing the unaltered two mica granite, the greisenized granite and the massive greisen of Panasqueira.

Figure 22 SEM-CL image and chemical maps of Ti, Li and B of a snowball quartz grain composing the unaltered two-mica granite. The chemical maps were performed by LA-ICP-MS following the same analytical procedure described in the subsection 5.2.

Figure 23 SEM-CL image and compositional profiles (Al, Ti, Na, Li, B and Ge) performed across a representative grain of snowball quartz overprinted by the greisenization (overgrowth). Abbreviations, c: core and r: rim.

Figure 24 Spider diagrams displaying trace element contents in the different generations of quartz considered in this study. The grey dashed line corresponds to the detection limit. Color lines correspond to median values for each quartz generation. Color domains were defined from maximal and minimal concentrations for each element.

Table 3 Summary of trace elements composition for quartz composing the unaltered two-mica granite and the massive greisen of Panasqueira

Table 4 Summary of trace elements composition for quartz composing the quartz tourmaline stage and the W-Sn mineralization stage of the mineralized veins of Panasqueira

Figure 25 Chemical evolution trends from magmatic to hydrothermal quartz displaying the behavior of Ti, Al, Ge, Li, Rb and B during magmatic-hydrothermal evolution of the Panasqueira ore deposit.

Figure 26 Temperatures of quartz crystallization obtained for the different generations of magmatic and hydrothermal quartz of the unaltered two-mica granite, greisen and mineralized veins. Temperatures were obtained by applying the TitaniQ geothermometer defined by Thomas et al. (2010) at (a) 1 and (b) 2 kbar for Ti activity ranging from 0.2 to 1. Red and blue dashed lines give respectively the ranges of temperatures obtained from primary magmatic muscovite and from hydrothermal muscovite of greisen and veins.

Figure 27 Compilation of chemical signatures (Ge/Ti vs Al/Ti) of quartz from different magmatic and magmatic-hydrothermal systems. Data were compiled from the synthesis of Breiter et al., (2017) and from data of Monnier et al., (2018) for the rare-metal granite of Beauvoir.

Figure 28 Tera-Wasserburg concordia diagrams, in which apatite analyses were reported to define lower intercept date. (a) Results obtained for magmatic apatite from the unaltered two-mica granite. (b) Results obtained for altered magmatic apatite from greisen. Black ellipses correspond to analyses of altered magmatic apatite and red ellipses correspond to hydrothermal oscillatory zoning overgrowth (c) Results obtained for hydrothermal apatite from mineralized veins (veins selvages). The black dashed lines represent the unforced discordias used for age determination, the $^{207}Pb/^{206}Pb$ values obtained from the upper intersect of discordias are also indicated. Ellipses and errors on ages are reported at 2σ.

Figure 29 Comparison and compilation of dating data from this study (U-Pb on apatite) and from Snee et al. (1981) (Ar/Ar on muscovite) on the magmatic-hydrothermal system of Panasqueira. The Ar/Ar ages were reported here with 2σ error bars.

Figure 30 Average concentrations and standard deviations of elements detected in fluid inclusions associated with the main oxide silicate stage (MOSS, W-Sn mineralization event) in veins. Data from Lecumberri-Sanchez et al. (2017). Fluid inclusions were analyzed at different distance of the cupola.

Chapitre V

Figure 1 (a) Location of the Panasqueira ore deposit in the Iberian Variscan belt (red star) (b) Geological map of the Panasqueira W-Sn-(Cu) ore deposit including the location of the drill hole SCB2 (white star) used in this study. (c) The (A-A') geological cross section displays the spatial relationship between the mineralized veins and the massive greisen constituting the top of the granite intrusion (data source Beralt Tin & Wolfram S.A.) (modified from Launay et al., 2018). Abbreviations, CZ: Cantabrian Zone, WALZ: West Asturian-Leonese Zone, GTOMZ: Galicia Tràs-os-Montes Zone, CIZ: Central Iberian Zone, OMZ: Ossa-Morena Zone and SPZ: South Portuguese Zone.

Figure 2 (a) Drill hole SCB2 showing the vertical mineral zoning of the greisen alteration (b) Macroscopic textural characteristics of 1:facies of the most altered greisen displaying a well-developed porosity, 2: quartz-muscovite greisen in which it is possible to observe pieces of less altered granite (white dashed lines correspond to the alteration front and white arrows to the expected direction of propagation), 3: propagation of the pervasive greisenization toward the Panasqueira granite, 4: propagation of alteration from fracture in deeper part of the drill hole and 5: the porphyritic two-mica granite of Panasqueira. Mineral abbreviation from Whitney and Evans (2010) Ab: albite, Bt: biotite, Kfs: K-feldspar, Ms: muscovite, Qz: quartz.

Figure 3 Apparatus used for the experiment of greisenization coupled with permeability measurement (a) External heated pressure vessel equipped with two metering pumps used for the pore fluid system and the permeability measurement (b) Connection between the granite core (encapsulated in the Au jacket) and the pore fluid system. Red arrows give the sense of fluid flow in the pore fluid system. (c) log(NaCl/HCl) vs. log(KCl/HCl diagram displaying the stability fields of albite, muscovite and k-feldspars at the experimental conditions used for the greisenization experiment (300°C and 300 bar). The white star gives the composition of the starting solution used for the experiment. This diagram was established from the thermodynamic database of SUPCRTLB (Zimmer et al., 2016 and Johnson et al., 1992).

Figure 4 Mineralogical and microtextural characteristics of the two-mica granite of Panasqueira. (a) Photomicrograph displaying the general view of the two-mica granite (transmitted light). (b) Photomicrograph of matrix k-feldspars exhibiting typical perthitic textures (polarized transmitted light). (c) Phenocryst of k-feldspar marked by poikilitic textures (inclusions of biotite, albite and apatite) (transmitted light). (d) Cathodoluminescence image of the same k-feldspar phenocryst displayed in c. This grain exhibits blue and red luminescent zones corresponding to different chemical compositions (indicated on image) and are related to K-metasomatism of primary magmatic alkali feldspars (blue luminescent zones). (e) Large euhedral flake of biotite comprising numerous zircon and apatite inclusions (transmitted light). (f) Phenocryst of albite comprising quartz and apatite inclusions. The chemical composition of albite is indicated on the photomicrograph (polarized transmitted light). (g) and (h) SEM-BSE images of albite displaying typical pitted textures marked by the occurrence of a dense network of micropores. Abbreviations from Whitney and Evans (2010) Ab: Albite, Ap: Apatite, Bt: Biotite, Kfs: k-feldspar, Ms: Muscovite, Or: Orthoclase; Qz: Quartz, Zrn: Zircon

Figure 5 SEM microphotographs and element mapping of Na, K and Al displaying the replacement textures of (a) albite, (b) K-feldspar and (c) biotite involved during the greisen alteration. Note the development of micro-porosity in the altered sections of K-feldspar and albite. Abbreviations from Whitney and Evans (2010) Ab: Albite, Bt: Biotite, Kfs: k-feldspar, Ms: Muscovite, Qz: Quartz.

Figure 6: SEM-BSE images displaying the microtextural evolution induced by the greisenization of the Panasqueira granite. (a) Porous texture in a greisenized granite sample showing the heterogeneous distribution of the porosity. A microporous pocket and a microcrack are labelled on image. (b) Zoom on a microporous pocket showing the intergranular porosity corresponding to spaces around muscovite grains. (c) Porous texture in greisen showing large pores corresponding to spaces around muscovite grains (This section was made from sample displayed in Figure 2b-1). (d) Porous greisen, in which a large amount of hydrothermal apatite have crystallized during the late hydrothermal stages. (e) Large void space fringed by euhedral quartz, which have crystallized from the pore edge. (f) SEM-BSE image displaying hydrothermal overgrowth of muscovite composing greisen and pore space partially infilled by hydrothermal apatite. (g) Fe and (h) Al chemical maps performed on section displayed on (f). Abbreviations from Whitney and Evans (2010) Ab: Albite, Ap: Apatite, Ms: Muscovite, Qz: Quartz.

Figure 7 Isocon diagram comparing the chemical composition of the least altered granite and the greisen of Panasqueira. Granite composition is an average of 5 analyses. Oxides analyses are in wt% and trace elements in ppm, values are scaled with the factors indicated for each element. The best fit isocon (blue line) defined from P_2O_5, Al_2O_3, MnO and Fe_2O_3 is compatible with an immobile alumina during the greisen alteration. This best fit is characterized by a slope of 1.12 corresponding to a volume decrease of about 12.4 %. For comparison isocon based on hypotheses of constant mass (black line) and constant volume (dashed line) are also plotted.

Table 1 Molar volume changes (ΔV) induced by the replacement reactions related to the greisen alteration of the least altered granite of Panasqueira. ΔV (cm^3/mol) are calculated at 400°C and 100 MPa using the thermodynamic database of SUPCRTBL. ΔV (%) is the molar volume change relative to the molar volume of the reactant minerals.

Figure 8 Time evolution of permeability during the greisenization experiment. This time evolution depicts cycles of permeability increases followed by stages of gradual decrease that can respectively attributed to porosity generation during the replacement reactions and sealing by closing of the neoformed pathways. The stages of permeability decrease fit with exponential functions commonly observed in experimental studies.

Table 2 Rock petrophysical properties measured in samples of granite, greisenized granite and greisen of Panasqueira. AI corresponds to the chemical alteration index defined in section 4.3

Figure 9 Texture of the alteration products obtained during the greisenization experiment. (a-d) SEM-BSE images and element maps showing the distribution of Na, K and Fe in a partially altered part of the granite core. These maps display the pathways along which fluids have preferentially flowed and altered albite into muscovite during the experiment. (e) SEM photomicrograph showing the dissolution and enlargement of pathway along the grain boundary between quartz and albite and the development of micropore along the cleavage planes of albite. (f) SEM photomicrograph showing the microporous texture of a partially altered albite. (g) Zoom on a micropore developed during the experiment that was partially coated by euhedral quartz and muscovite. Abbreviations from Whitney and Evans (2010) Ab: Albite, Ms: Muscovite, Qz: Quartz.

Figure 10 Evolution of (a) matrix density, (b) connected porosity and (c) permeability as a function of the chemical alteration index (AI). The AI increases upon the greisen alteration (see the top horizontal qualitative axis and section 4.3 for explanation).

Figure 11 (a) Relationship between the matrix density and the connected porosity deduced from measurements performed on the granite-greisen samples of Panasqueira. (b) Relationship between the connected porosity and the permeability deduced from granite greisen samples in which porosity and permeability have been measured. Black and white dots correspond respectively to permeability values obtained at 25°C and 400°C. The dashed lined correspond to modelled permeability evolutions as a function of the rock porosity using power law equations (see text for explanations).

Figure 12 (a) Vertical evolution of the permeability and the content in Sn, W and Cu of the whole rock in the drill hole SCB2. The spatial correlation between the rock permeability and the content in metals suggest that greisen was probably a preferential pathway for fluids related to the main mineralization stages occurring in the vein system of Panasqueira. Greisen porosity infilled by ore bearing minerals (b) cassiterite (transmitted light) (b) chalcopyrite (reflected light) and (d-e) chalcopyrite and sphalerite (SEM-BSE images). Note the presence of sulphides within the cleavage planes of muscovite suggesting that these weakness planes can be potential pathway for fluids. Abbreviations from Whitney and Evans (2010) Ccp: Chalcopyrite, Cst: Cassiterite, Ms: Muscovite, Py: Pyrite, Qz: Quartz, Sp: Sphalerite.

Figure 13 (a) Compilation of the matrix density and porosity data measured in different granite-greisen systems. This compilation shows that the matrix density and porosity increase are common in greisen systems. This compilation suggests that feedback between greisen alteration and permeability can be a common process in this type of deposit. (b) Grade versus metal content for different types of large and high-grade, primary tin deposits (modified from Mlynarczyk et al., 2003). Note that greisen systems can constitute a high tonnage low grade tin deposits.

Figure 14 Conceptual model integrating the time evolution of permeability induced by the replacement reactions related to the greisenization of the Panasqueira granite. (a) Initiation of the granite cooling and fluid flow, which triggers the greisenization of the Panasqueira granite along the granite schist contact (permeable interface). (b) Alteration of the Panasqueira granite leading to the progressive replacement of feldspars and biotite into muscovite. This mineralogical transformation is accompanied by the porosity generation owing to the molar volume decreases associated to these replacement reactions. A positive feedback between the greisen alteration and permeability is assumed here to explain the propagation of the greisenization front and the development of massive greisens (c) The porosity generation induced by the greisen alteration enhance permeability and develop a potential permeable zone which can enhance fluid flow and metal transport. The presence of minerals bearing-metals (cassiterite and sulfides) in the newly formed porosity in greisen seems to confirm the role of massive greisen as drain for mineralizing fluids and explain the formation of this type of deposit.

Figure 15 Schematic illustration of the experimental apparatus used for the experiment of greisenization (modified from Seyfried et al., 1987). Note the connection between the syringe used for the sampling of solutions and the Ti-reaction cell.

Table 3 Time evolution of concentrations of selected dissolved species and pH obtained during the greisenization experiment.xd

Figure 16: Evolution of pH and the concentrations (ppm and ppb) in Si, Ba, Ca, Sr, Mn, Mg and Fe with time. The data suggest that equilibrium between fluid and granite powder was attained at the end of the experiment.

Figure 17 SEM photomicrographs displaying the alteration products obtained during the greisenization experiment. (a) to (c) grains of albite and k-feldspar partially replaced by muscovite. (e) and (f) grains of albite partially replaced by k-feldspar. Abbreviations from Whitney and Evans 2010, Ab: albite, Kfs: k-feldspar and Ms: muscovite. Muscovite replacing feldspars exhibit a microporous texture compared to the parental feldspars.

Figure 18 (a) Evolution of the Sn solubility as a function of the HCl fugacity in fluids at 100 bar from 300 to 350°C (Mgdisov and Williams-Jones, 2005). (b) Evolution of the W solubility as a function of the HCl concentration in fluids at 1 kbar and from 300 to 600°C (Wood, 1992).

Figure 19 Conceptual model of greisen formation at the mineral scale. This model integrates the time evolution of permeability induced by the replacement reactions and effects of fluid rock interactions on the fluid chemistry. (t_1) Initial texture of the Panasqueira granite. (t_2) Replacement of feldspars and biotite induced by the greisenization. This mineralogical transformation induced permeability increase by porosity generation and the neutralization of the fluid acidity leading to a pH increase. The breakdown of feldspars and biotite releases Ba, Sr Na, K, Fe, Mg and Mn, whereas the crystallization of muscovite traps a part of Li, Cs, Rb and F from fluids. (t_3). The pathways developed by the replacement reactions enhance metal transport, while the fluid neutralization causes the precipitation of cassiterite in the newly formed porosity.

Chapitre VI

Figure 1 (a) Tectonic map displaying the tectonostratigraphic domains composing the Iberian massif (modified from Julivert et al., 1972). The location of the Panasqueira deposit is marked by a red star. CZ: Cantabrian Zone, WALZ: West Asturian-Leonese Zone, GTOMZ: Galicia Tràs-os-Montes Zone, CIZ: Central Iberian Zone, OMZ: Ossa-Morena Zone and SPZ: South Portuguese Zone. (b) Regional geological map of the W-Sn-(Cu) Panasqueira ore deposit, in which the lithogeochemical anomalies in W are represented (compiled from data of Oosterom et al., 1984). (c) The (A-A') geological cross section displaying the spatial relationships between the mineralized vein system, the greisen and the Panasqueira granite. (d) Cumulative vein thickness along the vertical sections of drill holes showing the vertical distribution of the mineralized vein network of Panasqueira (n refers to the number of veins crosscut by the drill holes) (drill holes data compiled from Foxford et al., 2000 and Wheeler, 2015).

Figure 2 Meshing and model geometry with a laccolith magma chamber of about 6 km of width for 2 km of height and a cupola at 2.7 km of depth. This geometry corresponds to the inferred geometry of the Panasqueira granite. The boundary and the initial conditions used for the modelling are also displayed. Cross-sections B-B' and C-C' refer to horizontal and vertical profiles used in Figures 6 to 9.

Table 1 Initial physical properties of rocks and fluid used for models. Eq(n) refers to equations presented in the text

Figure 3 Model of dynamic permeability in the country rocks domain describing the permeability increase induced by fluid overpressure conditions. (a) Permeability profile as function of depth (adapted from Ingebristen and Manning, 1999). Permeability increase induced by fluid overpressure conditions ($\lambda_v > 0.4$) are also displayed. For a given depth, the permeability increases by 2 orders of magnitude from the background value when the fluid pressure conditions are lithostatic ($\lambda_v = 1$). (b) Permeability evolution at 2 km of depth as function of the pore fluid factor (λ_v), shown here with a logarithmic scale. We assume that the permeability increases linearly with the pore fluid factor until lithostatic pressure conditions ($\lambda_v = 1$).

Figure 4 Alteration mineral phase diagram displaying crystallization and breakdown of minerals for the Butte granite as a function of the water/rock ratio and temperature conditions (modified from Reed et al., 2013). The red dashed line marks the total breakdown of primary magmatic minerals (albite, k-feldspars and biotite) and corresponds to the total greisenization of granite. Mineral abbreviations: Ab = Albite, Bt= Biotite, Kfs= k-feldspar, Ms= Muscovite.

Figure 5 Model of dynamic permeability in the granite intrusion describing the feedback between the greisenization, the porosity and the permeability (Experimental data after Launay et al., (submitted)). (a) Model of porosity evolution in greisen as a function of the water/rock (W/R) ratio and the alteration index ($AI = 100.(Al_2O_3/(Al_2O_3+K_2O+Na_2O))$). The conversion of the alteration index (AI) in water rock (W/R) ratio is detailed in the text. (b) Model of permeability evolution in greisen as function of the porosity generated during the greisenization. The red curves correspond to functions (Eq.(12) and Eq.(13)) used in numerical modeling to describe the porosity and the permeability evolution during the greisenization.

Figure 6 Results of time evolution of the fluid flow patterns and the time integrated fluid flux obtained for modeling with static granite permeability and without magmatic fluid production. After 50 kyrs a near steady state conditions are achieved

Figure 7 Results of time evolution of the fluid flow patterns and the time integrated fluid flux obtained for modeling with static granite permeability considering magmatic fluid production during the granite crystallization. Fluid flow is mainly controlled by expulsion processes during the first 10 kyrs and by convective circulation after 50 kyrs. (the localization of the vertical and the horizontal profiles are given in Figure 2).

Figure 8 Results of time evolution of the fluid flow patterns and the time integrated fluid flux obtained for modeling with static granite permeability considering dynamic permeability during the greisenization process and without fluid production. Fluid flow is mainly controlled by convective processes.

Figure 9 Results of time evolution of the fluid flow patterns and the time integrated fluid flux obtained for modeling considering both dynamic permeability and magmatic fluid production during the granite crystallization. Fluid flow is mainly controlled by expulsion processes during the first 10 kyrs and by convective circulation after 50 kyrs.

Figure 10 Time evolution of pore fluid factor and fluid flow velocity above and within the cupola (emplacements indicated by the blue and the red stars) in cases of magmatic fluid production without (left) and with (right) dynamic permeability in granite. Light grey areas correspond to the timespan of fluid production and dark grey areas highlight the sharp increase of fluid velocity and overpressure in the M4 model.

Figure 11 Effects of the dynamic permeability and the magmatic fluid production on the time evolution of fluid flux above the cupola (red area).

Figure 12 Time evolution of the greisen thickness resulting from fluid-rock interactions during fluid flow (for M1 to M4). We assume that W/R ratio of 2 marks the total breakdown of feldspars present in the granite and corresponds to the complete greisenization of granite (see explanation in section 3.6.3). The red line indicates the emplacement of profile along which, the time evolution of the greisen thickness has been determined.

Chapitre VII

Figure 1 Synthetic metallogenic model of formation of the W-Sn-(Cu) Panasqueira ore deposit integrating hydrodynamic and geological processes highlighted from results obtained in this study. Fluid flow between (t_1) and (t_2) is controlled by expulsion of magmatic ore-bearing fluids released and expelled during the magmatic-hydrothermal transition. Fluid flow related to the later stages (t_3) involved convective processes during which sulfide mineralization was deposed. More details are given in the main text.

Figure 2 Measured and modelled isotopic compositions of ore forming fluids related to the Main Oxide Silicate Stage (MOSS) and the Main Sulfide Stage (MSS) of the Panasqueira deposit (modified from Polya et al., 2000). Dashed orange and red curves correspond respectively to modelled equilibrium isotopic composition of meteoric water exchanged with coal rich metasediments and granite-schist. Water/Rock exchange ratios of 0.2, 0.02 and 0.002 are also reported.

Figure 3 Mineralogical and microtextural characteristics of the episyenitization of the Toki granite (Japan) (Nishimoto et al., 2010 and 2014). (a) Macroscopic characteristics of the unaltered Toki granite and the episyenite. (b) Photomicrograph showing porous texture of the episyenite and its mineralogical composition. (c) to (f) Photomicrographs showing occurrences of secondary minerals in vugs formed during the episyenitization.

Figure 4 (a) and (b) Macroscopic characteristics of partial epidotised pillow lavas composing oceanic crust (photo from Brett et al., 2017). (c) and (d) SEM-BSE images showing the development of porosity during epidotization (images from Cann et al., 2015). Note the crystallization of euhedral quartz in the void spaces. Mineral abbreviations, C: Chlorite, E: Epidote, Q: Quartz, V: void spaces.

Figure 5 Geological and textural characteristics of hydrothermal alterations involved during the formation of high sulphidation (HS) epithermal deposits. (a) Spatial zoning of hydrothermal alterations commonly observed in epithermal deposits (b) and (c) Textural characteristics of vuggy silica, which exhibits extremely porous texture (photographs from http://www.mininggeologyhq.com/epithermal/). (d) Textural characteristics of quartz-alunite zone whose the formation is accompanied by the development of porosity. (e) Conceptual model proposed by Mayer et al, (2016) considering the increase of permeability induced by acidic alterations related to the circulation of ore-bearing fluids. In this model the increase of permeability promotes the circulation of hydrothermal fluids.

Annexes

Supporting information for:

Chapter III: Deciphering fluid flow at the magmatic-hydrothermal transition: a case study from the world-class Panasqueira W-Sn-(Cu) ore deposit (Portugal)

Gaëtan Launay[1], Stanislas Sizaret[1], Laurent Guillou-Frottier[1], Eric Gloaguen[1] and Filipe Pinto[3,4]

(1) Université d'Orléans/CNRS/ISTO/BRGM, UMR 7327, 1A rue de la Férollerie, 45071 Orléans, France
(2) Beralt Tin & Wolfram, S.A., Geology Department, Barroca Grande, Portugal
(3) Institute of Earth Sciences (ICT), Pole of University of Porto, Rua do Campo Alegre 687, 4169-007 Porto, Portugal

---

1. Structural setting of the Panasqueira deposit

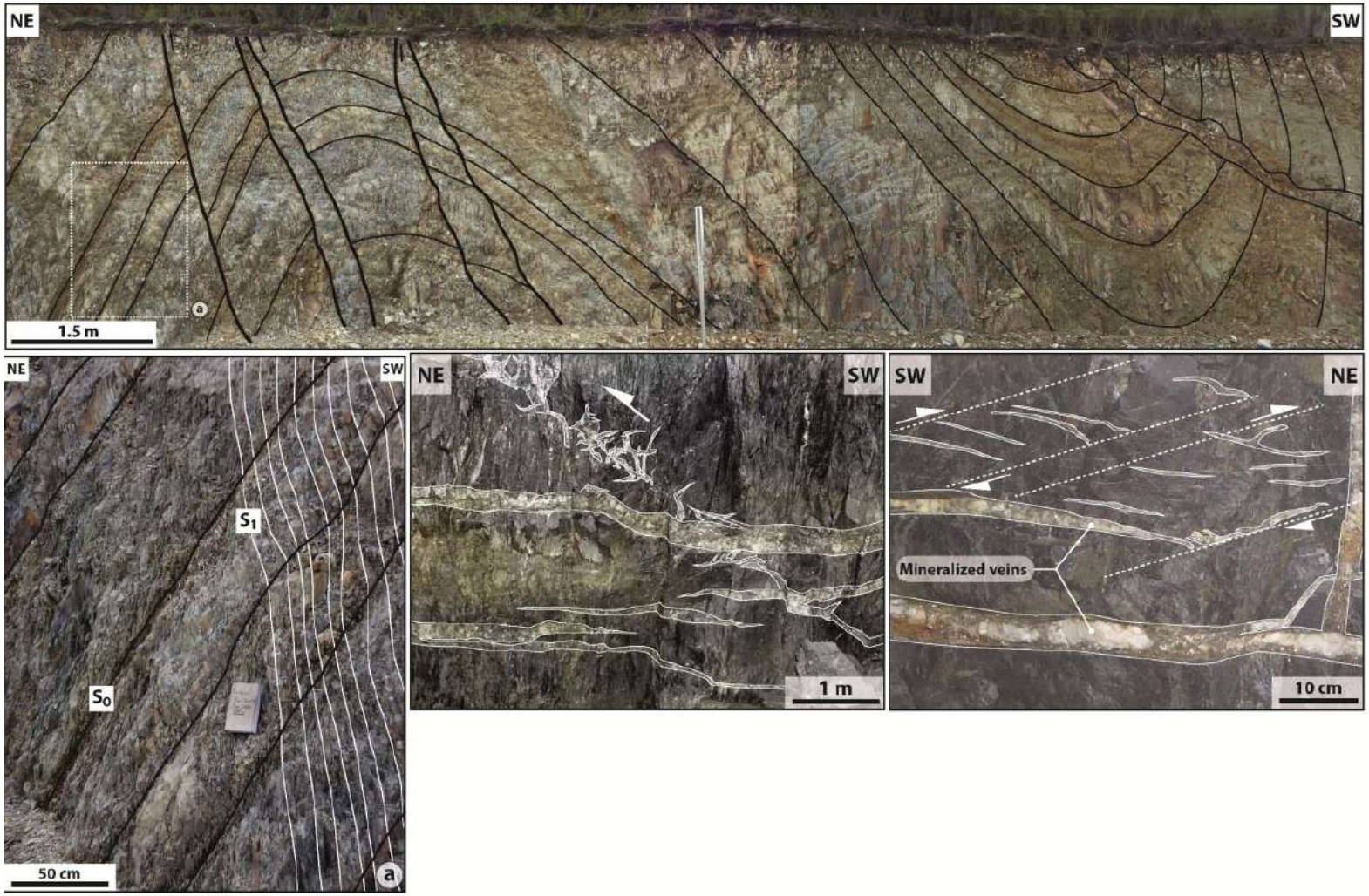

Figure 9 Field observations illustrating the structural setting of Panasqueira. The photo at the top shows the tight upright folds formed during the NE-SW shortening. The photo on the left shows the regional foliation S1 developed parallel to the axial planes of folds. Photos in the center and on the right show the relationship between horizontal tension gashes, thrusts and mineralized veins, all of these structures being formed in response to a regional NE-SW shortening and a vertical stretching.

2. EPMA configuration used for the analysis of tourmaline

Element	Calibration standard	Crystal	Counting time peak (s)	Average detection limit (ppm)	Average standard deviation 2σ (%)
K	Orthose	LPET	120	160	45
Ti	MnTiO3	LPET	10	600	12
Si	Albite	TAP	10	870	12
Al	Al2O3	TAP	10	800	13
Fe	FeO/Olivine	LIF	10	2550	18
Mn	MnTiO3	LIF	10	2080	22
Na	Albite	LTAP	10	620	17
Mg	Olivine	LTAP	10	380	14
Ca	Andradite	LPET	10	500	22
Cl	Vanadinite	LPET	10	450	21
F	Topaze	PC1	120	600	30

3. Field observations of tourmaline present in the mineralized system of Panasqueira

Figure 14 Macroscopic characteristics of tourmaline in the mineralized system of Panasqueira. (a) to (c) veins with tourmalines along the schist vein-contact. (d) Field evidence of the preferential crystallization of tourmaline in the vertical foliation planes. (e) and (f) examples of tourmalinite haloes developed around veins. (g) Example of mineralized vein in mine with tourmaline along the vein edge, (h) zoom on the schist vein contact showing the vertical growth of tourmaline.

4. Microscopic occurrences of tourmaline in the mineralized system of Panasqueira

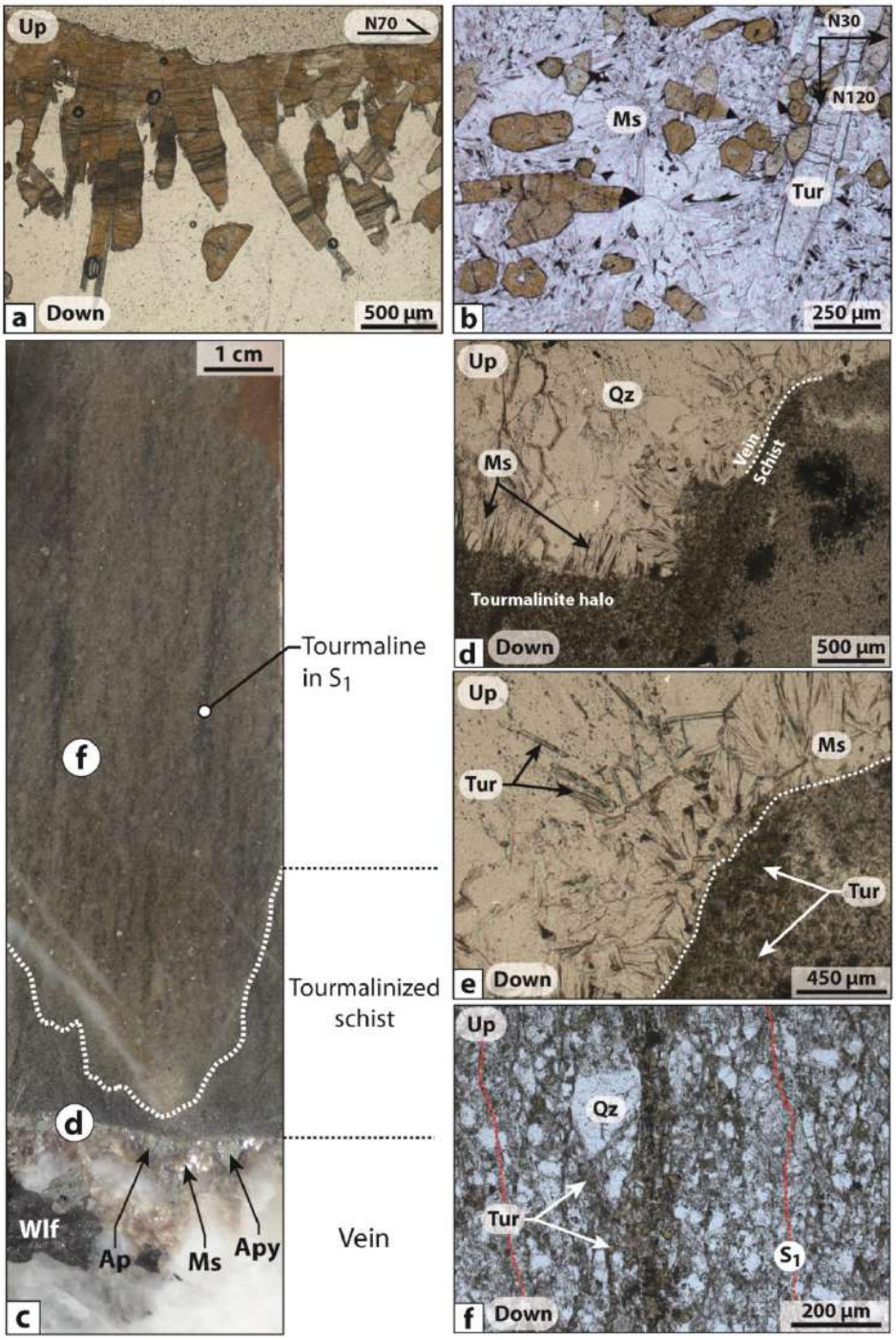

Figure 15 Microscopic characteristics of tourmaline present in the mineralized systems of Panasqueira. Sections of veins tourmaline (a) parallel and (b) perpendicular to the trigonal axis of tourmaline. (c) Sample showing the relationship between a mineralized vein and the tourmalinization of the wall-rock, d and f give the location of the thin sections d and f (note the preferential crystallization of tourmaline in the foliation planes). (d) Photomicrograph showing the contact between mineralized vein and tourmalinized wall-rocks. (e) Zoom on tourmalines present in the altered schist. Note the preferential crystallization of tourmaline in an inherited more pelitic layer. (f) Zoom on tourmaline present in the foliation planes.

5. Evidences of the anisotropic growth of the tourmaline of Panasqueira

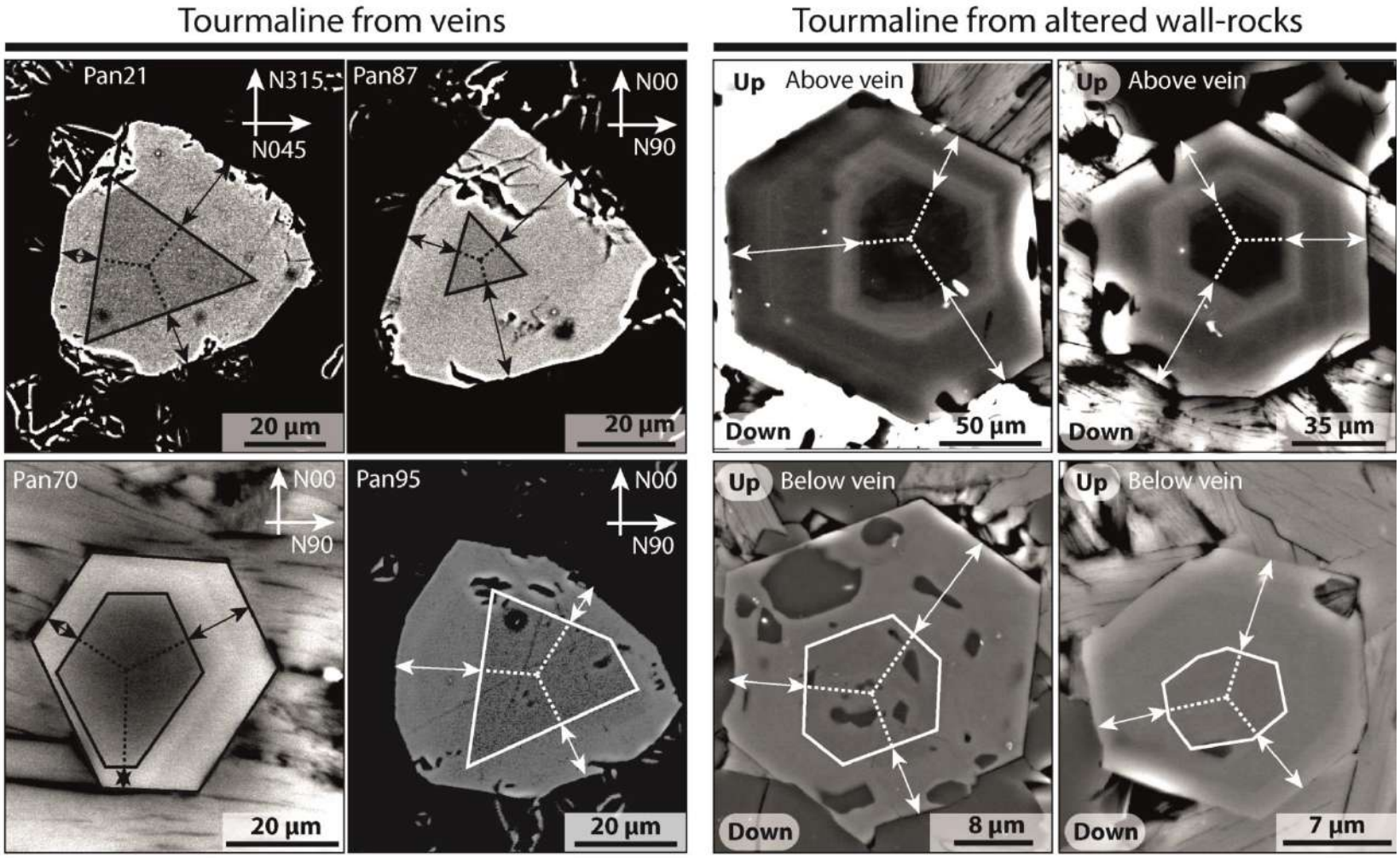

Figure 16 Scanning electronic photomicrographs (SEM) showing some representative examples of basal sections of tourmaline for different sample sites. Note the asymmetric shape of these tourmalines resulting of an anisotropic growth due to a directional fluid flow.

6. Evidence of trace element zoning in tourmaline

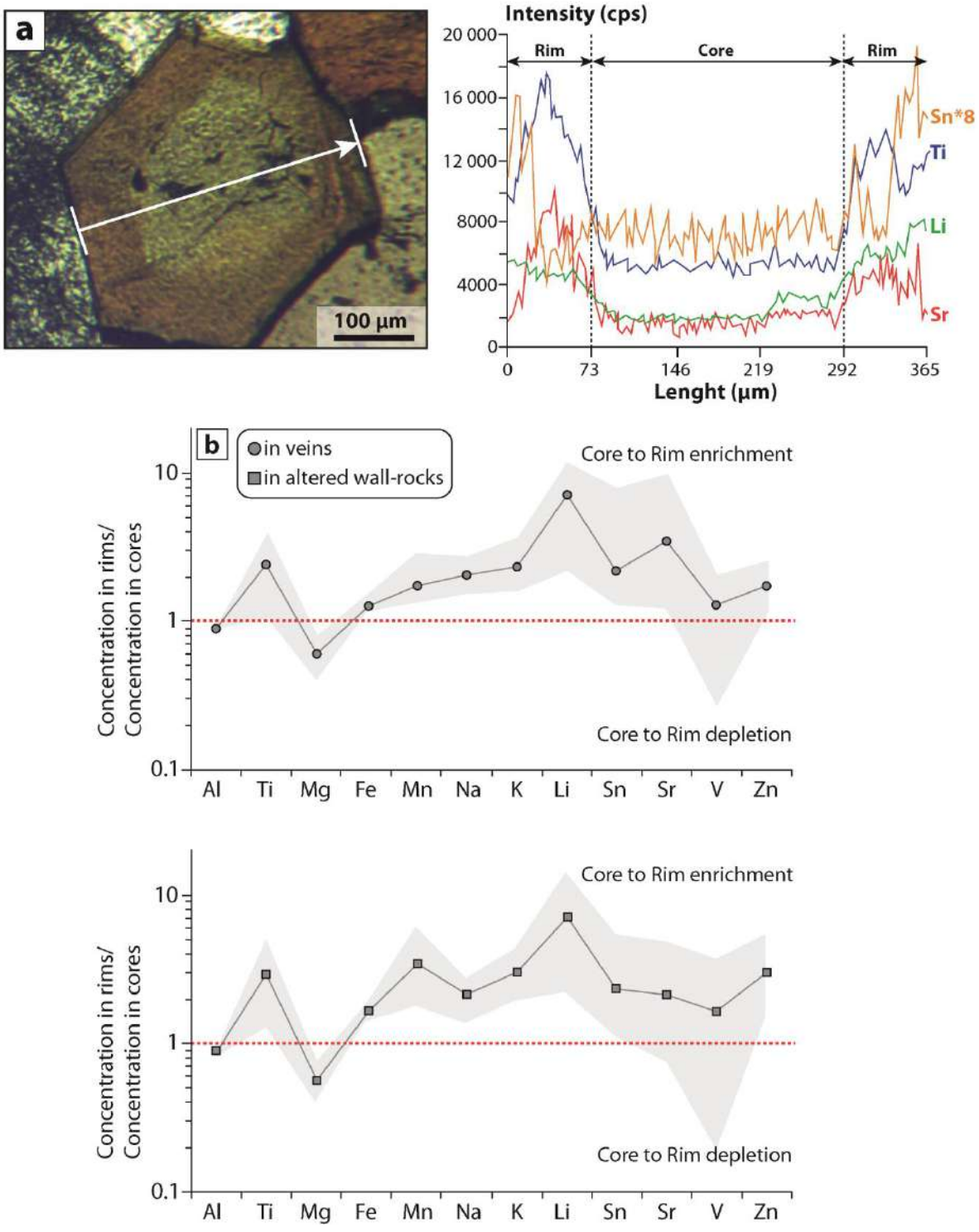

Figure 17 (a) LA-ICP-MS profile through a vein tourmaline showing the core to rim enrichment in Li, Sn, Sr and Ti. (b) and (c) Relative enrichment/depletion for major and trace elements between cores and rims for tourmalines of veins (b) and altered wall-rocks (c). The grey area corresponds to the standard deviation.

7. Microprobe analyses of tourmaline (wt%)

Tourmaline from altered wall-rocks (cores)										
Sample	**P20_core_1**	**P20_core_2**	**P20_core_3**	**P20_core_4**	**P20_core_5**	**P20_core_6**	**P20_core_7**	**P20_core_8**	**P20_core_9**	**P20_core_10**
SiO_2	35.0	35.9	35.6	35.7	36.0	35.3	36.2	36.1	36.5	35.7
TiO_2	0.12	0.30	0.24	0.14	0.30	0.12	0.20	0.12	0.13	0.15
Al_2O_3	34.8	34.6	34.5	35.1	34.9	36.2	33.9	34.5	33.2	34.5
FeO	9.6	8.9	9.7	8.5	8.0	9.4	8.7	9.7	7.2	9.4
MnO	0.0	0.1	0.0	0.0	0.0	0.0	0.0	0.0	0.0	0.1
MgO	3.3	3.2	3.9	4.4	4.3	3.5	4.4	3.3	4.9	3.6
CaO	0.0	0.0	0.0	0.1	0.1	0.0	0.1	0.1	0.1	0.1
Na_2O	1.8	1.8	1.6	1.9	1.8	1.8	1.6	1.9	1.6	1.5
K_2O	0.019	0.015	0.011	0.021	0.029	0.021	0.023	0.029	0.011	0.017
F	0.0	0.0	0.0	0.0	0.0	0.0	0.0	0.0	0.0	0.0
Cl	0.0	0.0	0.0	0.0	0.0	0.0	0.0	0.0	0.0	0.0
Total	84.7	84.8	85.5	85.8	85.5	86.3	85.2	86.0	83.6	85.2
B_2O_3	10.4	10.4	10.5	10.7	10.6	10.7	10.5	10.6	10.4	10.5
H_2O	3.3	3.3	3.3	3.3	3.3	3.3	3.3	3.3	3.3	3.3
Total*	98.4	98.5	99.3	99.7	99.5	100.3	99.1	99.9	97.3	98.9

Tourmaline from altered wall-rocks (cores)										
Sample	**P20_core_11**	**P20_core_12**	**P20_core_13**	**P20_core_14**	**P20_core_15**	**P20_core_16**	**P20_core_17**	**P20_core_18**	**P20_core_19**	**P20_core_20**
SiO_2	34.7	32.1	32.3	32.7	32.3	35.1	34.7	35.9	35.9	35.1
TiO_2	0.2	0.1	0.1	0.2	0.2	0.3	0.1	0.3	0.3	0.1
Al_2O_3	33.4	32.7	33.4	33.1	33.1	35.8	35.1	35.6	36.2	33.4
FeO	9.4	9.4	9.4	9.9	8.3	8.6	9.9	7.2	8.1	8.6
MnO	0.2	0.0	0.1	0.0	0.0	0.0	0.0	0.0	0.0	0.2
MgO	3.4	3.3	3.2	3.4	3.9	3.9	3.2	4.7	4.5	3.9
CaO	0.0	0.1	0.1	0.1	0.1	0.2	0.1	0.1	0.2	0.1
Na_2O	1.8	1.6	1.6	1.8	1.5	1.8	2.0	1.6	1.8	1.5
K_2O	0.0	0.0	0.0	0.0	0.0	0.0	0.0	0.0	0.0	0.0
F	0.0	0.0	0.0	0.0	0.0	0.0	0.0	0.0	0.0	0.0
Cl	0.0	0.0	0.0	0.0	0.0	0.0	0.0	0.0	0.0	0.0
Total	83.2	79.4	80.2	81.1	79.5	85.6	85.1	85.4	87.0	82.8
B_2O_3	10.3	9.8	9.9	10.0	9.9	10.6	10.5	10.6	10.8	9.9
H_2O	3.2	3.0	3.1	3.1	3.1	3.3	3.3	3.3	3.4	3.1
Total*	96.7	92.2	93.1	94.2	92.4	99.5	98.9	99.4	101.1	95.8

Tourmaline from altered wall-rocks (rims)										
Sample	**P20_rim_1**	**P20_rim_2**	**P20_rim_3**	**P20_rim_4**	**P20_rim_5**	**P20_rim_6**	**P20_rim_7**	**P20_rim_8**	**P20_rim_9**	**P20_rim_10**
SiO_2	34.8	35.7	35.3	36.1	35.4	35.0	34.5	34.8	35.0	34.8
TiO_2	0.6	0.4	0.3	0.5	0.6	0.6	0.4	0.5	0.5	0.6
Al_2O_3	30.6	30.2	30.2	31.6	30.1	30.2	30.4	30.3	30.2	29.9
FeO	13.8	13.9	14.1	14.4	13.9	14.3	13.9	13.7	14.0	14.4
MnO	0.0	0.0	0.1	0.0	0.2	0.0	0.1	0.1	0.0	0.0
MgO	2.4	2.4	2.4	1.8	2.0	2.1	2.0	2.2	2.2	2.1
CaO	0.1	0.1	0.0	0.2	0.0	0.0	0.0	0.0	0.0	0.0
Na_2O	2.3	2.2	2.2	2.1	2.3	2.2	2.3	2.3	2.1	2.2
K_2O	0.1	0.1	0.0	0.1	0.1	0.1	0.0	0.0	0.0	0.0
F	0.0	0.0	0.0	0.0	0.0	0.0	0.0	0.0	0.0	0.0
Cl	0.0	0.0	0.0	0.0	0.0	0.0	0.0	0.0	0.0	0.0
Total	84.6	85.0	84.7	86.9	84.5	84.5	83.8	83.9	84.1	84.1
B_2O_3	10.3	10.3	10.2	10.5	10.2	10.2	10.1	10.2	10.2	10.1
H_2O	3.2	3.2	3.2	3.2	3.1	3.1	3.1	3.1	3.1	3.1
Total*	98.0	98.5	98.1	100.6	97.9	97.8	97.0	97.2	97.4	97.3

Tourmaline from altered wall-rocks (rims)										
Sample	**P20_rim_11**	**P20_rim_12**	**P20_rim_13**	**P20_rim_14**	**P20_rim_15**	**P20_rim_16**	**P20_rim_17**	**P20_rim_18**	**P20_rim_19**	**P20_rim_20**
SiO_2	34.9	35.8	35.1	35.5	36.0	35.7	35.8	35.6	35.8	35.2
TiO_2	0.6	0.5	0.4	0.4	0.5	0.5	0.4	0.3	0.4	0.4
Al_2O_3	29.9	30.2	29.6	29.7	30.0	30.1	31.0	29.8	29.9	29.6
FeO	13.6	12.7	12.8	12.5	10.8	12.2	13.0	12.7	13.4	11.9
MnO	0.1	0.2	0.2	0.1	0.1	0.1	0.2	0.1	0.0	0.1
MgO	2.1	3.3	3.1	3.5	4.0	3.1	2.4	3.5	2.5	3.3
CaO	0.0	0.0	0.0	0.0	0.0	0.0	0.0	0.1	0.0	0.0
Na_2O	2.3	2.4	2.4	2.3	2.4	2.3	1.9	2.4	2.2	2.3
K_2O	0.0	0.1	0.0	0.0	0.1	0.1	0.1	0.1	0.1	0.1
F	0.0	0.0	0.0	0.0	0.0	0.0	0.0	0.0	0.0	0.0
Cl	0.0	0.0	0.0	0.0	0.0	0.0	0.0	0.0	0.0	0.0
Total	83.5	85.2	83.6	84.1	83.9	84.0	84.7	84.5	84.5	83.0
B_2O_3	10.1	10.4	10.2	10.3	10.3	10.3	10.3	10.3	10.2	10.2
H_2O	3.1	3.2	3.1	3.2	3.2	3.2	3.2	3.2	3.2	3.1
Total*	96.7	98.8	96.9	97.5	97.4	97.5	98.2	98.0	97.9	96.3

Tourmaline from mineralized veins (cores)

Sample	Pan78_core_1	Pan78_core_2	Pan78_core_3	Pan78_core_4	Pan78_core_5	Pan78_core_6	Pan78_core_7	Pan78_core_8	Pan78_core_9	Pan78_core_10
SiO_2	36.1	36.1	35.3	35.8	35.8	35.2	35.7	36.0	35.5	36.2
TiO_2	0.2	0.2	0.2	0.2	0.1	0.2	0.2	0.1	0.3	0.2
Al_2O_3	33.6	34.2	33.9	34.0	33.3	34.1	33.8	34.1	34.4	34.1
FeO	11.7	11.4	10.7	11.6	11.3	11.4	10.2	11.4	10.9	11.5
MnO	0.1	0.0	0.0	0.1	0.0	0.0	0.0	0.2	0.1	0.0
MgO	2.4	2.4	2.6	2.5	2.8	2.3	2.1	2.0	2.7	2.4
CaO	0.0	0.1	0.1	0.0	0.0	0.0	0.0	0.0	0.0	0.1
Na_2O	1.3	1.6	1.5	1.4	1.4	1.5	1.4	1.3	1.6	1.4
K_2O	0.0	0.0	0.0	0.0	0.0	0.0	0.0	0.0	0.0	0.0
F	0.0	0.0	0.0	0.0	0.0	0.0	0.0	0.0	0.0	0.0
Cl	0.0	0.0	0.0	0.0	0.0	0.0	0.0	0.0	0.0	0.0
Total	85.4	86.0	84.3	85.6	84.9	84.8	83.5	85.2	85.4	85.9
B_2O_3	10.4	10.5	10.3	10.4	10.3	10.3	10.2	10.3	10.4	10.4
H_2O	3.3	3.3	3.2	3.3	3.2	3.2	3.2	3.3	3.3	3.3
Total*	99.1	99.8	97.9	99.3	98.4	98.4	96.9	98.8	99.1	99.6

Tourmaline from mineralized veins (cores)

Sample	Pan78_core_11	Pan78_core_12	Pan78_core_13	Pan78_core_14	Pan78_core_15	Pan78_core_16	Pan78_core_17	Pan78_core_17	Pan78_core_18	Pan78_core_19	Pan78_core_20
SiO_2	35.9	35.7	37.0	36.8	35.4	35.3	35.7	35.7	34.6	35.2	35.7
TiO_2	0.2	0.1	0.2	0.2	0.2	0.2	0.2	0.1	0.1	0.2	0.1
Al_2O_3	33.9	33.5	34.5	33.7	33.9	34.1	33.4	33.9	31.8	33.3	34.1
FeO	11.1	9.9	11.3	11.5	9.7	11.0	10.4	9.5	9.9	11.4	10.2
MnO	0.1	0.0	0.0	0.1	0.0	0.1	0.0	0.0	0.0	0.1	0.0
MgO	2.3	2.3	2.7	2.2	3.2	2.1	2.8	2.8	5.0	2.2	2.9
CaO	0.0	0.0	0.0	0.0	0.0	0.0	0.1	0.1	0.2	0.0	0.0
Na_2O	1.4	1.4	1.3	1.4	1.4	1.4	1.4	1.3	1.1	1.3	1.3
K_2O	0.0	0.0	0.0	0.0	0.0	0.0	0.0	0.0	0.0	0.0	0.0
F	0.0	0.0	0.0	0.0	0.0	0.0	0.0	0.0	0.1	0.0	0.0
Cl	0.0	0.0	0.0	0.0	0.0	0.0	0.0	0.0	0.0	0.0	0.0
Total	84.9	82.9	87.0	85.9	83.9	84.2	84.0	83.5	82.9	83.6	84.4
B_2O_3	10.3	10.1	10.6	10.4	10.3	10.2	10.3	10.2	10.2	10.1	10.3
H_2O	3.2	3.2	3.3	3.3	3.2	3.2	3.2	3.2	3.2	3.2	3.2
Total*	98.4	96.2	100.9	99.6	97.4	97.6	97.5	96.9	96.2	96.9	97.9

Tourmaline from mineralized veins (rims)										
Sample	**Pan78_rim_1**	**Pan78_rim_2**	**Pan78_rim_3**	**Pan78_rim_4**	**Pan78_rim_5**	**Pan78_rim_6**	**Pan78_rim_7**	**Pan78_rim_8**	**Pan78_rim_9**	**Pan78_rim_10**
SiO_2	34.4	35.1	35.7	35.0	35.2	35.7	35.8	35.6	35.2	35.7
TiO_2	0.5	0.5	0.5	0.5	0.5	0.5	0.5	0.5	0.5	0.5
Al_2O_3	30.5	30.7	30.6	30.3	31.2	30.7	31.1	31.2	31.3	31.0
FeO	13.4	14.5	14.1	14.7	13.9	13.7	14.6	13.7	13.8	15.0
MnO	0.1	0.2	0.2	0.1	0.0	0.1	0.1	0.0	0.0	0.2
MgO	1.8	1.5	1.1	1.0	1.0	1.9	1.8	1.6	1.4	0.8
CaO	0.1	0.1	0.1	0.1	0.0	0.0	0.1	0.1	0.1	0.1
Na_2O	2.2	2.2	2.2	2.3	2.2	2.2	2.2	2.2	2.1	2.2
K_2O	0.1	0.1	0.0	0.0	0.0	0.0	0.0	0.0	0.1	0.0
F	0.0	0.0	0.0	0.0	0.0	0.0	0.0	0.0	0.0	0.0
Cl	0.0	0.0	0.0	0.0	0.0	0.0	0.0	0.0	0.0	0.0
Total	83.1	84.8	84.7	84.1	83.9	84.9	86.3	84.9	84.6	85.5
B_2O_3	10.0	10.2	10.2	10.1	10.1	10.3	10.4	10.3	10.2	10.2
H_2O	3.1	3.1	3.2	3.1	3.1	3.2	3.2	3.2	3.2	3.2
Total*	96.2	98.2	98.0	97.3	97.2	98.4	99.9	98.4	98.0	98.9

Tourmaline from mineralized veins (rims)

Sample	Pan78_rim_11	Pan78_rim_12	Pan78_rim_13	Pan78_rim_14	Pan78_rim_15	Pan78_rim_16	Pan78_rim_17	Pan78_rim_18	Pan78_rim_19	Pan78_rim_20
SiO_2	35.7	35.2	35.1	35.6	35.3	34.7	34.0	34.0	35.0	35.0
TiO_2	0.5	0.3	0.3	0.4	0.4	0.5	0.5	0.5	0.5	0.6
Al_2O_3	30.9	30.4	30.2	30.1	30.5	32.7	32.4	32.3	32.7	31.0
FeO	13.3	14.5	15.3	14.4	15.1	14.5	14.7	13.9	14.1	13.4
MnO	0.3	0.1	0.3	0.1	0.0	0.1	0.1	0.1	0.1	0.1
MgO	1.3	1.5	1.5	1.6	1.6	0.8	1.0	1.0	1.1	0.8
CaO	0.1	0.1	0.0	0.1	0.0	0.1	0.1	0.0	0.1	0.1
Na_2O	2.1	1.9	2.1	2.0	2.0	1.5	1.9	1.8	1.9	2.2
K_2O	0.0	0.0	0.1	0.0	0.0	0.1	0.1	0.1	0.1	0.0
F	0.0	0.0	0.0	0.0	0.0	0.0	0.0	0.0	0.0	0.0
Cl	0.0	0.0	0.0	0.0	0.0	0.0	0.0	0.0	0.0	0.0
Total	84.2	84.1	84.9	84.4	85.0	85.0	84.8	83.8	85.5	83.2
B_2O_3	10.1	10.1	10.2	10.1	10.2	10.2	10.2	10.1	10.3	10.0
H_2O	3.2	3.1	3.1	3.1	3.2	3.2	3.2	3.1	3.2	3.1
Total*	97.5	97.3	98.2	97.6	98.4	98.4	98.2	97.1	98.9	96.3

8. LA-ICP-MS analyses of tourmaline (ppm)

Tourmaline from altered wall-rocks										
Sample	**Li7**	**Na23**	**Mg24**	**Al27**	**Ti47**	**V51**	**Mn55**	**Zn66**	**Sr88**	**Sn118**
p20core-1	56.59	5682.3	9038.75	69859.34	2450.04	15.84	200.69	297.38	23.01	9.42
p20core-2	66.72	6188.68	5697.92	83872.37	2070.88	20.44	283.82	462.67	10.37	5.79
p20core-3	46.15	5500.21	9752.99	70132.74	2514.42	86.67	136.04	275.56	25.74	6.73
p20core-4	33.8	8211.69	17600.39	112610.54	1600.35	31.15	131.46	264.26	44.87	18.31
p20core-5	90.69	6131.8	4513.09	79225.09	2172.45	16.54	271.78	497.01	8.48	3.81
p20core-6	16.17	7352.23	15455.9	105837.59	1781.33	37.2	144.49	208.81	50.43	4.98
p20core-7	44.8	5146.18	6851.39	61173.64	2880.32	22.92	166.79	280.11	13.92	3.67
p20core-8	24.56	11221.16	31733.32	193113.86	974.03	219.19	153.44	337.79	62.7	19.94
p20core-9	59.81	5794.51	6615.74	57567.32	2948.34	22.9	201.63	334.37	14.97	3.9
p20core-10	14.69	8777.5	25230.6	154576.98	1136.69	127.68	115.13	234.3	30.51	8.9
p20core-11	18.09	5265.11	12323.47	67466.02	2532.1	65.57	79.66	134.21	30.55	15.08
p20rim-1	212.41	14187.92	16183.61	156634.95	3221.89	41.09	519.78	847.5	43.79	9.3
p20rim-2	176.99	14061.91	15099.13	150754.31	3259.38	44.08	530.59	871.43	48.25	12.26
p20rim-3	226.52	12880.55	13748.96	140522.52	3531.87	40.47	533.11	796.71	43.69	12.91
p20rim-4	191.54	14393.89	13302.97	156463.42	3177.48	36.53	579.07	972.32	36.13	9.35
p20rim-5	199.35	12565.1	11358.46	134577.13	3867.07	47.21	491.81	759.82	41.93	14.23
p20rim-6	205.92	12668.22	11839.05	144091.95	3542.1	43.47	499.84	793.87	38.54	13.54
p20rim-7	177.07	13497.11	12653.19	147491.89	3620.05	44.77	567.32	821.68	48.44	18.63
p20rim-8	286.06	15248.66	18714.82	160113.53	3181.46	42.18	634.39	875.94	46.89	19.9
p20rim-9	190.25	15656.44	14730.87	152547.13	3223.83	84.97	553.65	790.69	40.12	21.55
p20rim-13	168.49	16407.94	18040.25	164180.39	3400.84	59.69	537.61	939.36	42.58	12.2
p20rim-10	260.35	14182.57	13408.41	148148.73	3042.29	83.61	493.05	747.33	28.76	16.31
p20rim-11	201.24	15040.75	16406.7	157383.3	2779.33	71.4	512.79	875.5	37	13.37
p20rim-12	234.88	17796.83	19535.72	178706.47	3201.14	62.01	613.01	1009.72	36.19	11.07
p20rim-14	222.43	14610.82	14019.22	155139.13	3399.2	64.46	517.91	834.08	38.33	18.06

Tourmaline from mineralized veins										
Sample	**Li7**	**Na23**	**Mg24**	**Al27**	**Ti47**	**V51**	**Mn55**	**Zn66**	**Sr88**	**Sn118**
Pan_cor_1	36.59	7238.56	15188.92	110180.66	1619.74	69.68	295.9	305.47	18.17	2.24
Pan_cor_2	35.99	6774.5	9986.39	115909.44	1519.33	65.47	342.26	444.57	8.62	7.36
Pan_cor_3	49.39	9059.21	12779.48	154065.47	1010.29	64.47	423.95	511.9	14.26	9.08
Pan_cor_4	29.5	7966.79	12239.87	152089.61	1219.19	53.2	449.57	582.07	10.86	11.2
Pan_cor_5	36.92	7608.65	11806.97	135890.73	1287.43	50.85	387.5	516.51	11.95	11.9
Pan_cor_6	17.98	8613.92	16144.72	183483.52	1066.73	85.01	443.72	604.2	14.37	11.35
Pan_cor_7	20.37	8792.42	16416.34	176359.44	1045.48	109.26	440	581.06	17.38	11.72
Pan_cor_8	23.65	8530.08	14161.18	169925.72	1094.57	77.38	426.49	562.09	12.09	12.47
Pan_cor_9	27.79	7997.54	13102.89	148638.89	1191.68	77.04	386.99	535.05	12.88	11.75
Pan_cor_10	23.76	7514.66	12125.47	149343.94	1226.27	92.87	421.14	562.11	6.86	7.55
Pan_cor_11	18.87	7236.97	12362.62	148047.34	1234.82	81.78	408.73	535.24	8.02	6.87
Pan_cor_12	38.42	9615.63	16836.47	179932.5	1031.45	151.93	441.91	543.5	19.24	12.39
Pan_cor_13	14.25	10609.11	22703.54	228194.33	829.15	68.29	421	649.59	32.15	5.67
Pan_cor_14	18.83	8124.65	13609.31	168084.95	1073.93	60.87	429.7	570.66	7.16	11.52
Pan_cor_15	21.32	9851.6	16543.52	194694.94	832.24	113.68	458.96	632.67	18.81	11.12
Pan_cor_16	27.72	8847.41	15012.67	177255.05	1056.85	130.12	430.2	582.02	13.04	10.06
Pan_rim_1	191.09	19878.88	23888.67	264711.03	1967.85	118.3	865.62	793.94	48.04	17.56
Pan_rim_2	156.43	16221.21	22060.2	170960.28	2835.22	88.05	633.41	822.35	42.35	15.99
Pan_rim_3	107.09	16115.19	23717.31	184072.86	2782.16	91.98	628.74	805.74	42.38	14.73
Pan_rim_4	209.33	18156.84	22581.15	191858.39	2609.28	88.58	702.48	951.05	41.86	14.79
Pan_rim_5	119.96	14992.58	24080.72	151554.11	3215.52	105.58	513.07	673.2	38.8	9.03
Pan_rim_6	187.4	15486.52	21012.78	205241.69	2564.88	118.22	678.39	750.39	39.15	31.77
Pan_rim_7	194.19	19486.73	27914.14	278989.84	1923.76	123.18	844.2	1041.88	40.22	29.79
Pan_rim_8	236.2	20096.1	14891.03	254164.97	2040.12	45.82	967.65	1289.67	36.56	23.58
Pan_rim_9	123.16	15700.82	23731.39	222580.55	2444.94	128.3	666.78	898.39	33.64	19.87

Pan_rim_10	94.82	15399.89	22724.79	225774.84	2382.22	122.28	670.19	869.41	34.29	17.51
Pan_rim_11	113.96	16897.93	24434.09	244245.52	2136.18	125.61	739.98	985.35	29.84	17.37
Pan_rim_12	444.59	20008.37	14801.86	245372.66	2139.45	39.11	875.78	1316.37	28.77	18.31
Pan_rim_13	167.86	16151.49	24255.49	174231.8	2821.41	96.24	564.26	754.98	38.05	10.41
Pan_rim_14	184.75	17749.33	26784.79	254634.19	1993.24	101.71	675.31	815.74	70.61	21.17
Pan_rim_15	211.48	16477.03	17621.18	201342.05	2602.11	59.22	663.35	1051	33.53	14.02
Pan_rim_16	111.27	17353.14	25097.12	203118.3	2445.25	109.21	637.52	846	44.48	17.75
Pan_rim_17	128.8	16051.88	23557.04	172784.14	3003.21	104.3	537.52	768.17	40.21	11.45

Supporting information for:

Chapter IV: Relationships between the greisenization and the mineralized veins of Panasqueira: petrological and geochemical constrains

---

1. Operating conditions for trace elements analyses of muscovite

Trace elements analyses in muscovite	
Laboratory and sample preparation	
Laboratory name	Laboratoire Géosciences Océan, Brest, France
Sample type/mineral	Magmatic and hydrothermal muscovite and apatite
Sample preparation	Polished thin section (~30 µm)
Laser ablation system	
Make, model and type	
Laser wavelenght	193 nm
Fluence	10 $J.cm^{-2}$
Repetition rate	8 Hz
Spot size	85 µm
Sampling mode/pattern	Single spot
Carrier gas	100% He (250mL/min)
Background collection	20 seconds
Ablation duration	60 seconds
ICP-MS instrument	
Make, model and type	ThermoScientific X series II quadrupole
Sample introduction	Via conventional tubing
Data acquisition protocol	Time-resolved analysis
Masses measured	Li, Be, B, Na, Al, Si, S, Ti, Ge, As, Rb, Sr, Nb, Sn, Sb, Ta, W
Data processing	
Gas blank	20 seconds on-peak
Calibration strategy	NIST-612 SRM
Reference Material info	NIST-612 SRM (Pearce et al., 1997)
Data processing package used	Glitter 4.0
Quality control / Validation	NIST-612, relative standard deviation (RSD) between the measured and reference concentrations are below 10% for all elements

2. Operating conditions for trace elements analyses of quartz

Trace elements analyses in Quartz	
Laboratory and sample preparation	
Laboratory name	BRGM (lab), Orléans, France
Sample type/mineral	Magmatic and hydrothermal quartz
Sample preparation	Polished thick section (~100 μm)
Laser ablation system	
Make, model and type	Cetac Excite 193
Laser wavelenght	193 nm
Fluence	10 $J.cm^{-2}$
Repetition rate	8 Hz
Spot size	85 μm
Sampling mode/pattern	Single spot
Carrier gas	100% He (250mL/min)
Background collection	20 seconds
Ablation duration	60 seconds
ICP-MS instrument	
Make, model and type	ThermoScientific X series II quadrupole
Sample introduction	Via conventional tubing
Data acquisition protocol	Time-resolved analysis
Masses measured	Li, Be, B, Na, Al, Si, S, Ti, Ge, As, Rb, Sr, Nb, Sn, Sb, Ta, W
Data processing	
Gas blank	20 seconds on-peak
Calibration strategy	NIST-612 SRM
Reference Material info	NIST-612 SRM (Pearce et al., 1997)
Data processing package used	Glitter 4.0
Quality control / Validation	NIST-612, relative standard deviation (RSD) between the measured and reference concentrations are below 10% for all elements

3. Operating conditions for U-Pb dating of apatite

U-Pb apatite analyses	
Laboratory and sample preparation	
Laboratory name	Géosciences Rennes, UMR CNRS 6118, Rennes, France
Sample type/mineral	Magmatic and hydrothermal apatite
Sample preparation	Polished thin section
Imaging	CL: RELION CL instrument, Olympus Microscope BX51WI, Leica Color Camera DFC 420C
Laser ablation system	
Make, model and type	ESI NWR193UC, Excimer
Ablation cell	ESI NWR TwoVol2
Laser wavelenght	193 nm
Pulse width	< 5 ns
Fluence	6.5 $J.cm^{-2}$
Repetition rate	5 Hz
Spot size	50 µm
Sampling mode/pattern	Single spot
Carrier gas	100% He, Ar make-up gas and N_2 combined using in-house smoothing device
Background collection	20 seconds
Ablation duration	60 seconds
Wash-out delay	15 seconds
ICP-MS instrument	
Make, model and type	Agilent 7700x, Q-ICP-MS
Sample introduction	Via conventional tubing
RF power	1350 W
Sampler, skimmer cones	Ni
Extraction lenses	X type
Make-up gas flow (Ar)	0.87 l/min
Detection system	Single collector secondary electron multiplier
Data acquisition protocol	Time-resolved analysis
Scanning mode	Peak hopping, one point per peak
Detector mode	Pulse counting, dead time correction applied, and analog mode when signal intensity > ~10^6 cps
Masses measured	^{43}Ca, ^{204}(Hg + Pb), ^{206}Pb, ^{207}Pb, ^{208}Pb, ^{232}Th, ^{238}U
Integration time per peak	10-30 ms
Sensitivity / Efficiency	28000 cps/ppm Pb (50µm, 10Hz)
Dwell time per isotope	5-70 ms depending on the masses
Data processing	
Gas blank	20 seconds on-peak
Calibration strategy	Madagascar apatite used as primary reference material, Durango and McClure apatites used as secondary reference material (quality control)
Reference Material info	Madagascar (Thomson et al. 2012)
	Durango (McDowell et al. 2005)
	McClure (Schoene and Bowring 2006)
Data processing package used	Iolite (Paton et al. 2010), VizualAge_UcomPbine (Chew et al. 2014), ISOPLOT (Ludwig, 2012)
Quality control / Validation	Durango: Weighted average ^{207}Pb corrected age = 32.29 ± 0.90 Ma (n= 29; MSWD = 0.74; probability = 0.83)
	McClure: Weighted average ^{207}Pb corrected age = 524.1 ± 5.7 Ma (n = 23; MSWD = 1.3; probability = 0.16)

4. Microprobe analyses of muscovite (wt%). Li_2O contents were estimated following Tischendorff et al. (1997)

Primary magmatic muscovite from the less altered two-mica granite												
Sample	**Granite_D4**	**Granite_D4**	**Granite_D4**	**Granite_D4**	**Granite_D5**	**Granite_D5**	**Granite_D5**	**Granite_D5**	**Granite_D5**	**Granite_D5**	**Granite_D5**	**Granite_D5**
SiO_2	45.1	44.1	45.0	44.9	44.8	45.5	45.3	45.6	44.9	45.4	45.5	45.8
TiO_2	0.9	0.6	0.9	0.7	0.8	0.7	0.6	0.6	0.8	0.7	0.5	0.5
Al_2O_3	33.9	34.7	33.1	34.5	34.3	34.2	32.9	33.8	31.6	32.2	33.7	33.6
FeO	2.8	3.5	3.0	2.3	2.3	1.7	2.4	2.0	3.0	2.8	1.9	2.5
MnO	0.1	0.0	0.2	0.1	0.2	0.0	0.1	0.2	0.0	0.0	0.0	0.0
MgO	1.0	0.9	1.0	0.8	0.6	0.6	0.8	0.6	1.0	0.9	0.6	0.7
CaO	0.0	0.0	0.0	0.0	0.0	0.0	0.0	0.0	0.0	0.0	0.0	0.0
Na_2O	0.7	0.5	0.6	0.8	0.5	0.9	0.7	0.7	0.7	0.6	0.8	0.5
K_2O	10.0	10.3	10.2	10.2	10.6	10.2	10.5	10.3	10.4	10.3	10.4	10.8
P_2O_5	0.1	0.0	0.0	0.0	0.0	0.0	0.2	0.1	0.0	0.0	0.2	0.0
Cr_2O_3	0.0	0.0	0.1	0.0	0.0	0.1	0.0	0.0	0.0	0.0	0.0	0.0
Cl	0.0	0.0	0.0	0.0	0.0	1.1	1.1	1.0	1.0	0.8	0.0	0.0
F	0.9	0.9	0.6	0.8	0.7	0.0	0.0	0.0	0.0	0.0	0.5	1.0
Li_2O	0.4	0.4	0.2	0.3	0.3	0.0	0.0	0.0	0.0	0.0	0.2	0.4
OH	4.0	4.0	4.1	4.1	4.1	4.2	4.1	4.2	4.1	4.2	4.2	4.0
Total	99.8	100.0	99.0	99.4	99.2	99.1	98.6	99.1	97.5	97.9	98.3	99.8

Primary magmatic muscovite from the less altered two-mica granite												
Sample	**Granite_D4**	**Granite_D4**	**Granite_D4**	**Granite_D4**	**Granite_D4**	**Granite_D4**	**Granite_D4**	**Granite_D4**	**Granite_D4**	**Granite_D4**	**Granite_D4**	**Granite_D4**
SiO_2	46.7	45.5	45.4	45.9	46.5	47.5	45.9	45.3	45.6	46.6	45.7	45.4
TiO_2	0.9	0.5	0.4	0.6	0.9	0.7	0.8	0.7	0.7	0.6	0.6	0.5
Al_2O_3	34.0	34.5	34.1	34.9	33.9	33.7	34.5	33.9	34.0	33.2	33.6	34.1
FeO	2.0	2.0	1.9	2.1	2.3	2.2	1.7	1.9	1.5	2.1	1.8	1.6
MnO	0.1	0.0	0.1	0.0	0.1	0.0	0.0	0.0	0.0	0.0	0.1	0.0
MgO	0.7	0.6	0.6	0.6	0.7	0.7	0.7	0.6	0.6	0.6	0.6	0.5
CaO	0.0	0.0	0.0	0.0	0.0	0.0	0.0	0.0	0.0	0.0	0.0	0.0
Na_2O	0.7	0.7	0.6	0.7	0.7	0.7	0.8	0.8	0.9	0.8	0.8	0.7
K_2O	10.2	10.7	10.6	9.9	10.2	10.2	10.3	9.6	9.6	9.9	10.0	10.2
P_2O_5	0.2	0.0	0.0	0.0	0.0	0.2	0.1	0.0	0.2	0.0	0.0	0.0
Cr_2O_3	0.0	0.0	0.0	0.0	0.0	0.0	0.0	0.0	0.0	0.0	0.0	0.0
Cl	0.0	0.0	0.0	0.0	0.0	0.0	0.0	0.0	0.0	0.0	0.0	0.0
F	1.0	0.6	0.6	1.1	1.1	1.1	0.8	1.0	0.5	0.7	0.5	0.5
Li_2O*	0.4	0.2	0.2	0.4	0.4	0.5	0.3	0.4	0.2	0.3	0.2	0.2
OH	4.1	4.2	4.2	4.0	4.0	4.1	4.1	4.0	4.2	4.1	4.2	4.2
Total	100.8	99.5	98.6	100.3	100.8	101.6	99.9	98.3	97.8	98.9	98.2	97.8

Primary magmatic muscovite					Muscovite from greisenized granite (magmatic cores)							
Sample	**Granite_D5**	**Granite_D7**	**Granite_D7**	**Granite_D7**	**Greisen_P3**	**Greisen_P3**	**Greisen_P3**	**Greisen_P3**	**Greisen_P3**	**Greisen_P3**	**Greisen_P3**	**Greisen_P3**
SiO_2	45.9	46.2	46.5	45.8	46.4	45.4	45.5	45.3	45.0	45.5	44.4	45.1
TiO_2	0.5	0.5	0.7	0.7	0.6	0.6	0.7	0.7	0.8	0.7	0.7	0.8
Al_2O_3	34.6	34.4	35.2	34.6	34.3	32.3	33.9	34.4	33.5	31.9	35.1	34.8
FeO	1.7	1.8	1.8	1.8	2.3	1.7	1.9	2.4	1.7	4.8	2.6	2.0
MnO	0.0	0.0	0.0	0.0	0.1	0.0	0.0	0.1	0.0	0.0	0.1	0.0
MgO	0.6	0.6	0.6	0.6	0.3	0.6	0.4	0.3	0.2	0.2	0.4	0.3
CaO	0.0	0.0	0.0	0.0	0.0	0.1	0.0	0.0	0.0	0.0	0.0	0.0
Na_2O	0.6	0.7	0.6	0.7	0.6	0.5	0.4	0.7	0.6	0.6	0.7	0.7
K_2O	10.1	10.3	10.0	10.2	10.1	9.4	9.8	10.1	10.2	9.9	10.0	9.6
P_2O_5	0.0	0.0	0.1	0.0	0.2	0.0	0.0	0.2	0.1	0.2	0.0	0.1
Cr_2O_3	0.0	0.0	0.0	0.0	0.0	0.0	0.0	0.0	0.0	0.0	0.0	0.0
Cl	0.0	0.0	0.0	0.0	0.0	0.0	0.0	0.0	0.0	0.0	0.0	0.0
F	1.1	0.6	0.5	0.5	0.7	0.9	0.9	0.8	0.8	1.1	1.1	0.7
Li_2O*	0.5	0.2	0.2	0.2	0.2	0.4	0.3	0.3	0.3	0.4	0.4	0.3
OH	4.0	4.2	4.3	4.2	4.2	3.9	4.0	4.1	4.0	3.9	4.0	4.1
Total	99.7	99.5	100.5	99.5	100.0	95.9	97.9	99.4	97.3	99.3	99.5	98.7

Muscovite from greisenized granite (magmatic cores)												
Sample	**Greisen_P3**	**Greisen_P3**	**Greisen_P3**	**Greisen_C4**	**Greisen_C4**	**Greisen_C4**	**Greisen_C4**	**Greisen_C4**	**Greisen_C4**	**Greisen_C4**	**Greisen_C4**	**Greisen_C4**
SiO_2	45.3	45.7	45.4	45.1	45.8	45.6	45.3	45.5	45.9	46.6	46.7	45.0
TiO_2	0.7	0.8	0.7	0.6	0.5	0.6	0.6	0.5	0.4	0.5	0.5	0.7
Al_2O_3	34.0	33.5	33.1	34.2	34.3	35.4	34.9	32.7	35.0	33.4	34.6	34.8
FeO	2.7	2.4	3.2	1.9	1.9	1.9	1.4	2.1	2.5	2.2	1.5	2.5
MnO	0.0	0.0	0.0	0.0	0.0	0.0	0.0	0.0	0.0	0.0	0.0	0.1
MgO	0.1	0.1	0.1	0.1	0.1	0.0	0.0	0.0	0.2	0.4	0.4	0.1
CaO	0.0	0.0	0.0	0.0	0.0	0.0	0.0	0.0	0.0	0.0	0.0	0.1
Na_2O	0.6	0.7	0.6	0.5	0.5	0.6	0.5	0.6	0.6	0.4	0.4	0.5
K_2O	10.6	9.9	10.4	9.5	9.9	10.4	10.0	10.6	10.4	10.2	10.3	10.3
P_2O_5	0.0	0.0	0.0	0.0	0.2	0.1	0.0	0.0	0.0	0.0	0.2	0.1
Cr_2O_3	0.0	0.0	0.0	0.0	0.0	0.0	0.0	0.0	0.0	0.0	0.0	0.0
Cl	0.0	0.0	0.0	0.0	0.0	0.0	0.0	0.0	0.0	0.0	0.0	0.0
F	0.5	0.6	0.6	0.6	0.6	0.5	0.6	0.6	0.5	0.5	0.5	0.5
Li_2O*	0.2	0.2	0.2	0.2	0.2	0.2	0.2	0.2	0.2	0.2	0.2	0.2
OH	4.2	4.1	4.1	4.1	4.2	4.3	4.1	4.1	4.2	4.2	4.3	4.2
Total	98.8	98.1	98.3	96.8	98.2	99.6	97.7	97.0	99.8	98.6	99.6	98.9

Muscovite from greisenized granite (magmatic cores)											
Sample	**Greisen_P4**	**Greisen_P4**	**Greisen_P4**	**Greisen_P4**	**Greisen_P4**	**Greisen_P4**	**Greisen_P4**	**Greisen_P4**	**Greisen_P4**	**Greisen_P4**	**Greisen_P4**
SiO_2	45.7	46.0	45.3	43.9	46.0	46.2	45.4	46.2	47.2	45.6	44.4
TiO_2	0.7	0.9	0.9	0.7	0.7	0.6	0.7	0.8	0.5	0.3	0.6
Al_2O_3	34.1	34.7	34.0	35.4	33.8	35.0	33.9	34.8	34.3	34.0	34.9
FeO	2.1	1.8	1.9	2.0	2.0	1.9	2.3	2.5	2.0	2.4	2.6
MnO	0.1	0.1	0.1	0.1	0.0	0.0	0.1	0.1	0.1	0.1	0.0
MgO	0.2	0.0	0.2	0.0	0.1	0.1	0.1	0.0	0.0	0.4	0.1
CaO	0.0	0.0	0.0	0.0	0.0	0.0	0.0	0.0	0.0	0.0	0.1
Na_2O	0.8	0.6	0.6	0.7	0.5	0.6	0.6	0.7	0.6	0.4	0.6
K_2O	9.7	9.7	10.0	10.6	9.9	9.9	10.1	9.8	9.9	10.4	9.5
P_2O_5	0.0	0.6	0.0	1.2	0.2	0.0	0.3	0.1	0.0	0.0	0.2
Cr_2O_3	0.0	0.0	0.0	0.0	0.0	0.0	0.0	0.0	0.0	0.0	0.0
Cl	0.0	0.0	0.0	0.0	0.0	0.0	0.0	0.0	0.0	0.0	0.0
F	0.4	0.6	0.5	0.6	0.6	0.6	0.6	0.8	1.1	1.1	0.8
Li_2O*	0.1	0.2	0.2	0.2	0.2	0.2	0.2	0.3	0.5	0.4	0.3
OH	4.2	4.2	4.2	4.2	4.1	4.2	4.2	4.2	4.0	4.0	4.0
Total	98.1	99.5	97.9	99.5	98.2	99.3	98.4	100.1	100.4	99.2	98.2

Muscovite from greisenized granite (hydrothermal overgrowths)												
Sample	**Greisen_P3**	**Greisen_P3**	**Greisen_P3**	**Greisen_P3**	**Greisen_P3**	**Greisen_P3**	**Greisen_P3**	**Greisen_P3**	**Greisen_P3**	**Greisen_P3**	**Greisen_P3**	**Greisen_P3**
SiO_2	45.5	44.3	46.9	45.1	45.4	44.3	44.3	44.3	44.9	44.8	45.5	45.2
TiO_2	0.2	0.3	0.2	0.2	0.4	0.3	0.3	0.3	0.2	0.2	0.0	0.1
Al_2O_3	28.4	27.3	28.2	29.2	29.0	29.0	29.9	29.8	28.7	30.0	30.4	30.0
FeO	8.7	11.7	7.9	7.0	6.8	7.1	8.3	8.1	7.7	6.9	5.8	6.3
MnO	0.1	0.4	0.0	0.1	0.1	0.1	0.0	0.0	0.2	0.1	0.2	0.3
MgO	0.7	1.3	0.9	0.7	0.6	0.7	0.6	0.7	0.6	0.6	0.7	0.6
CaO	0.0	0.0	0.0	0.0	0.0	0.0	0.0	0.0	0.0	0.0	0.0	0.0
Na_2O	0.1	0.1	0.2	0.2	0.2	0.2	0.2	0.2	0.1	0.1	0.2	0.2
K_2O	10.2	9.4	9.9	10.0	9.4	9.7	10.6	9.1	9.9	10.2	9.7	9.7
P_2O_5	0.0	0.1	0.0	0.0	0.0	0.0	0.0	0.0	0.0	0.0	0.1	0.1
Cr_2O_3	0.0	0.0	0.0	0.0	0.0	0.0	0.0	0.0	0.0	0.0	0.0	0.0
Cl	0.0	0.0	0.0	0.0	0.0	0.0	0.0	0.0	0.0	0.0	0.0	0.0
F	1.5	1.8	1.2	1.0	1.0	1.2	1.2	1.1	1.0	1.1	1.1	1.0
Li_2O*	0.7	0.9	0.5	0.4	0.4	0.5	0.5	0.4	0.4	0.4	0.5	0.4
OH	3.7	3.5	3.8	3.8	3.8	3.7	3.8	3.8	3.8	3.8	3.8	3.9
Total	99.8	101.0	99.6	97.8	97.2	97.0	99.7	97.8	97.6	98.2	98.0	97.8

Muscovite from greisenized granite (hydrothermal overgrowths)										Hydrothermal muscovite (Greisen)		
Sample	**Greisen_P4**	**Greisen_P4**	**Greisen_P4**	**Greisen_P4**	**Greisen_P4**	**Greisen_P4**	**Greisen_P4**	**Greisen_P4**	**Greisen_P4**	**Greisen_B1**	**Greisen_B1**	**Greisen_B1**
SiO_2	44.6	42.1	41.9	42.4	42.6	43.0	42.5	46.1	45.8	45.2	46.0	46.5
TiO_2	0.0	0.0	0.0	0.0	0.0	0.0	0.0	0.0	0.1	0.3	0.3	0.2
Al_2O_3	29.5	28.4	28.6	30.0	30.7	29.3	28.3	29.3	27.8	30.3	29.8	29.3
FeO	5.6	6.7	7.8	5.3	6.6	6.5	6.7	7.2	8.1	6.6	7.1	7.3
MnO	0.1	0.2	0.2	0.2	0.2	0.2	0.1	0.2	0.1	0.1	0.1	0.1
MgO	0.7	0.6	0.5	0.5	0.6	0.6	0.5	0.8	0.6	0.6	0.7	0.5
CaO	0.0	0.0	0.0	0.1	0.0	0.0	0.0	0.0	0.0	0.0	0.0	0.0
Na_2O	0.1	0.2	0.2	0.2	0.1	0.2	0.1	0.1	0.1	0.2	0.2	0.1
K_2O	9.8	10.4	9.6	10.2	9.6	9.7	9.9	10.1	9.8	9.9	10.0	9.5
P_2O_5	0.0	0.0	0.0	0.0	0.0	0.0	0.0	0.0	0.0	0.1	0.0	0.0
Cr_2O_3	0.0	0.0	0.0	0.0	0.0	0.0	0.0	0.0	0.0	0.0	0.0	0.0
Cl	0.0	0.0	0.0	0.0	0.0	0.0	0.0	0.0	0.0	0.0	0.1	0.0
F	1.2	1.1	1.2	1.2	1.2	1.2	1.1	1.0	1.6	1.3	1.2	1.3
Li_2O*	0.5	0.5	0.5	0.5	0.5	0.5	0.5	0.4	0.7	0.5	0.5	0.6
OH	3.7	3.6	3.5	3.6	3.7	3.6	3.6	3.9	3.6	3.8	3.8	3.8
Total	95.9	93.9	94.0	94.2	95.8	94.6	93.4	99.1	98.3	99.0	99.7	99.3

Hydrothermal muscovite (Greisen)												
Sample	**Greisen_B1**	**Greisen_B1**	**Greisen_B1**	**Greisen_B1**	**Greisen_B1**	**Greisen_B1**	**Greisen_B1**	**Greisen_B1**	**Greisen_B1**	**Greisen_P4**	**Greisen_P4**	**Greisen_P4**
SiO_2	48.8	44.4	45.4	43.1	44.1	44.6	44.6	44.6	43.5	44.3	44.3	46.7
TiO_2	0.1	0.1	0.1	0.1	0.1	0.0	0.2	0.2	0.4	0.2	0.2	0.1
Al_2O_3	29.1	30.2	29.5	29.7	30.3	29.4	29.2	30.9	30.2	30.6	30.6	25.8
FeO	5.6	8.2	6.3	7.2	6.6	7.5	9.7	6.3	5.6	6.9	6.2	8.9
MnO	0.1	0.2	0.3	0.3	0.3	0.3	0.2	0.2	0.3	0.2	0.2	0.2
MgO	0.6	0.6	0.7	0.7	0.7	0.6	0.6	0.6	0.5	0.6	0.6	1.3
CaO	0.0	0.1	0.0	0.0	0.0	0.0	0.1	0.0	0.0	0.0	0.0	0.0
Na_2O	0.0	0.1	0.2	0.2	0.2	0.1	0.1	0.2	0.3	0.3	0.3	0.1
K_2O	9.7	9.6	10.1	10.4	10.5	9.2	9.5	9.8	9.3	9.5	9.5	9.8
P_2O_5	0.1	0.0	0.1	0.0	0.0	0.0	0.0	0.0	0.0	0.0	0.1	0.0
Cr_2O_3	0.0	0.0	0.0	0.0	0.0	0.0	0.0	0.0	0.0	0.0	0.0	0.0
Cl	0.0	0.1	0.0	0.0	0.0	0.0	0.0	0.0	0.0	0.0	0.0	0.0
F	1.1	1.4	1.8	1.5	1.5	1.1	1.6	1.0	0.8	1.1	0.9	1.7
Li_2O*	0.5	0.6	0.9	0.7	0.7	0.5	0.7	0.4	0.3	0.4	0.4	0.8
OH	3.9	3.7	3.5	3.6	3.6	3.8	3.6	3.9	3.9	3.8	3.9	3.5
Total	99.7	99.3	98.9	97.4	98.6	96.9	100.3	98.2	95.0	97.9	97.1	98.0

	Hydrothermal muscovite (Greisen)									Veins selvages		
Sample	**Greisen_P4**	**Greisen_P4**	**Greisen_P4**	**Greisen_P4**	**Greisen_P4**	**Greisen_P4**	**Greisen_P4**	**Greisen_P4**	**Greisen_P4**	**P20B**	**P20B**	**P20B**
SiO_2	45.8	45.2	46.8	46.7	46.0	48.0	47.5	47.1	46.1	46.3	46.6	46.0
TiO_2	0.2	0.2	0.2	0.2	0.3	0.4	0.2	0.1	0.5	0.2	0.2	0.3
Al_2O_3	30.2	31.0	31.8	32.4	33.0	31.8	30.3	27.7	24.4	32.1	31.8	32.0
FeO	4.7	3.5	3.7	3.0	2.5	4.0	4.9	7.4	12.8	3.6	3.8	3.7
MnO	0.1	0.1	0.1	0.0	0.1	0.2	0.1	0.2	0.2	0.0	0.1	0.0
MgO	1.0	0.9	1.0	0.9	0.8	0.8	1.2	1.3	1.5	0.9	0.9	0.7
CaO	0.0	0.0	0.0	0.0	0.0	0.0	0.0	0.0	0.0	0.0	0.0	0.0
Na_2O	0.3	0.4	0.5	0.5	0.7	0.3	0.3	0.1	0.1	0.5	0.6	0.6
K_2O	10.2	10.2	10.5	9.7	9.9	10.0	10.6	11.3	9.7	8.4	9.5	9.2
P_2O_5	0.0	0.2	0.1	0.0	0.0	0.0	0.0	0.2	0.0	0.1	0.1	0.0
Cr_2O_3	0.0	0.0	0.0	0.0	0.0	0.0	0.0	0.0	0.0			
Cl	0.0	0.0	0.0	0.0	0.0	0.0	0.0	0.0	0.0	0.0	0.0	0.0
F	1.1	1.0	1.2	1.2	0.9	1.1	1.4	1.6	1.9	1.2	1.5	1.2
Li_2O*	0.4	0.4	0.5	0.5	0.4	0.4	0.6	0.7	0.9	0.5	0.7	0.5
OH	3.8	3.8	3.9	3.9	4.0	4.0	3.8	3.7	3.4	3.8	3.8	3.9
Total	97.3	96.5	99.8	98.5	98.2	100.4	100.3	100.6	100.5	97.6	99.6	98.1

Veins selvages												
Sample	**P20B**	**P20B**	**P20B**	**P20B**	**P20B**	**P20B**	**P20B**	**P20B**	**P20B**	**P20B**	**P20B**	**P20B**
SiO_2	45.6	45.3	45.6	46.0	46.0	46.2	46.6	46.2	47.8	42.7	41.2	42.9
TiO_2	0.4	0.1	0.1	0.3	0.2	0.1	0.4	0.1	0.3	0.1	0.4	0.4
Al_2O_3	31.0	30.0	31.7	31.8	32.1	32.1	32.9	32.0	32.8	30.8	30.3	29.6
FeO	3.2	6.3	3.6	4.2	3.9	5.0	3.1	4.5	3.7	3.0	3.2	3.4
MnO	0.2	0.2	0.0	0.0	0.1	0.1	0.1	0.1	0.1	0.2	0.1	0.1
MgO	0.9	0.9	0.7	1.0	0.8	0.8	0.9	1.1	1.0	0.6	0.6	1.3
CaO	0.0	0.0	0.0	0.0	0.0	0.0	0.0	0.0	0.0	0.0	0.0	0.0
Na_2O	0.4	0.4	0.5	0.5	0.5	0.5	0.6	0.5	0.5	0.4	0.7	0.5
K_2O	9.4	9.6	8.0	8.3	10.5	10.4	10.2	10.5	10.3	8.0	10.2	10.4
P_2O_5	0.0	0.0	0.1	0.1	0.0	0.1	0.0	0.0	0.0	0.0	0.1	0.0
Cr_2O_3												
Cl	0.0	0.0	0.0	0.0	0.0	0.0	0.0	0.0	0.0	0.0	0.0	0.0
F	1.2	1.5	1.4	1.3	1.1	1.4	1.6	1.5	1.5	1.6	1.3	1.4
Li_2O*	0.5	0.7	0.6	0.6	0.5	0.6	0.7	0.7	0.7	0.8	0.6	0.6
OH	3.8	3.7	3.7	3.8	3.9	3.8	3.8	3.8	3.9	3.4	3.5	3.5
Total	96.6	98.6	96.0	97.6	99.7	101.2	100.9	101.0	102.6	91.6	92.1	94.1

Veins selvages												
Sample	**P20B**	**P20B**	**P20B**	**P20B**	**P20B**	**P20B**	**P20B**	**P20B**	**P32**	**P32**	**P32**	**P32**
SiO_2	45.8	46.3	45.7	46.0	45.4	45.8	45.1	45.9	46.5	46.4	45.7	46.7
TiO_2	0.4	0.2	0.5	0.5	0.3	0.4	0.1	0.1	0.4	0.1	0.1	0.4
Al_2O_3	31.6	31.4	31.4	31.1	32.0	31.7	32.2	32.8	32.5	31.9	30.3	32.4
FeO	3.6	4.3	3.9	3.7	3.5	3.2	3.0	2.5	2.7	3.6	4.9	3.4
MnO	0.0	0.1	0.1	0.2	0.0	0.0	0.0	0.1	0.0	0.1	0.0	0.0
MgO	0.9	0.9	0.8	0.8	0.7	0.9	0.7	0.6	0.6	0.9	0.9	0.8
CaO	0.0	0.0	0.0	0.0	0.0	0.0	0.0	0.0	0.0	0.0	0.0	0.0
Na_2O	0.5	0.5	0.5	0.5	0.4	0.4	0.4	0.6	0.4	0.4	0.4	0.4
K_2O	9.5	9.3	9.6	9.1	9.5	9.2	8.8	8.1	8.4	8.9	9.8	8.9
P_2O_5	0.0	0.0	0.0	0.0	0.0	0.1	0.0	0.1	0.1	0.0	0.0	0.0
Cr_2O_3												
Cl	0.0	0.0	0.0	0.0	0.0	0.0	0.0	0.0	0.0	0.0	0.0	0.0
F	1.0	1.1	1.1	1.0	0.8	0.9	0.8	1.1	0.8	1.0	1.1	1.0
Li_2O*	0.4	0.4	0.4	0.4	0.3	0.3	0.3	0.4	0.3	0.4	0.4	0.4
OH	3.9	3.9	3.9	3.9	4.0	4.0	3.9	3.9	4.0	3.9	3.8	4.0
Total	97.6	98.4	98.0	97.2	97.0	96.9	95.3	96.2	97.0	97.7	97.5	98.5

Veins selvages												
Sample	**P32**	**P32**	**P32**	**P32**	**P32**	**P32**	**P32**	**P32**	**P32**	**P32**	**P32**	**P32**
SiO_2	46.8	45.2	46.5	46.7	46.6	47.0	46.1	41.7	40.4	41.9	42.5	42.8
TiO_2	0.2	0.1	0.4	0.4	0.4	0.2	0.3	0.5	0.2	0.2	0.4	0.4
Al_2O_3	33.8	31.6	32.9	33.4	33.8	32.7	33.8	29.5	29.8	30.8	29.5	31.3
FeO	2.7	3.4	3.8	3.3	3.2	3.5	3.0	3.9	3.1	3.1	3.0	3.2
MnO	0.0	0.1	0.1	0.0	0.1	0.1	0.1	0.1	0.0	0.0	0.1	0.1
MgO	0.6	0.8	0.8	0.9	0.9	1.1	0.5	0.9	0.7	0.7	0.9	0.6
CaO	0.0	0.0	0.0	0.0	0.0	0.0	0.0	0.0	0.0	0.0	0.0	0.0
Na_2O	0.4	0.3	0.3	0.4	0.4	0.4	0.6	0.4	0.5	0.5	0.5	0.5
K_2O	10.7	10.8	10.6	10.6	10.9	10.6	10.2	10.1	9.8	10.4	10.1	10.3
P_2O_5	0.0	0.0	0.1	0.0	0.1	0.0	0.0	0.0	0.0	0.0	0.1	0.1
Cr_2O_3												
Cl	0.0	0.0	0.0	0.0	0.0	0.0	0.0	0.0	0.0	0.0	0.0	0.0
F	0.8	0.7	0.8	1.0	0.8	1.1	1.0	0.8	0.8	0.6	1.2	1.0
Li_2O*	0.3	0.3	0.3	0.4	0.3	0.4	0.4	0.3	0.3	0.2	0.5	0.4
OH	4.1	4.0	4.1	4.1	4.2	4.0	4.0	3.7	3.6	3.8	3.6	3.8
Total	100.3	97.3	100.8	101.3	101.5	101.2	100.0	91.9	89.3	92.2	92.3	94.3

5. LA-ICP-MS analyses of muscovite (ppm)

Primary magmatic muscovite									
Sample	**Li^{7}**	**Zn^{67}**	**Rb^{85}**	**Nb^{93}**	**Sn^{118}**	**Cs^{133}**	**Ba^{138}**	**Ta^{181}**	**W^{183}**
Ms_D4_1	396	93	204	24	10	13	2	3	1
Ms_D4_2	426	96	741	22	20	60	40	3	5
Ms_D4_3	193	162	1387	10	50	84	8	2	7
Ms_D4_4	270	170	1616	4	52	87	9	1	6
Ms_D4_5	582	93	690	13	35	59	29	2	3
Ms_D4_6	434	86	1001	2	102	46	18	1	8
Ms_D4_7	520	106	874	2	82	43	15	1	10
Ms_D4_8	223	179	1852	14	77	82	59	2	8
Ms_D4_9	332	124	1408	7	53	63	37	1	6
Ms_D4_10	349	152	1403	2	111	56	34	0	8
Ms_D4_11	366	132	1754	2	75	54	26	0	4
Ms_D4_12	370	138	1489	1	110	61	29	0	7
Ms_D4_13	480	65	473	12	9	38	42	1	0
Ms_D4_14	1203	88	684	39	56	30	24	15	23
Ms_D4_15	1165	91	775	31	62	53	41	14	11
Ms_D4_16	1096	78	643	27	53	39	32	9	12
Ms_D4_17	947	63	623	24	44	38	35	7	5
Ms_D4_18	1148	83	774	37	65	41	43	11	11
Ms_D4_19	1211	88	759	40	69	23	19	9	46
Ms_D4_20	1170	85	805	40	77	30	15	9	24
Ms_D4_21	1227	88	653	16	53	33	38	4	17

Muscovite from greisenized granite									
Magmatic cores									
Sample	**Li^{7}**	**Zn^{67}**	**Rb^{85}**	**Nb^{93}**	**Sn^{118}**	**Cs^{133}**	**Ba^{138}**	**Ta^{181}**	**W^{183}**
Ms_P3_core_1	987	99	1245	64	88	66	54	57	19
Ms_P3_core_2	926	147	1511	44	110	68	78	34	23
Ms_P3_core_3	854	121	2031	139	54	102	10	73	28
Ms_P3_core_4	999	108	1493	115	48	63	23	106	30
Ms_P3_core_5	313	66	1748	86	47	69	65	75	27
Ms_P3_core_6	864	119	1574	131	58	62	42	111	31
Ms_P3_core_7	910	112	1673	133	54	60	29	125	33
Ms_P3_core_8	859	117	1636	137	53	60	20	118	29
Ms_P3_core_9	986	118	1831	134	58	92	16	107	31
Ms_P3_core_10	893	114	1793	138	57	100	11	71	30
Ms_P3_core_11	929	117	1968	146	54	105	7	60	31
Ms_P3_core_12	328	140	2218	107	60	113	24	53	28
Ms_P3_core_13	367	109	1349	61	68	58	61	59	22
Ms_P3_core_14	346	128	2017	136	58	99	21	96	34
Hydrothermal overgrowths									
Ms_P3_rim_1	4123	202	2622	36	275	156	230	34	24
Ms_P3_rim_2	3915	224	2782	47	328	153	239	43	26
Ms_P3_rim_3	1473	266	3154	54	382	180	328	53	34
Ms_P3_rim_4	1505	300	3513	71	489	235	397	69	45
Ms_P3_rim_5	1561	224	3191	46	334	179	317	43	28
Ms_P3_rim_6	1372	236	3243	55	348	177	276	48	34
Ms_P3_rim_7	1486	306	3681	64	551	244	550	65	51
Ms_P3_rim_8	1461	292	3411	55	506	246	434	55	45
Ms_P3_rim_9	1473	266	3534	50	414	201	386	48	35
Ms_P3_rim_10	1544	235	2916	29	225	158	227	25	21
Ms_P3_rim_11	1535	272	3141	53	336	213	299	54	33
Ms_P3_rim_12	1697	235	2944	18	177	147	245	19	16
Ms_P3_rim_13	1713	317	3229	52	404	226	340	55	40
Ms_P3_rim_14	1406	321	3201	42	358	205	345	41	32
Ms_P3_rim_15	1701	259	2965	20	205	165	268	20	18
Ms_P3_rim_16	1673	244	2951	20	201	151	254	20	20

Hydrothermal muscovite (Greisen)									
Sample	**Li^{7}**	**Zn^{67}**	**Rb^{85}**	**Nb^{93}**	**Sn^{118}**	**Cs^{133}**	**Ba^{138}**	**Ta^{181}**	**W^{183}**
Ms_B4_1	2159	420	4797	197	313	262	111	67	60
Ms_B4_2	2289	346	4958	190	429	290	185	59	66
Ms_B4_3	2842	358	4036	132	462	241	224	36	65
Ms_B4_4	3445	253	3008	51	317	162	186	6	30
Ms_B4_5	2437	393	4756	215	236	297	192	59	63
Ms_B4_6	3413	290	3151	68	349	162	193	8	37
Ms_B4_7	1700	79	4400	49	210	236	50	9	17
Ms_B4_8	2176	107	3624	36	63	209	59	4	21
Ms_B4_9	2429	464	4509	204	291	263	146	75	63
Ms_B4_10	3176	293	3097	71	352	167	201	10	36
Ms_B4_11	3279	297	2979	69	343	155	198	8	34
Ms_B4_12	2962	263	3164	76	414	199	217	12	38
Ms_B4_13	3443	257	2704	57	285	156	170	8	33
Ms_B4_14	2395	443	4121	161	404	264	179	56	73
Ms_B4_15	2344	457	4134	162	377	263	180	57	73
Ms_B4_16	2794	417	3933	142	467	241	194	35	64
Veins selvages									
Ms_P20_1	1674	180	2827	58	328	136	433	15	101
Ms_P20_2	1909	188	2770	79	317	153	388	25	100
Ms_P20_3	1598	165	2388	44	272	97	316	9	56
Ms_P20_4	1398	252	3134	99	339	152	522	41	136
Ms_P20_5	1802	211	2664	50	310	145	399	15	93
Ms_P20_6	1820	183	2858	76	282	133	458	30	116
Ms_P20_7	1618	203	2745	76	321	146	397	27	111
Ms_P20_8	1716	227	2706	57	299	134	407	21	92
Ms_P20_9	1592	206	2465	63	258	127	288	23	92
Ms_P20_10	1652	218	2835	60	327	143	469	16	106
Ms_P20_11	1740	185	2831	77	307	145	370	28	113
Ms_P20_12	1724	174	2231	52	229	141	314	14	85
Ms_P20_13	1725	173	2227	52	229	141	314	14	85
Ms_P20_14	1747	194	2916	53	298	148	529	14	106
Ms_P20_15	2009	179	2558	55	262	124	329	18	86

6. Microprobe analyses of rutile (wt%)

Less altered two-mica granite								
Sample	**TiO_2**	**MnO**	**FeO**	**Nb_2O_5**	**SnO_2**	**Ta_2O_5**	**WO_3**	**Total**
E5	95.9	0.0	2.6	0.2	0.0	0.0	0.0	98.9
E5	96.7	0.1	1.3	0.1	0.0	0.0	0.0	98.2
E5	97.0	0.2	1.3	0.1	0.0	0.0	0.0	98.6
E5	95.5	0.1	2.5	0.1	0.0	0.0	0.0	98.3
E5	97.0	1.5	2.5	0.1	0.0	0.0	0.1	101.1
E5	97.7	0.0	1.5	0.2	0.0	0.1	0.0	99.4
E5	96.4	0.3	3.1	0.2	0.0	0.1	0.0	100.1
E5	97.7	0.0	1.6	0.2	0.0	0.0	0.0	99.5
E5	98.0	0.0	1.4	0.2	0.0	0.0	0.0	99.7
E5	97.4	0.0	1.6	0.2	0.0	0.0	0.0	99.3
E5	96.2	0.0	3.7	0.2	0.0	0.0	0.0	100.1
Greisenized granite								
J4	97.6	0.0	1.2	0.6	0.0	0.1	0.0	99.7
J4	97.1	0.0	1.1	0.7	0.1	0.2	0.1	99.3
J4	96.5	0.0	1.1	0.6	0.1	0.1	0.8	99.3
J4	98.0	0.0	1.4	0.2	0.0	0.0	0.0	99.7
J4	97.1	0.0	2.3	0.2	0.0	0.0	0.0	99.7
J4	93.2	0.0	2.1	1.0	0.1	0.2	4.1	100.7
J4	98.3	0.0	0.8	0.1	0.0	0.1	0.0	99.4
J4	93.2	0.0	2.1	1.0	0.0	0.2	4.2	100.7
J4	97.0	0.0	2.4	0.4	0.0	0.1	0.0	99.9
J4	95.8	0.0	2.2	1.3	0.0	0.2	0.1	99.6
J4	96.3	0.0	1.9	1.4	0.0	0.4	0.1	100.2
J4	94.2	0.0	2.7	2.5	0.1	0.5	0.1	100.1
J4	95.7	0.0	2.8	0.8	0.1	0.2	0.0	99.6
J4	95.2	0.0	2.1	1.9	0.1	0.3	0.4	99.9
J4	96.3	0.0	2.2	0.9	0.1	0.2	0.2	99.9

Greisen								
Sample	**TiO_2**	**MnO**	**FeO**	**Nb_2O_5**	**SnO_2**	**Ta_2O_5**	**WO_3**	**Total**
C5	95.4	0.0	1.5	1.0	0.2	0.7	2.1	100.8
C5	96.5	0.0	1.5	0.6	0.2	0.2	1.7	100.7
C5	97.5	0.0	1.1	0.6	0.1	0.1	1.6	101.0
C5	95.6	0.0	1.4	1.0	0.2	0.4	1.8	100.5
C5	96.5	0.0	1.1	0.9	0.2	0.4	1.8	100.9
C5	98.5	0.0	0.8	0.3	0.2	0.2	0.2	100.2
C5	98.8	0.0	0.5	0.5	0.1	0.1	0.8	100.9
C5	95.0	0.0	1.4	1.1	0.1	0.3	2.1	100.1
C5	94.3	0.0	1.5	1.1	0.2	0.6	3.1	100.8
C5	97.0	0.0	1.1	0.9	0.1	0.3	0.8	100.1
C5	95.9	0.0	1.2	0.8	0.1	0.3	2.3	100.7
C5	98.6	0.0	0.6	0.5	0.1	0.0	0.6	100.4
C5	97.6	0.0	1.0	0.5	0.1	0.1	0.9	100.1
C5	98.6	0.0	0.5	0.5	0.1	0.1	0.7	100.6
C5	98.7	0.0	0.6	0.5	0.1	0.2	0.6	100.6
C5	98.4	0.0	0.5	0.6	0.1	0.1	0.9	100.6
C5	95.3	0.0	1.4	1.1	0.2	0.7	2.3	100.9
C5	98.5	0.0	0.5	0.5	0.1	0.1	0.8	100.6
C5	95.3	0.0	1.4	1.1	0.2	0.6	2.3	100.9
C5	98.0	0.0	0.8	0.4	0.1	0.1	0.5	99.9
C5	95.9	0.0	1.2	1.2	0.2	1.0	1.4	100.9
C5	94.7	0.0	1.8	1.1	0.1	0.2	3.4	101.4
C5	93.9	0.1	2.4	1.0	0.1	0.2	3.3	101.1
C5	99.2	0.0	0.6	0.3	0.1	0.1	0.2	100.5
C5	98.9	0.0	1.4	0.3	0.1	0.0	0.1	100.9
C5	95.0	0.0	1.5	0.9	0.1	0.2	2.8	100.6
C5	98.3	0.0	1.0	0.4	0.1	0.0	1.1	101.0

7. LA-ICP-MS analyses of quartz (ppm)

Magmatic quartz from two-mica granite												
Core of snowball quartz												
Sample	**E2-C1-3**	**E2-C1-4**	**E2-C1-5**	**E2-C1-6**	**E2-C1-7**	**E2-C1-12**	**E2-C1-10**	**E2-C1-15**	**E2-C1-11**	**E2-C1-8**	**E2-C1-17**	**E2-C1-18**
Li	28.71	28.6	28.37	23.76	25.11	21.82	26.81	24.97	27.75	22.52	19.73	20.4
Be	0.151	<0.095	0.158	<0.068	<0.071	<0.076	0.101	0.141	0.102	0.142	0.199	<0.094
B	2.52	1.99	1.68	2.26	2.16	1.59	1.72	1.55	2.09	2.88	2.54	2.12
Na	11.88	14.26	12.09	25.24	14.58	8.97	10.5	10.96	10.67	14.62	23.34	12.3
Al	379.72	415.67	379.52	388.68	472.59	406.8	395.42	420.1	386.23	350.08	343.04	420.11
S	17.78	17.48	15.51	16.34	15.82	14.29	13.63	14.14	16.89	11.48	17.75	22.11
Ti	148.55	194.94	192.76	224.01	257.95	200.25	196.52	179.77	136.21	161.42	203.28	222.08
Ge	0.558	0.627	0.605	0.553	0.585	0.626	0.627	0.586	0.688	0.713	0.637	0.554
As	0.137	0.102	<0.065	0.165	<0.066	<0.059	0.076	0.082	<0.073	0.448	0.083	0.166
Rb	2.27	1.89	1.34	1.8	2.57	2.57	1.82	2.45	1.21	1.11	1.74	2.22
Sr	0.0345	0.0497	0.0462	0.0447	0.0226	0.0363	0.0367	0.0353	0.034	0.0589	0.0461	0.0541
Nb	<0.0053	<0.0040	<0.0054	<0.0042	0.0095	<0.0049	<0.0037	0.0056	<0.0037	0.0069	<0.0043	0.0263
Sn	0.1156	0.0819	0.0511	0.0795	0.1009	0.159	0.0843	0.0977	0.0446	0.223	0.232	0.21
Sb	0.198	0.1779	0.1025	0.481	0.144	0.0884	0.181	0.227	0.1445	0.1665	0.1526	0.0924
Ta	0.00052	0.00099	<0.00094	0.00145	0.00036	0.00105	<0.00	<0.00	<0.00105	<0.00096	<0.00	0.00117
W	0.0256	0.0165	0.0158	0.0384	0.0103	0.0136	0.0238	0.0152	0.0276	0.0268	0.0259	0.0597

Magmatic quartz from two-mica granite												
Core of snowball quartz												
Sample	**E2-C1-19**	**E2-C1-20**	**E2-C1-21**	**E2-C1-24**	**E2-C1-23**	**E2-C1-25**	**E2-C2-3**	**E2-C2-4**	**E2-C2-5**	**E2-C2-6**	**E2-C2-7**	**E2-C2-8**
Li	25.06	21.56	28.11	32.77	22.85	28.37	17.37	15.21	19.13	25.58	23.74	19.64
Be	0.166	0.136	0.151	0.103	0.093	0.122	0.052	0.321	0.253	0.172	0.236	<0.073
B	1.85	1.87	1.9	2.27	1.47	2.06	1.96	2.34	2.63	3.38	2.02	2.38
Na	13.81	16	10.56	9.62	6.06	15.98	13.93	22.22	24.12	32.7	33.93	15.14
Al	474.4	434.83	397.78	481.38	403.81	410.61	294.55	481.34	381.6	518.34	441.01	440.03
S	17.72	16.26	16.56	16.73	13.97	14.13	19.57	17.82	18.04	16.48	14.12	16.91
Ti	246.44	244.12	178.62	278.47	145.97	198.85	159.99	217.69	154.29	180.57	163.75	185.99
Ge	0.635	0.623	0.706	0.619	0.774	0.558	0.783	0.758	0.799	0.712	0.726	0.533
As	0.187	0.313	0.247	<0.064	0.097	0.104	0.301	1.26	1.33	0.768	0.431	0.104
Rb	3.28	2.22	1.88	2.5	2.35	1.25	1.116	2.38	1.66	2.34	3.17	2.43
Sr	0.0506	0.071	0.0471	0.0577	0.045	0.0373	0.0487	0.131	0.157	1.52	0.114	0.0398
Nb	<0.0063	0.0088	0.0067	<0.0052	<0.0050	0.007	<0.0057	0.0131	0.0173	0.03	<0.0049	<0.0071
Sn	0.185	0.137	0.1249	0.0971	0.144	0.0489	0.0726	0.229	0.125	0.326	0.0798	0.183
Sb	0.0857	0.0789	0.1087	0.45	0.415	0.1303	0.784	0.885	1.492	1.6	2.35	0.296
Ta	<0.00101	0.00266	0.00314	<0.00140	<0.00142	<0.00182	<0.00	<0.00231	0.0144	0.0087	0.00066	<0.00168
W	0.0066	0.0073	0.0186	0.0257	0.0247	0.0106	0.012	0.0187	0.0253	0.0357	0.0282	0.0461

Magmatic quartz from two-mica granite												
Core of snowball quartz					Rim of snowball quartz							
Sample	**E2-C2-9**	**D8-C1-50**	**D8-C1-51**	**D8-C1-52**	**E2-C1-1**	**E2-C1-2**	**E2-C1-14**	**E2-C1-9**	**E2-C1-13**	**E2-C1-16**	**E2-C1-22**	**E2-C1-26**
Li	15.19	10.01	14.28	12.88	10.43	16.11	17.9	15.61	15.55	4.81	12.63	16.4
Be	0.221	0.147	0.236	0.212	0.196	0.245	0.25	<0.089	0.133	0.372	0.25	0.145
B	1.97	3.05	2.77	2.64	4.1	4.65	5.27	3.83	3.25	5.39	6.37	6.56
Na	13.5	17.1	16.71	13.82	<1.48	40.7	20.91	27.52	23.23	<1.33	26.83	22
Al	369.12	487.71	557.49	378.32	175.63	292.67	271.08	354.53	188.95	306.71	292.17	238.51
S	13.27	16.94	16.44	14.46	27.75	23.48	12.47	14.24	12.24	20.94	23.01	22.61
Ti	138.73	137.55	148.47	153.43	15.73	14.79	100.29	61.64	63.82	64.87	13.95	18.27
Ge	0.706	0.946	0.822	0.744	2.47	0.773	0.808	0.896	1.53	1.57	0.925	1.77
As	0.137	0.247	0.143	0.291	0.358	0.35	0.403	0.329	0.313	0.357	0.436	0.372
Rb	2.2	2.84	3.1	1.51	0.091	0.477	0.97	1.91	1.25	1.34	0.741	0.376
Sr	0.0613	0.0906	0.0633	0.0729	0.0461	0.195	0.0851	0.0572	0.299	0.097	0.149	0.0759
Nb	<0.0050	0.0429	<0.0077	0.0136	<0.0060	0.1135	0.0983	0.0141	0.0108	0.0315	0.027	0.0116
Sn	0.1229	0.176	0.231	0.142	0.0414	0.0377	0.0762	0.0887	0.0163	0.0685	0.0436	0.0301
Sb	0.733	0.494	0.418	0.197	0.621	0.462	0.188	0.478	0.622	0.222	1.093	0.25
Ta	0.00076	0.007	0.0017	0.00492	0.00671	0.0177	0.0201	0.00273	0.0111	0.0393	0.0103	0.031
W	0.095	0.121	0.0578	0.0314	0.0126	0.159	0.082	0.0731	0.0337	0.0308	0.109	0.0265

Magmatic quartz from two-mica granite

Rim of snowball quartz

Sample	E2-C1-27	E2-C1-29	E2-C1-30	E2-C2-12	E2-C2-13	E2-C2-14	E2-C2-15	E2-C2-1	E2-C2-2	E2-C2-10	E2-C2-11	D8-C1-46
Li	13.09	11.77	15.64	11.93	10.76	7.72	16.79	9.85	10.65	10.66	7.92	10.62
Be	0.217	0.394	0.31	0.264	0.433	0.152	5.58	0.22	0.126	0.267	0.245	0.307
B	3.69	5.13	3.17	4.18	5.24	4.14	5.67	4.31	3.18	3.2	4.23	3.59
Na	7.31	14.96	27.8	14.27	57.59	26.6	20.07	5.7	29.09	11.76	21.13	12.29
Al	262.13	263.51	235.66	191.2	193.4	174.4	102.505	246.44	316.83	311.57	236.35	330.18
S	15.73	13.61	15.35	15	14.65	15.53	14.86	26.49	21.53	13.2	14.54	23.02
Ti	65.81	81.29	48.8	65.27	13.294	44.62	50.87	96.7	108.44	122.67	76.93	64.47
Ge	0.85	0.94	1.11	0.93	0.99	1.52	1.09	1.12	0.961	0.777	1.18	1.1
As	0.189	0.205	0.119	0.753	1.12	0.207	4.98	0.309	0.232	0.262	0.281	0.414
Rb	0.466	0.656	0.239	0.787	2.34	0.214	1.76	1.77	1.14	1.03	0.478	1.24
Sr	0.089	0.116	0.095	0.137	1.32	0.0515	6.49	0.0558	0.0486	0.0704	0.0953	0.0504
Nb	0.0064	0.0103	0.0164	0.0098	0.0222	0.0239	1.7	<0.0059	<0.0048	0.0105	<0.0056	0.0098
Sn	0.014	0.061	0.0187	0.0384	0.156	<0.0167	2.41	0.095	0.0613	0.1057	0.0238	0.207
Sb	0.19	0.308	0.0952	0.471	3.99	0.156	2.49	0.55	0.89	1.015	0.324	0.241
Ta	0.00544	0.01	0.0067	0.0076	0.0194	0.0063	1.28	<0.00	<0.00162	0.00207	0.0055	0.004
W	0.0394	0.0401	0.0091	0.138	0.96	0.0463	1.71	0.129	0.2	0.0592	0.0356	0.0173

Magmatic quartz from two-mica granite														
Rim of snowball quartz				Quartz from granite matrix										
Sample	**D8-C1-47**	**D8-C1-48**	**D8-C1-49**	**D8-c1-34**	**D8-c1-36**	**D8-c1-37**	**D8-c1-38**	**D8-C1-54**	**D8-C1-55**	**D8-C1-56**	**D8-C1-57**	**D8-C1-58**	**D8-C1-59**	**D8-C1-60**
Li	13.41	16.6	13.13	8.44	8.5	7.32	6.03	10.06	9.32	7.64	7.56	7.07	8.03	7.04
Be	0.257	0.326	0.1	0.333	0.304	0.199	0.444	0.164	0.385	0.503	0.363	0.229	0.427	0.348
B	4.1	4.05	5.35	5.5	4.72	4.28	4.69	3.51	2.72	3.92	4.5	4.9	4.27	4.26
Na	11.84	24.28	28.6	71.83	18.63	22.44	35.31	18.63	8.87	16.06	16.25	60.33	24.75	17.9
Al	354.21	380.03	386.73	315.9	194.89	244.84	233.96	204.53	266.7	285.94	356.93	207.64	349.65	253.54
S	21.72	21.06	17.98	20.29	17.26	16.83	13.35	14.23	15.07	13.35	13.51	15.68	13.15	15.06
Ti	72.42	63.85	92.49	64.29	20.75	76.09	60.61	44.28	80.63	112.72	104.51	15.11	86.24	42
Ge	1.11	1.12	0.97	0.965	1.44	0.889	0.975	1.17	0.916	0.757	0.9	1.6	0.876	1.27
As	<0.069	<0.060	0.354	0.219	0.248	0.13	0.294	0.226	0.331	0.139	0.622	0.279	0.424	0.155
Rb	1.045	1.084	1.46	0.526	0.219	0.509	0.726	0.152	0.68	0.742	1.48	0.162	1.16	0.565
Sr	0.0384	0.0594	0.0425	0.124	0.1039	0.072	0.1005	0.06	0.099	0.115	0.196	0.103	0.149	0.095
Nb	<0.0060	<0.0096	0.0237	0.0068	0.0113	0.062	0.0141	0.0303	0.0246	0.0318	0.0498	0.0235	0.0144	0.0287
Sn	0.094	0.082	0.1079	0.0972	0.0475	0.2	0.1658	0.0536	0.1208	0.631	0.442	0.0815	0.134	0.0623
Sb	0.071	0.083	0.154	0.152	2.42	0.194	0.1241	0.343	0.189	0.179	0.179	0.215	0.258	0.285
Ta	<0.00	0.00275	0.015	0.0198	0.0146	0.0356	0.0268	0.0067	0.0052	0.0084	0.0208	0.0088	0.0339	0.0063
W	<0.0044	0.0099	0.0154	0.0227	0.0332	0.0372	0.0406	0.0344	0.09	0.0343	0.0488	0.014	0.0354	0.0611

Massive greisen												
Snowball quartz conserved in greisen (cores)												
Sample	**O6-C1-3**	**O6-C1-4**	**O6-C1-5**	**O6-C1-6**	**O6-C1-7**	**O6-C1-8**	**O6-C1-9**	**O6-C1-10**	**O6-C1-11**	**O6-C2-5**	**O6-C2-6**	**O6-C2-7**
Li	14.31	13.55	10.68	21.32	21.21	20.82	20.53	15.9	14.54	8.16	12.87	22.24
Be	0.171	<0.077	0.134	<0.071	0.105	<0.077	0.094	0.111	0.118	0.321	0.083	0.081
B	2.44	2.21	2.53	2.6	2.08	2.06	2.18	2.94	3.24	2.72	2.42	2.95
Na	11.94	11.86	14.36	14.92	19.32	11.92	10.66	8.22	10.25	9.46	15.77	11.85
Al	268.38	350.14	306.52	356.99	280.55	332.02	374.08	328.37	303.48	254.85	384.62	381.24
S	18.42	15.96	15.23	15.16	14.63	13.96	13.58	15.11	12.53	17.89	16.18	16.46
Ti	86.08	151.94	137.74	152.32	104.34	106.64	161.43	138.51	110.08	82.89	165	137.39
Ge	0.744	0.615	0.748	0.677	0.804	0.732	0.69	0.662	0.725	0.559	0.605	0.8
As	0.221	0.128	0.594	0.136	0.176	<0.053	0.057	0.08	0.061	<0.069	0.109	0.066
Rb	0.377	1.011	0.898	0.739	0.554	0.676	1.36	0.638	0.791	0.523	1.53	1.02
Sr	0.0818	0.36	0.0478	0.0475	0.0523	0.0228	0.0376	0.0578	0.0481	0.0627	0.0412	0.0456
Nb	0.0263	<0.0101	0.0086	<0.0051	<0.0053	0.0059	<0.0082	<0.0050	0.0102	<0.0082	<0.0072	0.0054
Sn	0.203	0.0822	0.0627	0.0453	0.0628	0.0409	0.0827	0.0801	0.196	0.0754	0.0742	0.0466
Sb	0.243	0.196	0.611	0.436	0.835	0.181	0.26	0.301	0.251	0.102	0.0502	0.137
Ta	0.0052	0.00056	0.00059	0.00166	0.0048	<0.00237	<0.00150	<0.00236	0.00055	<0.00	0.00041	0.0027
W	0.0136	0.0172	0.0297	0.0253	0.0182	0.016	0.0242	0.0174	0.0224	0.0214	0.0043	0.0064

Massive greisen												
Snowball quartz conserved in greisen (cores)						Snowball quartz conserved in greisen (overgrowth)						
Sample	**O6-C2-8**	**O6-C2-9**	**O6-C2-10**	**O6-C2-11**	**O6-C2-12**	**O6-C1-1**	**O6-C1-2**	**O6-C1-12**	**O6-C1-13**	**O6-C1-14**	**O6-C1-15**	**O6-C2-1**
Li	24.07	21.33	15.2	9.44	8.66	5.31	9.01	3.38	4.05	4.97	3.84	3.36
Be	0.075	0.085	<0.067	0.273	0.219	0.128	0.191	0.162	0.075	0.76	0.09	0.171
B	2.74	2	2.16	2.55	2.42	3.46	3.94	3.64	3.94	5.5	3.07	7.53
Na	10.55	12.4	9.34	11.46	11.84	26.13	29.91	21.17	31.682	29.38	91.93	41.06
Al	365.06	371.72	372.38	292.98	321.54	110.92	126.9224	141.35	113.98	128.41016	134.15	134.87
S	12.7	14.5	13.55	16.14	13.97	23.68	17.35	18.63	16.31	22.89	19.95	27.05
Ti	158.02	156.96	170.12	139.12	98.36	12.48	35.88	16.1	15.44	9.37	11	9.19
Ge	0.682	0.71	0.631	0.643	0.76	2.46	2.25	1.77	1.96	2.64	2.58	2.59
As	0.057	<0.068	<0.060	0.126	<0.068	0.226	0.97	0.213	0.08	6.77	<0.082	0.64
Rb	0.97	0.93	0.91	0.694	1.24	0.125		0.106	0.077	0.459	0.019	0.067
Sr	0.0376	0.0137	0.039	0.0246	0.0266	0.0447	0.365	0.124	0.143	7.52	0.029	0.237
Nb	0.0354	<0.0091	0.0057	0.0129	0.0203	0.032	0.553	<0.0066	<0.0065	<0.0085	<0.0060	<0.0068
Sn	0.0297	0.0328	0.0834	0.144	0.167	0.0398	0.559	0.021	0.038	0.263	0.0161	0.135
Sb	0.16	0.043	0.104	0.0577	0.097	0.338	2.42	0.443	0.498	1.98	0.112	1.131
Ta	0.00086	<0.00	<0.00	0.0039	0.0042	0.0083	0.163	0.0058	<0.00263	0.008	0.0027	0.0087
W	0.0114	0.0043	0.0384	0.0048	0.0218	0.0374	0.223	0.073	0.099	3.45	0.0258	0.111

Massive greisen												
Snowball quartz conserved in greisen (overgrowth)						Quartz from greisen matrix						
Sample	**O6-C2-2**	**O6-C2-3**	**O6-C2-4**	**O6-C2-13**	**O6-C2-14**	**O6-C1-16**	**O6-C1-17**	**O6-C1-18**	**O6-C1-19**	**O6-C1-20**	**O6-C1-21**	**O6-C1-23**
Li	1.73	5.05	3.92	6.98	1.82	5.2	2.39	8.27	5.13	2.44	1.82	1.68
Be	0.103	<0.076	<0.053	<0.084	0.311	0.107	<0.072	<0.093	0.133	<0.064	0.093	<0.068
B	4.83	3.28	3.31	5.5	5.18	3.64	3.77	3	5.06	3.65	3.26	3.54
Na	26.7	41.33	45.3	20.29	49.42	11.36	66.64	5.46	138.22	29.47	74.77	10.94
Al	108	108.37	193.53	98	184.55	132.89	83.536	202.28	274.585	114.11	70.99	122.44
S	20.31	24.55	17.64	17.79	17.41	38.51	25.43	27.28	27.82	19.03	21.29	19.14
Ti	9.47	9.5	15.3	18.23	9.6	10.85	8.53	17.25	10.85	8.47	7.51	10.98
Ge	2.64	2.49	2.5	2.68	2.49	2.44	2.3	1.55	2.75	2.72	2.09	2.62
As	<0.067	0.438	0.312	0.174	0.102	0.184	<0.072	0.14	0.145	0.309	0.271	0.185
Rb	0.1	0.0264	1.16	0.0338	0.068	0.0212	0.045	0.0381	0.044	0.103	0.0302	0.0612
Sr	0.0567	0.0592	0.162	0.105	0.077	0.0326	0.226	0.0465	0.554	0.0334	0.0281	0.0445
Nb	0.0435	0.0185	0.0153	0.0105	<0.0047	<0.0105	0.0108	<0.0081	0.0204	<0.0075	0.0068	<0.0109
Sn	<0.0133	0.0206	0.0305	0.0233	0.0874	0.0136	0.053	0.0225	0.037	<0.0186	0.0792	0.013
Sb	0.15	0.184	1.014	0.161	0.137	0.25	0.384	0.0805	0.149	1.019	1.72	0.414
Ta	0.0113	0.009	0.004	0.00145	0.0044	<0.00156	<0.0029	0.00098	<0.00213	0.0048	<0.00	<0.00
W	0.0129	0.092	0.041	0.0184	0.0066	0.236	<0.0033	0.165	0.098	0.306	0.305	0.051

Massive greisen													
Quartz from greisen matrix							Quartz from greisen porosity						
Sample	**O6-C1-25**	**O6-C2-15**	**O6-C2-16**	**O6-C2-19**	**O6-C2-24**	**O6-C2-25**	**O6-C1-27**	**O6-C1-28**	**O6-C1-29**	**O6-C1-30**	**O6-C2-27**	**O6-C2-29**	**O6-C2-30**
Li	5.78	6.13	7.77	9.52	6.57	11.36	6.08	3.26	7.27	5.6	6.96	5.31	3.64
Be	0.118	0.345	0.271	0.165	0.143	0.342	0.218	0.397	0.213	0.125	<0.079	<0.090	<0.046
B	5.41	2.53	5.4	5.09	3.96	7.54	2.99	5.34	4	4.91	4.21	3.9	4.34
Na	96.81	12.82	75.84	125.83	20.63	105.87	6.12	47.75	12.95	50.07	49.73	75.68	33.75
Al	126.46	156.43	300.14	195.47	137.72	179.36	160.56	71.9079	159.92	151.17	163.38	216.45	105.45
S	18.67	16.15	28.14	23.95	17.81	17.65	19.33	17.97	16.43	18.48	20.8	20.78	16.44
Ti	11.92	12.28	38.86	18.65	10.36	14	29.95	9.19	10.89	11.13	13.83	11.59	9.74
Ge	2.22	2.31	1.2	1.86	2.53	2.39	1.49	2.76	2.58	2.46	2.5	2.54	2.71
As	0.193	<0.060	0.131	0.4	0.074	0.251	<0.061	0.68	0.589	0.29	0.269	0.153	<0.056
Rb	0.22	0.0227	0.503	0.267	0.06	0.273	0.056	0.038	0.072	<0.0156	0.555	0.0433	0.047
Sr	0.071	0.0432	0.154	0.747	0.061	1.38	0.0343	1.64	0.0499	0.0306	0.144	0.072	0.0286
Nb	<0.0100	<0.0071	<0.0105	0.0285	0.0099	0.0421	<0.0094	<0.0061	<0.0108	0.0448	0.0136	0.0108	<0.0042
Sn	<0.0151	0.087	0.097	0.0802	<0.0150	0.22	0.0149	0.132	<0.0139	0.0307	0.391	0.0399	0.0292
Sb	0.291	0.0628	0.082	0.567	0.106	1.036	0.128	0.237	0.99	0.222	1.17	0.146	0.246
Ta	0.0068	0.00122	0.0076	0.0259	0.0037	0.0321	0.00182	0.0053	0.00333	0.0059	0.0031	0.0039	<0.00
W	0.0255	0.0063	0.038	0.0298	0.0118	0.05	0.0309	0.074	0.08	0.0516	0.61	0.0181	0.0121

Hydrothermal veins quartz-Tourmaline stage												
Sample	**P773C-1-1**	**P773C-1-2**	**P773C-1-3**	**P773C-1-4**	**P773C-1-5**	**P773C-1-6**	**P773C-1-7**	**P773C-1-8**	**P773C-1-9**	**P773C-1-10**	**P773C-1-11**	**P773C-1-12**
Li	0.458	5.37	4.58	4.89	5.12	8.1	4.6	7.26	2.54	0.117	0.12	6.53
Be	<0.121	0.195	<0.143	<0.152	<0.147	<0.159	0.171	<0.106	<0.127	0.106	<0.120	<0.182
B	6.52	7.68	7.03	6.42	7.24	7.41	7.07	8.89	7.69	4.64	6.45	7.46
Na	<2.00	20.35	84.12	18.31	24.04	6.59	8.77	12.47	5.91	5.59	21.38	10.9
Al	51.92	89.5	87.48	98.58	92.74	108.92	90.54	108.67	82.65	64.34	58.75	111.71
S	14.37	15.37	12.76	20.63	18.09	15.91	13.14	18.71	15.8	8.36	12.31	11.86
Ti	3.56	6.6	6.45	6.37	7.35	8.26	7.14	7.54	5.77	2.41	4.55	8.03
Ge	2.34	2.35	2.22	2.68	2.57	2.85	2.52	2.54	2.69	2.14	2.72	2.95
As	1.179	1.368	1.345	1.558	1.535	1.699	1.014	1.552	1.721	5.6	1.264	1.668
Rb	0.0632	0.0334	0.123	0.053	0.0341	<0.0258	0.0672	<0.026	<0.025	0.048	<0.0212	0.064
Sr	0.0335	0.059	0.1669	<0.0137	0.091	<0.0138	0.0159	0.0416	0.0393	0.115	0.0455	0.0396
Nb	0.0082	0.011	0.0488	<0.0087	<0.0087	0.0125	<0.0058	0.0308	0.0108	<0.0052	0.0224	<0.0089
Sn	0.099	0.101	0.109	0.072	0.093	0.121	0.0504	0.0667	0.069	1.182	0.092	0.107
Sb	0.086	0.0725	0.0649	0.0531	0.038	0.0143	0.0676	0.0633	0.0928	0.119	0.0359	0.0436
Ta	<0.00143	0.0098	0.0123	<0.00276	0.00454	0.00144	0.00214	<0.0024	0.00507	0.0026	0.0049	<0.00164
W	0.0908	0.05	0.0216	0.026	0.0373	0.0217	0.0379	0.046	0.0175	0.258	0.0121	0.0367

Hydrothermal veins quartz-Tourmaline stage												
Sample	**P773C-1-13**	**P773C-1-14**	**P773C-1-15**	**P773C-2-1**	**P773C-2-2**	**P773C-2-3**	**P773C-2-4**	**P773C-2-5**	**P773C-2-6**	**P773C-2-7**	**P773C-2-8**	**P773C-2-9**
Li	0.118	10.84	8.76	2.55	7.8	5.48	9.01	7.45	9.24	8.36	10.81	11.12
Be	<0.113	<0.142	<0.129	<0.109	<0.146	<0.103	0.135	<0.128	0.21	<0.087	<0.132	<0.127
B	4.77	5.78	7.8	4.79	5.5	6.22	6.91	6.8	7.23	6.42	5.62	7.48
Na	15.78	6.34	36.92	<2.11	10.19	5.14	21.43	6.66	83.74	11.78	13.11	10.73
Al	54.09	121.37	142.32	74.3	96.67	103.86	108.48	104.22	130.2	105.76	122.01	119.53
S	14.43	14.9	13.85	18.19	18.26	15.78	16.36	19.36	13.46	16.54	19.11	13.67
Ti	3.23	9.53	10.12	6	7.69	7.74	8.6	8.12	9.43	8.62	10.04	8.98
Ge	2.3	3.29	3.12	2.55	2.68	2.61	2.71	2.75	2.2	3.13	3.15	2.87
As	1.228	1.327	1.551	1.658	1.63	1.545	1.588	1.663	1.213	1.766	1.642	1.443
Rb	0.0328	<0.0234	0.153	0.0319	<0.0243	<0.026	<0.0230	0.0248	<0.027	<0.0257	0.0441	<0.0235
Sr	0.0263	<0.0141	0.062	0.0166	0.0613	0.1167	0.0188	0.0478	0.0231	0.0163	0.0186	0.0238
Nb	<0.0061	0.0133	0.0308	<0.0079	<0.0074	<0.0068	0.0082	0.0117	0.0098	0.0136	0.0084	<0.0078
Sn	0.0788	0.049	0.0373	0.076	0.0751	0.071	0.22	0.0667	0.607	0.124	0.068	0.0553
Sb	0.0198	0.0482	0.0647	0.0125	0.0391	0.0735	0.0891	0.028	0.0531	0.0154	0.0517	0.0464
Ta	0.00327	0.00125	0.00421	<0.0030	0.00258	0.0093	0.0031	<0.00213	<0.0029	0.00182	0.0041	0.00257
W	0.0093	<0.0081	0.0297	<0.0053	0.0047	0.0056	<0.0055	0.0089	0.0075	0.0077	0.005	0.0053

Hydrothermal veins quartz-Tourmaline stage												
Sample	**P773C-2-10**	**P773C-2-11**	**P773C-2-12**	**P773C-2-13**	**P773C-2-14**	**P773C-2-15**	**P33-1-1**	**P33-1-2**	**P33-1-3**	**P33-1-4**	**P33-1-5**	**P33-1-6**
Li	9.62	10.31	3.77	4.3	16.36	7.58	28.75	17.8	2.59	11.18	18.59	21.32
Be	0.196	0.138	<0.113	<0.103	<0.122	<0.149	0.4	0.301	<0.097	0.22	<0.154	0.302
B	6.93	6.1	3.69	4.99	6.43	4.79	4.91	7.38	8.7	9.15	4.58	9.99
Na	8.73	12.87	12.2	<2.14	31.84	<2.18	<2.40	22.19	12.19	29.52	6.78	17.1
Al	130.77	127.58	88.51	97.87	169.46	112.49	374.31	208.5	82.93	333.56	208.62	453.09
S	11.41	14.46	18	12.49	12.73	12.1	36.74	29.14	36.19	35.11	32.82	32.29
Ti	12.3	9.65	6.98	7.12	10.83	9.32	14.1	12.58	6.11	20.54	14.49	13.94
Ge	3.04	2.89	2.49	2.76	3.09	3.48	3.27	2.69	2.67	3.54	3.56	3.41
As	1.506	1.617	1.631	1.551	1.207	1.276	3	2.53	2.81	3.25	2.96	3.61
Rb	<0.0224	0.0502	<0.0237	<0.0247	0.026	<0.027	<0.029	0.043	<0.0213	<0.027	0.036	0.0262
Sr	0.0241	0.058	0.0308	0.016	<0.0119	0.0318	<0.0164	0.0439	0.0326	0.192	0.0219	0.0303
Nb	0.009	0.0117	0.0125	<0.0073	0.013	0.0125	0.0099	<0.0096	0.0074	<0.100	<0.0082	0.0145
Sn	0.049	0.054	0.62	0.071	0.0743	0.0556	0.07	0.06	0.042	0.065	0.0526	0.113
Sb	0.0187	0.0212	0.0354	0.0134	0.0269	0.229	0.0875	0.1032	0.081	0.0974	0.0553	0.0903
Ta	0.00044	<0.00148	<0.00221	0.00174	0.00089	0.0167	0.0119	0.0074	0.0048	0.0034	0.0098	0.00404
W	<0.0072	0.0041	0.0449	<0.0039	0.021	0.0056	<0.0045	<0.0044	<0.0037	0.0084	0.0077	0.0138

Hydrothermal veins quartz-Tourmaline stage												
Sample	**P33-1-7**	**P33-1-8**	**P33-1-9**	**P33-1-10**	**P33-1-11**	**P33-1-12**	**P33-1-13**	**P33-1-14**	**P33-1-15**	**P33-1-16**	**P33-1-17**	**P33-1-18**
Li	29.12	23.72	22.2	22.41	20.99	17.31	3.47	11.05	31.54	15.99	11.54	0.692
Be	0.493	0.326	0.574	0.534	0.303	0.243	<0.159	0.31	0.609	<0.130	<0.189	<0.110
B	7.01	6.82	5.23	8.09	10.88	3.76	11.84	8.16	13.76	4.85	9.94	8.93
Na	10.89	8.38	17.35	5.4	10.74	8.69	4.84	6.58	9.8	<2.21	38.03	20.35
Al	435.13	280.28	333.78	309.65	216.64	215.53	103.79	172.34	401.33	208.07	235.43	257.28
S	29.92	22.85	28.31	27.68	23.98	21.22	22.68	18.93	20.51	23.19	27.09	27.36
Ti	15.59	16.83	11.91	11.24	12.92	9.94	9.14	12.2	15.23	14.07	12.74	6
Ge	3.37	3.25	2.98	2.7	2.74	2.72	2.72	3.05	3.56	2.92	2.87	2.84
As	3.17	2.4	3.18	3	2.89	2.57	2.88	2.52	3.13	2.81	3.17	2.97
Rb	0.099	<0.027	0.043	<0.027	<0.026	0.041	<0.031	0.0379	<0.027	<0.026	0.033	<0.0258
Sr	0.0591	0.451	0.0442	0.0377	0.052	0.0334	0.0404	0.0257	0.0475	0.0524	0.0385	0.0619
Nb	0.0535	0.0313	0.0239	0.0081	<0.0087	0.0127	0.0135	<0.0099	<0.0069	0.0223	0.0165	<0.0115
Sn	0.07	0.043	0.114	0.029	0.0398	0.075	0.086	0.051	0.0713	0.089	0.081	0.035
Sb	0.132	0.066	0.0696	0.0362	0.15	0.1023	0.0504	0.0644	0.0599	0.103	0.088	0.0242
Ta	0.0063	0.011	0.0051	<0.0025	0.00275	0.0079	<0.0035	0.0032	0.004	0.0513	0.0247	<0.0029
W	0.0072	0.0068	0.0049	<0.0062	<0.0042	<0.0072	0.008	<0.0038	0.0035	0.0188	<0.0068	<0.0059

Hydrothermal veins quartz-Tourmaline stage												
Sample	**P33-1-19**	**P33-1-20**	**P33-1-21**	**P33-1-22**	**P33-1-23**	**P33-1-24**	**P33-1-25**	**P33-1-26**	**P33-1-27**	**P33-1-28**	**P33-1-29**	**P33-1-30**
Li	14.46	19.34	13.71	4.93	8.06	12.52	11.34	15.41	14.74	20.53	11.65	15.7
Be	0.406	0.372	0.31	0.107	0.134	0.265	0.175	0.513	0.435	0.314	0.222	0.262
B	5.53	9.24	5.44	6.15	3.79	6.7	4.03	3.91	5.05	5.4	4.97	7.02
Na	<2.27	21.77	9.92	13.81	14.15	19.39	21.2	5.66	3.9	8.01	6.46	17.55
Al	264.09	312.29	229.21	104.47	132.17	183.73	219.38	281.49	298.89	317.39	251.12	250.15
S	27.99	24.72	22.49	21.75	27.25	23.45	17.93	22.07	22.03	16.24	15.49	17.61
Ti	11.27	12.42	15.38	7.34	11.52	13.9	11.71	11.86	13.16	11.78	9.71	9.1
Ge	3.17	3.14	2.93	2.8	2.8	2.92	2.98	3	3.4	3.19	3.11	2.77
As	3.24	3.14	2.63	3.08	2.94	2.76	2.94	2.71	3.47	3.27	3.04	3.07
Rb	<0.0237	0.079	0.0354	<0.026	<0.029	0.043	0.027	0.046	<0.029	0.044	0.028	0.043
Sr	0.0544	0.0884	0.0448	0.021	0.0524	0.0311	0.0392	0.04	0.0319	0.0465	0.0606	0.0323
Nb	0.015	0.0152	<0.0065	<0.0088	0.0142	0.0087	<0.0098	<0.0097	<0.0083	0.0233	<0.0071	<0.0102
Sn	0.043	0.028	0.0697	0.067	0.031	0.091	0.0441	0.093	0.05	0.04	0.073	<0.028
Sb	0.0596	0.0509	0.0642	0.0688	0.0511	0.148	0.0901	0.0221	0.0448	0.042	0.167	0.0404
Ta	0.0071	<0.00233	0.0095	0.0087	0.006	<0.0038	0.0045	0.00229	0.003	0.0081	0.0055	0.0085
W	0.00221	<0.0082	0.0066	0.0099	0.007	0.009	<0.0058	0.0057	<0.0046	<0.0040	0.011	<0.0078

Hydrothermal veins W-Sn mineralization stage												
Sample	**12H-c-2**	**12H-c-3**	**12H-c-4**	**12H-c-6**	**12H-c-7**	**12H-c-8**	**12H-c-9**	**12H-c-10**	**12H-c-12**	**12H-b-4**	**12H-b-8**	**12H-c-15**
Li	16.21	6.58	8.28	6.64	5.17	11.44	10.54	5.63	10.78	11.68	12.74	8.38
Be	0.327	<0.170	<0.100	<0.101	<0.272	0.251	<0.171	<0.094	<0.50	<0.44	<0.099	<0.073
B	3.9	6.88	4.84	6.36	2.84	4.04	3.31	5.52	6.74	13.35	4.32	3.84
Na	<4.33	37.89	21.6	51.49	43.58	37.5	44.15	29.5	<6.79		26.12	23.49
Al	171.6	100.33	106.03	92.27	75.15	113.09	114.15	69.32	83.32	241.41	101.26	96.04
S	13.66	17.91	19.04	20.04	21.87	29.74	23.4	28.72	21.97	13.39	18.91	17.18
Ti	7.67	8.25	6.21	5.7	6.24	5.63	5.54	5.27	4.81	21.89	5.69	4.42
Ge	3.17	3.17	3.08	3.03	2.42	2.45	2.67	2.94	3.15	2.36	1.068	3.11
As	<0.206	6.01	0.174	0.17	0.226	0.348	<0.231	0.356	0.536	3.89	1.092	0.166
Rb	<0.075	0.19	0.035	0.065	<0.078	<0.089	<0.067	0.038	<0.106	0.719	<0.033	0.031
Sr	0.07	0.665	0.0131	0.0782	0.0312	0.0387	0.0282	0.0483	0.091	1.699	0.241	0.0589
Nb	0.0283	0.1138	0.0095	<0.0063	<0.0101	0.01	0.0152	0.0075	0.0197	0.0588	0.0065	<0.0061
Sn	0.0508	0.157	0.0275	0.0381	<0.042	<0.052	0.064	<0.0172	0.0574	0.877	0.0376	0.0267
Sb	0.572	0.707	1.088	0.496	0.0496	0.06	0.133	0.0625	0.881	2.5	0.1286	0.544
Ta	<0.0056	0.0127	0.0085	0.0025	0.00208	0.0254	0.00455	0.00149	0.0081	0.0276	<0.00210	0.00274
W	0.0342		0.021	0.02	<0.0113	0.0221	0.0062	0.1224	0.0487		1.676	0.1006

Hydrothermal veins W-Sn mineralization stage												
Sample	**12H-c-16**	**P12H-c-1**	**P12H-c-2**	**P12H-c-3**	**P12H-c-4**	**P12H-c-5**	**P12H-c-6**	**P12H-clair-1**	**P12H-clair-2**	**p12F-c-1**	**p12F-c-2**	**p12F-c-3**
Li	9.79	14.19	13.44	12.14	15.38	10.71	14.29	19.67	28.12	4.37	2.42	3.77
Be	0.74	0.105	<0.116	<0.092	0.12	<0.094	0.096	<0.112	<0.097	<0.138	<0.100	<0.110
B	2.96	3.91	4.02	4.54	3.77	4.3	3.82	4.98	4.24	2.45	11.72	4.95
Na	<7.98	<2.21	<1.99	<2.11	<1.91	<1.98	31.35	<1.94	<1.87	<2.42	27.9	60.91
Al	146.93	138.58	111.04	117.19	131.6	109.85	149.07	258.16	231.39	55.96	46.83	52.31
S	15.23	19.16	17.82	18.46	17.71	16.99	23.53	19.57	17.65	24.73	25.75	20.93
Ti	7.25	6.48	6.8	6.05	5.99	6.33	6.79	8.21	7.36	5.16	5.41	5.28
Ge	2.25	3.09	3.22	3.43	3.28	3.43	2.8	3.01	3.1	2.58	2.74	2.9
As	<0.36	<0.112	<0.097	<0.094	0.601	0.156	0.285	0.244	0.263	0.21	0.275	0.726
Rb	<0.131	0.106	<0.033	<0.036	<0.032	<0.033	0.095	0.278	0.07	<0.039	0.287	<0.034
Sr	0.0875	0.202	0.0533	0.0711	0.0717	0.0322	0.187	0.22	0.1461	0.0431	0.0606	0.03
Nb	0.094	0.0173	<0.0054	0.0164	<0.0050	<0.0067	0.0091	0.017	<0.0067	0.0074	<0.0077	<0.0062
Sn	0.197	0.0192	0.0287	0.0255	0.0356	0.0551	0.0728	0.159	0.785	0.0647	0.0279	0.1003
Sb	0.083	0.146	0.1144	0.1007	0.169	0.0793	0.506	0.83	0.581	0.0516	0.191	0.1074
Ta	0.0263	0.0058	<0.00115	0.00367	0.00293	0.00201	0.0066	0.00165	0.00321	0.00433	0.00135	0.00261
W		0.0238	0.191		0.94	0.0687	1.13	2.146		0.0109	0.0261	0.152

Hydrothermal veins W-Sn mineralization stage												
Sample	**p12F-c-4**	**p12F-c-5**	**p12F-c-7**	**p12F-c-8**	**p12F-c-9**	**p12F-c-10**	**P882D-1-1**	**P882D-1-2**	**P882D-1-3**	**P882D-1-4**	**P882D-1-5**	**P882D-1-6**
Li	2.91	2.78	10.97	8.81	10.98	9.44	0.631	0.81	7.36	8.46	9.7	9.5
Be	<0.080	0.062	0.073	<0.080	0.133	<0.067	<0.192	<0.172	0.136	<0.132	<0.153	<0.169
B	4.71	5.64	2.58	5.03	7.1	8.39	5.61	4.91	5.44	4.47	4.85	4.15
Na	<1.81	23.38	<1.87	33.79	20.47	<2.17	18.05	35.21	<1.95	5.07	30.56	64.15
Al	52.43	65.86	119.61	131.9	160.76	112.03	43.62	44.15	86.7	90.47	92.13	97.32
S	14.99	19.77	20.48	17.06	20.2	19.87	26.08	25.5	16.58	19.7	24.45	14.86
Ti	4.56	5.36	6.55	6.38	5.86	7.09	4.09	4.65	3.83	3.87	3.81	4.73
Ge	2.28	2.86	3.16	3.1	3.16	3.16	1.408	1.563	2.15	2.06	2.03	2.24
As	0.248	0.407	<0.089	0.808	0.309	0.17	2.43	2.46	2.025	2.14	2.32	1.992
Rb	<0.029	0.093	<0.029	0.072	0.177	0.095	<0.028	<0.025	<0.0238	<0.0235	<0.025	<0.025
Sr	0.0314	0.0403	0.0126	0.0583	0.0538	0.0273	0.0391	0.0148	0.0266	0.0236	0.0402	0.0337
Nb	0.0157	0.1336	<0.0037	0.0078	<0.0061	0.0118	0.0078	<0.0075	<0.0081	<0.0080	<0.0091	<0.0066
Sn	0.0326	0.0814	<0.0143	0.0891	0.0131	0.0254	0.072	0.055	0.064	0.0771	0.08	0.102
Sb	0.0456	0.251	0.1341	0.135	0.192	0.121	0.0267	0.0358	0.341	0.363	0.702	0.384
Ta	0.00168	0.024	<0.00116	0.0029	0.00097	0.00377	0.00156	<0.00215	0.0043	<0.00127	0.00105	0.0005
W	0.0563	0.491	<0.0043	0.256	0.0352	0.0386	0.0073	0.0114	0.068	<0.0054	<0.0034	0.0092

Hydrothermal veins W-Sn mineralization stage												
Sample	**P882D-1-7**	**P882D-1-8**	**P882D-1-9**	**P882D-1-10**	**P882D-1-11**	**P882D-1-12**	**P882D-1-13**	**P882D-1-14**	**P882D-1-15**	**P882D-2-1**	**P882D-2-2**	**P882D-2-3**
Li	10.18	10.92	9.7	8.61	8.34	4.58	2.24	2.14	16.73	6.71	0.486	5.42
Be	<0.136	<0.173	<0.113	<0.210	<0.216	<0.124	<0.202	<0.165	0.148	0.159	<0.159	<0.157
B	4.5	5.77	4.46	7.56	7	6.62	5.55	4.83	4.21	5.46	6.78	5.74
Na	<1.89	40.26	11.4	<2.47	<2.57	22.55	<2.22	4.33	10.78	<2.73	30.68	26.52
Al	96.06	96.43	97.76	87.04	85.76	68.83	56.36	52.08	126.63	87.31	50.58	80.1
S	18.11	17.32	18.07	15.05	19.52	17.12	18.53	18.74	16.29	21.5	15.57	17.32
Ti	2.97	4.25	4.04	3.55	2.65	3.61	4.49	4.35	3	4.14	4.31	3.77
Ge	2.07	2.03	2.17	2.1	2.25	2.1	1.588	1.437	1.955	2.1	1.86	2.39
As	2.08	1.96	1.858	2.32	1.82	1.77	1.855	1.724	1.881	1.568	1.79	1.861
Rb	0.0372	0.059	0.031	<0.030	<0.031	<0.0229	<0.026	<0.0247	<0.0245	<0.033	0.042	0.059
Sr	0.0128	0.038	0.0286	0.0233	0.027	0.0167	<0.0127	0.0505	0.0322	<0.0155	0.0311	0.0338
Nb	<0.0064	<0.0078	0.0066	<0.0091	<0.0097	0.0099	0.0193	<0.0101	0.0066	0.011	<0.0071	<0.0086
Sn	0.107	0.0401	0.0634	0.0388	0.052	0.0578	0.042	0.0303	0.0957	0.074	0.083	0.088
Sb	0.605	0.915	0.662	0.0959	0.0644	0.0648	0.0578	0.223	0.116	0.264	0.0506	0.529
Ta	0.00353	0.0061	<0.00147	<0.00	0.00356	0.00273	0.0083	0.00336	0.00323	0.00396	0.0039	0.00626
W	0.0459	0.0062	0.0127	0.0088	<0.0043	0.0344	0.0091	0.0298	0.0448	0.0081	0.0102	0.0241

Hydrothermal veins W-Sn mineralization stage												
Sample	**P882D-2-4**	**P882D-2-5**	**P882D-2-6**	**P882D-2-7**	**P882D-2-8**	**P882D-2-9**	**P882D-2-10**	**P882D-2-11**	**P882D-2-12**	**P882D-2-13**	**P882D-2-14**	**P882D-2-15**
Li	5.77	6.62	1.152	1.759	2.14	1.99	0.149	0.545	6.85	0.375	0.457	0.635
Be	<0.126	<0.113	<0.113	0.148	<0.176	<0.196	<0.172	0.244	<0.137	<0.166	<0.187	<0.111
B	6.08	5.01	4.44	4.85	5.62	5.94	6.53	7.79	9.29	7.31	7.68	6.79
Na	<1.97	<1.86	25.57	<2.45	<2.01	14.8	25.21	<2.28	21.8	31.68	39.35	19.71
Al	87.34	93.81	56.62	57.34	62.73	64.1	46.95	56.13	87.14	54.43	55.85	49.51
S	17.42	17.8	17.53	15.45	12.57	16.61	13.42	15.47	13.31	17.42	15.68	15.36
Ti	4.21	4.98	3.02	4.69	4.58	3.73	2.7	3.94	3.94	3.36	3.25	3.86
Ge	1.858	2.44	1.718	2.15	2.38	2.46	2.2	2.54	0.985	2.51	2.67	2.02
As	1.462	1.57	1.797	1.85	1.793	1.589	1.595	1.428	1.85	1.718	1.552	1.711
Rb	0.0543	<0.0237	<0.0224	<0.030	0.0253	<0.026	<0.0251	0.034	<0.026	0.036	0.08	0.0506
Sr	0.0275	<0.0107	0.1279	<0.0164	0.0575	<0.0144	0.0275	<0.0145	0.0515	0.0213	0.0353	0.0846
Nb	<0.0064	<0.0074	<0.0066	0.0165		0.0242	0.0149	<0.0097	0.0226	0.0087	0.012	0.0107
Sn	0.0783	0.0848	0.0766	0.074	0.065	0.067	0.0802	0.088	0.21	0.0454	0.0535	0.084
Sb	0.0671	0.375	0.0231	0.0688	0.0623	0.1082	0.0471	0.0409	0.0814	0.0543	0.0685	0.0507
Ta	0.00149	<0.00134	0.00269	0.0073		0.0041	<0.0027	0.0064	0.0115	0.0057	0.00242	0.00346
W	0.962	0.0383	0.0163	0.027	0.746	0.0148	0.18	0.0891	0.185	0.0724	0.0288	0.0466

8. Representative LA-ICP-MS U-Pb apatite data used for geochronology

Magmatic apatite from the two-mica granite						
Sample	**U (ppm)**	**Pb (ppm)**	**$^{238}U/^{206}Pb$**	**Error (2σ)**	**$^{207}Pb/^{206}Pb$**	**Error (2σ)**
ApatMagma_1	116.9	17.1	12.52	0.42	0.3942	0.0065
ApatMagma_2	83.4	7.3	14.88	0.49	0.2948	0.0046
ApatMagma_3	78.4	5.8	15.80	0.52	0.2731	0.0040
ApatMagma_4	93.0	15.4	11.64	0.42	0.4167	0.0085
ApatMagma_5	82.3	6.7	15.41	0.57	0.2940	0.0250
ApatMagma_6	92.2	30.1	8.22	0.27	0.5553	0.0071
ApatMagma_7	59.2	60.9	3.41	0.15	0.7430	0.0150
ApatMagma_8	56.0	205.0	1.09	0.07	0.8390	0.0180
ApatMagma_9	87.1	8.1	14.73	0.48	0.3030	0.0044
ApatMagma_10	106.4	17.3	12.14	0.40	0.3983	0.0064
ApatMagma_11	55.0	62.1	3.28	0.24	0.7450	0.0120
ApatMagma_12	38.8	9.0	10.48	0.38	0.4658	0.0095
ApatMagma_13	28.4	13.0	6.74	0.25	0.6010	0.0140
ApatMagma_14	35.5	16.1	7.24	0.35	0.6020	0.0120
ApatMagma_15	64.6	9.9	13.44	0.72	0.3590	0.0110
ApatMagma_16	94.3	22.1	10.12	0.41	0.4700	0.0110
ApatMagma_17	42.0	14.1	8.37	0.30	0.5389	0.0096
ApatMagma_18	95.7	19.6	11.15	0.45	0.4530	0.0093
ApatMagma_19	32.1	10.5	8.62	0.31	0.5360	0.0110
ApatMagma_20	45.0	14.0	8.98	0.39	0.5270	0.0120
ApatMagma_21	134.0	10.9	16.00	0.69	0.2624	0.0059
ApatMagma_22	119.8	12.7	14.51	0.67	0.3162	0.0073
ApatMagma_23	56.5	9.0	12.00	0.45	0.4078	0.0087
Apat121316c_17	26.9	11.72	7.194245	0.2432586	0.5871	0.0084
Apat121316c_18	10.94	9.5	4.166667	0.1371528	0.7	0.01
Apat121316c_19	29.37	112.1	1.054852	0.04450854	0.821	0.011
Apat121316c_20	43.64	12.75	9.398496	0.3356606	0.506	0.011
Apat121316c_21	31.04	12.23	7.604563	0.2602322	0.556	0.011

Altered magmatic apatite (greisen)

Sample	U (ppm)	Pb (ppm)	$^{238}U/^{206}Pb$	Error (2σ)	$^{207}Pb/^{206}Pb$	Error (2σ)
Apat_Hydro_1	8.75	18.5	1.941748	0.08671882	0.798	0.02
Apat_Hydro_2	6.87	19.76	1.468429	0.06468849	0.818	0.016
Apat_Hydro_4	22.12	30.12	2.809778	0.1184228	0.754	0.014
Apat_Hydro_5	30.01	20.44	4.819277	0.2322543	0.678	0.016
Apat_Hydro_6	28	22.98	4.385965	0.307787	0.675	0.017
Apat_Hydro_7	50.2	30.9	5.422993	0.2646797	0.665	0.03
Apat_Hydro_9	28.19	11.16	7.843137	0.319877	0.576	0.014
Apat_Hydro_10	2.151	5.27	1.730104	0.09877755	0.812	0.023
Apat_Hydro_11	10.44	7.36	4.938272	0.2438653	0.683	0.019
Apat_Hydro_12	2.956	7.54	1.612903	0.07023933	0.812	0.013
Apat_Hydro_13	38.83	103.6	1.533742	0.07762806	0.806	0.014
Apat_Hydro_14	63.4	61.2	3.90625	0.3967285	0.696	0.032
Apat_Hydro_15	16.63	180.9	0.3903201	0.01675847	0.849	0.014
Apat_Hydro_16	48.35	122.1	1.612903	0.0962539	0.802	0.015
Apat_Hydro_17	11.21	87.4	0.5617978	0.02367125	0.85	0.014
Apat_Hydro_18	19.65	25.1	3.116236	0.1359529	0.758	0.014
Apat_Hydro_19	7.7	18.6	1.404494	0.1321645	0.811	0.016
Apat_Hydro_20	83.1	34.3	6.91085	1.576075	0.596	0.015
Apat_Hydro_21	24.55	142.1	0.7132668	0.03255997	0.835	0.014
Apat_Hydro_22	29.46	20.74	5.045409	0.2341966	0.658	0.024
Apat_Hydro_23	18.5	23.5	3.154574	0.2288808	0.747	0.026
Apat121316c_1	0.86	4.15	0.8340284	0.023	0.845	0.022
Apat121316c_2	17.68	136.7	0.5800464	0.03162666	0.832	0.022
Apat121316c_3	20.9	24.1	2.967359	0.2377409	0.733	0.02
Apat121316c_4	9.75	51.6	0.798722	0.03955333	0.851	0.022
Apat121316c_5	36.4	10.73	8.467401	0.4516903	0.533	0.02
Apat121316c_7	22.48	30.7	2.48139	0.1477751	0.766	0.027
Apat121316c_8	10.09	40.5	0.9259259	0.03600823	0.832	0.015
Apat121316c_9	22.33	69.2	1.153403	0.05454383	0.798	0.02
Apat121316c_10	3.291	8.47	1.665556	0.05548156	0.8	0.012
Apat121316c_11	28.88	10.53	8.143322	0.2851489	0.5408	0.0092
Apat121316c_12	4.61	59.2	0.3521127	0.02851617	0.825	0.024
Apat121316c_13	2.145	57.4	0.1610306	0.00777926	0.843	0.011
Apat121316c_14	14.68	42	1.49925	0.06743255	0.811	0.023
Apat121316c_15	34.5	17.48	6.17284	0.6477671	0.614	0.015
Apat121316c_16	24.73	27.68	3.388682	0.1263148	0.734	0.0086

Hydrothermal apatite from mineralized veins

Sample	U (ppm)	Pb (ppm)	$^{238}U/^{206}Pb$	Error (2σ)	$^{207}Pb/^{206}Pb$	Error (2σ)
Apat_Veines_1	31.91	13.82	6.872852	0.3212055	0.6012	0.0069
Apat_Veines_2	34.76	13.14	7.564297	0.3661989	0.5781	0.0065
Apat_Veines_3	89.7	17.7	11.80638	0.6133182	0.452	0.0081
Apat_Veines_4	30.93	14.36	6.69344	0.3180952	0.6017	0.0064
Apat_Veines_5	34.91	16.25	6.626905	0.3161943	0.6086	0.0066
Apat_Veines_6	62.7	18.62	8.810573	0.4191814	0.5223	0.0054
Apat_Veines_7	53.38	17.38	8.196721	0.3963988	0.5327	0.0054
Apat_Veines_8	71.43	22.82	8.285004	0.4049836	0.5283	0.0059
Apat_Veines_9	128.5	20.19	12.93661	0.652688	0.378	0.0036
Apat_Veines_10	26.59	11.82	6.480881	0.3192139	0.602	0.0071
Apat_Veines_11	65.42	19.35	8.403361	0.4025139	0.5206	0.0056
Apat_Veines_12	98.4	23.43	9.624639	0.4631684	0.4841	0.0052
Apat_Veines_13	35.9	23.1	5.408329	0.3802503	0.65	0.0094
Apat_Veines_14	31.84	15.15	6.501951	0.3128377	0.6012	0.0064
Apat_Veines_15	32.76	15.83	6.480881	0.9240401	0.61	0.013
Apat_Veines_16	33.82	17.76	6.071645	0.294919	0.619	0.0081
Apat_Veines_17	42.98	14.42	8.176615	0.4679992	0.531	0.0083
Apat_Veines_18	35.22	20.78	5.800464	0.2859858	0.6442	0.008
Apat_Veines_19	37.18	17.8	6.715917	0.3247455	0.6097	0.0072
Apat_Veines_20	153.3	20.69	14.403	0.6845728	0.3531	0.0034
Apat_Veines_21	57.2	16.59	9.149131	0.418533	0.514	0.0047
Apat_Veines_22	67.48	19.28	9.259259	0.4372428	0.5153	0.0059

Supporting information for:

Chapter V: Dynamic permeability related to greisenization reactions in Sn-W ore deposits: Quantitative petrophysical and experimental evidence

Gaëtan Launay[1], Stanislas Sizaret[1], Laurent Guillou-Frottier[1], Colin Fauguerolles[1], Rémi Champallier[1] and Eric Gloaguen[1]

(1) Université d'Orléans/CNRS/ISTO/BRGM, UMR 7327, 1A rue de la Férollerie, 45071 Orléans, France

---

Electronic Supplementary Materials 1 (ESM 1)

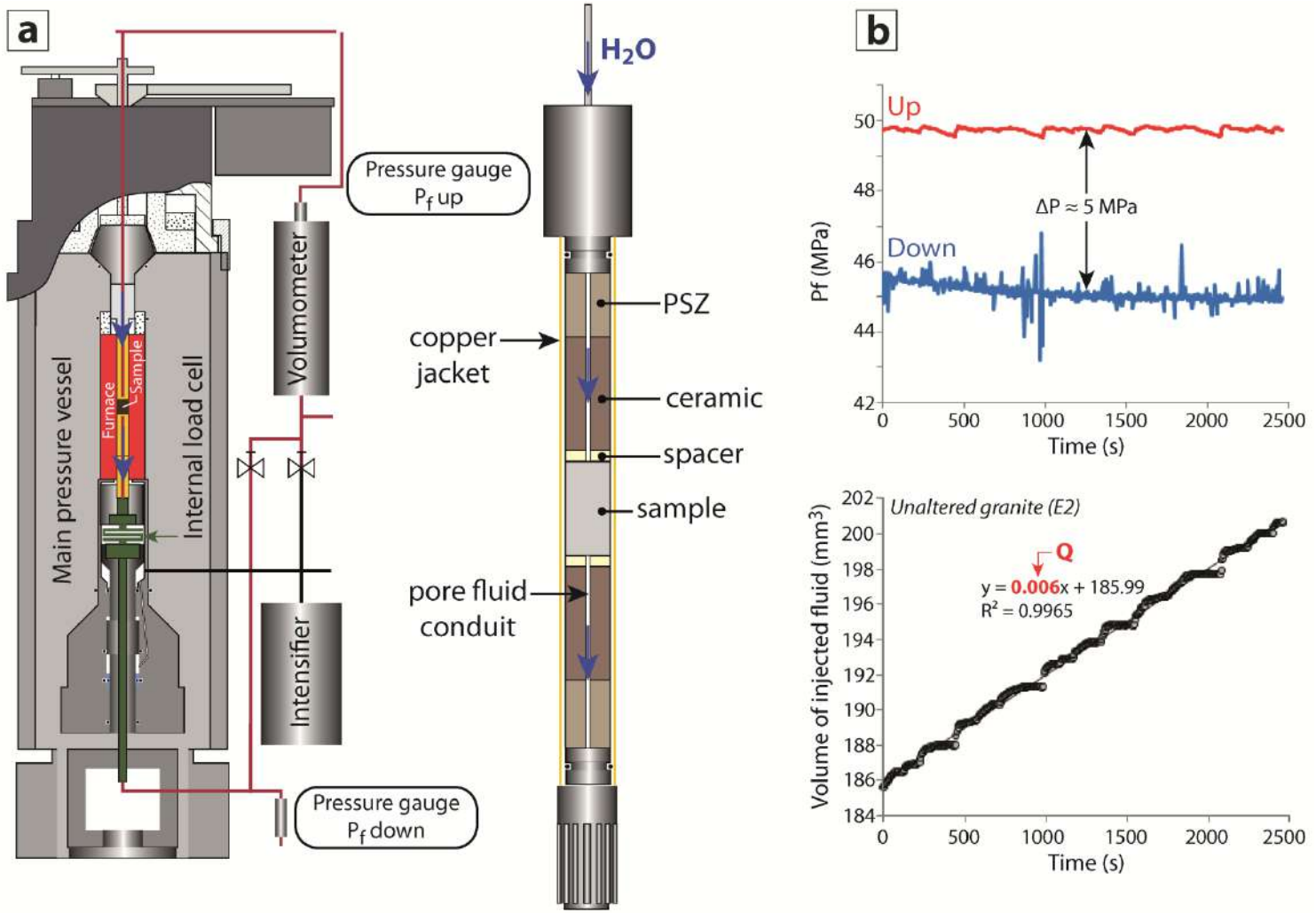

Figure 15: (a) Schematic representation of the Paterson apparatus and the pore fluid pressure system used for the permeability measurements (modified from Kushnir et *al.*, 2017). (b) Monitoring of the pressure fluid difference across the sample (ΔP) and the volume of fluid injected into the sample over the experiment time. The flow rate through the sample core was calculated from the linear regression shown in the diagram (Q = 0.006 mm3/s). From this flow rate and the pressure difference the permeability was estimated. This figure represents the measurement performed on the unaltered granite sample (E2).

Electronic Supplementary Materials 2 (ESM 2)

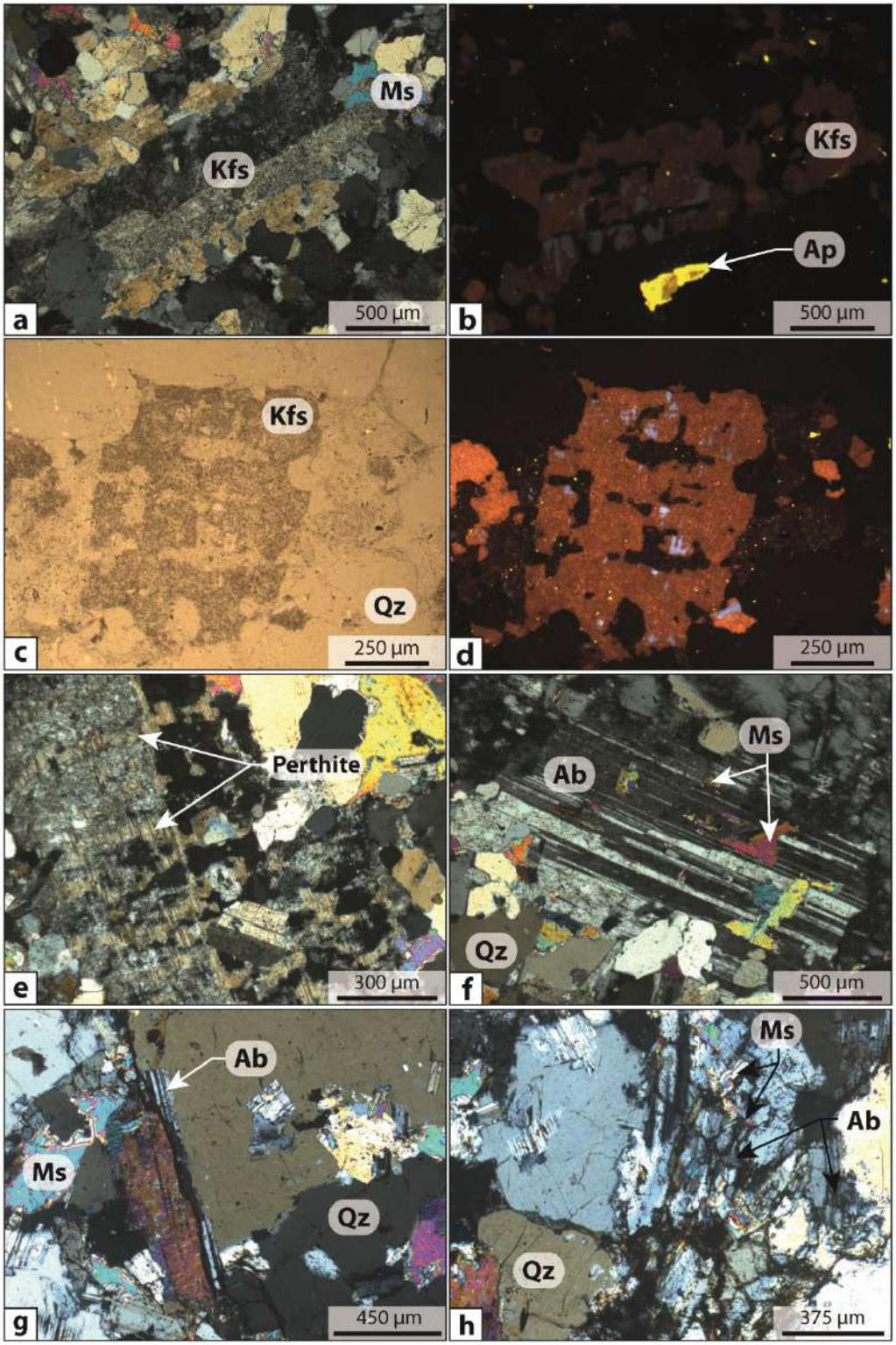

Figure 16 Photomicrographs of k-feldspars and albite composing the two-mica granite and the greisenized granite of Panasqueira. (a) to (c) Photomicrograph of matrix k-feldspars exhibiting replacement textures related to the early alkali metasomatism (a and c photomicrograph in transmitted light, b and d cathodoluminescence images). (e) Photomicrograph of k-feldspars exhibiting perthitic texture (transmitted polarized light). (f) Photomicrograph of albite in granite matrix (polarized transmitted light). (g) and (h) relics of albite partially replaced by muscovite (polarized transmitted light).

Electronic Supplementary Materials 3 (ESM 3)

wt%	Primary magmatic alkali feldspars (blue cathodoluminescence zones)										Metasomatized alkali feldspars (red cathodoluminescence zones)									
SiO_2	63.6	63.4	63.4	62.7	63.0	62.4	62.5	61.2	63.2	61.6	62.9	63.7	64.0	61.1	61.3	62.1	61.8	62.8	63.5	62.2
TiO_2	0.0	0.0	0.0	0.0	0.0	0.1	0.0	0.0	0.0	0.0	0.0	0.0	0.0	0.0	0.0	0.0	0.0	0.0	0.1	0.1
Al_2O_3	18.9	19.2	18.3	18.7	18.5	18.9	18.3	18.6	18.3	18.5	17.8	18.5	17.9	17.1	17.2	17.3	17.3	17.6	17.6	18.2
FeO	0.0	0.1	0.0	0.0	0.0	0.0	0.1	0.2	0.1	0.0	0.1	0.3	0.1	0.0	0.2	0.0	0.1	0.0	0.0	0.0
MnO	0.0	0.0	0.0	0.0	0.0	0.0	0.0	0.0	0.0	0.0	0.1	0.0	0.0	0.0	0.0	0.0	0.0	0.1	0.0	0.0
MgO	0.0	0.0	0.0	0.0	0.0	0.0	0.0	0.0	0.0	0.0	0.0	0.0	0.0	0.0	0.0	0.0	0.0	0.0	0.0	0.0
CaO	0.0	0.0	0.0	0.0	0.0	0.0	0.0	0.0	0.0	0.0	0.0	0.0	0.0	0.0	0.0	0.0	0.0	0.0	0.0	0.0
Na_2O	1.2	1.2	0.8	1.3	1.4	1.4	1.1	0.7	1.7	0.9	0.2	0.2	0.3	0.2	0.3	0.2	0.2	0.3	0.2	0.3
K_2O	15.1	15.1	16.1	15.0	14.7	14.6	15.2	15.3	13.6	15.8	16.1	16.5	16.5	16.5	16.9	16.6	16.6	16.5	16.7	15.7
P_2O_5	0.4	0.5	0.3	0.2	0.3	0.2	0.3	0.2	0.3	0.1	0.4	0.2	0.1	0.1	0.1	0.0	0.0	0.1	0.2	0.2
Total	99.1	99.6	99.0	98.1	97.9	97.6	97.5	96.3	97.0	97	97.6	99.4	98.8	95.2	95.9	96.4	96.1	97.3	98.1	96.8
Ab (%)	11	11	7	12	12	13	10	7	16	8	2	2	3	2	2	2	2	2	2	3
Or (%)	89	89	93	88	88	87	90	93	84	92	98	98	97	98	98	98	98	98	98	97
An (%)	0	0	0	0	0	0	0	0	0	0	0	0	0	0	0	0	0	0	0	0

Table 3 EPMA analyses of alkali feldspars composing the least altered two-mica granite of Panasqueira.

wt%	Plagioclase from least altered two-mica granite									
SiO_2	65.4	66.6	68.0	68.4	68.2	68.7	68.9	68.5	68.0	69.2
TiO_2	0.0	0.0	0.0	0.0	0.0	0.0	0.0	0.0	0.0	0.0
Al_2O_3	18.6	21.4	19.2	19.2	19.1	19.3	19.4	19.5	19.3	18.9
FeO	0.0	0.1	0.0	0.0	0.0	0.0	0.0	0.0	0.0	0.1
MnO	0.0	0.0	0.0	0.0	0.0	0.0	0.0	0.0	0.0	0.0
MgO	0.0	0.0	0.0	0.0	0.0	0.0	0.0	0.0	0.0	0.0
CaO	0.6	0.2	0.1	0.0	0.0	0.0	0.0	0.0	0.3	0.0
Na_2O	11.5	9.8	11.4	11.2	11.2	11.1	11.2	9.9	10.7	10.3
K_2O	0.1	0.9	0.1	0.1	0.1	0.2	0.1	0.1	0.2	0.0
P_2O_5	0.2	0.2	0.0	0.0	0.0	0.1	0.1	0.0	0.0	0.0
Total	96.4	99.1	98.9	99.0	98.7	99.4	99.8	98	98.5	98.6
Ab (%)	96	93	99	99	99	99	99	99	97	1
Or (%)	1	6	1	1	1	1	1	1	1	0
An (%)	3	1	0	0	0	0	0	0	3	0

Table 4 EPMA analyses of plagioclase composing the least altered two-mica granite of Panasqueira.

Electronic Supplementary Materials 4 (ESM 4)

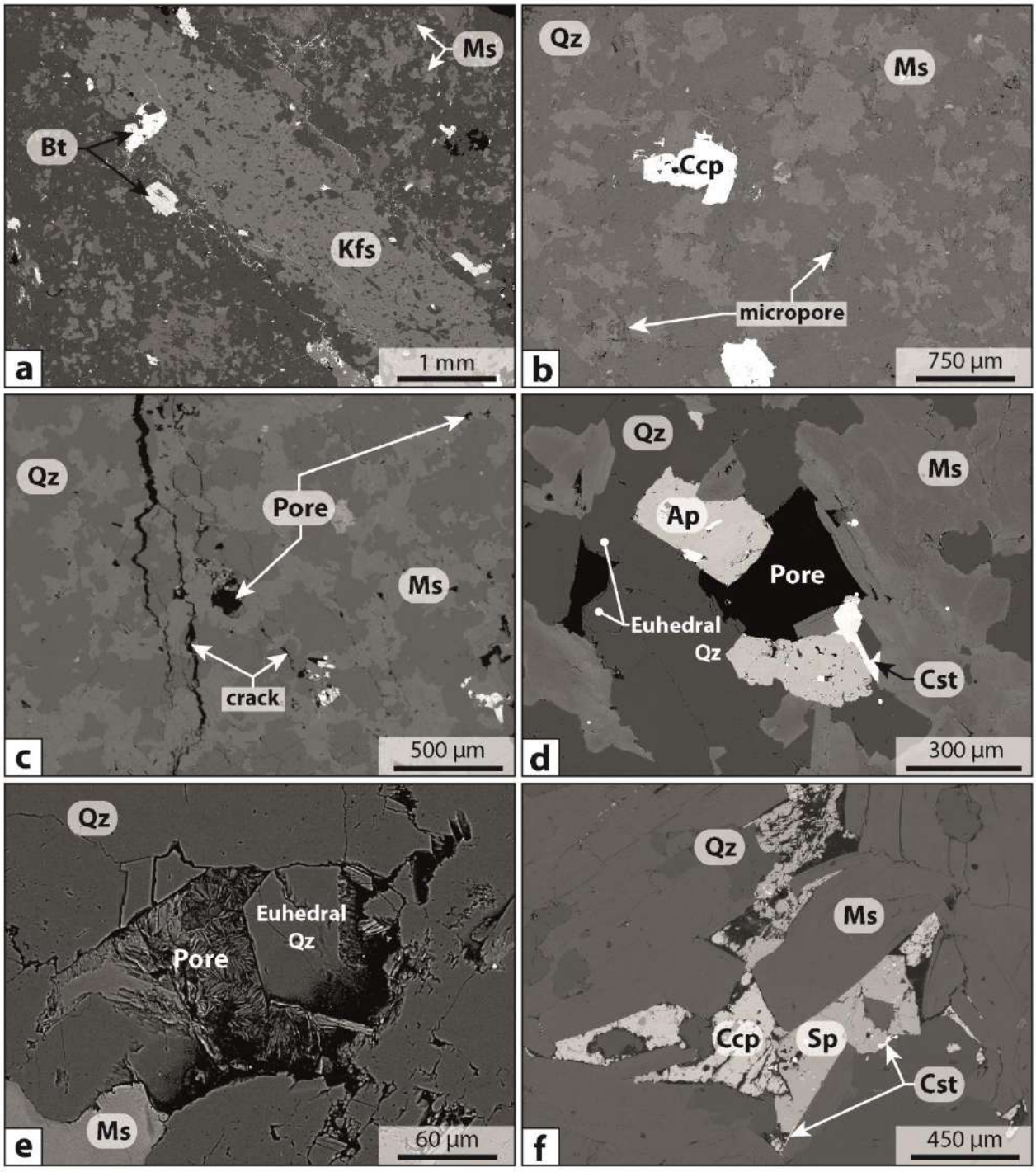

Figure 17: More SEM-BSE images showing the microtextural characteristics of greisenized granite and greisen of Panasqueira. (a) Section of k-feldspars partially altered into muscovite during greisenization. Note the presence of micropores and microcracks, which were completely infilled by sulfide minerals (pyrite and chalcopyrite) during the late sulfide stage. (b) Section of greisenized granite displaying microporous texture. (c) Section of quartz-muscovite greisen displaying large pores, cracks and microcracks. (d) and (e) zoom on greisen porosity, in which apatite, cassiterite and euhedral quartz have crystallized. (f) Greisen porosity completely infilled by sphalerite and chalcopyrite.

Electronic Supplementary Materials 5 (ESM 5)

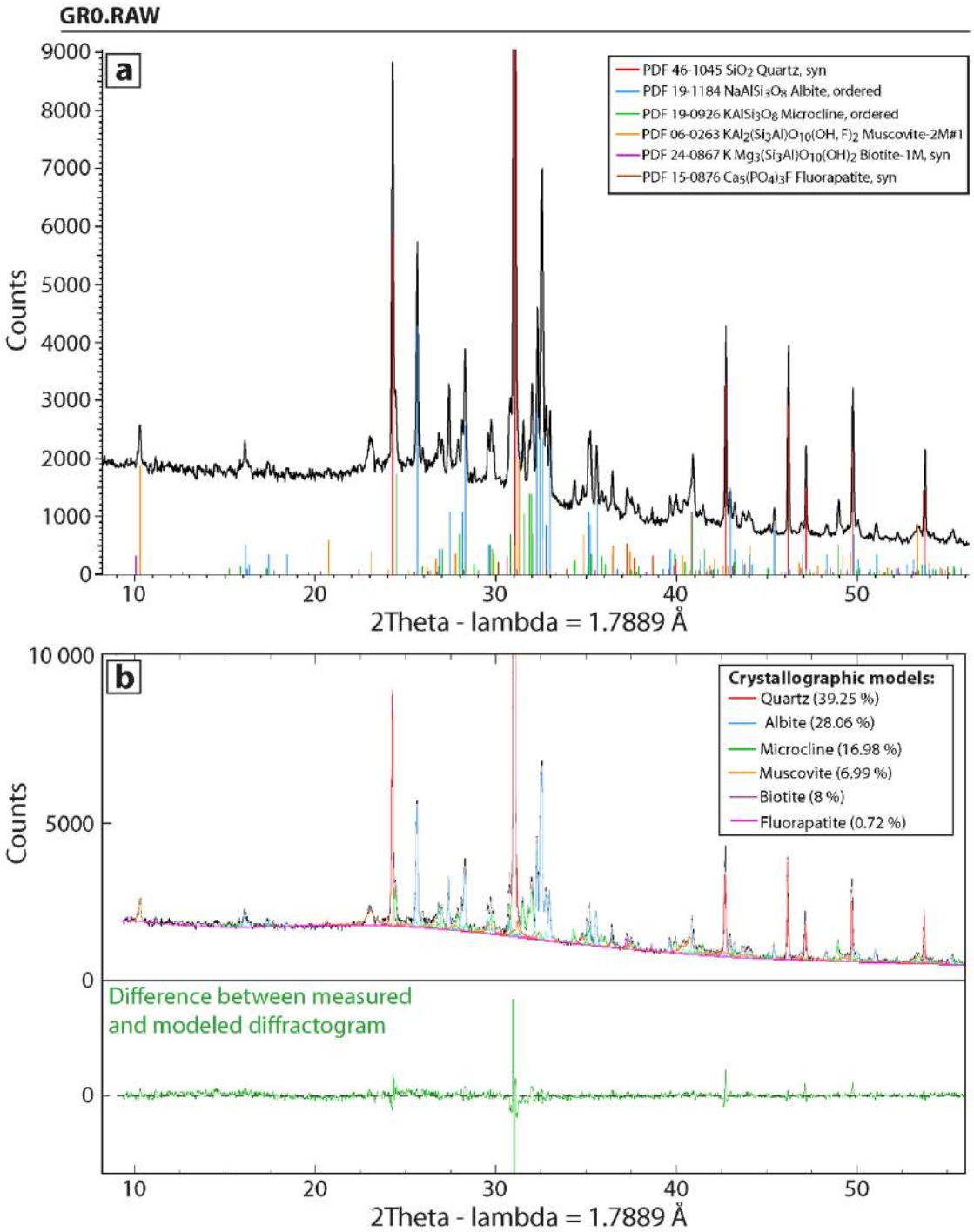

Figure 18: (a) X-Ray Diffractogram (XRD) obtained from powder of the unaltered Panasqueira granite. The XRD acquisitions were performed on an INEL diffractometer using a curve position-sensitive detector (CPS-120). The mineral identification was realized using the mineral database of Profex. (b) Results of mineral quantification obtained from Profex-Rietveld method. This method consists of simulating a diffractogram from crystallographic models and adjusts the mineral abundances to obtain a simulated diffractogram as close as possible to the measured diffractogram. The mineral abundances are indicated for each minerals and the difference between the measured and modeled diffractogram are displayed below the spectra.

Electronic Supplementary Materials 6 (ESM 6)

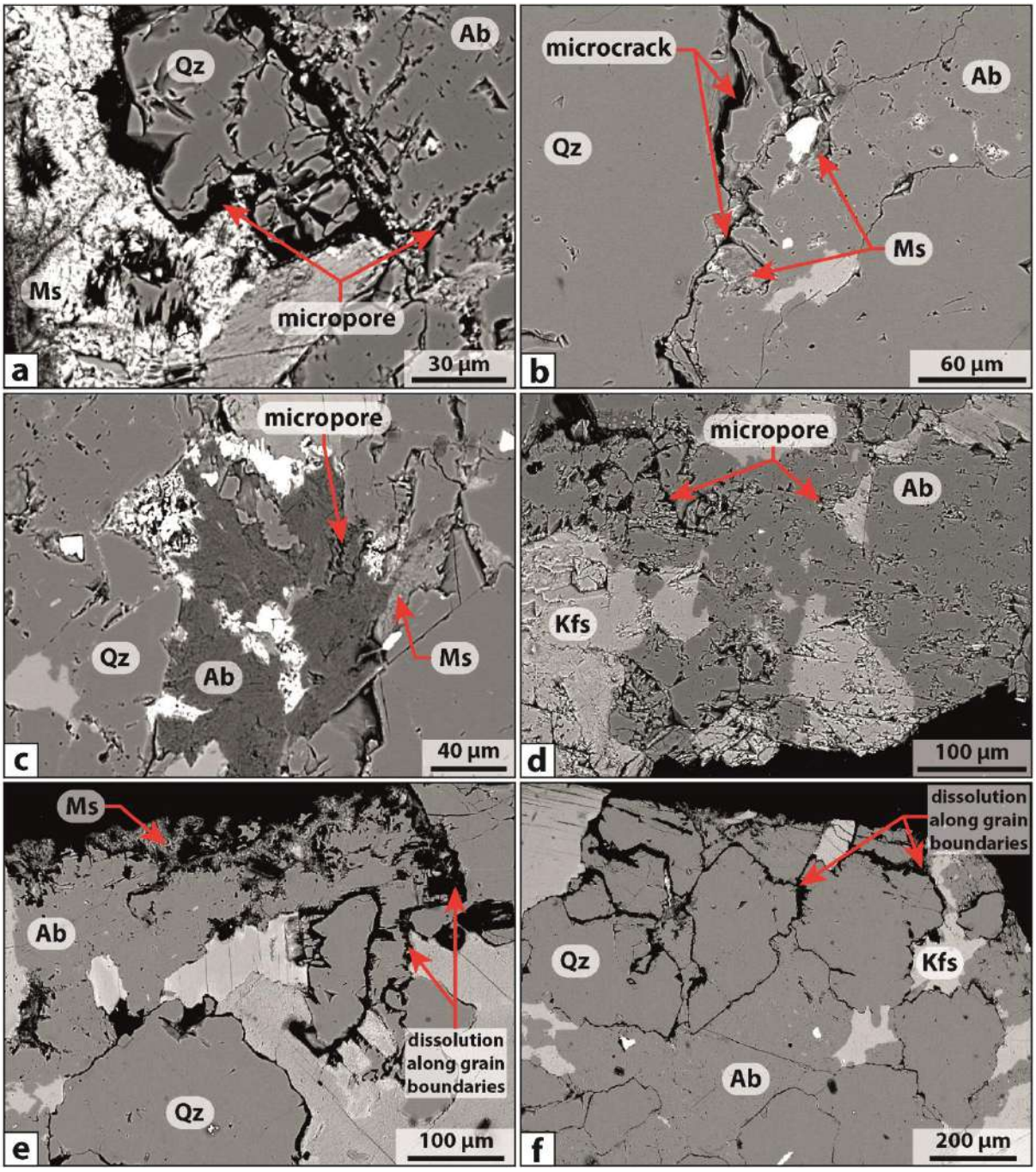

Figure 19: SEM-BSE images showing the alteration products and textures produced during the greisenization experiment. (a to c) Grains of albite partially replaced by muscovite along the grain boundaries and along microcracks. (d) Micropores developed in grains of albite and k-feldspar emphasizing the partial dissolution of feldspars during the greisenization. (e to f) Dissolution of albite along the grain boundaries and precipitation of muscovite along the edge of the granite core. All of these textures highlight that replacement reactions related to greisenization generate new pathways in greisenized facies.

Electronic Supplementary Materials 7 (ESM 7)

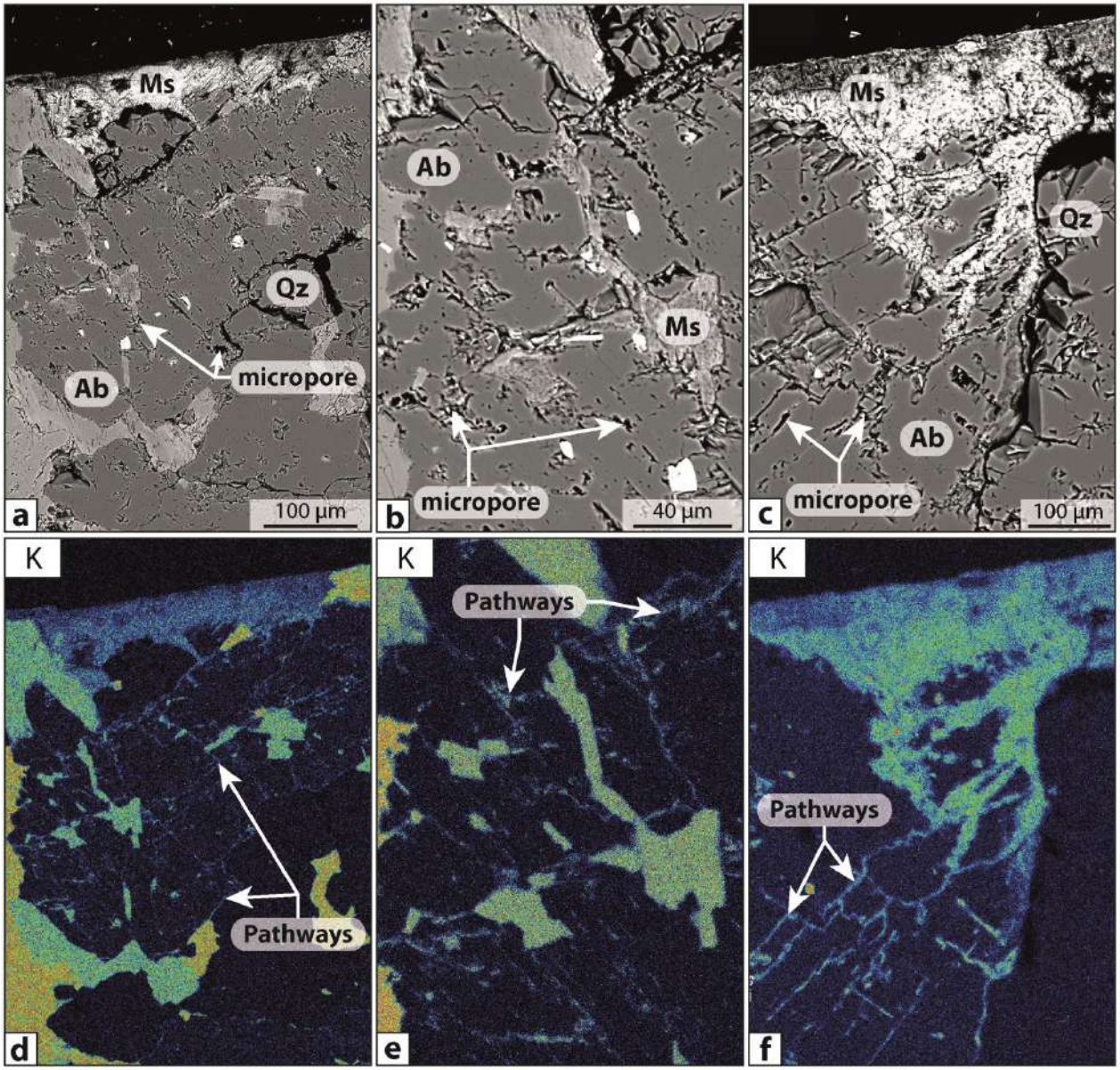

Figure 20: (a to c) SEM-BSE images and (d to f) geochemical mapping of K showing the pathways along which fluids have preferentially flowed and altered albite into muscovite during the greisenization experiment. The transformation of albite into muscovite occurred mainly along the grain boundaries and along the cleavage planes of albite. Note the presence of micropores in partially altered section of albite.

Electronic Supplementary Materials 8 (ESM 8)

	SiO_2	Al_2O_3	Fe_2O_3	CaO	MgO	Na_2O	K_2O	TiO_2	MnO	P_2O_5	LOI	Total
Granite												
D3	72.3	13.4	2.33	0.56	0.25	3.72	3.89	0.19	0.05	0.43	1.03	98.15
D1	72.7	13.65	1.91	0.66	0.27	3.41	4.21	0.2	0.05	0.44	0.96	98.46
D4	75.1	14	2.18	0.56	0.26	3.12	4.1	0.19	0.06	0.38	0.89	100.84
D2	73.2	13.9	2.19	0.64	0.31	3.32	4.35	0.22	0.05	0.4	1	99.58
E2	73.9	13.5	2.1	0.53	0.26	3.82	3.97	0.19	0.05	0.39	1.12	99.83
Greisenized granite												
C1	73.5	14.25	2.57	0.53	0.19	3	3.67	0.14	0.07	0.43	1.83	100.18
O4	78.3	12	1.34	0.24	0.02	4.06	1.86	0.01	0.05	0.2	0.94	99.02
P3D	80.7	12.05	1.51	0.23	0.02	3.66	2.04	0.01	0.05	0.21	0.93	101.41
P3E	74.9	14.5	1.92	0.71	0.04	3.62	2.85	0.01	0.09	0.58	1.31	100.53
P3C	74.1	14.6	2.46	0.56	0.22	2.72	3.56	0.12	0.07	0.45	1.76	100.62
O3	74.4	14	2.06	0.85	0.04	3.74	2.6	0.01	0.12	0.71	1.14	99.67
O1	73.1	14.9	2.5	0.55	0.23	2.79	3.48	0.11	0.06	0.45	1.88	100.05
O5	76.6	12.55	2.36	0.27	0.05	1.47	3.55	0.02	0.05	0.25	1.21	98.38
P4-2	79.4	10.55	2.69	0.3	0.04	0.22	3.52	0.02	0.06	0.25	1.25	98.3
P4-3	78.7	11.95	1.92	0.3	0.05	1.73	3.13	0.02	0.05	0.27	1.31	99.43
P4-A	77.2	12.55	2.38	0.27	0.07	1.47	3.29	0.02	0.05	0.23	1.38	98.91
Greisen												
B2	71.6	16.55	3.07	0.48	0.23	0.21	5.46	0.12	0.07	0.39	2.45	100.63
B1	70.1	16	2.97	0.49	0.23	0.2	5.1	0.13	0.07	0.45	2.37	98.1
P57-A	72.1	16.65	3.08	0.47	0.25	0.22	5.61	0.13	0.07	0.38	2.4	101.36

Table 5 Major elements composition (in wt%) for granite, greisenized granite and greisen used to establish the chemical alteration index (AI).

	Least altered granite							Less altered	Intermediate	Most altered
(wt%)	**D2**	**D3**	**D5-A**	**D1**	**D5-B**	**Average**	**SD**	**C1**	**C2-A**	**B1**
SiO_2	73.2	72.3	73.9	72.7	73.5	73.12	0.63	73.5	74.6	70.1
Al_2O_3	13.9	13.40	13.5	13.65	13.45	13.58	0.20	14.25	14.7	16
Fe_2O_3	2.19	2.33	2.1	1.91	2.12	2.13	0.15	2.57	2.54	2.97
CaO	0.64	0.56	0.53	0.66	0.51	0.58	0.07	0.53	0.56	0.49
MgO	0.31	0.25	0.26	0.27	0.25	0.27	0.02	0.19	0.23	0.23
MnO	0.05	0.05	0.05	0.05	0.05	0.05	0.00	0.06	0.06	0.06
Na_2O	3.32	3.72	3.82	3.41	3.7	3.59	0.22	3	2.79	0.2
K_2O	4.35	3.89	3.97	4.21	3.65	4.01	0.27	3.67	3.34	5.1
TiO_2	0.22	0.19	0.19	0.2	0.18	0.19	0.02	0.14	0.12	0.13
P_2O_5	0.4	0.43	0.39	0.44	0.35	0.40	0.04	0.43	0.45	0.45
LOI	1	1.03	1.12	0.96	1.28	1.08	0.13	1.83	1.84	2.37
Total	99.58	98.15	99.83	98.46	99.04	99.01		100.18	101.23	98.1
(ppm)										
Ba	66.9	53.7	55.6	59.1	54.6	57.98	5.39	27.3	29	27.1
Eu	0.23	0.16	0.22	0.22	0.19	0.204	0.03	0.1	0.11	0.1
Sr	23.1	22.4	23.1	23.9	23.2	23.14	0.53	15.5	13.1	10.2
Cs	21.5	17.45	17.8	18.9	17.95	18.72	1.64	35.8	51.1	42.1
Li	340	300	300	300	310	310	17.32	560	590	600
Sn	35	28	27	27	24	28.2	4.09	57	131	138
W	14	10	9	9	9	10.2	2.17	28	33	36
Zr	86	89	79	82	78	82.8	4.66	42	40	31
As	8	5	6	5	5	5.8	1.30	220	220	261
Cu	3	1	2	1	1	1.6	0.89	97	99	102
Zn	78	59	61	65	64	65.4	7.44	318	326	294
Rb	494	457	456	477	452	467.2	17.85	737	907	1065

Table 6 Major and trace elements composition of granite and sample representative of different degree of greisenization used to realize the isocon diagram

Résumé étendu de la thèse :

Les gisements à étain-tungstène (Sn-W) de type veine-stockwork et greisens sont des systèmes magmatiques-hydrothermaux qui fournissent une part importante de la production mondiale de tungstène et qui représentent une source importante d'étain. L'objectif de cette étude est d'améliorer la compréhension des processus géologiques et hydrothermaux impliqués lors du transport et le dépôt des métaux au cours de la formation de ce type de gisement. Cette étude complète comporte : (i) des études sur le terrain (contexte géologique et géologie structurale) ; (ii) la reconstruction des écoulements de fluides à la transition magmatique-hydrothermale, (iii) de la géochimie fine des minéraux et de la pétrologie des roches concernées, (iv) des déterminations expérimentales du changement de la perméabilité durant la formation du greisen et (v) des modélisations numériques des écoulements de fluides autour d'un granite en prenant en compte la production de fluides magmatiques et la perméabilité dynamique résultant des interactions eau-roche. Cette méthodologie a été appliquée au cas du gisement à W-Sn-(Cu) de Panasqueira (Portugal). Ce gisement expose en surface des roches représentatives de la transition magmatique-hydrothermale et représente donc un site de référence pour étudier les processus physico-chimiques associés à cette transition entrainant la formation de gisements à Sn-W de type veines et greisens.

Ce résumé contient les principaux résultats et conclusions développés dans les six premiers chapitres de la thèse, ainsi que le modèle métallogénique détaillé dans le dernier chapitre. La Figure 1 détaille ce modèle métallogénique déduit des observations géologiques et des processus hydrothermaux étudiés.

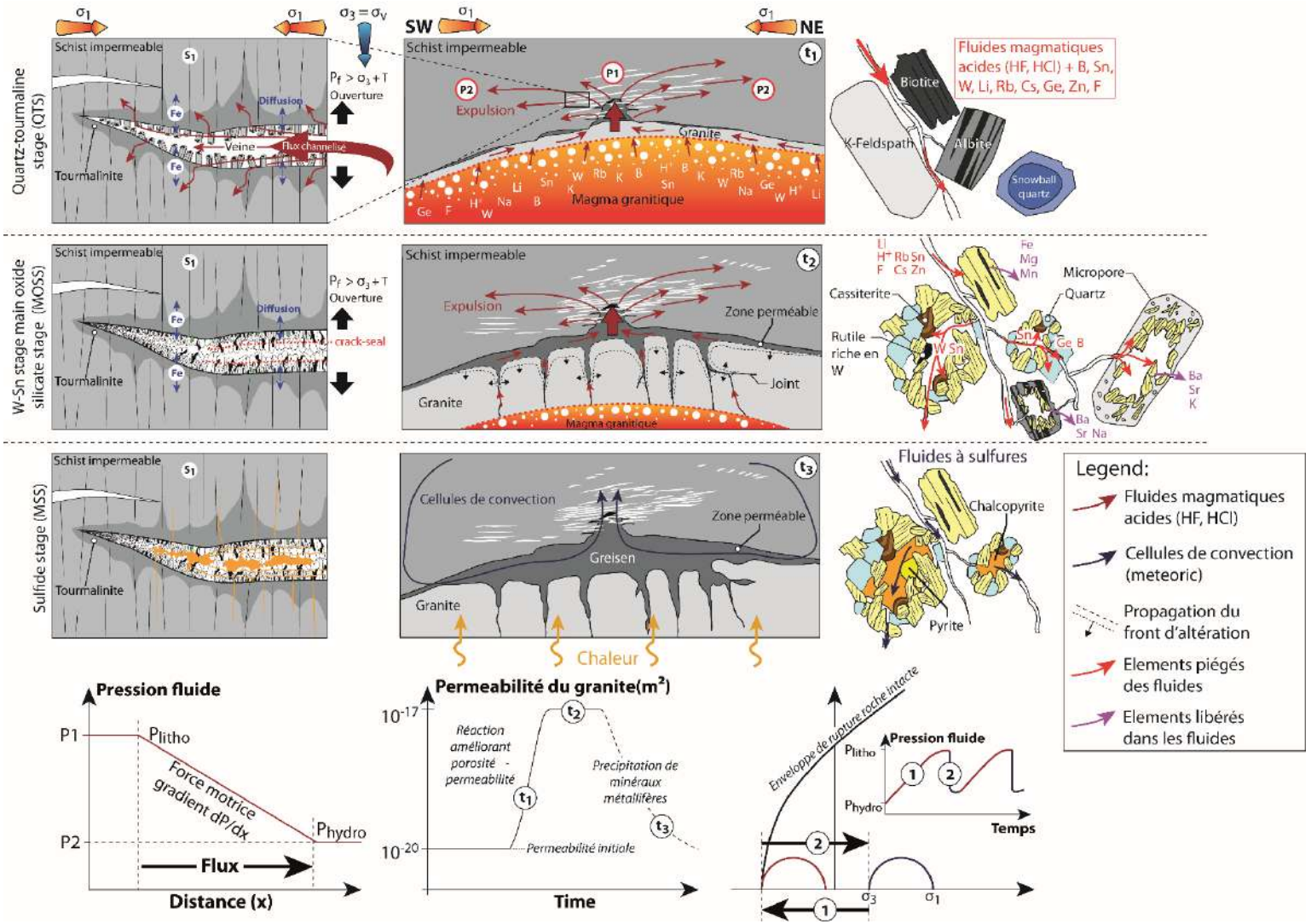

Figure 1 Modèle métallogénique de formation du gisement à W-Sn-(Cu) de Panasqueira intégrant les processus géologiques et hydrodynamiques mis en évidence dans cette étude. La circulation entre (t1) et (t2) est contrôlée par l'expulsion de fluides magmatiques libérés lors de la transition magmatique-hydrothermale. La circulation liée aux phases tardives (t3) implique des processus convectifs apportant la minéralisation en sulfures.

1. Formation du système des veines minéralisées à Panasqueira : contrôle structural et rôle des conditions de pression du fluide

Les analyses structurales de cette étude montrent que le réseau de veines minéralisées sub-horizontales correspondent à des veines d'extension (mode I) dont la formation est probablement liée à des surpressions de fluide et à des contraintes différentielles modérées (σ_d < 4T). Ces veines se sont préférentiellement ouvertes dans l'encaissant métasédimentaire au-dessus de la coupole granitique, suggérant ainsi (i) un fort contrôle rhéologique sur la localisation de la déformation, (ii) une localisation préférentielle des instabilités thermo-mécaniques autour de la coupole. L'arrangement de la géométrie des veines met l'accent sur un régime crustal compressif avec un raccourcissement horizontal régional NE-SW, et un étirement vertical comme en témoignent les structures observées au sein de l'encaissant métasédimentaire (schistes de Beira).

L'analyse des bandes de croissances des tourmalines montre que les vitesses de circulation des fluides sont de l'ordre de 10^{-4} à 10^{-3} $m.s^{-1}$ dans les filons de quartz, et de l'ordre de 10^{-6} to 10^{-5} $m.s^{-1}$ dans l'encaissant. Les faibles vitesses suggèrent que l'encaissant méta-sédimentaire reste relativement peu perméable. Les fluides s'écoulent depuis la coupole vers l'encaissant et le mettent en charge. Les textures minérales observées pour la tourmaline et les quartz à croissance libre suggèrent une pression de fluide supralithostatique. Par ailleurs les analyses géochimiques des éléments en traces dans les tourmalines montrent que celles-ci marquent la transition magmatique hydrothermale.

L'expulsion des fluides à partir des filons vers l'encaissant méta-sédimentaire est donc compatible avec des conditions de surpression de fluide durant le stade initial et est assisté par la formation des veines. Le fort gradient de pression vertical est responsable i) de l'ouverture et de la dilatation verticale des veines minéralisées et ii) des écoulements pervasifs dans les roches encaissantes. Ces migrations sont aussi à l'origine de la formation des fronts de tourmalinisation observés de part et d'autres des filons minéralisés. Les réouvertures en «crack-seal» montrent un fonctionnement cyclique du champ filonien alternant les phases d'ouverture et de remplissage par la minéralisation. Finalement l'orientation particulière subhorizontale des filons minéralisés est à mettre en relation avec un continuum de déformation régionale marqué par le raccourcissement NE-SW. Cette géométrie particulière est interprétée comme un réseau de fentes en échelon dans un système cisaillant avec un jeu inverse.

Ce model conceptuel géologique est compatible avec les évènements tectono-métamorphiques de la zone Centrale Ibérique.

2. Greisenisation : un processus clef pour améliorer l'écoulement des fluides et promouvoir la formation de grands gisements de type veine et greisens

Le toit du granite de Panasqueira est affecté par une intense altération de type greisen qui résulte de l'altération hydrothermale du granite. Les feldspaths et les biotites du granite ont été entièrement remplacés par la muscovite hydrothermale et le quartz. Cependant l'étude des textures des feldspaths et de leurs compositions montrent que ces minéraux ont été altérés préalablement à très haute température, juste après la cristallisation du magma. Lors de ce métasomatisme alcalin (altération potassique et albitisation), les feldspaths et les plagioclases ont été transformés en albite pure et en orthoclase. Ces réactions s'accompagnent de la formation d'une première porosité qui est le lieu des premières circulations de fluides et qui a permis le développement du greisen.

Les éléments en trace mesurés dans les muscovites hydrothermales du greisen et dans les veines montrent un enrichissement en éléments incompatibles granitophiles (K, Na, F, Li, Rb, Cs, Ge et B). La similitude des signatures suggère que le remplissage précoce des veines et la formation du greisen sont contemporains de l'expulsion d'un fluide d'origine magmatique lié à la progression de la cristallisation du magma granitique en profondeur. Ces fluides hydrothermaux acides migrent vers les parties externes du pluton déjà cristallisé. A plus faible température ces fluides entrent en déséquilibre avec leur encaissant granitique et déclenchent une réaction de greisenisation : les feldspaths potassiques, les albites et les biotites sont transformés en muscovite et en quartz.

La réaction de greisenisation s'accompagne d'une baisse du volume molaire. Les mesures sur échantillons montrent une augmentation de la porosité de 0,5% à 8,5% et une augmentation de la perméabilité de 3 ordres de grandeur (de $2\ 10^{-20}$ m² à 10^{-17} m²). Le rétrocontrôle positif de l'altération hydrothermale de type greisen sur la perméabilité est un processus potentiellement décisif lors de la formation des gisements de type veines et greisen. En effet, ce dernier permet d'expliquer (i) la migration du front d'altération depuis le toit vers les parties plus profondes du granite et (ii) la formation d'un vaste greisen comme observé couramment dans les gisements à Sn-W.

Le développement d'une zone de haute perméabilité au toit de l'intrusion granitique constitue un drain important pour conduire l'expulsion des fluides produits par la cristallisation du granite. La convergence des lignes de courant dans cette région est susceptible de contribuer fortement à établir et à stabiliser dans le temps une zone à forte pression fluide. Ces pressions fluides contribuent à ouvrir les veines au-dessus du toit du granite avec un fonctionnement cyclique alternant les périodes de fracturation et de cristallisation comme décrit précédemment dans le modèle géologique conceptuel. Ce fonctionnement rappelle les valves sismiques décrites dans la littérature.

Ce phénomène d'augmentation de la porosité au cours d'une altération de type greisen est un processus généralisable à l'ensemble des systèmes hydrothermaux connaissant ce type de réaction. Le rétrocontrôle positif sur la circulation des fluides par augmentation de la perméabilité est probablement un processus généralisable à l'ensemble des gisements à Sn-W de classe mondiale.

3. Modélisation numérique : rôle des coupoles granitiques et des apophyses sur la focalisation des fluides minéralisateurs et les flux

La reconstruction des paléo-circulations a mis en lumière le rôle déterminant de la coupole granitique. Cette observation a été confirmée par un travail de modélisation numérique des circulations fluides. En effet les travaux montrent que quelles que soient les hypothèses de travail, (expulsion de fluides magmatiques et/ou convection des fluides de l'encaissant) les lignes de courant ascendantes sont resserrées au niveau de la coupole granitique.

L'introduction dans le modèle numérique d'une perméabilité dynamique, c'est-à-dire qui varie avec le flux hydrothermal a été conduite en reliant la perméabilité à la température et au rapport fluide / roche et en utilisant les résultats expérimentaux acquis lors des mesures de perméabilités. Les simulations mettent en évidence que cet effet de focalisation au niveau des coupoles est amplifié par le développement du greisen. Cette situation a pour conséquence d'établir une région de surpression de fluide au toit de la coupole et par là même de favoriser l'ouverture de fractures. Par ailleurs les instabilités thermo-mécaniques sont généralement localisées autour des apex granitiques. La combinaison de la zone d'endommagement avec une région d'accumulation des fluides est donc très favorable à l'ouverture de structures perméables drainant les circulations de fluides. Là encore, il est

possible de parler de rétrocontrôle positif mais cette fois en lien avec la déformation de l'encaissant.

L'ensemble des simulations montrent que les coupoles et les apophyses sont des zones favorables pour la formation de gisements de forte teneur. Ces morphologies particulières constituent des centres d'émanation hydrothermale, à partir des quels les fluides minéralisateurs sont expulsés latéralement dans l'encaissant. Cette intensité est accentuée par les rétrocontrôles en lien avec i) l'altération du toit du granite en greisen, ii) la fracturation de l'encaissant induite par les pressions fluides et les endommagements de l'encaissant.

4. Evolution des figures d'écoulement et des forces motrices au cours du temps et modèle metallogénique

L'évolution de la succession paragénétique peut être décrite simplement par un stade à silicate et oxydes associé aux minéralisations à Sn-W (MOSS) suivi par un stade à sulfure (MSS). La formation du gisement de Panasqueira implique donc deux fluides minéralisateurs qui impliquent des mécanismes et des forces motrices différentes.

Les travaux de modélisation numérique mettent en évidences deux stades minéralisateurs. Les liens entre les stades modélisés et ceux observés sont interprétés de la façon suivante :

- Un premier stade magmatique-hydrothermal est enregistré par la tourmalinisation de l'encaissant et la formation de veines à quartz et tourmaline. Ce stade est marqué par un cristallisation progressive du granite qui expulse un fluide enrichi en éléments incompatibles et en métaux (W, Sn et Zn). Ce premier stade est responsable de l'altération de la coupole en greisen et de la formation d'une zone de surpression de fluide au-dessus de la coupole. A cause de la faible perméabilité de l'encaissant, les fluides ont été chenalisés principalement au sein d'un réseau de fractures dans lesquelles la minéralisation a précipité en interagissant avec un fluide météorique extérieur. Au cours de ce stade les forces motrices principales correspondent aux suppressions de fluides qui ont pour origine la cristallisation du magma. Les cycles de réouverture des veines suggèrent un activité magmatique polyphasée et pulsatile de type valve sisimique.
- Le second stade est clairement contrôlé par la fin de de la mise en place du pluton granitique et de son refroidissement. Les fluides de l'encaissant méta-sédimentaire entrent en convection par instabilité thermique et gravitaire. Au cours de leur

migration, ils lessivent les sulfures disséminés dans l'encaissant (pyrite) et mobilisent les métaux contenus (Cu et Zn) par ces derniers. Ces fluides réempruntent les zones les plus perméables, c'est-à-dire le greisen et les fractures de l'encaissant où les métaux précipitent sous forme de sulfures. Au cours de ce second stade, la force motrice principale est la variation de densité du fluide induite par l'augmentation de la température à proximité du granite.

Les simulations numériques mettent en évidence ces deux stades successifs. Le premier stade est en lien direct avec la fin de cristallisation du magma, il peut être lié à une source des métaux qui est dominée par le magma. Le second marque le refroidissement du pluton par des boucles de convection et la source des métaux est principalement l'encaissant. Cette évolution est extrêmement classique dans les gisements à Sn – W et le modèle établi à Panasqueira semble pouvoir être étendu à de nombreux systèmes similaires.

5. Conséquences des interactions fluide-roche sur le dépôt des métaux

Les interactions fluides-roches impliquées dans la formation des gisements à Sn-W modifient fortement la chimie des fluides et contribuent à favoriser le dépôt des métaux. Les réactions de tourmalinisation et de muscovitisation (altération de la chlorite) déclenchées par la migration des fluides depuis les veines vers l'encaissant ont pour effets de neutraliser le pH et de relâcher une grande quantité de fer dans le fluide et, ainsi, de favoriser la cristallisation de la wolframite dans les veines.

Les expériences de greisenisation menées dans cette thèse indiquent que l'altération des feldspaths et de la biotite consomme une grande quantité de protons (H^+). Ces réactions tamponnent le pH des fluides hydrothermaux en les neutralisant. Cette augmentation de pH est susceptible de réduire significativement la solubilité de l'étain. Vraisemblablement ces réactions permettent d'expliquer la présence de cassitérite dans la porosité des greisens.

Finalement, les altérations mises en scènes lors des interactions fluides-roches sont importantes pour la compréhension des systèmes minéralisateurs : i) elles sont capables d'augmenter les flux hydrothermaux en augmentant la perméabilité des roches ; ii) elles neutralisent l'acidité des fluides et par conséquent baissent la solubilité de nombreux minéraux.

6. **Implications pour l'exploration minière**

L'ensemble des résultats de ces travaux de thèse confirment, avec de nouveaux arguments, que les coupoles granitiques sont des points de focalisation des décharges hydrothermales et par conséquent sont des zones potentiellement minéralisées. De même les greisens développés aux toits des granites sont des cibles potentielles pour des minéralisations à cassitérite et sont aussi des guides d'exploration pour découvrir indirectement des gisements filoniens.

De mêmes les axes de tourmalinisation dans les roches métasédimentaires marquent potentiellement la transition magmatique-hydrothermale, et la tourmalisation peut être un mécanisme décisif pour induire la cristallisation de wolframite. Par ailleurs la tourmaline peut être utilisée pour évaluer les directions d'écoulement et, par reconstruction, conduire à la découverte de coupoles cachées.

Enfin la modélisation numérique est une approche complémentaire aux travaux de terrain. Elle permet d'expérimenter les effets des différents paramètres géologiques et hydrodynamiques contrôlant la formation des gisements hydrothermaux. Le développement de cette méthode pourra à terme devenir un outil pour l'exploration minière, permettant de prédire les zones favorables à la formation de concentrations minérales.

En conclusion ce travail centré sur l'hydrodynamique des systèmes hydrothermaux et plus particulièrement sur les systèmes étain-tungstène clarifie l'importance des rétrocontrôles des altérations sur les flux hydrothermaux en les décrivant sur un objet naturel et en les quantifiant par des modélisations numériques. La nature de ces rétrocontrôles pour les altérations de type greisen est liée à une modification de la pétrophysique des roches en augmentant la porosité et la perméabilité. La prise en compte de la modification de ces propriétés dans les simulations numériques permet de comprendre l'augmentation des flux et met en lumière l'existence de zones de surpression qui à son tour va induire une fracturation au toit du granite. Ces mécanismes d'amplification de circulations des fluides sont vraisemblablement applicables à l'ensemble des réactions hydrothermales provoquant une baisse du volume molaire. Les méthodes utilisées dans ces travaux pourront être déployées pour analyser l'hydrodynamique mise en jeu dans d'autres types de gisements hydrothermaux.

Gaëtan LAUNAY

Hydrodynamique des systèmes minéralisés péri-granitiques : étude du gisement à W-Sn-(Cu) de Panasqueira (Portugal)

Résumé : Les gisements à Sn-W de type veine et greisen sont des systèmes magmatiques-hydrothermaux dont l'exploitation fournit une part importante de la production mondiale de tungstène et qui représentent également une source importante d'étain. La formation de ces gisements résulte d'un continuum de processus magmatiques et hydrothermaux et implique un transport efficace et la focalisation des fluides minéralisateurs. Cette étude vise à améliorer la compréhension des processus hydrodynamiques et géologiques impliqués lors du transport et du dépôt de métaux conduisant à la formation de ces gisements. Nous avons réalisé une étude pluridisciplinaire combinant (i) travail de terrain (étude géologique et structurale), (ii) reconstruction des paléo-circulations hydrothermales via l'analyse texturale des bandes de croissance des tourmalines, (iii) détermination expérimentale des changements de perméabilité induits par la greisenisation et (iv) modélisation numérique des écoulements péri-granitiques prenant en compte l'évolution de la perméabilité dynamique lors des interactions fluide-roche. Cette méthodologie a été appliquée au cas du gisement W-Sn-(Cu) de Panasqueira, qui constitue un site de référence pour étudier les processus magmatiques et hydrothermaux conduisant à la formation de gisements à Sn-W de classe mondiale. Les résultats obtenus démontrent que l'expulsion des fluides magmatiques minéralisés a déclenché la greisenisation des parties apicales (coupoles et apex) de l'intrusion granitique, entraînant la création de porosité (~ 8,5%) qui améliore significativement la perméabilité (de 10^{-20} à 10^{-17} m²) au sein du greisen massif composant le toit de l'intrusion. Le développement de ce niveau perméable constitue un drain important favorisant l'expulsion et la focalisation des fluides magmatiques minéralisateurs exsolvés lors de la cristallisation du granite sous-jacent. Cette focalisation des décharges hydrothermales (i) améliore significativement le transport des métaux, et (ii) favorise l'établissement de conditions de pression de fluide élevées qui couplées aux contraintes régionales compressives causent l'ouverture des veines minéralisées au toit de l'intrusion. Cette étude souligne l'importance des rétrocontrôles entre perméabilité dynamique et altération hydrothermale. Ces derniers constituent des mécanismes majeurs permettant d'améliorer significativement la circulation des fluides minéralisateurs et donc la formation de gisements hydrothermaux de grandes tailles

Mots-clés : veine et greisen, gisement à Sn-W, transition-magmatique hydrothermale, hydrodynamique, circulation hydrothermal péri-granitique approches expérimentales, modélisation numérique, greisenisation, perméabilité dynamique, Panasqueira

Hydrodynamics of peri-granitic mineralized systems: study of the W-Sn-(Cu) Panasqueira ore deposit

Abstract: The vein and greisen Sn-W deposits are magmatic-hydrothermal systems that provide an important part of the world W production and represent an important source of Sn. The formation of these deposits involves continuum of magmatic-hydrothermal processes and implies the transfer and the focusing of a large amount of mineralizing fluids. This study aims to improve understanding of hydrodynamic and geological processes involved during the transport and the deposition of metals leading to the formation of these deposits. We have performed a complete study combining (i) field works (geological and structural studies), (ii) fluid flow reconstruction via the textural analysis of tourmaline growth bands, (iii) experimental determination of permeability changes during greisenization, and (iv) numerical modeling of peri-granitic fluid flow accounting for magmatic fluid production and dynamic permeability related to fluid-rock interactions. This methodology was applied in the case of the world-class W-Sn-(Cu) Panasqueira deposit, which represents a reference site to study magmatic-hydrothermal processes leading to the formation of large vein and greisen deposit. Our results demonstrate that the releasing and the expulsion of ore-bearing magmatic fluids triggered greisenization of the apical part of granite intrusion, which caused generation of porosity (~8.5%) and therefore a significant increase of permeability (from 10^{-20} to 10^{-17} m²) in massive greisen composing the granite's roof. The development of this permeable pathway constitutes an important drain promoting the expulsion and the focusing of magmatic fluids produced during the crystallization of the underlying granite. This enhancement of magmatic fluids expulsion (i) promotes significantly fluid flux and transfer of metals, and (ii) the establishment of high fluid pressure conditions, which coupled with the regional compressive crustal regime, triggered the opening of mineralized veins above the granite roof. Finally, this study emphasizes that reactive hydrothermal fluids are able to generate their own pathways in initially impermeable rocks. This process represents an important mechanism to enhance fluid flow and promote the formation of large hydrothermal deposits.

Keywords: vein and greisen, Sn-W deposits, magmatic-hydrothermal transition, hydrodynamics, peri-granitic fluid flow, experimental approaches, numerical modeling, greisenization, dynamic permeability, Panasqueira

Institut des Sciences de la Terre d'Orléans
UMR 7327 – CNRS/Université d'Orléans
1A, Rue de la Férollerie
45071 Orléans Cedex 2 France